



Technische Universität München

Fakultät für Chemie

Investigation of Materials Degradation and Hysteresis Phenomena in High-Energy Cathodes used for Lithium-Ion Batteries

Franziska Friedrich

Vollständiger Abdruck der von der Fakultät für Chemie der Technischen
Universität München zur Erlangung des akademischen Grades einer
Doktorin der Naturwissenschaften (Dr. rer. nat.)

genehmigten Dissertation.

Vorsitz: Prof. Dr. Barbara A. J. Lechner

Prüfer der Dissertation: 1. Prof. Dr. Hubert A. Gasteiger
2. Prof. Dr.-Ing. Andreas Jossen
3. Prof. Dr. Matteo Bianchini

Diese Dissertation wurde am 05.04.2022 bei der Technischen Universität
München eingereicht und durch die Fakultät für Chemie am 02.06.2022
angenommen.

Abstract

The focus of current lithium-ion battery research is mainly on decreasing the cost and increasing the energy density of the battery by investigating and improving electrode active materials. One way to achieve this is increasing the nickel content in layered transition metal oxides ($\text{LiNi}_x\text{Mn}_y\text{Co}_z\text{O}_2$ with $x+y+z = 1$, NCM) used as cathode active material (CAM). Another promising class of cathodes are the Li- and Mn-rich NCMs (LMR-NCMs).

The first part of this thesis addresses the aging mechanisms occurring in a Ni-rich NCM (NCM-811) over long-term cycling. While the bulk structure remains relatively stable, a reconstruction of the near-surface region of the CAM particles leads to the growth of a resistive surface layer, which ultimately results in two capacity loss terms: (i) an irreversible capacity loss due to the fraction of CAM lost for the formation of the surface layer; (ii) a reversible capacity loss due to an increasing charge-transfer resistance at the surface, which can be overcome at low currents. Comparing the results at ambient and elevated temperatures indicates that the reconstruction of the surface is accelerated at higher temperatures.

The second part of this thesis deals with the investigation of LMR-NCM with regards to its pronounced OCV hysteresis. Since the associated loss of electrical energy is expected to be converted into waste heat during cycling, the heat generation was investigated using isothermal micro-calorimetry (IMC). In addition, entropy measurements were conducted with the aim of determining the reversible heat. The OCV hysteresis mostly leads to heat evolution during discharge and is quantified as a function of state-of-charge. The heat generation during the first activation cycle was also investigated with the result that a considerable amount of heat is evolved during the first charge, leading to a unique heat evolution profile. The analysis of the heat flow curves thereby gives valuable insights into the processes correlated with the OCV hysteresis.

Kurzfassung

Die aktuelle Lithium-Ionen Batterieforschung beschäftigt sich hauptsächlich mit der Reduzierung der Kosten und der Erhöhung der Energiedichte der Batterie, unter anderem mittels Untersuchung und Implementierung neuer Elektrodenmaterialien. Eine Möglichkeit dies zu erreichen, ist die Erhöhung des Nickelgehalts in Schichtoxiden, sogenannten NCMs ($\text{LiNi}_x\text{Mn}_y\text{Co}_z\text{O}_2$ mit $x+y+z = 1$), die als Kathoden verwendet werden. Eine andere vielversprechende Materialklasse sind Li- und Mn-reiche Schichtoxide (LMR-NCMs).

Der erste Teil dieser Doktorarbeit beschäftigt sich mit Alterungsmechanismen, die bei der Langzeit-Zyklisierung von Ni-reichen NCMs (NCM-811) auftreten. Während die Kristallstruktur des NCMs weitgehend stabil ist, bildet sich an der Oberfläche der Partikel eine sauerstoffarme Schicht mit erhöhtem Widerstand aus. Der Verlust von Aktivmaterial für die Bildung dieser Schicht führt zu einem irreversiblen Kapazitätsverlust. Der erhöhte Widerstand an der Partikeloberfläche führt außerdem zu einem reversiblen Kapazitätsverlust, der aber bei niedrigen Stromraten überwunden werden kann. Ein Vergleich der Ergebnisse bei Raumtemperatur und 45°C zeigt, dass die Rekonstruktion der Oberfläche bei erhöhter Temperatur schneller abläuft.

Im zweiten Teil dieser Arbeit geht es um die Analyse von LMR-NCM mit Hinblick auf dessen ausgeprägte OCV (open-circuit voltage) Hysterese. Der damit einhergehende Verlust an elektrischer Energie wird erwartungsgemäß als Abwärme freigesetzt, die mittels kalorimetrischer Messungen untersucht wurde. Ergänzend dazu wurden Entropie-Messungen durchgeführt, um den Beitrag der reversiblen Wärme zu bestimmen. Die OCV Hysterese führt vorwiegend zu einer Wärmefreisetzung beim Entladen der Zelle und wurde als Funktion des Ladezustands quantifiziert. Zudem wurde die Wärmegeneration während des ersten Aktivierungszyklus analysiert, mit dem Ergebnis, dass insbesondere beim ersten Laden der Zelle viel Wärme freigesetzt wird. Die Analyse der Wärmeflussprofile gibt wertvolle Einblicke in die Prozesse, die mit der OCV Hysterese zusammenhängen.

Contents

Abstract.....	i
Kurzfassung.....	ii
Contents.....	iii
List of Abbreviations	v
1 INTRODUCTION	1
1.1 THEORETICAL BACKGROUND ON LITHIUM-ION BATTERIES	4
1.2 CHALLENGES OF NI-RICH LAYERED OXIDES.....	13
1.3 CHALLENGES OF LI- AND MN-RICH LAYERED OXIDES.....	17
2 EXPERIMENTAL METHODS.....	20
2.1 X-RAY POWDER DIFFRACTION	20
2.2 ELECTROCHEMICAL IMPEDANCE SPECTROSCOPY	27
2.3 ISOTHERMAL MICRO-CALORIMETRY	29
2.4 ENTROPY MEASUREMENTS.....	39
2.5 MATERIAL CHARACTERIZATION.....	42
3 RESULTS.....	45
3.1 CAPACITY FADING MECHANISMS OF NI-RICH LAYERED OXIDES DURING LONG-TERM CYCLING	46
3.1.1 <i>In-situ X-ray study at ambient temperature</i>	46
3.1.2 <i>Ex-situ study at elevated temperatures</i>	94
3.2 HYSTERESIS AND HEAT GENERATION IN LI- AND MN-RICH LAYERED OXIDES.....	111
3.2.1 <i>Entropy measured via linear temperature variation</i>	111
3.2.2 <i>Implications of hysteresis on heat generation during cycling</i>	139
3.2.3 <i>Heat generation during the first activation cycle</i>	157
4 CONCLUSIONS	159
5 APPENDIX	166
References	205
List of figures.....	217
Acknowledgements	219
Scientific Contributions.....	221
Curriculum Vitae	223

List of Abbreviations

Abbreviation	Description
BET	Brunauer-Emmett-Teller (theory)
BEV	battery electric vehicle
CAM	cathode active material
CC	constant current
CE	counter-electrode
CV	constant voltage
E_{eq}	hypothetical equilibrium potential of the cell
E_{load}	cell voltage under load
E_{OC}	cell voltage under open-circuit conditions
$\frac{\partial E_{OC}}{\partial T}$	variation of the OCV with temperature (=TD-OCV)
F	Faraday constant
GWRE	gold-wire micro-reference electrode
HAADF-STEM	high angle annular dark field scanning transmission electron microscopy
ICEV	internal combustion engine vehicle
ICP-AES	inductively coupled plasma atomic emission spectroscopy
IMC	isothermal micro-calorimetry
LCO	lithium cobalt oxide (LiCoO ₂)
LFP	lithium iron phosphate (LiFePO ₄)
LIB	lithium-ion battery
LMO	lithium manganese oxide (LiMn ₂ O ₄)
LMR-NCM	lithium- and manganese-rich NCM Li _{1+x} M _{1-x} O ₂ (M=Ni, Co, Mn; x typically >0.1)
LNMO	lithium nickel manganese oxide (LiNi _{0.5} Mn _{1.5} O ₄)
n	molar amount of charge
NCA	lithium nickel cobalt aluminum oxide (Li[Ni _{1-x-y} Co _x Al _y]O ₂)
NCM-abc	lithium nickel cobalt manganese oxide (Li[Ni _a Co _b Mn _c]O ₂ , a + b + c = 1)

List of Abbreviations

OCV	open-circuit voltage
PEIS	potentiostatic electrochemical impedance spectroscopy
Q	heat [mWh]
\dot{Q}	heat flow [mW]
\dot{Q}_{hys}	heat flow due to OCV hysteresis
\dot{Q}_{irrev}	irreversible heat flow
\dot{Q}_{par}	parasitic heat flow
\dot{Q}_{rev}	reversible heat flow
RE	reference-electrode
$\frac{dS}{d\xi}(\xi)$	partial molar entropy change as a function of ξ
SEI	solid electrolyte interphase
SEM	scanning electron microscopy
SOC	state-of-charge
T	temperature
TD-OCV	temperature-dependent OCV ($=\frac{\partial E_{OCV}}{\partial T}$)
TM	transition-metal
WE	working-electrode
XPD	X-ray powder diffraction
XPS	X-ray photo-electron spectroscopy
ξ	reaction turnover
η	overpotential

1 Introduction

Climate change is one of the biggest challenges humankind has to face in the near and far future. Limiting global warming to 1.5°C would help to significantly reduce the risks and impacts of climate change in comparison to even higher temperature rises. For this reason, the Paris Agreement was signed by more than 180 countries in 2016, committing to reducing the greenhouse gas emissions in order to limit the global average temperature rise to well below 2°C. In Germany, $\approx 23\%$ of the CO₂ equivalents (including CO₂, CH₄, and N₂O) are caused by the traffic sector¹ and roughly two thirds of this is due to private transport.² In a study by the Wuppertal Institut, key points for the German contribution to the compliance of the 1.5°C target are identified.³ For the private traffic sector, the authors conclude that most internal combustion engine powered vehicles (ICEVs) have to be replaced by battery electric vehicles (BEVs) by 2035.³ To achieve this goal, more than 2 million BEVs would need to be sold per year.³ In comparison, in 2019 a total number of 3.6 million cars were newly registered in Germany, from which only 63.000 were BEVs.⁴ Global carmakers hence need to speed up the pace for the development of affordable BEVs that are compatible to ICEVs. Among the available battery technologies, including lead-acid batteries (energy density $\approx 40\text{-}60$ Wh/kg)⁵, nickel-metal hydride batteries (energy density $\approx 40\text{-}110$ Wh/kg)⁵, and lithium-ion batteries (LIB, energy density > 150 Wh/kg)^{5,6}, LIBs are the most suitable technology to fulfill the requirements of electric vehicles owing to their energy and power density, lower cost, and flexibility in terms of material and cell design.

The development of LIBs, as we know them today, started in 1976 with a rechargeable TiS₂/Li cell presented by M. Stanley Whittingham.⁷ In order to increase the energy density of the cathode, John B. Goodenough introduced the material class of so-called layered oxides LiMO₂ (M = Ni, Co, Mn), from which in particular LiCoO₂ offered a good cycling stability and energy density.⁸ By replacing

the lithium metal anode with a carbon based material, Akira Yoshino achieved a safe battery using only intercalation compounds in 1985.⁹ Soon after, Sony introduced the first commercial LIB with graphite as anode and LiCoO_2 as cathode for consumer electronics in 1991.¹⁰ For the development of lithium-ion batteries, Whittingham, Goodenough, and Yoshino were honored with the Nobel Prize in Chemistry in 2019.¹¹ Over the past 30 years, extensive research effort was directed at the development of electrode materials and electrolytes to enhance the performance of LIBs. Compared to the original Sony cell, the energy density has increased from 80 Wh/kg⁹ to 260 Wh/kg¹² (Tesla Model 3) at cell level. With such a high energy density, driving ranges of ≈ 500 km are possible. So far, however, this is only commercialized for some premium vehicle models, while the driving range performance of affordable BEVs (e.g., $<25.000\text{€}$) is still far from that of conventional ICEVs.¹³ To enable both a comparable driving range and price for BEVs, the US Department of Energy estimated that the energy density of LIBs needs to be above 350 Wh/kg at a price of $\approx 62\text{€}/\text{kg}$ at cell level (corresponding to ≈ 235 Wh/kg at $\approx 80\text{€}/\text{kg}$ at pack level).¹⁴

Since it is mostly the cathode that limits the available specific capacity and determines the average operating voltage, it is still the main bottleneck when it comes to increasing the energy density of the cell. The manufacturing costs of LIBs are dominated by the costs for the raw materials ($\approx 75\%$)¹⁵, whereby the cathode is the largest compound ($\approx 50\%$ of material costs)¹⁵. This is why the main research focus is on the development of cathode active materials. Currently, layered oxides LiMO_2 ($M = \text{Ni}, \text{Co}, \text{Mn}$), as introduced by Goodenough 40 years ago, dominate the battery market.^{13,16} By increasing the nickel content, the energy density of the cathode is increased and the amount of cobalt is decreased. Cobalt is considered as the most critical raw material with respect to cost, material reserves, and supply reliability.¹² Using nickel-rich variants of LiMO_2 with $\geq 80\%$ nickel, the intermediate milestone of 300 Wh/kg on cell-level can already be reached today (CATL with NCM-811, Panasonic with NCA, explanation of cell chemistry in the following sections).¹³ The disadvantage of the high nickel content is its relatively high raw material cost ($7.40\text{€}/\text{kg}$ Ni_2SO_4 compared to $1.50\text{€}/\text{kg}$ Mn_2SO_4)^{17,18} leading to overall cell prices on the order of 80-140€/kg_{cell} for cells with Ni-rich layered oxides.¹³ In order to decrease the cathode material cost and further increase the

energy density, another focus in battery research is the development of Li- and Mn-rich layered oxides, which can even be synthesized without the use of cobalt.^{19,20} There are, however, still some serious drawbacks hindering the commercial application of this type of cathode materials.²¹

In the light of the current importance of cathode active material development in battery research, this thesis covers two main subjects. One is the investigation of fading mechanisms of Ni-rich layered oxides on a material level. The second focus is on the understanding of Li- and Mn-rich layered oxides with respect to the unique hysteresis of the open-circuit voltage (OCV) that is an intrinsic material property displayed by this type of cathode active material, and which still impedes its commercial application.

1.1 Theoretical background on lithium-ion batteries

Working principle

Figure 1.1 shows a schematic illustration of a Li-ion battery (LIB). It consists of two intercalation electrodes coated on metal current collectors and an electrolyte-filled porous separator. Today's LIBs work according to the "rocking chair" concept. This means that Li-ions are shuttled back and forth between the electrodes. The electrode with the higher lithiation potential is hereby the positive electrode (right side in Figure 1.1). By convention, it is referred to as "cathode", independent of whether the discharge or charge direction is considered. In today's LIBs, lithium transition metal oxides (LiMO_2 , $M = \text{Ni, Co, Mn, ...}$) or phosphates are frequently used as cathode materials. These lithium intercalation compounds provide the active lithium that can be shuttled between the electrodes. The typical anode consists of graphite (C_6) that can accommodate lithium between its graphene layers. The electrodes are electronically separated by a porous polymer membrane soaked with a Li^+ ion conducting electrolyte, the so-called separator. During charge, Li-ions de-intercalate from the LiMO_2 cathode (see equation (1.1)), move through the electrolyte and insert into the graphite anode (equation (1.2)) while the electrons are transferred via an external electrical circuit. During discharge, the reaction is reversed, releasing the stored electrical energy via the external circuit.

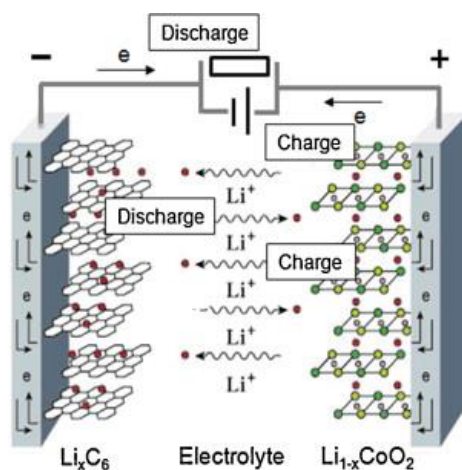
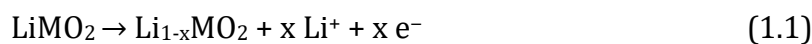


Figure 1.1: Schematic illustration of the main components and the operating principle of a Li-ion battery taken from Hausbrand et al.²². Reprinted under a Creative Commons BY-NC-ND 3.0 license.



 Battery testing

In the following, some important terms central to the LIB research are defined. The specific capacity of an active material (C_{spec}) is directly linked to the amount of lithium ions (n), which can be (de-)intercalated per formula unit. It is calculated with equation (1.3):

$$C_{spec} = \frac{n \cdot F}{M} \quad (1.3)$$

Here, F is the Faraday constant (96485 As/mol) and M is the molar mass of the active material (in g/mol). Note that, in case of the cathode active material, the molar mass of the lithiated compound is considered while for the anode active material, the molar mass of the delithiated material is taken. C_{spec} is usually given in units of mAh/g referring to the mass of the active material. However, equation (1.3) only describes the theoretical capacity of a material where all lithium ions are extracted from the host structure. For typical cathode materials, this would lead to an instability of the structure and a poor cycling performance. The reversible capacity corresponding to the amount of Li that can reversibly be (de-)intercalated is hence smaller than the theoretical value. The capacity of a cell is usually limited by the specific capacity of the cathode, which represents the available Li reservoir. The ratio of the discharge to charge capacity of a cell is the coulombic efficiency. It is a quality criterion describing how reversible the cell reaction is and should be close to 100%.

The cell voltage (V_{cell}) corresponds to the potential difference between the two electrodes. It can be calculated from the respective half-cell voltages: $V_{cathode} - V_{anode}$. It is important to differentiate the cell voltage under load from that under open-circuit voltage (OCV) conditions. The difference between them arises from various overpotentials (η) caused by a combination of resistive effects within the cell (e.g., the ionic resistance of the separator, the contact and charge-transfer resistances of the electrodes, etc.).

The specific charge or discharge energy ($E_{cha/dis}$) is calculated by integrating the cell voltage curve, V_{cell} , versus the specific capacity, C_{spec} , for a complete charge or discharge process (i.e., from a nominal capacity C_0 to C'):

$$E_{cha/dis} = \int_{C_0}^{C'} V_{cell}(C_{spec}) dC_{spec} \quad (1.4)$$

The specific energy is thus given in units of mWh/g. Analogously to C_{spec} , it is referenced to the mass of the active material of interest (in case of all studies presented here, this is the cathode active material). Since a high energy is desired for batteries, researchers try to increase both the cell capacity and voltage. The ratio of the discharge to charge energy of a full cycle is the energy round-trip efficiency. It is a measure of the electrical energy lost during the cycle, i.e., as waste heat.

An important term for battery testing is the so-called C-rate. According to equation (1.5), it defines the ratio of the applied current, I (in A), and the cell capacity, C_{cell} (in Ah).

$$\text{C-rate} = \frac{I}{C_{cell}} \quad (1.5)$$

The C-rate is thus given in units of 1/h, and a C-rate of one corresponds to a charging or discharging process, during which the cell capacity is exchanged in one hour.

The state-of-charge (SOC) of a battery is usually given in percentage, where 100% means a charged state and 0% a discharged state. Since this definition of the SOC is relative and depends on the chosen upper and lower cell voltage cutoffs, the respective reference capacity needs to be known for an unambiguous interpretation (see above for the difference between the theoretical and the reversible capacity). In the present work, the term SOC is instead used synonymous to the nominal full specific capacity of the cathode (in mAh/g). This means that a direct link between the amount of Li in the cathode and the so-called SOC is established.

Anode materials

To achieve a high energy density for LIBs, the anode should have a low reaction potential and a high specific capacity (see equation (1.4)). The anode of most present LIBs consists of graphite with a reversible capacity of ≈ 360 mAh/g (theoretical capacity = 372 mAh/g). For graphite electrode coatings, low weight percentages (<5%) of binder (e.g., polyvinylene difluoride, PVDF) are used to enable adhesion of the coating to the current collector and cohesion within the coating ensuring mechanical stability. Copper foil is used as current collector for

graphite anodes because it does not alloy with lithium even at the low potential (≈ 0.1 V vs. Li^+/Li) and has a high electronic conductivity. The intercalation of lithium into graphite leading to Li_xC_6 occurs via two main stages, which give rise to characteristic plateaus in the voltage profile of graphite vs. exchanged capacity. During the first plateau at ≈ 125 mV vs. Li^+/Li ($0.2 < x < 0.5$), LiC_{12} is formed, where every second graphene layer is occupied by lithium. This is followed by the intercalation of lithium into every layer, leading to the formation of LiC_6 at ≈ 70 mV vs. Li^+/Li ($0.5 < x < 1$).²³ However, no organic electrolyte is stable at the operating potential of lithiated graphite.²⁴ While this would lead to a continuous decomposition of electrolyte at the anode and a consequent consumption of lithium, it is prevented by the formation of a so-called solid-electrolyte interface (SEI) at the surface of the graphite particles.²⁵ The SEI has a thickness of several nanometers and consists of reduction products of the electrolyte such as lithium carbonate and lithium fluoride.^{26,27} It allows ionic conduction of Li^+ but inhibits electron transport, so that further electrolyte decomposition is prevented. For the formation of the SEI, some lithium is irreversibly lost during the first cycle, leading to a low coulombic efficiency in the range of 80 – 95%.²⁸ After its initial formation, graphite cycles reversibly and coulombic efficiencies close to 100% can be achieved. Another contribution to lithium loss at the anode is the dissolution of transition metals from the cathode and their reduction and deposition on the anode. This can lead to a continuous loss of active lithium because of the catalytic activity of the transition metals at the anode.^{29,30} As a result of the proximity of the graphite lithiation potential to the Li^+/Li potential, graphite is at risk for Li plating at high degrees of lithiation during charging. Li plating causes a loss of active lithium and can lead to the formation of Li dendrites, which can ultimately lead to a short circuiting of the cell. To prevent this, anodes are capacitively and geometrically oversized. Furthermore, graphite has a limited fast-charging capability since high kinetic overpotentials can push the anode potential below 0 V vs. Li^+/Li and lead to Li plating.

Another anode material is lithium-titanate (LTO) with a specific capacity of ≈ 175 mAh/g.³¹ Owing to its high operating voltage plateau of ≈ 1.5 V vs. Li^+/Li ,³¹ no SEI is formed and fast kinetics enable high charging rates.³² However, the absence

of the SEI leads to the formation of significant H₂ gassing when LTO gets in contact with carbonate electrolytes.³³ Another drawback of the high potential is the low energy density of the resulting cell due to the low cell voltage.

With respect to maximizing the energy density of future LIBs, silicon is one of the most promising anode materials owing to its high specific capacity of 3579 mAh/g and low average potential of ≈ 0.2 V vs. Li⁺/Li.^{34,35} Silicon forms alloys with lithium and can thereby be lithiated up to Li₁₅Si₄.³⁶ A drawback of this alloying reaction is the large volume expansion of $\approx 270\%$ accompanied with it.^{35,37} This leads to a destabilization of the SEI and to breakage and electronic isolation of Si particles, causing the loss of cyclable lithium and of Si active material.³⁶ As a result, rapid capacity fading is observed. These undesired phenomena must be mitigated to enable the commercial application of silicon as anode material.

Initially, lithium metal was used as anode in LIBs. With regards to energy density, it is one of the most desirable materials, with a high specific capacity of 3862 mAh/g and a low potential.³⁸ In the 1980s, LIBs with lithium anodes and MoS₂ cathodes were commercialized by Moli Energy but failed due to dendrite formation that would lead to short circuits and fire incidents during operation.^{24,39} Today, lithium metal anodes are possible candidates for use in all-solid-state-batteries.

Electrolytes

The electrodes of a LIB are ionically connected via a liquid electrolyte consisting of a lithium salt dissolved in an aprotic solvent. LiPF₆ is typically used as lithium salt. It ensures the ionic conductivity and is able to passivate the aluminum current collector against anodic dissolution.⁴⁰ Major drawbacks of LiPF₆ are its disproportionation into insoluble LiF and gaseous PF₅ at temperatures above 60°C,⁴¹ and its high reactivity with trace water leading to the formation of HF, which is known to decrease the cycle life of LIBs.^{42,43} To minimize these undesired side reactions, electrolytes are kept under inert atmosphere and electrodes as well as all cell parts are vigorously dried before the cells are assembled in a dry-room (or under inert atmosphere). LiPF₆ is typically dissolved in a mixture of the cyclic carbonate ethylene carbonate (EC) and linear carbonates such as ethyl methyl carbonate (EMC) or diethyl carbonate (DEC). Owing to its high dielectric constant,

EC ensures the dissolution of the salt and the formation of a stable SEI, which is formed upon EC reduction below 0.8 V vs. Li⁺/Li.^{44,45} The linear carbonates keep the viscosity of the mixture low to ensure good ionic conductivity and furthermore decrease the freezing point.⁴² The electrochemical stability window of the resulting electrolyte is between ≈ 0.8 V and 4.8 V vs. Li⁺/Li, whereby lower potentials lead to a reduction on the anode (SEI formation) and higher potentials to an oxidation at the cathode.⁴⁶ Another component, which is often contained in electrolyte mixtures, are additives such as vinylene carbonate (VC). Additives improve the properties of the SEI and thus the long-term cyclability of LIBs.⁴⁴ To achieve a high energy density of the battery on cell level, the electrolyte to active material is kept low in commercial cells.

Cathode active materials

The cathode active material (CAM) provides the lithium that is shuttled between the electrodes and thus directly governs the capacity of the full cell. To maximize the energy density of LIBs, a high operating potential and a high specific capacity of the cathode are desired. All currently used CAMs rely on 3d transition metals (i.e., Mn, Fe, Co, Ni), which are oxidized during the charge of the battery to compensate for the deintercalation of Li⁺. Besides the energy density, also the cost of the metals used is an important factor for the development of cathode materials.

Figure 1.2 shows the most relevant CAMs classified by their practical energy density and the cathode cost. The energy density of the CAM is calculated by multiplying the specific capacity with the average voltage according to equation (1.4). The underlying values for the calculation are presented in Table 1.1. The cathode cost was estimated by calculating the price of 1 kg of CAM based on the respective raw material prices of the metal precursors but neglecting any production costs. The raw materials include Li₂CO₃, NiSO₄, MnSO₄, CoSO₄ and FePO₄. For all transition metal sources, the calculation is based on the raw material prices from March 11, 2022 (with an exchange rate of 1USD = 0.91 €).^{17,18,47,48} The respective costs are shown in the description of the table. For Li₂CO₃, however, the average price of the year 2021 (15.50 €/kg)⁴⁹ was considered for the calculation because the lithium

raw material price was subject to strong fluctuations⁵⁰ and reached an all-time high in March 2022 with ≈ 72 €/kg⁵¹, which would distort the results.

Table 1.1: Overview of various CAMs with their respective cathode cost (in €/kg referenced to the CAM mass), specific capacity (in mAh/g), average voltage (V vs. Li⁺/Li), specific energy density (Wh/kg referenced to the CAM mass) and the resulting cathode cost in €/kWh referenced to the CAM energy density.^{9,21,52-55} The cathode cost in €/kg was calculated according to Nelson et al.⁵⁶ but neglecting any costs for processing or profit margin. The cost only includes contributions from the raw material precursors (15.50 €/kg for Li₂CO₃,⁵¹ 7.40 €/kg for NiSO₄,¹⁷ 1.50 €/kg for MnSO₄,¹⁸ 17.20 €/kg for CoSO₄,⁴⁷ and 3.50 €/kg for FePO₄⁴⁸).

CAM	Cathode cost in € kg ⁻¹	Specific capacity in mAh g ⁻¹	Average voltage in V	Energy density in Wh kg ⁻¹	Cathode cost in € kWh ⁻¹
NCM111	16.98	160	3.9	624	27.21
NCM622	16.06	180	3.85	693	23.18
NCM811	15.36	210	3.8	798	19.25
LCO	30.20	190	3.9	741	40.76
LNO	14.66	240	3.7	888	16.51
NCA	16.75	200	3.8	760	22.04
LFP	5.35	160	3.4	550	9.73
LMO	4.21	130	4.0	520	8.10
LNMO	6.67	135	4.7	635	10.50
LMR-NCM	11.38	250	3.6	900	12.64
LMR-NCM (Co free)	8.35	250	3.6	900	9.28

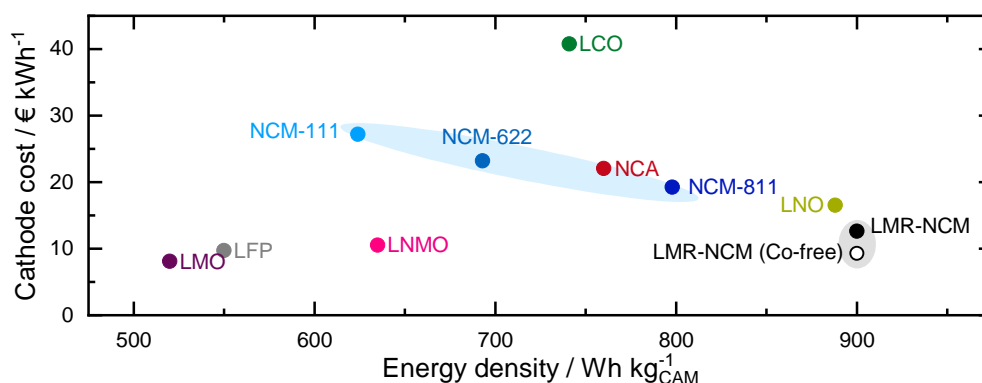


Figure 1.2: Classification of the most relevant cathode active materials (CAMs) according to their practical energy density^{9,21,52-55} (in Wh/kg referenced to the CAM mass) and the cathode cost^{17,18,47-49} (in €/kWh referenced to the CAM energy density). The calculation is based on the values shown in Table 1.1. For the cathode cost, only the raw material prices were considered as described in the text.

Based on their structure, all currently used cathode materials can be classified into three groups: (i) spinel oxides with the general formula LiM_2O_4 , (ii) phospho-olivines with the formula LiMPO_4 , and (iii) layered oxides with the structure LiMO_2 (with the overlithiated version $\text{Li}_{1+x}\text{M}_{1-x}\text{O}_2$).

The spinel oxide LiMn_2O_4 (LMO) is a cobalt-free, thus cost attractive material ($\approx 4.20\text{€}/\text{kg}$, see Table 1.1) with a high thermal stability.^{35,57} However, its reversible capacity is limited to $\approx 130\text{ mAh/g}$ at an average voltage of $\approx 4.0\text{ V vs. Li}^+/\text{Li}$ leading to an energy density of only $\approx 520\text{ Wh/kg}$.^{35,52} The LiMn_2O_4 structure moreover suffers from severe material degradation during extended cycling.^{30,58} The energy density is improved by substituting parts of the manganese with nickel. The resulting so-called high-voltage spinel $\text{LiNi}_{0.5}\text{Mn}_{1.5}\text{O}_4$ (LNMO) offers a capacity of $\approx 135\text{ mAh/g}$ at an average voltage of $\approx 4.7\text{ V vs. Li}^+/\text{Li}$ (resulting in $\approx 635\text{ Wh/kg}$).⁵² It, however, also suffers from capacity fading due to electrolyte oxidation and manganese dissolution at high potentials.^{59,60}

The commercially most successful representative of the group of phospho-olivines is lithium iron phosphate (LFP) with the chemical composition LiFePO_4 . LFP is a two-phase material with a voltage plateau at $3.45\text{ V vs. Li}^+/\text{Li}$ over the whole SOC range and a specific capacity of $\approx 160\text{ mAh/g}$.⁹ The advantages of LFP are its low cost due to the use of inexpensive iron ($3.50\text{ €}/\text{kg}$ for FePO_4)⁴⁸, and its high structural and thermal stability.³⁵ However, because of the low energy density ($\approx 550\text{ Wh/kg}$) it is preferably used in applications requiring long lifetimes rather than high energies, such as stationary energy storage systems or electrical buses.⁶¹

Layered oxides with the structure LiMO_2 ($M = \text{Ni, Co, Mn}$) are currently the most prevalent cathode active materials in Li-ion batteries.¹⁶ Their application has its beginnings in 1991, when the first commercial LIB was introduced using LiCoO_2 (LCO) as cathode active material. LCO offers a high energy density of $\approx 740\text{ Wh/kg}$ (capacity = 190 mAh/g , average voltage $\approx 3.9\text{ V vs. Li}^+/\text{Li}$)²¹ but is also a very expensive material due to the high cobalt content ($17.20\text{€}/\text{kg}$ for CoSO_4)⁴⁷. This is why it is mostly used for portable electronics that require only small amounts of active material.⁹ By partially replacing cobalt by manganese and nickel, the so-called NCM materials with the chemical formula $\text{LiNi}_x\text{Mn}_y\text{Co}_z\text{O}_2$ ($x+y+z = 1$) are

obtained (highlighted in blue in Figure 1.2). Current research efforts focus on increasing the nickel content in order to decrease the material cost and increase the specific capacity at a reasonable cutoff potential ($\approx 4.1 - 4.3$ V vs. Li^+/Li). Figure 1.2 shows this trend by comparing NCM-111 ($\text{LiNi}_{0.33}\text{Mn}_{0.33}\text{Co}_{0.33}\text{O}_2$, capacity = 160 mAh/g, average voltage ≈ 3.9 V vs. Li^+/Li) to NCM-622 ($\text{LiNi}_{0.60}\text{Mn}_{0.20}\text{Co}_{0.20}\text{O}_2$, capacity = 180 mAh/g, average voltage ≈ 3.85 V vs. Li^+/Li) and NCM-811 ($\text{LiNi}_{0.80}\text{Mn}_{0.10}\text{Co}_{0.10}\text{O}_2$, capacity = 210 mAh/g, average voltage ≈ 3.8 V vs. Li^+/Li). By substituting manganese with aluminum, the so-called NCA-material is obtained (e.g., $\text{LiNi}_{0.80}\text{Co}_{0.15}\text{Al}_{0.05}\text{O}_2$). NCA offers a comparable energy density (≈ 760 Wh/kg) at similar CAM costs as NCMs with similar nickel contents (see Figure 1.2). The NCM and NCA materials are discussed in more detail in section 1.2.

In order to increase the energy density of NCM materials even further, Li-ions are incorporated into the transition metal layer, leading to the so-called Li- and Mn-rich NCMs (LMR-NCM, highlighted in gray in Figure 1.2). As a result of the higher amount of accessible lithium (capacity = 250 mAh/g) and the high operating potential (≈ 3.6 V vs. Li^+/Li), a high energy density of ≈ 900 Wh/kg²¹ is achieved at relatively low cathode material costs ($\approx 8-11$ €/kg, see Table 1.1). This class of cathode materials will be discussed in detail in section 1.3. Current research in the field of cathode active material hence focuses on Ni-rich NCMs and Li- and Mn-rich NCMs in order to increase energy density and reduce material cost by using less cobalt. The aim of this thesis is to contribute to the understanding of these two layered oxides on a material level.

1.2 Challenges of Ni-rich layered oxides

Layered oxides (LiMO_2) crystallize in the trigonal space group $R\bar{3}m$. Lithium and the transition metals occupy octahedral sites in alternating layers separated by a cubic closed package of oxide ions, leading to a stacking sequence of Li-O-M-O. In case of NCMs, the transition metal layer is filled with a solid solution of nickel, cobalt, and manganese ($\text{LiNi}_x\text{Mn}_y\text{Co}_z\text{O}_2$ with $x+y+z = 1$). By using aluminum instead of manganese, NCA is obtained (e.g., $\text{LiNi}_{0.80}\text{Co}_{0.15}\text{Al}_{0.05}\text{O}_2$). In general, both advantages and disadvantages of this class of compounds scale with the Ni content: a higher Ni content thereby implies a higher capacity and an improved rate capability, but also a lower cycling and thermal stability.⁶ Cobalt improves the rate capability and capacity but increases the cost of the material.¹² Manganese stabilizes the layered structure and reduces the cathode costs, but also decreases the specific capacity due to its redox inactivity.^{62,63}

The NCM material with the lowest nickel content commercially used is NCM-111 ($\text{LiNi}_{0.33}\text{Mn}_{0.33}\text{Co}_{0.33}\text{O}_2$). For example, it found application in the first generation of the BMW i3.^{6,12,64} To meet future demands for automotive applications, BMW proposed a target value of ≈ 800 Wh/kg on the cathode active material level for 2025.⁶ This cannot be reached with NCM-111 (≈ 620 Wh/kg, see Figure 1.2). To further increase the energy density of NCM cathodes, a widely adapted strategy is to maximize the nickel content (highlighted in blue in Figure 1.2). Although all NCM materials have a very similar theoretical capacity of ≈ 275 mAh/g due to the similar molar masses of Ni, Mn, and Co, Ni-rich NCMs (Ni content $>60\%$) deliver a larger share of their capacity at lower voltage and thus effectively increase the practical capacity for a given upper cut-off potential. This goes along with a decrease in the cobalt content, which lowers the CAM costs (see Figure 1.2).¹² Accordingly, the next generation of the BMW i3 employed NCM-622 as cathode active material (≈ 690 Wh/kg).⁶⁴ To meet the target value of 800 Wh/kg,⁶ even higher amounts of nickel are required. NCM-811 delivers ≈ 800 Wh/kg (see Figure 1.2) and will thus be used as cathode in the upcoming BMW iX3.^{5,65} NCA with a high Ni content (80%) also delivers up to ≈ 760 Wh/kg and is used by Tesla for its electric vehicles.¹² NCA and NCM-811 provide similar practical capacities (≈ 200 mAh/g for NCA, ≈ 210 mAh/g for NCM-811). NCA thereby shows advantages regarding capacity

retention and power, while NCM-811 offers a higher thermal stability.¹² The maximum possible nickel content is reached for LiNiO_2 (LNO, capacity = 240 mAh/g, average voltage ≈ 3.7 V vs. Li^+/Li). Figure 1.2 shows that it offers the highest energy density for layered oxides and the lowest material costs. With this high Ni content, however, the layered structure becomes more unstable, particularly at high states of charge. LNO thus shows a decreased cycle life, strong gassing during cycling and severe safety issues.^{54,66}

The strive for a higher energy density by increasing the nickel content in layered oxides comes at the price of a lower thermal stability⁶², a higher sensitivity when exposed to ambient air or moisture^{67,68}, and a reduced cycling stability.¹³ The investigation of the capacity fading of Ni-rich NCMs is one focus of this PhD thesis and is presented in the Results section 3.1. Figure 1.3 illustrates the most important aging mechanisms of LIBs with NCM cathodes and graphite anodes. The cathode thereby causes – directly or indirectly – most of the observable capacity fading processes, which are explained in the following.

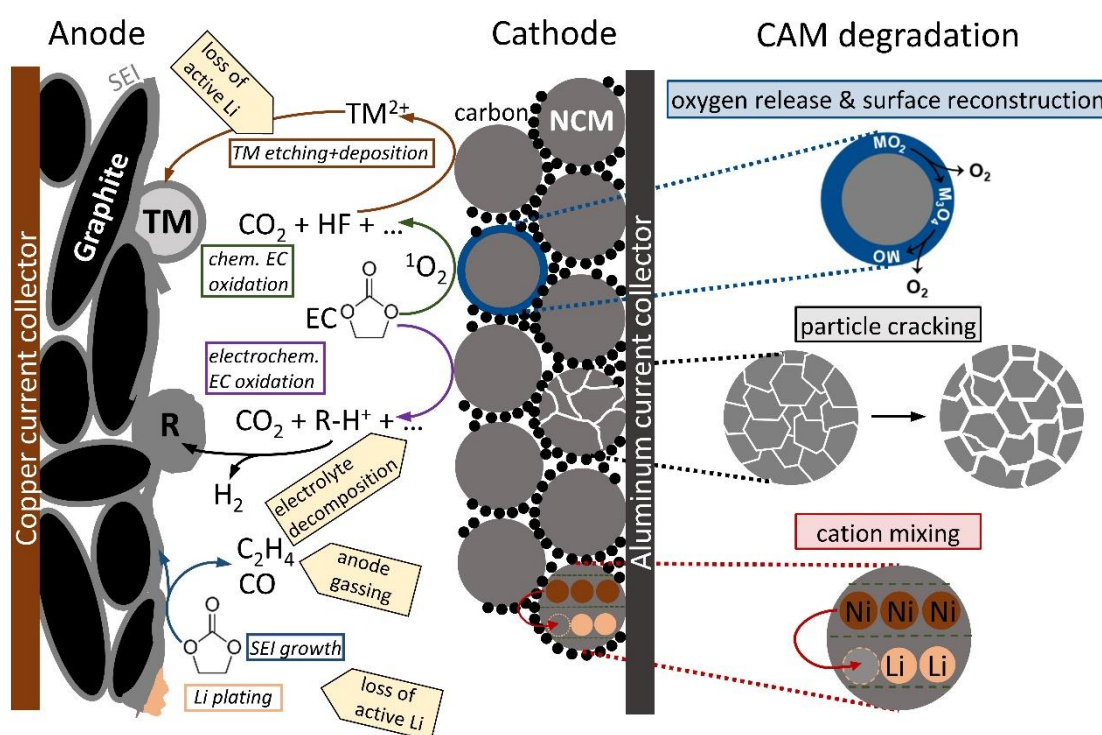


Figure 1.3: Schematic illustration of the most important aging mechanisms in a Li-ion battery with a graphite anode and an NCM cathode. Text in colored boxes describes the respective process. The yellow arrows indicate the effect on the cell performance. The right hand side shows the three major degradation phenomena of the cathode active material in more detail. For further explanations, see text.

When layered NCMs are charged beyond an SOC of $\approx 80\%$ ($x_{\text{Li}} \leq 0.2$), oxygen is released from surface-near regions and a spinel and/or rock-salt surface layer is formed.^{53,69} The reconstruction of the surface is accompanied with an increased charge-transfer resistance, leading to a significant capacity fading.^{70,71} On the other hand, the released oxygen can react with the electrolyte, thereby forming CO and CO₂, since the evolved O₂ is – at least partially – highly reactive singlet oxygen.^{72,73} This chemical electrolyte decomposition entails the formation of HF, which can etch transition metals from the cathode active material, causing another aging mechanism.^{74–76} Subsequent deposition of transition metals on the graphite anode leads to a loss of active lithium because of ongoing SEI formation.^{29,30} Electrolyte decomposition can also happen via an electrochemical pathway, as shown in Figure 1.3. The occurrence of this oxidation reaction increases with the potential⁷⁷ and is thus a more significant problem for cells with Ni-rich cathodes, which are typically cycled to higher upper cut-off potentials. Since this decomposition reaction is driven by the potential, it also occurs for other CAMs like LNMO and LMR-NCM, which are also cycled to high upper cut-off voltages. The decomposition products of the electrolyte oxidation can diffuse to the anode and cause gas evolution or a decomposition of the SEI.^{53,78} Both the chemical and electrochemical electrolyte decomposition lead to a consumption of the available electrolyte and might even lead to cell failure by electrolyte dry-out.

When layered oxides are delithiated, they experience a considerable anisotropic volume contraction, which is more severe for a higher nickel content (e.g., $\approx 1\%$ for NCM-111 and $\approx 5\%$ for NCM-811 charged until 4.3 V vs. Li⁺/Li).⁷⁹ These repeated volume changes during cycling can lead to cracking of the secondary particle but also to micro-cracks within the primary particles as illustrated in Figure 1.3.^{80–82} Particle cracking might deteriorate the electrical contact between primary NCM crystallites and even lead to electronically isolated particles (loss of active material).^{83,84} Furthermore, the increased surface area at the interior of the secondary agglomerate means that the electrolyte can penetrate further into the particle. This increase in the interfacial surface area between the electrolyte and the CAM might enhance side reactions such as the electrolyte decomposition discussed above.^{53,82,85}

At high SOC, the amount of lithium remaining in the NCM structure is low and transition metals can irreversibly migrate from the transition metal layer to the empty lithium sites. This so-called cation mixing is a bulk process. It can lead to capacity fading due to an increased cathode impedance as a result of a deteriorated solid-state lithium diffusion.^{86,87} Moreover, the amount of available Li sites is reduced by the presence of transition metals in the Li layer.

One focus of this PhD thesis is the investigation of the capacity fading mechanisms in cells with Ni-rich NCM-811 cathodes. In order to exclusively analyze the effects caused by the cathode active material, the studies presented in section 3.1 were set up in a way that other degradation phenomena were minimized or excluded as good as possible by the design of the experiments. The arrows colored in yellow in Figure 1.3 indicate possible reasons for capacity fading, which are not directly occurring at the cathode. The loss of active lithium resulting from an ongoing growth of the SEI on the anode was counter-balanced by using a pre-lithiated graphite that offers a large lithium reservoir. The prelithiation also mitigates lithium plating by ensuring that the anode potential is well above 0 V vs. Li⁺/Li. The dissolution of transition metals from the NCM by HF formed during the electrolyte oxidation is reduced by employing a glass fiber separator that acts as an HF scavenger.^{88,89} Moreover, this porous separator offers a high void volume to contain a large electrolyte excess. This ensures that capacity fading due to electrolyte depletion is mitigated. The focus of the studies presented in section 3.1 is therefore the analysis of capacity fading due to intrinsic CAM degradation phenomena, which are sketched on the right hand side of Figure 1.3: surface reconstruction, particle cracking and cation mixing.

1.3 Challenges of Li- and Mn-rich layered oxides

Taking layered NCMs as a starting point, the energy density can be further increased by incorporating lithium into the transition metal layer, yielding the overlithiated Li- and Mn-rich layered oxides (LMR-NCM). There are generally two ways of describing the LMR-NCM formula. When regarding it as a two-phase material of nano-domains of NCM and Li_2MnO_3 existing next to each other, the composition can be expressed as $x \text{Li}_2\text{MnO}_3 \cdot (1-x) \text{LiMO}_2$ ($M=\text{Ni, Co, Mn}$).⁹⁰ On the other hand, LMR-NCM can also be described as a one-phase material by writing $\text{Li}_{1+x}\text{M}_{1-x}\text{O}_2$ ($M=\text{Ni, Co, Mn}$; x typically >0.1). The first cycle of LMR-NCM is characterized by a unique charge voltage profile, featuring a plateau at ≈ 4.5 V vs. Li^+/Li and a high irreversible capacity (difference between charge and discharge capacity is ≈ 40 mAh/g). The electrical energy efficiency of the first cycle is hence very low ($\approx 73\%$). This will be discussed in more detail in section 3.2.3. After the unique voltage profile in the first charge/discharge cycle, the so-called activation cycle, LMR-NCM offers a reversible capacity of ≈ 250 mAh/g at an average operating voltage of ≈ 3.6 V vs. Li^+/Li . As briefly mentioned in section 1.1., this class of materials has the advantage of a low material cost because of the high fraction of manganese used. Since it can also be synthesized without cobalt, the cathode cost can be further decreased (see Figure 1.2).^{19,20}

However, the commercial application of LMR-NCM is still impeded by several serious issues limiting the lifetime and performance of these materials. During cycling, a considerable voltage fading is observed. This means that the average voltage during charge and discharge decreases and hence leads to a decreasing (dis-)charge energy.^{91,92} Furthermore, pronounced oxygen release from the LMR-NCM adversely affects the cycling performance in several ways. On the one hand, the surface reconstruction from a layered to an oxygen-deficient spinel/rock-salt structure, which is linked to the oxygen evolution, leads to an impedance build-up on the cathode.⁹³⁻⁹⁵ On the other hand, the evolved oxygen triggers electrolyte decomposition.⁹³⁻⁹⁵ Thereby, a considerable amount of gas is formed, in particular during initial cycling, which needs to be removed in a degassing step for large-format cells to allow further stable and safe cycling.⁹⁶ The relatively high operating potential of cells with LMR-NCM cathodes (up to 4.8 V vs. Li^+/Li)

furthermore enhances electrochemical electrolyte oxidation, in particular at elevated temperatures. Another factor are the relatively slow charge-transfer kinetics of LMR-NCM, leading to poor rate capabilities in comparison to classical layered oxides.^{19,97,98}

Another disadvantage when using LMR-NCM cathodes is the pronounced voltage difference between the charge and discharge voltage curve. This voltage hysteresis is still present under open-circuit conditions (OCV hysteresis, Figure 1.4a) and thus represents an intrinsic bulk material property of LMR-NCM. The voltage hysteresis significantly decreases the energy efficiency of a charge-discharge cycle. The energy round-trip efficiency describes to what fraction the charge energy can be extracted during discharge for a complete cycle. For example, in comparison to an NCA/graphite cell with an energy efficiency of 98% (at C/10, 25°C), an LMR-NCM/graphite cell only reaches a value of 89% at the same cycling conditions.⁹⁹ The energy loss, which is caused by this round-trip inefficiency, generates waste heat. This will be discussed in more detail in section 3.2.2. Interestingly, the hysteresis as a function of state-of-charge is not only observed for the voltage. Figure 1.4 shows two other examples of parameters that show a path dependence between charge and discharge direction: (i) the unit cell volume (Figure 1.4b), which resembles the behavior of the lattice parameters; and (ii) the charge-transfer resistance of the cathode (Figure 1.4c). The data shown in Figure 1.4 were collected within the course of this thesis and are in agreement with published data on the LMR-NCM lattice parameters¹⁰⁰ and the cathode resistance¹⁰¹. Also, the Li site occupation¹⁰², atomic distances¹⁰³ and the oxidation states of the transition metals^{104,105} and oxygen^{105,106} are reported to show a path dependence between charge and discharge direction.

Several reasons for the OCV hysteresis in LMR-NCM are discussed in the literature, mainly focusing on reversible transition metal migration^{97,107,108} and changes of oxygen redox^{105,106} or a combination of both¹⁰⁶, causing the re-entrant Li environment during discharge to be energetically different from that during charge^{102,109}. The migration of transition metals hereby means that transition metals (ir-)reversibly move from their original layer into the lithium layer.^{97,107,108} Anionic redox refers to the (reversible) redox activity of lattice oxygen O^{2-}/O^{n-}

($n \leq 2$).^{105,106} A clear consensus on the exact mechanism explaining all the observed hysteresis phenomena is however lacking.

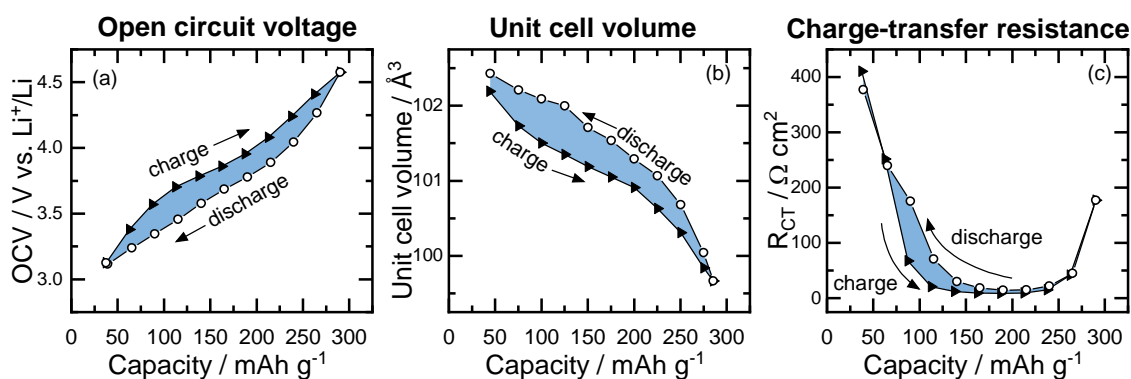


Figure 1.4: Examples of 0.33 LMR-NCM ($0.33 \text{ Li}_2\text{MnO}_3 \cdot 0.67 \text{ LiMO}_2$; $M = \text{Ni, Co, Mn}$) material properties that show a path dependent behavior between charge and discharge direction as a function of state-of-charge (=capacity, given in $\text{mAh/g}_{\text{CAM}}$). Charge direction indicated by black triangles, discharge direction by white circles. The resulting hysteresis is highlighted in blue. All data shown here originate from LMR-NCM/Li cells after complete activation, cycled at a C-rate of $C/10$ at 25°C between $2.0 - 4.7 \text{ V vs. Li}^+/\text{Li}$: (a) open-circuit voltage (OCV, 4th cycle); (b) unit cell volume obtained from in-situ X-ray diffraction in accordance with data reported by Strehle et al.¹⁰⁰ (2nd cycle); (c) charge-transfer resistance as published¹¹⁰ and presented in the Results section 3.2.2 (4th cycle). For experimental details, see section 2.

The second part of this thesis focuses on LMR-NCM cathode active materials and in particular on the hysteresis phenomena observed with this type of material. In the Results section 3.2.1, the hysteresis in LMR-NCM is discussed on a fundamental level and the partial molar entropy of LMR-NCM/Li cells is presented. The results suggest that the entropy also exhibits a path dependence as a function of SOC, which vanishes when plotted as a function of OCV. The practical implications of the OCV hysteresis and the corresponding waste heat are discussed in the Results section 3.2.2. All hysteresis phenomena are only observable after a full activation of the LMR-NCM. During this activation, irreversible processes occur, causing the material at the end of the cycle to differ significantly from the pristine one. The corresponding loss of electrical energy and the generation of waste heat during this activation process are discussed in the Results section 3.2.3.

2 Experimental Methods

2.1 X-ray powder diffraction

In an X-ray powder diffraction experiment, a crystalline powder sample is analyzed with respect to its structural parameters, crystallinity, and morphological properties such as strain and crystal size. The incoming X-rays are scattered at the lattice planes of the sample and are measured by the detector. The resulting diffractogram shows the observed X-ray intensity as a function of scattering angle θ . Thereby, only constructively interfering scattered waves contribute to the diffractogram. Constructive interference is only possible when the scattered waves are in phase, i.e., when the difference between their path lengths is equal to an integer multiple (m) of the wavelength (λ). Bragg's law correlates this condition ($m\lambda$) with the inter-planar spacing of the lattice planes within the sample (d) and the angle between the incoming beam and the respective parallel lattice planes (θ):

$$m\lambda = 2d \sin\theta \quad (2.1)$$

The number of reflections, their intensity and position are hence governed by the crystal structure of the sample (determining d) and the wavelength of the X-ray beam (λ). The inter-planar spacing d is determined by the lattice parameters of the unit cell a , b , and c . Since layered oxides such as NCM-811 belong to the hexagonal $R\bar{3}m$ space group, the following constraints apply for their unit cell: $a = b$, $\alpha = \beta = 90^\circ$, and $\gamma = 120^\circ$. The fact that the lattice parameters a and c are linked to the amount of lithium in the structure (x_{Li})^{79,111,112}, is used to establish a correlation between the state-of-charge of the cathode and its structural parameters in form of a calibration curve (see the $c/a = f(x_{\text{Li}})$ relationship given in the Results section 3.1). In the diffractogram, the apparent peak shape is determined by instrumental contributions and by sample properties such as strain and crystallite size. By

measuring highly crystalline standard reference materials, the instrumental contribution to the peak broadening is determined. Any additional peak broadening originating from the sample can then be modeled.

For the analysis of X-ray powder diffractograms (XPDs), the Rietveld method is applied. It uses a least-squares approach to refine a theoretical pattern in order to approximate it to the observed XPD. The theoretical pattern is generated based on various input parameters describing the crystal symmetry, further sample contributions, and the instrument function. The quality of the refinement can be assessed by comparing the calculated pattern to the observed one and by looking at the generated difference plot. Statistical agreement factors such as R_{wp} , R_{Bragg} , and χ^2 furthermore help to quantitatively follow the refinement process. They are, however, not suitable for a comparison of different samples or measurement setups. All refined parameters are reported with their estimated standard deviation. The Rietveld refinements conducted for this thesis were performed using the software package TOPAS (Coelho, Version 6, 2016)¹¹³ in combination with the text editor jEdit. The refinement approach including applied constraints and simplifications is described in detail in the respective experimental section of the manuscripts presented in the Results section 3.1.

The cells used for the XPD studies were pouch cells with NCM-811 as cathode active material, a pre-lithiated graphite as anode, and two glass-fiber separators in between. The potential of the cathode was controlled versus a lithium reference electrode as shown in Figure 2.1. Further experimental details can be found in the manuscripts in section 3.1.

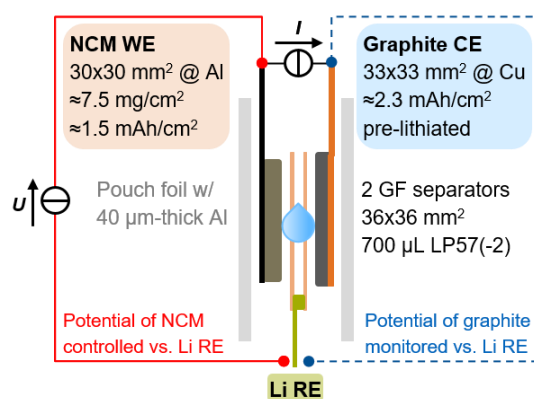


Figure 2.1: Schematic drawing of the NCM-811/graphite pouch cell used for XPD experiments with NCM-811 working electrode (WE, 30x30 mm², contacted by an aluminum tab), a pre-lithiated graphite as counter electrode (CE, 33x33 mm², contacted by a nickel tab), and two glass-fiber separators in between (GF, 36x36 mm²). The potential of the cathode was controlled versus a lithium reference electrode (RE).

In our XPD studies, we investigated structural changes of the NCM-811 CAM over the course of cycling in order to correlate them with the observable capacity fading of the cell. The focus of these studies were therefore aging mechanisms solely originating from the cathode, as shown in the right part of Figure 1.3 (surface reconstruction, particle cracking, and cation mixing). Any other degradation phenomena were excluded or minimized by the design of the experiment. By using a pre-lithiated graphite anode, electrolyte excess, and glass-fiber separators, capacity fading due to Li loss, electrolyte depletion, and electrolyte side reactions was minimized, as described in section 1.2.

The first XPD study, presented in section 3.1.1, was performed at the Diamond Light Source synchrotron (I11 beamline, UK). The advantages of using a synchrotron source rather than a lab instrument include a high X-ray intensity leading to a superior signal-to-noise ratio and faster acquisition times, but also a better angular resolution and a tunable wavelength. We aimed at monitoring structural changes such as the lattice parameters, but also the Li-Ni mixing over the course of cycling by collecting XPDs in regular intervals in charged and discharged state. As shown in section 3.1.1, the cells were cycled over 1000 cycles at room temperature. The XPDs were measured in-situ during rest phases in charged and discharged state, with an acquisition time of ≈ 5 minutes and a wavelength of ≈ 0.494 Å. Since the X-ray beam penetrates the whole cell stack, not only the NCM-811 phase contributes to the resulting diffractogram, but also the graphite anode, the aluminum and copper current collectors, and the aluminum of the pouch cell envelope. The electrolyte

moreover gives rise to a complex background. The advantages of the synchrotron source are hence somewhat compromised by the disadvantages of the in-situ measurement configuration. Additionally, the I11 beamline operates with a 2D Pixium area detector to achieve fast acquisition times for dynamic experiments. For our experiments however, the measurement time was not crucial, since the measurements were conducted during OCV rest phases. By using an area detector, however, the resolution offered by the synchrotron source cannot be exploited. In the course of this synchrotron XPD study, we were thus not able to refine the sensitive Li-Ni mixing parameter from the in-situ data sets and could only monitor the evolution of the lattice parameters.

After 1000 cycles, the cells were stopped and ex-situ XPDs were collected with the harvested CAM at our in-house diffractometer (STOE, Germany). Using Mo-K α_1 radiation (0.7093 Å), the wavelength is sufficiently short to ensure a good resolution (one data point every 0.015°/2 θ), and by measuring XPDs over night (\approx 14 h), a reasonably good signal-to-noise ratio was achieved. The CAM was harvested under inert conditions and filled into 0.3 mm borosilicate capillaries. This means that no reflections from the anode or the current collectors contribute to the diffractograms, which improves the refinement quality of the data. From these measurements, the Li-Ni mixing could be determined. In addition, we conducted in-situ and operando experiments with NCM-811/Li half-cells at our in-house diffractometer to measure the lattice parameters as a function of SOC. For the in-situ experiments, the cells were (dis-)charged in defined SOC steps and the XPD data were collected during intermittent OCV phases. For the operando experiments, the cells were continuously (dis-)charged and only selected reflections were analyzed (i.e., the 003 and 110 reflections). By limiting the measurement to a small part of the 2 θ range, a sufficient time resolution could be ensured (\approx 8 minutes/diffractogram). Further experimental details are described in the supporting information in section 3.1.1. With the resulting $c/a=f(x_{\text{Li}})$ calibration curve, the lattice parameter changes obtained from the synchrotron data could be interpreted in terms of an effective SOC window shrinkage, as explained in section 3.1.1.

Based on the experiences with the different X-ray sources, our follow-up XPD study was performed using solely the in-house instrument (Mo-K α_1). For this purpose, various NCM-811/pre-lithiated graphite pouch cells were cycled at 45°C, and one cell was stopped every 150 cycles in discharged state (i.e., one cell cycled to 150 cycles, one cell for 300 cycles, etc.). The CAM harvested from a given cathode electrode was filled into a capillary and an ex-situ XPD was collected. Furthermore, from the pouch cell cathode, a smaller electrode was punched out and used as cathode in a coin cell. In the coin cell, the NCM-811 was charged and subsequently another XPD was measured from the CAM harvested in the charged state. In this way, XPD data from the discharged and charged state could be collected ex-situ at our in-house instrument every 150 cycles. As discussed in section 3.1.2, with this ex-situ approach it was also possible to conduct other complementary measurements to monitor different NCM properties every 150 cycles, such as the CAM surface by BET or the cathode impedance by impedance spectroscopy.

After conducting X-ray diffraction studies on a synchrotron and a lab instrument, we have gained valuable experience with both approaches. The advantages and disadvantages of both methods will be summarized in the following. The advantages of the synchrotron include the high X-ray intensity and the high angular resolution allowing for a good signal-to-noise ratio, which is especially beneficial for our in-situ experiments with pouch-cells with all the side phases and background signals from the pouch foil material, electrolyte, graphite anode, binder etc. Moreover, using a synchrotron with an area detector allows for fast data collection (≈ 5 minutes), which minimizes the beam damage of the sample and is useful for monitoring dynamic processes. In contrast, the use of the lab instrument required long acquisition times (≈ 45 minutes) in order to reach a sufficient signal-to-noise ratio. The monitoring of dynamic processes was only possible by collecting diffraction data of selected reflections instead of the full pattern. Moreover, the use of synchrotron radiation during in-situ experiments means that the sample is not prone to unintended manipulation by any sort of harvesting or sample preparation, as is the case for the capillary measurements at our in-house instrument. The design of the experiment at the synchrotron also allows for a continuous monitoring of the same cell while for the lab experiments, a number of identical cells is required since the CAM needs to be harvested from the cells to be analyzed in capillaries. On the

other hand, the experiments at the synchrotron source require severely more effort (proposal for beamtime, transportation of cells to the beamline, design of experiment depends on schedule of the beamline, etc.). Long-term experiments at a synchrotron source are also less flexible meaning that the researcher can hardly interfere if something unexpected happens during the long-term cycling. In our case, one cell showed a connection problem during the long-term study at the synchrotron and it was not possible for us to make a remote diagnosis of the source of the problem. Another disadvantage of conducting a study at a synchrotron source is that only a limited number of cells can be analyzed while at the in-house instrument numerous cells can be investigated. Thereby, the experimental plan of the study is also more flexible in-house regarding new questions, which might arise during such a long-term study, that can be addressed readily using the in-house instrument without the need to apply for a new beamtime at a synchrotron. Another advantage of the use of numerous cells with the in-house instrument is that complementary experiments can be conducted in regular intervals with the same CAM, which was used for the diffraction. In contrast, for a synchrotron study such complementary methods are only possible at beginning of test and end of test but not during the course of the long-term cycling.

In summary, we learnt a lot from the in-situ study at the synchrotron, which enabled us to design the follow-up study at 45°C, using the ex-situ approach. Key learnings from the synchrotron study include: (i) a lot can be gained from the lattice parameters of NCM in combination with electrochemical data and for this purpose, a synchrotron is not necessarily required; (ii) complementary experiments (e.g., impedance, BET) in regular intervals add valuable information to the diffraction data but are not possible at a synchrotron source; (iii) an area detector is not suitable for answering research questions, such as the cation mixing in NCM, due to its low resolution compared to slower angle dispersive or angle scanning detectors,¹¹⁴ commonly used at synchrotron beamlines. Based on these learnings, we conclude that diffraction experiments in the OCV rest phase can be conducted at our lab instrument while dynamic experiments (e.g., under current flow or when initial relaxation processes are of interest) should be conducted at a synchrotron source with an area detector. Furthermore, if experiments are conducted at a

synchrotron, one could complement the results with other experiments (e.g., impedance, BET, etc.) using identical cells cycled in-house, where the CAM can be harvested in regular intervals.

2.2 Electrochemical impedance spectroscopy

Throughout this thesis, potentiometric electrochemical impedance spectroscopy (PEIS) was applied to analyze the various resistances within lithium ion battery cells. For the long-term study with NCM-811 presented in section 3.1.1, a gold-wire micro-reference electrode¹¹⁵ was used in a T-cell setup to investigate the impedance of the NCM-811 cathode individually. For this purpose, a circular electrode was punched out of the cathode harvested after 1000 cycles and transferred to a T-cell. The impedance analysis was hence limited to the harvested CAM at the end of life and to a new electrode sample prepared for the beginning of test. This was improved for the follow-up study at 45°C, where several identical cells were cycled with the same protocol and one cell was stopped every 150 cycles (see Results section 3.1.2). Based on the PEIS experiments in these regular intervals, the impedance of the cathode could be monitored over the course of cycling. In this case, we used a coin cell setup with a Li counter-electrode covered by a free-standing graphite (FSG), as described by Morasch et al.¹¹⁶ The use of such a Li/FSG composite electrode results in a comparably small impedance contribution for the counter-electrode (imaginary and real part $<5 \Omega \text{ cm}^2$). This means that the measured cell impedance is reasonably well approximated to correspond to that of the NCM-811 cathode.

In both studies, we used the following equivalent circuit to describe the impedance spectra: $R_{\text{HF}} + \text{TLM}[R_{\text{ion}}, R_{\text{CT}}/Q_{\text{CT}}] + R_{\text{contact}}/Q_{\text{contact}}$. This equivalent circuit contains the following elements: (i) R_{HF} , which is the high-frequency resistance of the cell; (ii) TLM, which is the transmission line model including the ionic resistance R_{ion} and an $R_{\text{CT}}/Q_{\text{CT}}$ parallel circuit element with the charge transfer resistance R_{CT} and a constant phase element Q_{CT} ; (iii) the $R_{\text{contact}}/Q_{\text{contact}}$ parallel circuit element with the contact resistance between the cathode electrode and the aluminum current collector, and the respective constant phase element. Fitting was performed with a MATLAB-based application ("EIS Breaker", © J. Landesfeind) based on the `fminsearch` MATLAB function using a Nelder-Mead simplex algorithm and modulus weighing. The assignment of the fitting parameters to the semicircles was verified by a rough order-of-magnitude estimation of the double layer capacitances (C_{calc})

related to the charge transfer and to the contact resistance (R), using the frequency at the maximum of the semicircle (f_{max}):^{101,117}

$$C_{calc} = \frac{1}{R 2\pi f_{max}} \quad (2.2)$$

When the calculated capacitances are normalized to the proper interface, they should be on the order of 10 $\mu\text{F}/\text{cm}^2$.¹¹⁷ Further experimental details are explained in the supporting information in section 3.1.1 and in both experimental parts in section 3.1.

For the investigation of the Li- and Mn-rich NCMs (LMR-NCMs), coin cells with a Li counter-electrode were used. The resulting impedance spectra hence contain the contribution of the Li electrode as well as of the LMR-NCM cathode. The aim of these PEIS experiments was the quantification of heat sources in LMR-NCM/Li cells. This is why the impedance was conducted in the same half-cell setup as used for the calorimetric measurements. The resulting spectra were fitted with the simplified equivalent circuit $R^* + \text{TLM}[R_{ion}, R_{CT}/Q_{CT}]$. Hereby, R^* includes the high frequency resistance of the cell but also the impedance of the Li anode and the contact resistance of the cathode. This simplified equivalent circuit is applicable because the aim of these studies is the quantification of different heat sources, i.e., the contribution of the cathode electrode as a function of SOC. The impedance data were used to explain the results from overpotential analysis, where the difference between the voltage on load and that under open-circuit conditions was measured. For a more detailed discussion of these measurements, the reader is referred to section 3.2.2 and 3.3.3.

2.3 Isothermal micro-calorimetry

The focus of the studies presented in section 3.2 is on the LMR-NCM material. It shows a unique hysteresis in the open-circuit voltage (OCV), resulting in a reduced electrical energy round-trip efficiency. Since the corresponding energy loss is expected as waste heat, we aimed at quantifying the heat generated during cycling of cells with LMR-NCM cathodes using isothermal micro-calorimetry (IMC). Equation (2.3) describes the different sources of heat in a battery with an LMR-NCM cathode:

$$\begin{aligned}\dot{Q} &= I \cdot (E_{load} - E_{OC}) + I \cdot (E_{OC} - E_{eq}) + T \cdot I \cdot \frac{\partial E_{OC}}{\partial T} + \dot{Q}_{par} \\ &= \dot{Q}_{irrev} + \dot{Q}_{hys} + \dot{Q}_{rev} + \dot{Q}_{par}\end{aligned}\quad (2.3)$$

The irreversible heat (\dot{Q}_{irrev}) originates from polarization processes causing the measured cell potential under load (E_{load}) to deviate from the open-circuit potential (E_{OC}). \dot{Q}_{irrev} is determined by impedance spectroscopy and intermittent cycling, as explained in section 3.2.2. The reversible heat (\dot{Q}_{rev}) is typically calculated from entropy measurements, as discussed in section 2.4. The parasitic heat (\dot{Q}_{par}) refers to all sources of heat caused by any side or parasitic reactions, such as electrolyte decomposition. There is no direct method to measure \dot{Q}_{par} during cycling, but its contribution is estimated to be negligible for the studies presented in section 3.2.2 and 3.2.3. Using IMC, the sum of all sources of heat is measured as a function of SOC (\dot{Q}). For materials with a pronounced OCV hysteresis such as LMR-NCM, another heat term needs to be added, namely the heat due to the OCV hysteresis (\dot{Q}_{hys}). For its description, a similar situation to that of the irreversible heat can be created by establishing a potential difference between the open-circuit potential (E_{OC}) and the (hypothetical) equilibrium potential (E_{eq}), which, however, is not measurable. For an electrode material with no OCV hysteresis, $E_{OC} = E_{eq}$ and hence $\dot{Q}_{hys} = 0$. Note that the potential difference building the basis of \dot{Q}_{irrev} is a function of the applied current ($\Delta E(I) = E_{load}(I) - E_{OC}$), because E_{load} depends on the current. \dot{Q}_{irrev} thus becomes very small when the current is decreased. In contrast, for \dot{Q}_{hys} , the potential difference $\Delta E = E_{OC} - E_{eq}$ is independent of the current, since the OCV hysteresis is a material

specific property. It hence gives a significant contribution even at low currents. \dot{Q}_{hys} is the sought quantity for LMR-NCM.

Using IMC, the sum of all sources of heat is measured as a function of SOC. For this purpose, the calorimeter setup has to meet certain requirements. They are described in the following and are listed in Table 2.1, where different instruments are compared. An important criterion is how much of the expected heat can be detected by the IMC. This is a measure of the sensitivity of the instrument. Ideally, the ratio between measured and expected heat should be 100%. Values below that can be explained by a non-ideal setup causing a loss of heat, e.g., through the cables connecting the battery cell, so that the generated heat cannot be quantified accurately by the detector. A ratio above 100% indicates that there are additional sources of heat (e.g., the resistance of the cables or the contacting of the cell) which are not reflected in the electrochemical data. This is possible if a 4-probe measurement setup is used, where there are two power cables and two sensing cables. The resistance of the power cables does not lead to an overpotential observable in the potential profile of the cell, since the latter is measured by the sensing cables. On the other hand, the sensitivity and precision of the detector also determine how accurately the expected heat can be measured, and values both above and below 100% can be caused by the detector. Another aspect is the stability of the baseline. A pronounced drift of the baseline signal over the course of the experiment affects the accuracy of the measurement and complicates the integration of the signal. A fluctuating baseline signal moreover indicates that temperature changes in the surrounding of the calorimeter affect the experiment and hence means that the measurement is not isothermal. Yet another factor is the signal-to-noise ratio, which determines the resolution of features in the heat flow curves. It should at least be high enough to enable a clear differentiation between measured heat flow and the baseline.

For the work in this thesis (see Results sections 3.2.2 and 3.2.3), a suitable calorimeter had to be selected and purchased. Table 2.1 gives an overview of the various calorimeter instruments tested with regards to the above described requirements. For the implementation of calorimetric measurements, we also needed to evaluate which cell type is required and whether we can build it in our

labs and how the contacting of the cell is ensured inside the calorimeter. Figure 2.2 shows three exemplary heat flow curves normalized to the active material mass recorded for coin cells with LMR-NCM cathodes at a C-rate of C/10 and 25°C.

Table 2.1: Comparison of different calorimeter setups with regards to the required cell type, the ratio of measured to expected heat, the drift of the baseline, the signal-to-noise ratio, and the contacting of the cell. The rating of the various parameters is illustrated by the black circles, where five filled circles is equal to the best rating. Calorimeter A: EV-ARC (THT); B: C80 (Setaram); C: MMC 274 Nexus® (Netzsch); D: μ BC (THT); E: TAM IV Micro-calorimeter (TA Instruments).

	Cell type	$\frac{\text{measured heat}}{\text{expected heat}}$	Baseline drift $\mu\text{W}/(\text{gh})$	Signal/noise ratio	Contacting of the cell
A	pouch-cell	●●○○○ 55-82%	●●●○○ ≈ 7	●●○○○	●●●●○ no compression
B	CR1020 coin cell	●●●○○ 65-95%	●○○○○ ≈ 140	●●●○○	●○○○○ cables stuck to the cell
C	CR2032 coin cell	●●●○○ 93-120%	●●○○○ <30	●○○○○	●●○○○ current flows through Peltier elements
D	CR2032 coin cell	●○○○○ 41-78%	●○○○○ $\approx 45 - 3000$ (severe fluctuation)	●○○○○ only 1C possible	not known
E	CR2032 coin cell	●●●●● 97-104%	●●●●● <2	●●●●●	●●●●○ custom-made holder

Instrument A (EV-ARC from THT) is designed to measure the heat evolution of large-format cells during use and abuse tests.¹¹⁸ For this purpose, we built multi-layer pouch cells with a capacity of ≈ 400 mAh. The cells were connected via crocodile clamps. The generated heat was measured using thermocouples and heat flow sensors attached to the pouch cell surface. The cell was placed inside a steel container (the so-called bomb) with a large void volume. The calorimeter was operated in a quasi-isothermal mode by keeping the temperature of the bomb constant. The advantage of using large-format cells is that the amplitude of the generated heat is comparably large, since it scales with the amount of active material. This was however outweighed by the use of such an inaccurate measurement setup with a large void volume and an insufficient temperature control. The detection of heat with a couple of temperature sensors attached to the cell surface moreover deteriorates the signal quality and significance. As shown in Table 2.1 (first row), the ratio between measured and observed heat is

consequently insufficient, with values between 55% and 82% (depending on the applied C-rate). Moreover, a compression of the pouch-cells was not possible in this setup, which affects the cycling performance of the cells, especially at high C-rates. The signal-to-noise ratio is also rather poor even though the baseline was relatively stable. This was achieved by placing the calorimeter in an isolated room, which was not entered until the end of the experiment to avoid a fluctuation of the temperature around the calorimeter. Figure 2.2 contains no data from these experiments because, in contrast to the other calorimeters, the measured quantity here was the temperature and not directly the heat flow.

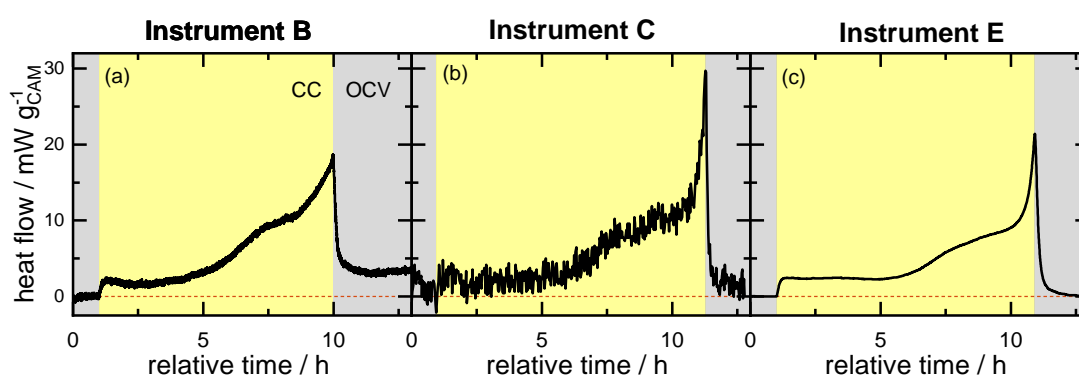


Figure 2.2: Comparison of measurement results from the calorimeters B, C, and E. The mass-normalized heat flow is shown as a function of time for coin cells with LMR-NCM cathodes discharged at C/10 and 25°C. The constant-current phases (CC) with heat generation from the cell are highlighted in yellow, the subsequent open-circuit phases (OCV) in gray. The baseline determined prior to the CC-phase is indicated by the dashed orange line.

For the experiments with instrument B (C80 from Setaram), small coin cells with a diameter of 10 mm were required because the measurement chamber is very narrow. Because of the special cell size, we could not build the coin cells in-house but had to make them in the lab of the cooperation partner. Since the calorimeter was commercialized for use with powder or liquid samples filled into ampoules, there was no cell holder available for contacting of the cells. Instead, cables were attached to the cell using conductive varnish. Depending on the C-rate, up to $\approx 95\%$ of the expected heat were detected by the calorimeter. For small currents, however, only $\approx 65\%$ were observed. The signal-to-noise ratio was acceptable, as can be seen in Figure 2.2a. The biggest disadvantage of this instrument is that it can only ensure isothermal conditions if the measurement temperature is chosen to be well above room temperature. Otherwise, a climate chamber would be required in which the

calorimeter is placed. Still, even with the climate chamber the baseline drift of this setup is unacceptable (see Table 2.1). Figure 2.2a shows that the heat signal after a constant-current (CC) discharge does not approach the baseline, but instead stabilizes at a new value.

Instrument C (MMC 274 Nexus[®] from Netzsch) is sold with a coin cell holder offering space for two CR2032 cells (sample and reference cell). The cells are contacted with metal clips pressing them onto Peltier elements measuring the generated heat flow. This means that the current passing through the cell, however, also flows through the sensitive Peltier elements, which potentially affects the signal detection. The measured heat was mostly above the expected value, indicating that either the Peltier elements were influenced by the current from the cell or other sources of heat (e.g., resistance of the cables) contributed to the heat signal but were not observed in the electrochemical data, because a 4-probe measurement setup was used. In addition to the poor measurement accuracy, also the signal-to-noise ratio was very low, as shown in Figure 2.2b.

For the tests with instrument D (μ BC from THT), CR2032 cells built in-house were shipped to a laboratory of the producer in England. This is why we could not examine the calorimeter setup ourselves. Based on our previous measurement results, the researchers on-site decided to only measure the heat evolution at the highest C-rate of 1C, since they expected the heat flow at lower C-rates to be too small to be accurately quantified. Table 2.1 shows that even at the high C-rate, the sensitivity of the instrument is not sufficient to measure the expected heat flow. In addition, there was a severe fluctuation of the baseline and the signal-to-noise ratio was comparably poor considering the high signal amplitudes at 1C. The measurement results are not shown in Figure 2.2, because the absolute heat flow signal at 1C is not comparable to the other data sets recorded at C/10.

Instrument E (TAM IV Micro-calorimeter from TA Instruments) was already used by other research groups investigating the heat generation of batteries.¹¹⁹⁻¹²¹ There is a micro-calorimeter available that allows for the passing of cables from the outside into the measurement position. With a custom-made coin cell holder, CR2032 coin cells can be contacted and positioned inside the micro-calorimeter. At the reference side, a dummy cell with a similar heat capacity and heat conductance

but no electrochemically active materials is placed. Table 2.1 shows that this calorimeter offers the highest sensitivity in comparison to all other instruments tested. The exemplary data set in Figure 2.2c moreover illustrates the superior signal-to-noise ratio. To ensure a stable baseline signal, the background signal is measured prior to the insertion of the cell and subtracted from the data. After insertion of the cell, waiting times of several hours are typically necessary until the signal approaches the previously calibrated zero value. This procedure leads to the very low baseline drift shown in Table 2.1.

The measurements at instrument E presented in section 3.2.2 were conducted in cooperation with Dr. Alexander Hoefling from the Helmholtz Institute Ulm, using his optimized measurement setup. Subsequently, an identical calorimeter was installed at TUM in a cooperation project with Prof. Jossen's Chair for Electrical Energy Storage. We continuously strive to improve the cell holder for our in-house instrument, which will be subject to a future publication.¹²² Figure 2.3 shows the main components of the micro-calorimeter measuring assembly. The measurements discussed in section 3.2.3 were conducted at this in-house instrument using an in-house designed coin cell holder made of aluminum. The cell was connected to a Biologic potentiostat (SP200, BioLogic, France) by special Cu-P bronze cables (Duo-Twist wire WDT-36-25, 36 AWG, Lakeshore, USA) in a 4-point probe measurement setup. The cables are very thin and offer the advantage of a low thermal conductivity, which is important to minimize the loss of heat generated at the cell through the connected cables. At the same time, the material of the cables still provides a sufficient electrical conductivity. Further details of the setup will soon be described in a publication by Kunz and Berg et al.¹²² The experimental approach is furthermore explained in section 3.2.3. The heat balance considering the various sources of heat during cycling of LMR-NCM/Li half-cells is explained in detail in the theoretical part of the publications in section 3.2.2 and 3.2.3.

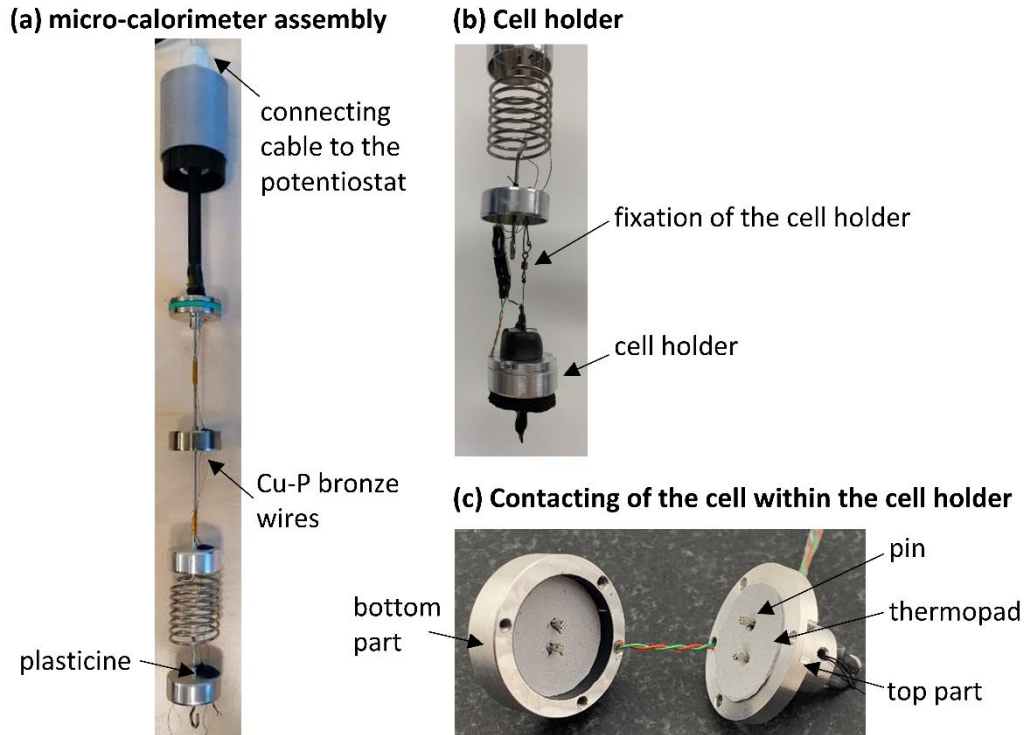


Figure 2.3: Pictures of the micro-calorimeter assembly used for measurements in section 3.2.3, with the whole assembly in (a), the custom-made cell holder in (b), and the opened cell holder in (c). A detailed discussion of the setup will be published by Kunz and Berg et al.¹²²

The following section summarizes the mathematical derivation and physical description of the heat flow measurement by a TAMIV instrument according to the PhD thesis of L. E. Downie¹²³ and the material provided by TA instruments¹²⁴. For the isothermal calorimeter used for the studies presented in section 3.2.2 and section 3.2.3, the heat flow produced by the sample (\dot{Q}_s) is given by:

$$\dot{Q}_s = \Phi + C_s \left(\frac{dT_s}{dt} \right) \quad (2.4)$$

Here, Φ is the rate of heat exchange between the cell and its surrounding, and the second term on the right hand side is the rate of heat accumulation with the heat capacity of the sample (C_s) and the sample temperature (T_s). The rate of heat exchange is given by

$$\Phi = k_s \Delta T_s \quad (2.5)$$

ΔT_s is the difference between the sample and the environment temperature (i.e., the temperature of the oil bath of the calorimeter), and k_s is the sample heat conductance. It can be expressed by equation (2.6), where τ_s is the time constant of the sample system and C_s is the heat capacity of the sample.

$$k_s = \frac{C_s}{\tau_s} \quad (2.6)$$

The calorimeter measures the heat flow using a number of thermopiles arranged around the sample. The temperature gradient ΔT_s between the sample and the environment (i.e., the isothermal oil bath) creates a voltage difference (V_s) at the thermopiles. This correlation is described by the Seebeck coefficient (S_b) of the thermopiles:

$$S_b = \frac{V_s}{\Delta T_s} \quad (2.7)$$

Consequently, the heat flow can be expressed by combining the equations above, leading to the Tian-Calvet equation:

$$\dot{Q}_s = \epsilon_s \left(V_s + \tau_s \frac{dV_s}{dt} \right) \quad (2.8)$$

Here, ϵ_s is the calibration constant, which is given by

$$\epsilon_s = \frac{C_s}{S_b \cdot \tau_s} \quad (2.9)$$

The time constant, τ_s , is determined by a so-called General Performance Test where a known heat flow signal is applied on the sample side by external heaters and the time delay is measured until $1 - 1/e$ ($\approx 63.2\%$) of the final value is reached. For the IMC used here, the time constant is 67 s on average.

The here used IMC is a twin system with a sample and a reference side, which decreases the signal noise.¹²⁵ For the reference system, the heat flow \dot{Q}_r can be derived as shown above, leading to equation (2.10), where ϵ_r , V_r , and τ_r are the calibration constant, voltage difference and time constant for the reference side, respectively.

$$\dot{Q}_r = \epsilon_r \left(V_r + \tau_r \frac{dV_r}{dt} \right) \quad (2.10)$$

Since there is no heat generation in the reference cell, \dot{Q}_r is equal to zero. The subtraction of equation (2.10) from equation (2.8) hence gives the heat flow of the sample measured in the twin system:

$$\dot{Q} = \epsilon_s \left(V_s + \tau_s \frac{dV_s}{dt} \right) - \epsilon_r \left(V_r + \tau_r \frac{dV_r}{dt} \right) \quad (2.11)$$

For the evaluation of the data, it is assumed that the heat conductance and the heat capacity of the sample and the reference system are the same, so that the calibration constant is given by $\varepsilon_s = \varepsilon_r = \varepsilon$ and the time constant by $\tau_s = \tau_r = \tau$. Since the cell holders at both sides are identical, it is important that the heat conductance and capacity of the reference cell used are as close to that of the sample cell as possible. For this purpose, we used a coin cell with a lithium electrode, the same amount of spacers, separators, and a spring, but without electrolyte and cathode at the reference side. Equation (2.11) thus simplifies to

$$\dot{Q} = \varepsilon \left[(V_s - V_r) + \tau \frac{d(V_s - V_r)}{dt} \right] \quad (2.12)$$

The second term on the right hand side of equation (2.12) is the so-called Tian correction, which can be applied to consider the effect of the time delay of the calorimeter on the measured heat flow. This is only necessary for rapid, dynamic processes and requires a special form of internal calibration prior to the actual measurement, the so-called dynamic calibration. For the measurements conducted throughout this thesis, this correction was not applied and hence the measured heat flow is given by:

$$\dot{Q} = \varepsilon \cdot (V_s - V_r) \quad (2.13)$$

The output signal of the instrument is given in units of Watt and measured as a function of time, with a resolution of one data point every second. In order to convert the time into an SOC axis, a constant current is applied to the cell. In that manner, a certain charge/discharge capacity can be directly converted into units of time. The time delay of the heat measurement, however, introduces an uncertainty when trying to relate the heat flow to a given SOC. For this purpose, the effective time constant of the calorimeter was determined. A detailed description will be published soon.¹²² Generally, the time delay can be determined by applying a defined current to a dummy cell with a precisely known resistor. The current is applied in form of a square wave signal, which should give rise to a heat flow following the same signal shape. The observed signal can be described by a dynamical 2nd order system (PT2 system) with two time constants (T1 = 57 s and

$T_2 = 131$ s). The time difference until the measured heat flow reaches 99% of the expected value is ≈ 682 s for the study presented in section 3.2.3.

The calorimeter was calibrated in regular intervals (every ≈ 10 -14 days) to ensure comparability of the measurement results. For this purpose, the built-in so-called “gain calibration” function was used, where a pulse of $200 \mu\text{W}$ is applied to the sample side for 1 h. The calibration was started after reaching the internally defined “high signal stability”. For the gain calibration, two dummy cells consisting of identical cell parts (housing, spring, 1 mm spacer), 2 glass-fiber separators, and a piece of Li with the same dimensions as in a real cell were placed in the reference and the sample side, respectively. With the dummy cells, the heat capacity and heat conductance of a real cell are mimicked while ensuring that no (electro-)chemical reactions take place, which might generate heat.

2.4 Entropy measurements

As mentioned in the previous chapter and shown in equation (2.14), the partial molar entropy of the cell ($\frac{dS}{d\xi}(\xi)$) needs to be known as a function of SOC in order to calculate the reversible heat (Q_{rev}). We define here the reaction turnover parameter ξ to describe the progress of the charging/discharging reaction. It is zero for no reaction (fully lithiated CAM) and $1+x$ for a complete delithiation of the LMR-NCM material according to the nomenclature $\text{Li}_{1+x}\text{M}_{1-x}\text{O}_2$ explained in section 1.3. Theoretical considerations and derivations of the equations regarding the partial molar entropy are discussed in detail in the article presented in section 3.2.1.

$$Q_{\text{rev}} = \int T \cdot \left(\frac{dS}{d\xi}(\xi) \right) \cdot d\xi \quad (2.14)$$

The partial molar entropy of a battery cell is typically determined by measuring the OCV (E_{OC}) as a function of temperature (T). With the resulting temperature-dependent OCV (TD-OCV), $\frac{dS}{d\xi}(\xi)$ is calculated according to equation (2.15), where n is the molar amount of charge transported when ξ changes by one unit and F is the Faraday constant.

$$\frac{dS}{d\xi}(\xi) = -n \cdot F \cdot \frac{d}{dT} E_{OC}(\xi) \quad (2.15)$$

The TD-OCV needs to be measured at different SOCs during charge and discharge in order to obtain the partial molar entropy curve for both directions. A common method to determine the TD-OCV is the temperature step procedure. During OCV conditions, the temperature of the cell is changed and after giving the cell some time to equilibrate, the OCV is measured as a function of the applied temperature. By repeating this for a number of different temperatures, the TD-OCV is determined from the slope of the linear regression of the OCV vs. temperature data. In the article presented in section 3.2.1, it is discussed in detail, why this temperature step method is prone to errors that are mainly caused by the hereby encountered difficulty when trying to determine an accurate OCV value for each temperature.

To overcome these difficulties, we used a so-called temperature ramp method, which was only used by a few other research groups before.^{126–128} The methodical

approach and a comparison to the temperature step method are shown in section 3.2.1. For our entropy study, we used T-cells with LMR-NCM cathodes, Li anodes and a Li-RE. The potential of the LMR-NCM was monitored versus the Li-RE to ensure that Li plating/stripping do not contribute to the result. We used several identical cells, each charged or discharged to a certain SOC and allowed to rest in open-circuit conditions until the change of OCV with time was less than ≈ 0.2 mV/h. This typically took 100-200 h. The cells were then transferred to a temperature chamber (Espec LU114), which allows applying a linear temperature ramp. Starting at the initial cell temperature of 25°C, the temperature ramping commenced to 35°C and then to 5°C at a rate of 0.5 K/min. Three cycles of cooling to 5°C and heating to 35°C were conducted, followed by a final cooling step to 25°C. Based on the known temperature variation with time (0.5 K/min), the OCV variation measured as a function of time is translated into the TD-OCV. The advantages of the ramping method are described in section 3.2.1.

Since both anode and cathode contribute to the overall TD-OCV, we wanted to determine the contribution of Li in order to understand the contribution of LMR-NCM better. For this purpose, we built special pouch-cells with a U-shaped geometry, as shown in the Supporting Information in section 3.2.1. In the spatially non-isothermal cell setup, one side of the U-cell is exposed to temperature changes induced by a surrounding water bath, while the other side is kept at a constant temperature. With this approach, we determined the contribution of Li to the TD-OCV of the cell. It needs to be stressed (and it is also discussed in section 3.2.1) that in the spatially non-isothermal setup, the Soret effect and the Seebeck effect possibly influence the measurement result. The Seebeck effect describes the potential build-up due to a metal-metal thermocouple.¹²⁹⁻¹³¹ It is negligibly small for the materials used here (nickel tab). The Soret effect is caused by thermal diffusion and cannot be excluded. It is discussed in the article presented in section 3.2.1 why we estimate that it only gives a minor contribution to the spatially non-isothermal TD-OCV.

The initial motivation for determining the entropy of LMR-NCM was the calculation of the reversible heat. It will be explained in section 3.2.1, why this was not achievable for a whole cycle. For a CAM like LMR-NCM, the integration of $\frac{dS}{d\xi}(\xi)$ over

ξ according equation (2.14) is not possible for a whole charge/discharge cycle, because ξ is no unique descriptor of the (de-)lithiation processes in LMR-NCM. The fact that the charge follows a different pathway than the discharge as a function of SOC is well known for several LMR-NCM material properties, as mentioned in section 1.3. These hysteresis phenomena are observed for the OCV, the resistance¹⁰¹, the lattice parameters^{100,104}, and also the partial molar entropy¹³², which indicate that the (de-)lithiation follows metastable pathways away from thermodynamic equilibrium. The integration of $\frac{dS}{d\xi}(\xi)$ over ξ – although mathematically possible – would not lead to physically meaningful values when a complete cycle is considered. A detailed discussion can be found in section 3.2.1.

2.5 Material Characterization

In addition to the methods described before, further experimental techniques were used in this PhD thesis. BET physisorption measurements were deployed for the determination of the surface area of the active materials examined in section 3.1. We used nitrogen and krypton as gas adsorbates, whereby krypton has the advantage of a lower saturation pressure and thus enables the analysis of lower surface area samples compared to nitrogen. For the samples harvested from cycled electrodes in section 3.1.2., we therefore exclusively used krypton physisorption. Prior to the measurement, the samples were washed to remove residuals from the electrolyte.⁸⁵

In order to determine the exact composition of the NCM-811 material studied in section 3.1, the active material was sent to the Mikroanalytisches Labor Pascher (Remagen, Germany) for elemental analysis. After dissolving the powder by pressurized acid digestion in aqua regia, the mass fractions of Li, Ni, Co and Mn were quantified by inductively coupled plasma atomic emission spectroscopy (ICP-AES).

The morphology of the NCM-811 particles in section 3.1 was evaluated by cross-sectional scanning electron microscopy (SEM). The SEM measurements were conducted in cooperation with Katia Rodewald from the Wacker-Chair of Macromolecular Chemistry at TUM, using a JEOL scanning electron microscope (JSM-7500F, JEOL, Japan) in backscattering mode at an accelerating voltage of 5 kV. To further analyze the structure of the NCM-811 particles, high angle annular dark field scanning transmission electron microscopy (HAADF-STEM) images were collected at the Competence Center Material Physics of BASF SE. For this purpose, the samples were prepared by focused ion beam (FIB) milling using a Helios G4 CX dualbeam machine (Thermo Fischer Scientific, USA). Subsequently, the samples were imaged at 300 keV by HAADF-STEM using a Thermo Fisher Themis Z 3.1 microscope.

To analyze the surface of the NCM-811 particles before and after cycling, X-ray photo-electron spectroscopy (XPS) measurements were conducted with a monochromatic Al K_{α} source (1486.6 eV) using an Axis Supra system (Kratos, UK) with an operating pressure of $2 \cdot 10^{-8}$ Torr. XPS spectra were collected with

focus on the O 1s region. Fitting was done with a mixture of Lorentzian and Gaussian shape function and a Shirley background. The results are shown in section 3.1.1.

3 Results

This chapter contains the published work. The manuscript which is to be submitted soon is shown in the Appendix. Section 3.1. presents the results of long-term cycling studies with cells using Ni-rich NCM-811 as cathodes. The aim of these studies was the investigation of capacity fading mechanisms in Ni-rich NCMs at ambient (section 3.1.1) and elevated temperatures (section 3.1.2). For this purpose, a variety of different analysis methods was combined with X-ray diffraction as the key method in both studies. While we used a rather complicated in-situ measurement approach relying on synchrotron radiation during the first study at ambient temperatures (section 3.1.1), we designed the cycling stability study at elevated temperatures in a way that allowed ex-situ analysis at our in-house diffractometer (section 3.1.2).

In section 3.2, the focus is on Li- and Mn-rich NCM (LMR-NCM) and particularly on the investigation of the hysteresis phenomena exhibited by this type of CAM. The main goal was the quantification of the waste heat associated with the hysteresis of the open-circuit voltage. This analysis was conducted using isothermal micro-calorimetry (section 3.2.2). In order to analyze the heat flow generated by cells with LMR-NCM cathodes, a quantification of the different sources of heat was required. Measurements of the entropy in LMR-NCM/Li half-cells were initially conducted with the aim of determining the reversible heat. However, the entropy in LMR-NCM turned out to be more complex, and a translation of the entropy measurement data into a physically meaningful value for the reversible heat was not possible (section 3.2.1). Since LMR-NCM shows a unique voltage curve during the first charge that is associated with irreversible structural rearrangements, another isothermal micro-calorimetry study was conducted to investigate the waste heat generated during the first activation cycle (section 3.2.3).

3.1 Capacity fading mechanisms of Ni-rich layered oxides during long-term cycling

3.1.1 In-situ X-ray study at ambient temperature

The article “Capacity Fading Mechanisms of NCM-811 Cathodes in Lithium-Ion Batteries Studied by X-ray Diffraction and Other Diagnostics” was submitted in September 2019 and published in November 2019 as an Editor’s choice publication in the peer-reviewed Journal of the Electrochemical Society. It is available as an “open access” article under the terms of the Creative Commons Attribution Non-Commercial No Derivates 4.0 License. The permanent web link can be found under: <https://iopscience.iop.org/article/10.1149/2.0821915jes>. Benjamin Strehle presented the article at the 235th Meeting of the Electrochemical Society in Dallas, USA in May 2019 (Paper 559). To support the main article, additional information is provided in the Supporting information, including details about the diffraction and impedance experiments, and microscopy images of cathodes.

Ni-rich layered oxides such as NCM-811 are promising cathode active material candidates for use in LIBs in order to meet the requirements for a high energy density, e.g., for application in BEVs. By increasing the Ni content, the specific capacity at a given voltage is increased. This, however, comes at the price of a reduced structural, cycling and thermal stability.¹³³⁻¹³⁵ As outlined in section 1.2, several degradation phenomena are reported to occur when cycling Ni-rich NCMs, especially when charging to high SOCs (>80%). Figure 1.3 summarizes the three main contributions from the cathode: (i) oxygen release from surface-near regions^{53,69}, associated with the reconstruction of the surface and an increased charge-transfer resistance;^{53,69-71} (ii) particle cracking due to an anisotropic volume contraction at high SOCs, leading to a deterioration of electrical contact^{80-82,84} and to an increased surface area;^{82,85} (iii) irreversible migration of TMs from the TM-layer to the Li-layer (cation mixing), causing an increased cathode impedance^{86,87} and a reduced number of available Li sites. In addition to the degradation of the CAM, other reasons for capacity fading are possible, which are not directly occurring at the cathode. Those are highlighted by yellow arrows in Figure 1.3. By the design of the experiment, they were minimized or excluded as good as possible. A prelithiated graphite was used as anode to prevent loss of active material by the

ongoing SEI growth and to prevent Li plating by ensuring an anode potential well above 0 V vs. Li⁺/Li. By using a glass fiber separator, HF, which might be formed during electrolyte oxidation, is scavenged. A large electrolyte excess moreover mitigates electrolyte depletion. Thus, we focused quasi exclusively on the three main degradation phenomena occurring in the CAM: surface reconstruction, particle cracking, and cation mixing.

We investigated the capacity fading of NCM-811/graphite pouch cells cycled at C/2 (3.0-4.5 V vs. Li⁺/Li) at $\approx 22^\circ\text{C}$ for 1000 cycles by a combination of in-situ synchrotron X-ray powder diffraction (XPD), impedance spectroscopy (EIS) and X-ray photoelectron spectroscopy (XPS). Of the three main aging phenomena in CAMs, presented above, we found no evidence for particle cracking (no crystallographic side phase due to isolated particles) and observed a stable bulk structure with a constant cation mixing. We observed that a growing resistive surface layer is responsible for the capacity fading. On the one hand, this leads to an irreversible capacity loss due to the fraction of CAM lost for its formation. On the other hand, it causes an increasing charge-transfer resistance accompanied by a reversible capacity loss, since the associated overpotentials can be overcome at low C-rates. By establishing a quantitative correlation between the NCM-811 lattice parameters and the capacity fading, those two fading mechanisms were monitored over the course of cycling. At the end of test, harvested cathodes were used for EIS and XPS measurements, verifying the increasing resistance and the oxygen-depleted nature of the surface layer.

Author contributions

F.F. and B.S. conducted the electrochemical measurements and the diffraction experiments at the in-house laboratory diffractometer and evaluated all diffraction data. The beamline scientists K.K. and S.J.D. collected the synchrotron diffractograms. A.T.S.F. conducted the XPS measurements and evaluated the XPS data. C.E. provided the cathode electrode sheets and initiated the microscopy measurements. F.F. wrote the manuscript, which was edited by B.S. and H.A.G. All authors discussed the data. F.F. and B.S. contributed equally as co-shared first authors.



Capacity Fading Mechanisms of NCM-811 Cathodes in Lithium-Ion Batteries Studied by X-ray Diffraction and Other Diagnostics

Franziska Friedrich,^{1,*,*z} Benjamin Strehle,^{1,*,*} Anna T. S. Freiberg,^{1,*} Karin Kleiner,^{1,2} Sarah J. Day,² Christoph Erk,³ Michele Piana,^{1,**} and Hubert A. Gasteiger^{1,***}

¹Chair of Technical Electrochemistry, Department of Chemistry and Catalysis Research Center, Technical University of Munich, D-85748 Garching, Germany

²Harwell Science and Innovation Campus, Diamond Light Source, Didcot, Oxfordshire OX11 0DE, UK

³BASF SE Ludwigshafen, Lithium-Ion Battery Research, D-67056 Ludwigshafen, Germany

Ni-rich layered oxides, like NCM-811, are promising lithium-ion battery cathode materials for applications such as electric vehicles. However, pronounced capacity fading, especially at high voltages, still lead to a limited cycle life, whereby the underlying degradation mechanisms, e.g. whether they are detrimental reactions in the bulk or at the surface, are still controversially discussed. Here, we investigate the capacity fading of NCM-811/graphite full-cells over 1000 cycles by a combination of in situ synchrotron X-ray powder diffraction, impedance spectroscopy, and X-ray photoelectron spectroscopy. In order to focus on the NCM-811 material, we excluded Li loss at the anode by pre-lithiating the graphite. We were able to find a quantitative correlation between NCM-811 lattice parameters and capacity fading. Our results prove that there are no considerable changes in the bulk structure, which could be responsible for the observed $\approx 20\%$ capacity loss over the 1000 cycles. However, we identified the formation of a resistive surface layer, which is responsible for (i) an irreversible loss of capacity due to the material loss for its formation, and (ii) for a considerable impedance growth. Further evidence is provided that the surface layer is gradually formed around the primary NCM-811 particles.

© The Author(s) 2019. Published by ECS. This is an open access article distributed under the terms of the Creative Commons Attribution Non-Commercial No Derivatives 4.0 License (CC BY-NC-ND, <http://creativecommons.org/licenses/by-nc-nd/4.0/>), which permits non-commercial reuse, distribution, and reproduction in any medium, provided the original work is not changed in any way and is properly cited. For permission for commercial reuse, please email: oa@electrochem.org. [DOI: 10.1149/2.0821915jes]



Manuscript submitted September 3, 2019; revised manuscript received October 23, 2019. Published November 14, 2019. This was Paper 559 presented at the Dallas, Texas, Meeting of the Society, May 26–May 30, 2019.

Introduced by Sony in 1991, lithium-ion batteries (LIB) now dominate the battery market. However, a large-scale commercialization of battery electric vehicles (BEVs) and storage systems for renewable energy sources requires higher energy density, lower price, and longer cycle life, all of which critically depend on the cathode active material (CAM). Layered transition-metal oxides (LiTMO₂, where TM refers to one or a combination of the transition-metals (TMs) Ni, Co, and/or Mn, so-called NCMs) have been successfully used as CAMs in LIBs owing to their high specific capacity and high thermal stability. For example, the currently sold BMW i3 BEV uses NCM-111, which is expected to be replaced by NCM-622 in the near future in order to increase energy density and to reduce the cobalt content,¹ as the latter is problematic from a sustainability and geopolitical point of view.^{2–4} For these reasons, the more Ni-rich NCM variants (e.g., NCM-811) are the most promising candidates for future BEV applications, particularly as a higher Ni content leads to an increase in specific capacity at a given cut-off voltage compared to the less Ni-rich NCMs. However, large amounts of Ni in the CAM result in reduced structural, cycling and thermal stability.^{5–7} Especially at high potentials (>4 V vs. Li⁺/Li), structural instabilities such as bulk structural transformations^{6,8–10} and cation disorder (anti-site disorder between lithium and a transition-metal)¹¹ are reported to deteriorate the electrochemical performance of layered oxides. Some authors identified micro-strain and intergranular cracking as major causes for capacity fading in Ni-rich NCMs.^{12–14}

Other research activities focus on the structural evolution of the CAM surface, because it happens simultaneously with electrochemical cycling and determines the interaction between active material and the other components of the battery. Recent on-line electrochemical mass spectrometry (OEMS) and transmission electron microscopy (TEM) studies on NCMs and their over-lithiated variants (referred to as HE-

NCMs) report oxygen release at the particle surface^{15–18} accompanied by the formation of rock-salt and spinel-type surface layers.^{17–20} The low conductivity of these reconstructed phases is believed to cause an increased impedance on the cathode side and therefore contribute considerably to the capacity loss.^{18,20} Furthermore, the literature reports that transition-metal dissolution from the CAM deteriorates cycling performance in NCM/graphite full-cells. While on the cathode side active material is lost and the particle surface is reconstructed, the deposition of dissolved transition-metals on the anode side leads to enhanced electrolyte decomposition and an impedance rise.^{21–23}

In view of the required lifetime of 15 years and a cycle life over 1000 cycles for large-scale commercialization of LIBs for applications such as electric vehicles,^{24,25} it is essential to gain a fundamental understanding of the underlying mechanisms and their interrelations contributing to battery failure. As ex situ techniques may lead to deviations from the original state of the CAMs during electrode harvesting (e.g., changes in the state-of-charge (SOC) of the CAMs), much more authoritative information can be achieved by in situ and operando techniques, which allow for the characterization of electrode materials under real operating conditions. In situ X-ray powder diffraction (XPD) is a powerful analytical tool, which provides insights about bulk structural changes in cathode and anode over the course of cycling.

In the present study, detailed information on the fading mechanisms of NCM-811/graphite full-cells is obtained from the combination of X-ray powder diffraction, electrochemical impedance spectroscopy (EIS), rate tests, X-ray photoelectron spectroscopy (XPS) and scanning electron microscopy (SEM). To get unambiguous insights about the cathode active material fading mechanisms, the graphite counter-electrode was pre-lithiated to eliminate capacity fading from active lithium loss at the anode, while allowing for long-term cycling which is more problematic with a metallic lithium anode. In situ synchrotron X-ray powder diffraction experiments were conducted with pouch cells cycled over 1000 times at the long duration experiment (LDE) facility of beamline I11 at the Diamond Light Source, UK. The results from the LDE synchrotron XPD study were combined with operando XPD measurements using a lab diffractometer with a molybdenum

^zThese authors contributed equally to this work.

*Electrochemical Society Student Member.

**Electrochemical Society Member.

***Electrochemical Society Fellow.

^zE-mail: franziska.friedrich@tum.de

source to allow for a quantitative correlation between lattice parameter changes in the CAM and capacity losses, seeking to clarify whether bulk or surface related phenomena are responsible for capacity fading in NCM-811 CAMs.

Experimental

Battery assembly and cycling.—NCM-811 cathode electrode sheets (94 wt% BASF SE NCM-811, 2 wt% Timcal SFG6L graphite, 1 wt% Timcal C65 conductive carbon, 3 wt% Kynar PVDF binder HSV900) with a loading of ≈ 7.4 mg_{CAM}/cm² (corresponding to ≈ 1.5 mAh/cm² based on 200 mAh/g) and with a precise composition of Li_{1.01}Ni_{0.79}Co_{0.1}Mn_{0.1}O₂ (Mikroanalytisches Labor Pascher, Germany; see below) were provided by BASF SE (Germany). The pristine NCM-811 has a BET surface of ≈ 0.27 m²/g (determined by N₂ and Kr physisorption; see below). Cathodes with a geometric area of 9 cm² (30 × 30 mm²) were assembled in single layer pouch cells (with a 40 μm-thick Al layer) versus graphite counter-electrodes (CE, geometrically oversized, 33 × 33 mm²) in an argon-filled glove box (<0.1 ppm O₂ and H₂O, MBraun, Germany). These capacitively oversized graphite sheets (96 wt% active material, ≈ 7.1 mg_{Graphite}/cm², reversible capacity of ≈ 2.3 mAh/cm²) were also provided by BASF SE. To avoid capacity fading due to the loss of cyclable lithium caused by the formation of the solid electrolyte interphase (SEI) as well as during cycling, the graphite anodes were pre-lithiated to \approx Li_{0.3}C₆ (corresponding to ≈ 0.7 mAh/cm²) versus a lithium counter-electrode (450 μm, 99.9%, Rockwood Lithium) in LP57-2 electrolyte (1M LiPF₆ in EC:EMC = 3:7 by weight with 2% VC, BASF SE). In full-cells, two glass-fiber (GF) separators (36 × 36 mm², glass microfiber filter 691, VWR, Germany) with a projecting tab (10 × 10 mm²) were used with 700 μL LP57-2 electrolyte. A piece of lithium (10 × 5 mm²) positioned at the tab, was used as reference-electrode (RE). For a homogeneous compression of the cells at ≈ 2 bar, a homemade spring-loaded pouch cell holder with a 1.5 mm diameter hole as X-ray window was used, similar to that reported in our previous work.²⁶

The first two formation cycles were performed at constant current (CC) at a C-rate of C/10 (based on 200 mAh/g, which corresponds to a current density of ≈ 1.5 mA/cm² at a rate of 1C). Subsequent CC cycling was carried out at C/2 (without any constant voltage hold step). The cathode voltage window was 3.0–4.5 V vs. Li⁺/Li as controlled versus the Li-RE. All voltages in this work are reported vs. Li⁺/Li if not stated otherwise. Initial cycling (2 cycles at C/10 and 6 cycles at C/2) was performed at the Technical University of Munich (Maccor cyler, series 4000, USA) in a thermostatic chamber at 25°C. At the long duration experiments (LDE) facility of beamline I11 at the Diamond Light Source, two nominally identical pouch cells were cycled at C/2 and $\approx 22^\circ\text{C}$. The following nomenclature will be used: (i) “pristine” refers to the as-received NCM-811 powder or to pristine electrode sheets (i.e., never assembled into a battery); (ii) “fresh” corresponds to data collected within the first 10 cycles (including formation cycles); (iii) “begin-of-test” (BOT) refers to a NCM-811 cathode electrode, which has gone through formation (initial 2 cycles at C/10) and 16 cycles at C/2, corresponding to our first LDE XPD data point; and, (iv) “end-of-test” (EOT) refers to a cathode at the end of the LDE test, more specifically, it refers to the LDE XPD data collected in cycle 968 for cell 1 and in cycle 975 for cell 2, although the electrochemical cycling continued until cycle 995 for cell 1 and cycle 1003 for cell 2. Subsequently, further tests were conducted (e.g., C-rate test, relaxation test), which are also denominated as EOT.

For elemental analysis, inductively coupled plasma atomic emission spectroscopy (ICP-AES) was performed at the Mikroanalytisches Labor Pascher (Remagen, Germany), for which the CAM powder was dissolved by pressurized acid digestion in aqua regia. Considering surface impurities such as Li₂SO₄, Li₂CO₃, and transition-metal carbonates, which amount in total to ≈ 2.2 wt% of the sample, the composition of NCM-811 was determined as Li_{1.01}Ni_{0.79}Co_{0.10}Mn_{0.10}O₂, giving a theoretical capacity of 280 mAh/g_{NCM} or 274 mAh/g_{CAM} (including the surface impurities) for complete Li extraction. Note that capacity values are given for the total CAM powder and that we used

the latter notation throughout the entire work. The layered oxide is doped with ≈ 0.3 mol% Al (relative to the transition-metal amount), which is however not taken into further consideration.

X-ray powder diffraction measurements.—The in situ long-duration study of two nominally identical NCM-811/graphite pouch cells was performed using synchrotron X-ray powder diffraction on the LDE facility of beamline I11, Diamond Light Source; this will further on be referred to as “in situ S-XPD”. Patterns were collected with an exposure time of 5 minutes with an X-ray beam of ≈ 25 keV energy (≈ 0.494 Å) and a 2D Pixium area detector at a distance of ≈ 0.25 m. NIST Standard Reference Material CeO₂ (NIST SRM 674b) was measured before every sample data collection in order to refine the wavelength and detector distance and to evaluate the instrumental broadening. Detailed information on the LDE instrument is given by Murray et al.²⁷ The diffraction data were reduced with the software package DAWN^{28,29} and refined with the software package Topas (version 6).³⁰ XPD data collection was performed once a week at open circuit voltage (OCV) after 3–5 h of relaxation, both in the discharged state of the cathode at the lower cathode cut-off potential of 3.0 V vs. Li⁺/Li and, after subsequent charging, in the charged state of the cathode at the upper cathode cut-off potential of 4.5 V vs. Li⁺/Li. In this way, data collection was intended to be performed every ≈ 50 cycles at both SOC. However, due to a beam shut-down no XPD data could be collected for several months. The cycling protocol was nevertheless continued including OCV holds every week (i.e., every ≈ 50 cycles).

In addition, XPD experiments were conducted at our in-house STOE STADI P diffractometer (STOE, Germany) in transmission mode using Mo-K_{α1} radiation (0.7093 Å, 50 kV, 40 mA) and a Mythen 1K detector with one data point every 0.015°/2θ. For the determination of instrumental broadening, a silicon standard material (NIST SRM 640c) was used. In-house measurements comprise three different types of experiments for the pristine, fresh, and harvested EOT NCM-811 materials: (i) structural information from ex situ capillary data; (ii) determination of lattice parameters and of a calibration curve correlating the lithium content x_{Li} with the *c/a* lattice parameter ratio ($x_{\text{Li}} = f(c/a)$), which was performed both in operando (i.e., data collection during charge-discharge cycling) and in situ mode (i.e., data collection during intermediate OCV holds), and, (iii) relaxation tests of the (003) reflection upon the transition from CC charge to OCV. XPD experiments conducted with the Mo-K_{α1} laboratory XPD will further on be referred to as “L-XPD” experiments.

Ex situ L-XPD measurements were conducted over night (≈ 14 h) in 0.3 mm borosilicate capillaries in a 2θ range of 3–60° (with detector step size/step time of 0.15°/5 s). Cycled samples were scratched off the electrode and filled into the capillary in an argon-filled glove box.

In situ and operando L-XPD experiments were performed in pouch cells with a lithium counter-electrode and a relatively thin pouch foil (12 μm-thick Al layer). During the measurement, the cell was connected to a SP200 potentiostat (SP200, Biologic, France). For the determination of lattice parameters from the fresh NCM-811 electrode, all cycles were conducted at a C-rate of C/7.5. The first charge was limited to a maximum capacity of 180 mAh/g (corresponding to a cathode potential of ≈ 4.1 V vs. Li⁺/Li) to avoid any side reactions of the electrolyte. By limiting the SOC window and using a Li counter-electrode, the observed irreversible capacity loss could be solely related to the NCM-811 CAM. Afterwards, the cell was cycled for several cycles at C/7.5 between cathode potentials of 3.0 and 4.6 V vs. Li⁺/Li; the accumulated irreversible capacity loss caused by side reactions amounted to ≈ 9 mAh/g during the operando measurement, and the SOC scale in the respective figures was corrected for this value. The *c/a* ratio was measured operando at C/7.5 with a time resolution of 8 minutes (see below), translating to one diffractogram every ≈ 4 mAh/g; for in situ measurements (i.e., during a 50 min OCV hold), diffractograms were taken every 10 mAh/g. The EOT sample was cycled in situ using the cycling protocol for the LDE experiment (i.e., at C/2 between 3.0 and 4.5 V vs. Li⁺/Li) with data points every 15 mAh/g. In situ L-XPD data collection was performed during intermittent OCV periods in the cycling procedure in a 2θ range of 6–48° (detector step size/step time

of 0.15°/5 s), leading to L-XPD acquisition times of 40 minutes. For operando L-XPD data collection, only small 2θ sections with non-overlapping NCM reflections were measured in repetition mode. To determine the c/a calibration curve from operando L-XPD, the (003) reflection was monitored in the 2θ range of 8.000–9.215° (0.405°/3 s), and the (110) reflection in the 2θ range of 28.500–29.715° (0.405°/3 s), with an overall acquisition time of about 8 minutes. Lattice parameter values determined by the operando L-XPD method perfectly overlap with those from in situ L-XPD data (see Figure S5 in paragraph S3 of the Supporting Information), whereby the operando method has the advantage that more data points are collected.

Finally, additional operando L-XPD lattice parameter relaxation experiments were conducted with fresh and EOT samples. After C/2 charging to a comparable state of delithiation (i.e., cathode potential cut-offs of 4.3 V vs. Li^+/Li for the fresh and of 4.5 V vs. Li^+/Li for the EOT sample), the cell was allowed to relax at OCV while monitoring only the relaxation of the (003) reflections in the 2θ range of 8.000–9.215° (0.405°/3 s), resulting in a time resolution of about 4 minutes per L-XPD pattern.

Rietveld refinement.—As the X-ray beam penetrates through the entire pouch cell, the synchrotron diffractogram contains reflections of (i) Al from the pouch foil and the cathode current collector, (ii) Cu from the anode current collector, (iii) graphite phases (graphite as conductive agent in the cathode, Li_xC_6 in the anode), and, (iv) the actual NCM reflections of interest. The scattering from the electrolyte-soaked separator and from polymers of the binder and pouch cell give rise to a complex background, which was fitted by different approaches. Initially, the background signal was defined by fitting a linear interpolation between selected data points in non-overlapping regions, as was done by Dolotko et al.³¹ However, a more elegant way – because its inclusion in the refinement process is possible – is a user-defined background modeled by eight pseudo-Voigt peaks, similar to what was used by Bo et al.,³² and which was used throughout our analysis. From the refinement of one pattern, the positions and relative intensities of the pseudo-Voigt peaks were determined and fixed across all scans with a single scale factor allowing for a free variation of the overall background intensity. Due to preferred orientation effects in the metal foils, a structure-independent Pawley fit was used for the respective phases. The peak profile was described as isotropic broadening with the Thompson-Cox-Hastings pseudo-Voigt function (TCHZ, as implemented into Topas). The instrumental contribution to the broadening was determined with the CeO_2 standard (NIST SRM 674b), giving a value of ≈ 0.006 for the θ -independent parameter W in the TCHZ function. Additional isotropic reflection broadening caused by the sample was taken into account as phase-specific micro-strain ($\tan \theta$ -dependent parameter X) or crystallite size effects ($1/\cos \theta$ -dependent parameter Y) in the TCHZ function of each individual phase. For a more detailed discussion see paragraph S1 in the SI.

NCM-811 is a layered transition-metal oxide known to exhibit an $\alpha\text{-NaFeO}_2$ -type structure with $R\bar{3}m$ symmetry.³³ The unit cell of NCM-811 contains Li atoms on the 3a site (fractional coordinates: 0, 0, 0) and the transition-metals randomly distributed on the 3b site (0, 0, 1/2). The oxygen atoms are on the 6c site (0, 0, $z_{6c,O}$), with $z_{6c,O}$ ranging between 0.23 and 0.24. According to literature reports³⁴ and our own experience, a more stable refinement is achieved if the number of refined parameters is minimized. Therefore, the following constraints were applied: (i) the site occupancy factors of Co and Mn were both fixed to 0.10 on the 3b site (as determined from the ICP-AES analysis); (ii) the overall Ni content was fixed to 0.79 per formula unit; and, (iii) for the refinement of cation disorder, the Ni distribution between 3a and 3b sites was constrained by assuming the same amount of Li on the transition-metal 3b site as the amount of Ni on the Li 3a site (\equiv Li-Ni mixing, cation disorder). The chosen kind of constraints have already been applied in the literature and were found to give chemically reliable results and a stable refinement.^{10,31,35–38} Furthermore, the atomic displacement parameter was constrained for all sites to be the same, because otherwise physically meaningless (sometimes negative) values were obtained. However, when refining data obtained from ex situ

L-XPD capillary measurements, site-specific atomic displacement parameters could be implemented, which were in good agreement with literature values.^{39,40} We used ionic scattering factors for all atoms in the structure. Generally, there is no commonly accepted rule whether to use ionic or neutral atomic form factors.⁴¹ However, recently the advantages of the use of composite structure factors were reported.³⁴

At this point, it is important to note that structure factors are a (theoretical) model of the electron density of an atom which scatters X-rays. Usually, a scattering factor of a free neutral atom deviates substantially from that of an atom in a crystal lattice. However, full charge-transfer between atoms rarely occurs, so that the actual charge density of an ion in a crystal lattice is not equal to its formal charge.^{34,42,43} Accurate scattering factors therefore need to be determined for the respective structural model. As such data are not available for NCM-811, the scattering factors were chosen so that the resulting oxidation states (Li^+ , Ni^{3+} , Co^{2+} , Mn^{4+} , and O^{2-}) give a chemically meaningful, neutral sum formula for the pristine material. The effects of the scattering factors might be mitigated by excluding the low 2θ region from the Rietveld refinement.³⁴ In our case, however, this is not possible because strong reflections are in this range and discarding them would mean a detrimental loss of information.

Any anisotropic strain introduced by changes in the lattice due to Li de-/intercalation (especially pronounced at high state-of-charge, SOC) was taken into account by the hexagonal Stephens model (see paragraph S1 in the SI for equations and Figure S3 for the Williamson-Hall plot).⁴⁴ The simultaneous refinement of the four micro-strain parameters (S_{004} , S_{004} , S_{202} , S_{301}) during the sequential Rietveld analysis of the LDE pouch cell data did not yield stable results. Therefore, only S_{004} and S_{202} were used, because these parameters had the largest effect on the fit quality. This procedure is in agreement with the literature.⁴⁵ For the refinement of the capillary data measured at the in-house diffractometer, all four strain parameters were used successfully, underlining the fact that the Stephens model is phenomenological and only helps to describe the peak shape but does not directly correspond to a physical meaning. In case of the refinement of capillary data obtained at the in-house diffractometer, absorption correction was applied. For further details on the structural parameters, constraints, and refinement results see paragraphs S1 and S2 in the SI.

In addition to the NCM phase, graphite phases of the anode were observed in the XPD patterns from NCM-811/graphite full-cells. It is known in the literature^{31,46} that the lithiation of graphite is a step-wise process leading to three phases which are distinguishable by X-ray diffraction analysis: graphite (space group $P6_3/mmc$), LiC_{12} ($P6/mmm$), and LiC_6 ($P6/mmc$). The pre-lithiation of the anode results in a lithium reservoir which ensures that even in the fully discharged cell, graphite is not formed. The nevertheless observed (002) graphite reflection therefore stems from the conductive graphite additive in the NCM-811 cathode coating. Structural parameters for the refinement of the Li_xC_6 phases ($0 < x < 1$) were taken from a neutron study conducted by Dolotko et al.⁴⁷ As just the small (002) reflection of graphite appears, only the lattice parameters were refined for this phase. For the LiC_{12} phase, lattice parameters and peak broadening due to size effects could be refined. At high SOC, also LiC_6 is present, from which the lattice parameters and crystallite size broadening could be refined. Results from the structural refinement of the LDE data with respect to the different graphite phases are shown in Tables S7–S9 in the SI.

Impedance measurements and rate tests.—Electrochemical impedance spectroscopy (EIS) experiments were conducted in spring-compressed Swagelok-type T-cells (≈ 1 bar), in which both cathode and anode had a diameter of 11 mm. Pre-lithiated graphite was used as counter-electrode. A gold wire micro-reference (GWRE) with a Au wire diameter of 50 μm insulated with a 7 μm polyimide shrouding (Goodfellow Ltd., UK) was used as reference-electrode,⁴⁸ placed between two GF separators with 60 μL LP57-2 electrolyte. The GWRE was lithiated with a constant current of 150 nA for 1 h and yielded a constant potential of 0.31 V vs. Li^+/Li . Potential-controlled electrochemical impedance measurements (PEIS) were conducted with a potentiostat (VMP300, BioLogic, France) in a frequency range of

100 kHz to 100 mHz with an AC voltage perturbation of 10 mV (taking 20 data points per decade and 3 period repetitions). PEIS measurements were performed during the first formation cycle, the 18th cycle, and at end-of-test during charge and discharge at intervals of 20 mAh/g. Prior to measurements, the cells were allowed to rest at OCV for 1 h. Harvested cathode material from the pouch cells of the LDE study was used for the PEIS experiments and for rate tests at EOT. For the other two cycles of interest, new cells were assembled. To fit the impedance spectra, the transmission line model (TLM) was used as described in paragraph S4 of the Supporting Information.⁴⁹

Rate tests were done in 2325-type coin cells with cathode electrodes of 11 mm (EOT) and 14 mm (BOT) in diameter, a lithium counter-electrode (15 mm), two GF separators (16 mm), and 80 μ L LP57 electrolyte (1M LiPF₆ in EC:EMC = 3:7 by weight, BASF SE).

X-ray photoelectron spectroscopy measurements.—X-ray photoelectron spectroscopy (XPS) measurements were conducted on pristine, BOT, and EOT electrode samples with focus on the O1s region. The electrodes were used as-received (pristine) or harvested without washing in the completely discharged state (i.e., after a constant voltage hold step at 3.0 V vs. Li⁺/Li until a C/100 current cut-off). 4 mm diameter samples were cut out of the electrode sheets inside an argon-filled glove box (<0.1 ppm O₂ and H₂O, MBraun, Germany), mounted floating onto a stainless steel stub, and transferred into the loadlock of the XPS system without air exposure using the transfer device from Kratos (UK). XPS spectra were recorded with a monochromatic Al K _{α} source (1486.6 eV), using an Axis Supra system (Kratos, UK) with an operating pressure of 2·10⁻⁸ Torr. A pass energy of 20 eV, step size of 0.1 eV and dwell time of 200 ms were chosen for a spot size of 800 × 300 μ m². Binding energies were corrected based on the adventitious carbon signal at 284.8 eV in the C 1s spectrum. Fitting of the spectra was done with a mixture of Lorentzian (30%) and Gaussian (70%) shape function on top of a Shirley background.

Surface area determination.—Surface area measurements were performed on a gas sorption analyzer (Autosorb-iQ, Quantachrome, USA) at 77 K using either nitrogen or krypton as adsorbent. Beforehand, the pristine NCM-811 powder was degassed at 350°C for 3 h, whereas treated powders were degassed at 80°C for 24 h. The CAM

was either treated with (i) H₂O for 30 min or (ii) LP57 + 1000 ppm H₂O for 7 days, whereby in the latter case, previous work showed that the 1000 ppm H₂O will be converted to \approx 2000 ppm HF within the course of roughly 2–3 days.⁵⁰ The CAM-to-solvent ratio was 1:10 g:ml in both cases. Afterwards, the CAM was filtrated and additionally washed with dimethyl carbonate for the HF-treated sample. The specific surface area was determined from adsorption isotherms in the relative pressure range of 0.05 < p/p₀ < 0.30 according to the Brunauer-Emmet-Teller (BET) theory. As N₂ and Kr sorption provide similar surface areas for the pristine material (N₂: 0.26 m²/g, Kr: 0.28 m²/g), the following experiments were only done with krypton, since it should be more accurate with a low sample amount (\approx 1 g).

Overview.—Figure 1 summarizes the main techniques which we have used in this study and which will be discussed in detail in the Results and Discussion section. It might be helpful for the reader to go back to this overview from time to time, especially with respect to the different XPD techniques, as it shows the targeted parameter(s) of each experiment and the different aging states of the NCM-811 CAM.

Results and Discussion

LDE electrochemical data.—Figure 2a shows the specific discharge capacity of two NCM-811/graphite full-cells cycled at the long duration experiment (LDE) facility of beamline I11 at the Diamond Light Source, UK. Initially, there is a first cycle irreversible capacity loss (ICL) of \approx 25 mAh/g (not shown), which compares well with the ICL reported for NCM-111 of \approx 24 mAh/g⁵¹ and which results in a CAM stoichiometry of Li_{0.92}Ni_{0.79}Co_{0.10}Mn_{0.10}O₂ after the first cycle. This irreversible capacity loss of NCMs was also reported by other groups,^{51–55} and Buchberger et al.⁵¹ discussed various reasons for the ICL and were able to prove the mechanism first proposed by Kang et al.,^{54,55} who suggested that the Li diffusion at the end of discharge is very sluggish because of the lack of Li-ion vacancies. These authors were able to recover the full capacity by giving the diffusion process enough time at voltages lower than 3.0 V. The capacity drops after the second cycle by \approx 16 mAh/g when increasing the C-rate from C/10 to C/2 (see inset of Figure 2a), a typical rate-induced capacity loss observed for NCMs.⁵⁶ In addition, between cycle 8 and 9 there

Technique	Target	Figure	Pristine CAM powder	Fresh <10 cycles	BOT Cycle 18	LDE Cycling	EOT \approx 1000 cycles
In situ S-XPD	$\Delta C_{\text{Material}}$ & $\Delta C_{\text{Overpotential}}$	Fig. 5			✓	✓	✓
Operando L-XPD	$c/a = f(x_{\text{Li}})$	Fig. 5a		✓			
In situ L-XPD	$c/a = f(\text{OCV})$	Fig. 6a		✓			✓
Ex situ L-XPD	Li-Ni mixing	Fig. 3	✓				✓
Operando L-XPD	Relaxation	Fig. 9		✓			✓
In situ EIS	R_{CT}	Fig. 6b		✓	✓		✓
Rate test	$\Delta C_{\text{Material}}$	Fig. 7			✓		✓
XPS	Nature of surface layer	Fig. 8	✓		✓		✓

Figure 1. Overview of the main techniques used in this work, highlighting the targeted parameter(s), the figure where the respective results are shown in the Results and Discussion section, and the different aging states of the NCM-811 CAM which have been investigated with the respective technique.

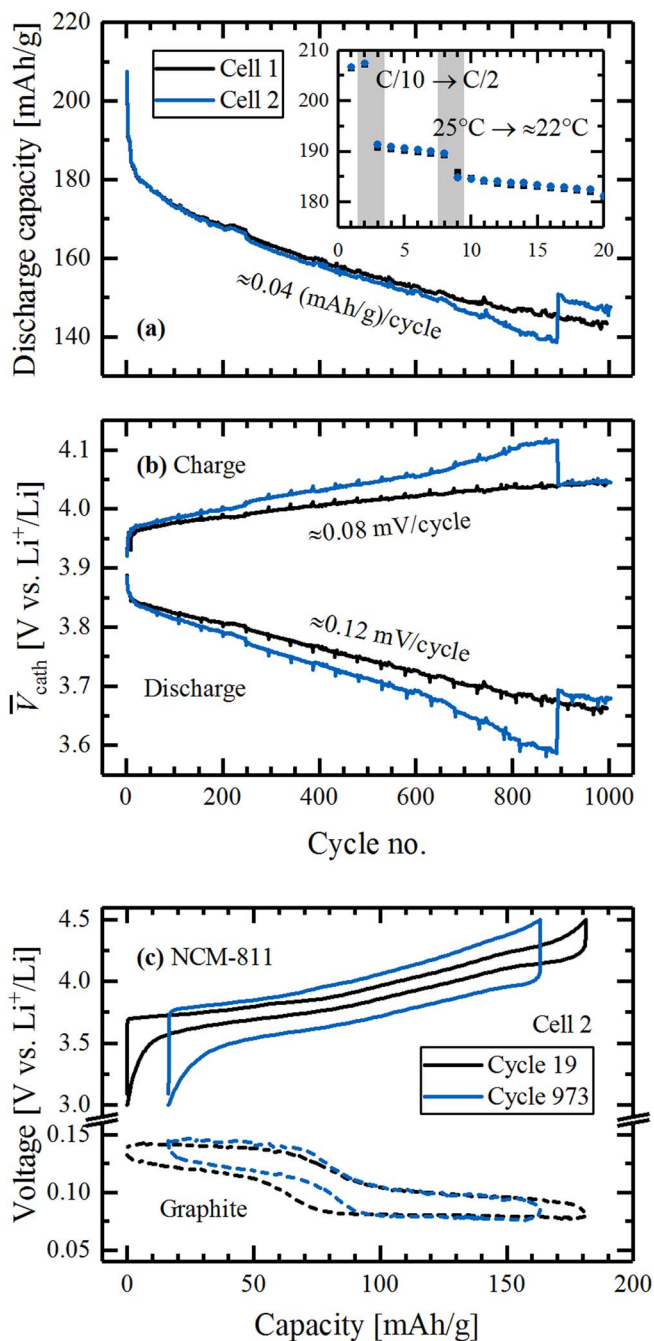


Figure 2. (a) Specific discharge capacity, (b) charge-averaged mean charge and discharge voltage of the cathode vs. Li⁺/Li (\bar{V}_{cath}), and (c) voltage profile of anode and cathode of NCM-811/graphite full-cells cycled at $\approx 22^\circ\text{C}$ with C/2 between 3.0–4.5 V vs. Li⁺/Li at beamline I11 (Diamond Light Source, UK). The inset in panel (a) highlights the first 20 cycles, where (i) the C-rate was increased from C/10 (cycles 1 and 2) to C/2, and (ii) the cells were moved to the Diamond Light Source (between cycle 8 and 9), where the cycling temperature was $\approx 22^\circ\text{C}$ compared to 25°C during cycles 1–8. Slight deviations from the characteristic mean voltage curves in panel (b) originate from the OCV phases for XPD data collection (every ≈ 50 cycles). The half-cell voltage profiles of cycle 973 in panel (c) were shifted arbitrarily along the x-axis relative to cycle 19 in order to illustrate the overpotential leading to capacity fading.

is another capacity drop of $\approx 3\text{--}5$ mAh/g at the same C-rate, which unfortunately is due to a temperature difference between the cycling experiments conducted in our laboratory at the Technical University Munich (25°C , until cycle 8) and in the beamline hutch at the Diamond Light Source ($\approx 22^\circ\text{C}$, from cycle 9 onwards). This difference

in discharge capacity is consistent with the temperature dependence of the discharge capacity of ≈ 0.8 (mAh/g)/K, determined in a separate experiment (not shown) with fresh NCM-811/graphite cells cycled at C/2 at varying temperatures ($19\text{--}33^\circ\text{C}$). The mean capacity drop in the subsequent cycles is ≈ 0.04 mAh/g per cycle (see Figure 2a), resulting in a capacity retention (at 22°C and C/2) of 77–80% after 1000 cycles, referenced to 185 mAh/g in cycle 9. The instantaneous regain of capacity for cell 2 (blue line) in cycle 893 must have been caused by a sudden improvement of the cell contact (i.e., the electrical contact between the current collector tab of the cell and the crocodile clamp of the current cable). This becomes apparent from the voltage profiles of cell 2 in cycles 892–894, which show a ≈ 100 mV lower charge and discharge voltage after the event in cycle 893 (corresponding to a ≈ 15 Ω lower resistance; see paragraph S5 and Figure S8 in the SI). However, the capacity fading rate after this event remains unchanged for the subsequent cycles.

Figure 2b shows the charge-averaged mean charge and discharge voltage of the cathode electrodes vs. Li⁺/Li of cells 1 and 2 (for a given charge or discharge cycle, $\bar{V}_{\text{cath}} \equiv \int V_{\text{cath}} \times dq / \int dq$).⁵⁷ After the initial rapid increase of \bar{V}_{cath} due to the increase in C-rate (from C/10 to C/2 in the 3rd cycle) and change in temperature (from 25°C to $\approx 22^\circ\text{C}$ in cycle 9), the \bar{V}_{cath} curves for charge and discharge show a relatively linear behavior, with the mean discharge voltage decreasing by ≈ 0.12 mV per cycle and the mean charge voltage increasing by ≈ 0.08 mV per cycle. The increase of the overpotential during both charge and discharge suggests an increase in cathode impedance over extended cycling. The small spikes in the \bar{V}_{cath} curves every ≈ 50 cycles are caused by the OCV holds for XPD data collection, where the cell potential relaxes. The \bar{V}_{cath} jump of cell 2 at cycle 893 is due to the above discussed change in the cell contact resistance.

Figure 2c shows a comparison of the half-cell voltage profiles of graphite and NCM-811 vs. Li⁺/Li of cell 2 for the 19th cycle (black curves, after the first LDE XPD data point, BOT) and for the 973rd cycle (blue curves, close to the last LDE XPD data point in the 975th cycle, EOT). It can be seen that the overpotential of the cathode (solid lines) increases drastically with cycling, as already indicated by its mean voltage evolution. Because cycling was carried out between fixed cathode voltage limits (3.0 and 4.5 V vs. Li⁺/Li), this increase of overpotential contributes significantly to the observed capacity fading, as the accessible capacity window gets narrowed from both sides.^{19,58} On the other hand, the voltage profile of the graphite anode (dashed lines) shows no significant change with cycling.

In the literature, various factors are discussed which might cause the capacity fading for Ni-rich NCMs in the absence of a loss of cyclable lithium (i.e., in half-cells with lithium anodes or, as in this study, in full-cells with pre-lithiated graphite anodes), as seen in Figure 2. Amongst others, bulk structural changes such as cation disorder are identified as possible reason.⁵² A notably increased fraction of Ni in the Li layer would not only reduce the number of active Li sites, but also gives rise to an increased polarization.⁵⁹ Contact loss in the CAM due to pronounced particle cracking¹³ and surface instabilities,²⁰ however, are also reported to lead to a capacity loss due to impedance build-up. At the same time, both cracking and surface instabilities might cause a capacity loss due to material loss in the form of isolated particles or reconstructed phases, which are electrochemically inactive. In the following, the reasons for the continuous capacity fading observed in Figure 2 are analyzed by a combination of various techniques, with emphasis on the long-duration experiment XPD data.

XPD analysis with respect to bulk stability and cation mixing.— Starting our XPD analysis, we first examined whether any reversible phase transformations could be observed. For instance, for LiNiO₂, there are literature reports on the reversible phase transformation from a hexagonal to a monoclinic structure (H1-M transformation) and further on to new hexagonal versions (M-H2 and H2-H3 transformations) upon delithiation.⁷ The H1-M transformation is accompanied by the splitting of the original (101), (012), and (104) reflections in the hexagonal symmetry, whereas the H2-H3 transformation involves an abrupt contraction of the lattice parameter *c*. In our study, no peak splitting

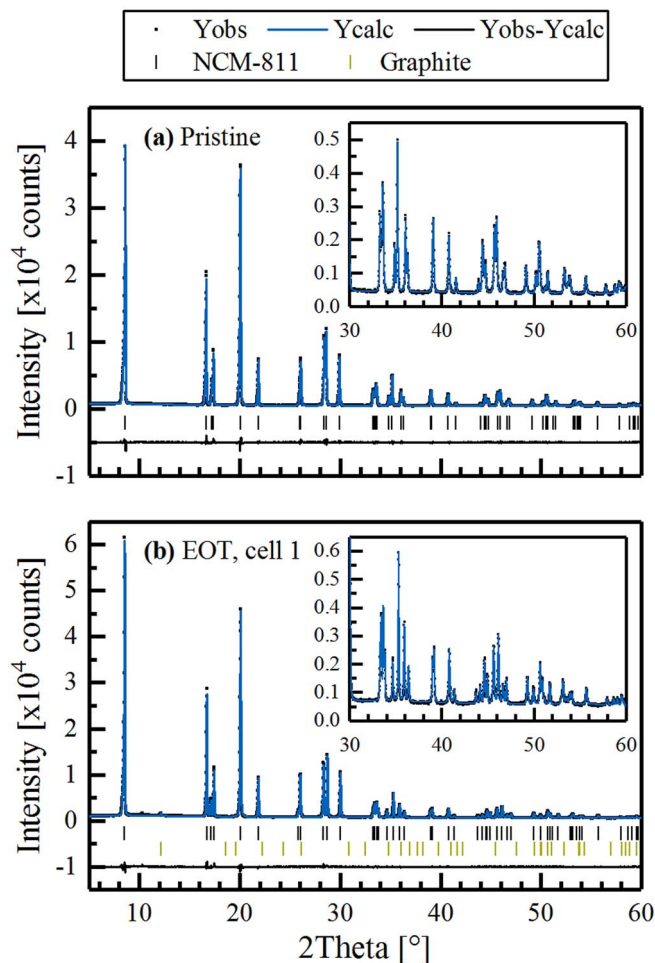


Figure 3. Refinement of ex situ L-XPD data based on capillary measurements of (a) pristine and (b) harvested EOT NCM-811 powder (from cell 1) in the common $R\bar{3}m$ space group. The data were collected at the in-house Mo-diffractometer ($\lambda = 0.7093 \text{ \AA}$). The observed (black points), calculated (blue lines), and difference diffraction profiles (black lines) are shown together with the position of the Bragg peaks of NCM-811 (black ticks) and graphite (green ticks). The insets show a magnification of the high-angular range. Note that the EOT NCM-811 electrode sample contains 2 wt% conductive graphite, which was included into the refinement (strongest reflection at $\approx 12^\circ$). The refinement results are summarized in Table I.

and only a gradual contraction of the c parameter were observed. In the study of Ryu et al.,⁶⁰ these LiNiO_2 -like transformations were only seen for NCM materials with a Ni content of 90% or higher. Other authors report on an irreversible thermal reconstruction of the rhombohedral to a spinel structure of $\text{Li}_{0.5}\text{NiO}_2$, indicated by a coalescence of the (018) and (110) reflections,⁶¹ which we could not observe here by electrochemical cycling.

Next, we examined the XPD patterns for any sign of cation disorder between the Li and transition-metal layer, i.e., for Li-Ni mixing. The refinement of this sensitive parameter has proved to be difficult, especially in the case of in situ XPD data due to the overlapping reflections from other cell components (Al and Cu) and the complex background patterns (see paragraphs S1 and S2 in the SI). Furthermore, we observed a significant correlation between the Li occupancy and cation disorder, as it is also known from the literature.³⁴ The refinement of the cation disorder was therefore conducted with ex situ L-XPD data from capillary measurements with pristine NCM-811 powder and discharged NCM-811 cathodes harvested at EOT. These data are shown in Figure 3, and the refinement results are summarized in Table I, whereby the remaining Li content, x_{Li} , of the EOT samples was determined from the c/a calibration curves discussed in the following

Table I. Refinement results of pristine NCM-811 and NCM-811 electrodes harvested at EOT, based on ex situ L-XPD capillary measurements at a Mo-diffractometer and refined in the common $R\bar{3}m$ space group. The diffractograms for pristine NCM-811 and the electrode harvested at EOT from cell 1 are shown in Figure 3. The table summarizes quality factors (R -values), lattice parameters and the thereof determined Li content and atomic site-specific information (including Li-Ni mixing, fractional z -coordinate of O, and thermal displacement parameters). The b values were constrained to be the same for all elements on one site. Errors given in parenthesis.

	Pristine	EOT, cell 1	EOT, cell 2
R_{wp} [%]	4.52	4.48	4.84
R_{bragg} [%]	1.14	1.04	1.49
χ^2	1.99	2.63	2.04
a [\AA]	2.87212(2)	2.85945(2)	2.85931(3)
c [\AA]	14.2058(2)	14.2902(2)	14.2820(3)
c/a [-]	4.94609(7)	4.99756(7)	4.9949(1)
x_{Li} [-]	1.01 ^a	0.79 ^b	0.80 ^b
Li-Ni mixing [%] ^c	3.1(1)	2.0(1)	3.1(1)
$z_{6c,O}$ [-]	0.24156(7)	0.23908(8)	0.2396(1)
$b_{3a,\text{Li}}$ [\AA^2]	1.22(9)	0.7(1)	1.1(2)
$b_{3b,\text{TM}}$ [\AA^2]	0.171(8)	0.298(9)	0.08(1)
$b_{6c,O}$ [\AA^2]	0.62(2)	0.82(3)	0.47(3)

^aThe Li content of the pristine material was fixed to the elemental analysis results ($\text{Li}_{1.01}\text{Ni}_{0.79}\text{Co}_{0.10}\text{Mn}_{0.10}\text{O}_2$).

^bThe Li content of the EOT materials was calculated from the low-SOC c/a calibration curve, as shown in Figure 5a and in paragraph S1 in the SI.

^cLi-Ni mixing gives the percentage of Ni on the 3a site of the Li layer relative to the total available occupancy of the 3a site.

section (see Figure 5a). These refinements give a Li-Ni mixing of 3.1(1)% for the pristine and EOT sample of cell 2. The EOT sample of cell 1 gives a reproducible cation disorder of 2.0(1)%.

For the refinement of the in situ S-XPD data, the cation disorder was therefore fixed to the value obtained from the ex situ L-XPD capillary data, because there the parameter could be determined reliably and without any overlapping reflections. In the Rietveld refinement, the very sensitive cation disorder parameter correlates strongest to the thermal displacement parameter $b_{3a,\text{Li}}$ ($\approx 75\%$) and the scale factor ($\approx 65\%$). However, all b values are in a reasonable range.^{34,39} Fixing the EOT b values to the pristine b values increases the Li-Ni disorder only by $\approx 0.2\%$. Thus, we can conclude with confidence that the Li-Ni mixing is barely affected by 1000 charge/discharge cycles and does not contribute to the observed capacity loss. Since the peak broadening of the samples is also very similar (see Table S2 in the SI for the in situ S-XPD data), all these results prove that there are no remarkable bulk structural changes observed in the NCM-811 CAM upon long-term cycling with an upper cut-off voltage of 4.5 V vs. Li^+/Li . This is in agreement with a study over 300 cycles for NCM-811/graphite full-cells including XPD data performed by Kim et al.,⁶² even though it should be noted that the upper cut-off voltage in their study was only 4.2 V. Furthermore, there are literature reports (without specifically refining Li-Ni mixing) on the bulk stability of Ni-rich CAMs like $\text{LiNi}_{0.76}\text{Co}_{0.14}\text{Al}_{0.10}\text{O}_2$, which was cycled over 1000 cycles also to 4.2 V,⁶³ and NCM-523 cycled 50 times to a cut-off potential as high as 4.8 V vs. Li^+/Li .⁵⁸ This is in contrast to a study of Li et al.,¹¹ claiming the structural instability of Ni-rich CAMs, $\text{LiNi}_{0.80}\text{Co}_{0.15}\text{Al}_{0.05}\text{O}_2$ and $\text{LiNi}_{0.70}\text{Co}_{0.15}\text{Mn}_{0.15}\text{O}_2$, which showed an increase of Li-Ni disorder from 2–3% to 9–13% after cycling over 1500 charge/discharge cycles between 3.0 V and a relatively high upper cut-off voltage of 4.4 V. In our case, it can be concluded that the NCM-811 bulk structure is stable over 1000 cycles, even if a cut-off potential as high as 4.5 V vs. Li^+/Li is chosen.

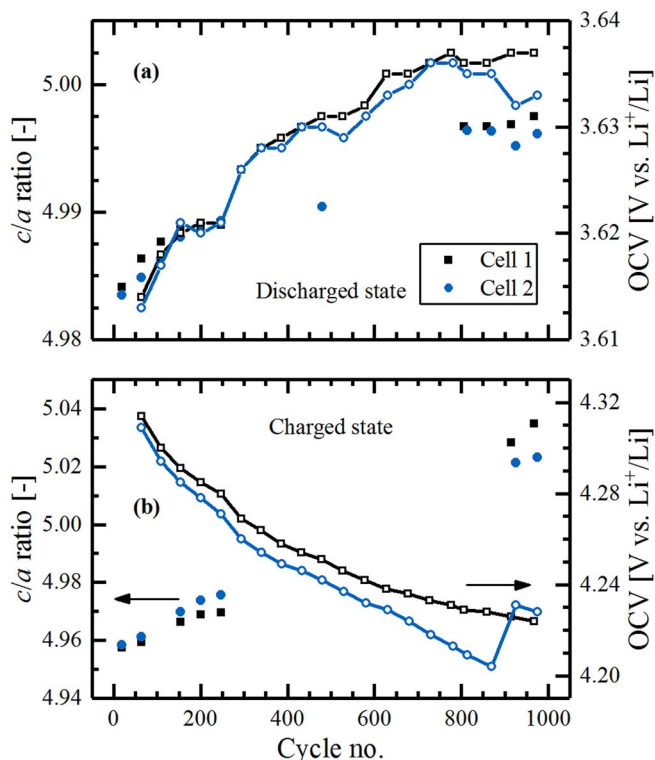


Figure 4. Evolution of the c/a ratio (filled symbols, left y-axes) and the OCV (line and empty symbols, right y-axes) in the (a) discharged and (b) charged state of NCM-811, determined from the in situ S-XPD data obtained from the two cells cycled at the Diamond Light Source. Missing c/a data points are due to a long beam shut-down.

Lattice parameter evolution monitored via XPD analysis.—From the refinement of the in situ S-XPD patterns, the lattice parameters of NCM-811 were obtained in charged and discharged state over the course of almost 1000 cycles for the two cells (more refinement results shown in paragraph S2 in the SI). The lattice parameter ratio c/a is shown in Figure 4 (filled symbols, left y-axes) together with the OCV at which the respective data were measured (empty symbols, right y-axes). According to literature data, the c/a ratio is the most reliable measure of lattice expansion (in c -direction) and compression (in a, b direction) induced by Li extraction and insertion in NCM materials.⁶⁴ It can be seen that in both charged and discharged state the c/a ratio increases during the experiment (see filled symbols). Furthermore, the OCV was found to change over the course of extended cycling, increasing in the discharged state (empty symbols in Figure 4a) and decreasing in the charged state (empty symbols in Figure 4b). For a stable bulk material – which we can assume based on the ex situ L-XPD data discussed above – it is known that the OCV scales with the SOC of the material, i.e., the higher the SOC, the higher the respective OCV value. Thus, from the OCV evolution shown in Figure 4, we can conclude that the effective SOC window becomes smaller over the course of cycling. This is in agreement with the observed capacity loss and overpotential increase of the NCM-811 electrode (see Figure 2). Here, we should note that the jump in the OCV (≈ 30 mV) observed for cell 2 after ≈ 900 cycles is related to the change in cell contacting resistance at this point and also reflected in an increase in cell capacity (see Figure 2a), as discussed above.

To understand whether this is consistent with the observed increase of the c/a ratio over cycling in both the charged and discharged state (filled symbols in Figures 4a, 4b), one has to consider the relationship between the c/a ratio and the lithium content, x_{Li} , or the SOC of NCM materials: the c/a ratio initially increases upon charging until it reaches a maximum at $\approx 60\%$ SOC (i.e., $x_{\text{Li}} \approx 0.4$) and then decreases upon

further increasing the SOC.^{51,60,64,65} Thus, the observed increase in the c/a parameter in the discharged state (SOC $\ll 60\%$) and in the charged state (SOC always $>60\%$), clearly indicates a shrinkage in the capacity window, which at least qualitatively is consistent with the OCV evolution.

To convert the qualitative OCV and c/a analysis into a quantification of capacity losses in the charged and discharged state, the c/a curve for the first two/three cycles was measured to serve as a calibration curve of the c/a ratio vs. capacity (more precisely x_{Li}) or OCV, as will be described in the following. The detailed approach and the respective data sets from in situ XPD (i.e., complete XPD pattern collected at OCV conditions at different SOC steps over 2 cycles) and operando XPD (i.e., continuous data collection of (003) and (110) reflection during 3 cycles) are described in the Experimental section and are discussed in detail in paragraph S3 in the SI. The thus obtained relationship between the c/a ratio and the lithium content x_{Li} of NCM-811 is shown exemplarily for the 2nd discharge cycle in Figure 5a (measured in operando mode), which is in agreement with literature reports.^{60,65,66}

Next, the lattice parameters obtained from the in situ S-XPD data during long-term cycling were used to compute the changes of the c/a ratio, from which the Li content x_{Li} in the cycled NCM-811 (i.e., in $\text{Li}_x\text{Ni}_{0.79}\text{Co}_{0.10}\text{Mn}_{0.10}\text{O}_2$) could be determined, as was done by Buchberger et al.⁵¹ The relationship between the c/a ratio and x_{Li} is given in Figure 5a and in paragraph S1 in the SI. Here, the advantages of using the c/a ratio instead of only the lattice parameters becomes evident: (i) the c/a ratio is close to linearity in the x_{Li} ranges of interest; and, (ii) small misalignments of the cells in the geometry of the diffractometer would not falsify the result, because the error gets cancelled out by taking the ratio of both lattice parameters. From the S-XPD analysis shown in Figure 4, we know that the c/a ratio in both the discharged state (low SOC) and the charged state (high SOC) increases with cycling. The grey bars in Figure 5a mark the c/a ratio changes over 1000 cycles in both the discharged state (left bar) and the charged state (right bar), based on the data in Figure 4 (filled symbols). With the obtained operando L-XPD calibration curve (black symbols and interpolating line in Figure 5a), a mathematical relationship between x_{Li} and c/a can now be established. At low SOC ($0.62 \leq x_{\text{Li}} \leq 0.91$), i.e., in the discharged state, this is best described by a quadratic equation of c/a as function of x_{Li} (highlighted in blue in Figure 5a, with the equation given in the figure, and also as x_{Li} as a function of c/a in equation (S1) in the SI). At high SOC ($0.12 \leq x_{\text{Li}} \leq 0.23$), i.e., in the charged state, there is a linear dependence between c/a and x_{Li} (highlighted in green, with the equation given in the figure and as equation (S2) in the SI).

With the values for c/a in the discharged and charged state over 1000 cycles (from Figure 4), the capacity losses at low and high SOC in the i^{th} cycle ($\Delta C_{\text{Discharge}}^{\text{BOT} \rightarrow i}$ and $\Delta C_{\text{Charge}}^{\text{BOT} \rightarrow i}$) relative to the first in situ S-XPD data point in the 18th cycle (BOT) can now be quantified and then compared to the electrochemical capacity loss ($\Delta C_{\text{EC}}^{\text{BOT} \rightarrow i}$). The applied calculations are explained in the following, whereby a “ Δ ” represents a difference between two specific states. Firstly, the electrochemical capacity loss between the i^{th} cycle and at BOT (18th cycle), $\Delta C_{\text{EC}}^{\text{BOT} \rightarrow i}$, is defined by the difference of the discharge capacity in the i^{th} cycle, C_{EC}^i , and that at BOT, $C_{\text{EC}}^{\text{BOT}}$:

$$\Delta C_{\text{EC}}^{\text{BOT} \rightarrow i} = C_{\text{EC}}^{\text{BOT}} - C_{\text{EC}}^i \quad [1]$$

This can be compared to the capacity loss inferred from the in situ S-XPD data, namely to the sum of the calculated capacity losses referenced to BOT in the discharged state, $\Delta C_{\text{Discharge}}^{\text{BOT} \rightarrow i}$, and in the charged state, $\Delta C_{\text{Charge}}^{\text{BOT} \rightarrow i}$:

$$\Delta C_{\text{Overpotential}}^{\text{BOT} \rightarrow i} = \Delta C_{\text{Discharge}}^{\text{BOT} \rightarrow i} + \Delta C_{\text{Charge}}^{\text{BOT} \rightarrow i} \quad [2]$$

Both of these XPD-deduced capacity loss values can be calculated for the i^{th} cycle relative to BOT by taking the difference between the respective x_{Li} values between the i^{th} cycle and BOT (Δx_{Li}) in either the discharged state ($x_{\text{Li,dis}}^i - x_{\text{Li,dis}}^{\text{BOT}}$) or the charged state ($x_{\text{Li,cha}}^{\text{BOT}} - x_{\text{Li,cha}}^i$), which are obtained by the measured c/a ratios using the mathematical

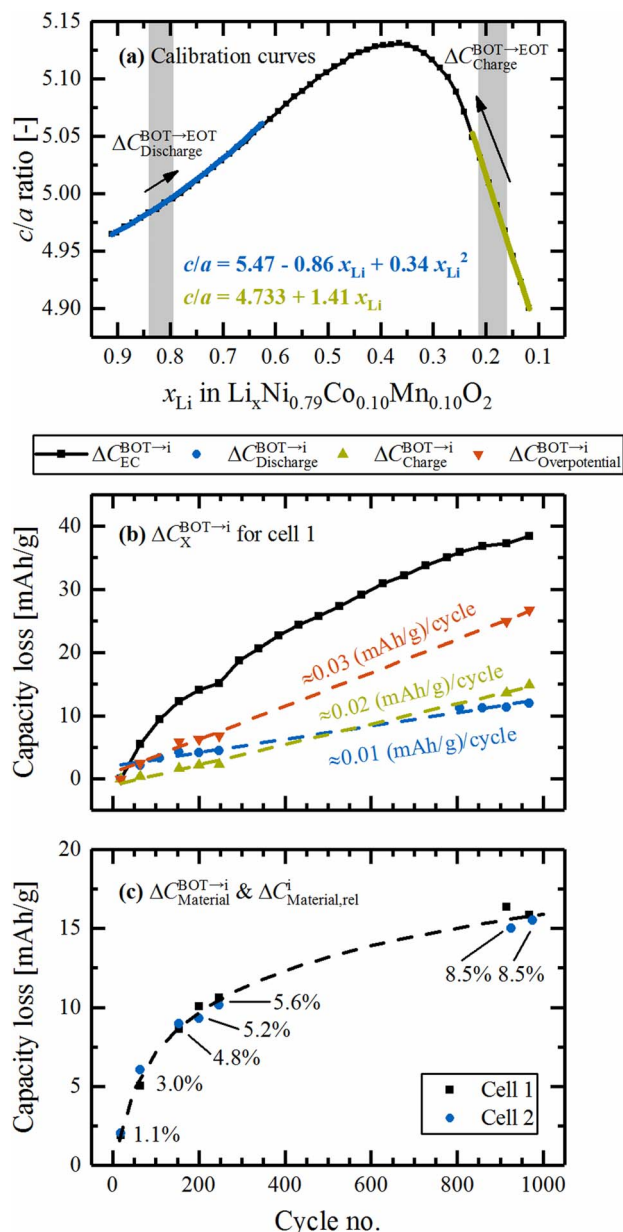


Figure 5. (a) Dependence of the c/a ratio on the Li content x_{Li} for the pristine NCM-811 CAM determined by operando L-XPD (black symbols and interpolating line, shown exemplarily for the 2nd discharge cycle). The quadratic and linear fits at low and high SOC are shown in blue and green, respectively (average from the first three discharge cycles, equations given in the plot and in paragraph S1 of the SI). Furthermore, the evolution of the c/a ratio from BOT to EOT during the long-term cycling study is indicated by the grey bars and arrows (based on the filled symbols in Figure 4). (b) Capacity loss relative to BOT calculated from electrochemical data ($\Delta C_{EC}^{BOT \rightarrow i}$, Eq. 1) and from changes of x_{Li} obtained by in situ S-XPD in the discharged ($\Delta C_{Discharge}^{BOT \rightarrow i}$, Eq. 3) and charged state ($\Delta C_{Charge}^{BOT \rightarrow i}$, Eq. 4) as well as the sum of both ($\Delta C_{Overpotential}^{BOT \rightarrow i}$, Eq. 2). (c) Capacity loss attributed to a material loss depicted in absolute values ($\Delta C_{Material}^{BOT \rightarrow i}$, Eq. 6, individual data points for cell 1 and 2) and relative to the pristine CAM ($\Delta C_{Material,rel}^i$, Eq. 7, percentages given for each cycle as mean value from cell 1 and 2).

relationships between the c/a ratio and x_{Li} (see equations (S1) and (S2) in paragraph S1 of the SI). To convert this Δx_{Li} difference into a specific capacity, the second term on the right-hand side of Equations 3 and 4 serves as a conversion factor relating 1.01 mol Li to the theoretical capacity of 274 mAh/g for complete Li extraction in the

here used NCM-811 material ($Li_{1.01}Ni_{0.79}Co_{0.10}Mn_{0.10}O_2$, theoretical capacity includes surface impurities, see Experimental section).

$$\Delta C_{Discharge}^{BOT \rightarrow i} = (x_{Li,dis}^i - x_{Li,dis}^{BOT}) \cdot \frac{274 \text{ mAh/g}}{1.01} \quad [3]$$

$$\Delta C_{Charge}^{BOT \rightarrow i} = (x_{Li,cha}^{BOT} - x_{Li,cha}^i) \cdot \frac{274 \text{ mAh/g}}{1.01} \quad [4]$$

In this case, $\Delta C_{Overpotential}^{BOT \rightarrow i}$ (Equation 2) accounts for the accumulated capacity loss between BOT and the i^{th} cycle due to an increasing overpotential, as deduced from the in situ S-XPD data. If the capacity loss over cycling were only due to an increasing NCM-811 overpotential, $\Delta C_{Overpotential}^{BOT \rightarrow i}$ would have to be identical with the electrochemically determined capacity loss $\Delta C_{EC}^{BOT \rightarrow i}$ (see Equation 1). On the other hand, if part of the NCM-811 would either become electrochemically inactive by a loss of material (e.g., by dissolution) or by the formation of an inactive phase, $\Delta C_{EC}^{BOT \rightarrow i}$ would be larger than $\Delta C_{Overpotential}^{BOT \rightarrow i}$.

The application of these calculations is shown for cell 1 in Figure 5b, where we compare the electrochemically measured capacity losses, $\Delta C_{EC}^{BOT \rightarrow i}$ (black symbols), with those calculated based on the lattice parameter changes, namely the sum of $\Delta C_{Discharge}^{BOT \rightarrow i}$ (blue symbols) and $\Delta C_{Charge}^{BOT \rightarrow i}$ (green symbols), equating to $\Delta C_{Overpotential}^{BOT \rightarrow i}$ (red symbols). The capacity loss $\Delta C_{Overpotential}^{BOT \rightarrow i}$ is caused by the increased overpotential of the NCM-811 CAM (see Figure 2c), which results in a smaller effective SOC window because the upper and lower cut-off potentials are reached earlier, corresponding to a smaller cyclable Δx_{Li} . In the lithiated state, the capacity loss calculated via $\Delta(c/a)$ is ≈ 0.01 (mAh/g)/cycle ($\Delta C_{Discharge}^{BOT \rightarrow i}$, blue curve in Figure 5b), while it is roughly doubled in the delithiated state ($\Delta C_{Charge}^{BOT \rightarrow i}$, green curve in Figure 5b). This corresponds to a shrinkage of the SOC window from initially $0.16 \leq x_{Li} \leq 0.84$ ($\Delta x_{Li} = 0.68$) for cell 1 in cycle 18 to $0.21 \leq x_{Li} \leq 0.79$ ($\Delta x_{Li} = 0.58$) after 1000 cycles. This shrinkage of the exchanged amount of lithium per cycle determined by in situ S-XPD translates into a capacity loss between BOT and EOT of $\Delta C_{Overpotential}^{BOT \rightarrow i} = 26.8$ mAh/g (\equiv value of the red curve at EOT in Figure 5b), which is substantially smaller than the electrochemically measured capacity loss from BOT to EOT of $\Delta C_{EC}^{BOT \rightarrow i} = 38.4$ mAh/g (\equiv value of the black curve at EOT in Figure 5b). The discrepancy between $\Delta C_{Overpotential}^{BOT \rightarrow i}$ and $\Delta C_{EC}^{BOT \rightarrow i}$ must be caused by a loss of active NCM-811, meaning that a portion of the material has either disappeared or is no longer participating in the electrochemical processes. As described in the literature, the capacity loss could be caused by the formation of an oxygen-deficient and electrochemically inactive phase formed at the surface of the NCM-811 particles, which transforms gradually into an insulating spinel/rock-salt-type layer and thereby also causes an impedance growth of the CAM.^{18,19,67,68} Another possible scenario is the formation of electronically isolated particles caused by cracking phenomena, which would then become electrochemically inactive.¹³ As we observe no second NCM-811 phase with shifted reflections (i.e., constant lattice parameters) in the patterns in neither discharged nor charged state, the formation of electronically isolated particles can be ruled out. Moreover, *post mortem* elemental analysis revealed only a minor amount of TMs deposited on the graphite anode at EOT (corresponding to ≈ 0.22 mol%_{TM} when referenced to the original NCM-811 material, which would amount to a maximum capacity loss of ≈ 2.4 mAh/g as described in paragraph S3 of the SI), indicating that CAM dissolution is a rather negligible contribution to the overall capacity loss after ≈ 1000 cycles of the NCM-811 CAM between 3.0 and 4.5 V vs. Li^+/Li . This further supports the hypothesis that the loss of active material may be due to the formation of an electrochemically inactive surface layer.

To more precisely quantify the loss of electrochemically active material over cycling, one can compare the absolute electrochemically observed capacity in the i^{th} cycle, C_{EC}^i , to the effective capacity window in the i^{th} cycle expected from the Δx_{Li} range (i.e., $x_{Li,cha}^i - x_{Li,dis}^i$), as determined from the in situ S-XPD analysis and converted into a

capacity, C_{XPD}^i :

$$C_{\text{XPD}}^i = (x_{\text{Li,cha}}^i - x_{\text{Li,dis}}^i) \cdot \frac{274 \text{ mAh/g}}{1.01} = \Delta x_{\text{Li}}^i \cdot \frac{274 \text{ mAh/g}}{1.01} \quad [5]$$

If 100% of the original NCM-811 material were active, the electrochemical capacity in the i^{th} cycle, C_{EC}^i , and the capacity predicted by the Δx_{Li} range, C_{XPD}^i , would have to be equal. If, however, a part of the CAM becomes electrochemically inactive, the capacity expected from the XPD data, C_{XPD}^i , would be larger than what can be observed, C_{EC}^i , because the Δx_{Li} range determined from XPD is applied for the whole CAM (i.e., the CAM fraction from XPD analysis appears always as 100%). Therefore, a loss of electrochemically active material by the i^{th} cycle, $\Delta C_{\text{Material}}^i$, would correspond to the difference between C_{XPD}^i (capacity if no cyclable material would have been lost) and the actual electrochemical capacity in the i^{th} cycle:

$$\Delta C_{\text{Material}}^{\text{BOT} \rightarrow i} = (C_{\text{XPD}}^i - C_{\text{EC}}^i) \cdot \frac{\Delta x_{\text{Li}}^{\text{BOT}}}{\Delta x_{\text{Li}}^i} \quad [6]$$

The correction factor of $\Delta x_{\text{Li}}^{\text{BOT}}/\Delta x_{\text{Li}}^i$ takes into account that the material loss goes typically hand in hand with an increased overpotential (i.e., $\Delta x_{\text{Li}}^{\text{BOT}} > \Delta x_{\text{Li}}^i$). Consequently, the material loss relative to BOT has to be referred to the broader $\Delta x_{\text{Li}}^{\text{BOT}}$ range and BOT should ideally be a state where no material loss has yet occurred (i.e., one of the very first cycles). More intuitively, the material loss can also be expressed in percentage terms as the electrochemically inactive phase fraction relative to the pristine CAM:

$$\Delta C_{\text{Material,rel}}^i = \frac{C_{\text{XPD}}^i - C_{\text{EC}}^i}{C_{\text{XPD}}^i} \quad [7]$$

Here, no correction is necessary since the equation only involves data from the i^{th} cycle, with C_{XPD}^i being the maximum capacity, which can be achieved with the actually present overpotential of the aged CAM in the i^{th} cycle.

The thus calculated capacity loss due to the loss of electrochemically active material, $\Delta C_{\text{Material}}^{\text{BOT} \rightarrow i}$, for both cell 1 and cell 2 as well as the average share of lost material relative to the pristine CAM, $\Delta C_{\text{Material,rel}}^i$, are shown in Figure 5c. The curve of the material loss shows a steep increase during the first 300 cycles and levels out afterwards, suggesting that most material losses happen in the first 300 cycles. It is known for regular NCMs^{15,18} as well as for Li-rich NCMs^{17,69} that a surface reconstruction is triggered by the loss of oxygen, which happens mainly in the very first cycles, especially if the cathode is charged over 80% SOC. Here, an SOC of $\approx 85\%$ is reached during the first two C/10 formation cycles. On the other hand, HR-TEM images have shown that the actual reconstruction happens within 20–50 cycles for Li-rich NCMs at 25°C.¹⁷ As vacancies in the transition-metal layer probably facilitate the reconstruction in Li-rich NCMs, it is reasonable to assume that this process takes longer for regular NCMs (here 200–300 cycles). At the end-of-test, the material loss for both cells adds up to $\approx 15.8 \text{ mAh/g}$ or 8.5% (average of the data for both cells at ≈ 1000 cycles in Figure 5c). As we propose that this materials loss is due to the formation of a thin surface layer in the nm range with a possibly amorphous character, it is not unexpected that it is not visible as additional phase in the diffractograms, similar to the finding for aged NCMs in the literature.^{18,51} For this reason, we also tried to quantify the electrochemically active NCM-811 fraction over the course of the cycling study by normalizing its scale factor (measure of the intensity of this phase) to the intensity of stable “internal standards” in the cell (see Figure S4 in the SI). For this analysis, we used the polymer peaks from the pouch foil as well as the intensity of the (111) reflection of Al and Cu, which were both refined with a structure-independent Pawley fit. As can be seen in Figure S4, the results have a relatively large scatter, but a loss of a fraction of the active NCM-811 phase from BOT to EOT can be concluded as general trend.

The above analysis has shown that we can differentiate two main contributions to the capacity loss of NCM-811, namely the overpotential-induced loss and the actual loss of cyclable material. As only the electrochemically active material can undergo a capacity

loss due to an increasing overpotential, $\Delta C_{\text{Overpotential}}^{\text{BOT} \rightarrow i}$ has to be corrected by the NCM-811 phase fraction which has been lost up to the respective cycle:

$$\Delta C_{\text{Overpotential,corr}}^{\text{BOT} \rightarrow i} = \Delta C_{\text{Overpotential}}^{\text{BOT} \rightarrow i} \cdot (1 - \Delta C_{\text{Material,rel}}^i) \quad [8]$$

The same correction applies to the individual contributions in the discharged ($\Delta C_{\text{Discharge}}^{\text{BOT} \rightarrow i}$) and charged state ($\Delta C_{\text{Charge}}^{\text{BOT} \rightarrow i}$, see Equation 2). Since the material loss amounts to 8.5% at the end-of-test, $\Delta C_{\text{Overpotential}}^{\text{BOT} \rightarrow \text{EOT}} = 26.8 \text{ mAh/g}$ for cell 1 in Figure 5b reduces to 24.5 mAh/g after correction. Thus, the sum of both loss terms from BOT to EOT, $\Delta C_{\text{Overpotential,corr}}^{\text{BOT} \rightarrow \text{EOT}}$ and $\Delta C_{\text{Material}}^{\text{BOT} \rightarrow \text{EOT}}$ (15.8 mAh/g), amounts to 40.3 mAh/g for cell 1. This calculated value is slightly higher than the actual capacity loss of $\Delta C_{\text{EC}}^{\text{BOT} \rightarrow \text{EOT}} = 38.4 \text{ mAh/g}$ due to the material loss which was already acquired until the begin-of-test (1.9 mAh/g in the 18th cycle, see Figure 5c).

Bulk stability vs. surface instability.—In the following, XPD data from which we have inferred the stability of the bulk of NCM-811 (Figure 6a) are contrasted with impedance data from which we will get insights into the long-term stability of the NCM-811 surface (Figure 6b). Let us first focus on Figure 6a, where the c/a ratio is shown as a function of the open circuit voltage for the in situ L-XPD data (i) from the first two cycles of the NCM-811 cathode (black symbols/lines) and (ii) from the harvested EOT cathode of cell 1 (blue symbols/lines)

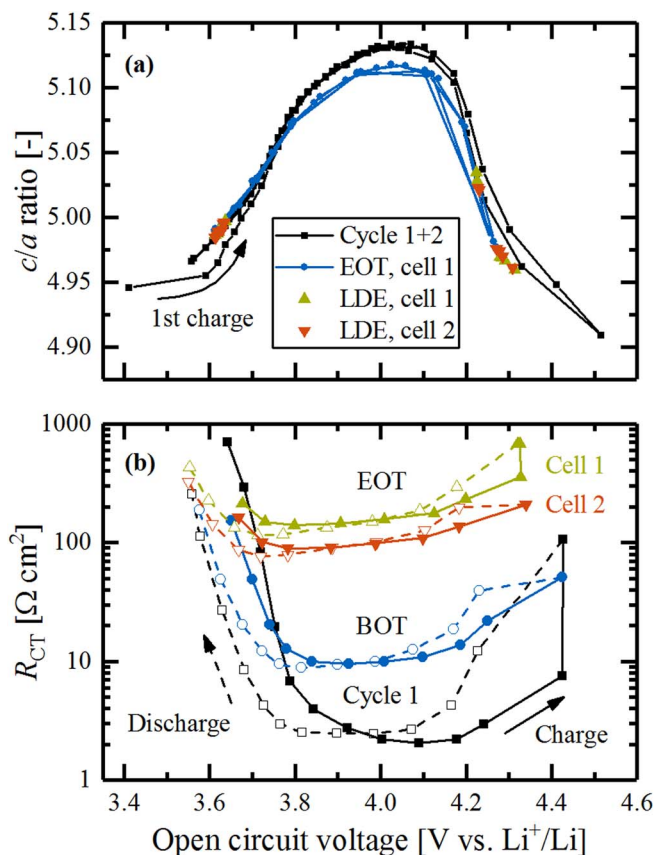


Figure 6. (a) Comparison of the in situ L-XPD c/a curves of a fresh NCM-811 cathode in cycle 1 and 2 (black symbols/lines) and for the EOT cathode (harvested from cell 1, blue symbols/lines) cycled vs. a lithium anode with the c/a data points collected during the long-term S-XPD study from cells 1 and 2 (green and red symbols, labeled as LDE, same data as in Figure 4). (b) Comparison of the charge-transfer resistance of NCM-811 cathodes in the first cycle, at BOT, and at EOT for both long-term cycled cells, measured with a GWRE in a NCM-811/pre-lithiated graphite setup at 25°C. The electrodes in cycle 1 and BOT are a different set than that at EOT. Both the c/a data in panel (a) and the R_{CT} data in panel (b) are shown as a function of the OCV value, at which the data points were measured.

as well as for the in situ S-XPD data from both cells over the course of cycling (green and red symbols, labeled as LDE cells). Note that the OCV values versus the Li-CE (for the L-XPD data) or the Li-RE (for the S-XPD data cycled vs. a pre-lithiated graphite CE) are exactly known from each in situ measurement, i.e., the datasets can be directly compared with each other without any correction. The Rietveld refinement of the capillary data (Figure 3) already indicated the bulk stability over the course of the 1000 cycles. The LDE S-XPD *ca* data (green and red points in Figure 6a, which are the same data as in Figure 4) agree fairly well with the in situ L-XPD calibration curves of the first two cycles (black points/lines) and the EOT sample (blue points/lines). This proves that the *ca* calibration curve taken for NCM-811 in the first few cycles and used to quantify the lithium content x_{Li} at low or high SOC, is also valid for NCM-811 aged over the course of 1000 cycles, so that the XPD analysis conducted in Figure 5 is feasible. The small deviation of the first *ca* points in the first charge from the first discharge and the subsequent cycle is discussed in paragraph S3 in the SI and shown in more detail in Figure S6. Furthermore, the discrepancy of the EOT curve in the mid-voltage region is probably caused by a minor amount of dissolved transition-metals (≈ 0.22 mol% TMs detected by ICP-OES on the graphite anode at EOT). The observed discrepancy is also discussed in context with Figure S6 in paragraph S3 of the SI.

As described above, a growing overpotential on the cathode was identified to be a major reason for the observed capacity loss in NCM-811/graphite full-cells based on the XPD analysis, as shown by $\Delta C_{\text{Overpotential}}^{\text{BOT} \rightarrow \text{EOT}}$ in Figure 5b. It has been reported in the literature that the formation of a spinel or rock-salt-like structure at the surface of NCM cathode materials leads to a drastic increase in the charge-transfer resistance.^{15,18,19} To further analyze the overpotential build-up deduced from our XPD analysis (Figure 5) and the charge/discharge curve profiles (Figure 2a and Figure S9), we determined the cathode impedance of NCM-811 cathodes after a different number of cycles, using a three-electrode setup with a micro-reference electrode. Figure S7 in the SI shows exemplary cathode impedance spectra taken at ≈ 4.0 V during charge of NCM-811 cathodes in the first cycle, in the 18th cycle (corresponding to BOT), and after 1000 cycles (EOT) from a harvested NCM-811 cathode. The spectra exhibit a semicircle at low frequencies, which could be assigned to the charge-transfer resistance, R_{CT} , as described in paragraph S4 in the SI. As the value of R_{CT} is SOC-dependent, these impedance measurements were conducted during OCV at different points during charge and discharge, namely at steps of 20 mAh/g, in a similar fashion as the in situ XPD measurements in Figure 6a. The resulting R_{CT} values are plotted versus OCV in Figure 6b. As was already mentioned above, there is no need to correct for any shift in capacity (x-axis) when plotting vs. OCV, because this is already a measure of the bulk state-of-charge or the lithium content. All R_{CT} curves depicted in Figure 6b have a characteristic minimum around ≈ 4.0 V and increasing values toward the SOC limits, analogous to what has been reported for HE-NCM.⁷⁰ A comparison of the curves during charge at ≈ 4.0 V is consistent with the observed increase of the NCM-811 cathode overpotential, with the charge-transfer resistance found to increase from $\approx 2 \Omega \text{ cm}^2$ to $\approx 10 \Omega \text{ cm}^2$ over the first 18 cycles (black vs. blue curve) and further up to $\approx 100\text{--}150 \Omega \text{ cm}^2$ after 1000 cycles (green and red curve for EOT cell 1 and 2). This means that the impedance growth for cell 2 amounts to $\approx 90 \Omega \text{ cm}^2$ from BOT to EOT, which at a rate of $C/2$ ($\equiv 0.75 \text{ mA/cm}^2$) would equate to an additional overpotential of $\approx 70 \text{ mV}$ (a slightly higher impedance growth of $140 \Omega \text{ cm}^2$ and a higher projected overpotential of $\approx 105 \text{ mV}$ is obtained for cell 1). The overpotential growth calculated from the R_{CT} increase for cell 2 is reasonably consistent with what we observed from the cathode half-cell voltage profiles of cell 2 shown in Figure 2c. There, the difference between charge and discharge voltage at mid-SOC (near 4 V) increases by $\approx 240 \text{ mV}$ between cycle 19 and cycle 973, compared to the R_{CT} -based prediction of $\approx 140 \text{ mV}$. A more detailed description of this overpotential build-up plotted over the whole SOC window is depicted in Figure S9 of the SI. In addition, there is also a difference plot between the cathode half-cell voltage profiles at EOT and cycle 250 versus BOT, indicating that the

overpotential increase can be seen over the whole SOC window and that it is more pronounced during the discharge than during charge, an observation which for yet unknown reasons is at variance with the R_{CT} data in Figure 6b. Overall, however, the cathode potential vs. capacity curves can be used as an indicator for the impedance build-up, as they correlate reasonably well with cathode impedance based R_{CT} values. This fact is further utilized to analyze the evolution of the overpotential build-up over cycling.

While the impedance growth over the 1000 cycles shown in Figure 6b can account for a significant part of the NCM-811 capacity loss, our XPD analysis shown in Figure 5 also indicates that there must be an additional loss of cyclable material, which was found to be most pronounced during the first 300 cycles (see Figure 5c). In this context, it has been suggested that oxygen release takes place in surface-near regions of NCMs or HE-NCMs, leading to a highly disordered oxygen-deficient surface layer which during subsequent cycling transforms into a resistive spinel/rock-salt-like layer, accompanied by an impedance build-up.^{15–19,71} If material at the NCM-811 particle surface were to transform directly into a resistive layer, the impedance build-up should follow the same trend over cycling as the material loss derived from the $\Delta C_{\text{Material}}^i$ data, namely increasing rapidly until cycle 300, followed by a more gradual increase afterwards (see Figure 5c). However, the evolution of the overpotential on the cathode half-cell voltage profile does not follow the trend of the material loss (see comparison of cycle 250 with BOT in Figure S9 in the SI). Indeed, the voltage profile in cycle 250 does not exhibit a significant overpotential ($\approx 40 \text{ mV}$ for cell 2 near 4.0 V during charge, highlighted by a grey bar in Figure S9 in the SI), although at the same cycle number, $\Delta C_{\text{Material}}^i$ shown in Figure 5c already indicates a substantial loss of cyclable material. Thus, we could further confirm the observations made in the literature^{18,19} on the early transformation of the surface-near region of NCM, then followed by a subsequent, more gradual transformation into a resistive surface layer. Summarizing our findings so far: R_{CT} is the origin of the growing cathode overpotential developing gradually over the course of cycling. This, in turn, causes the cell to run earlier into its voltage limits, thereby shrinking the effective capacity window (Δx_{Li}). We showed that this capacity loss due to an increased overpotential can be monitored by XPD, as shown in Figure 5 and Figure 6a. Thus, the surface instability of the NCM-811 cathode active material is the dominant factor contributing to capacity fading.

Reversible vs. irreversible capacity losses.—To analyze the observed overpotential, which is a kinetic hindrance of the (de)lithiation process, a rate test with BOT and EOT samples was conducted to evaluate how much of the lost capacity can be recovered at very low C-rates. For a C-rate approaching zero in combination with a lithium anode, the increased NCM-811 impedance over cycling and the associated overpotential should become negligible and lead to a regain of the original capacity, except for the capacity loss which is caused by an irreversible loss of electrochemically active material. The capacity share due to the loss of active CAM would then be equal to $(C_{\text{BOT}} - C_{\text{EOT}})/C_{\text{BOT}}$ ($= \Delta C/C_{\text{BOT}}$) at a given C-rate, as the C-rate approaches zero. The scheme in Figure 7a shows why the relative values (i.e., the comparison of BOT and EOT) should be used in this analysis. It is based on the fact that the cycling conditions, including C-rate, potential cut-offs, and temperature, determine the actual capacity that can be extracted from the CAM and which for NCMs is always below the theoretical capacity of $\approx 280 \text{ mAh/g}_{\text{NCM}}$. Let us compare two scenarios where either 100% (case A, e.g., with a very high cut-off voltage) or only 50% (case B, e.g., with an intermediate cut-off voltage) of the NCM capacity is accessed at BOT (i.e., in the absence of any loss of active material). The absolute capacity loss caused by an inactive surface layer (of the same thickness) at EOT will definitely be different for the two cases, meaning that the absolute loss for case B would only be half compared to that for case A (i.e., $\Delta C_B = 0.5 \cdot \Delta C_A$). In contrast, the BOT-normalized relative capacity loss is the same in both cases (i.e., $\Delta C/C_{\text{BOT}}$ would be identical) and is thus the correct measure for the loss of active material. However, as stated above, to quantify the irreversible capacity loss due to cyclable material loss

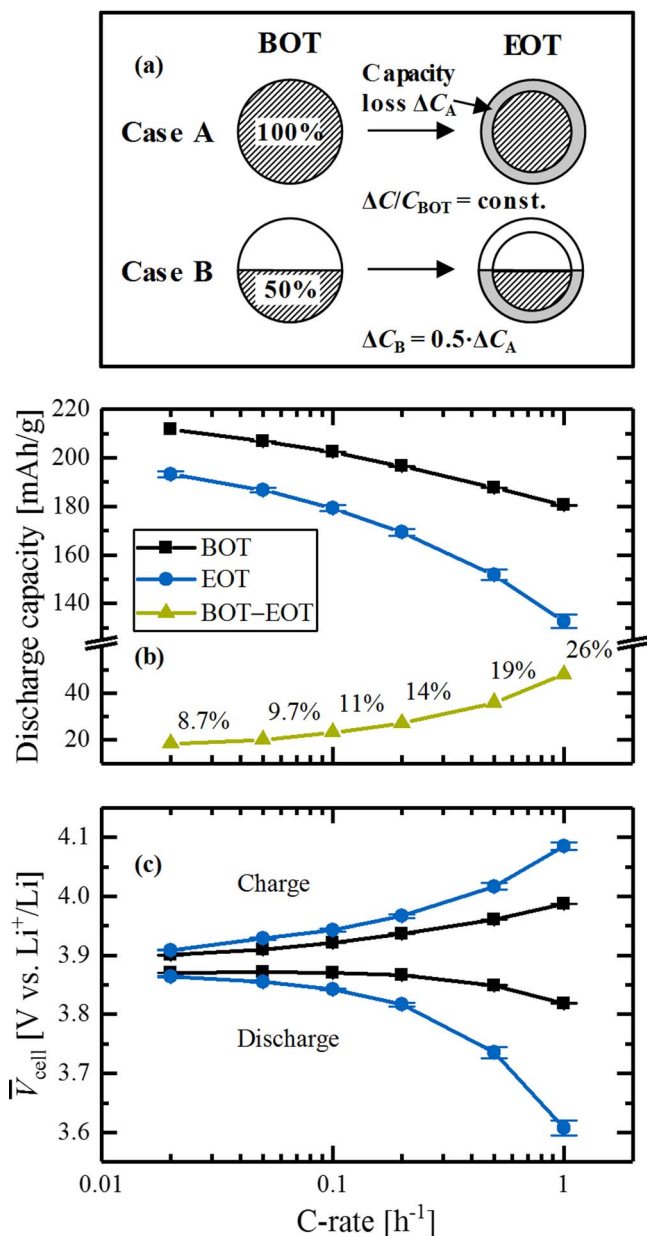


Figure 7. Rate test of BOT (i.e., test started after 18 regular cycles of the LDE protocol) and EOT NCM-811 cathodes harvested from cell 1 and 2, measured in a NCM-811/lithium coin-cell setup at 25°C. (a) Scheme illustrating the difference between absolute and relative capacity loss caused by an inactive phase. (b) Discharge capacities at BOT and EOT as well as their difference; the percentages marked on the latter are the difference between BOT and EOT capacity normalized to the BOT discharge capacity at the respective C-rate. (c) Mean charge and discharge cell voltages (\bar{V}_{cell}) of the NCM-811/Li cells. For EOT samples, the average capacity and \bar{V}_{cell} values for the NCM-811 cathodes harvested from cell 1 and cell 2 of the long-duration experiment are shown (error bars are min/max values); for the BOT samples, two nominally identical cells were measured.

by these means, the C-rate must be small enough so that overpotentials play no role anymore. This condition should be satisfied once the charge-averaged mean charge and discharge voltages (\bar{V}_{cell}) for NCM-811 cathodes harvested at EOT start to become sufficiently close to that of the BOT cells. In Figure 7c, this recovery of \bar{V}_{cell} during charge and discharge for the EOT cells (blue curve) is compared to the BOT cell (black curve) as the C-rate is decreased from 1C to C/50, reaching essentially identical \bar{V}_{cell} values for BOT and EOT cells at C/50 (less than 10 mV difference).

The effect of a decreasing overpotential with decreasing C-rate on the discharge capacity is shown in Figure 7b. Comparing the performance of the BOT (black curve) and EOT NCM-811 cathodes (blue curve) indicates that a large fraction of the discharge capacity is regained for the EOT cells by applying a slow cycling rate of C/50. In the light of our previous analysis, the remaining (irreversible) capacity loss should arise from the NCM-811 fraction that is lost to a reconstructed and electrochemically inactive surface layer. Thus, the irreversible capacity loss of ≈ 18 mAh/g at C/50 (green symbols in Figure 7b) that translates into a loss of cyclable material of 8.7% (from $\Delta C/C_{BOT}$) has to be compared to the relative material loss of 8.5%, which we calculated from the XPD analysis in Figure 5c. Considering the errors, which might occur in the XPD analysis (e.g., accuracy of the calibration curves) and the rate test (e.g., weighing error of the EOT electrodes, mean voltages even at C/50 not perfectly identical), the estimates for the loss of cyclable material are reasonably close and consistent. Summarizing the presented findings: The share of the electrochemically inactive material at EOT can be calculated from both our XPD analysis and the rate test, whereby the respective reference state has to feature the same overpotential and thus the same Δx_{Li} range as at end-of-test. At a rate of C/50 at which the overpotential is minor, this reference state is the begin-of-test, whereas the overpotential build-up at C/2 during long-term cycling is significant and only the theoretical XPD capacity of the same cycle (EOT in this case) can be used as reference state (see Equations 5 and 7).

Nature of the surface layer.—XPS measurements were conducted with pristine NCM-811 electrodes as well as harvested BOT and EOT NCM-811 cathode samples to further clarify the nature of the resistive surface layer. In order to ensure a comparable SOC between the pristine and cycled electrodes (as close as possible to 0%), the latter were regularly discharged to 3.0 V vs. Li⁺/Li, followed by constant voltage hold step with a C/100 current cut-off. Figure 8 is a zoom of the low-binding energy region of the O1s spectrum of pristine and aged NCM-811 samples (for the complete O1s spectrum and the used fitting parameters see Figure S10 and Table S11 in paragraph S6 of the SI). The O1s spectrum of the pristine sample shown in Figure 8a suggests the presence of a pure layered oxide with an O1s binding energy of 529.3 eV (indicated by the green line), similar to a different study conducted at our instrument.⁷² After 18 charge/discharge cycles, the spectrum already shows some intensity at energies higher than the layered oxide binding energy (529.9 eV, indicated by the blue line in Figure 8b), which can be attributed to an oxygen-deficient surface layer (blue marked area). The correlation between a shift to higher binding energies and oxygen depletion in surface-near regions is established based on reference spectra of layered MnO₂, spinel Mn₃O₄, and rock-salt MnO (see paragraph S6 in the SI). It is shown there, that the O-depleted Mn-samples, i.e., spinel and rocksalt, show a peak at 0.3–0.4 eV higher energy than the layered MnO₂. After 1000 cycles (Figure 8c), the intensity of the low binding energy O1s peak shifts considerably to higher binding energy, indicating a considerable oxygen depletion at the NCM-811 surface. Therefore, at least qualitatively, the XPS analysis supports our above hypothesis that an oxygen-depleted layer is formed upon extended cycling of NCM-811 between 3.0–4.5 V vs. Li⁺/Li.

Effect of the O-depleted surface layer on the SOC distribution.—Our XPD analysis showed that neither bulk structural changes, nor significant Ni-Li disorder are observable in NCM-811 over 1000 cycles (see Table I and Figure 3). However, a detailed analysis of the capacity losses indicates a loss of electrochemically active CAM (Figure 5), while the XPS analysis suggests that an oxygen-depleted surface film on the NCM-811 particles is formed upon cycling (Figure 8). Impedance data (Figure 6b) as well as rate tests (Figure 7) suggest an increased charge-transfer resistance, which is presumably caused by a resistive surface film. This poses the question whether a resistive surface layer is being formed on the external surface of each secondary NCM-811 particle with diameters of ≈ 5 –10 μm (see Figure S11 in paragraph S8 of the SI) or whether it is being formed around each of the

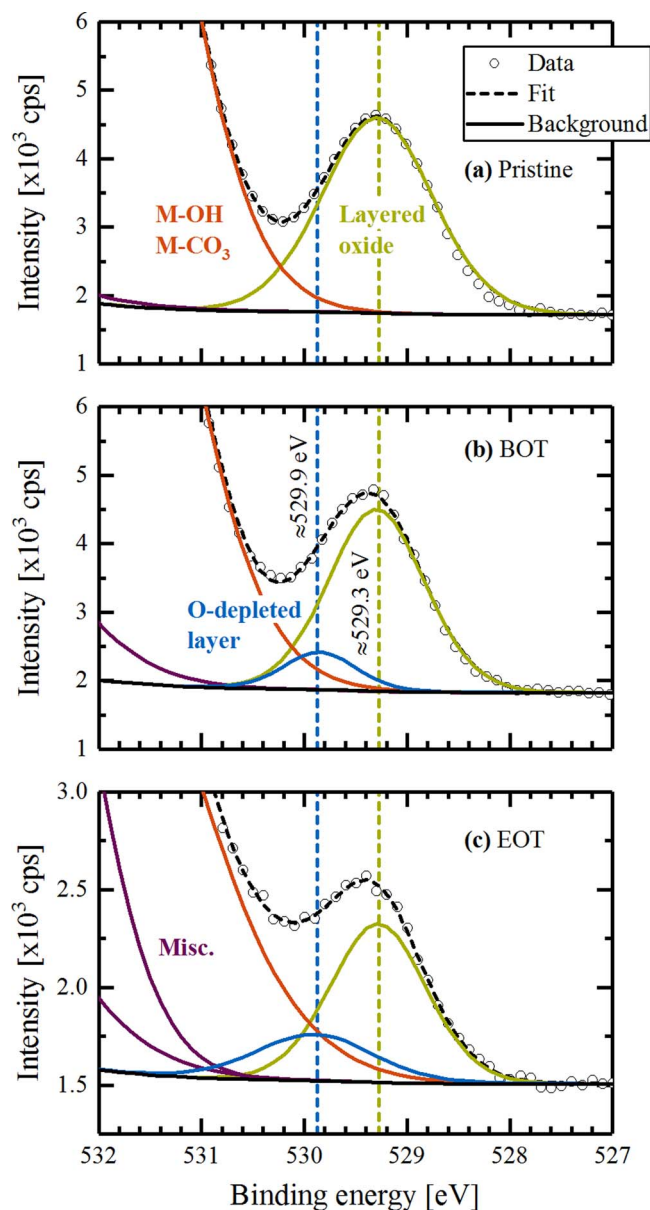


Figure 8. XPS O1s spectra of (a) pristine NCM-811 powder and of NCM-811 electrodes harvested at (b) BOT and (c) EOT. The binding energies of the layered oxide (green line) and an O-depleted surface layer (highlighted in blue) were inferred from MnO_2 , Mn_3O_4 , and MnO reference samples (see SI S6). Surface contaminants (hydroxides and carbonates) are fitted with one peak at higher binding energies (red line). The purple peaks referred to as miscellaneous (misc.) originate from organic surface impurities. For details on the XPS analysis and fitting procedure see paragraph S6 in the SI.

primary particles ($\approx 0.5\text{--}1\ \mu\text{m}$ in size) of which the secondary particle is composed. These two scenarios are sketched into the SEM cross-section image of a secondary NCM-811 particle shown in Figure 9a. As will be explained in the following, we will seek to examine these two scenarios by an operando XPD relaxation experiment, where the lattice parameter c is monitored upon the transition from a $C/2$ charge to OCV.

With an operando XPD relaxation experiment, the inhomogeneity of the lithium distribution (i.e., of x_{Li}) over the fresh NCM-811 electrode (after 9 cycles) and harvested EOT NCM-811 samples is compared. Thereby, the full width at half maximum (FWHM) of the reflections correlates with the homogeneity of the lattice spacing, meaning that a broader d -spacing distribution leads to a larger FWHM, whereas a homogenous d -spacing results in a sharp peak shape. Be-

cause the lattice parameters are closely linked to the lithium content x_{Li} in the NCM-811 material, the FWHM is a measure of the inhomogeneity of the SOC distribution. In this experiment, relative differences between the FWHMs of fresh and EOT samples are compared, wherefore the instrumental contribution to the broadening can be neglected (since the instrument provides a constant offset). In the relaxation experiment, selected reflections of the NCM-811 phase were monitored during the OCV period after a $C/2$ charge to a comparable SOC, as determined by the respective OCV (cut-off voltage of 4.3 V for fresh and 4.5 V for EOT NCM-811). The resulting OCV relaxation is shown in Figure 9b, whereby the initial potential drop from 4.3 V (fresh sample) and 4.5 V (EOT sample) to below 4.3 V occurred within the first 10 s of the OCV period. The final OCV of the fresh sample ($\approx 4.25\ \text{V}$ vs. Li^+/Li) is reasonably close to that of the EOT sample ($\approx 4.23\ \text{V}$ vs. Li^+/Li), indicating that indeed a very similar lithium content x_{Li} was established by the preceding charge at $C/2$. At such high SOCs (corresponding to OCV values higher than 4.2 V), the lattice parameter a is virtually constant, while the lattice parameter c depends very strongly on x_{Li} in this region (see Figure S6 in the SI). Therefore, in order to minimize the XPD data acquisition time, only the 003 reflection, which uniquely describes the lattice parameter c , was recorded for the data shown in Figure 9. This resulted in an acquisition time for the relevant 2θ region of ≈ 4 minutes (see Experimental section). Analogous relaxation measurements recording both the (110) and the (003) reflection (≈ 8 minutes acquisition time) were also recorded to verify that the a parameter indeed remains essentially constant during the OCV transients (data not shown).

As can be seen in Figure 9c, the lattice parameter c exhibits a slight increase during the OCV phase. In the case of the EOT sample, this could be attributed to relaxation processes within the NCM-811 material, meaning the distribution of Li ions across the bulk of the NCM-811 structure, because the FWHM (Figure 9d) also indicates such a relaxation process. Assuming a constant a value of $\approx 2.815\ \text{\AA}$ during relaxation (estimation based on data shown in Figure S6 in the SI), the SOC change can be calculated from the c/a change and the high-SOC calibration curve (shown in Figure 5a). Thus, the observed relaxation of the lattice parameter c for the EOT sample correlates to $\Delta x_{\text{Li}} \approx 0.015$ and $\Delta \text{SOC} \approx 4.1\ \text{mAh/g}$ (vs. $\Delta x_{\text{Li}} \approx 0.009$ and $\Delta \text{SOC} \approx 2.4\ \text{mAh/g}$ for the fresh sample). Both values show that the net capacity change during the OCV period is minor. For the fresh sample however, this process cannot be correlated to the equilibration of an initially inhomogeneous SOC distribution across the bulk of NCM-811 particles, because in this case no relaxation of the FWHM is observed. Currently, we cannot provide a solid explanation for the apparent re-lithiation of the material. One hypothesis is that electrolyte oxidation (possibly also triggered by the permanent X-ray beam) might lead to a small re-lithiation of the CAM, as suggested by Xia et al.⁷³ It is important to note here that the XPD data collection during the LDE study was usually performed after a 3–5 h long OCV phase, meaning that the LDE XPD data are expected to depict a well-equilibrated state.

From the FWHM of the reflections, conclusions on the heterogeneity of the lattice spacing can be drawn. Assuming a virtually constant a parameter, a broader FWHM of the (003) reflection thereby translates into a more pronounced inhomogeneity of the Li distribution within the NCM-811 particles. For a fresh material, no relaxation process can be seen for the FWHM (black symbols/curve in Figure 9d), and the OCV relaxation is rather small ($\approx 30\ \text{mV}$ between $\approx 5\ \text{s}$ and $\approx 5\ \text{h}$ into the OCV period, black curve in Figure 9b; initial voltage drop of $\approx 20\ \text{mV}$ within the first 5 s not shown here), which we believe is due to both the relaxation of concentration gradients within the electrolyte phase and the above discussed slight extent of re-lithiation. In contrast, the EOT sample shows a significantly larger decrease in both OCV ($\approx 50\ \text{mV}$ between $\approx 10\ \text{s}$ and $\approx 5\ \text{h}$ into the OCV period, blue curve in Figure 9b; initial voltage drop of $\approx 220\ \text{mV}$ in the first 10 s not shown here) and FWHM curves (blue symbols/curve in Figure 9d). The initial FWHM for the EOT NCM-811 is more than double compared to that of the fresh cathode material, indicating a severe d -spacing heterogeneity in the c direction. The final FWHM value after relaxation is the same for both samples, suggesting that an equally homogeneous Li distribution

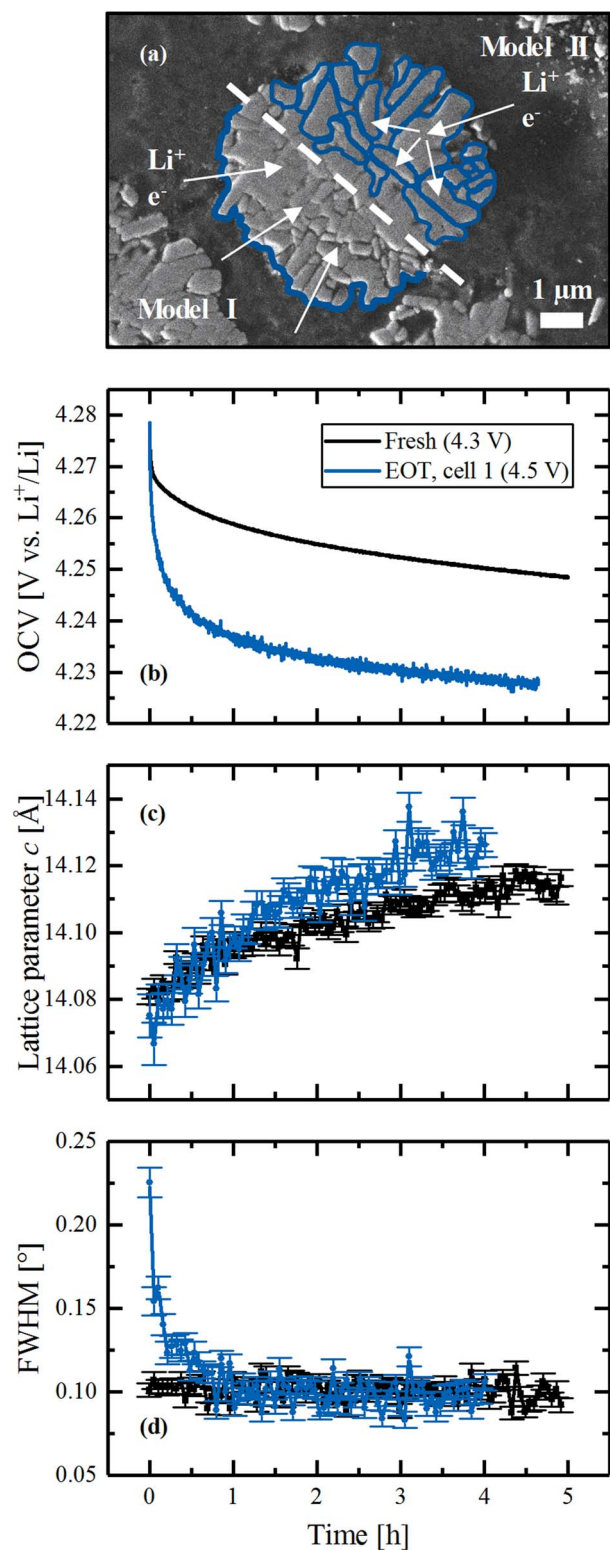


Figure 9. (a) SEM image of an NCM-811 particle, with a scheme illustrating the two discussed models for the formation of the O-deficient surface layer (sketched in blue): (i) either around the external surface of the secondary agglomerates (model I) or (ii) around each individual primary particle (model II). (b-d) Operando L-XPD relaxation experiment at the in-house diffractometer with fresh (measured in the 9th cycle, black curve) and EOT NCM-811 samples (from cell 1, blue curve) after charging to a comparable SOC with C/2: Evolution of (b) the NCM-811 cathode OCV, (c) the lattice parameter *c* determined from the (003) reflection, and (d) the FWHM of the (003) reflection during OCV period. The XPD data were acquired with a time resolution of ≈ 4 minutes.

across the bulk of the NCM-811 particles can be achieved in the EOT sample after prolonged relaxation times. This is another strong support for our above conclusion that the bulk structure of the NCM-811 material is not significantly altered by cycling over 1000 cycles.

On the other hand, the observed FWHM relaxation behavior for the EOT sample could in principle have several causes: (i) an inhomogeneous degree of NCM-811 delithiation across the cathode thickness, if the ionic resistance within the electrolyte phase (R_{ion}) were sufficiently large; (ii) an inhomogeneous lithium distribution within the bulk phase of each of the primary particles due to hindered lithium diffusion in the solid phase; and/or, (iii) different degrees of delithiation within the secondary particles.¹³ Despite the increase of the ionic resistance over cycling (from initially $R_{\text{ion}} \approx 3 \Omega \text{ cm}^2$ to $R_{\text{ion}} \approx 9 \Omega \text{ cm}^2$ after 1000 cycles; see paragraph S4 in the SI), the absolute potential drop at C/2 due to R_{ion} is only ≈ 7 mV even after 1000 cycles, which would imply an essentially homogeneous delithiation across the cathode thickness upon charge, so that the first possible cause (i) should be negligible. With regards to the second possible cause (ii), our XPD analysis clearly indicates that there is no significant change in the Li-Ni disorder over 1000 cycles, so that one would not expect any differences in the lithium diffusion within the NCM-811 bulk phase between fresh and EOT NCM-811. This leaves the third possible cause (iii) as an explanation for the slow FWHM relaxation of the EOT NCM-811, namely an uneven degree of delithiation within the secondary particles. This must be due to the formation of the O-depleted surface layer upon cycling. Addressing our initial question, this surface layer can either be formed around (i) the secondary particles (model I in Figure 9a, sketched by the blue lines) or (ii) around the primary particles (model II) which agglomerate to the former.

For the first scenario (model I), the poor lithium ion conductivity through the resistive layer (as suggested by the large increase in R_{CT} upon cycling, see Figure 6b) around the secondary particle would be rate determining. After overcoming this barrier, the SOC distribution in the primary particles within each secondary particle would be homogeneous, in which case no initial broadening of the FWHM recorded during the OCV period following the C/2 charge would be expected for the EOT sample, contrary to what is observed in Figure 9d. For the other scenario (model II) with a resistive surface layer formed around every primary particle within a secondary particle, a homogenous degree of delithiation would also be expected within a given primary particle, but assuming that the transport of lithium ions and/or electrons is hindered by the surface film and must proceed through the NCM-811 solid phase, the degree of delithiation would be lower for primary particles deeper within the secondary particle compared to those at its outer surface. This would correspond to a SOC variation between primary particles, which would result in an initially broad FWHM in the OCV period following the C/2 charge. Over an extended OCV period, an equilibration of the different SOCs of the primary particles within a secondary particle would occur, so that the FWHM should ultimately narrow to the value observed for a fresh NCM-811 sample. This is exactly what is observed during relaxation of the EOT NCM-811 sample (see Figure 9d). Therefore, on the basis of this analysis of the operando L-XPD relaxation experiment, strong evidence is provided that the resistive O-depleted surface layer must be forming around primary particles in the cycled NCM-811 CAM.

Quite clearly, an aging mechanism according to model II is most consistent with our experimental observation so far. However, the question remains whether the delithiation of the primary particles toward the center of the secondary particles is limited by the transport of Li-ions or of electrons. Seeking to examine this question, the particle morphology of pristine and discharged EOT NCM-811 samples was analyzed by SEM, hoping that it might answer the extent of particle cracking (see paragraph S8 in the SI). Interestingly, the particle morphology at BOT compared to that at EOT shows no significant difference, indicating that NCM-811 particles are not cracked into clearly separate pieces over the 1000 cycles. However, it needs to be stressed out here that the samples were mechanically polished to obtain cross-sectional SEM images, which renders it impossible to differentiate

between small cracks and grain boundaries that are present even in the pristine NCM-811 CAM.

The formation of cracks, however, can also be examined by Kr-BET surface area measurements, as cracks would have to lead to an increase in the specific surface area. The pristine NCM-811 powder has a BET surface area of $\approx 0.28 \text{ m}^2/\text{g}$, which for non-porous spherical particles would predict a particle diameter of $\approx 4.5 \text{ }\mu\text{m}$ (see equation (S11) in paragraph S7 of the SI). This is reasonably consistent with the secondary particle size observed by SEM (see Figure S11 in paragraph S8 of the SI), suggesting that essentially only the external surface of the pristine NCM-811 would be accessible to the electrolyte. However, it may be the case that there are simply surface impurities on the external surfaces of the secondary and/or primary particles (e.g., Li_2CO_3 or LiOH), which prevent gas (and electrolyte) access to within the secondary particles. Therefore, as these could be removed during cycling,⁵⁶ or by protons/HF formed during (electro)chemical electrolyte oxidation,^{74,75} we conducted two more Kr-BET measurements to mimic this conditions in a real cell. NCM-811 was treated either with (i) water for 30 min or (ii) over a period of 7 days with LP57 electrolyte containing $\approx 2000 \text{ ppm HF}$ (see Experimental section). After these treatments, the BET surface area has increased by ≈ 4 -fold to $\approx 1.2 \text{ m}^2/\text{g}$ in both cases. For the solid sphere approximation, this would correspond to a particle diameter of $\approx 1 \text{ }\mu\text{m}$, which is on the order of the dimensions of the primary particles (see Figure S11), indicating that the pores within the thus treated secondary NCM-811 particles become accessible for gas adsorption. Considering the known formation of protons/HF during (electro)chemical oxidation,⁷⁵ which is expected to be substantial over extensive cycling of NCM-811 to potentials of 4.5 V vs. Li^+/Li , one would also expect that the surface of the primary particles within the secondary particles gradually becomes accessible to the electrolyte over the course of cycling. The fact that the primary particles shrink by up to $\approx 6\%$ when NCM-811 is charged to 4.5 V vs. Li^+/Li (see unit cell volume change in Figure S6) provides an additional argument for the electrolyte penetration into pores during cycling.

These pores would enable the release of O_2 gas from inside the secondary particles, thereby enabling the formation of an O-depleted resistive surface layer on the primary particles, ultimately leading to the morphology termed as model II in Figure 9a. The limiting transport mechanism, which leads to the initial broadening of the FWHM observed for the EOT NCM-811 sample during the OCV relaxation experiment (Figure 9d), would thus have to be due to a poor electronic conduction pathway into the aged secondary NCM-811 particle (across now loosely connected primary particles covered by a resistive O-depleted film), as a relatively fast lithium ion transport could proceed through the electrolyte within the pores.

In summary, while many literature reports claim that particle cracking is a major degradation process in NCM cathodes,^{12–14} our analysis suggests that it is rather the interplay of cracks formed due to structural changes during cycling in conjunction with the dissolution of surface impurities that gradually increase the specific surface area of NCMs. As this goes along with an increasing accessibility of the electrolyte to the primary particles in the interior of the secondary particles, an O-depleted resistive surface layer can be formed on the primary particles, which in turns leads to the observed capacity fading. Based on the here proposed aging mechanism, the cycling stability of single-crystal NCMs would be predicted to be superior to poly-crystalline materials.

Estimated thickness of the O-depleted surface layer.—Assuming that the BET surface area of $1.2 \text{ m}^2/\text{g}$ for the washed or HF-treated NCM-811 is representative for NCM-811 after 1000 cycles, the thickness of the O-depleted surface could be estimated by a similar approach as described in literature (for the calculation see paragraph S7 in the SI).^{16,57} Assuming a solid sphere, a primary particle size of $\approx 1 \text{ }\mu\text{m}$ is obtained, which is in good agreement with what can be seen in the SEM images (Figure 9a and paragraph S8 in the SI). The material loss of $\approx 8.5\%$ from the XPD analysis in Figure 5c equals to the phase fraction of the O-depleted surface layer, which translates to a layer thickness of $\approx 15 \text{ nm}$. This is in good agreement with literature values, which

also include transmission electron microscopy images.^{67,76} Watanabe et al.⁷⁶ cycled NCA full-cells to 4.2 V for 1000 cycles and found a $\approx 8 \text{ nm}$ thick NiO-like surface layer at 25°C (and $\approx 25 \text{ nm}$ at 60°C), supporting our model of a surface reconstruction around primary particles. Jung et al.⁶⁷ performed half-cell cycling with NCM-523 cathodes to upper cut-off voltages of 4.5 V and 4.8 V vs. Li^+/Li , respectively, observing a gradual surface transformation from layered via spinel to rock-salt structure, with a layer thickness of ≈ 15 –20 nm, depending on the cut-off voltage. Note, that in Figure 9a, the surface layer of model I is depicted thicker to stress that in this case, based on a smaller BET surface area of $0.28 \text{ m}^2/\text{g}$, the layer thickness would be around $\approx 66 \text{ nm}$, which is much thicker than the typical values reported in the literature, providing further support for model II shown in Figure 9a. We finally tried to validate the layer thickness from cross-sectional HAADF-STEM images of pristine, BOT, and EOT samples, which were prepared by focused ion beam milling (for details and images see paragraph S9 in the SI). While the pristine CAM exhibits no defects at the surface, proving its purely layered nature, transition-metals partially occupy the inter-slabs in the surface-near region of the BOT and EOT samples, as it would be the case for the spinel and/or rock-salt structure. The disordered surface layer was identified on numerous of the primary NCM-811 particles, but it was not possible to accurately quantify the surface layer thicknesses due to several reasons: (i) in many cases, the primary particles could not be tilted into the desired low-indexed zone axes, and, (ii) no clear boundary could be observed between the different phases, as they probably merge gradually into each other.⁶⁷

Conclusions

In this work, we investigated the capacity fading in NCM-811/graphite full-cells over 1000 cycles, whereby focusing on the cathode by pre-lithiating the anode, to identify fading mechanisms with a combination of diagnostics, such as in situ and operando XPD, EIS, and XPS. From an ex situ XPD refinement of the NCM-811 before and after 1000 cycles, we concluded the bulk stability of the CAM with an unaltered Ni-Li disorder of $\approx 3\%$. Based on data from in situ XPD analysis, we were able to establish a quantitative correlation between lattice parameter changes and capacity losses in NCM-811 over the course of cycling. We concluded that the thereby identified capacity losses are caused by a shrinkage of the effective SOC window at both low and high SOC due to an increased cathode polarization. This overpotential build-up was further confirmed by cathode EIS measurements using a gold wire micro-reference electrode showing a 10-fold increase of the charge-transfer resistance. Furthermore, the difference between the capacity loss predicted by the in situ XPD analysis and that obtained from the electrochemical data reveals a CAM loss of $\approx 8.5\%$. These observations are consistent with the formation of an O-depleted resistive surface layer, which was found by XPS measurements and is assumed to show no Li intercalation. An operando XPD relaxation experiment leads us to conclude that the impedance build-up across a secondary particle is caused by the formation of a resistive O-depleted surface layer around the individual primary particles. This conclusion is further supported by BET measurements and cross-sectional SEM as well as HAADF-STEM pictures. The observed surface reconstruction on the one hand means a loss of CAM, which results in an irreversible capacity loss. On the other hand, it causes a significant overpotential thereby shrinking the apparent SOC window. This reversible capacity loss could be regained at very low C-rates. To avoid a surface reconstruction, less resistive and protective coatings for Ni-rich CAMs are essential to improve capacity retention and cycle life in future LIBs.

Acknowledgments

Financial support by BASF SE through its Scientific Network on Electrochemistry and Batteries is gratefully acknowledged. We also wish to acknowledge the Diamond Light Source for provision of beamtime at the Beamline I11 (proposal EE16866) and financial support. Further gratitude is expressed to Sophie Solchenbach for her con-

tribution to the impedance measurements, to Katia Rodewald from the Wacker-Chair of Macromolecular Chemistry at the Technical University of Munich for the SEM measurements, and to the Competence Center Material Physics of BASF SE for the STEM measurements.

ORCID

Franziska Friedrich  <https://orcid.org/0000-0001-9400-1212>

Benjamin Strehle  <https://orcid.org/0000-0001-8878-1160>

Michele Piana  <https://orcid.org/0000-0002-3310-6587>

References

- Pedro Lima, Pushevs, can be found under <https://pushevs.com/2018/04/05/samsung-sdi-94-ah-battery-cell-full-specifications>, accessed October 2019.
- E. A. Olivetti, G. Ceder, G. G. Gaustad, and X. Fu, *Joule*, **1**, 229 (2017).
- A. H. Tkaczyk, A. Bartl, A. Amato, V. Lapkovskis, and M. Petranikova, *J. Phys. D Appl. Phys.*, **51**, 203001 (2018).
- C. B. L. Nkulu, L. Casas, V. Haufroid, T. De Putter, N. D. Saenen, T. Kayembe-Kitenge, P. M. Obadia, D. K. W. Mukoma, J.-M. L. Ilunga, T. S. Nawrot, O. L. Numbi, E. Smolders, and B. Nemery, *Nat. Sustain.*, **1**, 495 (2018).
- M. H. Kim, H. S. Shin, D. Shin, and Y. K. Sun, *J. Power Sources*, **159**, 1328 (2006).
- T. Ohzuku, A. Ueda, and M. Nagayama, *J. Electrochem. Soc.*, **140**, 1862 (1993).
- H. Li, N. Zhang, J. Li, and J. R. Dahn, *J. Electrochem. Soc.*, **165**, A2985 (2018).
- W. Li, J. Reimers, and J. Dahn, *Solid State Ionics*, **67**, 123 (1993).
- H. Arai, S. Okada, H. Ohtsuka, M. Ichimura, and J. Yamaki, *Solid State Ionics*, **80**, 261 (1995).
- J.-M. Kim and H.-T. Chung, *Electrochim. Acta*, **49**, 3573 (2004).
- W. Li, X. Liu, H. Celio, P. Smith, A. Dolocan, M. Chi, and A. Manthiram, *Adv. Energy Mater.*, **8**, 1703154 (2018).
- K. Ishidzu, Y. Oka, and T. Nakamura, *Solid State Ionics*, **288**, 176 (2016).
- H. Liu, M. Wolf, K. Karki, Y.-S. Yu, E. A. Stach, J. Cabana, K. W. Chapman, and P. J. Chupas, *Nano Lett.*, **17**, 3452 (2017).
- E. J. Lee, Z. Chen, H.-J. Noh, S. C. Nam, S. Kang, D. H. Kim, K. Amine, and Y.-K. Sun, *Nano Lett.*, **14**, 4873 (2014).
- R. Jung, M. Metzger, F. Maglia, C. Stinner, and H. A. Gasteiger, *J. Electrochem. Soc.*, **164**, A1361 (2017).
- B. Strehle, K. Kleiner, R. Jung, F. Chesneau, M. Mendez, H. A. Gasteiger, and M. Piana, *J. Electrochem. Soc.*, **164**, A400 (2017).
- T. Teufl, B. Strehle, P. Müller, H. A. Gasteiger, and M. A. Mendez, *J. Electrochem. Soc.*, **165**, A2718 (2018).
- D. Streich, C. Erk, A. Guéguen, P. Müller, F.-F. Chesneau, and E. J. Berg, *J. Phys. Chem. C*, **121**, 13481 (2017).
- F. Lin, I. M. Markus, D. Nordlund, T. C. Weng, M. D. Asta, H. L. Xin, and M. M. Dieff, *Nat. Commun.*, **5**, 3529 (2014).
- S. Sallis, N. Pereira, P. Mukherjee, N. F. Quackenbush, N. Faenza, C. Schlueter, T. L. Lee, W. L. Yang, F. Cosandey, G. G. Amatucci, and L. F. Piper, *J. Appl. Phys. Lett.*, **108**, 263902 (2016).
- H. Zheng, Q. Sun, G. Liu, X. Song, and V. S. Battaglia, *J. Power Sources*, **207**, 134 (2012).
- K. Amine, Z. Chen, Z. Zhang, J. Liu, W. Lu, Y. Qin, J. Lu, L. Curtis, and Y.-K. Sun, *J. Mater. Chem.*, **21**, 17754 (2011).
- S. Solchenbach, G. Hong, A. T. S. Freiberg, R. Jung, and H. A. Gasteiger, *J. Electrochem. Soc.*, **165**, 3304 (2018).
- USABC, USABC Goals for Advanced Batteries for EVs - CY2020 Commercialization, can be found under https://www.energy.gov/sites/prod/files/2014/05/f15/APR13_Energy_Storage_d_III_Adv_Battery_Dev_0.pdf, accessed October 2019.
- D. Andre, S. Kim, P. Lamp, F. Lux, and F. Maglia, *J. Mater. Chem. A Mater. Energy Sustain.*, **3**, 6709 (2015).
- K. Kleiner, B. Strehle, A. R. Baker, S. J. Day, C. C. Tang, I. Buchberger, F.-F. Chesneau, H. A. Gasteiger, and M. Piana, *Chem. Mater.*, **30**, 3656 (2018).
- C. A. Murray, J. Potter, S. J. Day, A. R. Baker, S. P. Thompson, J. Kelly, C. G. Morris, S. Yang, and C. C. Tang, *J. Appl. Crystallogr.*, **50**, 172 (2017).
- M. Basham, J. Filik, M. T. Wharmby, P. C. Y. Chang, B. El Kassaby, M. Gerring, J. Aishima, K. Levik, B. C. A. Pulford, I. Siharulidze, D. Sneddon, M. Webber, S. S. Dhesi, F. Maccherozzi, O. Svensson, S. Brockhauser, G. Náray, and A. W. Ashton, *J. Synchrotron Radiat.*, **22**, 853 (2015).
- J. Filik, A. W. Ashton, P. C. Y. Chang, S. J. Day, M. Drakopoulos, M. W. Gerring, M. L. Hart, O. V. Magdysyuk, S. Michalik, A. Smith, C. C. Tang, N. J. Terril, M. T. Wharmby, and H. Wilhelm, *J. Appl. Crystallogr.*, **50**, 959 (2017).
- O. Coelho, Coelho Software (2016).
- O. Dolotko, A. Senyshyn, M. J. Mühlbauer, K. Nikolowski, and H. Ehrenberg, *J. Power Sources*, **255**, 197 (2014).
- S. H. Bo, K.-W. Nam, O. J. Borkiewicz, Y.-Y. Hu, X.-Q. Yang, P. J. Chupas, K. W. Chapman, L. Wu, L. Zhang, F. Wang, C. P. Grey, and P. G. Khalifah, *Inorg. Chem.*, **53**, 6585 (2014).
- T. A. Hewstone and B. L. Chamberland, *J. Phys. Chem. Solids*, **48**, 97 (1987).
- H. Liu, H. Liu, S. H. Lapidus, Y. S. Meng, P. J. Chupas, and K. W. Chapman, *J. Electrochem. Soc.*, **164**, A1802 (2017).
- Y. Arachi, H. Kobayashi, S. Emura, Y. Nakata, M. Tanaka, T. Asai, H. Sakaebe, K. Tatsumi, and H. Kageyama, *Solid State Ionics*, **176**, 895 (2005).
- O. Sekizawa, T. Hasegawa, N. Kitamura, and Y. Idemoto, *J. Power Sources*, **196**, 6651 (2011).
- Y. J. Gu, Y. B. chen, H. Q. Liu, Y. M. Wang, C. L. Wang, and H. K. Wu, *J. Alloys Compd.*, **509**, 7915 (2011).
- M. Ma, N. A. Chernova, B. H. Toby, P. Y. Zavalij, and M. S. Whittingham, *J. Power Sources*, **165**, 517 (2007).
- P. Whitfield, I. Davidson, L. Cranswick, I. Swainson, and P. Stephens, *Solid State Ionics*, **176**, 463 (2005).
- A. Hirano, K. Kanie, T. Ichikawa, N. Imanishi, Y. Takeda, R. Kanno, T. Kamiyama, and F. Izumi, *Solid State Ionics*, **152–153**, 207 (2002).
- L. Yin, G. S. Mattei, Z. Li, J. Zheng, W. Zhao, F. Omenya, C. Fang, W. Li, J. Li, Q. Xie, J.-G. Zhang, M. S. Whittingham, Y. S. Meng, A. Manthiram, and P. G. Khalifah, *Rev. Sci. Instrum.*, **89**, 093002 (2018).
- S. Sasaki, K. Fujino, and Y. Takéuchi, *Proc. Japan Acad. Ser. B Phys. Biol. Sci.*, **55**, 43 (1979).
- S. Sasaki, K. Fujino, Y. Takéuchi, and R. Sadanaga, *Acta Crystallogr. Sect. A*, **36**, 904 (1980).
- P. W. Stephens, *J. Appl. Crystallogr.*, **32**, 281 (1999).
- A. O. Kondrakov, H. Geßwein, K. Galdina, L. de Biasi, V. Meded, E. O. Filatova, G. Schumacher, W. Wenzel, P. Hartmann, T. Brezesinski, and J. Janek, *J. Phys. Chem. C*, **121**, 24381 (2017).
- A. Senyshyn, O. Dolotko, M. J. Mühlbauer, K. Nikolowski, H. Fuess, and H. Ehrenberg, *J. Electrochem. Soc.*, **160**, A3198 (2013).
- O. Dolotko, A. Senyshyn, M. J. Mühlbauer, K. Nikolowski, F. Scheiba, and H. Ehrenberg, *J. Electrochem. Soc.*, **159**, A2082 (2012).
- S. Solchenbach, D. Pritzl, E. J. Y. Kong, J. Landesfeind, and H. A. Gasteiger, *J. Electrochem. Soc.*, **163**, A2265 (2016).
- J. Landesfeind, D. Pritzl, and H. A. Gasteiger, *J. Electrochem. Soc.*, **164**, A1773 (2017).
- D. Strmcnik, I. E. Castelli, J. G. Connell, D. Haering, M. Zorko, P. Martins, P. P. Lopes, B. Genorio, T. Østergaard, H. A. Gasteiger, F. Maglia, B. K. Antonopoulos, V. R. Stamenkovic, J. Rossmeisl, and N. M. Markovic, *Nat. Catal.*, **1**, 255 (2018).
- I. Buchberger, S. Seidlmayer, A. Pokharel, M. Piana, J. Hattendorff, P. Kudejova, R. Gilles, and H. A. Gasteiger, *J. Electrochem. Soc.*, **162**, A2737 (2015).
- J. Choi and A. Manthiram, *Solid State Ionics*, **176**, 2251 (2005).
- F. German, A. Hintennach, A. LaCroix, D. themig, S. Oswald, F. Scheiba, M. J. Hoffmann, and H. Ehrenberg, *J. Power Sources*, **264**, 100 (2014).
- S. H. Kang, D. P. Abraham, W. S. Yoon, K. W. Nam, and X. Q. Yang, *Electrochim. Acta*, **54**, 684 (2008).
- S. H. Kang, W. S. Yoon, K. W. Nam, X. Q. Yang, and D. P. Abraham, *J. Mater. Sci.*, **43**, 4701 (2008).
- R. Jung, R. Morasch, P. Karayaylali, K. Philips, F. Maglia, C. Stinner, Y. Shao-Horn, and H. A. Gasteiger, *J. Electrochem. Soc.*, **165**, A132 (2018).
- R. Jung, M. Metzger, F. Maglia, C. Stinner, and H. A. Gasteiger, *J. Phys. Chem. Lett.*, **8**, 4820 (2017).
- S.-K. Jung, H. Gwon, J. Hong, K.-Y. Park, D.-H. Seo, H. Kim, J. Hyun, W. Yang, and K. Kang, *Adv. Energy Mater.*, **4**, 1300787 (2014).
- Y. Makimura, T. Sasaki, T. Nonaka, Y. F. Nishimura, T. Uyama, C. Okuda, Y. Itou, and Y. Takeuchi, *J. Mater. Chem. A*, **4**, 8350 (2016).
- H. H. Ryu, K. J. Park, C. S. Yoon, and Y. K. Sun, *Chem. Mater.*, **30**, 1155 (2018).
- S. Choi and A. Manthiram, *J. Electrochem. Soc.*, **149**, A1157 (2002).
- H. R. Kim, S. G. Woo, J. H. Kim, W. Cho, and Y. J. Kim, *J. Electroanal. Chem.*, **782**, 168 (2016).
- S. Watanabe, T. Hosokawa, K. Morigaki, M. Kinoshita, and K. Nakura, *ECS Trans.*, **41**, 65 (2012).
- N. Yabuuchi, Y. Makimura, and T. Ohzuku, *J. Electrochem. Soc.*, **154**, A314 (2007).
- L. de Biasi, A. O. Kondrakov, H. Geßwein, T. Brezesinski, P. Hartmann, and J. Janek, *J. Phys. Chem. C*, **121**, 26163 (2017).
- A. O. Kondrakov, A. Schmidt, J. Xu, H. Geßwein, R. Mönig, P. Hartmann, H. Sommer, T. Brezesinski, and J. Janek, *J. Phys. Chem. C*, **121**, 3286 (2017).
- S. K. Jung, H. Gwon, J. Hong, K.-Y. Park, D.-H. Seo, H. Kim, J. Hyun, W. Yang, and K. Kang, *Adv. Energy Mater.*, **4**, 1300787 (2014).
- D. Mohanty, K. Dahlberg, D. M. King, L. A. David, A. S. Sefat, D. L. Wood, C. Daniel, S. Shar, V. Mahajan, M. Lee, and F. Albano, *Sci. Rep.*, **6**, 26532 (2016).
- K. Luo, M. R. Roberts, R. Hao, N. Guerrini, D. M. Pickup, Y.-S. Liu, K. Edström, J. Guo, A. V. Chadwick, L. C. Duda, and P. G. Bruce, *Nat. Chem.*, **8**, 684 (2016).
- T. Teufl, D. Pritzl, S. Solchenbach, H. A. Gasteiger, and M. A. Mendez, *J. Electrochem. Soc.*, **166**, A1275 (2019).
- H. Koga, L. Croguennec, M. Ménétrier, P. Mannesiez, F. Weill, and C. Delmas, *J. Power Sources*, **236**, 250 (2013).
- H. Sclar, J. Sicklinger, E. M. Ericson, S. Maiti, J. Grinblat, M. Talianker, L. Burstein, H. Beyer, G. Avruschenko, H. A. Gasteiger, B. Markovsky, and D. Aurbach, *to be submitted*.
- J. Xia, K. J. Nelson, Z. Lu, and J. R. Dahn, *J. Power Sources*, **329**, 387 (2016).
- M. Metzger, B. Strehle, S. Solchenbach, and H. A. Gasteiger, *J. Electrochem. Soc.*, **163**, 798 (2016).
- J. Wandt, A. T. S. Freiberg, A. Ogródnik, and H. A. Gasteiger, *Mater. Today*, **21**, 825 (2018).
- S. Watanabe, M. Kinoshita, T. Hosokawa, K. Morigaki, and K. Nakura, *J. Power Sources*, **258**, 210 (2014).

Supporting Information

Capacity Fading Mechanisms of NCM-811 Cathodes in Lithium-Ion Batteries Studied by X-ray Diffraction and Other Diagnostics

Franziska Friedrich,^{1,=} Benjamin Strehle,^{1,=} Anna T. S. Freiberg,¹ Karin Kleiner,^{1,2} Sarah J. Day,²
Christoph Erk,³ Michele Piana,¹ and Hubert A. Gasteiger¹

¹ *Chair of Technical Electrochemistry, Department of Chemistry and Catalysis Research Center,
Technical University of Munich, D-85748 Garching, Germany*

² *Harwell Science and Innovation Campus, Diamond Light Source, Didcot, Oxfordshire OX11 0DE, UK*

³ *BASF SE Ludwigshafen, Lithium-Ion Battery Research, D-67056 Ludwigshafen, Germany*

⁼ *These authors contributed equally to this work.*

Contents

S1: Supplementary Information on Refinement Strategy	2
S2: Rietveld Refinement Results	7
S3: Lattice Parameter and <i>c/a</i> Calibration Curves	12
S4: Impedance Measurements	17
S5: Selected Cathode Half-Cell Voltage Profiles	20
S6: XPS Reference Data	22
S7: Calculation of O-depleted Surface Layer Thickness	25
S8: SEM Cross-Sectional Images of Pristine and EOT NCM-811	26
S9: HAADF-STEM Images of Pristine, BOT and EOT NCM-811	28
S10: Literature	30

S1: Supplementary Information on Refinement Strategy

Background fit.— As mentioned in the Experimental section of the main text, two different approaches were applied to fit the complex background. In the following, both fits are compared. One option is fitting a linear interpolation between selected data points, which results in an approximately linear background for single reflections, even for the (003) reflection which is located in the 2θ range with a clearly apparent nonlinear background. Therefore, the integrated area of the peaks and the structural information derived from them is assumed to be rather reproducible. On the other hand, this fit gives rise to an irregular background curve as can be seen in the following figure. The limited amount of data points, which are manually selected for the background fit, is the reason for this poor fit quality. Therefore, another method was applied to fit the complex background. A combination of eight pseudo-Voigt peaks was used to model the broad and high background of the cell components diffracting in the 2θ range below 12° . In addition, the standard background functions implemented in Topas (polynomial and $1/X$) are used. The thereby obtained background is smooth in comparison to the linear interpolated background. Although the fit of the complex background below 12° 2θ is not perfect, the reflections of interest can be refined based on a continuous and smooth background, which improves the quality of the refinement.

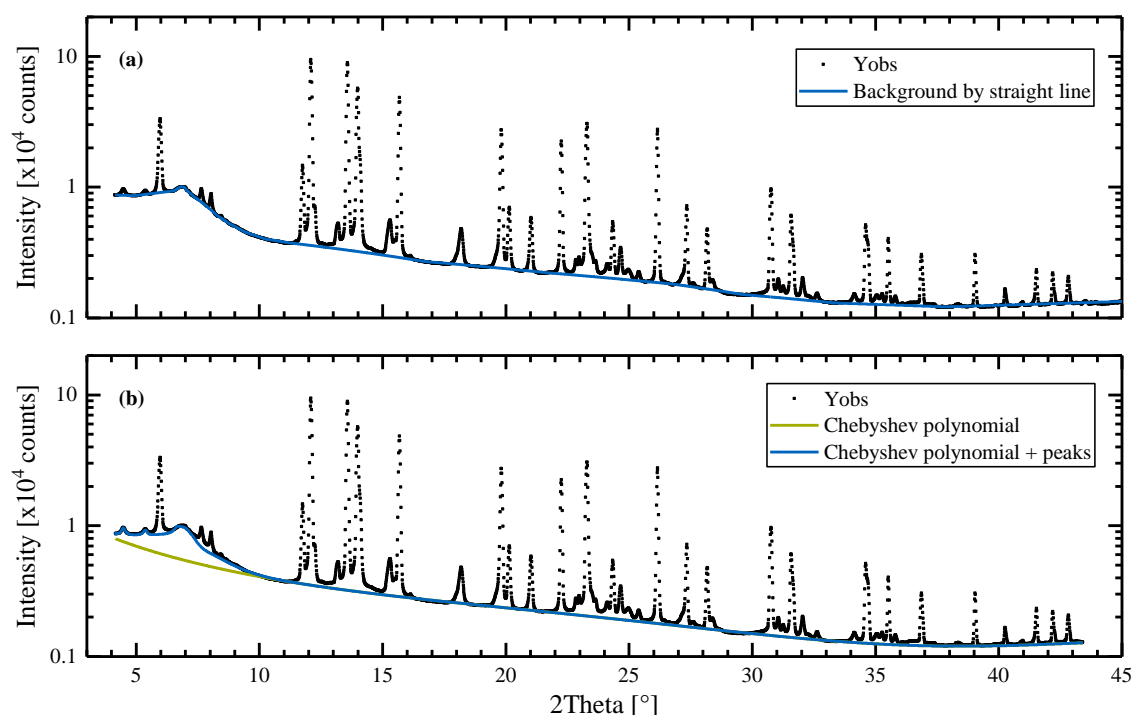


Figure S1. In situ S-XPD of an NCM-811/graphite full-cell (LDE cell 1 in the charged state in the 968th cycle) measured at beamline I11 of the Diamond Light Source, showing the measured data points and the fitted background: (a) a straight-line background fit in comparison to (b) a combination of pseudo-Voigt peaks and standard Topas background functions (polynomials and $1/X$).

Applied constraints and calculation of Li occupancy in $\text{Li}_x\text{Ni}_{0.79}\text{Co}_{0.1}\text{Mn}_{0.1}\text{O}_2$.— Underlying structural parameters and constraints for the refinement of the NCM phase are summarized in **Table S1**. An example of a refinement of an NCM-811/graphite pattern is given in **Figure S2**.

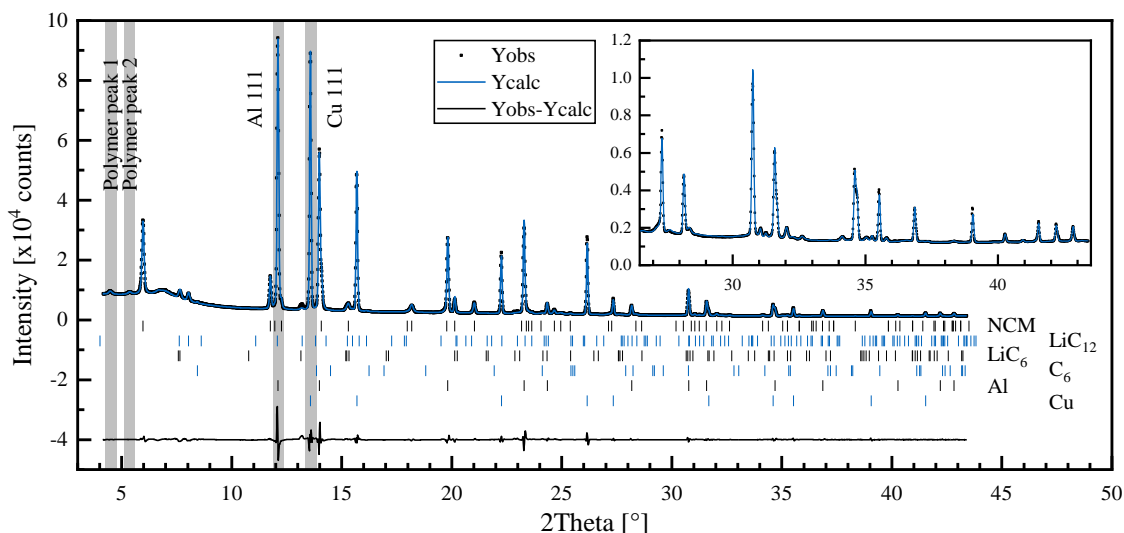


Figure S2. In situ S-XPD pattern of an NCM-811/graphite full-cell (LDE cell 1 in the charged state in the 968th cycle) with the experimental data points (points), the calculated fit (blue line), and the difference plot (black line). The inset shows the reflections at high angles. The reflection positions of NCM-811, LiC_{12} , LiC_6 , C_6 , Al, and Cu phases are shown as ticks below the diffractogram. Highlighted peaks were used as “internal standards” for the quantification of the material loss discussed in paragraph S2.

The parameter x_{Li} stands for the Li occupancy, calculated based on the fit of the operando L-XPD c/a calibration curve as discussed in the main text. For the low SOC range ($0.62 \leq x_{\text{Li}} \leq 0.91$), the quadratic fit gives the following equation when solved for x_{Li} :

$$x_{\text{Li}} = \frac{73.80 - \sqrt{c/a \cdot 10^4 - 49222}}{58.36} \quad (\text{S1})$$

The linear fit for the high SOC range ($0.12 \leq x_{\text{Li}} \leq 0.23$) results in the following equation for x_{Li} :

$$x_{\text{Li}} = \frac{c/a - 4.733}{1.41} \quad (\text{S2})$$

With equations (S1) and (S2), the occupancy of Li on the Li site can be calculated. However, the cation disorder between Ni and Li has to be taken into account to get the true number of Li atoms on the Li site and, in turn, also the number of Ni atoms on the Li site. Therefore, the parameter *dis* in **Table S1** stands for the amount of Li (Ni) which was found to be on the TM (Li) site by refining pristine and EOT samples from ex situ L- XPD measurements at our in-house diffractometer. A disorder (Li-Ni mixing) of 3% equals to a *dis* parameter of 0.03.

Table S1. Structural parameters from the Rietveld refinement of the NCM-811 phase with Wyckoff positions, fractional coordinates, and site occupancy factors. The thermal displacement parameter was constrained for all sites in case of the in situ S-XPD data and refined site-specific for the ex situ L-XPD data collected at the in-house diffractometer. Refined values for z_O are given in paragraph S2.

Li _x Ni _{0.79} Co _{0.10} Mn _{0.10} O ₂ : Space group $R\bar{3}m$ (166) with x_{Li} = Li content and <i>dis</i> = disorder					
Atom	Wyckoff position	x	y	z	S.O.F.
Li(1)	3a, Li	0	0	0	x_{Li} - <i>dis</i>
Li(2)	3b, TM	0	0	0.5	<i>dis</i>
Ni(1)	3b, TM	0	0	0.5	0.79 - <i>dis</i>
Ni(2)	3a, Li	0	0	0	<i>dis</i>
Co	3b, TM	0	0	0.5	0.10
Mn	3b, TM	0	0	0.5	0.10
O	6c, O	0	0	$z_{6c,O} \approx 0.24$	1

Stephens model.— In agreement with the literature,^{S1,S2} anisotropic reflection broadening was also observed in this study for samples at high degrees of delithiation. The anisotropy can be caused by inhomogeneous Li (de)intercalation, oxygen deficiency and lattice distortions. For perfectly isotropic samples, the FWHM (Γ_{total}) is supposed to be the sum of the particle size broadening Γ_{size} and the micro-strain broadening Γ_{strain} , as described by the following equations:

$$\Gamma_{total} = \Gamma_{strain} + \Gamma_{size} \quad (S3)$$

$$\Gamma_{total} = 4 \varepsilon \tan \theta + \frac{K \lambda}{L \cos \theta} \quad (S4)$$

where ε = strain, K = Scherrer constant ($0.89 < K < 1$; usually $K = 0.9$ for spherical particles),^{S3} λ = wavelength of the X-rays in nm, L = diameter of the (spherical) particles in nm, and 2θ = Bragg angle of the respective reflection.

By the following transformation, a linear correlation (the so-called Williamson-Hall plot) between $\Gamma_{total} \cdot \cos \theta$ and $\sin \theta$ can be established, with the micro-strain broadening as slope and the apparent particle size as intercept.

$$\Gamma_{total} \cdot \cos \theta = 4 \varepsilon \sin \theta + \frac{K \lambda}{L} \quad (S5)$$

For an ideal material with isotropic broadening, like the herein used CeO₂ standard material, the Williamson-Hall plot gives a straight line as can be seen in **Figure S3** ($R^2 = 0.84$). The data points of

the discharged NCM-811 are also reasonably close to a straight line ($R^2 = 0.07$). However, the reflections of the charged NCM-811 do not follow a Williamson-Hall behavior.

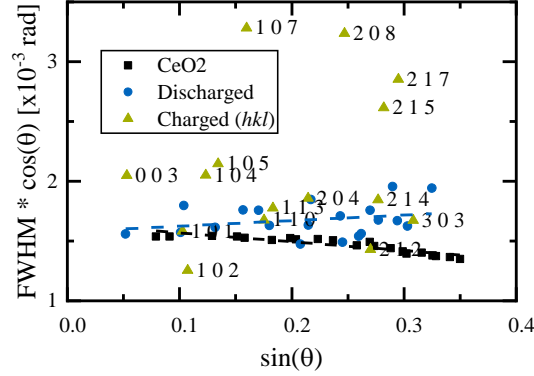


Figure S3. Williamson-Hall plot of the NCM-811 phase (from in situ S-XPD at BOT in the discharged and charged state) compared to the CeO₂ standard material, as determined by single reflection fitting with a pseudo-Voigt function. For the charged state, the reflections are labeled with the corresponding hkl indices.

This so-called anisotropic line shape broadening is accommodated by a phenomenological model of the multi-dimensional distribution of lattice metrics within a sample. It was first introduced by Peter Stephens in 1999 and is therefore called Stephens model.^{S4} The investigated samples belong to the $R\bar{3}m$ space group. According to the literature, a trigonal Bravais lattice with hexagonal indexing was employed, leading to four independent anisotropic strain parameters S_{400} , S_{202} , S_{004} , and S_{301} ,^{S2,S4,S5} of which only S_{004} and S_{202} were used for fitting the in situ S-XPD data. The anisotropic broadening contribution is thereby given by

$$\Gamma_A(hkl) = \left[\sum_{\text{HKL}} S_{\text{HKL}} h^{\text{H}} k^{\text{K}} l^{\text{L}} \right]^{1/2} d^2 \tan \theta \quad (\text{S6})$$

with

$$\begin{aligned} \sum_{\text{HKL}} S_{\text{HKL}} h^{\text{H}} k^{\text{K}} l^{\text{L}} = & S_{400} (h^4 + k^4 + 3h^2k^2 + 2h^3k + 2hk^3) + \\ & S_{004} l^4 + \\ & S_{202} 3 (h^2l^2 + k^2l^2 + hkl^2) + \\ & S_{301} (3h^2kl - 3hkl^2 + 2h^3l - 2k^3l) \end{aligned} \quad (\text{S7})$$

It is important to note that Γ_A is given in radians. For a conversion to degrees, as used in the Topas software, the factor $180^\circ/\pi$ must be applied. For an easier handling of the strain parameters, another factor of 10^{-5} is implemented in the Topas macros. The Gaussian and Lorentzian contributions of Γ_A are implemented into the pseudo-Voigt function (TCHZ) describing the overall reflection shape as follows:

$$\Gamma_G = [U \tan^2 \theta + V \tan \theta + W + Z/\cos^2 \theta + (1 - \xi)^2 \Gamma_A^2(hkl)]^{1/2} \quad (\text{S8})$$

$$\Gamma_L = X \tan \theta + Y/\cos \theta + \xi \Gamma_A (hkl) \quad (\text{S9})$$

where ξ is a mixing parameter to interpolate between the Gaussian and Lorentzian line shape. In the following tables, the refinement results of the LDE data for the anisotropic strain parameters S_{004} and S_{202} are shown. The mixing parameter ξ always converges to 1 (i.e., mainly Lorentzian line shape). The isotropic strain parameter of the TCHZ function (X) was set to zero when the Stephens model was applied. The evolution of the S_{004} and S_{202} strain parameters in the charged state of the LDE cells is summarized in **Table S2**, which shows that the line shape broadening of the NCM-811 phase stays basically constant over the course of almost 1000 cycles.

Table S2. Anisotropic strain parameters used in the Stephens model in the refinement of the LDE data of cell 1 and 2 in the charged state. Errors are given in parenthesis.

Cell 1			Cell 2		
Cycle	S_{004}	S_{202}	Cycle	S_{004}	S_{202}
18	95(6)	270(50)	18	99(6)	280(50)
64	82(5)	250(50)	64	83(5)	230(50)
155	69(5)	240(50)	155	68(5)	200(50)
201	64(5)	260(50)	201	62(5)	210(50)
248	64(5)	260(50)	248	58(5)	230(50)
915	63(5)	280(50)	926	64(6)	290(60)
969	57(5)	320(50)	976	56(6)	310(60)

S2: Rietveld Refinement Results

Refinement results of the NCM-811 phase.— The results from the in situ S-XPD refinement of the NCM-811 phase during the LDE study are summarized in the following tables sorted by cell number (cell 1 and 2) and SOC (first in the discharged state and then in the charged state). During the refinement, the Li-Ni disorder was fixed to the value determined from the ex situ L-XPD data (3.1%) as is described in the main text.

Table S3. Refined structural parameters for $\text{Li}_x\text{Ni}_{0.79}\text{Co}_{0.10}\text{Mn}_{0.10}\text{O}_2$ in the discharged state (cell 1) with errors given in parenthesis.

Cycle	a [Å]	c [Å]	V [Å ³]	c/a [-]	x_{Li} [-]	$z_{6c,\text{O}}$ [-]	b_{all} [Å ²]	R_{bragg} [%]
18	2.8618(1)	14.2641(7)	101.169(8)	4.9841(3)	0.838	0.2397(3)	1.31(6)	1.24
63	2.8613(1)	14.2675(7)	101.161(8)	4.9863(3)	0.831	0.2396(3)	1.33(6)	1.31
108	2.8613(1)	14.2711(7)	101.185(9)	4.9876(3)	0.826	0.2389(3)	1.33(7)	1.83
154	2.8611(1)	14.2735(7)	101.185(9)	4.9887(3)	0.823	0.2394(3)	1.49(7)	1.41
200	2.8620(1)	14.2775(7)	101.281(8)	4.9886(3)	0.823	0.2386(3)	1.20(6)	2.00
247	2.8620(1)	14.2782(7)	101.284(8)	4.9890(3)	0.822	0.2389(3)	1.30(6)	1.68
806	2.8654(1)	14.3171(7)	101.799(8)	4.9967(3)	0.797	0.2387(3)	1.34(6)	1.60
859	2.8654(1)	14.3174(7)	101.804(8)	4.9967(3)	0.797	0.2384(3)	1.27(6)	1.92
914	2.8653(1)	14.318(7)	101.800(9)	4.9969(3)	0.796	0.2382(3)	1.28(7)	2.14
968	2.8651(1)	14.3183(7)	101.788(9)	4.9975(3)	0.794	0.2385(3)	1.32(7)	1.77

Table S4. Refined structural parameters for $\text{Li}_x\text{Ni}_{0.79}\text{Co}_{0.10}\text{Mn}_{0.10}\text{O}_2$ in the discharged state (cell 2) with errors given in parenthesis.

Cycle	a [Å]	c [Å]	V [Å ³]	c/a [-]	x_{Li} [-]	$z_{6c,\text{O}}$ [-]	b_{all} [Å ²]	R_{bragg} [%]
18	2.8682(1)	14.2937(6)	101.831(8)	4.9835(3)	0.840	0.2401(3)	1.37(6)	1.38
63	2.8682(1)	14.2977(7)	101.859(8)	4.9848(3)	0.836	0.2397(3)	1.35(7)	1.27
108	2.8681(1)	14.3011(7)	101.877(9)	4.9863(3)	0.831	0.2392(3)	1.32(7)	1.45
154	2.8676(1)	14.3031(7)	101.855(8)	4.9880(3)	0.825	0.2399(3)	1.53(7)	1.17
200	2.8673(1)	14.3050(8)	101.85(1)	4.9891(3)	0.821	0.2399(3)	1.37(8)	1.51
247	2.8674(1)	14.306(1)	101.86(1)	4.9893(4)	0.821	0.2402(3)	1.5(1)	1.71
814	2.8658(1)	14.3179(7)	101.834(9)	4.9964(3)	0.798	0.2398(3)	1.42(7)	1.29
869	2.8657(1)	14.3179(7)	101.830(9)	4.9963(3)	0.799	0.2395(3)	1.31(7)	1.30
925	2.8661(1)	14.3166(8)	101.85(1)	4.9952(3)	0.802	0.2395(3)	1.34(7)	1.28
975	2.8658(1)	14.3175(7)	101.835(9)	4.9961(3)	0.799	0.2398(3)	1.35(7)	1.52

Table S5. Refined structural parameters for $\text{Li}_x\text{Ni}_{0.79}\text{Co}_{0.10}\text{Mn}_{0.10}\text{O}_2$ in the charged state (cell 1) with errors given in parenthesis.

Cycle	a [Å]	c [Å]	V [Å ³]	c/a [-]	x_{Li} [-]	$z_{6c,\text{O}}$ [-]	b_{all} [Å ²]	R_{bragg} [%]
18	2.81434(8)	13.952(1)	95.701(9)	4.9576(4)	0.159	0.2337(3)	1.66(6)	1.66
63	2.81472(8)	13.960(1)	95.779(9)	4.9595(4)	0.161	0.2335(3)	1.72(6)	1.50
154	2.81532(8)	13.982(1)	95.973(8)	4.9663(4)	0.165	0.2340(3)	1.86(6)	1.29
200	2.81625(8)	13.994(1)	96.118(9)	4.9689(4)	0.167	0.2337(3)	1.68(5)	1.52
247	2.81643(8)	13.997(1)	96.150(9)	4.9695(4)	0.168	0.2338(3)	1.70(6)	1.57
914	2.82367(9)	14.199(1)	98.04(1)	5.0282(4)	0.209	0.2330(3)	1.80(6)	1.45
968	2.82389(8)	14.218(1)	98.189(9)	5.0347(4)	0.214	0.2332(3)	1.75(6)	1.63

Table S6. Refined structural parameters for $\text{Li}_x\text{Ni}_{0.79}\text{Co}_{0.10}\text{Mn}_{0.10}\text{O}_2$ in the charged state (cell 2) with errors given in parenthesis.

Cycle	a [Å]	c [Å]	V [Å ³]	c/a [-]	x_{Li} [-]	$z_{6c,\text{O}}$ [-]	b_{all} [Å ²]	R_{bragg} [%]
18	2.82028(8)	13.985(1)	96.330(9)	4.9584(4)	0.160	0.2339(3)	1.78(6)	1.44
63	2.82074(8)	13.995(1)	96.435(9)	4.9612(4)	0.162	0.2336(3)	1.79(6)	1.42
154	2.82141(8)	14.022(1)	96.668(9)	4.9699(4)	0.168	0.2341(3)	2.08(6)	1.38
200	2.82164(9)	14.035(1)	96.77(1)	4.9739(5)	0.171	0.2337(3)	1.80(7)	1.74
247	2.82187(9)	14.040(1)	96.82(1)	4.9756(4)	0.172	0.2339(3)	1.77(7)	1.76
925	2.8302(1)	14.212(1)	98.59(1)	5.0214(5)	0.205	0.2336(3)	1.87(7)	1.46
975	2.82380(9)	14.184(1)	97.95(1)	5.0233(5)	0.206	0.2343(3)	1.89(7)	1.47

Refinement results of the Li_xC_6 phases.— Refinement results from the graphite phases are shown in **Table S7** (C), **Table S8** (LiC_{12}), and **Table S9** (LiC_6). Starting values were taken from Dolotko *et al.*,^{S6} and the thermal displacement parameters were kept constant at their respective values. For graphite, only the lattice parameters were refined. For the LiC_{12} and the LiC_6 phase, lattice parameters and peak broadening due to size effects and fractional coordinates of carbon could be refined.

Table S7. Structural data of graphite added as conductive agent to the cathode coating. Exemplary data for cell 1 in cycle 968 in the charged state.

Graphite: Space group $P6_3/mmc$ (194), $a = 2.49(1)$ Å, $c = 6.68(1)$ Å, $R_{\text{bragg}} = 2.0\%$					
Atom	Wyckoff position	x	y	z	b_{all} [Å ²] ^{S6}
C(1)	2b	0	0	1/4	1.62
C(2)	2c	1/3	2/3	1/4	1.62

Table S8. Structural data of LiC_{12} determined by Rietveld refinement of cell 1 in cycle 968 in the charged state.

LiC_{12} : Space group $P6/mmm$ (191), $a = 4.293(3)$ Å, $c = 7.038(2)$ Å, $R_{\text{bragg}} = 4.8\%$					
Atom	Wyckoff position	x	y	z	b_{all} [Å ²] ^{S6}
Li	1a	0	0	0	1.49
C	12n	0.361(6)	0	0.165(2)	1.49

Table S9. Structural data of LiC_6 determined by Rietveld refinement of cell 1 in cycle 968 in the charged state.

LiC ₆ : Space group P6/mmc (191), $a = 4.315(3)$ Å, $c = 3.700(2)$ Å, $R_{\text{bragg}} = 4.9\%$					
Atom	Wyckoff position	x	y	z	b_{all} [Å ²] ^{S6}
Li	1a	0	0	0	1.65
C	12n	0	0.34(1)	1/2	1.65

Quantitative phase analysis.— For a quantitative phase analysis using XPD data, an internal standard is necessary. In order to quantify the CAM phase loss, the NCM-811 scale factor was normalized to the intensity of different reflections. The respective reflection intensity is assumed to correlate solely with the beam intensity and to show no change in the phase fraction. This is why no Li_xC_6 phases were used. However, due to preferred orientation, the Al and Cu phases were refined structure-independent as Pawley fits. Therefore, no classical phase quantification by Rietveld refinement was possible. For this reason, the small polymer reflections at $4.5^\circ 2\theta$ and $5.4^\circ 2\theta$ as well as the 111 reflections from Al and Cu were chosen as “internal standards” (see highlighted reflections in **Figure S2**). The polymer reflections arise from the pouch foil. As can be seen in **Figure S2**, the 111 reflection of Cu is most suitable for such an analysis because there is no significant overlap with any reflections of the NCM-811 phase. In **Figure S4**, the results of the performed estimation are shown for cell 1 and 2 in the discharged and charged state. All three different normalization methods have in common that an NCM-811 material loss over the course of cycling becomes evident (despite for cell 1 when normalized to the Cu 111 reflection). However, the resulting absolute values scatter substantially. From the analysis in **Figure 5c**, a material loss of 8.5% is expected. Small changes in the NCM-811 phase fraction are expected to give rise to minor intensity changes and they proved to be very hard to quantify with the herein applied “internal standards”. In conclusion, we can say that a quantitative analysis of the NCM-811 phase fraction was not possible using a ratio between scale factors and reflection intensities, but the results at least qualitatively follow the observed trend for the NCM-811 material loss.

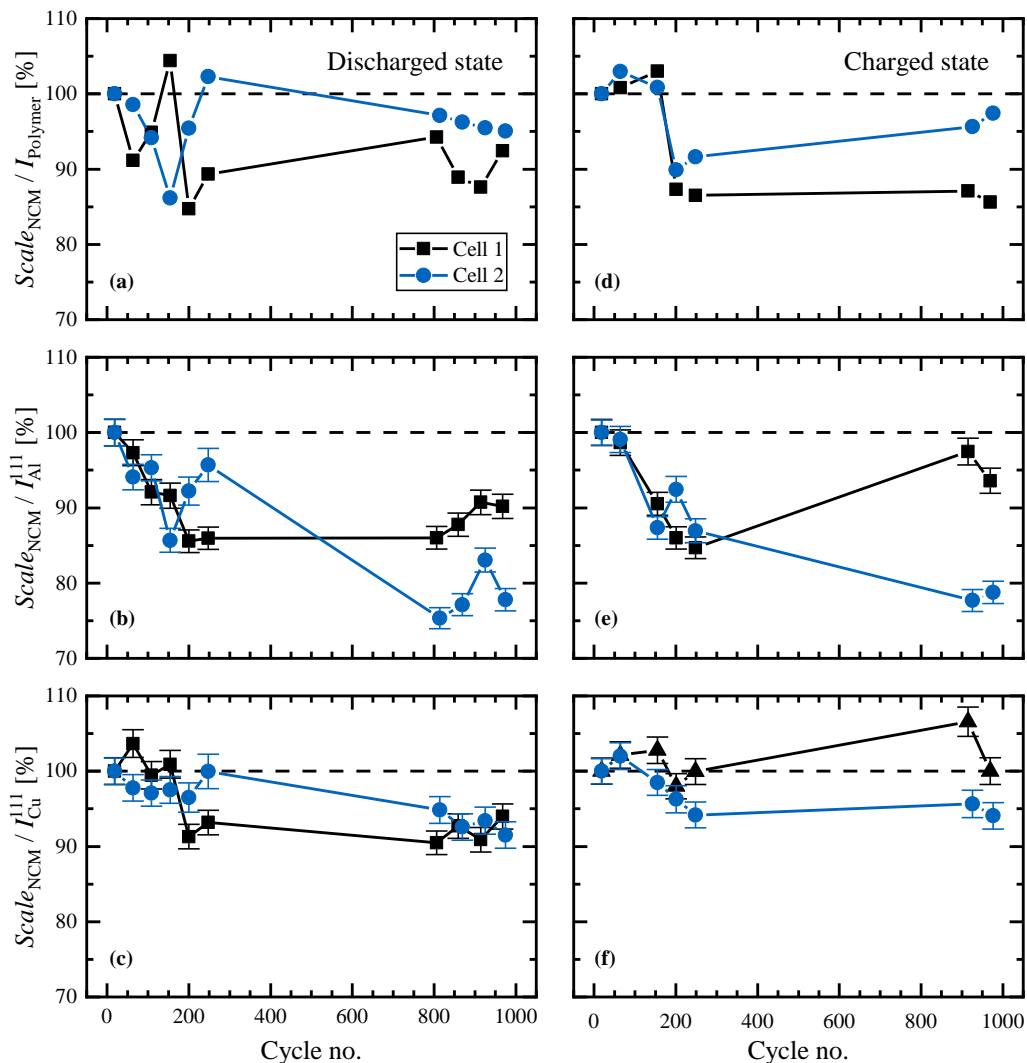


Figure S4. Results of the NCM-811 phase quantification from the in situ S-XPD data for both cells in the discharged (left panels) and charged state (right panels) over the course of cycling, making use of different “internal standards”: (a,d) the intensity of the polymer peaks; (b,e) the intensity of the 111 reflection of the Al current collector; (c,f) the intensity of the 111 reflection of the Cu current collector. The error bars for the polymer-based normalization are not shown because they are too large for the chosen scale.

S3: Lattice Parameter and c/a Calibration Curves

To obtain a calibration curve for the c/a ratio, diffraction data over the whole charge/discharge cycle are necessary. We tried two different approaches to collect this data:

- (a) In situ L-XPD measurements: The cell is cycled at $C/7.5$ and at defined capacity steps (e.g., every 10 or 15 mAh/g), XPD data are collected during OCV periods. The main advantage is that data over a large 2θ range are collected, thus most NCM reflections contribute to the refinement. A disadvantage is that just a limited amount of c/a data points are collected during cycling, especially at high SOC, where the c/a curve is very steep. Thus, the intervals between the c/a data points in this region are rather large.
- (b) Operando L-XPD measurements: The cell is cycled at a rate of $C/7.5$ while a small part of the 2θ range is measured continuously. Thereby, selected non-overlapping reflections of the NCM-811 phase, namely 003 and 110, are monitored alternately during cycling. The main advantage is that a time resolution of ≈ 8 minutes (corresponding to SOC intervals of ≈ 4 mAh/g) allows for a sufficient amount of c/a data points for interpolation of the c/a curve. A disadvantage is that only two reflections contribute to the refinement, so that the accuracy of the obtained lattice parameter values has to be verified.

Figure S5 compares the two differently obtained data sets, showing that the lattice parameter values obtained by the operando L-XPD technique ($\Delta\text{SOC} \approx 4$ mAh/g) are in good agreement with those obtained by in situ L-XPD ($\Delta\text{SOC} = 10$ mAh/g). While no actual structural information can be obtained from the single reflection fits, the operando L-XPD method can be used to track the evolution of the lattice parameter with rather short acquisition times, so that we could use it also to monitor the evolution of the c parameter upon a transition from constant-current charge to OCV (see **Figure 8** in the main text).

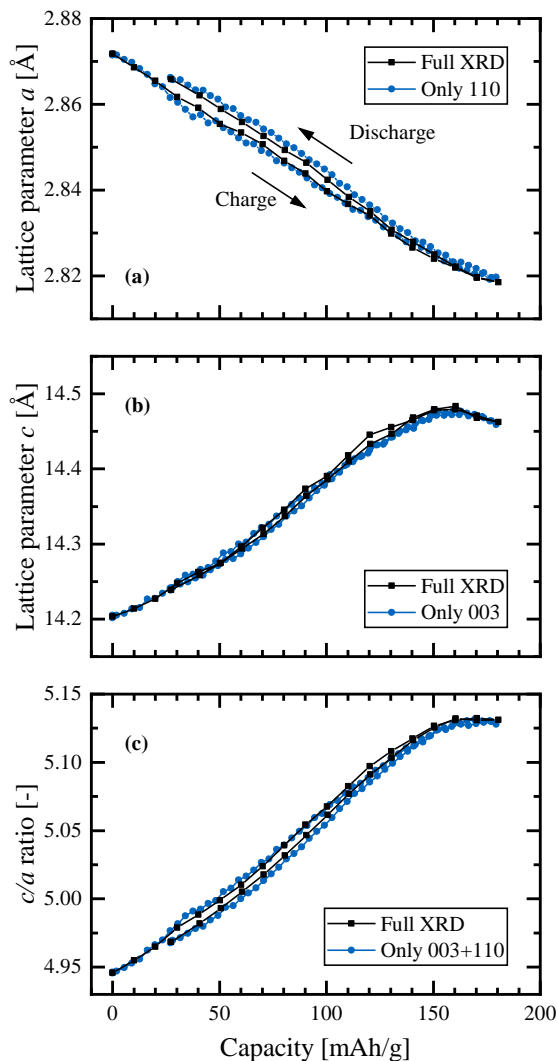


Figure S5. Comparison of lattice parameter values vs. capacity of NCM-811/lithium cells obtained by refining in situ L-XPD data (i.e., fitting the full XPD pattern measured during intermediate OCV phases) versus those obtained by refining operando L-XPD data (i.e., continuous measurements of the 003 and 110 reflections, determining a and c by single reflection fitting). Data were collected at the in-house Mo-diffractometer and show the first cycle at C/7.5 charged to 180 mAh/g and then discharged to 3.0 V.

Next, we will use in situ L-XPD data to examine the evolution of the lattice parameters over the first two formation cycles (cycle 1 and 2) at C/7.5 and compare them to the lattice parameter values which are obtained by in situ L-XPD with an NCM-811 cathode harvested from cell 1 at EOT (both cells are assembled with metallic lithium anodes). The determined lattice parameters and the unit cell volume versus OCV are shown in **Figure S6**, whereby the observed evolution of structural parameters is in agreement with literature reports.^{S2,S7-S10} With increasing OCV of the fresh NCM-811 cathode, i.e., with increasing extent of delithiation, the lattice parameter a drops from ≈ 2.87 Å to ≈ 2.81 Å, and then remains essentially constant at OCV values exceeding ≈ 4.2 V (see **Figure S6a**). It is reported that the TM-O distance closely follows the behavior of the lattice parameter a upon delithiation, because both values directly depend on the oxidation states and the ionic radii of the transition metals. When Li-ions are removed from the structure, this charge is compensated for by the oxidation of TMs, resulting in decreased ionic radii and hence a decrease in the lattice parameter a .

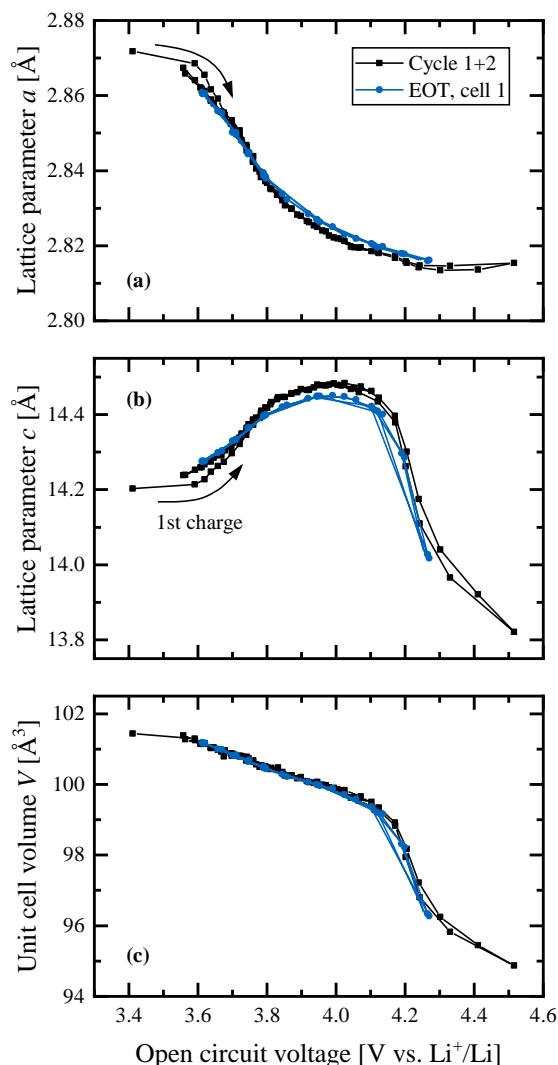


Figure S6. Dependence of (a) lattice parameter a , (b) lattice parameter c , and (c) unit cell volume V on the OCV of NCM-811 during charge/discharge, as determined by in situ L-XPD. The black lines/symbols are obtained with fresh NCM-811 (cycle 1+2, $C/7.5$, $\Delta\text{SOC} = 10$ mAh/g) and the blue lines/symbols are obtained with an EOT sample harvested from the LDE cell 1 ($C/2$, $\Delta\text{SOC} = 15$ mAh/g). The counter-electrode is metallic lithium.

The lattice parameter c , which correlates to the Li-O distance, exhibits a more complex behavior. After an initial increase from ≈ 14.2 Å to ≈ 14.5 Å, a broad maximum is reached at an OCV of ≈ 4.0 V, followed by a steep decrease to ≈ 13.8 Å upon further delithiation (see **Figure S6b**). The initial rise is interpreted as a result of the increasing coulombic repulsion between negatively charged oxygen anions remaining in the layered structure upon removal of the Li-ions between them. The interaction of Li with lattice oxygen is reported to be accompanied with a partial charge transfer from oxygen to lithium, resulting in a screening effect that diminishes the inter-slab repulsion. Upon delithiation, this screening effect is minimized and thereby leads to an increase in c . On the other hand, the observation of a decreasing c at an OCV exceeding ≈ 4.0 V must imply a decrease in the inter-slab repulsion. It is known in the literature^{S11} that TM 3d and O 2p states are highly hybridized in layered Ni-rich compounds. This means that electrons can be extracted from both TM and O states, which decreases the effective charge of the oxygen atoms and thereby the inter-slab repulsion, resulting in a decrease in c . While the decreasing

screening effect by Li should induce an elongation in the c direction, the decreasing effective oxygen charge due to TM-O hybridization would cause a shrinkage. Both effects seem to be present, with the elongation in the c direction being dominant until an OCV of ≈ 4.0 V, and the shrinkage in the c direction occurring at higher degrees of delithiation. At the beginning of charge, the change in the unit cell volume is dominated by the changes in a , which contributes to the cell volume by the second power. At high OCV values, i.e., at low lithium contents, where the lattice parameter a remains essentially constant and c shows a steep decrease with OCV, the change in the unit cell volume is mostly dominated by the changes in c .

When we now compare the evolution of the lattice parameters of fresh NCM-811 upon cycling with that of the harvested EOT sample (black vs. blue lines/symbols in **Figure S6**), the advantage of the ability to plot the structural parameters versus the NCM-811 OCV becomes clear: In operando XPD, the degree of (de)lithiation at a given SOC is not anymore defined, as it changes due to capacity losses upon aging (e.g., by increased polarization, CAM loss, and/or loss of cyclable lithium if used in a full-cell without a pre-lithiated anode). In contrast, for in situ XPD data taken at OCV, the degree of (de)lithiation at a given OCV value is identical for fresh and aged samples. The first data points of the first charge in **Figure S6** indicate that the structural evolution of a material with a full Li site and no cycling history deviates slightly from that of a cycled CAM. This, however, has no influence on our analysis. Apart from that, lattice parameter a shows the same trend for the aged NCM-811 harvested at EOT as for the fresh material, although its absolute value is slightly higher for the EOT material at OCV values >3.8 V (see **Figure S6a**). An increased a for the aged NCM-811 would suggest a lower oxidation state of the transition-metals compared to the fresh NCM-811. Lattice parameter c for the aged NCM-811 is slightly decreased at OCV values of >3.8 V (see **Figure S6b**) compared to fresh NCM-811, indicating that the observed repulsion between the negatively charged oxygen layers is less severe. This might be caused by a more covalent TM-O bond, with significant charge transfer from O to the transition-metals. The resulting decreased TM oxidation state is in agreement with the results for the lattice parameter a . Although there are literature reports on a small lowering of the Co and Mn oxidation states upon extended cycling,^{S12} it has to be noted that so far these observations were only made on the near-surface region of cathodes. Interestingly, the deviations of the lattice parameters between the fresh and the EOT sample do not affect the net cell volume, as the values for the unit cell volume before and after 1000 cycles agree almost perfectly over the entire OCV range (see **Figure S6c**).

To get an idea of what might have happened to the transition-metals of the cathode, we conducted ICP-AES measurements of the graphite anode at EOT and found that over the course of the ≈ 1000 cycles, an amount of transition-metals corresponding to 0.22 mol%_{TM} of the NCM-811 material was deposited on the anode. The relative distribution of Ni, Co, and Mn amongst the metals deposited on the anode is 84%, 2%, and 14%, which at least for Ni and Mn is close to the stoichiometric metal ratio in the fresh NCM-811, suggesting that there is no strong indication for a preferential metal loss (e.g., of Mn).

Different mechanisms are reported for the transition metal dissolution from NCM CAMs.^{S9} The possible extent of dissolution of Ni and Mn out of the pouch cell components (pouch foil, current collector and tabs) is not known. However, Al current collectors generally have a Mn contamination on the order of 100 ppm due to production processes. Assuming that a loss of one transition-metal in NCM-811 will result in a maximum loss of 4 cyclable lithium due to charge compensation (e.g., for 1 removed Mn⁴⁺, 4 Li⁺ would have to remain in the structure), the maximum capacity loss based on a transition-metal loss of 0.22 mol%_{TM} would be ≈ 2.4 mAh/g, similar values as those suggested by Buchberger *et al.* for NCM-111.^{S9}

S4: Impedance Measurements

To fit the cathode impedance spectra obtained with a gold wire micro-reference electrode (GWRE), the transmission line model (TLM) was used as described in the literature.^{S13} The fitted equivalent circuit is described by $R_{HF} + \text{TLM}[R_{ion}, R_{CT}/Q_{CT}] + R_{contact}/Q_{contact} + W$, with R_{HF} as the high-frequency resistance, TLM as a transmission line model with ionic resistance R_{ion} and an R_{CT}/Q_{CT} parallel circuit element of the charge transfer resistance R_{CT} and a constant phase element (CPE; $Z_{CPE} = [Q \cdot (i\omega)^\alpha]^{-1}$) denoted with Q_{CT} , the $R_{contact}/Q_{contact}$ parallel circuit element of the contact resistance $R_{contact}$ and a $Q_{contact}$ CPE, and, finally a Warburg diffusion element W . W and $R_{contact}/Q_{contact}$ were only used when appropriate. The fitted value for the ionic resistance was $R_{ion} \approx 3 \Omega \text{ cm}^2$ during the first and 18th cycle and $R_{ion} \approx 9 \Omega \text{ cm}^2$ at EOT. **Figure S7** shows three representative cathode impedance spectra of NCM-811 measured in NCM-811/graphite full-cells (with a GWRE) during charge at an OCV of $\approx 4.0 \text{ V}$ in the first, the 18th cycle, and after 1000 cycles.

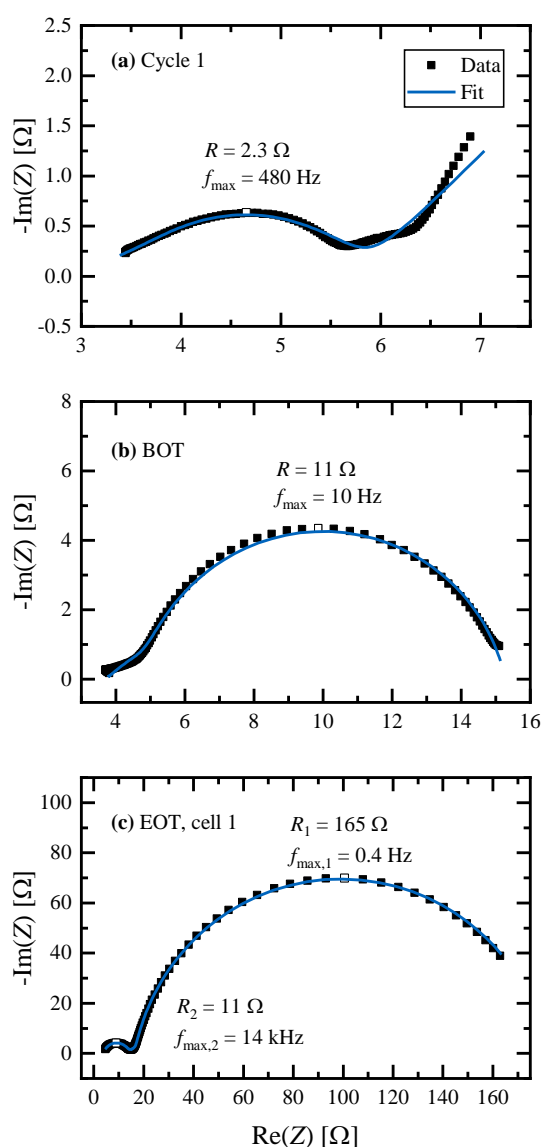


Figure S7. Exemplary cathode impedance spectra of NCM-811/graphite full-cells with a micro-reference electrode (GWRE) measured after a C/10 charge to an OCV of $\approx 4.0 \text{ V}$: (a) in the first charging cycle; (b) in the

18th cycle (BOT); and, (c) for the harvested NCM-811 cathode from the LDE experiment after 1000 cycles (EOT). The data (black symbols) were fitted (blue lines) to: $R_{HF} + TLM[R_{ion}, R_{CT}/Q_{CT}] (+ R_{contact}/Q_{contact}) (+ W)$ (see text for assignments). Spectra were recorded from 100 kHz to 100 mHz with a voltage perturbation of 10 mV at 25°C.

For both the fresh NCM-811 and the NCM-811 at BOT (18th cycle), no feature indicating a contact resistance could be observed (see **Figure S7a,b**) and the fit was conducted without the $R_{contact}/Q_{contact}$ element. On the other hand, an apparent contact resistance feature was observed at high frequencies for the EOT sample (see **Figure S7c**). A rough order-of-magnitude estimation of the capacitances related to charge transfer and to the contact resistance by neglecting the constant phase exponent α was conducted to verify the assignment of the fitting parameters to the semicircles:^{S13-S15}

$$C_{calc} = \frac{1}{R 2\pi f_{max}} \quad (S10)$$

This calculation yields values of $C_{calc,CT} \approx 0.14$ mF for the first charge cycle, $C_{calc,CT} \approx 1.5$ mF for the BOT sample, and $C_{calc,CT} \approx 2.4$ mF and $C_{calc,contact} \approx 1.0$ μ F for the EOT sample. An overview of the all values is shown in **Table S10**.

Table S10: Overview of the resistances (R) and the maximum frequencies (f_{max}) of the R/Q elements determined from the Nyquist plots in Fig. S7, together with the calculated capacitances (C_{calc}) according to eq. S10. Based on the assigned interfaces, the calculated capacitances were normalized to the total surface area (A_{total}) to calculate an estimated capacitance (C_{est}), for which different NCM-811 BET surface areas ($A_{BET,CAM}$) were used as described in the text. Note that for the EOT sample (from cell 1), two clearly pronounced semicircles were observed (denoted below as low-f and high-f).

Sample	R [Ω]	f_{max} [Hz]	C_{calc} [mF]	Assigned interface	$A_{BET,CAM}$ [m ² /g]	A_{total} [cm ²]	C_{est} [μ F/cm ²]
Cycle 1	2.3	480	0.14	Electrode/electrolyte	0.27	95	≈ 1.5
BOT	11	10	1.5	Electrode/electrolyte	1.2	160	≈ 9.4
EOT (low-f)	165	0.4	2.4	Electrode/electrolyte	1.2	160	≈ 15
EOT (high-f)	11	$14 \cdot 10^3$	$1.0 \cdot 10^{-3}$	Al foil/electrode	-	0.95	≈ 1.1

The C_{calc} values of the BOT and EOT samples were normalized to the total surface area of the cathode electrode, including the BET surface area of SFG6L (≈ 20 m²/g), C65 (≈ 62 m²/g), and of either the fresh NCM-811 (≈ 0.27 m²/g) or of aged NCM-811 after removal of the surface impurities with the HF treatment (≈ 1.2 m²/g, see discussion in context of Figure 8 in the main text). This results in an estimated total cathode electrode surface area of either ≈ 95 cm² for fresh or of ≈ 160 cm² for aged NCM-811. When normalizing the C_{calc} values by the total electrode surface area and when neglecting the α exponent of the CPE elements, one would expect to obtain estimated specific capacitances (C_{est}), which are comparable to the typical double layer capacitance of ≈ 10 μ F/cm².^{S13,S16} For the BOT and EOT samples, $C_{est,CT}$ is ≈ 9.4 μ F/cm² and ≈ 15 μ F/cm², respectively, which is consistent with the expected value and suggests that our assignment is correct. On the other hand, $C_{est,CT}$ for the NCM-811 in the first cycle is only ≈ 1.5 μ F/cm², which must be due to the fact that the “semicircle” seen in the Nyquist plot for the

first cycle (**Figure S7a**) must contain at least two different processes, as indicated by the very low α value of 0.6 (vs. 0.9 for the other semicircles in the BOT and EOT samples), so that the associated $Q_{\text{est,CT}}$ value can only be taken as an order-of-magnitude estimate. A reason for this relatively small capacitance might be the fact that this electrode has never been cycled to voltages above 4.0 V where this impedance spectrum was recorded. As mentioned in the main text in context with the shift of the R_{CT} vs. OCV curve of the first charge (**Figure 5**), it is known from the literature^{S17} that surface species, such as Li_2CO_3 , are removed upon the first charge, a process which might not be completed at this point and their continuous slow removal during the first-cycle impedance measurements at 4.0 V might lead to artefacts as the surface might be changing while recording the impedance data.

Finally, let us examine the high-frequency semicircle clearly apparent in the EOT sample, which is likely related to a contact resistance at the interface between the Al current collector and the cathode electrode. This can be verified by normalizing C_{calc} to the exposed area of the Al current collector ($\approx 0.95 \text{ cm}^2$), yielding an estimated capacitance of $C_{\text{est,contact}} \approx 1.1 \text{ } \mu\text{F}/\text{cm}^2$, which is on the same order of magnitude than a double layer capacitance,^{S13,S16} thus proving that the assignment of this impedance feature to a contact resistance is correct.

S5: Selected Cathode Half-Cell Voltage Profiles

Figure S8 shows cathode voltage profiles of cell 2 at $C/2$ ($\equiv 0.72 \text{ mA/cm}^2$ or 6.46 mA), for which a sudden jump in capacity and in the average charge and discharge voltages is observed during cycle 893 (see **Figure 1a** and **b**), plotting the voltage profiles before and after this event. Quite clearly, both the charge and the discharge voltages between cycle 892 (black line) and cycle 894 (green line) differ by $\approx 100 \text{ mV}$ along the entire capacity range, which corresponds to a resistance decrease of $\approx 15 \Omega$ (from $100 \text{ mV}/6.46 \text{ mA}$, $\approx 140 \Omega \text{ cm}^2$). As evident from the voltage profile of cycle 893 (blue symbols), this decrease in potential, i.e., this drop in resistance, occurred instantaneously, indicating that it cannot be caused by any structural change within the cathode, but must be related to a sudden improvement of the electronic contacting of the cell. This was likely caused by obtaining a better electronic contact between the current collector tabs of the pouch cell and the crocodile clamp by some random movement. While we cannot prove this hypothesis, due to the fact that both cells showed again rather similar capacities and average charge/discharge voltages after cycle 893 (see **Figure 1a** and **b**), we are very confident that this contacting issue does not influence the observations and conclusions made in our work.

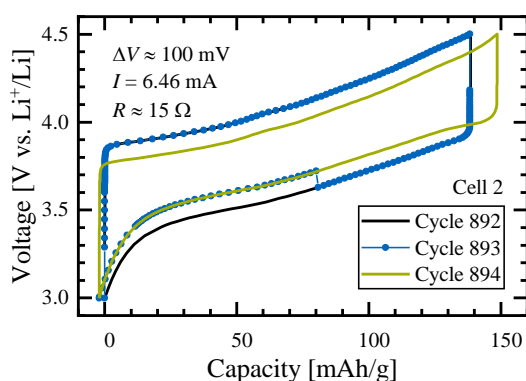


Figure S8. Cathode half-cell voltage profiles at $C/2$ of the LDE cell 2 during cycles 892 (black line), 893 (blue line/symbols), and 894 (green line), where a sudden jump in capacity and average charge/discharge voltage occurred.

An additional figure of cathode half-cell voltage profiles serves to support the line of argument that the impedance build-up happens with a considerable time delay compared to the material loss, because the surface oxygen-depleted surface layer restructures only gradually into a resistive surface layer. To show this, the cathode voltage profiles and the respective difference plots of the 250th cycle, at EOT, and at BOT are shown for cell 1 and 2 in **Figure S9**. Here, the capacity axis used in **Figure 1c** in the main text is converted into the lithium content (x_{Li}) scale for the NCM-811 bulk material, as determined by the XPD analysis (see **Figure 4**). Independent of the degree of material loss, this visualization allows the best comparison between voltage curves of the retained bulk material over the course of extended cycling (assuming that the surface layer is electrochemically inactive and does not contribute to the obtained capacities). The increase of cathode overpotential observable in the 250th cycle is slightly higher than at BOT (cycle 19), but much lower than at EOT (cycle 970/973), while in the 250th cycle

the material loss at the surface was found to be already $\approx 65\%$ of that at EOT (5.6% after 250 cycles vs. 8.5% at EOT, see **Figure 4c**). In **Figure S9**, the grey bars highlight the x_{Li} region where the OCV is ≈ 4.0 V, i.e., the region from which the overpotential estimates are derived in the main text. It can therefore be concluded that the loss of active material by the formation of the oxygen-depleted surface layer initially does not substantially increase the cathode impedance (i.e., the surface layer has a relatively low resistance), but that it gradually transforms into a substantially more resistive structure which gives rise to the observed impedance build up (see **Figure 5b**).

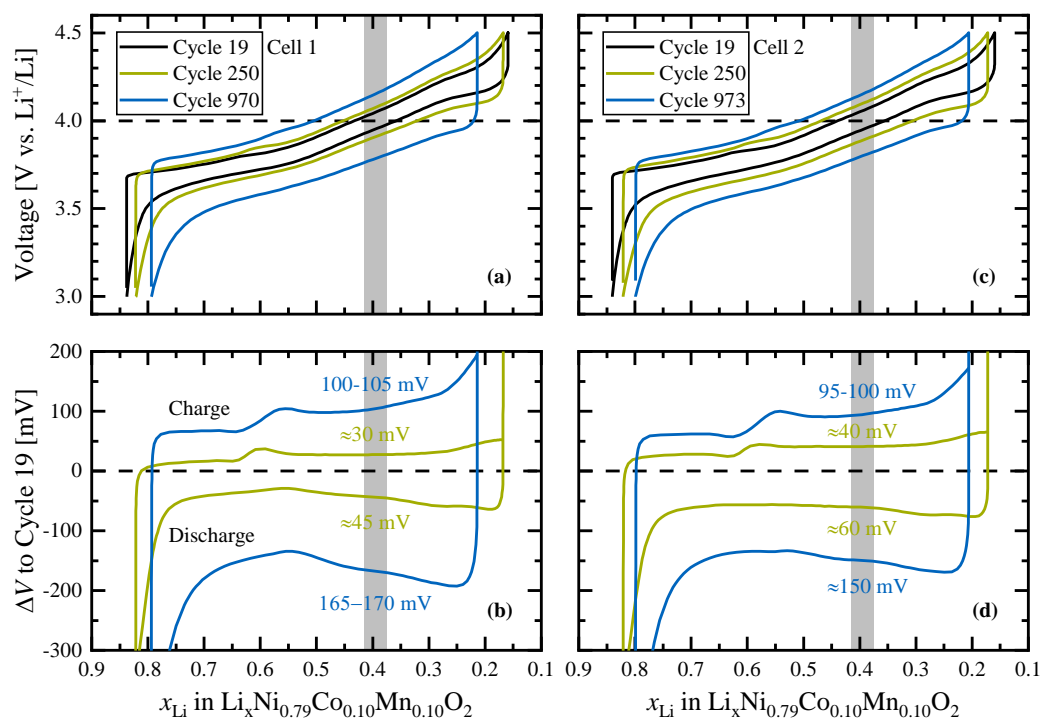


Figure S9. (a,c) Cathode voltage profiles of both LDE cells from the 19th (close to BOT, black line), the 250th (green line), and the 970th/973rd cycle (close to EOT, blue line) plotted vs. the lithium content (x_{Li}) of the retained bulk material, which was determined by the c/a ratio from the charged and discharged state of the respective in situ S-XPD data. (b,d) Voltage difference of the curves from the 250th and 970th/973rd cycle relative to the 19th cycle. The grey bars highlight the overpotential increase for the x_{Li} region at which the OCV of ≈ 4.0 V vs Li^+/Li is expected.

S6: XPS Reference Data

To establish a correlation between intensity shifts in the O1s XPS spectrum of our sample and structural information, reference spectra are necessary. For this purpose, layered MnO_2 (purity >99%), spinel Mn_3O_4 (purity >97%) and rock-salt MnO samples (purity >99%, all samples from Sigma-Aldrich) were analyzed by X-ray photoelectron spectroscopy. The focus thereby lies on the peak at lower binding energies (green and blue fits in **Figure S10**) because the one at higher energies derives from surface impurities like carbonates and hydroxides (red fits in **Figure S10**). A comparison of the reference spectra (**Figure S10g-i**) shows that the low-energy O1s peak shifts to higher binding energy as the oxygen content of the materials decreases, namely from 529.3 eV for layered MnO_2 (panel g) to 529.6 eV for spinel Mn_3O_4 (panel h) and to 529.7 eV for rock-salt MnO (panel i). Based on this observation, a correlation between the shifts of the low-energy O1s peaks towards higher binding energies upon cycling of the NCM-811 sample (pristine \rightarrow BOT \rightarrow EOT) deduced from the fits in **Figure S10d-f** is consistent with an increasing oxygen deficiency in the surface-near regions upon cycling. The detailed fitting values and applied constraints for peak energy and FWHM are listed in **Table S11**. The position of the peak of the O-depleted layer in NCM-811 (\approx 529.9 eV, marked by the dashed blue lines in **Figure S10d-f**) likely deviates from the reference samples because of the different local environment around the oxygen (only Mn in reference samples vs. Ni, Co and Mn in NCM-811).

In addition, the intensity of the peak around \approx 533.5 eV (and an additional peak for the EOT sample at \approx 532.8 eV) is evolving with cycling (**Figure S10a-c**), which we denominated as “miscellaneous”. In the literature,^{S18,S19} a similar feature is reported in the O1s XPS spectra of cycled NCA cathodes and ascribed to a CEI-type (cathode electrolyte interphase) film forming on the cathode by electrolyte decomposition (e.g., lithium alkyl carbonates, Li-O-CO-O-R), which is also possible in our case.

Table S11: XPS fitting parameters for the fits in **Figure S10** for pristine, BOT, and harvested EOT NCM-811 as well as for three reference compounds: peak energy with constrained deviation and FWHM with respective range constraint. Additionally, parameters for the main surface impurity peak are shown.

Sample (panel)	Assigned species	Energy [eV] (constrained deviation)	FWHM [eV] (constrained range)
Pristine (a,d)	Layered (green)	529.3 (± 0.1)	1.26 (0.8-1.35)
	M-OH/M-CO ₃ (red)	531.9 (± 0.1)	1.62 (0.8-2.35)
BOT (b,e)	Layered (green)	529.3 (± 0.1)	1.10 (0.8-1.35)
	O-depleted (blue)	529.9 (fixed)	1.08 (0.8-1.35)
	M-OH/M-CO ₃ (red)	531.9 (± 0.1)	1.66 (0.8-2.35)
EOT (c,f)	Layered (green)	529.3 (± 0.1)	1.10 (0.8-1.35)
	O-depleted (blue)	529.9 (fixed)	1.24 (0.8-1.35)
	M-OH/M-CO ₃ (red)	531.9 (± 0.1)	2.26 (0.8-2.35)
MnO ₂ (g)	Layered (green)	529.3 (-)	0.88 (0.8-1.35)
Mn ₃ O ₄ (h)	Spinel (blue)	529.6 (-)	1.17 (0.8-1.35)
MnO (i)	Rock-salt (blue)	529.7 (-)	0.95 (0.8-1.35)

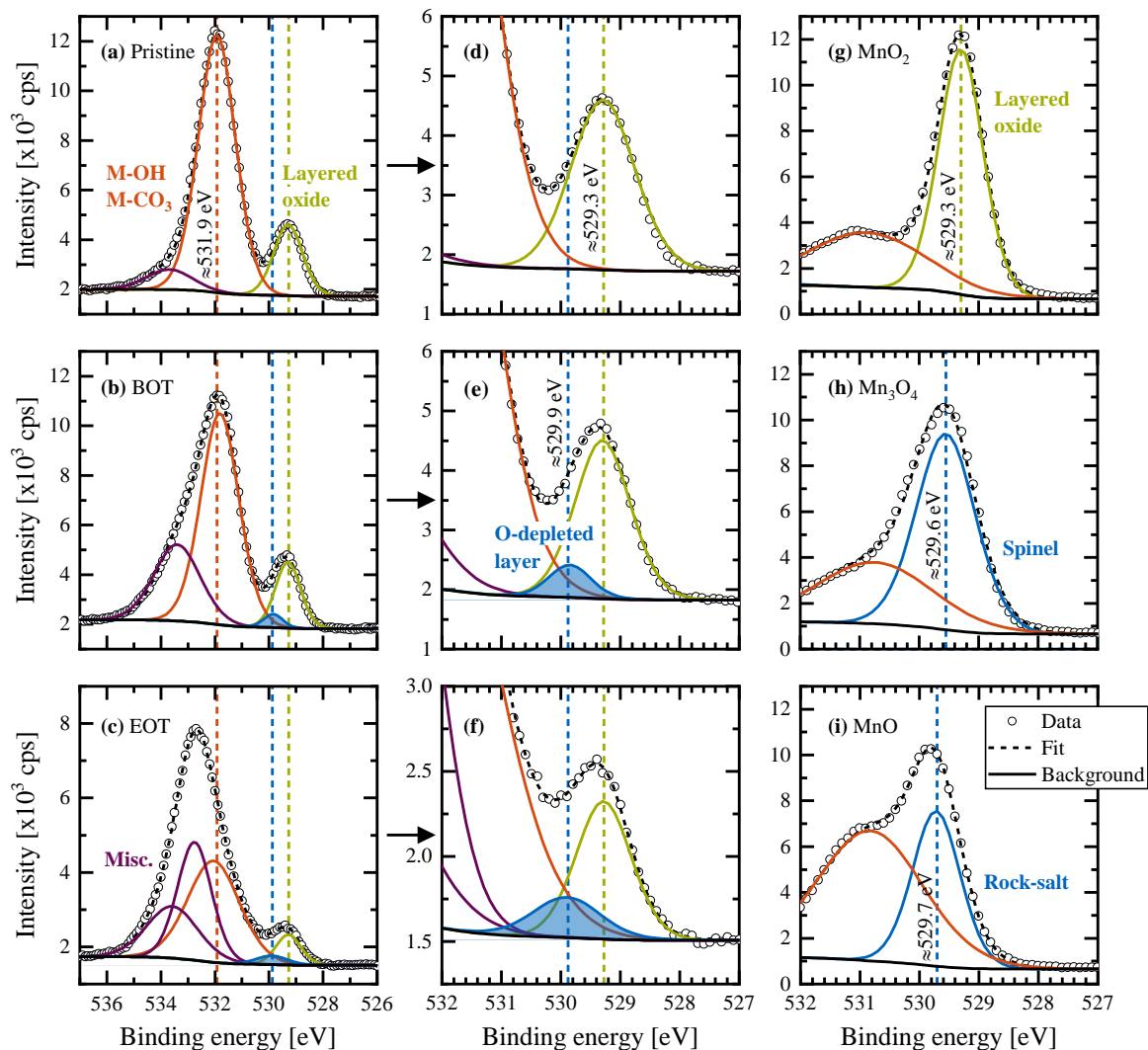


Figure S10. XPS O1s spectra of pristine, BOT, and EOT NCM-811 samples with surface hydroxide and carbonate impurities highlighted by a red dashed line in panels a-c; close-ups of the peak at lower binding energies are shown in panels d-f. Reference XPS O1s spectra of layered (MnO_2), spinel (Mn_3O_4), and rock-salt (MnO) manganese reference compounds are shown in panels g-i. The peak position of a layered and an oxygen-deficient (spinel and rock-salt) structure are highlighted by green and blue dashed lines in panels d-i. All spectra are shown with Shirley background in black line, data points as empty symbols, and the overall fit as black dashed line. The colored lines corresponding to the respective surface species as indicated in the plots give a deconvolution of the overall fitting. The fitting parameters and their constrained values for the low-energy O1s peaks (green and blue) and for the main surface impurity peak (red) are listed in **Table S12**.

S7: Calculation of O-depleted Surface Layer Thickness

Based on the discrepancy between the absolute capacity losses observed by electrochemical measurement (C_{EC}^{EOT}) and calculated from the change in lattice parameters ($C_{Material}^{EOT}$), we deduced a loss of cyclable CAM as is discussed in context with **Figure 5c** in the main text. This evaluation provides the capacity loss due to material loss, $\Delta C_{Material}^{BOT \rightarrow EOT} = 15.8$ mAh/g, or in percentage terms relative to the pristine CAM, $\Delta C_{Material,rel}^{EOT} = 8.5\%$. This ratio gives the estimated molar fraction of NCM-811, which is no longer taking part in Li intercalation ($x_{surface-layer}$). To translate the molar fraction into a surface layer thickness, the approximate particle radius is estimated from the BET surface area (A_{BET}) and the crystallographic density of the CAM (ρ_{cryst}) as given in equation (S11) and **Table S13**. For this calculation, the surface area of the aged NCM-811 is used (1.2 m²/g after HF treatment, as discussed in context with **Figure 8** in the main text), because this is the actual surface area, on which the layer will form upon extended cycling. The surface layer thickness ($t_{surface-layer}$) can then be estimated from the particle radius and the molar fraction using equations (S12) and (S13). All calculated values and measurement data are summarized in **Table S13**. Detailed information about these calculations are reported in the literature.^{S20,S21}

$$r = \frac{3}{A_{BET} \rho_{cryst}} \quad (S11)$$

$$r' = r (1 - x_{surface-layer})^{1/3} \quad (S12)$$

$$t_{surface-layer} = r - r' \quad (S13)$$

Table S13. Parameters for calculating the thickness of a presumably inactive surface layer formed upon ≈ 1000 cycles. The BET surface area (A_{BET}) was measured by both Kr and N₂ physisorption (yielding identical values) after exposure of the NCM-811 CAM to 1000 ppm HF in LP57 (see main text); the crystallographic density (ρ) was obtained from Rietveld refinement. The average radius of the NCM-811 particles was based on a spherical approximation using (S10), while the molar fraction of material lost in the surface layer ($x_{surface-layer}$) is based on the EOT value given in **Figure 5c**. The approximate surface layer thickness ($t_{surface-layer}$) then follows from (S11) and (S12).

Parameter	Value
A_{BET} [m ² /g]	1.2
ρ_{cryst} [g/cm ³]	4.75
r [nm]	526
$x_{surface-layer}$ [%]	8.5
$t_{surface-layer}$ [nm]	15

S8: SEM Cross-Sectional Images of Pristine and EOT NCM-811

The morphology of CAM secondary particles was evaluated from cross-sectional SEM images. For that purpose, 1 x 1 cm² pieces were punched out of pristine and end-of-test electrodes in their fully lithiated state. The samples were fixed in a Teflon holder, embedded in epoxy resin (EpoThin 2 resin and hardener, Buehler, USA), and subjected to reduced pressure in order to remove gas bubbles. After hardening overnight at 40°C, the resin block was removed from the holder, ground on SiC paper in two steps (grade P320 and P1200, CarbiMet S, Buehler), and subsequently polished with 9 and 3 μm diamond polishing pastes (MetaDi Supreme Polycrystalline Diamond Suspension, Buehler) on a micro cloth (MicroCloth, Buehler). The final polishing step was done with a 0.05 μm Al₂O₃ agent (MasterPrep Alumina Suspension, Buehler) on a micro cloth (ChemoMet, Buehler). The contact pressure was set to 5 N for every step. SEM analysis was performed with a JEOL scanning electron microscope (JSM-7500F, JEOL, Japan) in the backscattering mode at an accelerating voltage of 5 kV.

In context with **Figure 8** in the main text, the SEM images presented in **Figure S11** indicate that the contact area between electrolyte and primary particles is quite large and that most primary particles indeed are in direct contact with the electrolyte.

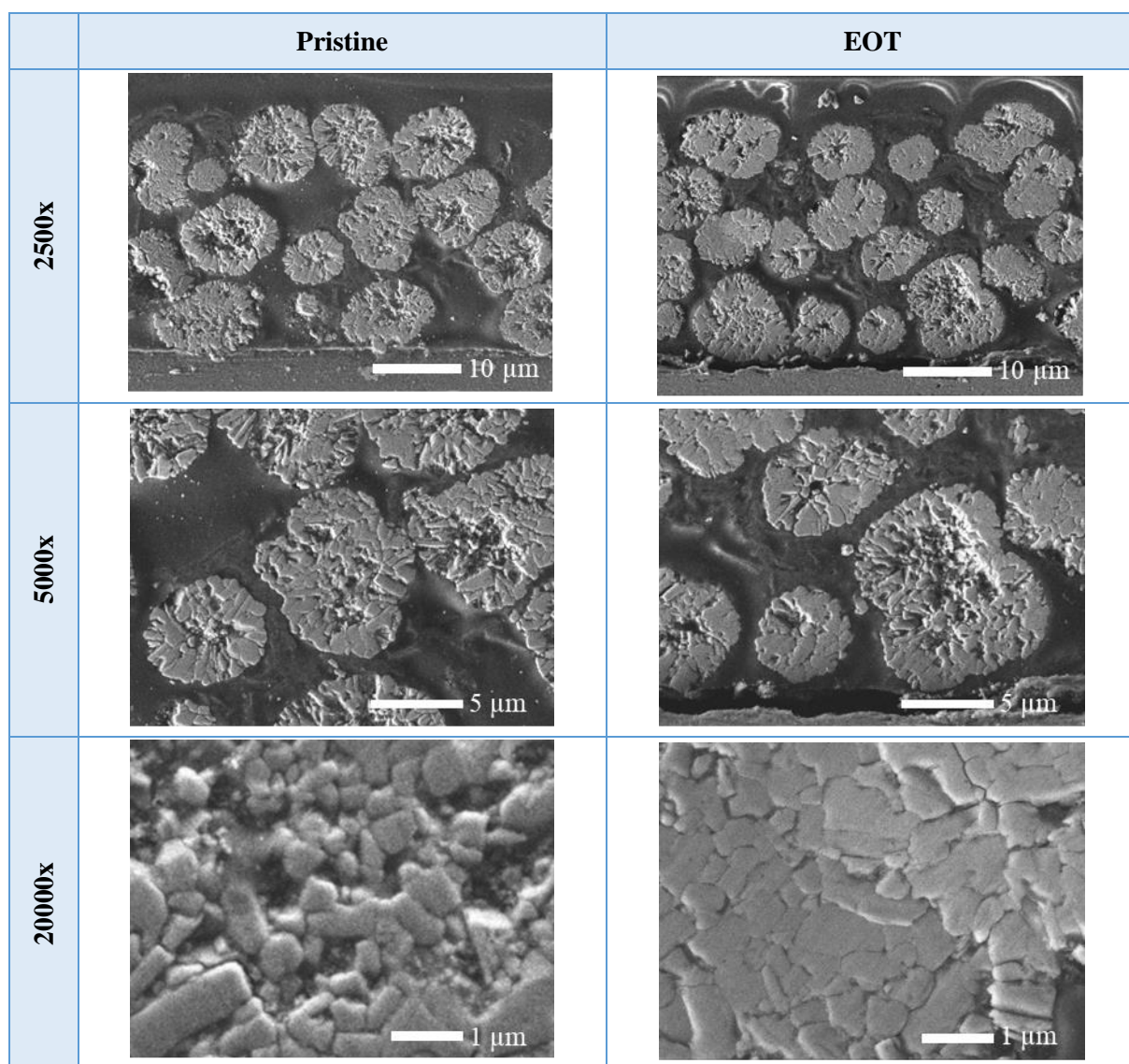


Figure S11: Cross-sectional SEM pictures of pristine (calandered electrode sheets, left) and EOT NCM-811 (discharged state, right) at different magnifications measured in backscattering mode at an accelerating voltage of 5 kV.

S9: HAADF-STEM Images of Pristine, BOT and EOT NCM-811

High Angle Annular Dark Field – Scanning Transmission Electron Microscopy (HAADF-STEM) images were measured from a pristine NCM-811 electrode, a BOT electrode which was cycled according to the LDE protocol, and a harvested EOT electrode. The BOT and EOT electrodes (in the discharged state) were first washed thoroughly with dimethyl carbonate (DMC, BASF SE) in an argon-filled glove box to remove LiPF_6 salt residuals and then dried overnight at room temperature. Afterwards, all samples were prepared by focused ion beam (FIB) milling using a Helios G4 CX dualbeam machine (Thermo Fisher Scientific, USA). The samples were immediately imaged at 300 keV by HAADF-STEM using a Thermo Fisher Themis Z 3.1 microscope.

The HAADF-STEM images are summarized in **Figure S12**. The two primary particles of the pristine NCM-811 in the left picture are imaged in the desired low-indexed zone axes in order to differentiate any disordered spinel/rock-salt structure from the regular layered structure. The pristine particle on the left (as well as in the right picture) seems to be imaged along the ab plane, highlighting the hexagonal arrangement of the transition-metals within their layer (which appear as bright spots due to the high Z number). In contrast, the pristine particle on the right shows the layered structure along the c direction, highlighting the alternating stacking of the transition-metal (bright lines) and lithium layers (inter-slab, dark lines). If transition-metals (partially) occupy the lithium layers, the intensity of these atomic columns would be increased and the region would therefore appear brighter in the image. This is however not the case for the pristine NCM-811, i.e., the layered structure ranges from the bulk of the particles to their surface without any defects. On the other hand, the BOT and EOT primary NCM-811 particles feature inter-slabs in the surface-near region (as indicated either (i) with arrows for the representation along the c direction in the left pictures or (ii) by dashed lines for the representation along the ab plane in the right figures), which are partially occupied with transition-metals, as it would be expected for spinel/rock-salt structures. However, no clear boundary between the layered bulk structure and the disordered spinel/rock-salt surface structure can be discerned from these images. The phases seem to merge gradually into each other, which makes it difficult to quantify the surface layer thickness.

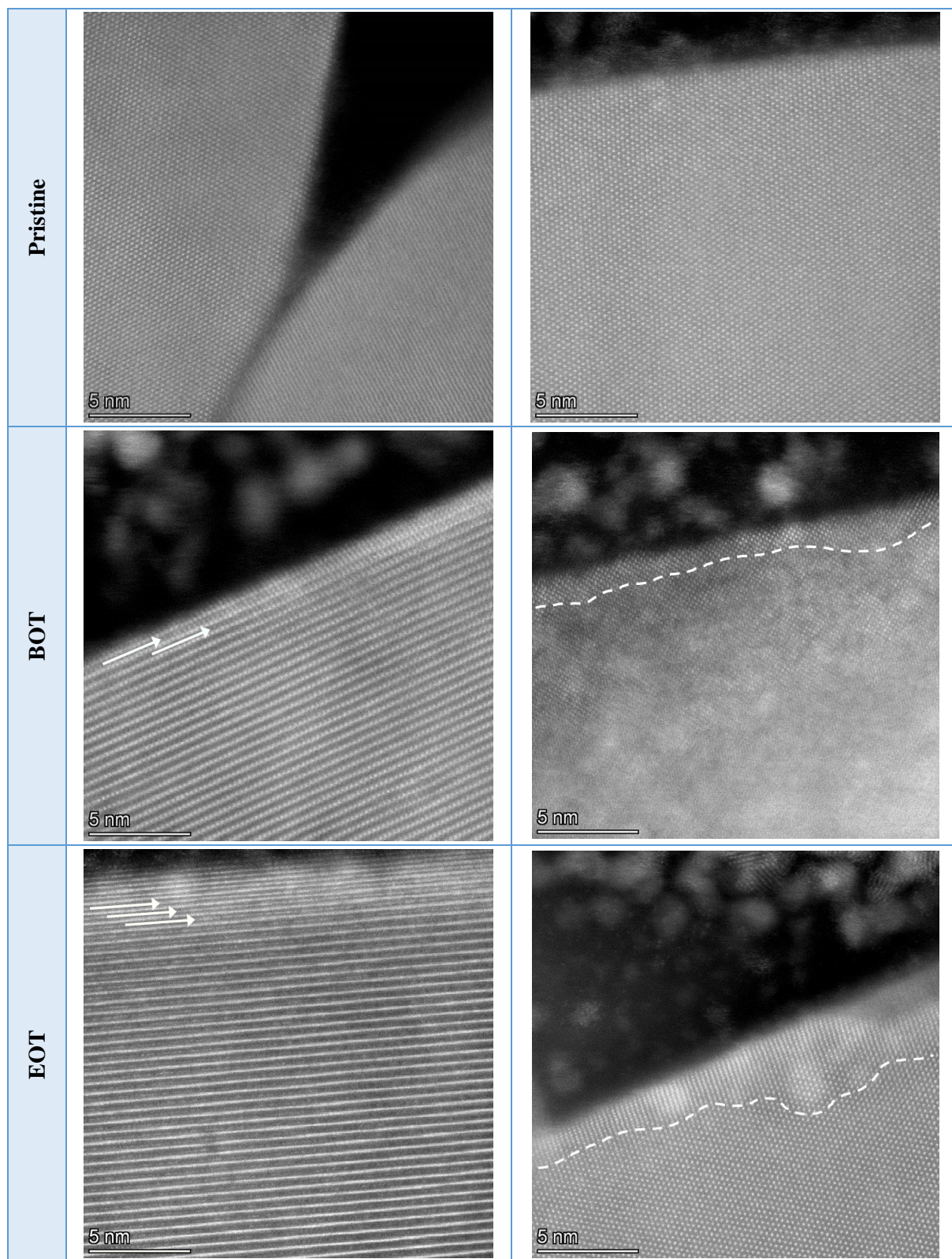


Figure S12: HAADF-STEM pictures of pristine (top), BOT (18th cycle, middle), and EOT NCM-811 particles (after 1000 cycles, bottom). The arrows/dashed lines in the BOT and EOT images exemplary indicate surface-near inter-slabs/regions which are partially populated with transition-metals (and which appear as bright spots/lines in these images).

S10: Literature

- S1. K. Kleiner, B. Strehle, A. R. Baker, S. J. Day, C. C. Tang, I. Buchberger, F.-F. Chesneau, H. A. Gasteiger, and M. Piana, *Chem. Mater.*, **30**, 3656 (2018).
- S2. A. O. Kondrakov, A. Schmidt, J. Xu, H. Geßwein, R. Mönig, P. Hartmann, H. Sommer, T. Brezesinski, and J. Janek, *J. Phys. Chem. C*, **121**, 3286 (2017).
- S3. V. K. Pecharsky and P. Y. Zavalij, *Fundamentals of Powder Diffraction and Structural Characterization of Materials*, Springer, New York (2005).
- S4. P. W. Stephens, *J. Appl. Crystallogr.*, **32**, 281 (1999).
- S5. J. Frantti, S. Eriksson, S. Hull, V. Lantto, H. Rundlöf, and M. Kakihana, *J. Phys. Condens. Matter*, **15**, 6031 (2003).
- S6. O. Dolotko, A. Senyshyn, M. J. Mühlbauer, K. Nikolowski, F. Scheiba, and H. Ehrenberg, *J. Electrochem. Soc.*, **159**, A2082 (2012).
- S7. A. O. Kondrakov, H. Geßwein, K. Galdina, L. de Biasi, V. Meded, E. O. Filatova, G. Schuhmacher, W. Wenzel, P. Hartmann, T. Brezesinski, and J. Janek, *J. Phys. Chem. C*, **121**, 24381 (2017).
- S8. L. de Biasi, A. O. Kondrakov, H. Geßwein, P. Hartmann, T. Brezesinski, and J. Janek, *J. Phys. Chem. C*, **121**, 26163 (2017).
- S9. I. Buchberger, S. Seidlmayer, A. Pokharel, M. Piana, J. Hattendorff, P. Kudejova, R. Gilles, and H. A. Gasteiger, *J. Electrochem. Soc.*, **162**, A2737 (2015).
- S10. O. Dolotko, A. Senyshyn, M. J. Mühlbauer, K. Nikolowski, and H. Ehrenberg, *J. Power Sources*, **255**, 197 (2014).
- S11. D.-H. Seo, A. Urban, and G. Ceder, *Phys. Rev. B Condens. Matter Mater. Phys.*, 115118 (1998).
- S12. F. Lin, I. M. Markus, D. Nordlund, T.-C. Weng, M. D. Asta, H. L. Xin, and M. M. Doeff, *Nat. Commun.*, **5**, 1 (2014).
- S13. J. Landesfeind, D. Pritzl, and H. A. Gasteiger, *J. Electrochem. Soc.*, **164**, A1773 (2017).
- S14. J. Landesfeind, J. Hattendorff, A. Ehrl, W. A. Wall, and H. A. Gasteiger, *J. Electrochem. Soc.*, **163**, A1373 (2016).
- S15. T. Teufl, D. Pritzl, S. Solchenbach, H. A. Gasteiger, and M. A. Mendez, *J. Electrochem. Soc.*, **166**, A1275 (2019).
- S16. T. Teufl, B. Strehle, P. Müller, H. A. Gasteiger, and M. A. Mendez, *J. Electrochem. Soc.*, **165**, A2718 (2018).
- S17. A. Grenier, H. Liu, K. M. Wiaderek, Z. W. Lebens-Higgins, O. J. Borkiewicz, L. F. J. Piper, P. J. Chupas, and K. W. Chapman, *Chem. Mater.*, **29**, 7345 (2017).
- S18. S. Watanabe, M. Kinoshita, T. Hosokawa, K. Morigaki, and K. Nakura, *J. Power Sources*, **258**, 210 (2014).

S19. M. Shikano, H. Kobayashi, S. Koike, H. Sakaebe, E. Ikenaga, K. Kobayashi, and K. Tatsumi, *J. Power Sources*, **174**, 795 (2007).

S20. B. Strehle, K. Kleiner, R. Jung, F. Chesneau, M. Mendez, H. A. Gasteiger, and M. Piana, *J. Electrochem. Soc.*, **164**, A400 (2017).

S21. R. Jung, M. Metzger, F. Maglia, C. Stinner, and A. H. Gasteiger, *J. Electrochem. Soc.*, **164**, A1361 (2017).

3.1.2 Ex-situ study at elevated temperatures

The article “A Comparative Study on Structural Changes during Long-Term Cycling of NCM-811 at Ambient and Elevated Temperature” was submitted in February 2021 to the peer-reviewed Journal of The Electrochemical Society and published in May 2021 as a part of the Focus Issue on Future of Intercalation Chemistry for Energy Storage and Conversion in Honor of M. Stanley Whittingham. The permanent web link of this work is available under <https://iopscience.iop.org/article/10.1149/1945-7111/abf780>. Franziska

Friedrich presented the article at the PRiME Meeting in October 2020 (digital, Abstract No. 254).

Based on the long-term cycling study at ambient temperatures (section 3.1.1), we conducted a follow-up study at 45°C in order to investigate the capacity fading mechanisms within NCM-811 at elevated temperature and compare them to our previous study conducted at $\approx 22^\circ\text{C}$. Cycling batteries at high temperatures is useful for two main reasons. First, battery failure is accelerated at elevated temperatures, which enables the evaluation of the underlying fading mechanisms on a shorter time span compared to experiments at room temperature. Another factor is that LIBs are used for BEVs, which must operate both in colder and hotter regions. The knowledge of the aging of LIBs at elevated temperatures thus plays an important role for commercial application.

During the in-situ study at ambient temperatures presented in section 3.1.1, we gained experience with regards to the necessity of various measurement methods (e.g., the in-situ XPD at the synchrotron) and how they are best used to answer the research question. This means that we changed from the in-situ setup at the synchrotron source to six identical cells, which were cycled with the same protocol, whereby every 150 cycles one of the cells was stopped in order to conduct ex-situ analysis on the harvested CAM, while keeping the cell setup and the cycling procedure largely similar to that of the previous study. Ex-situ methods include rate tests in NCM-811/Li half-cells, EIS experiments, Kr-BET measurements, and XPD analysis of harvested CAM filled into capillaries and analyzed at the in-house diffractometer.

We observed that the capacity loss at 45°C is more than doubled in comparison to that at ≈22°C. In accordance with the results from the previous study, we found that the capacity fading in NCM-811 is due to the formation of a resistive oxygen-depleted surface layer. The corresponding increase in the charge-transfer resistance was quantified by ex-situ EIS measurements of NCM-811 versus a lithium/free standing graphite electrode, as presented by Morasch et al.¹¹⁶ The capacity loss due to the increased cathode resistance is reversible, i.e., it can be regained when cycling at very low C-rates (here C/50) in NCM-811/half-cells. The results from the rate tests indicate that ≈40% of the observed capacity fading is due to the increased charge-transfer resistance. XPD analysis proves that the other ≈60% can be ascribed to the loss of CAM caused by the formation of the resistive surface layer. The XPD experiments furthermore show that the bulk structure is stable, since the Li-Ni mixing only increased by ≈1-2%. The contribution of this increase on the lithium bulk diffusivity, however, remains elusive. Kr-BET measurements show that virtually all primary CAM particles are exposed to the electrolyte in charged state due to the severe volume contraction of NCM-811, which can also lead to particle cracking as discussed in section 1.2. Based on the surface area measurements from Kr-BET, the CAM loss translates into a surface layer thickness around the primary particles. For the study at ambient temperatures, this surface layer is estimated to be ≈6 nm thick (after 1000 cycles). After 700 cycles at 45°C, the surface layer thickness is around ≈12-14 nm.

Author contributions

F.F. built the pouch-cells and conducted the EIS and Kr-BET measurements. B.S. was in charge of the structural analysis and the rate tests. B.S. wrote the manuscript which was edited by F.F. and H.A.G. All authors discussed the results. F.F. and B.S. contributed equally to this work as co-shared first authors.



A Comparative Study of Structural Changes during Long-Term Cycling of NCM-811 at Ambient and Elevated Temperatures

Benjamin Strehle,^{*,*,z}  Franziska Friedrich,^{*,*}  and Hubert A. Gasteiger^{*,*} 

Chair of Technical Electrochemistry, Department of Chemistry and Catalysis Research Center, Technical University of Munich, D-85748 Garching, Germany

Lithium-ion batteries operate predominantly at room temperature, but some applications such as electric vehicles also demand operation at higher temperature. This is especially challenging for cathode active materials (CAMs), which undergo an accelerated failure at elevated temperature. Here, we systematically compare the capacity fading of the Ni-rich NCM-811 at two different temperatures. The first dataset over 1000 cycles at 22 °C stems from a former study, while the NCM-811/graphite full-cells are investigated now under similar conditions at 45 °C for 700 cycles. We focus on the CAM by using pre-lithiated graphite anodes. The capacity loss due to NCM-811 degradation at 45 °C is more than doubled compared to 22 °C. The underlying mechanisms related to the bulk and the surface of the CAM are quantified by several ex situ techniques such as X-ray powder diffraction, half-cell cycling with impedance spectroscopy, and Kr-BET. The aging happens mainly at the surface of the primary particles, forming a resistive, disordered surface layer, whose thickness is estimated to reach ≈ 6 nm at 22 °C and ≈ 12 –14 nm at 45 °C by the end-of-test. Furthermore, the Li-Ni mixing in the bulk increases by $\approx 1\%$ – 2% at elevated temperature, but its contribution to the capacity loss remains elusive.

© 2021 The Author(s). Published on behalf of The Electrochemical Society by IOP Publishing Limited. This is an open access article distributed under the terms of the Creative Commons Attribution Non-Commercial No Derivatives 4.0 License (CC BY-NC-ND, <http://creativecommons.org/licenses/by-nc-nd/4.0/>), which permits non-commercial reuse, distribution, and reproduction in any medium, provided the original work is not changed in any way and is properly cited. For permission for commercial reuse, please email: permissions@iopublishing.org. [DOI: [10.1149/1945-7111/abf780](https://doi.org/10.1149/1945-7111/abf780)]



Manuscript submitted February 25, 2021; revised manuscript received March 29, 2021. Published May 13, 2021. *This was Paper 254 presented during PRiME 2020, October 4–9, 2020.*

Layered transition-metal oxides are the most widely applied class of cathode active materials (CAMs) in lithium-ion batteries (LIBs). They dominate the fast-growing market of electric vehicles (EVs), combining high energy and power density with long cycle-life.¹ On a structural level, layered oxides can be written as $\text{Li}_{1+\delta}[\text{TM}]_{1-\delta}\text{O}_2$, with alternating layers of lithium and transition-metals (TMs) in octahedral coordination and with a small degree of over-lithiation (typically $0 < \delta < 0.05$). Depending on the choice of transition-metals, layered oxides are referred to as NCMs (combining Ni, Co, and Mn) or NCAs (replacing Mn by Al, which is actually not a TM). Making efforts to reduce the cobalt content due to sustainability and geopolitical aspects,^{2,3} there is an ongoing trend to increase the nickel content as much as possible. This strategy goes along with a higher specific capacity at a given cell voltage compared to less Ni-rich counterparts, but Ni-rich CAMs are also prone to structural and thermal instabilities.^{4,5} In this respect, NCM-811 ($\text{Li}_{1+\delta}[\text{Ni}_{0.8}\text{Co}_{0.1}\text{Mn}_{0.1}]_{1-\delta}\text{O}_2$) is currently one of the most Ni-rich NCM materials with proven cycling stability.^{6–8}

In a recent study from 2019, we investigated the long-term cycling stability of NCM-811 at ambient temperature (≈ 22 °C).⁹ Using in situ X-ray powder diffraction (XPD) in combination with other diagnostics such as electrochemical impedance spectroscopy (EIS) and X-ray photoelectron spectroscopy (XPS), we elucidated the capacity fading mechanism of an NCM-811 cathode active material and quantified its main contributions to cell capacity fading over the duration of 1000 cycles. We provided evidence that the high-voltage operation until 4.5 V vs Li^+/Li leads to the formation of a resistive, oxygen-depleted surface layer around the primary particles. Consequently, the capacity fading intrinsic to the NCM-811 CAM can be divided into two contributions, one originating from the irreversible cathode active material loss (due to the surface reconstruction of the CAM) and one originating from the growing charge-transfer resistance and the associated overpotential loss (due to the resistive nature of the surface layer). The latter is particularly pronounced at high charge/discharge rates.

Even though the majority of applications are designed to operate at/near room temperature, there is a growing demand for lithium-ion batteries to operate and survive also under more extreme thermal conditions.^{10,11} Electric vehicles, e.g., should run both in colder and hotter regions. The United States Advanced Battery Consortium (USABC) aims at a survival temperature ranging from -40 °C to $+66$ °C for 24 h.¹² This goal for EV applications might be one of the reasons why the focus of academic research is increasingly placed on performing cycling studies at elevated temperatures (in the range of ≈ 40 °C– 60 °C).^{13–16} Furthermore, high-temperature cycling accelerates the battery failure and can thus be used as an accelerated stress test (AST) to evaluate new or optimized CAMs. Alternative AST strategies that have been reported are potential hold or open circuit voltage (OCV) rest phases at high voltages as well as cycling with low salt concentrations.¹⁷

On the other hand, the evaluation of ASTs requires facile characterization methods to extract important battery parameters over the course of (long-term) cycling. With respect to CAM evaluation, such parameters are the percentage of active material loss and the increase of the charge-transfer resistance, which were deduced from in situ XPD and EIS in our former work. In situ and operando techniques can generate much more authoritative information than ex situ (or post-mortem) experiments, because they characterize the material under real operating conditions. At the same time, they are often cumbersome and need advanced instrumentation (e.g., custom-made cell designs or synchrotron radiation), which is not readily available in every laboratory. Thus, high-throughput ASTs should be accompanied by some basic ex situ techniques.

In the present work, we want to systematically compare the long-term cycling performance of NCM-811 at ambient and elevated temperatures. Using the cycle-life analysis over 1000 cycles at 22 °C from our precedent study as Ref. 9, the same NCM-811 cathode active material is cycled here at 45 °C for up to 700 cycles. To ensure comparability, the other cycling conditions are kept constant. As in our previous study, the graphite counter-electrode (CE) is pre-lithiated to eliminate cell capacity fading contributions from the anode and the NCM-811 potential is controlled vs the lithium reference-electrode (RE). Every ≈ 150 cycles, one of the pouch cells is stopped and the harvested cathode electrode is subjected to several ex situ techniques such as XPD, EIS, and surface area determination

[†]These authors contributed equally to this work.

*Electrochemical Society Student Member.

**Electrochemical Society Fellow.

^zE-mail: benjamin.strehle@tum.de

by Kr-BET. Here, the NCM-811 cathode active material loss is quantified by two independent approaches, either by XPD or purely by electrochemical means, while the charge-transfer resistance from EIS is compared to direct current internal resistance (DCIR) measurements in the pouch cells. Furthermore, we are seeking to clarify whether the NCM-811 CAM aging at elevated temperature is mechanistically similar, or different, to its fading at ambient temperature. This question addresses the relative importance of bulk vs surface related degradation phenomena, in particular Li-Ni mixing in the bulk vs surface reconstruction.

Experimental

Battery assembly and cycling.—The materials and battery design used here are identical to our previous aging study of NCM-811 at ambient temperature and can be looked up in detail there.⁹ Briefly, the CAM composition was determined to be $\text{Li}_{1.01}\text{Ni}_{0.79}\text{Co}_{0.10}\text{Mn}_{0.10}\text{O}_2$ by elemental analysis, which gives a theoretical capacity of 274 mAh g^{-1} (including $\approx 2.2 \text{ wt\%}$ surface impurities). Cathode electrode sheets with 94 wt% CAM, 2 wt% Timcal SFG6L graphite, 1 wt% Timcal C65 conductive carbon, and 3 wt% Kynar PVDF binder (HSV900) were provided by BASF SE (Germany). The electrode sheets were calendered to a porosity of $\approx 30\%$ and have a CAM loading of $\approx 7.0 \text{ mg}_{\text{CAM}} \text{ cm}^{-2}$ ($\pm 1\%$), corresponding to $\approx 1.4 \text{ mAh cm}^{-2}$ for a practical capacity of 200 mAh g^{-1} . The CAM loading is lower than the previously reported value of $\approx 7.4 \text{ mg}_{\text{CAM}} \text{ cm}^{-2}$, probably due to a small variation along the electrode spool. Single-layer pouch cells with 9 cm^2 cathode area ($30 \times 30 \text{ mm}^2$) were manufactured with a geometrically as well as capacitively over-sized graphite counter-electrode (CE, $33 \times 33 \text{ mm}^2$, $\approx 7.1 \text{ mg}_{\text{graphite}} \text{ cm}^{-2}$, corresponding to $\approx 2.3 \text{ mAh cm}^{-2}$, BASF SE), two glass-fiber (GF) separators ($36 \times 36 \text{ mm}^2$, glass microfiber filter 691, VWR, Germany), a lithium metal reference-electrode (RE), and $700 \mu\text{L}$ LP57 electrolyte (1M LiPF_6 in EC:EMC = 3:7 by weight; electrolyte-to-CAM mass ratio of $\approx 13/1$). In contrast to our former study that used LP57-2 with 2% vinylene carbonate (VC), the VC additive was omitted in the full-cells in this work due to its oxidative instability at elevated temperatures.¹⁸ To ensure a stable solid electrolyte interface (SEI), the graphite counter-electrode was however pre-formed and pre-lithiated in a half-cell configuration at $45 \text{ }^\circ\text{C}$ in LP57-2 electrolyte. The pre-lithiation to $\approx \text{Li}_{0.24}\text{C}_6$ (corresponding to $\approx 0.55 \text{ mAh cm}^{-2}$) provides a sufficiently large lithium reservoir for the full-cells ($0.55/1.4 \approx 40\%$ of the cathode capacity). This approach avoids any capacity fading due to the loss of cyclable lithium and thus, the Li-RE can be used for the potential control of the cathode. Furthermore, the anode/cathode balancing after pre-lithiation amounts to $(2.3-0.55)/1.4 \approx 1.25/1$, i.e., the remaining storage capability of the anode does not pose a risk for lithium plating during charge. The pouch cells were compressed in a spring-loaded holder at a homogeneous pressure of $\approx 2 \text{ bar}$.

The pouch cells were tested at $45 \text{ }^\circ\text{C}$ in a temperature-controlled chamber (Binder, Germany) with a battery cyler (Series 4000, Maccor, USA). The cycling protocol consists of a loop of 50 cycle segments, which are further divided into three sequential steps:

- (i) The first two cycles were done at constant-current (CC) mode at a C-rate of C/10 and in the cathode potential window of 3.0–4.5 V vs Li^+/Li , as controlled vs the Li-RE. All C-rates throughout this study are based on a nominal specific capacity of 200 mAh g^{-1} and the unit “V” refers to ‘V vs Li^+/Li ’, unless stated otherwise.
- (ii) The third cycle is a direct current internal resistance (DCIR) measurement at a relative state of charge (SOC) of 65%, as referenced to the discharge capacity of the preceding C/10 cycle. The partial charge to 65% SOC, where the DCIR measurement was taken, and the subsequent discharge back to a cathode potential of 3.0 V were also carried out at C/10. The DCIR measurement itself was done after a 2 h rest period

at open circuit voltage (OCV, $\approx 4.0 \text{ V}$), applying a discharge pulse of C/5 for 10 s. The area specific resistance (R_{DCIR} in $\Omega \text{ cm}^2$) was computed by the Maccor MIMS Client according to:¹⁹

$$R_{\text{DCIR}} = \frac{V_1 + V_3 - V_2}{2j_2} \quad [1]$$

Here, V_1 is the OCV right before the pulse, V_2 is the voltage at the end of the 10 s pulse, V_3 is the OCV 10 s after the pulse, and j_2 is the current density of the C/5 discharge pulse ($\approx 0.28 \text{ mA cm}^{-2}$). Please note that the induced change of $\approx 0.1 \text{ mAh g}^{-1}$ (corresponding to an SOC variation of $\approx 0.05\%$) is negligible and that R_{DCIR} relates solely to the resistance of the cathode due to the potential control vs the Li-RE.

- (iii) The remaining 47 cycles were done in CC mode at C/2 between cathode potentials of 3.0–4.5 V, which are, for the sake of comparability, the same cycling conditions than in our previous study at $\approx 22 \text{ }^\circ\text{C}$.⁹

This iterative protocol of 50 cycle segments was applied to six cells, which passed through an increasing total number of cycles, ranging from only six cycles (i.e., two cycles at C/10, one DCIR test cycle, and three cycles at C/2; referred to as begin-of-test, BOT), to 100 cycles and then in steps of 150 cycles to a maximum of 700 cycles (end-of-test, EOT). Each cell was stopped in the discharged state (i.e., after a final C/2 cycle until 3.0 V) and the cathode OCV was measured for $\approx 5 \text{ h}$ at $45 \text{ }^\circ\text{C}$ and finally for another $\approx 5 \text{ h}$ at $25 \text{ }^\circ\text{C}$. The final OCV values taken at $45 \text{ }^\circ\text{C}$ and $25 \text{ }^\circ\text{C}$ agree within less than $\pm 10 \text{ mV}$ for a given cell. After cell disassembly, the NCM-811 cathode electrodes were stored for further ex situ analyses in an argon-filled glove box.

X-ray powder diffraction and Rietveld refinement.—XPD measurements aimed at monitoring the evolution of the lithium content (x_{Li} in $\text{Li}_x\text{Ni}_{0.79}\text{Co}_{0.10}\text{Mn}_{0.10}\text{O}_2$) and the Li-Ni mixing (Ni_{Li}) in the NCM-811 CAM upon cycling. The experiments were conducted at our in-house STOE STADI P diffractometer (STOE, Germany) in transmission mode, using $\text{Mo-K}_{\alpha 1}$ radiation (0.7093 \AA , 50 kV , 40 mA), a Ge(111) monochromator, and a Mythen 1K detector with one data point every $0.015^\circ/2\theta$. A silicon standard material was used for the determination of the instrumental broadening. The CAM powder was measured ex situ in air-tight sealed 0.3 mm borosilicate capillaries in the 2θ range of 5° – 90° for $\approx 17 \text{ h}$. For measurements with the discharged CAM, the material was scratched off with a scalpel from the harvested electrodes of each of the six pouch cells and loaded into two capillaries without further washing (for two independent XPD repeat measurements). On the other hand, for measurements with the charged CAM, the $30 \times 30 \text{ mm}^2$ cathodes harvested from the cycled pouch cells were punched out into disk-shaped electrodes with a diameter of 14 mm . These smaller electrodes were assembled with a $\varnothing 15 \text{ mm}$ Li-CE, two $\varnothing 16 \text{ mm}$ GF separators, and $80 \mu\text{L}$ LP57 electrolyte in CR2032-type coin cells, which were cycled at C/2 and $45 \text{ }^\circ\text{C}$ for 1.5 cycles between 3.0–4.5 V and then stopped at 4.5 V. Due to electrolyte residuals, the CAM mass could not properly be determined and we used the average loading of the pristine electrodes instead, which leads to an uncertainty of $\approx 1\%$ for the applied current and the extracted capacity. In order to minimize self-discharge effects, which would lead to an apparently erroneous increase of the determined x_{Li} value in the charged state at 4.5 V, the OCV periods at $45 \text{ }^\circ\text{C}$ and $25 \text{ }^\circ\text{C}$ that followed these 1.5 cycles were not longer than 30 min each (change in the OCV at $25 \text{ }^\circ\text{C}$ of less than 15 mV over the max. 30 min). Afterwards, the coin cells were immediately opened and the charged CAM was prepared for the XPD measurement at the same day.

The Rietveld refinements were performed with the software package Topas.²⁰ NCM-811 exhibits a layered α - NaFeO_2 -type

structure with $R\bar{3}m$ symmetry and we therefore used the following structural model: $[\text{Li}_{x-\nu}\text{Ni}_{\nu}]_{3a}[\text{Li}_{\nu}\text{Ni}_{0.79-\nu}\text{Co}_{0.10}\text{Mn}_{0.10}]_{3b}[\text{O}]_{6c}$. Here, the overall lithium content (x_{Li}) was calculated according to the c/a lattice parameter ratio of the cycled samples. The calibration curves, $x_{\text{Li}} = f(c/a)$, were determined by operando XPD from the initial cycles of this particular CAM in our previous publication and they look as follows in the discharged (i.e., at low SOC, $0.62 \leq x_{\text{Li,dis}} \leq 0.91$) and charged state (i.e., at high SOC, $0.12 \leq x_{\text{Li,cha}} \leq 0.23$):⁹

$$x_{\text{Li,dis}} = \frac{73.80 - \sqrt{c/a \cdot 10^4 - 49222}}{58.36}, \quad \text{for } 0.62 \leq x_{\text{Li,dis}} \leq 0.91 \quad [2]$$

$$x_{\text{Li,cha}} = \frac{c/a - 4.733}{1.41}, \quad \text{for } 0.12 \leq x_{\text{Li,cha}} \leq 0.23 \quad [3]$$

The Li-Ni mixing was treated as a paired anti-site defect ($\nu_{\text{Li}} = \nu_{\text{Ni}}$). This means that the amount of Ni in the Li layer (Ni_{Li}) is the same as the amount of Li in the TM layer (Li_{TM}). Please note that in the special case of the pristine CAM, ν_{Li} equals $\nu_{\text{Ni}} + 0.01$ due to full occupation of all layers (at $x_{\text{Li}} = 1.01$). The Li-Ni mixing is reported in percentage terms as $\text{Ni}_{\text{Li}} = \nu_{\text{Ni}} \cdot 100\%$.

The refinements included the following non-structural parameters:

- background: Chebyshev polynomial with 15 parameters
- instrument: zero shift and axial divergence
- absorption: cylindrical absorption correction ($\mu_{\text{R}} \approx 0.75$, assuming a packing density of 40%)

The structure-related refinement parameters are the following:

- scale factor
- broadening: isotropic contribution from crystallite size and anisotropic contribution from microstrain using the hexagonal Stephens model²¹
 - lattice parameters: a and c
 - fractional coordinate: $z_{6c,O}$
 - atomic displacement parameters: three site-specific and isotropic parameters ($b_{3a,\text{Li}}$, $b_{3b,\text{TM}}$, and $b_{6c,O}$)
 - site occupancy factors: ν_{Ni} (and x_{Li}) as outline above, using ionic scattering factors for all elements (Li^+ , Ni^{3+} , Co^{2+} , Mn^{4+} , and O^{2-})

Furthermore, the 2 wt% of conductive graphite (Timcal SFG6L) in the cathode electrode sheet were included into the Rietveld fits by refining its scale factor, crystallite size broadening, and lattice parameters, while fixing the other structural parameters of the $P6_3/mmc$ graphite phase to the values from Dolotko et al.²² Due to the high intensity of the freshly replaced Mo source, we also noticed tiny reflections of the borosilicate capillary in some of the diffractograms, which were treated as additional reflections based on an empty capillary measurement.

Rate test and impedance analysis.—We punched out another \emptyset 14 mm electrode from each of the pouch cell cathodes harvested after cycling, reassembling them into coin cells with a lithium metal counter-electrode (separator and electrolyte as described above). These were used to perform a rate test towards slow C-rates in combination with electrochemical impedance spectroscopy (EIS). Since a conventional lithium metal foil would have a large contribution to the EIS response of the NCM-811 half-cells, we placed a free-standing graphite (FSG) electrode on top of the lithium metal foil (i.e., between the lithium metal and the separator), as it was described by Morasch et al.²³ Using this Li/FSG composite as counter-electrode, its impedance contribution (imaginary and real part of $<5 \Omega \text{ cm}^2$ over the measured frequency range²³) to the half-cell impedance is comparably small compared to that of the

NCM-811 cathode. Consequently, the measured cell impedance can be reasonably well approximated to correspond to that of the NCM-811 cathode. The coin cells were cycled between 3.0–4.5 V at 45 °C for two cycles each at C/2, C/10, C/50, and finally again at C/2. The two C/10 cycles over the entire voltage range were completed by a third DCIR-like cycle to 65% SOC (OCV of ≈ 4.0 V, see full-cells), at which we conducted potential-controlled EIS measurements with a potentiostat (VMP300, BioLogic, France) in the frequency range of 100 kHz to 100 mHz with an AC voltage perturbation of 15 mV (taking eight data points per decade and three repetitions per point).

To fit the impedance spectra acquired at 65% SOC and 45 °C, we used an equivalent circuit described by $R_{\text{HF}} + \text{TLM}[R_{\text{ion}}, R_{\text{CT}}/Q_{\text{CT}}] + R_{\text{contact}}/Q_{\text{contact}}$, with the elements defined as follows: (i) R_{HF} being the high-frequency resistance of the half-cell; (ii) TLM representing a transmission line model with the ionic resistance in the electrolyte phase between the pores of the electrode (R_{ion}), and a parallel circuit element of the charge-transfer resistance (R_{CT}) and a constant phase element (CPE, Q_{CT}); and, (iii) another parallel circuit element of the contact resistance (R_{contact}) and a Q_{contact} CPE that is generally observed as an interfacial resistance between the cathode electrode and the aluminum current collector.^{9,24} The last discharge of the half-cells at C/2 was to a cell voltage of 2.55 V, followed by constant voltage hold for 1–6 h before cell disassembly. The harvested electrodes were used for surface area measurements that are described in the following.

Surface area determination.—After the rate test, the discharged NCM-811 cathodes were subjected to Kr-BET measurements. Before that, the electrodes were thoroughly washed in three steps with an EC/EMC mixture and twice with DMC to remove any residuals from the conductive salt, as described by Oswald et al.,²⁵ and then dried at 120 °C under dynamic vacuum for at least 6 h. Surface area measurements were performed on a gas sorption analyzer (Autosorb-iQ, Quantachrome, USA) at 77 K using krypton as adsorbate and the obtained surface areas are referenced to the mass of the washed electrodes. Kr has the advantage over N_2 to be much more sensitive due to its ≈ 300 times lower saturation pressure (p_0), which minimizes the void volume correction and thus enables the analysis of low surface area samples. The specific surface area of the NCM-811 CAM ($A_{\text{BET,CAM}}$ in $\text{m}^2/\text{g}_{\text{CAM}}$) was determined from adsorption isotherms in the relative pressure range of $\approx 0.13 < p/p_0 < 0.29$ with seven data points according to the Brunauer-Emmett-Teller (BET) theory. The actually measured surface area of the entire electrode ($A_{\text{BET,elec}}$ in $\text{m}^2/\text{g}_{\text{elec}}$), consisting of 94 wt% CAM and 6 wt% inactive electrode additives (viz., 2 wt% SFG6L conductive graphite, 1 wt% C65 conductive carbon, and 3 wt% PVDF binder), was converted into $A_{\text{BET,CAM}}$ by subtracting the contribution of the inactive electrode additives ($A_{\text{BET,add}}$ in $\text{m}^2/\text{g}_{\text{add}}$):

$$A_{\text{BET,CAM}} = \frac{A_{\text{BET,elec}} - 0.06 \cdot A_{\text{BET,add}}}{0.94} \quad [4]$$

Here, $A_{\text{BET,add}}$ of the overall 6 wt% inactive electrode additives was measured separately, using electrodes comprising only the additives in the same ratio as in the actual NCM-811 electrodes. The pristine additives-only electrode yielded a specific surface area of $5.10 \pm 0.11 \text{ m}^2/\text{g}_{\text{add}}$ (average from two electrodes). To evaluate a possible change of $A_{\text{BET,add}}$ during cycling, we tried to mimic the full-cell conditions by cyclic voltammetry at a scan rate of 0.2 mV s^{-1} between 2.55–4.5 V (requiring a time comparable to that for C/2 cycling). After 10 or 20 cyclic voltammetry cycles at 45 °C vs a Li/FSG-CE, $A_{\text{BET,add}}$ rises by $\approx 9\%$ to $5.56 \pm 0.01 \text{ m}^2/\text{g}_{\text{add}}$ (average from these two cells). Using the specific surface area of the conductive additive powders (SFG6L: $\approx 20 \text{ m}^2/\text{g}$, C65: $\approx 62 \text{ m}^2/\text{g}$), one would expect $A_{\text{BET,add}}$ to be $\approx 17 \text{ m}^2/\text{g}_{\text{add}}$ for the additives-only electrode. This discrepancy is explained by prior observations that pore blocking by the PVDF binder can substantially lower the electrode surface area, depending on the type of conductive additives and the binder content.^{25,26} In Eq. 4, the first $A_{\text{BET,add}}$ value

($5.10 \text{ m}^2/\text{g}_{\text{add}}$) was used for the pristine NCM-811 electrode, while the latter ($5.56 \text{ m}^2/\text{g}_{\text{add}}$) was used for any cycled electrode. The inactive electrode additives contribute with $\approx 15\%$ – 20% to the total surface area of the cycled electrodes.

Results and Discussion

Electrochemical full-cell data.—To focus solely on the intrinsic degradation mechanisms of the NCM-811 cathode active material at elevated temperature, we designed the full-cells in such a way that common degradation processes originating from the anode and from the electrolyte are effectively suppressed during battery operation. Since the graphite anode is pre-lithiated to a cathode capacity of $\approx 40\%$ (see Experimental section), the loss of cyclable lithium on the anode side does not contribute to the observed capacity fading.²⁷ This approach allows the NCM-811 cathode to be operated between fixed cut-off potentials of 3.0 and 4.5 V vs Li^+/Li , as controlled vs a Li-RE. Furthermore, electrolyte changes such as oxidation reactions at the cathode side and LiPF_6 salt depletion could deteriorate the cell performance²⁸ at realistic mass ratios of $m_{\text{electrolyte}}/m_{\text{CAM}} \approx 1/1$.²⁹ Therefore, we employ highly porous glass-fiber separators in our full-cells, which enable a large electrolyte excess of $m_{\text{electrolyte}}/m_{\text{CAM}} \approx 13/1$, so that the bulk electrolyte properties remain unaltered. Assuming that electrolyte degradation is relevant under the applied conditions, the thereby released protic species could lead to transition-metal dissolution from the CAM surface;²⁷ however, the SiO_2 -containing GF separator acts as a proton scavenger.^{30,31} We want to stress that all these modifications distinguish this work from other studies using more realistic cell setups (i.e., graphite anode not pre-lithiated, less electrolyte volume, and polyolefin separators), but they are done on purpose to obtain an in-depth and quantitative understanding of the CAM degradation. To enhance its degradation processes, the NCM-811 CAM is further subjected to an accelerated stress test, because the upper cut-off potential of 4.5 V vs Li^+/Li is chosen deliberately higher than in commercial NCM/graphite cells. Here, the upper full-cell voltage (V_{FC}) typically amounts to 4.2–4.3 V_{FC} ,^{12,16} corresponding only to ≈ 4.3 – 4.4 V vs Li^+/Li .

Figure 1 shows from top to bottom the evolution of the discharge capacity at C/2 (including checkup cycles at C/10), the charge-averaged mean charge and discharge voltage, and the DCIR resistance measured at a relative state of charge (SOC) of 65% (based on the preceding C/10 cycle). For all six cells, the first charge at C/10 to 4.5 V yields $\approx 237 \text{ mAh g}^{-1}$ (not shown), corresponding to an absolute SOC of $\approx 86\%$ (referenced to the total amount of lithium in the NCM-811 CAM). This is well beyond the onset of oxygen evolution from the layered oxide surface at $\approx 80\%$.^{32,33} The following C/10 discharge yields a capacity of $\approx 221 \text{ mAh g}^{-1}$, which decreases to an initial discharge capacity of $\approx 207 \text{ mAh g}^{-1}$ at the faster rate of C/2 (see Fig. 1a). The capacity fading is very reproducible among the six cells, which were tested for an increasing number of cycles ranging from 6 to 700 cycles (see differently colored symbols in Fig. 1a). In the overlapping cycling segments, the average standard deviation between the cells amounts to $\pm 2 \text{ mAh g}^{-1}$.

Focusing first on the C/2 cycling, Table I compares the begin-of-test (BOT) discharge capacity values at 45°C with those from our previous study with the same CAM at 22°C as well as their end-of-test (EOT) values after 1000 and 750 cycles, respectively. The BOT capacity increases by $\approx 24 \text{ mAh g}^{-1}$ when comparing the BOT value after 18 cycles at 22°C and after 6 cycles at 45°C (for an explanation why BOT was defined after 18 cycles in our previous study, see Ref. 9) or by $\approx 17 \text{ mAh g}^{-1}$ when comparing cycle 6, which we ascribe to the enhanced kinetics at elevated temperature. However, the higher initial capacity at 45°C goes along with a faster degradation upon cycling, with the capacity fading of $\approx 0.04 \text{ mAh g}^{-1}$ per cycle at 22°C being more than doubled at 45°C ($\approx 0.10 \text{ mAh g}^{-1}$ per cycle). Consequently, the EOT capacity of $\approx 139 \text{ mAh g}^{-1}$ after 700 cycles at 45°C is already $\approx 6 \text{ mAh g}^{-1}$ lower than that after 1000 cycles at 22°C .

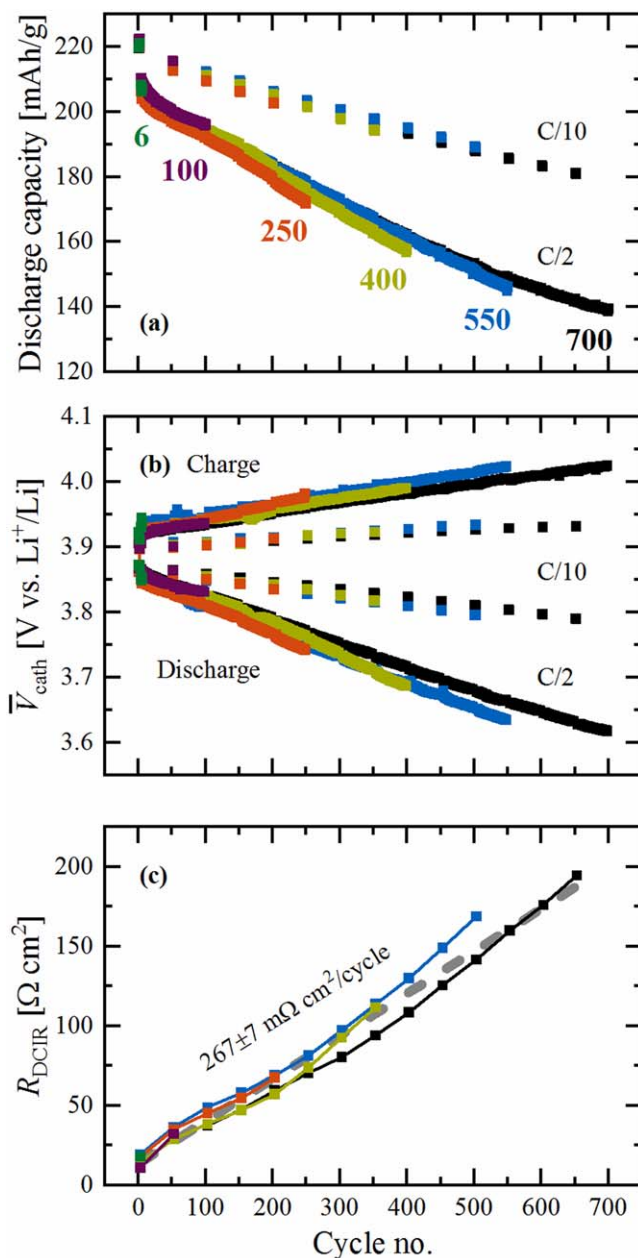


Figure 1. Cycle-life degradation of the NCM-811 CAM evaluated in NCM-811/graphite full-cells with a partially pre-lithiated graphite CE, which were cycled at 45°C and C/2 (with intermittent C/10 checkup cycles) between cathode potentials of 3.0–4.5 V measured vs a Li-RE. (a) Specific discharge capacities. (b) Charge-averaged mean charge and discharge cathode voltages vs Li^+/Li ($\bar{V}_{\text{cath}} \equiv \int V_{\text{cath}} dq / \int dq$). (c) Cathode resistance measured by a DCIR pulse at 65% SOC with respect to the preceding C/10 cycle (R_{DCIR} calculated according to Eq. 1). The discharge capacities and the mean voltages are shown for both the regular C/2 cycles and the intermittent C/10 checkup cycles, while the DCIR cycles to 65% SOC are excluded from these panels. Slight deviations from the characteristic mean voltage curves due to the change of C-rate or OCV periods were further omitted from panel (b). The numbers in panel (a) give the total number of cycles for each of the six cells. The increase of R_{DCIR} in panel (c) was determined to be $267 \pm 7 \text{ m}\Omega \text{ cm}^2/\text{cycle}$ by a linear fit through all data points, as marked by the dashed gray line ($R^2 = 0.975$).

Even though there is no study which investigates NCM-811 under similar conditions, it is useful to compare our results with literature data in order to validate that the performance degradation shown in Fig. 1a is reasonable. Li et al. tested $\text{LiNi}_{0.80}\text{Co}_{0.15}\text{Al}_{0.05}\text{O}_2$ (NCA) in multi-layer pouch cells at 40°C and various full-cell (FC)

Table I. Comparison of the C/2 discharge capacity, as reported in our previous publication at 22 °C⁹ and as measured in this work at 45 °C. The NCM-811/graphite full-cells were cycled between cathode potentials of 3.0–4.5 V vs Li⁺/Li and analyzed from the respective begin-of-test (BOT) to end-of-test (EOT).

C/2 capacity [mAh g ⁻¹]	Ambient temperature (22 °C)	Elevated temperature (45 °C)
BOT → EOT	Cycle 18 → 1000	Cycle 6 → 700
BOT	≈183	≈207
EOT	≈145	≈139
Capacity loss ($\Delta C_{\text{EC}}^{\text{BOT} \rightarrow \text{EOT}}$)	≈38 (≈0.04 per cycle)	≈68 (≈0.10 per cycle)
Capacity retention	≈79%	≈67%

cut-off conditions, including C/2 cycling between 3.0–4.2 V_{FC} and 3.0–4.3 V_{FC} with a constant voltage (CV) hold at the upper cut-off.¹³ Please note that the full-cell voltage (V_{FC}) is roughly 0.1 V lower than the cathode potentials vs Li⁺/Li given in our study and that we use a partially pre-lithiated graphite CE. After 700 cycles of these NCA/graphite full-cells, the capacity retention amounts to ≈86% (at an upper cathode potential of ≈4.3 V vs Li⁺/Li) and ≈78% (≈4.4 V vs Li⁺/Li), which is more than the ≈67% obtained for our NCM-811/graphite full-cells under the slightly harsher conditions of 45 °C and an upper cathode potential of 4.5 V vs Li⁺/Li (see Table I). Schweidler et al. investigated NCM-851005/graphite single-layer pouch cells at 45 °C and 1C between 2.8 and 4.2 V_{FC} (also with CV hold, CE not pre-lithiated).¹⁵ They report an initial capacity of ≈195 mAh g⁻¹ and a fairly linear fading of ≈0.07 mAh g⁻¹ per cycle. Since the capacity loss is again smaller than in our present work, it is reasonable to assume that the CAM aging, which strongly increases with increasing upper cathode potentials, is the dominant factor in all cases, and that any lithium inventory loss at the anode does not contribute much to the reported fading. In realistic full-cells, the amount of cyclable lithium could be reduced, e.g., due to TM dissolution from the cathode and the consequent attack of the SEI,³⁴ which potentially limits the lithiation of the CAM during discharge.³⁵ Here, the pre-lithiation of the graphite anode deliberately eliminates this effect in order to focus on the degradation of the NCM-811 CAM.

The ex situ diagnostic analyses presented later will try to answer the question if the aging mechanism of the NCM-811 CAM is mostly due to its surface reconstruction, as it was the case in our previous degradation study with the same CAM conducted at 22 °C,⁹ or if other (bulk) phenomena come into play at an elevated temperature. The reduced fading of ≈0.06 mAh g⁻¹ per cycle during the C/10 checkup cycles compared to ≈0.10 mAh g⁻¹ per cycle at C/2 (both taken from Fig. 1a) already points towards an overpotential-induced capacity loss, which might be caused by the formation of a resistive surface layer and/or by an increase of the bulk resistance of the CAM (e.g., due to sluggish lithium diffusion kinetics). Such a resistance build-up is further suggested by the evolution of the mean charge and discharge cathode voltages shown in Fig. 1b. Inspecting their average changes over cycling (see Table II), the decrease of the mean discharge voltage is always higher than the increase of the mean charge voltage (by a factor of 1.5–2.5). This discrepancy could potentially be ascribed to a path dependence of the cathode resistance (or one of its components) between charge and discharge. In this context, Pan et al. reported the chemical diffusion coefficient of Li (\bar{D}_{Li}) to be up to four times higher during delithiation (i.e., during charge) than during lithiation (i.e., during discharge) of LiCoO₂ thin-film electrodes at the H1-H2 phase transition.³⁶ This initial phase transition takes place at low SOC, where also NCM layered oxides exhibit largely different resistances: while the voltage vs capacity curve is relatively flat at the beginning of charge, indicating small overpotentials, it drops steeply at the end of discharge, i.e., the cathode resistance is much higher for the same lithium content during discharge.^{9,13} Besides the lithium diffusion kinetics in the bulk of the CAM, the charge-transfer resistance at its surface might also contribute to the different

changes of the cathode mean voltage during charge vs discharge (see Table II). The charge-transfer rises strongly towards the voltage cut-offs, especially at the low-SOC limit, which makes it however difficult to clearly resolve differences between charge and discharge under common measurement conditions (e.g., for EIS measurements with a capacity spacing of 20 mAh g⁻¹).⁹

Finally, Fig. 1c shows the evolution of the direct current internal resistance (R_{DCIR}) of the cathode, which was measured in the mid-SOC range (65% SOC based on the preceding C/10 cycle), so that it is only marginally affected by slight variations of the lithium content (x_{Li}) upon cycling: this relative SOC of 65% occurs within the narrow OCV range of 3.98–4.00 V over all cycles, indicating a small variation of x_{Li} , and furthermore lies in a region where the charge-transfer resistance varies little with x_{Li} (note that R_{CT} is at/near its minimum at an OCV of ≈4.0 V for any given cycle, as shown in Fig. 6 of our previous study with the same CAM⁹). Here, R_{DCIR} rises almost linearly for all six cells (see Fig. 1c), with an average slope of $267 \pm 7 \text{ m}\Omega \text{ cm}^2$ per cycle. This resistance increase can also be translated into a voltage change by multiplying the slope with the current densities applied at C/2 and C/10, respectively. Doing so in Table II, the calculated voltage changes of ≈0.19 and ≈0.04 mV/cycle resemble the evolution of the mean charge voltage, amounting to ≈0.14 mV/cycle at C/2 and ≈0.05 mV/cycle at C/10, whereas the evolution of the mean discharge voltages stays higher. This might be due to the fact that the mean discharge voltage is dominated by the very high R_{CT} (and/or very low \bar{D}_{Li}) at low SOC, so that R_{DCIR} taken near the minimum of the R_{CT} vs SOC curve is not representative of the much higher resistance toward the end of discharge.

Validation of the DCIR measurement by EIS.—Since the DCIR measurement does not tell us which component(s) of the cathode resistance increases upon cycling, we performed an ex situ EIS analysis with the harvested pouch cell electrodes. To enable this analysis in a coin cell setup, i.e., in the absence of a μ -RE, the Li-CE was extended by a free-standing graphite (FSG) electrode in contact with metallic lithium, which drastically lowers the impedance of the counter-electrode.²³ The coin cells with such a Li/FSG-CE ran through a multi-step cycling procedure, which includes an EIS measurement at a relative SOC of 65% within a DCIR-like cycle, analogous to that conducted with the full-cells (see Experimental section for more details). The results of the EIS analysis are illustrated in Fig. 2.

First, the feasibility of this approach was tested with a symmetrical cell of two Li/FSG electrodes, which was cycled similarly to the actual coin cells (by applying the same current densities and charging times). As shown in Fig. 2a, the imaginary part of the impedance of such a symmetrical Li/FSG cell is below ≈1 $\Omega \text{ cm}^2$ and the HFR-corrected real part of its impedance is below ≈5 $\Omega \text{ cm}^2$ (sum of both electrodes), consistent with the values reported in Ref. 23. As will be shown below, these impedances are very small compared to the HFR-corrected impedances of the coin cells composed of harvested NCM-811 cathodes and a Li/FSG-CE, so that the HFR-corrected impedance response of the latter closely corresponds to the impedance of the harvested NCM-811 electrodes.

Table II. Comparison of the mean voltage change of the NCM-811 cathode (\bar{V}_{cath}) during C/2 and C/10 cycling at either 22 °C over 1000 cycles or at 45 °C over 700 cycles. For charge and discharge, the slope from linear fits of the mean voltages presented in our previous publication⁹ and in Fig. 1b is given in absolute values. Furthermore, the mean voltage change was calculated from R_{DCIR} in Fig. 1c according to $\frac{d\bar{V}_{\text{cath}}}{d\text{cycle}} = \frac{dR_{\text{DCIR}}}{d\text{cycle}} \Delta j$, with $\frac{dR_{\text{DCIR}}}{d\text{cycle}} = 267 \text{ m}\Omega \text{ cm}^2/\text{cycle}$ and $j = 0.7 \text{ mA cm}^{-2}$ at C/2 and 0.14 mA cm^{-2} at C/10, respectively.

$\frac{d\bar{V}_{\text{cath}}}{d\text{cycle}}$ [mV/cycle]	Ambient temperature (22 °C)		Elevated temperature (45 °C)	
	C/2 cycling		C/2 cycling	C/10 cycling
Charge	≈0.08		≈0.14	≈0.05
Discharge	≈0.12		≈0.35	≈0.11
Discharge/charge ratio	≈1.5		≈2.5	≈2.2
From R_{DCIR}	n.d.		≈0.19	≈0.04

More precisely, the contribution of the Li/FSG-CE to the overall impedance would even be lower since the symmetric Li/FSG cell impedance represents the impedance of two rather than one Li/FSG electrodes.

The spectra in Fig. 2 feature two semicircles: (i) a small semicircle at high frequencies (with a frequency maximum of $f_{\text{max}} \approx 2.2\text{--}5.4 \text{ kHz}$ between 6 and 700 cycles), and (ii) another semicircle at low frequencies (with $f_{\text{max}} \approx 14.8\text{--}0.18 \text{ Hz}$ between 6 and 700 cycles), whose diameter increases significantly upon

cycling. As illustrated in our previous publications,^{9,37} the underlying processes that are represented by each of the two R/Q elements in our impedance model (see caption of Fig. 2) can be deduced from an estimate of the associated double layer capacitance, which normalized to the proper interface should be on the order of $10 \mu\text{F cm}^{-2}$.²⁴ Doing so, the high-frequency semicircle must correspond to the contact resistance between the cathode electrode coating and the current collector, since its capacitance when normalized to the geometric surface area of the current collector results in $2\text{--}4 \mu\text{F/cm}_{\text{geom}}^2$. The low-frequency semicircle on the other hand is described by a transmission line model (TLM) that represents a complex convolution of the ion conduction in the electrolyte phase within the porous electrode (R_{ion}) and the charge-transfer resistance (R_{CT}). Its capacitance should thus reflect the double layer capacitance of the CAM and the conductive additives, consistent with the fact that the capacitance normalized by the BET surface area of the cycled cathode electrodes results in $10\text{--}25 \mu\text{F/cm}_{\text{BET}}^2$. Here, the surface area of the cycled electrodes amounts to $A_{\text{BET,elec}} \approx 1.6\text{--}2.8 \text{ m}^2/\text{g}_{\text{elec}}$, as determined by Kr-BET (see Experimental section).

The contact resistance (R_{contact}) deduced from the high-frequency semicircle is in the range of $\approx 12\text{--}26 \Omega \text{ cm}^2$. The observed small variation of this value might be caused by artifacts from the assembly of the coin cells with harvested cathodes. The α value of the corresponding constant phase element (Q_{contact}) is on the order of ≈ 0.7 . The low-frequency semicircle was fitted by a transmission line model, consisting of R_{ion} and $R_{\text{CT}}/Q_{\text{CT}}$.²⁴ The values for R_{ion} are $\approx 0.75\text{--}1.5 \Omega \text{ cm}^2$ for the samples up to 250 cycles. Afterwards, as the charge-transfer resistance becomes very large, the deconvolution of R_{ion} and R_{CT} becomes rather error-prone, resulting in fitted R_{ion} values of $\approx 10\text{--}20 \Omega \text{ cm}^2$, which is likely incorrect. For cathode electrodes with $\approx 30\%$ porosity, as used in this study, we do not expect that R_{ion} significantly increases over cycling. Thus, for the fitting of the impedance spectra where a reasonable value for R_{ion} could not be determined due to the dominance of R_{CT} (after 400–700 cycles), we used a fixed value of $1.5 \Omega \text{ cm}^2$ for R_{ion} . The α value of Q_{CT} evolves gradually from 0.93 to 0.75. For these cycling data at 45 °C, R_{CT} increases from $\approx 7 \Omega \text{ cm}^2$ after 6 cycles to $\approx 246 \Omega \text{ cm}^2$ after 700 cycles. This is considerably higher than at 22 °C, where R_{CT} for the same CAM amounted to $\approx 100\text{--}150 \Omega \text{ cm}^2$ after 1000 cycles,⁹ which indicates the formation of a thicker resistive surface layer at elevated temperature.

In Fig. 2b, the R_{CT} values obtained from the fit of the EIS data of the harvested NCM-811 cathodes (see Fig. 2a) are compared to the averaged R_{DCIR} values of the six full-cells (data taken from Fig. 1c). Note that the DCIR pulse was conducted every 50 cycles at the beginning of the full-cell cycling loop, so that the last measurement was taken after 650 cycles, while the ex situ EIS measurements are taken up to 700 cycles. The charge-transfer resistance of the NCM-811 cathode fully describes the observed R_{DCIR} trend, with R_{CT} increasing in a similar fashion as R_{DCIR} . The observation that R_{CT} is consistently lower than R_{DCIR} is due to the fact that the latter also includes contributions from R_{HF} , R_{contact} , and R_{ion} . Therefore, a more rigorous comparison of the DCIR resistance with the EIS data would be to compare it with the EIS-derived low-frequency resistance, which corresponds to the magnitude of the impedance

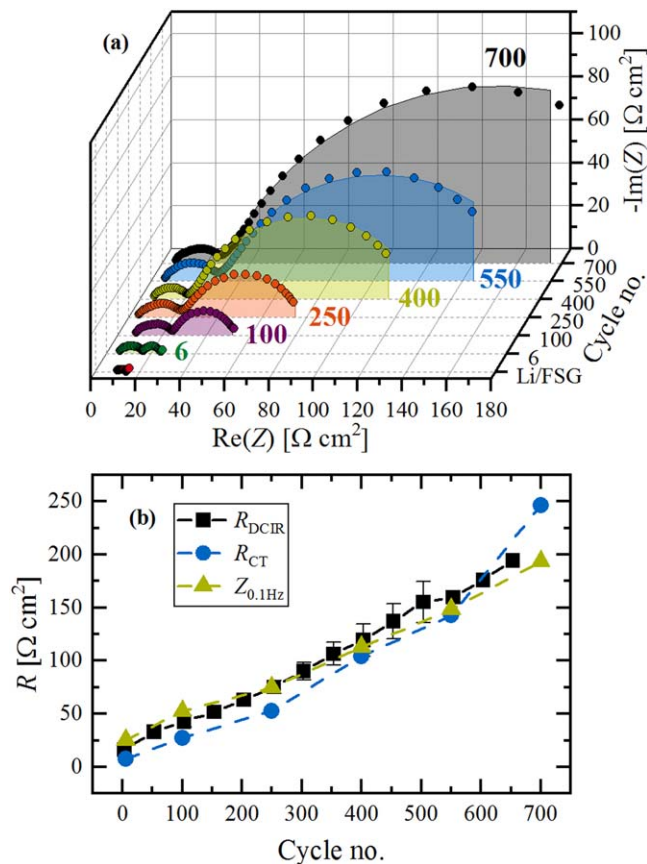


Figure 2. Ex situ EIS analysis of the harvested pouch cell cathodes, from which 14 mm diameter electrodes were punched out and re-assembled as working-electrode (WE) vs a Li/FSG-CE in a coin cell. (a) Impedance spectra were measured at the same conditions as the DCIR pulse in the full-cells (45 °C, 65% SOC, OCV $\approx 4.0 \text{ V}$). The data points (symbols) were fitted (lines) to: $R_{\text{HF}} + \text{TLM}[R_{\text{ion}}, R_{\text{CT}}/Q_{\text{CT}}] + R_{\text{contact}}/Q_{\text{contact}}$. The spectrum of a symmetrical Li/FSG cell, which underwent the same cycling procedure than the other coin cells prior to the EIS measurement, is also shown, demonstrating the negligible contribution of the Li/FSG-CE to the overall impedance beyond the high-frequency resistance. (b) Comparison of the averaged R_{DCIR} from Fig. 1c with the cathode charge-transfer resistance (R_{CT}) determined from the above fit of the EIS data and the low-frequency impedance at 0.1 Hz ($Z_{0.1\text{Hz}}$).

Table III. Rietveld refinement results of the NCM-811 CAM (pristine CAM powder, pristine electrode, as well as cycled and discharged electrodes). For the cycled electrodes, one of the two separately measured capillaries of the same electrode is exemplary given in the table (viz., the measurement with the lower Ni_{Li} value). The table summarizes quality factors (*R*-values), lattice parameters, and the therefrom determined Li content (according to Eq. 2 for the cycled electrodes), atomic site-specific information (including Li-Ni mixing, fractional z-coordinate of O, and atomic displacement parameters), and the fitted weight fraction of conductive graphite (nominally 2 wt%). Errors are given in parenthesis.

	Pristine powder	Pristine electrode	6	100	250	400	550	700
R_{wp} [%]	3.68	2.45	4.09	4.01	3.94	4.19	4.11	4.38
R_{bragg} [%]	0.906	0.648	0.898	0.989	1.06	1.30	1.12	1.55
χ^2	2.46	1.35	3.79	3.61	3.49	4.16	4.41	4.48
a [Å]	2.87214(1)	2.87246(1)	2.86888(2)	2.86873(2)	2.86738(2)	2.86690(2)	2.86606(2)	2.86693(2)
c [Å]	14.2081(1)	14.2080(1)	14.2409(1)	14.2516(1)	14.2622(2)	14.2712(2)	14.2735(2)	14.2756(2)
c/a [-]	4.94685(5)	4.94629(5)	4.96391(5)	4.96790(6)	4.97395(6)	4.97792(6)	4.98017(6)	4.97939(7)
x_{Li} [-]	1.01	1.01	0.915	0.898	0.875	0.861	0.852	0.855
Ni _{Li} [%]	1.98(7)	1.84(7)	1.71(8)	2.13(8)	2.54(8)	3.07(8)	2.75(8)	3.54(9)
$z_{6c,O}$ [-]	0.24113(5)	0.24092(5)	0.24029(6)	0.24016(6)	0.24011(6)	0.24000(7)	0.23993(6)	0.24006(7)
$b_{3a,Li}$ [Å ²]	0.73(5)	0.68(6)	0.76(8)	0.73(7)	0.80(8)	0.80(8)	0.85(8)	0.81(8)
$b_{3b,TM}$ [Å ²]	0.310(4)	0.473(5)	0.462(6)	0.482(6)	0.479(6)	0.432(7)	0.489(7)	0.445(7)
$b_{6c,O}$ [Å ²]	0.81(1)	0.97(2)	1.07(2)	1.12(2)	1.18(2)	1.23(2)	1.16(2)	1.25(2)
Graphite [wt%]	n.d.	1.9(1)	1.56(8)	1.44(8)	1.29(9)	1.47(9)	1.32(9)	1.30(9)

($|Z| = \sqrt{\text{Re}(Z)^2 + \text{Im}(Z)^2}$) at the nominal equivalent frequency than the DCIR pulse duration. For the here used 10 s DCIR pulse, this translates into 100 mHz, which is the lowest frequency measured during EIS analysis shown in Fig. 2a. Therefore, the magnitude of the impedance at 100 mHz ($Z_{0.1\text{Hz}}$) is compared with R_{DCIR} in Fig. 2b. R_{DCIR} and $Z_{0.1\text{Hz}}$ agree within $\pm 10 \Omega \text{ cm}^2$ throughout cycling, which is quite reasonable. For the first data points after 6 and 100 cycles, $Z_{0.1\text{Hz}}$ is slightly higher than R_{DCIR} , which most likely is due to the fact that the two more cycles at C/2 and C/10 that were applied to the harvested cathode electrodes prior to the ex situ EIS measurements might add some additional aging to the relatively fresh NCM-811 CAM.

Even though we believe that the here measured charge-transfer resistance predominantly originates from a reconstructed, spinel/rock-salt-type surface layer, which is caused by oxygen release and which grows from the CAM surface gradually into its interior, there is also the possibility that electrolyte decomposition products might form a resistive surface film, which is often referred to as cathode-electrolyte interphase (CEI).¹¹ This CEI-type surface film would grow on top of the CAM surface. The high-frequency semicircle obviously does not allow for discerning the occurrence of two different types of surface layers; however, we can try to evaluate the importance of the CEI on the basis of (i) the electrochemical stability of the electrolyte towards anodic oxidation and (ii) its chemical stability towards reactive lattice oxygen.³⁸ Regarding the first point, Metzger et al. have shown that EC-based electrolytes are oxidatively stable at potentials greater than 4.5 V vs Li⁺/Li, even at an elevated temperature of 50 °C.³⁹ This is further supported by an LNMO study by Pritzl et al.,¹⁸ where LNMO/graphite full-cells were cycled at 40 °C and with an LP57 electrolyte containing different concentrations of VC. LNMO is an ideal model electrode, because the spinel structure is inherently stable against oxygen release and the concomitant surface reconstruction.^{33,38} At the same time, it operates at a high potential of ≈ 4.7 V vs Li⁺/Li, which enables to study exclusively the influence of electrolyte oxidation on the cathode resistance. For the EC/EMC/LiPF₆ base electrolyte without VC, the cathode resistance remained constant over the duration of 100 cycles, i.e., we can exclude the formation of a resistive CEI-type surface layer. If VC was added in high concentrations, the cathode resistance however increased because VC gets already oxidized at ≈ 4.3 V vs Li⁺/Li, so that an organic film of poly(VC) deposits on the LNMO surface. For this reason, VC was omitted in our NCM-811/graphite full-cells.

The oxygen release from the CAM surface is accompanied by the chemical degradation of the electrolyte.⁴⁰ In case of EC, the attack of singlet oxygen leads to the in situ formation of VC at an intermediate

stage of the decomposition cascade. When NCM-622/graphite full-cells are cycled above the onset potential of oxygen release (until 4.6 V_{FC} at 25 °C), Teufl et al. reported a rapid rollover failure within ≈ 25 cycles using an EC-based electrolyte and a low $m_{\text{electrolyte}}/m_{\text{CAM}}$ ratio of $\approx 1.6/1$.⁴¹ The authors suggested that the cell resistance build-up that leads to this rollover failure is due to an increase of the cathode resistance, caused by the oxidation of VC at these high potentials. On the other hand, the capacity fading of very similar NCM-622/graphite cells with LP57 electrolyte (also cycled until 4.6 V_{FC} at 25 °C) is considerably less using a $m_{\text{electrolyte}}/m_{\text{CAM}}$ ratio of $\approx 8/1$.¹⁴ Here, the cells last for ≈ 300 cycles until they reach the same capacity drop than after the above rollover failure. In summary, we cannot entirely exclude the formation of a resistive CEI-type surface film also in our case, especially at the elevated temperature of 45 °C, where both the oxygen release and the electrolyte decomposition are increased compared to 25 °C operation.¹⁴ However, the here used ≈ 0.2 V lower upper cut-off potential of 4.5 V vs Li⁺/Li and the higher $m_{\text{electrolyte}}/m_{\text{CAM}}$ ratio of $\approx 13/1$ probably counteract these effects. Furthermore, we think that such an organic surface film, if present, does not contribute to the observed capacity losses, because its share in R_{CT} is expected to be independent of the state of charge (and thus not larger than measured for the medium SOC of 65% in Fig. 2). On the other hand, R_{CT} significantly increases towards the lower and upper SOC limit at the cut-off voltages,⁹ which is believed to be caused by the slowed Li diffusion within the reconstructed, spinel/rock-salt-type surface layer.⁴²

Bulk stability and Li-Ni mixing analyzed via XPD.—The bulk stability of layered oxides typically refers to the level of cation mixing, where a transition-metal moves irreversibly from the native TM layer into the Li layer. Due to similar ionic radii of Li⁺ and Ni²⁺, Ni is mainly believed to be the moving TM,^{4,43,44} but X-ray diffraction does not allow any distinction among the three TMs and Ni is just the most favorable representative in the investigated Ni-rich NCM-811. Refining the Li-Ni mixing as a paired anti-site defect of Ni_{Li} and Li_{TM} in the common $R\bar{3}m$ space group, we observed no systematic change in the extent of Li-Ni mixing between the pristine and EOT samples after 1000 cycles in our prior study with the same CAM at 22 °C.⁹ We thus concluded that the freely refined Ni_{Li} stays constant at a level of $\approx 3\%$, which was recently supported by Xu et al. for NCM-811 also cycled at room temperature.⁴⁵ The Rietveld refinement results of the present study at 45 °C are summarized in Fig. 3 and Table III.

Figure 3a shows exemplarily the XPD pattern of the discharged cathode at EOT after 700 cycles and the corresponding Rietveld

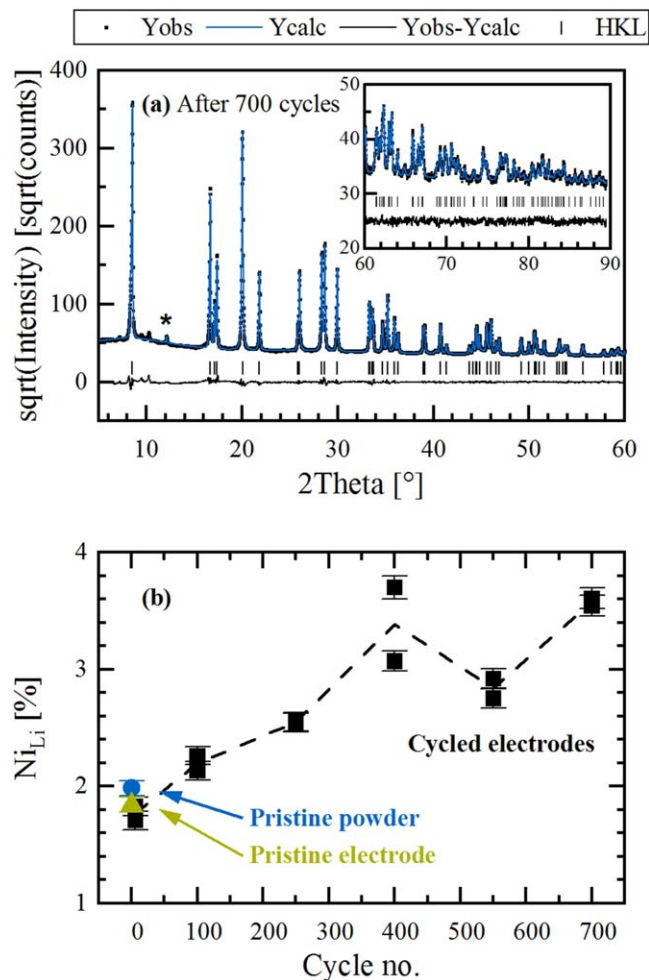


Figure 3. Determination of the Li-Ni mixing from ex situ XPD data of the harvested NCM-811 electrodes in the discharged state. (a) Rietveld refinement of the EOT NCM-811 CAM after 700 cycles. The data were collected at our in-house Mo-diffractometer ($\lambda = 0.7093 \text{ \AA}$) in the 2θ range of 5° – 90° . The observed (black points), calculated (blue line), and difference diffraction profile (black line) are shown together with the position of the Bragg peaks of NCM-811 (black ticks). The asterisk at $\approx 12^\circ$ indicates the strongest (002) reflection of conductive graphite, which was also included into the refinement. The inset shows the high-angular range from 60° to 90° . To visualize the increasingly smaller reflections at higher 2θ , the intensity is displayed on a square root scale on the y-axis. (b) Evolution of the Li-Ni mixing, labeled as Ni_{Li} , over the course of 700 cycles. The cycled electrodes were measured twice in two separate capillaries and are further compared with the pristine CAM powder and the pristine electrode (both heated at 120°C prior to loading the material into the capillaries). The dashed black line shows the average trend of the cycled electrodes.

refinement fit. Apart from 2 wt% conductive graphite in the electrode formulation, whose most intense peak is highlighted by an asterisk, there is no crystallographic side phase visible in the pattern. Regarding the NCM-811 material, its layered structure is well preserved and the applied model satisfactorily describes the bulk material, as can be also seen from the fairly constant R -values in Table III. Other structural parameters such as the atomic displacement parameters scatter in a sufficiently narrow range, which gives further confidence about the validity of the refined Ni_{Li} values (see Fig. 3b).

Ni_{Li} was determined from two separate capillaries of the same harvested cathodes, together with the pristine CAM powder and the pristine electrode. The deviation between the duplicate measurements amounts to less than 0.2%, which is close to the estimated

standard uncertainty from the Rietveld fit of $\approx 0.1\%$. Only the XPD data from the cathode harvested after 400 cycles differ in this respect with a deviation of $\approx 0.6\%$. Starting with the pristine CAM, its Li-Ni mixing of $\approx 1.8\%$ – 2.0% turns out to be lower than the $\approx 3.1\%$ reported in our previous study, despite using the identical NCM-811 sample and the same electrode sheets that had been stored under inert conditions in an argon-filled glove box. In comparison to the former study, we extended the 2θ range from 60° to 90° , but this does not alter the refinement outcome (within the margin of uncertainty); it only slightly reduces the extent of correlations for the sensitive Ni_{Li} parameter ($\approx 70\%$ to the scale factor and to $b_{3a,\text{Li}}$). Unfortunately, we cannot provide a solid explanation for this discrepancy. We speculate that the replacement of the Mo-source and the following re-adjustment of the diffractometer might have caused this difference in the refinement-based value of Ni_{Li} . To avoid any artefacts which might be caused by instrumental variations, we consequently tried to measure the samples in this study under fairly constant conditions within a short period of time. Yin et al. investigated 17 pristine NCM samples by high-resolution X-ray and neutron powder diffraction and they established a linear correlation between the Ni_{Li} amount and the Ni content of the NCM (more specifically, between % Ni_{Li} and Ni^{2+}).⁴⁶ For NCM-811, this correlation projects a Ni_{Li} amount of $3.4 \pm 0.5\%$, which would match the value reported in our earlier study.⁹ However, as discussed by the authors, the Li-Ni mixing further depends on the calcination temperature and the activation energy of defect formation (on the order of 200–300 meV), so the here reported value of $\approx 1.8\%$ – 2.0% is not unreasonable.

Analyzing the cycled NCM-811 electrodes with regards to Ni_{Li} , we find that for the cathode harvested after only 6 cycles, the extent of Li-Ni mixing agrees with that of the pristine CAM powder and the pristine electrode (see Fig. 3b). After increasingly more cycles, the Li-Ni mixing rises by $\approx 1\%$ – 2% until the end-of-test (700 cycles), depending on how one interprets the scatter of the Ni_{Li} values between 400, 550, and 700 cycles. At this point, we want to discuss shortly some aspects of the structural model: $[\text{Li}_{x-\nu}\text{Ni}_\nu]_{3a}[\text{Li}_i\text{Ni}_{0.79-\nu}\text{Co}_{0.10}\text{Mn}_{0.10}]_{3b}[\text{O}]_{6c}$ (see also Experimental section). Here, x_{Li} was deduced from the ca lattice parameter ratio according to Eq. 2, whereby x_{Li} of the discharged cathodes decreases upon cycling (see Table III). If x_{Li} would have been fixed to the pristine value of 1.01 for all samples (e.g., in default of a proper method to determine x_{Li} of cycled samples), the fitted value of Ni_{Li} , e.g., at EOT (700 cycles) would be reduced from $\approx 3.6\%$ to $\approx 2.4\%$ (so that one might mistakenly conclude there is hardly any change in comparison to $\approx 1.8\%$ – 2.0% of the pristine NCM-811). This is due to the fact that the required electron density of the Li layer would mainly be compensated by Li itself, so that there would be no need in the refinement routine to place additional Ni there. Alternatively, refining the Li-Ni mixing not as a paired anti-site defect of Ni_{Li} and Li_{TM} , but purely as Ni_{Li} (i.e., $\nu_{\text{Li}} = 0$), has not such a big impact: the absolute amount of Ni_{Li} would shift to lower values by a maximum of only $\approx 0.3\%$ after 700 cycles (because the remaining Li again partially provides the required electron density of the Li layer). It is thus very important to report all relevant aspects of the refinement, including a clear description what x_{Li} value was used for a given fit, in order to enable a comparison of the structural data reported in different publications.

Even though the absolute values of Ni_{Li} have to be treated with caution, we are quite confident that the observed trend of an increasing Li-Ni mixing by $\approx 1\%$ – 2% while cycling NCM-811 for 700 cycles at 45°C between cathode potentials of 3.0–4.5 V is correct. The trickier question, however, addresses the impact of an increasing extent of Li-Ni mixing on the electrochemical performance of the NCM-811 CAM. How would it affect the cathode resistance and finally the achievable capacity? Makimura et al. synthesized a series of $[\text{Li}_{1-y}\text{Ni}_y][\text{Ni},\text{Co},\text{Al}]\text{O}_2$ samples ($0 \leq y \leq 0.13$) and they found a perfectly linear correlation between the capacity (C) and y for C/10 cycling at 20°C between cathode potentials of 2.5 and 4.2 V, namely $C [\text{mAh g}^{-1}] = 181.4 - 725.5 \cdot y$.⁴⁷ When normalized to the highest capacity for $y = 0$ (C_0), this

equates to $C/C_0 [\%] = 100 - 400 \cdot y$, so that the observed capacity loss is four times higher than the loss that would be simply expected by the blocking of free Li sites by inactive Ni. The authors confirmed a strong polarization effect originating from slowed Li diffusion kinetics. This generalized $C/C_0 = f(y)$ correlation can be used to estimate the impact of a maximum of 2% increase in Ni_{Li} over 700 cycles (see Fig. 3b) on the capacity, since y equals approximately v_{Ni} in the structural model of NCM-811 (please note that $Ni_{Li} = v_{Ni} \cdot 100\%$). For a maximum increase of Ni_{Li} by 2% from BOT to EOT, the capacity fading predicted by the above relationship observed by Makimura et al. would amount to 8% or $\approx 18 \text{ mAh g}^{-1}$ (based on an initial capacity of $\approx 221 \text{ mAh g}^{-1}$ at $C/10$, see Fig. 1a). This is $\approx 45\%$ of the overall capacity loss of $\approx 40 \text{ mAh g}^{-1}$ at $C/10$ (same C-rate as applied by Makimura et al.⁴⁷). It is difficult to make any statement about the Li diffusion kinetics of NCM-811. The cathode mean charge voltage could be fully explained by the increase of R_{DCIR} at $\approx 4.0 \text{ V}$ (see Table II), which in turn is a direct measure of R_{CT} (see Fig. 2), but \tilde{D}_{Li} might potentially have an impact on the more pronounced change of the cathode mean discharge voltage. In this context, Makimura et al. observed a higher polarization during discharge than during charge with increasing y , but at the same time the capacity was more limited in the charge than discharge endpoint (ratio of $\approx 2/1$).⁴⁷ In summary, the cycling-induced increase of the Li-Ni mixing by $\approx 1\%$ – 2% over 700 cycles might appear negligible, but its contribution to the capacity fading due to the slowed Li diffusion kinetics in the bulk phase could indeed be relevant. Since the correlation reported for NCA samples by Makimura et al. might not be fully applicable to our NCM-811 CAM, however, the precise quantification of the capacity loss caused by increasing Li-Ni mixing remains elusive.

Finally, we want to look at a recent study of Li et al., where NCM-811 was cycled for 1000 cycles at 25°C to different upper cut-off voltages in NCM-811/graphite full-cells.⁴⁴ For cycling until 4.2 and 4.4 V_{FC} , which translates into ≈ 4.3 and $\approx 4.5 \text{ V vs Li}^+/\text{Li}$, the authors report the Li-Ni mixing to increase vastly by 6.7% and 11.9%, respectively. Unfortunately, their structural model is barely described in the publication, which makes it difficult to compare their results to ours. According to the $C/C_0 = f(y)$ correlation by Makimura et al.,⁴⁷ the Li-Ni mixing has to account completely (and beyond) for the observed capacity fading (78% and 52% capacity retention). This refinement result seems to be quite unlikely, because Li et al. also identified other important degradation mechanisms such as TM dissolution and deposition on the anode, surface NiO formation, and particle cracking.⁴⁴

Lithium content via XPD analysis.—The above evaluation of the XPD data from the cathodes harvested in the discharged state already indicated a steady decrease of the lithium content of the discharged NCM-811 CAM upon cycling (see x_{Li} in Table III). This behavior can be easily rationalized by the increasing overpotential (e.g., reflected by the changes in the mean charge/discharge cathode voltage, see Fig. 1b), which narrows the accessible SOC window from both sides in the completely discharged and charged states when cycling the NCM-811 electrode in the fixed cathode voltage window of 3.0–4.5 V. In our study conducted at 22°C ,⁹ the x_{Li} data from in situ XPD were the centerpiece to deconvolute the capacity loss into its contributions originating from the increase of R_{CT} related overpotentials and from a loss of cyclable cathode active material. This analysis shall also be applied here based on ex situ XPD data. Since the full-cells were stopped during $C/2$ cycling after running into the lower cut-off voltage, XPD data in the discharged state of the harvested NCM-811 cathodes could be acquired immediately. For XPD analysis in the charged state, we punched out smaller electrodes, which were cycled in half-cells at $C/2$ for 1.5 more cycles and which were then disassembled after running into the upper cut-off cathode voltage of 4.5 V. The c/a lattice parameter ratio from the diffractograms and the thereof determined lithium content are summarized in Fig. 4.

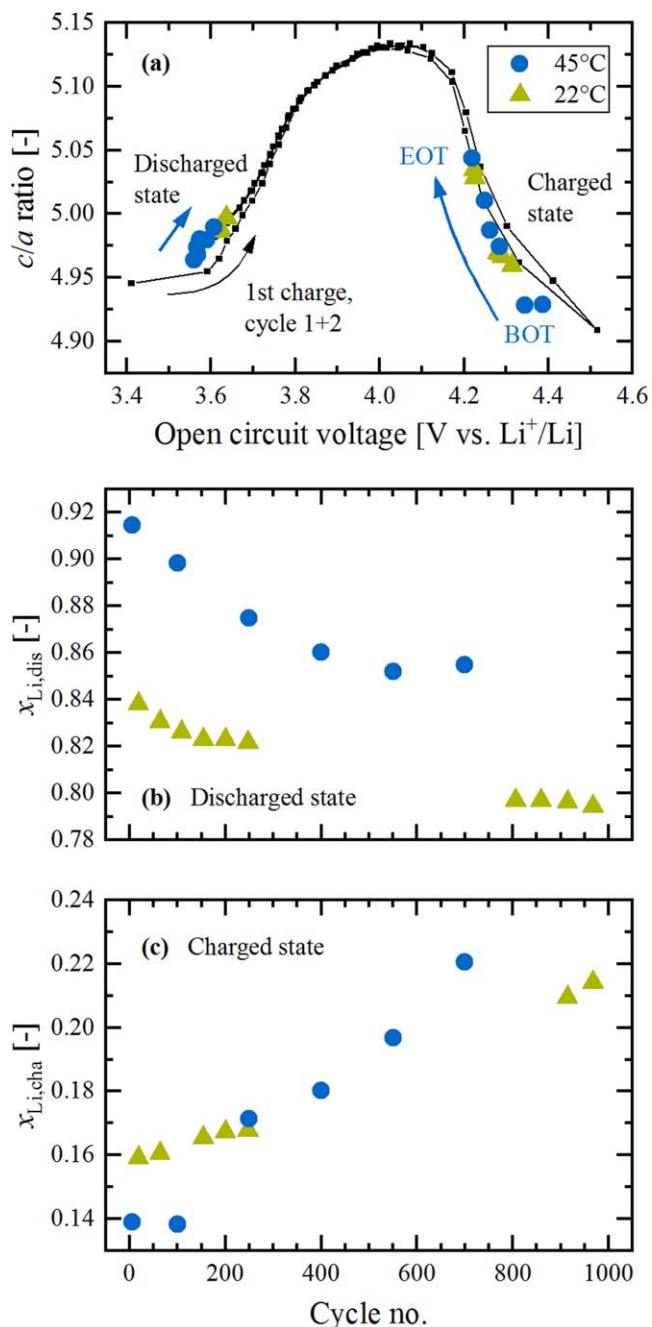


Figure 4. Determination of the lithium content in the discharged and charged state of NCM-811 electrodes operated between cathode potentials of 3.0–4.5 V at $C/2$ and different cycling temperatures. (a) Evolution of the underlying c/a lattice parameter ratio vs OCV and comparison to the c/a curve of a fresh NCM-811 cathode in cycle 1 and 2 (black squares/lines). The cycle 1 + 2 curve and the in situ XPD data for cycling at 22°C (green triangles) were taken from our previous publication (see curves labeled “Cycle 1 + 2” and “LDE, cell 1” in Fig. 6a of Friedrich et al.,⁹ published by ECS, licensed as CC BY 4.0). The ex situ XPD data at 45°C (blue circles) originate directly from the harvested full-cell electrodes (discharged state) or from harvested electrodes that were subjected to another 1.5 half-cell cycles (charged state) and are shown vs the final OCV value at 25°C (see Experimental section). The c/a data points are converted into the lithium content: (b) in the discharged state via Eq. 2, referred to as $x_{Li,dis}$; (c) in the charged state via Eq. 3, referred to as $x_{Li,cha}$. At 45°C , the BOT value of $x_{Li,dis} \approx 0.915$ slightly exceeds the margin of the c/a calibration curve, but additional ex situ points of fresh NCM-811 cathodes showed that Eq. 2 holds true until ≈ 0.95 .

The $x_{\text{Li}} = f(c/a)$ calibration curves were measured within the first cycles of a fresh NCM-811 cathode,⁹ where the lithium content (x_{Li}) can be deduced fairly accurately from the exchanged capacity (assuming purely faradaic currents from lithium de-/intercalation into the CAM). This approximation is not true anymore during prolonged cycling, due to the charge accumulation caused by tiny parasitic currents. Consequently, it is difficult to prove if the initially determined calibration curves and the extracted x_{Li} values are still valid, because there is no direct measure of the CAM's state of charge. On the other side, we continuously tracked the open circuit voltage (at 45 °C and finally also at 25 °C), and the c/a ratio is shown as a function of the OCV at 25 °C in Fig. 4a. Here, the c/a data from 45 °C cycling (blue circles in Fig. 4a) are contrasted with the data from 22 °C cycling (green triangles) and with the full $c/a = f(\text{OCV})$ curve of a fresh NCM-811 cathode (black squares/lines). Note that the OCV values are known for every measurement, i.e., all datasets can be compared with each other without any correction. We see that, independent of the cycling temperature, the c/a data in the completely discharged and charged state coincide nicely with the initial calibration curve. The c/a values increase with cycling in both the discharged and charged state, indicating a shrinking OCV window. Since the $c/a = f(\text{OCV})$ correlation is maintained upon cycling and since the OCV is an indirect measure of the absolute SOC (i.e., the SOC referenced to x_{Li}), we can continue to convert the c/a ratio into the lithium content. This is done by applying Eq. 2 for the discharged state (see $x_{\text{Li,dis}}$ in Fig. 4b) and by applying Eq. 3 for the charged state (see $x_{\text{Li,cha}}$ in Fig. 4c), respectively. For a more detailed explanation of this procedure see the Experimental section and Friedrich et al.⁹

Let us first look at the BOT values, where the 45 °C capacity is $\approx 24 \text{ mAh g}^{-1}$ higher than at 22 °C (see Table I). This capacity gain predominantly occurs in the discharged state, because $x_{\text{Li,dis}}$ is higher by ≈ 0.08 in the discharged state (see Fig. 4b), while $x_{\text{Li,cha}}$ is only lower by ≈ 0.02 in the charged state (see Fig. 4c), corresponding to a ratio in Δx_{Li} of $\approx 4/1$. Based on dQ/dV plots, Li et al. also reported that the low-SOC capacity (i.e., towards the discharged state) of NCA depends strongly on temperature (and mildly on C-rate), but the high-SOC limit (i.e., towards the charged state) is hardly affected by neither temperature nor C-rate.¹³ They explain this behavior by the kinetic hindrance from solid-state lithium diffusion, which hampers the lithium intercalation back into the layered oxide during discharge. In the following, $x_{\text{Li,dis}}$ continuously decreases while $x_{\text{Li,cha}}$ increases with cycling, as already anticipated from the $c/a = f(\text{OCV})$ raw data (see Fig. 4a). The changes are quite uniform, except for the $x_{\text{Li,cha}}$ value after 100 cycles at 45 °C that remains at the value of ≈ 0.14 obtained after 6 cycles (see Fig. 4c). Furthermore, $x_{\text{Li,dis}}$ does not continue to decrease anymore between 550 and 700 cycles (see Fig. 4b). Comparing the changes in x_{Li} from BOT to EOT between both temperatures, $\Delta x_{\text{Li,dis}}$ and $\Delta x_{\text{Li,cha}}$ are by a factor of ≈ 1.4 – 1.5 higher after 700 cycles at 45 °C compared to 1000 cycles at 22 °C ($|\Delta x_{\text{Li,dis}}|$: ≈ 0.044 at 22 °C vs ≈ 0.060 at 45 °C; $\Delta x_{\text{Li,cha}}$: ≈ 0.055 at 22 °C vs ≈ 0.081 at 45 °C). This result is in line with the more strongly increasing overpotential at the higher temperature, as outlined in the previous paragraphs. However, it is difficult to relate the Δx_{Li} differences quantitatively to the mean cathode voltages (Fig. 1b) or to the $R_{\text{DCIR}}/R_{\text{CT}}$ evolution (Fig. 2b), because only the resistances in the low- and high-SOC region towards the voltage cut-offs matter for the overpotential-induced capacity loss (but these resistances are not directly addressed by the former measures).

In light of the results from Figs. 3 and 4, we want to emphasize that the aged NCM-811 CAM could be always refined as a single phase based on the Rietveld refinement of the ex situ XPD data. This is in contrast to some operando studies about Ni-rich NCMs and NCAs (with 80%–85%_{Ni}), which detected the emergence of two to three simultaneously present layered phases over the course of long-term cycling, especially in the charged (delithiated) state.^{15,45,48,49} Xu et al. observed a so-called “fatigued” phase of NCM-811 (together with an “active” and “intermediate” phase), whose

upper SOC limit was fixed at approximately 75% (corresponding to $x_{\text{Li,cha}} \approx 0.25$).⁴⁵ They assign this threshold to the increasing interfacial lattice strain between the reconstructed rock-salt surface layer (caused by lattice oxygen release at high SOC) and the bulk layered structure beyond $\approx 75\%$ SOC. The segregation into several phases might however disappear in the charged state when the CAM is held long enough under constant voltage¹⁵ or open circuit voltage.⁴⁹ Despite forming a reconstructed surface layer, we could operate NCM-811 continuously to $x_{\text{Li,cha}}$ values below 0.25 (see Fig. 4c) without any evidence for an additional “fatigued” layered phase in the XPD data, contrary to the up to $\approx 70\%$ observed by Xu et al.⁴⁵ This is perhaps due to the observation that such a fatigued phase may only occur upon extensive particle cracking, in which case Schweidler et al. observed the occurrence of a fatigued phase that nevertheless could be fully accessed at very low currents.¹⁵

Capacity loss analysis.—With the XPD-derived x_{Li} data, we can now proceed to perform the capacity loss analysis. Here, the material loss is probably the most interesting parameter, which quantifies the fraction of the electrochemically active CAM lost and/or converted into an electrochemically inactive phase upon cycling. In the former 22 °C study, the material loss could be explained by the formation of a resistive, oxygen-deficient surface layer around the primary particles, and this loss of electrochemically active material was calculated in percentage terms relative to the pristine CAM as follows:⁹

$$\Delta C_{\text{Material,rel}}^i = \frac{C_{\text{XPD}}^i - C_{\text{EC}}^i}{C_{\text{XPD}}^i} \quad [5]$$

where C_{EC}^i (in mAh g^{-1}) is the electrochemically measured discharge capacity in the i th cycle and C_{XPD}^i (also in mAh g^{-1}) is the theoretically expected capacity inferred from XPD:

$$C_{\text{XPD}}^i = (x_{\text{Li,dis}}^i - x_{\text{Li,cha}}^i) \cdot \frac{274 \text{ mAh g}^{-1}}{1.01} \quad [6]$$

C_{XPD}^i is applied to the whole CAM and thus assumes no material to be lost while aging, but it considers the narrowed SOC window during C/2 cycling due to the actually present overpotential in the i th cycle. Thus, the difference between C_{XPD}^i and C_{EC}^i represents the loss of electrochemically active material in the i th cycle (in mAh g^{-1}); if this difference is normalized by C_{XPD}^i , it reflects the relative loss of electrochemically active material. Please note that 274 mAh g^{-1} correspond to the theoretical capacity for complete lithium extraction of 1.01 from the pristine CAM (see Experimental section).

Even though providing quantitative insights into CAM degradation, we admit that the XPD analysis is not really practical to be applied on a routine basis, since it requires a precise $x_{\text{Li}} = f(c/a)$ calibration curve for every CAM and that the bulk of the CAM stays fairly unaltered under the testing conditions (e.g., extensive Li-Ni mixing⁴⁴ or lattice dislocations⁵⁰ could potentially modify the $x_{\text{Li}} = f(c/a)$ relationship). These drawbacks call for alternative methods. Relying solely on electrochemical data, Dahn's group developed a differential voltage analysis software (which also requires that the bulk of the CAM does not change upon cycling).⁵¹ Here, dV/dQ vs Q curves of the cycled full-cell are compared to reference half-cells from anode and cathode. They are matched with each other by adjusting two parameters for each electrode: the electrochemically active mass of the electrodes and their capacity slippage. Other diagnostic and prognostic tools use a similar set of parameters to model battery aging from experimental data.^{52,53} The loss of electrochemically active material can then be calculated from the decrease of the cathode mass.

In our previous publication, we also tried to estimate the material loss by applying a C-rate test and comparing the electrochemical

capacity in the i th cycle (C_{EC}^i) to an adequate reference state (C_{EC}^0):

$$\Delta C_{\text{Material,rel}}^i = \frac{C_{EC}^0 - C_{EC}^i}{C_{EC}^0} \quad [7]$$

There are two important requirements to be fulfilled by the reference state: (i) it must not yet have experienced an electrochemically active material loss, which limits the reference state to the initial cycles; and, (ii) the overpotential must be negligible, which demands that C_{EC}^0 and C_{EC}^i are measured at a very slow C-rate. Under these conditions, any reversible capacity loss can be compensated for and only the irreversible loss of electrochemically active material remains. In our previous work with the same NCM-811 CAM, it turned out that a C-rate of $C/50$ was sufficiently slow to minimize the impact of overpotentials on the attained capacity.⁹ $C/50$ cycling at 45 °C between cathode potentials of 3.0–4.5 V delivers a discharge capacity of $C_{EC}^0 = 228 \pm 1 \text{ mAh g}^{-1}$ within the first two cycles of a pristine NCM-811 cathode (which is quite close to the $221 \pm 1 \text{ mAh g}^{-1}$ obtained a $C/10$, see Fig. 1a). Electrodes that were punched out from the cathodes harvested from the cycled pouch cells were also subjected to two $C/50$ cycles (following EIS at $C/10$, see Experimental section). The cathode mean discharge voltage of the cycled electrodes agrees within less than 35 mV (lower) with that of the pristine cathode, even though the mean discharge voltage after 700 cycles has decreased by $\approx 80 \text{ mV}$ at $C/10$ and $\approx 250 \text{ mV}$ at $C/2$ (see Fig. 1b). This implies that the resistance increase over cycling does not result in any significant overpotential at this very low C-rate of $C/50$, i.e., the above requirements for this analysis are satisfied.

Figure 5 compares the relative material loss of the electrodes cycled at 45 °C and calculated by this EC method (black squares, acc. to Eq. 7) to that calculated by the XPD analysis (acc. to Eq. 5) for the electrodes cycled at 45 °C (blue circles) and those cycled at 22 °C in our previous study (green triangles). Focusing first on the electrodes cycled at 45 °C, Fig. 5 shows that the electrochemically active material loss obtained by the EC vs the XPD method, both independent datasets, match extremely well within ± 1 percentage points. The only exception is the EOT sample after 700 cycles, where the XPD-derived material loss ($\approx 18.2\%$) exceeds that obtained from the EC method ($\approx 15.6\%$) by ≈ 2.6 percentage points. This difference could potentially be explained by a slightly too high $x_{\text{Li,dis}}$ value (see Fig. 4b), which in turn would increase C_{XPD}^i and thus the XPD-based $\Delta C_{\text{Material,rel}}^i$ value (see Eqs. 5 and 6).

For the electrodes cycled at 22 °C, most of the electrochemically active material get lost within the first 200–300 cycles, then leveling off and reaching $\approx 8.5\%$ after 1000 cycles. For the electrodes cycled at 45 °C, the progress of the material loss shows a similar trend in the beginning, but contrary to the 22 °C data, it does not diminish until 700 cycles. Even though the trend is not exactly clear, either possessing a sharp rise from 550 to 700 cycles (as indicated by the XPD method) or a more uniform increase (as suggested by the EC method), the EOT value after 700 cycles at 45 °C amounts to $\approx 15.6\%$ – 18.2% and is thus twice as big than after 1000 cycles at 22 °C. Using the dV/dQ analysis software,⁵¹ Li et al. tracked the CAM loss of their NCA/graphite full-cells cycled at 40 °C.¹³ For the upper cut-off voltage of 4.3 V_{FC} (corresponding to $\approx 4.4 \text{ V}$ vs Li^+/Li), the calculated CAM loss amounts to $4.3 \pm 0.5\%$ and $10.1 \pm 0.5\%$ after 400 and 800 cycles, respectively. While these losses for NCA are ≈ 2 -fold lower than those in this study for NCM-811, this may not only be due to the different active materials but also due to the here used $\approx 0.1 \text{ V}$ higher upper cathode potential and the 5 °C higher temperature. In an earlier publication from the Dahn group, they reported $\approx 8\%$ of lost NCM-811 after only 83 cycles under very similar conditions (again 40 °C and 4.3 V_{FC}),⁵⁴ which seems quite large compared to our data. All these datasets point towards the influence of the cycling conditions (e.g., temperature, upper cut-off voltage, and depth of discharge) and the nature of the CAM (e.g., NCM vs NCA) on

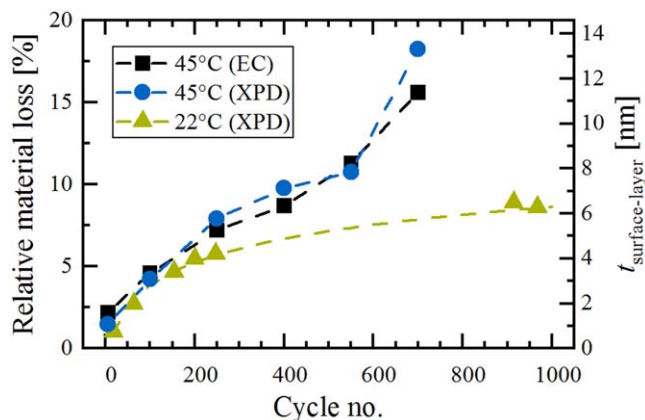


Figure 5. Determination of the NCM-811 material loss ($\Delta C_{\text{Material,rel}}^i$) upon extended cycling at 45 °C between cathode potentials of 3.0–4.5 V, either determined from slow $C/50$ cycling of the harvested cathodes (EC method using Eq. 7; black squares), or from our XPD analysis (using Eqs. 5 and 6; blue circles). The XPD data at 22 °C (green triangles) were taken from our previous publication (see data labeled “Cell 1” in Fig. 5c of Friedrich et al.,⁹ published by ECS, licensed as CC BY 4.0). The material loss in percentage terms is converted into the thickness of a resistive, O-depleted surface layer on the right. Here, we assumed spherical primary particles, whose average diameter of $\approx 410 \text{ nm}$ was estimated from the BET surface area of a charged electrode ($\approx 3.1 \text{ m}^2/\text{g}_{\text{CAM}}$, see later discussion); for details of this calculation see the supporting information of Ref. 9.

the extent of material loss, so that a quantitative comparison with other work in the literature is typically not possible.

But what causes the temperature dependence in this work? The more pronounced material loss at elevated temperature suggests a thicker reconstructed, oxygen-depleted surface layer. However, the upper SOC limit is almost not affected by the temperature rise, as was already seen for the BOT values of $x_{\text{Li,cha}}$ at $C/2$ (see Fig. 4c) as well as for the $C/10$ formation cycles (absolute SOC values of $\approx 85\%$ vs $\approx 86\%$). Since the oxygen release that leads to the surface transformation predominantly depends on the maximum SOC (i.e., the extent of delithiation),^{32,33} one would expect a similar driving force for oxygen release for the cycling conditions at both temperatures. On the other hand, the kinetics of the surface reconstruction would be expected to be faster (e.g., for oxygen transport and TM rearrangement), by which the O-depleted, spinel/rock-salt-like layer would be able to penetrate deeper into the primary particles. The temperature dependence of the initial oxygen release was studied by Jung et al. for an NCM-622 CAM.¹⁴ Taking the sum of evolved O_2 , CO , and CO_2 within the first four cycles until 4.8 V_{FC}, the gassing caused by oxygen release increased by a factor of ≈ 1.5 and ≈ 1.9 when increasing the temperature from 25 °C to 40 °C or to 50 °C, respectively. In our case, the NCM-811 CAM operates for most of the time above the SOC threshold for oxygen release at $\approx 80\%$, corresponding to an $x_{\text{Li,cha}}$ value of ≈ 0.20 at the upper cut-off potential. As shown in Fig. 4c, $x_{\text{Li,cha}}$ remains below 0.20 for the first ≈ 750 cycles during 22 °C operation (interpolated from a linear fit through the existing data) and for ≈ 550 cycles during 45 °C operation. Consequently, the oxygen release could proceed almost unlimited; however, Jung et al. further showed that the oxygen release diminishes from cycle to cycle.¹⁴ At 40 °C, e.g., the gassing of the NCM-622 CAM in cycle 2–4 reduced by a factor of ≈ 2.2 , ≈ 3.7 , and ≈ 4.0 compared to the first cycle. Even though we cannot finally say for how long oxygen is released from the CAM surface, we want to emphasize that the here quantified fraction of lost CAM does not directly correspond to the accumulated amount of evolved lattice oxygen until the respective cycle number. The transformation of the electrochemically active, layered structure into an electrochemically inactive, resistive surface layer is assumed to be a two-step process.⁹ After the initial oxygen release, the

Table IV. Deconvolution of the electrochemically measured capacity loss from BOT to EOT ($\Delta C_{EC}^{BOT \rightarrow EOT}$) into its contributions originating from the loss of cyclable CAM ($\Delta C_{Material}^{BOT \rightarrow EOT}$) and the overpotential-induced loss ($\Delta C_{Overpotential}^{BOT \rightarrow EOT}$). $\Delta C_{Overpotential}^{BOT \rightarrow EOT}$ can be further divided into capacity losses in the discharged ($\Delta C_{Discharge}^{BOT \rightarrow EOT}$) and charged state ($\Delta C_{Charge}^{BOT \rightarrow EOT}$), respectively. The underlying equations of the XPD analysis are provided in the Appendix and the values at ambient temperature stem from our previous publication of the same material.⁹ The sum of $\Delta C_{Material}^{BOT \rightarrow EOT}$ and $\Delta C_{Overpotential}^{BOT \rightarrow EOT}$ exceeds $\Delta C_{EC}^{BOT \rightarrow EOT}$ due to rounding errors and due to the fact that some material loss was already acquired until BOT.

C/2 capacity loss [mAh g ⁻¹]	Equation	Ambient temperature (22 °C)	Elevated temperature (45 °C)
BOT → EOT		Cycle 18 → 1000	Cycle 6 → 700
$\Delta C_{EC}^{BOT \rightarrow EOT}$	(A.1)	≈38	≈68
$\Delta C_{Material}^{BOT \rightarrow EOT}$	(A.2)	≈16	≈40
$\Delta C_{Overpotential}^{BOT \rightarrow EOT}$	(A.3)	≈25	≈31
$-\Delta C_{Discharge}^{BOT \rightarrow EOT}$	(A.4)	≈11	≈13
$-\Delta C_{Charge}^{BOT \rightarrow EOT}$	(A.5)	≈14	≈18

transition-metals in the then O-depleted structure have to rearrange to form a spinel/rock-salt-type surface layer, which is incapable of reversibly de-/intercalating a significant amount of lithium-ions. While both steps run basically in parallel during the thermal decomposition of charged NCM/NCA CAMs,^{5,55} the TM rearrangement is expected to be retarded during electrochemical cycling. For Li-rich NCMs at 25 °C, HR-TEM images have shown that the actual reconstruction happens within 20–50 cycles.⁵⁶ As vacancies in the TM layer probably facilitate the rearrangement in Li-rich NCMs, it is reasonable to assume that this process takes longer for regular NCMs (here >100 cycles).

Using the set of XPD-based equations introduced in our former study,⁹ which are shortly summarized in the Appendix of this work, Table IV deconvolutes the BOT-to-EOT capacity losses measured at 22 °C and 45 °C. Here, the electrochemically measured capacity losses at C/2 ($\Delta C_{EC}^{BOT \rightarrow EOT}$, see Eq. A.1) amount to ≈38 mAh g⁻¹ for cycling at 22 °C (cycles 18 to 1000) and to ≈68 mAh g⁻¹ for cycling at 45 °C (cycles 6 to 700; see also Table I). As already anticipated by the relative material losses in Fig. 5, this difference of ≈30 mAh g⁻¹ is largely dominated by the extent of surface reconstruction at ambient vs elevated temperature, which translates into absolute capacity losses ($\Delta C_{Material}^{BOT \rightarrow EOT}$, see Eq. A.2) of ≈16 mAh g⁻¹ for cycling at 22 °C and ≈40 mAh g⁻¹ for cycling at 45 °C, respectively. This is a ≈2.5-fold increase caused by the enhanced loss of cyclable NCM-811 CAM when increasing the cycling temperature. On the other hand, the overpotential-induced capacity loss ($\Delta C_{Overpotential}^{BOT \rightarrow EOT}$, see Eq. A.3) increases only by factor of ≈1.2 (from ≈25 mAh g⁻¹ at 22 °C to ≈31 mAh g⁻¹ at 45 °C), which is composed of contributions from the discharged state ($\Delta C_{Discharge}^{BOT \rightarrow EOT}$, see Eq. A.4) and from the charged state ($\Delta C_{Charge}^{BOT \rightarrow EOT}$, see A.5). At the first glance, this moderate rise of the overpotential-related losses is less than that projected from the underlying x_{Li} data: $\Delta x_{Li,dis}^{BOT \rightarrow EOT}$ (see Fig. 4b) and $\Delta x_{Li,cha}^{BOT \rightarrow EOT}$ (see Fig. 4c) increase by a factor of ≈1.4–1.5 when increasing the cycling temperature from 22 to 45 °C. This discrepancy is due to the fact that $\Delta C_{Overpotential}^{BOT \rightarrow EOT}$ (and its individual components in the discharged and charged state) have to be corrected by the phase fraction of lost NCM-811 CAM, because only the cyclable CAM can experience a capacity loss due to an increasing overpotential. Consequently, as the relative material loss is doubled after 700 cycles at 45 °C compared to 1000 cycles at 22 °C (see Fig. 5), the overpotential-induced capacity losses in units of mAh g⁻¹ turn out to be smaller than the shrinkage of the accessible Δx_{Li} window of the retained NCM-811 CAM.

Cracking and surface layer thickness.—Finally, we want to estimate the thickness of the reconstructed surface layer formed over extended cycling. This question requires to determine the surface area of the CAM, which will change upon cycling due to particle

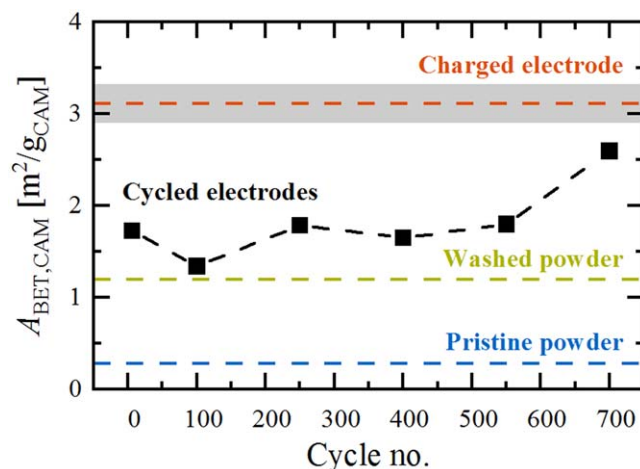


Figure 6. Evolution of the NCM-811 surface area ($A_{BET,CAM}$) during long-term cycling at 45 °C. The cycled electrodes (black data points) were measured in the discharged state by Kr-BET (following the rate test and washing steps with aprotic solvents; see Experimental section), whereby the surface area contribution of the CAM was calculated according to Eq. 4. In order to provide some reference points (depicted as horizontal lines), the $A_{BET,CAM}$ values of the cycled electrodes are compared to those of the pristine NCM-811 powder (blue line), of washed NCM-811 powder (either in water or HF-containing electrolyte; green line), and of a charged electrode (after a first charge at C/10 to a cathode potential of 4.5 V at 45 °C; red line).

cracking.^{9,25} Figure 6 shows the evolution of the specific NCM-811 surface area of the cycled electrodes harvested in the discharged state (black data points), as determined by Kr-BET measurements. Here, the contribution of the NCM-811 CAM was calculated according to Eq. 4 by subtracting the share of the electrode additives (2 wt% SFG6L graphite, 1 wt% C65 carbon black, and 3 wt% PVDF binder) in the composite cathode. Their surface area was determined from additives-only electrodes, consisting only of the inert components with the same weight ratio as in the actual cathodes, yielding $A_{BET,add} = 5.10 \text{ m}^2/\text{g}_{add}$ for fresh and $5.56 \text{ m}^2/\text{g}_{add}$ for cycled additives-only electrodes (see Experimental section). This approach assumes that the binder does not significantly alter the accessible surface area of the CAM in the cathode electrodes, even though the binder was found to reduce the surface area of the conductive agents by a factor of ≈3 in the additives-only electrodes (see Experimental section). To prove this assumption, we can compare the surface area of the pristine NCM-811 CAM in its form as pure powder of $0.28 \text{ m}^2/\text{g}_{CAM}$ (blue line in Fig. 6) with that obtained for the CAM in the fresh cathode electrode of $0.30 \pm 0.02 \text{ m}^2/\text{g}_{CAM}$ (determined from the electrode specific surface area of $A_{BET,elec} = 0.58 \pm 0.01 \text{ m}^2/\text{g}_{elec}$ by subtracting the weight-fraction-normalized value of $A_{BET,add}$ acc. to Eq. 4; average from two measurements). Since the CAM specific

surface areas of the pristine NCM-811 powder and cathode electrode agree nicely with each other, we can now continue with the surface area analysis of the cycled electrodes (black data points in Fig. 6).

In the cycled electrodes, the surface area of the NCM-811 CAM is on a rather constant level of $\approx 1.8 \text{ m}^2/\text{g}_{\text{CAM}}$ and only increases to $\approx 2.6 \text{ m}^2/\text{g}_{\text{CAM}}$ at the end-of-test after 700 cycles. To evaluate these numbers, some important reference points are shown as horizontal lines in Fig. 6. The afore-mentioned pristine CAM powder (blue line) has a significantly lower surface area of $0.28 \text{ m}^2/\text{g}_{\text{CAM}}$. Assuming solid spheres and using the crystallographic density of 4.75 g cm^{-3} , this value translates into an average particle diameter of $d_{\text{avg}} \approx 4.5 \text{ }\mu\text{m}$ ($d_{\text{avg}} = 6/(\rho_{\text{cryst}} \cdot A_{\text{BET,CAM}})$), which is on the order of the secondary agglomerates (d_{50} value of $10.2 \text{ }\mu\text{m}$ determined by laser scattering). Consequently, we predominantly see the outer surface of the secondary agglomerates, while the inner surface of the primary particles is not accessible for two reasons: (i) the crystallites are closely packed after calcination with little pore volume in between and (ii) the pore space between the primary crystallites is blocked due to the presence of surface impurities such Li_2CO_3 and LiOH . As shown in our first publication for the same NCM-811 CAM,⁹ these impurities can be removed by washing the CAM powder in water or by storing it in an HF-containing electrolyte, yielding in both cases $1.2 \text{ m}^2/\text{g}_{\text{CAM}}$ (green line). The surface area of the cycled electrodes is still higher ($\approx 1.3\text{--}2.6 \text{ m}^2/\text{g}_{\text{CAM}}$; see black squares in Fig. 6), because the crystallites experience a continuous contraction/expansion during charge/discharge cycling. Under the given conditions (C/2 cycling at $45 \text{ }^\circ\text{C}$ between cathode potentials of $3.0\text{--}4.5 \text{ V}$), the change of the unit cell volume, $\Delta V/V_{\text{dis}}$, evolves from -6.1% at BOT to -3.1% at EOT. Since the unit cell volume shrinks predominantly at high SOCs ($x_{\text{Li}} < 0.35$ for NCM materials),⁵⁷ $\Delta V/V_{\text{dis}}$ gets smaller over the course of cycling due to the gradual increase of $x_{\text{Li,cha}}$ at the upper cut-off voltage (see Fig. 4c). The reversible “breathing” in every single cycle accumulates a mismatch between the primary particles, so that their packing in the discharged state is not as dense as it was in the pristine state, exposing additional inner surface area.

When we develop this argument further, the contracted crystallites in the charged state should exhibit the highest surface area. For this reason, we also measured Kr-BET of the charged electrodes after the first charge at C/10 to a cathode potential of 4.5 V at $45 \text{ }^\circ\text{C}$, yielding a specific surface area of the CAM of $3.1 \pm 0.2 \text{ m}^2/\text{g}_{\text{CAM}}$ (average from two electrodes; red line). For solid spheres, this gives an average diameter of $d_{\text{avg}} \approx 0.41 \pm 0.03 \text{ }\mu\text{m}$, which indeed reflects the size of the primary particles (see Fig. S11 -in our former study⁹). Oswald et al. have visualized these alternating phenomena by cross-sectional FIB-SEM images of NCM-622, illustrating (i) the separation of primary particles in the charged state and (ii) their subsequent compaction in the discharged state.²⁵ After 303 cycles to a cathode potential of 4.5 V at $25 \text{ }^\circ\text{C}$, they reported a surface area of $\approx 3.1 \text{ m}^2/\text{g}_{\text{CAM}}$ in the discharged state, which resembles that of our NCM-811 CAM in the charged state of the first cycle.

Alternatively, Oswald et al. introduced an EIS-based method to monitor the surface area of electrodes by utilizing its correlation to the electrochemical double layer capacitance.²⁵ Kr-BET and EIS have some intrinsic differences. Most importantly, krypton atoms can access pores as small as $\approx 0.2 \text{ nm}$, while the penetration of solvated lithium-ions into pores requires pore diameters of greater than $\approx 1 \text{ nm}$, so that only pores above this value will contribute to the capacitance determined by EIS. This might explain why the here reported surface area changes determined by Kr-BET (see Fig. 6) occur mainly from the pristine state to BOT (6 cycles): after the initial few cycles, the surface impurities seem to be already removed and the particle disintegration seems to have already created permanent pores at least on the sub-nm scale, which can be detected right away by Kr-BET. In Oswald’s EIS data, there is also a sharp but less extensive rise in the first cycles and the capacitance increases notably in the later cycles as well. This is rationalized by the steady expansion of pores (or cracks) in the discharged state (due to the accumulating mismatch between the primary

crystallites), so that the further increase of CAM surface area only becomes detectable by EIS after a certain pore/crack size threshold has been reached.

The above discussion highlights the coexistence of solid/solid, solid/liquid, and solid/gas interfaces within the secondary agglomerates. As their relative ratio will change during cycling, we have to select a proper surface area for the calculation of the surface layer thickness. In this respect, recent publications address the question if the surface reconstruction requires the exposure of the surface to the electrolyte.^{15,58,59} In the work of Schweidler et al.¹⁵ and Zou et al.,⁵⁸ STEM imaging of cycled Ni-rich CAMs revealed reconstruction layers on open surfaces (exposed to the electrolyte), while the layered structure was maintained on sealed surfaces (not in contact with the electrolyte). For solid/solid interfaces, Zou et al. further differentiate between incoherent boundaries (stable against phase transitions) and twin boundaries (prone to phase transitions). All these different modes of surface reconstruction can be ascribed to intergranular cracking. In contrast, Ahmed et al. reported on the growth of rock-salt-like regions at the boundary of intragranular nanopores, which are encapsulated in the bulk of the CAM and thus not exposed to the electrolyte.⁵⁹ Yan et al. identified intragranular cracks, which are initiated from the grain interior and can generate completely new surfaces (in contrast to sealed surfaces, which are already present, but buried).⁵⁰ We conclude that the surface reconstruction depends on the type of grain boundary and its exposure to the electrolyte. Consequently, the calculated thickness can just provide an estimate, which averages over the heterogeneous surfaces. We decided to proceed with the $\approx 3.1 \text{ m}^2/\text{g}_{\text{CAM}}$ of the charged electrode, because this value represents in good approximation all available surfaces of the crystallites, which might potentially be exposed to the electrolyte (due to intergranular cracking, particularly in the charged state). Furthermore, the layered-to-spinel/rock-salt transformation is initiated by the release of lattice oxygen at these high SOCs.

Using the equations described in our former work,⁹ the relative material loss (left axis in Fig. 5) is converted into the average thickness, $t_{\text{surface-layer}}$ (right axis in Fig. 5). As already discussed beforehand, we want to mention that the here calculated thickness represents the electrochemically inactive surface layer, which yet might be thinner than the O-depleted surface layer at a given cycle number. The initial oxygen release has to be completed by the rearrangement of the transition-metals in order to be become detectable as lost CAM. Therefore, we assume several reaction fronts, which gradually grow from the surface of the primary particles into their interior, but only the fully reconstructed and non-intercalating layer can be measured by our approach. With the $\approx 3.1 \text{ m}^2/\text{g}_{\text{CAM}}$ of the charged electrode, the re-calculation of the EOT value after 1000 cycles at $22 \text{ }^\circ\text{C}$ now gives $\approx 6 \text{ nm}$, which agrees much better to the HAADF-STEM images in our previous study than the back then estimated $\approx 15 \text{ nm}$ on the basis of the $1.2 \text{ m}^2/\text{g}_{\text{CAM}}$ of the washed CAM. At $45 \text{ }^\circ\text{C}$, the surface layer thickness amounts to $\approx 12\text{--}14 \text{ nm}$ after 700 cycles. Even though all quantification methods, either XPD and Kr-BET (as applied here) or STEM imaging, should be taken with a grain of salt, the $45 \text{ }^\circ\text{C}$ trend line is in good agreement to the STEM data of Schweidler et al.¹⁵ Similar to our NCM-811, they cycled their NCM-851005 at $45 \text{ }^\circ\text{C}$ to $4.2 \text{ V}_{\text{FC}}$ (corresponding to $\approx 4.3 \text{ V}$ vs Li^+/Li) and reported a rock-salt-like phase of $\approx 2 \text{ nm}$ after 100 cycles and $\approx 14 \text{ nm}$ after 500 cycles, respectively. In light of the above arguments, the observed surface layer is however not perfectly uniform around the individual primary particles.¹⁵ Consequently, the average thickness of $\approx 14 \text{ nm}$ after 500 cycles reported by Schweidler et al.¹⁵ is in a reasonably good agreement with the here estimated $\approx 8 \text{ nm}$ for the NCM-811 electrode cycled for 550 cycles (see Fig. 5). In summary, the CAM surface area and the thickness of the reconstruction layer can be accessed by various methods, including microscopy, BET, and EIS. In order to evaluate how quantitative their agreement can be in the best case, all these methods have to be applied to the same material in a complementary manner.

Our data as well as all the discussed data and findings from other groups are based on poly-crystalline CAMs, but there is an ongoing trend to switch to single-crystalline layered oxides.^{16,60–62} In that case, the crystallites have a size in the μm range. As long as intragranular cracking of individual crystallites does not generate new surfaces, e.g., due to real particle fracture, we would expect the surface area of single-crystalline CAMs to stay below $1 \text{ m}^2/\text{g}_{\text{CAM}}$ also during cycling. The lower surface-to-bulk ratio would substantially decrease the loss of electrochemically active material (assuming that it is occurring mostly on CAM surfaces exposed to the electrolyte) and the associated degradation mechanism. This is an interesting working hypothesis for single-crystalline CAMs to look at in the future.

Conclusions

In the present work, we investigated in a comparative manner the degradation mechanisms of the Ni-rich layered oxide NCM-811 at ambient (22 °C) and elevated temperatures (45 °C). Apart from the temperature variation, the NCM-811/graphite full-cells were cycled in a very similar fashion at a constant-current of $C/2$ between cathode potentials of 3.0 and 4.5 V. In order to focus solely on the CAM degradation and to exclude any effects due to a lithium loss at the anode, the graphite CE was partially pre-lithiated and the potential was controlled vs the Li-RE. Furthermore, the large electrolyte excess prevents any capacity fading caused by the potential electrolyte breakdown.

The capacity loss during $C/2$ cycling was more than doubled at 45 °C operation (data generated in this work) compared to 22 °C operation (data acquired in our first study⁹). To elucidate the underlying degradation mechanisms, we switched from time-consuming in situ techniques to their simplified ex situ counterparts, including X-ray powder diffraction, electrochemical impedance spectroscopy, and Kr-BET. We could ascribe $\approx 60\%$ of the observed capacity loss after 700 cycles at 45 °C to the loss of electrochemically active material, which is caused by the formation of a reconstructed, electrochemically inactive surface. This compares to only $\approx 40\%$ material loss after 1000 cycles at 22 °C.

The formation of the reconstructed, oxygen-depleted surface results in a growth of the charge-transfer resistance of the NCM-811 CAM, which is also reflected by an analogous increase of the DCIR resistance and further leads to overpotential-induced capacity losses. After 700 cycles at 45 °C, the layer thickness around the primary particles exposed to the electrolyte is estimated to be $\approx 12\text{--}14 \text{ nm}$, reasonably consistent with the literature, while only $\approx 6 \text{ nm}$ are estimated after 1000 cycles at 25 °C. We attribute this difference to the faster kinetics for oxygen removal and/or transition-metal rearrangement at the higher temperature.

The overpotential-induced capacity losses occur in a similar ratio both in the discharged state (i.e., during lithiation of the CAM) and the charged state (i.e., during delithiation of the CAM). Whether these losses are predominantly caused by the increased charge-transfer resistance or by a decreased lithium diffusivity in the bulk phase cannot be finally answered. However, the extent of Li-Ni mixing stays constant at 22 °C and increases only by $\approx 1\%\text{--}2\%$ after 700 cycles after 45 °C. Furthermore, we could not observe the emergence of a so-called fatigued phase with a layered structure.

Acknowledgments

Financial support by BASF SE through its Scientific Network on Electrochemistry and Batteries is gratefully acknowledged.

Appendix

Equations used for the capacity loss analysis.—The XPD-derived variation of the lithium content (x_{Li}^i) over the course of cycling (see Fig. 4) enables the deconvolution of the electrochemically measured capacity loss, $\Delta C_{\text{EC}}^{\text{BOT} \rightarrow i}$ (in mAh g^{-1}):

$$\Delta C_{\text{EC}}^{\text{BOT} \rightarrow i} = C_{\text{EC}}^{\text{BOT}} - C_{\text{EC}}^i \quad [\text{A}\cdot 1]$$

which is defined by the difference of the discharge capacity in the i th cycle (C_{EC}^i) relative to that at the begin-of-test ($C_{\text{EC}}^{\text{BOT}}$). Please note that the following equations were established in our former publication by Friedrich et al., where they are explained in great detail.⁹

The first contribution is the absolute loss of electrochemically active material in the form of a reconstructed, O-depleted surface layer, which can be quantified as $\Delta C_{\text{Material}}^{\text{BOT} \rightarrow i}$ (in mAh g^{-1} , just like the other loss terms) by the following equation:

$$\Delta C_{\text{Material}}^{\text{BOT} \rightarrow i} = (C_{\text{XPD}}^i - C_{\text{EC}}^i) \cdot \Delta \frac{x_{\text{Li}}^{\text{BOT}}}{\Delta x_{\text{Li}}^i} \quad [\text{A}\cdot 2]$$

Here, the material loss corresponds to the difference between the theoretically expected capacity inferred from XPD (C_{XPD}^i , see Eq. 6) and the actually measured discharge capacity in the i th cycle (C_{EC}^i). To reference this difference to BOT, it has to be corrected by the accessible Δx_{Li} ranges between the discharged and charged state (e.g., $\Delta x_{\text{Li}}^i = x_{\text{Li,dis}}^i - x_{\text{Li,cha}}^i$), which typically shrink upon cycling due to the increasing overpotential (i.e., $\Delta x_{\text{Li}}^{\text{BOT}} > \Delta x_{\text{Li}}^i$).

The overpotential-induced loss ($\Delta C_{\text{Overpotential}}^{\text{BOT} \rightarrow i}$) is the second contribution, which can be further divided into capacity losses in the discharged ($\Delta C_{\text{Discharge}}^{\text{BOT} \rightarrow i}$) and in the charged state ($\Delta C_{\text{Charge}}^{\text{BOT} \rightarrow i}$):

$$\Delta C_{\text{Overpotential}}^{\text{BOT} \rightarrow i} = \Delta C_{\text{Discharge}}^{\text{BOT} \rightarrow i} + \Delta C_{\text{Charge}}^{\text{BOT} \rightarrow i} \quad [\text{A}\cdot 3]$$

where by the two individual contributions are calculated according to:

$$\Delta C_{\text{Discharge}}^{\text{BOT} \rightarrow i} = (x_{\text{Li,dis}}^{\text{BOT}} - x_{\text{Li,dis}}^i) \cdot \frac{274 \text{ mAh g}^{-1}}{1.01} \cdot (1 - \Delta C_{\text{Material,rel}}^i) \quad [\text{A}\cdot 4]$$

$$\Delta C_{\text{Charge}}^{\text{BOT} \rightarrow i} = (x_{\text{Li,cha}}^i - x_{\text{Li,cha}}^{\text{BOT}}) \cdot \frac{274 \text{ mAh g}^{-1}}{1.01} \cdot (1 - \Delta C_{\text{Material,rel}}^i) \quad [\text{A}\cdot 5]$$

by taking the difference of the respective x_{Li} values between BOT and the i th cycle in either the discharged ($x_{\text{Li,dis}}^{\text{BOT}} - x_{\text{Li,dis}}^i$) or charged state ($x_{\text{Li,cha}}^i - x_{\text{Li,cha}}^{\text{BOT}}$). Note that for this analysis it is irrelevant whether the difference in x_{Li} is due to an increase of the CAM's R_{CT} (caused by the formation of a resistive surface layer) or a decrease of the lithium diffusivity in the bulk of the CAM (caused by transition-metal migration into the lithium layer). Since only the electrochemically active material can undergo a capacity loss due to an increasing overpotential, Eqs. A.3–A.5 include a correction term that considers the NCM-811 phase fraction which has already been lost until the i th cycle ($\Delta C_{\text{Material,rel}}^i$, see Eq. 5).

ORCID

Benjamin Strehle  <https://orcid.org/0000-0001-8878-1160>
 Franziska Friedrich  <https://orcid.org/0000-0001-9400-1212>
 Hubert A. Gasteiger  <https://orcid.org/0000-0001-8199-8703>

References

- G. Zubi, R. Dufo-López, M. Carvalho, and G. Pasaoglu, *Renew. Sustain. Energy Rev.*, **89**, 292 (2018).
- E. A. Olivetti, G. Ceder, G. G. Gaustad, and X. Fu, *Joule*, **1**, 229 (2017).
- C. Banza Lubaba Nkulu et al., *Nat. Sustain.*, **1**, 495 (2018).
- H.-J. Noh, S. Youn, C. S. Yoon, and Y.-K. Sun, *J. Power Sources*, **233**, 121 (2013).

5. S.-M. Bak, E. Hu, Y. Zhou, X. Yu, S. D. Senanayake, S.-J. Cho, K.-B. Kim, K. Y. Chung, X.-Q. Yang, and K.-W. Nam, *ACS Appl. Mater. Interfaces*, **6**, 22594 (2014).
6. S.-T. Myung, F. Maglia, K.-J. Park, C. S. Yoon, P. Lamp, S.-J. Kim, and Y.-K. Sun, *ACS Energy Lett.*, **2**, 196 (2017).
7. H.-H. Ryu, K.-J. Park, C. S. Yoon, and Y.-K. Sun, *Chem. Mater.*, **30**, 1155 (2018).
8. W. Li, E. M. Erickson, and A. Manthiram, *Nat. Energy*, **5**, 26 (2020).
9. F. Friedrich, B. Strehle, A. T. S. Freiberg, K. Kleiner, S. J. Day, C. Erk, M. Piana, and H. A. Gasteiger, *J. Electrochem. Soc.*, **166**, A3760 (2019).
10. M.-T. F. Rodrigues, G. Babu, H. Gullapalli, K. Kalaga, F. N. Sayed, K. Kato, J. Joyner, and P. M. Ajayan, *Nat. Energy*, **2**, 17108 (2017).
11. G. Xu, X. Liu, A. Daali, R. Amine, Z. Chen, and K. Amine, *Adv. Funct. Mater.*, **30**, 2004748 (2020).
12. USABC, USABC Goals for Advanced Batteries for EVs (2020), https://www.energy.gov/sites/prod/files/2014/05/15/APR13_Energy_Storage_d_III_Adv_Battery_Dev_0.pdf.
13. J. Li, J. Harlow, N. Stakheiko, N. Zhang, J. Paulsen, and J. Dahn, *J. Electrochem. Soc.*, **165**, A2682 (2018).
14. R. Jung, P. Strobl, F. Maglia, C. Stinner, and H. A. Gasteiger, *J. Electrochem. Soc.*, **165**, A2869 (2018).
15. S. Schweißler, L. de Biasi, G. Garcia, A. Mazilkin, P. Hartmann, T. Brezesinski, and J. Janek, *ACS Appl. Energy Mater.*, **2**, 7375 (2019).
16. J. E. Harlow et al., *J. Electrochem. Soc.*, **166**, A3031 (2019).
17. C. P. Aiken, J. E. Harlow, R. Tingley, T. Hynes, E. R. Logan, S. L. Glazier, A. S. Keefe, and J. R. Dahn, *J. Electrochem. Soc.*, **167**, 130541 (2020).
18. D. Pritzl, S. Solchenbach, M. Wetjen, and H. A. Gasteiger, *J. Electrochem. Soc.*, **164**, A2625 (2017).
19. *MIMS Client, Version 1.4* (Maccor Inc, Tulsa, United States of America) (2019).
20. *TOPAS-Academic V6* (Coelho Software, Brisbane, Australia) (2016).
21. P. W. Stephens, *J. Appl. Crystallogr.*, **32**, 281 (1999).
22. O. Dolotko, A. Senyshyn, M. J. Muhlbauer, K. Nikolowski, F. Scheiba, and H. Ehrenberg, *J. Electrochem. Soc.*, **159**, A2082 (2012).
23. R. Morasch, B. Suthar, and H. A. Gasteiger, *J. Electrochem. Soc.*, **167**, 100540 (2020).
24. J. Landesfeind, D. Pritzl, and H. A. Gasteiger, *J. Electrochem. Soc.*, **164**, A1773 (2017).
25. S. Oswald, D. J. Pritzl, M. Wetjen, and H. Gasteiger, *J. Electrochem. Soc.* (2020).
26. S. Meini, M. Piana, H. Beyer, J. Schwämmlein, and H. A. Gasteiger, *J. Electrochem. Soc.*, **159**, A2135 (2012).
27. I. Buchberger, S. Seidlmayer, A. Pokharel, M. Piana, J. Hattendorff, P. Kudejova, R. Gilles, and H. A. Gasteiger, *J. Electrochem. Soc.*, **162**, A2737 (2015).
28. L. M. Thompson, W. Stone, A. Eldesoky, N. K. Smith, C. R. M. McFarlane, J. S. Kim, M. B. Johnson, R. Petibon, and J. R. Dahn, *J. Electrochem. Soc.*, **165**, A2732 (2018).
29. F. T. Wagner, B. Lakshmanan, and M. F. Mathias, *J. Phys. Chem. Lett.*, **1**, 2204 (2010).
30. R. Sharabi, E. Markevich, V. Borgel, G. Salitra, D. Aurbach, G. Semrau, M. A. Schmidt, N. Schall, and C. Stinner, *Electrochem. Commun.*, **13**, 800 (2011).
31. T. Yim, H.-J. Ha, M.-S. Park, K. J. Kim, J.-S. Yu, and Y.-J. Kim, *RSC Adv.*, **3**, 25657 (2013).
32. R. Jung, M. Metzger, F. Maglia, C. Stinner, and H. A. Gasteiger, *J. Electrochem. Soc.*, **164**, A1361 (2017).
33. J. Wandt, A. T. S. Freiberg, A. Ogrodnik, and H. A. Gasteiger, *Mater. Today*, **21**, 825 (2018).
34. S. Solchenbach, G. Hong, A. T. S. Freiberg, R. Jung, and H. A. Gasteiger, *J. Electrochem. Soc.*, **165**, A3304 (2018).
35. R. Jung, F. Linsenmann, R. Thomas, J. Wandt, S. Solchenbach, F. Maglia, C. Stinner, M. Tromp, and H. A. Gasteiger, *J. Electrochem. Soc.*, **166**, A378 (2019).
36. R. Pan, D. Rau, Y. Moryson, J. Sann, and J. Janek, *ACS Appl. Energy Mater.*, **3**, 6065 (2020).
37. T. Teufl, D. Pritzl, S. Solchenbach, H. A. Gasteiger, and M. A. Mendez, *J. Electrochem. Soc.*, **166**, A1275 (2019).
38. R. Jung, M. Metzger, F. Maglia, C. Stinner, and H. A. Gasteiger, *J. Phys. Chem. Lett.*, **8**, 4820 (2017).
39. M. Metzger, P. Walke, S. Solchenbach, G. Salitra, D. Aurbach, and H. A. Gasteiger, *J. Electrochem. Soc.*, **167**, 160522 (2020).
40. A. T. S. Freiberg, M. K. Roos, J. Wandt, R. de Vivie-Riedle, and H. A. Gasteiger, *J. Phys. Chem. A*, **122**, 8828 (2018).
41. T. Teufl, D. Pritzl, P. Krieg, B. Strehle, M. A. Mendez, and H. A. Gasteiger, *J. Electrochem. Soc.*, **167**, 110505 (2020).
42. R. Weber, A. J. Louli, K. P. Plucknett, and J. R. Dahn, *J. Electrochem. Soc.*, **166**, A1779 (2019).
43. H. Li, M. Cormier, N. Zhang, J. Inglis, J. Li, and J. R. Dahn, *J. Electrochem. Soc.*, **166**, A429 (2019).
44. W. Li, X. Liu, Q. Xie, Y. You, M. Chi, and A. Manthiram, *Chem. Mater.*, **32**, 7796 (2020).
45. C. Xu et al., *Nat. Mater.*, **20**, 84 (2020).
46. L. Yin et al., *Chem. Mater.*, **32**, 1002 (2020).
47. Y. Makimura, T. Sasaki, T. Nonaka, Y. F. Nishimura, T. Uyama, C. Okuda, Y. Itou, and Y. Takeuchi, *J. Mater. Chem. A*, **4**, 8350 (2016).
48. K. Kleiner, D. Dixon, P. Jakes, J. Melke, M. Yavuz, C. Roth, K. Nikolowski, V. Liebau, and H. Ehrenberg, *J. Power Sources*, **273**, 70 (2015).
49. H. Liu, M. Wolf, K. Karki, Y.-S. Yu, E. A. Stach, J. Cabana, K. W. Chapman, and P. J. Chupas, *Nano Lett.*, **17**, 3452 (2017).
50. P. Yan, J. Zheng, M. Gu, J. Xiao, J.-G. Zhang, and C.-M. Wang, *Nat. Commun.*, **8**, 14101 (2017).
51. H. M. Dahn, A. J. Smith, J. C. Burns, D. A. Stevens, and J. R. Dahn, *J. Electrochem. Soc.*, **159**, A1405 (2012).
52. M. Dubarry, C. Truchot, and B. Y. Liaw, *J. Power Sources*, **219**, 204 (2012).
53. F. Wang, Z. Lin, L. Liu, X. Wei, S. Lin, L. Dai, Y. Wei, C. Liang, and B. Liaw, *J. Electrochem. Soc.*, **167**, 090549 (2020).
54. J. Li, H. Liu, J. Xia, A. R. Cameron, M. Nie, G. A. Botton, and J. R. Dahn, *J. Electrochem. Soc.*, **164**, A655 (2017).
55. S.-M. Bak, K.-W. Nam, W. Chang, X. Yu, E. Hu, S. Hwang, E. A. Stach, K.-B. Kim, K. Y. Chung, and X.-Q. Yang, *Chem. Mater.*, **25**, 337 (2013).
56. T. Teufl, B. Strehle, P. Müller, H. A. Gasteiger, and M. A. Mendez, *J. Electrochem. Soc.*, **165**, A2718 (2018).
57. L. de Biasi, A. O. Kondrakov, H. Geßwein, T. Brezesinski, P. Hartmann, and J. Janek, *J. Phys. Chem. C*, **121**, 26163 (2017).
58. L. Zou, W. Zhao, H. Jia, J. Zheng, L. Li, D. P. Abraham, G. Chen, J. R. Croy, J.-G. Zhang, and C. Wang, *Chem. Mater.*, **32**, 2884 (2020).
59. S. Ahmed et al., *ACS Nano*, **13**, 10694 (2019).
60. J. Li, H. Li, W. Stone, R. Weber, S. Hy, and J. R. Dahn, *J. Electrochem. Soc.*, **164**, A3529 (2017).
61. J. Li, A. R. Cameron, H. Li, S. Glazier, D. Xiong, M. Chatzidakis, J. Allen, G. A. Botton, and J. R. Dahn, *J. Electrochem. Soc.*, **164**, A1534 (2017).
62. H. H. Sun, H.-H. Ryu, U.-H. Kim, J. A. Weeks, A. Heller, Y.-K. Sun, and C. B. Mullins, *ACS Energy Lett.*, **5**, 1136 (2020).

3.2 Hysteresis and heat generation in Li- and Mn-Rich Layered Oxides

3.2.1 Entropy measured via linear temperature variation

The article entitled “Entropy Measurements of Li-Ion Battery Cells with Li- and Mn-Rich Layered Transition Metal Oxides via Linear Temperature Variation” was submitted to the peer-reviewed Journal of the Electrochemical Society in September 2021 and published in December 2021 as an “open access” article under the terms of the Creative Commons Attribution Non-Commercial No Derivates 4.0 License. The permanent web link can be found under: <https://iopscience.iop.org/article/10.1149/1945-7111/ac3938>. Franziska Friedrich presented the results of this work at the PRiME Meeting in October 2020 (digital, Abstract No. 2851).

Figure 1.2 illustrates that LMR-NCMs are promising cathode active material candidates for future LIBs owing to their high energy density and low CAM cost. As outlined in section 1.3, they, however, suffer from several drawbacks limiting their lifespan and performance. An outstanding issue is the pronounced hysteresis of the OCV. Interestingly, this hysteresis between the charge and discharge direction is not only observable for the OCV, but also for the LMR-NCM structural parameters^{100,102,103}, the cathode resistance¹⁰¹, and the oxidation states of the transition metals^{104,105} and oxygen^{105,106}. In order to get a better understanding of the thermodynamic processes occurring during cycling of LMR-NCM cathodes, entropy measurements were conducted. Since the entropy is a sensitive parameter obtained by a non-destructive in-situ method, it is capable of monitoring even minor energetic differences in the environment of Li ions in the CAM structure. In addition, the acquisition of entropy data as a function of SOC in principle allows for the calculation of the reversible heat according to equation (2.14).

As described in section 2.4, the partial molar entropy ($\frac{dS}{d\xi}(\xi)$) is determined based on the measurement of the temperature-dependent OCV (TD-OCV). In contrast to the conventional method of applying a constant temperature to the cell and measuring the OCV as a function of temperature (step method), we linearly changed the temperature of the cell with a constant rate (ramp method). By monitoring the

corresponding OCV response, the TD-OCV can be calculated. Our study contains a comparison of both approaches, suggesting that the ramp method is advantageous. In order to evaluate the contribution of the lithium counter electrode to the overall TD-OCV, spatially non-isothermal entropy measurements in specially designed pouch-cells were conducted. We found that the contribution of the lithium electrode (≈ 1.2 mV/K) is one order of magnitude higher than the overall value of the TD-OCV of the cell (≈ 0.1 mV/K). This means that only the difference between the two large values of both electrodes (both in the order of ≈ 1 mV/K) leads to the small values observed for the LMR-NCM/Li cell.

We found a broad peak in the $\frac{dS}{d\xi}(\xi)$ curve, similar to a feature of a second order phase transition, which we correlate to changes in the local ordering or the energetics of the lattice. Our results reveal a hysteresis of the peak in the $\frac{dS}{d\xi}(\xi)$ curve between the charge and discharge direction when plotted as a function of SOC, which, however, vanishes when plotted as a function of OCV. This suggests that the entropy changes in LMR-NCM are governed by the OCV and not by the amount of Li in the structure. This trend was also observed for an LMR-NCM material with a higher degree of overlithiation. The absence of typical fingerprints for configurational entropy and the observed path dependence led us to the conclusion that the vibrational entropy is dominating the $\frac{dS}{d\xi}(\xi)$ vs. SOC curve of LMR-NCM/Li cells. In contrast, the partial molar entropy during the first activation charge shows a completely different curve shape, suggesting that the configurational entropy mainly contributes to the observed profile. Since ξ is no unique descriptor of the charge/discharge processes in LMR-NCM, we conclude that (de-)lithiation follows metastable pathways. Hence, the integration of $\frac{dS}{d\xi}(\xi)$ to calculate the reversible heat would include an additional term caused by the internal entropy production. Equation (2.14) is hence not applicable in case of LMR-NCM.

Author contributions

F.F. conducted the electrochemical measurements, evaluated the data and wrote the manuscript. S.P. contributed to the measurements in the course of her research internship. H.A.G. discussed the results and revised the manuscript.



Entropy Measurements of Li-Ion Battery Cells with Li- and Mn-Rich Layered Transition Metal Oxides via Linear Temperature Variation

Franziska Friedrich,^{*z}  Susanne Pieper, and Hubert A. Gasteiger^{**} 

Chair of Technical Electrochemistry, Department of Chemistry and Catalysis Research Center, Technical University of Munich, Munich, Germany

Changes in the partial molar entropy of lithium- and manganese-rich layered transition metal oxides (LMR-NCM) are investigated using a recently established electrochemical measuring protocol, in which the open-circuit voltage (OCV) of a cell is recorded during linear variation of the cell temperature. With this method, the entropy changes of LMR-NCM in half-cells were precisely determined, revealing a path dependence of the entropy during charge and discharge as a function of state of charge, which vanished as a function of OCV. This observation is in line with other hysteresis phenomena observed for LMR-NCM, of which the OCV hysteresis is the most striking one. For a systematic investigation of the entropy changes in LMR-NCM, measurements were conducted during the first activation cycle and in a subsequent cycle. In addition, two LMR-NCM materials with different degrees of overlithiation were contrasted. Contributions from configurational and vibrational entropy are discussed. Our results suggest that the entropy profile during activation exhibits features from the configurational entropy, while during subsequent cycling the vibrational entropy dominates the entropy curve.

© 2021 The Author(s). Published on behalf of The Electrochemical Society by IOP Publishing Limited. This is an open access article distributed under the terms of the Creative Commons Attribution Non-Commercial No Derivatives 4.0 License (CC BY-NC-ND, <http://creativecommons.org/licenses/by-nc-nd/4.0/>), which permits non-commercial reuse, distribution, and reproduction in any medium, provided the original work is not changed in any way and is properly cited. For permission for commercial reuse, please email: permissions@iopublishing.org. [DOI: [10.1149/1945-7111/ac3938](https://doi.org/10.1149/1945-7111/ac3938)]



Manuscript submitted September 20, 2021; revised manuscript received October 26, 2021. Published December 2, 2021. *This was paper 2851 presented during PRiME 2020, October 4–9, 2020.*

Supplementary material for this article is available [online](#)

For Li-ion battery development, lithium- and manganese-rich layered transition metal oxides (LMR-NCM, $\text{Li}_{1+\delta}[\text{TM}]_{1-\delta}\text{O}_2$ with $\text{TM} = \text{Ni, Co, Mn}$ and typically $0.1 < \delta < 0.2$), are currently under investigation as potential next generation cathode active materials (CAM). Their exceptionally high gravimetric capacity is, however, accompanied by a pronounced voltage hysteresis, of which a significant part is still present at open circuit conditions. This OCV hysteresis is a material-specific property. The hysteresis does not only affect the voltage profile, but also the cathode resistance,^{1–3} the Li site occupation⁴ as well as the LMR-NCM lattice parameters^{5,6} and atomic distances.⁷ To gain a better understanding of the thermodynamic processes upon cycling LMR-NCM cathodes, entropy measurements were conducted in this study. Hereby, the partial molar entropy, $\frac{dS}{d\xi}(\xi)$, is obtained in a sensitive, non-destructive way from the derivative of the OCV with respect to temperature. Such data complement information on free energy gained from OCV and allow for a more comprehensive characterization of thermodynamic processes in battery cells in situ.⁸ In contrast to other techniques, e.g. based on diffraction, entropy is capable of monitoring even minor changes in the environment of the Li ions.

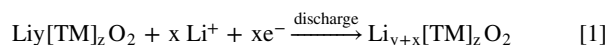
So far, the interpretation of experimental entropy data of battery active materials in the literature was mainly constricted to a quantification of the corresponding heat terms^{9–11} and to a relative comparison between materials.^{10–12} The shape of the entropy curve was either discussed in context of configurational entropy in studies including theoretical calculations and computational simulations^{13–15} or it was ignored. Here, we present a study on entropy changes of LMR-NCM/Li half-cells and will discuss different possible contributions to the shape of the entropy curve, including configurational and vibrational entropy. To overcome systematic experimental errors, a linear temperature variation method was established based on previous literature reports.^{16–18} With this method, partial molar entropy changes in LMR-NCM were measured, revealing an unusual resonance-like signature, which is typical of a second order transition. The center

and width of this transition differ when measured during charge and discharge and plotted as a function of SOC, while its appearance in both directions coincides when plotted against OCV. The correlation with OCV apparently reflects a Gibbs free energy driven process, which seems to be associated with only very subtle structural changes, since it escapes observation by other techniques so far. Due to the strong dependence of the entropy on the OCV rather than on the Li content, any significant contribution of configurational entropy can be discarded in LMR-NCM. We thus consider vibrational entropy being dominant in LMR-NCM.

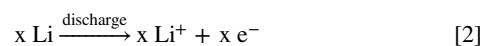
Theoretical Considerations

The focus of this study is on the thermodynamics of the Li (de-)intercalation processes of LMR-NCM, which for simplicity is abbreviated as NCM in the following equations. The commonly used structural formula of LMR-NCM ($\text{Li}_{1+\delta}[\text{TM}]_{1-\delta}\text{O}_2$, $\text{TM} = \text{Ni, Co, Mn}$) was simplified to $\text{Li}_y[\text{TM}]_z\text{O}_2$, where y describes the amount of lithium in the cathode active material (CAM) and where the maximum value of y is equal to $1+\delta$, as explained in the Experimental section. To simplify the investigated cell chemistry, Li metal is used as a counter electrode, giving the following reactions for the positive and negative electrodes during discharge:

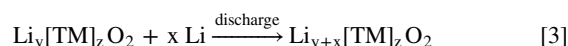
Positive electrode:



Negative electrode:



For the whole cell reaction during discharge ($\Delta G < 0$), it follows:



Thereby, the electrons supplied on discharge at the negative electrode are transferred to the positive electrode via the external

*Electrochemical Society Student Member.

**Electrochemical Society Fellow.

^zE-mail: franziska.friedrich@tum.de

circuit. For the charge reaction, the direction is reversed and $\Delta G > 0$.

The overall stoichiometric amount of Li can be summarized as $x_{Li} = x + y$. For the Li- and Mn-rich NCM used herein, the maximum value of x_{Li} is $1 + \delta$ as explained in the Experimental section. To describe the progress of the charging/discharging reaction, we will use the reaction turnover parameter ξ , which we define as $\xi = (1 + \delta) - x_{Li}$. It runs parallel to the SOC but is normalized in stoichiometric units. ξ is zero for the fully lithiated (pristine) CAM and 1.14 for a completely delithiated (charged) 0.33 LMR-NCM. Since it increases on charging (deintercalation of the LMR-NCM) and decreases on discharging, the sign of $d\xi$ explicitly reflects the direction of the reaction.

The partial molar entropy $\frac{dS}{d\xi}(\xi)$.— dS is the change in the total entropy of a cell with 1 mol of cathode material on charging with a differential amount of electrons $d\xi$ and thus releasing the same amount of Li^+ . For the half-cell reaction at the cathode side, the corresponding molar entropy change can be expressed as follows:

$$dS_{\text{cha,cathode}}(\xi) = \frac{dS_{\text{NCM}}(\xi)}{d\xi} d\xi + \frac{dS_{\text{solv}}}{d\xi} d\xi \quad [4]$$

Here, $\frac{dS_{\text{NCM}}(\xi)}{d\xi}$ describes the entropy change when a differential amount of Li^+ (corresponding to $d\xi$) is extracted from 1 mol of LMR-NCM, at an SOC at which a molar fraction ξ (of Li^+) was already extracted. We may likewise call $\frac{dS_{\text{NCM}}(\xi)}{d\xi}$ the partial molar intercalation entropy. The molar entropy of Li^+ solvation, $\frac{dS_{\text{solv}}}{d\xi}$, is the second contribution to the entropy change at the cathode interface since for any amount of Li^+ ($=d\xi$) extracted from the CAM, a corresponding number of Li^+ ions will be transferred to the electrolyte.

On the Li metal anode side, the molar entropy change upon charge is the sum of the entropy change for depositing Li at the metal anode and the entropy of desolvation of the Li^+ ions:

$$dS_{\text{charge,anode}}(\xi) = \frac{dS_{\text{Li}}}{d\xi} d\xi + \frac{dS_{\text{desolv}}}{d\xi} d\xi \quad [5]$$

In this study, entropy is measured vs a Li reference electrode. Since the Li reference electrode is practically unaffected in quantity and thus not altered in quality, its entropy is independent of the SOC.^{19,20} $\frac{dS_{\text{Li}}}{d\xi}$ is the change in entropy for adding 1 mol of Li to the Li metal anode.

For the whole cell reaction shown in Eq. 3, the differential change of the total entropy of the battery for the charging process, dS_{charge} , results from the combination of Eqs. 4 and 5. By assuming a negligible concentration gradient in the electrolyte, the entropy of solvation at the cathode is counterbalanced by the desolvation of Li^+ at the Li anode and the entropy of solvation/desolvation cancel.

$$dS_{\text{charge}}(\xi) = \frac{dS}{d\xi}(\xi) d\xi = \frac{dS_{\text{NCM}}(\xi)}{d\xi} d\xi - \frac{dS_{\text{Li}}}{d\xi} d\xi \quad [6]$$

Note that only the contribution from the cathode, $\frac{dS_{\text{NCM}}(\xi)}{d\xi}$, is expected to change with ξ (SOC).

In order to clarify sign conventions pertaining to our results, we will briefly sum up how $\frac{dS}{d\xi}(\xi)$ can be derived from a temperature dependent OCV (TD-OCV) measurement. First, we correlate changes of Gibbs free energy, dG , with the electrical work reversibly stored in the cell while charging:

$$dG = dw_{\text{el,rev}} = E_0(\xi) \cdot dq \quad [7]$$

If n is the net electric charge on the ion ($n = +1$ for Li^+), n mole of electrons will have to be transported from the external power source at each turnover ξ yielding: $dq = n \cdot F \cdot d\xi$. Here, F is the Faraday constant and E_0 is the OCV. Since we have chosen $d\xi$ to be positive on charging and since in that case work will be stored in the battery and should be counted positive, according to thermodynamic convention, we get:

$$dG(\xi) = n \cdot F \cdot E_0(\xi) \cdot d\xi \quad [8]$$

Note that a negative sign would appear on the right hand side if one used dx_{Li} instead of $d\xi$, as is often found in the literature.

According to the fundamental thermodynamic relation, the entropy can be derived from the temperature dependence of the Gibbs free energy:

$$\frac{dG}{dT}(T, p, \xi)|_{p,\xi} = -S(T, p, \xi)|_{p,T} \quad [9]$$

We obtain the partial molar values of G and S by combining Eqs. 8 and 9, and dividing by $d\xi$: $\frac{d}{dT}\left(\frac{dG}{d\xi}(\xi)\right) = -\frac{dS}{d\xi}(\xi)$. This finally gives:

$$\frac{dS}{d\xi}(\xi)|_{p,T} = -n \cdot F \cdot \frac{d}{dT} E_0(\xi)|_{p,\xi} \quad [10]$$

The entropy change due to a differential increase of the turnover parameter on the left side corresponds to a temperature induced change of E_0 measured at a constant ξ . Note that the differential increase of G (endergonic for charging) due to $d\xi$ is already implicitly included in E_0 . In our study, an increase in temperature was found to decrease the OCV, independent of whether the OCV was measured after charging or discharging and at all values of ξ . $\frac{\partial E_0}{\partial T}$ is thus negative and accordingly the partial molar entropy is always positive. As a consequence, the entropy of the cell increases on charging $dS = \frac{dS}{d\xi}(\xi) \cdot d\xi > 0$ because $d\xi > 0$ and vice versa decreases while discharging ($d\xi < 0$).

Depending on the electrode properties, $\frac{dS}{d\xi}(\xi)$ can change with ξ since for most electrode active materials, such as LMR-NCM, the structural and energetic properties change upon lithiation. As mentioned above, for the Li anode, the partial molar entropy can be assumed to be constant. Hence, for a LMR-NCM/Li cell, any changes of the partial molar entropy of the cell are exclusively governed by the properties of the cathode, while the value (and sign) of $\frac{dS}{d\xi}(\xi)$ includes the constant contribution from the Li anode.

The total molar entropy change $\Delta S(\xi)$.—When we start at an SOC value “a” (ξ_a) and charge or discharge to get to state “b” (ξ_b), the total entropy change referred to 1 mol of CAM is obtained by integrating the partial molar entropy of this process, as long as local reversibility is given:

$$\Delta S = S(\xi_b) - S(\xi_a) = \int_{\xi_a}^{\xi_b} \frac{dS}{d\xi}(\xi) d\xi = \Delta S_{\text{NCM, a} \rightarrow \text{b}} - S_{\text{Li}} \quad [11]$$

Thereby, the total molar entropy change ΔS is a measure of additional energetic disorder in the whole battery induced by (dis-)charging the cell by $\Delta\xi$. It contains the contribution from the cathode ($\Delta S_{\text{NCM, a} \rightarrow \text{b}}$) and the Li anode (S_{Li}). Basically, there are three possible contributions to ΔS and hence to its derivative $\frac{dS}{d\xi}(\xi)$: The configurational, vibrational, and electronic entropy, which will be discussed in the following.

The electronic molar entropy change $\Delta S_{\text{elec}}(\xi)$.— $\Delta S_{\text{elec}}(\xi)$ is associated with thermal disorder in electronic states near the Fermi

level and can be sensitive to the SOC. It can be calculated from the change of electronic density of states at the Fermi level with changing degree of lithiation. For Li_xCoO_2 , it was shown that $\Delta S_{elec}(\xi)$ is negligible.²⁰ Since for our system, electronic entropy calculations are not available, for the time being we neglect such contributions at room temperature.

The Li-configurational molar entropy change $\Delta S_{config}(x)$.—The Li-configurational entropy gives information about the distributional variability of Li atoms in the host structure. In a very simplified ideal solid solution model with Li atoms moving freely between a given number of empty sites, without changing interactions (among each other and with the host lattice), the molar entropy change is given by:

$$\Delta S_{config}(x) = -R \cdot \{x \cdot \ln x + (1-x) \cdot \ln(1-x)\} \quad [12]$$

Here, R is the molar gas constant and x the relative amount of exchangeable sites being occupied. When describing a simplified CAM, we assume the maximum number of x to be equal to one (as common for typical layered oxides but not for the LMR-NCM used in our study). Resulting from Eq. 12, $\Delta S_{config}(x) = 0$ for an ‘empty’ electrode ($x = 1$) and a completely filled electrode ($x = 0$). With increasing delithiation $\Delta S_{config}(x)$ increases and is categorically positive yielding a maximum at $x = 0.5$ with a value of $\Delta S_{config}(x = 0.5) = R \cdot \ln 2 = 0.693R = 5.76 \text{ J}/(\text{mol K})$. To both sides of the maximum, it symmetrically decreases to zero. In the ideal solid solution case, all Li sites are energetically equal and the interactions between the Li ions among each other and with the lattice do not change during the charge/discharge process (implying a constant value for ΔH). This leads to a practically horizontal voltage curve for such an electrode material with a maximum deflection of $\approx 17 \text{ mV}$ at $x = 0.5$ (according to the definition of the Gibbs free energy, $\Delta G = \Delta H - T\Delta S$ and Eq. 8).

Of course there are more sophisticated models, including interactions between Li and the host structure and among the Li ions at varying distances in the host, leading to more complicated entropy curves, which can even have several maxima (here, ΔH also changes as a function of SOC).^{13,14} However, these curve features must become increasingly smaller in amplitude, the more maxima are detected. All of these entropy curves are categorically positive and equal to zero at the endpoints.

The partial molar configurational entropy is the slope of the configurational entropy $\Delta S_{config}(x)$ obtained by differentiating Eq. 12:

$$\frac{\partial \Delta S_{config}}{\partial x} = -R \cdot \ln \left(\frac{x}{1-x} \right) \quad [13]$$

For the simplified solid solution model ($0 \leq x \leq 1$), it is a monotonically decreasing function starting at infinity, changing curvature at the maximum of $\Delta S_{config}(x = 0.5)$ and ending at $-\infty$ at $x = 0$.¹⁵ For the above mentioned models with several maxima in ΔS_{config} , the corresponding derivatives give inverse sigmoidal curves with pole signatures at their ends.^{13,14} In the data presented below, there is no indication of such features.

The vibrational entropy $\Delta S_{vib}(\xi)$.—Here we are interested in that part of vibrational entropy, also called phonon entropy, which is associated with changes of vibrational frequencies in the crystal lattice with the degree of lithiation. Any Li-induced changes of the vibrational density of states up to the Fermi level will lead to changes in the heat capacity (C_p) and to corresponding changes in the vibrational entropy (ΔS_{vib}).

$$\Delta S_{vib} = \int_0^T \frac{C_p(T)}{T} dT \quad [14]$$

As a rule of thumb, at room temperature, the main contribution will result from low-frequency phonons with rather large effective mass, hence from the transition metal oxide host lattice rather than from the intercalated Li atoms. On the other hand, the Grüneisen relation suggests that increased stiffness should reduce C_p , yielding lower lattice entropy. Such lattice strain may be accumulated while (de-)intercalating Li from/into a host structure during charge or discharge. In particular, phase transitions occurring during charge/discharge should be mirrored in the entropy profile. Accumulation of crystallographic defects leading to disruptions of long range vibrations are expected to influence vibrational entropy. Such changes can be induced by the intercalation of Li ions into the Li layer of LMR-NCM, but also by a change in the stiffness of the host lattice, e.g. by the oxidation/reduction of transition metals, by transition metal migration, and/or by oxygen redox. The formation of Li clusters can also modulate vibrational modes. With neutron-weighted phonon density of states (DOS) derived from inelastic neutron scattering data, the Li-induced vibrational entropies at different SOCs could be calculated for Li_xCoO_2 .²⁰ It was shown that the difference in vibrational entropy between the relatively stiff Li_xCoO_2 lattice and the soft metallic Li anode results in a significant negative but constant contribution to the partial molar entropy of the cell, which however could not explain obvious changes of $\frac{dS}{d\xi}(\xi)$ with ξ .²⁰ For the further discussion it is noteworthy that, in contrast to the configurational entropy, which in the simplest case is a direct function of the SOC, the vibrational entropy is closely linked to the structure of the host lattice.

Contribution of lithium to the partial molar entropy of the cell.—The contribution of the Li counter electrode is often neglected in the literature or even assumed to be zero.^{20–22} As explained above for Eq. 5, the entropy of Li is independent of the SOC^{19,20} but is not zero.^{20,23–25} In order to determine the contribution of Li to the overall cell-TD-OCV, spatially non-isothermal measurements were conducted, which are explained in the following. In the potentiometric measurement of the cell-TD-OCV, spatially isothermal conditions are implied, where the whole cell, i.e. both cathode and anode, are subjected to the same temperature variation. In contrast, one can take precautions to change the temperature of only one of the electrodes (the thermally working electrode) in a spatially non-isothermal arrangement (see Fig. S1 in the Supporting Information available online at stacks.iop.org/JES/168/120502/mmedia). Such asymmetric temperature changes can be applied to cells with electrochemically symmetric (identical) electrodes. Spatially non-isothermal measurements yield important entropy information pertaining to the thermal working electrode material, which is why resulting values will be denominated as electrode-TD-OCV in the following. The electrode-TD-OCV differs from the cell-TD-OCV in such a way that the temperature function of the electrode that is held at constant temperature does not contribute to the electrode-TD-OCV. However, even if it might seem that the electrode-TD-OCV value leads to the entropy of a single electrode, this is not true because the potential itself is still a cell property and not a single electrode quantity, as is always the case in electrochemistry.²³ As is shown in Eq. 15, the electrode-TD-OCV depends on three factors: (i) the actual entropy contribution of the electrode under investigation, $\frac{\partial E'_0}{\partial T}$, (E'_0 is the OCV between a working electrode subjected to variable temperature and a counter electrode held at constant temperature), (ii) a potential build-up due to thermal diffusion of ions in the electrolyte, the so-called Soret effect $\left\{ \frac{\partial E}{\partial T} \right\}_{\text{Soret}}$, and (iii) the metal-metal junction thermocouple Seebeck effect, $\left\{ \frac{\partial E}{\partial T} \right\}_{\text{Seebeck}}$.^{25–27}

$$\left\{ \frac{\partial E_0}{\partial T} \right\}_{\text{electrode}} = \left\{ \frac{\partial E'_0}{\partial T} \right\}_{\text{working electrode}} + \left\{ \frac{\partial E}{\partial T} \right\}_{\text{Soret}} + \left\{ \frac{\partial E}{\partial T} \right\}_{\text{Seebeck}} \quad [15]$$

When using a symmetrical Li/Li cell, the pure entropy contribution $\frac{\partial E_0}{\partial T}$ of the Li electrode can in principle be determined from Eq. 15 if the effects (ii) and (iii) can be minimized or determined as good as possible. The thermocouple effect (iii) can be estimated from the Seebeck coefficients of the materials, which are exposed to a temperature gradient. For the symmetrical Li/Li cell, this is nickel, since only at the nickel tab of the Li electrode a changing temperature gradient will build up. With $-18.0 \mu\text{V K}^{-1}$,²⁸ the Seebeck effect of nickel is negligibly small in comparison to the measured electrode-TD-OCV of Li, $\left\{\frac{\partial E_0}{\partial T}\right\}_{\text{Li}} = 1.12 \text{ mV K}^{-1}$. Furthermore, the Seebeck effect can be minimized by keeping all other metal-metal junctions isothermal.^{26,27} The Soret effect describes a mass separation induced by a temperature gradient.^{29,30} In the context of this study, the Soret effect plays a role in the spatially non-isothermal configuration, because a temperature-induced concentration gradient will cause a potential difference between the hot and the cold side, i.e. $\left\{\frac{\partial E}{\partial T}\right\}_{\text{Soret}}$. Comprehensive data of the Soret effect are lacking in the literature because experimental measurements of the thermodiffusion coefficient prove to be difficult and there is no universal technique to measure the Soret effect of binary mixtures.²⁹ In the Results part, we estimate the influence of the Soret effect on the value of the electrode-TD-OCV as rather insignificant, especially in comparison to other sources of error (cell to cell variation, accuracy of the temperature measurement, etc). This is in accordance with the “negligible thermal diffusion potential assumption” made by Swiderska-Mocek et al.²⁵

Experimental

Electrode preparation.—Li- and Mn-rich layered oxides (LMR-NCM) with two different degrees of overlithiation were obtained from BASF SE (Germany). According to the notation $\text{Li}_{1+\delta}[\text{TM}]_{1-\delta}\text{O}_2$ for the pristine LRM-NCM cathode active materials, the here examined LRM-NCM materials have $\delta = 0.14$ and $\delta = 0.20$; this corresponds to a composition of $0.33 \text{ Li}_2\text{MnO}_3 \cdot 0.67 \text{ LiTMO}_2$ (for $\delta = 0.14$; further on referred to as 0.33 LMR-NCM) and $0.50 \text{ Li}_2\text{MnO}_3 \cdot 0.50 \text{ LiTMO}_2$ (for $\delta = 0.20$; further on referred to as 0.50 LMR-NCM) in the two-phase notation applied by Teufl et al.³¹ (with TM = Ni, Co, Mn). The 0.33 LMR-NCM is the same material as used in previous studies of our group^{6,32} and has the composition $\text{Li}_{1.14}[\text{Ni}_{0.26}\text{Co}_{0.14}\text{Mn}_{0.6}]_{0.86}\text{O}_2$. The 0.50 LMR-NCM is a follow-up batch with similar composition and properties as the material used by Teufl et al.³¹

For inks of the 0.33 LMR-NCM cathode active material, 92.5 wt% LMR-NCM (BASF SE, Germany), 3.5 wt% polyvinylidene-fluoride binder (PVDF, Kynar, HSV 900, France), and 4 wt% conductive carbon (Super-C65, Timcal, Switzerland) were dispersed in N-methyl pyrrolidone (NMP, anhydrous, Sigma-Aldrich, Germany) and mixed in a planetary orbital mixer (solids content $\approx 54 \text{ wt}\%$; Thinky, USA). The resulting ink was coated onto aluminum foil ($\approx 15 \mu\text{m}$, MTI, USA) and the dried coatings were calandered (GK 300 L, Saueressig, Germany) to a porosity of $\approx 42\text{--}45\%$. For electrochemical testing, electrodes with a diameter of 11 mm (for Swagelok T-cells) or 14 mm (for 2032-type coin-cells) were punched out and dried at $120 \text{ }^\circ\text{C}$ under dynamic vacuum for at least 12 h (Büchi, Switzerland). The loading of the 0.33 LMR-NCM cathode active material (CAM) was $\approx 12 \text{ mg cm}^{-2}$, corresponding to $\approx 3 \text{ mAh cm}^{-2}$ (based on a nominal reversible capacity of $250 \text{ mAh g}_{\text{CAM}}^{-1}$). For experiments with the 0.50 LMR-NCM material, an industrially manufactured coating was obtained from BASF SE with a loading of $\approx 7.7 \text{ mg cm}^{-2}$, corresponding to $\approx 1.9 \text{ mAh cm}^{-2}$.

Electrochemical characterization.—Three different cell setups were used: (i) Swagelok T-cells with a Li reference electrode (Li-RE) for determination of the cell-TD-OCV in LMR-NCM/Li half-cells, (LMR-NCM potential measured vs the Li-RE); (ii) coin-cells

for electrochemical cycling experiments and recording of the OCV curves; (iii) U-shaped pouch-cells for spatially non-isothermal measurements of the electrode-TD-OCV (see Fig. S1 in the Supporting Information). All cells were assembled in an argon filled glovebox ($\text{O}_2, \text{H}_2\text{O} < 0.1 \text{ ppm}$, MBraun, Germany).

For Swagelok T-cells, anode and cathode were stacked with two glass fiber separators in between (11 mm diameter, $200 \mu\text{m}$ thickness, glass microfiber #691, VWR, Germany). The cells were filled with $60 \mu\text{l}$ of a FEC:DEC (12:64 v:v) based electrolyte with 1 M LiPF_6 and 24 vol% of an additional fluorinated co-solvent. The Li-RE (6 mm diameter, $450 \mu\text{m}$ thickness, 99.9%, Rockwood Lithium, USA) was in electrochemical contact with the cell *via* a separator onto which another $20 \mu\text{l}$ of electrolyte was added. The 3-electrode T-cell setup is identical to what is described by Solchenbach et al. as the “conventional design”.³³ Coin-cells were assembled using a Li counter electrode (16 mm diameter, CE), two glass fiber separators (17 mm diameter) and an LMR-NCM cathode, adding $80 \mu\text{l}$ of the same electrolyte as was used for the T-cells. The U-cell setup is described in the Experimental section and in the Supporting Information.

T-cells and coin-cells were cycled at $25 \text{ }^\circ\text{C}$ (if not stated otherwise) in a temperature-controlled oven (Binder, Germany) using a Biologic potentiostat (VMP300, Biologic, France). At first, one activation cycle at a C-rate of C/15 (2.0–4.8 V, all voltages reported vs Li^+/Li) and two stabilization cycles at C/10 (2.0–4.7 V) were conducted. All C-rates reported here refer to the nominal capacity of the LMR-NCM of 250 mAh g^{-1} (i.e. $1\text{C} \equiv 250 \text{ mA g}^{-1}$ or $\approx 3 \text{ mA cm}^{-2}$). Subsequent to the initial cycles, the electrochemical characterization (OCV curves, determination of the cell-TD-OCV) was carried out at C/10 in the 4th cycle. For measurements at a different C-rate, an additional cycle at that C-rate was done prior to the actual experiment to equilibrate to the new C-rate.

Measurement of the partial molar entropy of the cell.—All measurements were conducted in the 4th cycle subsequent to the initial activation and stabilization procedure explained above. To determine the SOC dependent cell-TD-OCV of LMR-NCM/Li cells, the T-cells were (dis)charged to a certain SOC-point at $25 \text{ }^\circ\text{C}$ and allowed to relax until the change of the OCV with time was less than $\approx 0.2 \text{ mV h}^{-1}$. For each SOC-point, such a relaxation took between 100 h and 200 h. The cells were then transferred to an Espec temperature chamber (LU114, Espec, Japan) to measure the cell-TD-OCV with a defined temperature ramp of 0.5 K min^{-1} . Starting at the initial cell temperature of $25 \text{ }^\circ\text{C}$, the temperature ramping commenced with a heating phase to $35 \text{ }^\circ\text{C}$. Subsequently, three cycles of cooling to $5 \text{ }^\circ\text{C}$ and heating to $35 \text{ }^\circ\text{C}$ were repeated, followed by a final cooling step to the initial $25 \text{ }^\circ\text{C}$. Figure 2 shows an exemplary curve of the temperature profile and the respective OCV response. After this measurement sequence, the cell was (dis)charged to the next SOC at $25 \text{ }^\circ\text{C}$. This procedure was repeated with several cells in charge and discharge direction to collect data with an SOC spacing of $\approx 5\%$ (12.5 mAh g^{-1}). Data treatment was conducted with a Matlab Script determining the slope of the measured OCV data vs time by a linear fitting of the individual ramps. The so derived $\frac{\partial E_0}{\partial T}$ values were averaged and transferred to cell-TD-OCV, $\frac{\partial E_0}{\partial T}$, by allocating them with the predefined temperature ramp $\left(\frac{\partial T}{\partial t}\right)$. For a detailed discussion on the ramping method, see the Results section. Moreover, the OCV value of the cell at the respective SOC was determined by averaging over the last hour of data points prior to initiating the temperature ramps.

To confirm the accuracy of the data acquired by the Biologic potentiostat, a high sensitivity Nanovoltmeter (Model 2182 A, Keithley Instruments, USA) was used with a Labview Script to record the potential of the cell during temperature variation.

Determination of the Li contribution to the partial molar entropy of the cell.—To accomplish a spatially non-isothermal

environment for the measurement of the electrode-TD-OCV of Li, pouch-cells with a U-shaped geometry were used. A schematic drawing is shown in Fig. S1 in the Supporting Information. For measurements of the electrode-TD-OCV of Li, symmetrical Li/Li U-cells with a Li metal ($\approx 1 \text{ cm}^2$, contacted *via* a Ni-tab) at both sides of the cell were used. Electrochemical contact was ensured with a U-shaped glass fiber separator soaked with 2 mL LP57 electrolyte (1 M LiPF₆ in EC:EMC = 3:7 by weight, BASF SE, Germany). Using this geometry, the temperature of one Li-electrode was kept constant in a water bath at room temperature while the temperature of the other one was varied between 0 °C and 40 °C using a double-walled glass beaker with an in-, and outlet for cooling fluid connected to a refrigerated-heating circulator (FP50, Julabo, Germany). The temperature at the vicinity of the cell surface of each of the immersed legs of the U-cell was recorded by two USB data loggers (Easylog-USB-2-LCD, Lascar Electronics Ltd, UK). The potential was monitored using the above described Nanovoltmeter. The measurement principle is similar to that described by Swiderska-Mocek et al.²⁵

Results and Discussion

Development of an accurate method to determine $\frac{\partial E_0}{\partial T}$.—The partial molar entropy, $\frac{dS}{d\xi}(\xi)$, can be obtained by potentiometric methods *via* determination of the temperature dependence of the OCV (cell-TD-OCV), $\frac{\partial E_0}{\partial T}$, or with calorimetric methods *via* measuring the reversible heat, \dot{Q}_{rev} . For calorimetric measurements, however, large cell formats are necessary to reach the required accuracy. In the following, we will focus on the potentiometric method where the TD-OCV is determined by collecting OCV data as a function of temperature. For this purpose, the battery is typically cycled to a certain SOC and allowed to relax in OCV conditions for some time before the temperature of the cell is changed in a step-like procedure.^{9,12,34–36} A typical data set for the step procedure is shown in Fig. 1a for a 0.33 LMR-NCM/Li cell at a nominal SOC of 140 mAh g⁻¹ in the 4th cycle in charge direction. After 24 h of relaxation at OCV conditions at 25 °C, the temperature of the cell is changed to 35 °C and the cell is given 1 h to accommodate to the new temperature. This is repeated at 25 °C, 15 °C and 5 °C before the temperature is again set to 25 °C. The OCV is thus measured as a direct function of the cell temperature. By making a linear regression of OCV vs temperature (Fig. 1b), the cell-TD-OCV can be determined from the slope. This is repeated at every SOC of interest.

However, there are some challenges when applying this method to determine the TD-OCV. Since the OCV is directly measured as a function of temperature, any relaxation phenomena leading to a change in OCV with time have to be excluded. For the data shown in Fig. 1a, the scatter in the OCV data lead to the error bars in Fig. 1b (standard deviation of calculating the average OCV value during the last 5 min of the respective 1 h temperature step in Fig. 1a). The overall error for the calculation of the cell-TD-OCV hence includes the error from the linear fit and the error of the respective OCV values. For the exemplary data set in Fig. 1, Table I shows that the calculated error is in the same order of magnitude as the resulting

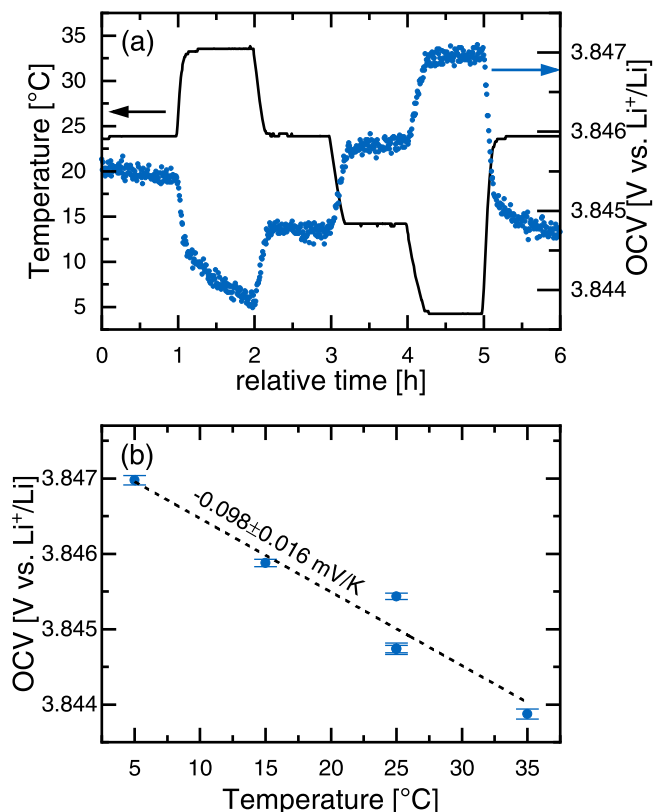


Figure 1. (a) Example of a temperature profile (black line) and the corresponding OCV response (blue symbols) when applying the temperature step method. After equilibrating at OCV conditions for 24 h at 25 °C, the temperature of the battery is varied in steps with a thermal equilibration time of 1 h per step. Here, data from a 0.33 LMR-NCM/Li T-cell at a nominal SOC of 140 mAh g⁻¹ during the 4th charge is shown. (b) The cell-TD-OCV is the slope of a linear fit (black dashed line) of the determined OCV values (blue symbols) as a function of the respective temperatures. The error bars of the OCV data are the standard deviation calculated from averaging over the last 5 min of every 1 h temperature step. The error of the resulting cell-TD-OCV includes the error from the linear fitting and the errors of the data points.

TD-OCV value after 24 h of relaxation. Voltage relaxation processes cannot be fully avoided and are reported to take up to six months depending on the cell chemistry.³⁷ However, a survey of entropy studies by Zhang et al.²² showed that typically waiting times of 3 h and 60 h were provided for voltage relaxation at each SOC point. Figure 1a serves to illustrate that a relaxation time of 24 h is not sufficient (for this cell chemistry, at this SOC) since ongoing voltage relaxation is observable, which is especially pronounced at higher temperatures. This leads to the fact that three different OCV values are determined at 25 °C during the step method. On the other hand, during prolonged relaxation periods, self-discharging phenomena within the battery have to be taken into account. Especially at high

Table I. Cell-TD-OCV of a 0.33 LMR-NCM/Li cell determined at an SOC of 140 mAh g⁻¹ during the 4th charge after 24 h and 96 h of relaxation in OCV conditions at 25 °C. Results from the step method and ramp method are contrasted (by comparing data from two identical cells). The difference between the absolute results after 96 h from the two different methods is caused by cell to cell variations. For the step method, the error is calculated from the fit through the OCV data as a function of temperature including the error from the OCV determination. For the ramp method, the error results from averaging over six dE/dt values including their respective error from the linear fitting of the ramps.

Equilibration time [h]	Cell TD-OCV [mV K ⁻¹] with error in parenthesis	
	Step method	Ramp method
24	-0.098 (0.016)	-0.127 (0.002)
96	-0.115 (0.006)	-0.123 (0.001)

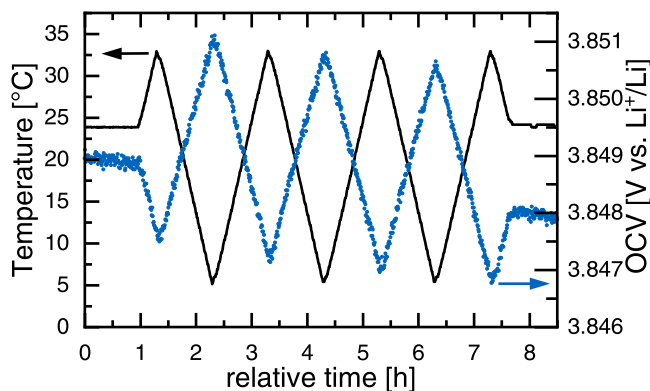


Figure 2. Typical OCV profile during the application of the linear temperature ramp method where the temperature is varied linearly between 5 °C and 35 °C with a rate of 0.5 K min⁻¹ (black line) while the OCV is recorded (blue symbols). Here, data from a 0.33 LMR-NCM/Li T-cell at a nominal SOC of 140 mAh g⁻¹ during the 4th charge is shown after equilibrating the cell at OCV conditions for 24 h at 25 °C.

SOCs, it may become difficult to maintain a stable voltage.^{12,35,38} Figure S2 in the Supporting Information exemplarily shows that a pronounced voltage relaxation at a high SOC considerably compromises the determination of the TD-OCV with the step method. To circumvent extended waiting times, Osswald et al.³⁹ suggested to extrapolate the stationary state voltage by fitting the truncated relaxation curve. By correcting for self-discharge³⁵ or by short charge/discharge phases at low currents,⁴⁰ attempts have been made to minimize the effects of self-discharging and parasitic side reactions. Another issue was identified by Zilberman et al.,³⁷ who found a temperature path dependent voltage behavior causing uncertainties in the determination of the true OCV values. Therefore, they suggested to limit the temperature amplitude and the thermal equilibration time, and use both cooling and heating temperature variations to determine accurate TD-OCVs.³⁷ Usually, a temperature range between 20 °C and 30 °C is applied,^{22,39,40} though some researchers use wider ranges (from 0 °C up to 55 °C) for a better signal-to-noise ratio.^{22,34,35} Of course, also appropriate measurements of the cell temperature are required for valid TD-OCV data. In summary, the step procedure, although widely used in the literature, faces some issues, pertaining to the accurate determination of an OCV value per temperature step.

To overcome these difficulties, we applied a linear temperature ramp method, which is less common in the field and was only used by a few other research groups before.^{16–18} This is why we want to discuss it in more detail. The here used temperature profile is similar to what was applied by Thomas et al.⁴⁰ and an exemplary data set of our ramp method is shown in Fig. 2. The temperature was varied linearly between 5 °C and 35 °C at a rate of 0.5 K min⁻¹. By doing so, the OCV is measured on the fly while the temperature is continuously changed, in contrast to the above discussed classical temperature step technique. Since the OCV is a linear function of the temperature (within a reasonable temperature range), the slope of the OCV change follows the linearity of the applied temperature profile. With the knowledge of the rate (e.g. $\frac{\partial T}{\partial t} = 0.5 \text{ K min}^{-1}$), the slope of the OCV ($\frac{\partial E_0}{\partial t}$ in mV h⁻¹) is easily converted to the TD-OCV ($\frac{\partial E_0}{\partial T}$ in mV K⁻¹). Figure 2 shows that the effective temperature range, which was monitored by a temperature sensor close to the cell surface, is slightly smaller ($\approx 5 \text{ °C}$ –33.5 °C) than what is given by the thermostat (5 °C–35 °C). This might be related to the accuracy of the temperature chamber and the temperature sensor used. To find an optimum temperature range, a compromise has to be reached between two requirements: A large temperature range is desirable to get as much data as possible. For the cell chemistry, the temperature range should be restricted to reasonable limits to avoid

side reactions. This is why the range between 5 °C and 35 °C was chosen.

To validate the results from the temperature ramp method, the cell-TD-OCV was first determined *via* the temperature step procedure and then compared to that determined by consecutive temperature ramp procedures with rates of 0.5 K min⁻¹ and 1 K min⁻¹. For this experiment, a cell was charged to a certain SOC, allowed to relax at OCV for ≈ 60 –150 h (until the change in OCV was less than $\approx 0.2 \text{ mV K}^{-1}$), and then the temperature was first changed according to the step profile and then according to the two ramp profiles. The results are shown in the Supporting Information in Fig. S4 and confirm that the temperature ramp method gives the same results as the temperature step method. Minor deviations may arise from the differences in calculating $\frac{\partial E_0}{\partial T}$ between the temperature ramp and the step method (see discussion of the data accuracy below), but are negligible with respect to other sources of errors (e.g. accurate determination of the SOC, cell to cell variations). Furthermore, it is proved that the results from the ramp method are independent of the applied rate (as long as a reasonably slow rate is applied). A detailed analysis of the temperature ramp data sets shows that the potential change is delayed with respect to the applied temperature change by about 2 to 5 min (see Fig. 2), which gives an idea about the thermal conductivity of the cell. Due to this deviation from the ideal triangular behavior, the OCV data at the boundaries of each ramp were not included into the linear fit (approx. the first and last 5 min of each 60 minute ramp, effectively reducing the analyzed temperature window to $\approx 8 \text{ °C}$ –30 °C). Since the voltage responses of interest have rather small absolute values, we validated the accuracy of the data obtained from the Biologic potentiostat (resolution of $\approx 100 \mu\text{V}$) with a high precision Nanovoltmeter (resolution of $\approx 1 \mu\text{V}$ in the mode used here). As a quality criterion, the residual sum of squares of linear fits of the obtained triangle wave data is used. For the data measured by the Nanovoltmeter (not shown here), this parameter is four orders of magnitude below the one for the Biologic, suggesting a significantly lower noise level. However, both data sets give very similar results for $\frac{\partial E_0}{\partial T}$ (differing by less than $\approx 0.01 \text{ mV K}^{-1}$). Since the data from the Biologic show only white noise, which is significantly smaller than the actual signal intensity (see Figs. 1 and 2), and since the results are practically the same as those obtained from the Nanovoltmeter, all further measurements were conducted with the Biologic potentiostat.

In the following, the temperature step and ramp method will be compared. Figure 2 shows data collected during a temperature ramp experiment with an identical cell as used for the temperature step method in Fig. 1 (both at 140 mAh g⁻¹ during the 4th charge after 24 h of relaxation at 25 °C). For the temperature ramp method, the TD-OCV is calculated based on the slope of the triangular OCV data. The error therefore includes the error of the linear fit of the respective ramps and the error from taking the average over six values. Table I shows that for the ramp method, the calculated error is one order of magnitude smaller compared to the error resulting from the step method. Both measurements were repeated after 96 h of relaxation, when the change of the OCV with time was sufficiently low ($<0.1 \text{ mV h}^{-1}$) to allow for a reliable determination of the TD-OCV. In case of the temperature ramp method, the result obtained after 24 h of relaxation is very close to the TD-OCV value determined after 96 h of relaxation. For the step method, however, the deviation between the two TD-OCV values is relatively large. This illustrates that the temperature ramp method is less sensitive to ongoing voltage relaxation compared to the step procedure. This is achieved by applying several heating and cooling ramps, which result in triangular OCV response curves with positive and negative slopes, so that any effects resulting from incomplete OCV relaxation are minimized. This is furthermore illustrated in Fig. S3 in the Supporting Information, where an ongoing relaxation at a high SOC leads to a gradual decrease of the OCV over time. The relaxation effect has an opposing sign, thus a weakening effect on the OCV

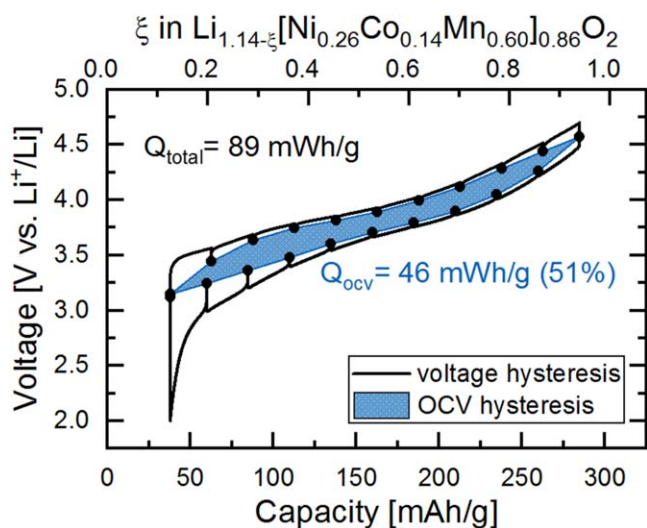


Figure 3. Voltage hysteresis at C/10 (25 °C) in a 0.33 LMR-NCM/Li cell shown vs specific capacity (lower x-axis) and extent of reaction (upper x-axis). The black line is the voltage curve at C/10 with intermittent 1 h OCV phases every $\approx 10\%$ SOC (i.e. every 25 mAh g⁻¹), leading to the black circles. The total voltage hysteresis amounts to 89 mWh g⁻¹ (area enclosed by the black line) and the OCV hysteresis at zero current equals 46 mWh g⁻¹ (blue area, enclosed by OCV points, amounting to 51% of the total area).

behavior during cooling and an amplifying effect during heating. By measuring both temperature pathways multiple times and averaging over the acquired slopes, any error due to OCV relaxation is minimized. This also means that even if the OCV is not perfectly stable, the entropy data obtained with the temperature ramp method are reliable. If sufficiently long relaxation times are applied, the advantage of the temperature ramp method is less pronounced. Table 1 shows that after 96 h of relaxation, the calculated errors of the TD-OCV of both methods are similar. We want to stress, however, that prolonged relaxation times can lead to self-discharge phenomena (especially at high SOC), which might again cause a pronounced change of the OCV with time. For these cases, the temperature ramp method is more suitable than the step procedure. The difference between the two final $\frac{\partial E_0}{\partial T}$ values might arise from minor deviations in the determination of the SOC for the two different cells and from cell to cell variations. The measurement was repeated after 220 h of relaxation and the respective TD-OCV values of both cells did not change significantly. The errors from the calculation are thus relatively small in comparison to experimental errors.

Although effects from voltage relaxation are minimized by the temperature ramp method, the cells of this study were allowed to rest at each SOC until the change in OCV was on the order of ≈ 0.2 mV h⁻¹, leading to relaxation times of 100–200 h per SOC step. Of course, such extended OCV periods, especially at high SOC, cause self-discharge and lead to an inaccuracy in the determination of the SOC. To avoid accumulated self-discharge during repeated, prolonged observation intervals using a single cell, a number of identical cells was used instead to measure the TD-OCV at given SOC points during charge and discharge, with every cell undergoing only three to five measurements. All OCV values determined prior to the temperature ramp method, were in good agreement with the nominal OCV curve (see Fig. 3). The use of a set of cells for these measurements not only increased the accuracy of the SOC determination, but also helped to speed up the collection of a complete entropy data set for a whole charge/discharge cycle significantly. Additionally, with the use of multiple cells, the reproducibility of the results could be verified by measuring at nominally identical SOC points. Small cell to cell variations were observable, which however were negligible within the limits of accuracy of the measurements.

Li electrode contribution to the partial molar entropy of LMR-NCM/Li cells.—As was explained in the Theoretical Considerations above, we aimed at clarifying the contribution of Li to the cell entropy by spatially non-isothermal measurements using custom-made U-shaped pouch cells (Figure S1 in the Supporting Information). In this setup, one side of the U-cell is exposed to temperature changes induced by a water bath, while the other side is held at a constant temperature, similar to the approach reported by Swiderska-Mocek.²⁵ In symmetrical Li/Li U-cells, the electrode-TD-OCV of Li was directly determined. When both electrode compartments are at the same temperature, the OCV is zero. As soon as the temperature of one side deviates from the other one, the potential changes. By measuring the OCV as a function of this temperature difference, the electrode-TD-OCV of Li can be determined. The average over multiple measurements with a number of different cells gives $\left\{\frac{\partial E_0}{\partial T}\right\}_{Li} = 1.12(\pm 0.06)$ mV K⁻¹. We found that the results are independent of whether a fresh piece of Li metal was used or one harvested from a cycled LMR-NCM/Li cell. This means that the contribution of Li to the cell TD-OCV is independent of the cycling history and nominal SOC of the Li, which is in agreement with literature reports.^{19,20} An exemplary data set of such a measurement is shown in Fig. S5 in the Supporting Information. However, as mentioned above in the theory section, this value includes the Soret effect, since in the spatially non-isothermal setup, thermodiffusion is present (see Eq. 15). A comparison to literature reports shows that Huang et al.⁴¹ have done a similar experiment with a cell consisting of two single-electrode tubes containing identical Li electrodes that are connected by an electrolyte filled plastic tube. The electrode tubes were placed in two oil-bath systems at different temperatures. With the above discussed temperature stepping method, they obtained a value of 1.17 mV K⁻¹,⁴¹ which is in good agreement with our result. As in the case of our U-cell experiment, their approach also includes the Soret effect. However, they have complemented their experiments with an electrochemical-calorimetric measurement where one Li electrode is inside the calorimeter and one outside. By cycling with small currents and subtracting the discharge from the charge heat, the irreversible heat is removed and the reversible heat can be determined. From that, they calculate the so-called “entropy of the Li single electrode reaction” to be 128.3 J (mol K⁻¹).⁴¹ Using Eq. 10, this value converts to an electrode-TD-OCV of 1.33 mV K⁻¹. Since there is no Soret effect present in their calorimetric measurement, the difference between their potentiometric value of 1.17 mV K⁻¹ and their calorimetry derived value of 1.33 mV K⁻¹, equating to -0.16 mV K⁻¹, would correspond to $\left\{\frac{\partial E}{\partial T}\right\}_{Soret}$ (based on Eq. 15 and assuming $\left\{\frac{\partial E}{\partial T}\right\}_{Seebeck}$ to be negligible). It should be noted that other measurement errors like the inaccuracy of the calorimeter might be affecting the result. Also, charge-neutral exothermic side reactions can contribute to the calorimetric signal and hence lead to an overestimation of the electrode-TD-OCV. The observed difference between the two reported values is therefore only a rough estimate for the contribution of the Soret effect. We can therefore conclude that the Soret effect is negligible in comparison to our $\left\{\frac{\partial E_0}{\partial T}\right\}_{Li}$ value of 1.12(±0.06) mV K⁻¹ and that our result agrees with the values reported in the literature.^{25,41} According to Eq. 10, a $\left\{\frac{\partial E}{\partial T}\right\}_{Li}$ value of 1.12 mV K⁻¹ converts to a molar entropy of 108 J (mol K⁻¹) for Li. We want to stress that this value cannot directly be compared to the textbook value of 29 J (mol K⁻¹)⁴² since the latter refers the entropy of formation of Li metal at standard conditions while we measure the molar entropy change for depositing Li at the metal anode and the entropy of desolvation of Li⁺ ions (see Eq. 5).

From similar spatially non-isothermal measurements with LMR-NCM electrodes, we determined the electrode-TD-OCV of LMR-NCM at certain SOC points (data not shown here). We found that the contribution of Li to the cell-TD-OCV of the LMR-NCM/Li cell is in the same order of magnitude as the one of the LMR-NCM

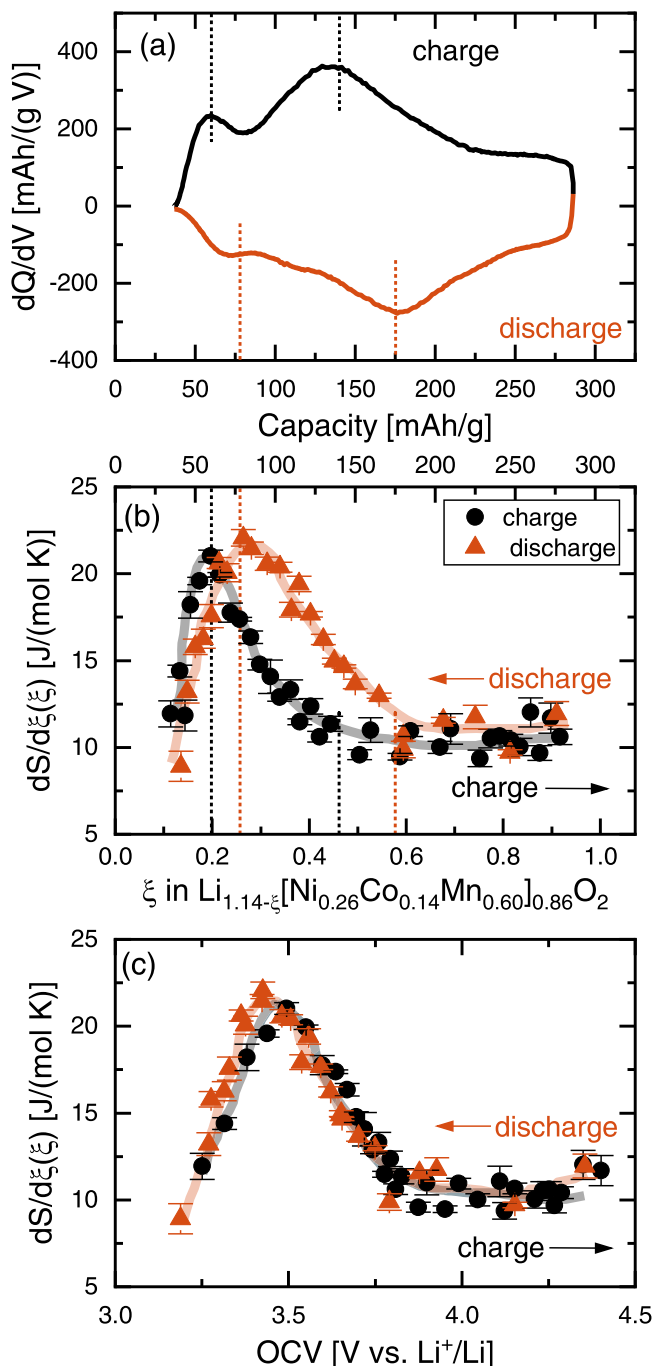


Figure 4. (a) dQ/dV vs capacity plot of a 0.33 LMR-NCM/Li cell recorded at C/10 (25 °C) in the 4th cycle. (b) Partial molar entropy for 0.33 LMR-NCM/Li cells obtained from cell-TD-OCV measurements using the temperature ramp procedure during charge (black circles) and discharge (orange triangles) in the 4th cycle as a function of capacity (upper x -axis) or reaction turn-over ξ (lower x -axis). (c) Same partial molar entropy data but plotted as function of OCV. Trendlines are shown as guide for the eye. The error bars are calculated mean standard deviations from the calculation of TD-OCV values. Dashed lines highlight common features in the different plots.

cathode (both on the order of $\approx 1 \text{ mV K}^{-1}$), and only the difference of both gives the observable small values around $\approx -0.1 \text{ mV K}^{-1}$ for the cell-TD-OCV. Swiderska-Mocek et al.²⁵ also report such high electrode-TD-OCV values for the CAMs used in their study.

Conclusively, the entropy contribution of Li as a counter electrode must not be assumed to be zero but has to be treated as an SOC-independent offset value. It is important to keep in mind that

any counter electrode will contribute to the measured entropy curve, even if the contribution is only an offset, as for Li. This is especially crucial when discussing an apparent change in the sign of the $\frac{dS}{d\xi}(\xi)$ curve, which, in the literature, is often solely ascribed to processes in the cathode active material.^{22,40} Such a hypothesis is not valid for the data presented here and any suppositions presented elsewhere need to be revisited.

Hysteresis phenomena in LMR-NCM cathode active materials.

The active material of interest in this study is Li-, and Mn-rich NCM and the main focus is on the material 0.33 LMR-NCM (Li_{1.14}[Ni_{0.26}Co_{0.14}Mn_{0.60}]O₂). LMR-NCM exhibits characteristic hysteresis phenomena, which are extensively discussed in the literature. In general, a hysteretic behavior occurs if sufficiently high energy barriers prevent an equilibration between stoichiometrically equivalent states located along energetically different charging and discharging pathways. In this case, changes in state will occur via thermodynamically metastable regions.⁴³ The resulting hysteresis loop as a whole is unidirectional but reversibility may hold within limited path sections. The most striking of these phenomena in LMR-NCM is the OCV hysteresis, which is shown in Fig. 3 (blue shaded area). The overall voltage hysteresis can be separated into two parts, (i) a voltage hysteresis due to charge transfer and concentration overpotentials, which is common for all types of active materials, scaling with the applied current and being zero at open circuit conditions, and (ii) the OCV hysteresis, which is independent of the applied current (see Fig. S6 in the SI and discussion below) and is hence a material specific property. At a low C-rate as C/10, the energy loss caused by the OCV hysteresis loop (represented by the blue shaded area in Fig. 3) can amount to 51% of the total voltage hysteresis loop (represented by the area that is enclosed by the black line).

Several reasons for the OCV hysteresis in LMR-NCM are discussed in the literature, mainly focusing on reversible transition metal migration⁴⁴ and changes of oxygen redox,⁴⁵ causing the re-entrant Li environment during discharge to be energetically different from that during charge.^{4,46} The phenomenon of hysteresis in LMR-NCM is not only observable in the voltage curve, but also in a path dependent cathode resistance¹⁻³ as well as in the SOC dependent hysteresis of LMR-NCM lattice parameters^{5,6} and atomic distances.⁷ The OCV hysteresis is of particular interest for this study, because it directly reflects the chemical potential, constituting a basic thermodynamic property. This is why we investigated the influence of different factors on the OCV hysteresis of LMR-NCM. For the analysis of the effect of the C-rate, we applied a special cycling protocol. Since the width of the SOC window in a voltage-limited cycling procedure depends on the applied current (and the resulting overpotential), a comparison of the overall energy associated with the OCV hysteresis (integration of the OCV hysteresis loop) at different C-rates is not directly possible. However, by using a cycling procedure that is controlled by specific capacity cutoffs (i.e. limiting the overall SOC window), the comparison of the OCV hysteresis obtained at different C-rates becomes possible. Figure S6 in the SI compares the OCV curves at 1C, C/2, and C/10, revealing a perfect overlap of the OCV hysteresis loops. Thus, the OCV hysteresis is independent of the applied current. This observation indicates that there is a static barrier causing the hysteresis, which is not subject to the dynamics of charging/discharging. Another influencing factor that was investigated is the temperature. To investigate the temperature dependence of the OCV hysteresis, OCV data were collected at 0 °C and 45 °C in a capacity limited cycling procedure. The resulting data are shown in Fig. S7 in the SI. The OCV hysteresis is larger at higher temperature, which is in agreement with literature reports on LMR-NCM.⁴⁷ Processes, which are kinetically hindered, are expected to accelerate with increasing temperature. It seems, however, that the energetic barriers leading to the OCV hysteresis in LMR-NCM cannot be overcome at the temperature of 45 °C. It is conceivable that the temperature

necessary to eliminate the OCV hysteresis is beyond the operating temperature of a battery and might even be beyond the thermal stability of the CAM.

Another factor affecting the OCV hysteresis is the degree of overlithiation of the LMR-NCM material. A higher degree of overlithiation leads to an increase of the OCV hysteresis loop. This will be discussed in more detail with regards to Fig. 6. The following entropy measurements are intended to investigate possible interrelations between entropy and hysteresis phenomena in LMR-NCM and to open a new perspective on the current discussion in literature.

Partial molar entropy of LMR-NCM.—*Path dependence of the partial molar entropy of LMR-NCM.*—By applying the temperature ramp method, cell-TD-OCVs of 0.33 LMR-NCM vs a Li-RE were acquired during charge and discharge at every $\approx 5\%$ SOC. In Fig. 4b, the resulting partial molar entropy, $\frac{dS}{d\xi}(\xi)$, is depicted as a function of SOC. During charge (black circles), the entropy curve shows a distinct peak at $\xi \approx 0.20$ and a plateau-like behavior above $\xi \approx 0.50$. Upon discharge (orange triangles), this plateau only extends down to $\xi \approx 0.58$, where a similar peak begins to evolve. Its maximum at $\xi \approx 0.26$ is significantly shifted as compared to the charge direction. As discussed above, any effects of self-discharge are minimized by the temperature ramp method and the SOC values are verified by comparing the OCV values collected after 1 h (Fig. 3) to that after extended waiting times (entropy measurements). Therefore we are confident that the observed shift of the partial molar entropy curve along the ξ axis during charge and discharge is relevant.

If however, $\frac{dS}{d\xi}(\xi)$ is plotted vs the OCV, this shift of the partial molar entropy peak vanishes, as can be seen in Fig. 4c. In this case, both peaks exhibit the same shape and coincide with each other. This important finding shows that the OCV, and not ξ , is a unique descriptor of the thermodynamic changes being responsible for the entropy change occurring at the observed peak. The same observation is reported for the lattice parameters in LMR-NCM, revealing a hysteresis when plotted as function of SOC, which, likewise, vanishes when plotted as a function of OCV.⁶ Since the OCV essentially mirrors the change of the Gibbs free energy of the LMR-NCM, these findings demonstrate that OCV, entropy and Gibbs free energy all experience a pronounced hysteresis while they remain thermodynamically correlated among each other.

Our entropy curves differ in shape from those of Shi et al.⁴⁸ who also investigated the entropy of Li- and Mn-rich cathodes with the classical temperature stepping method, however, using a rather short relaxation phase (90 min) and short-time temperature steps (15 min). It remains unclear, how far the differences to our data result from the use of a different LMR-NCM material or whether it is due to their very short OCV equilibration times, which we would consider far too short to yield reliable TD-OCV data. The magnitude of the entropy values of LMR-NCM is fairly comparable with the data for regular layered oxides.^{20,35,49}

Another interesting finding is that distinct features of the $\frac{dS}{d\xi}(\xi)$ curve vs SOC correlate well with peaks in the dQ/dV plot recorded at the same rate but without intermittent OCV periods (see Fig. 4a), as marked by the dashed lines in Figs. 4a and 4b. Schlüter et al.,¹³ also report a correlation between peaks in the dQ/dV plots of LiMn₂O₄ and features in the respective entropy profile. In charge direction, the position of the maximum of the entropy peak at $\xi \approx 0.20$ coincides with the location of a peak in the dQ/dV plot (see left-most set of black dashed lines). This dQ/dV peak is usually assigned to the Mn^{3+/4+} redox reaction.⁵⁰ Another peak in the dQ/dV plot during charge is observed where the entropy curve starts the plateau (near $\xi \approx 0.50$; marked by the second set of vertical black dashed lines). It is mainly assigned to Ni^{2+/3+/4+} and Co^{3+/4+} redox chemistry.⁵⁰ In the discharge direction, the same correspondence

between the peaks in the dQ/dV vs capacity plot and the partial molar entropy vs capacity plot is observed (marked by the vertical orange dashed lines). Since these redox reactions are guided by the Gibbs free energy, it is not surprising that the dQ/dV plot shows the same hysteresis as a function of SOC, as the OCV and the entropy curve.

Discussion of the configurational entropy.—The configurational entropy can be represented by a statistical distributional model of Li on available lattice sites. In the literature, two structural models are typically used to explain common features in entropy curves. One refers to an ideal solid solution, where all vacancies in the lattice are filled randomly.^{14,15} The other model is based on two or more energetically different sub-lattices, which are filled in energetic order.^{13–15} The entropy curves of LMR-NCM/Li, however, show none of the typical fingerprints of those configurational entropy profiles. There are several reasons why configurational entropy is not expected to be dominating the $\frac{dS}{d\xi}(\xi)$ curve in case of LMR-NCM/Li, which will be discussed in the following.

Configurational entropy should in principle always be a function of the distributional variability of Li in the CAM, hence the SOC of the cell. Because of the steep voltage curves of LMR-NCM/Li ($\frac{\partial U}{\partial x} \approx 1.5$ eV), the amount of thermally exchangeable Li sites near the Fermi level is very small ($\Delta x_{\text{exchange}} = \frac{RT}{F \cdot \frac{\partial U}{\partial x}} = 1.7\%$). We do

therefore not expect any significant contributions from the configurational entropy in our system. Another important consideration is the fact that there is a path dependence of $\frac{dS}{d\xi}(\xi)$ vs SOC, which vanishes as a function of OCV. This means that the entropy is a function of the OCV (= chemical potential of the LMR-NCM) and not directly of the amount of Li in the structure, which we would expect in case of a dominating configurational entropy. The broadness of the peak in the $\frac{dS}{d\xi}(\xi)$ curve can be explained by a continuous modification of the LMR-NCM structure during (de-)lithiation, which is proven by XRD measurements.^{5,6} The ongoing change in the chemical potential of lithium entering the host lattice during discharge (and leaving the CAM during charge) might lead to a smearing out of any contributions from configurational entropy in contrast to the situation of an ideal solid solution where all Li sites are energetically equal leading to distinct curve features from configurational entropy. Another reason why the contribution from the configurational entropy might not be visible is that the overlithiation of the LMR-NCM and hence the removal of Li from the transition metal layer might lead to the formation of domains with only a limited amount of Li vacancies. This would effectively suppress the distributional variability of Li ions over the host lattice and reduce the configurational entropy of the whole structure. In support of this argument, it was reported in the literature that the overlithiation of LiCoO₂⁵¹ and Li₂Mn₂O₄^{13,14} reduces the characteristic features of the configurational entropy by the formation of pinned Li in the host structure.

Discussion of the vibrational entropy.—The vibrational entropy was introduced in theory section above and was reported to give a constant offset.²⁰ In the case of LMR-NCM, where we observe a hysteretic behavior and a lack of typical fingerprints of configurational entropy, it is worth to discuss the possible influence of the vibrational entropy. Heubner et al.,⁵² who also observed a peak in the entropy profile of their active material NaFePO₄ followed by a flat behavior with increasing SOC, speculated that contributions from vibrational entropy are possible. For LMR-NCM, owing to the low mass of Li, any confined movement within the Li layer should lead to rather high frequency vibrations and is thus not expected to be active at ambient temperature. Therefore, any change of vibrational entropy in the LMR-NCM must be caused by the host lattice itself. It is conceivable that low-frequency translational vibronic

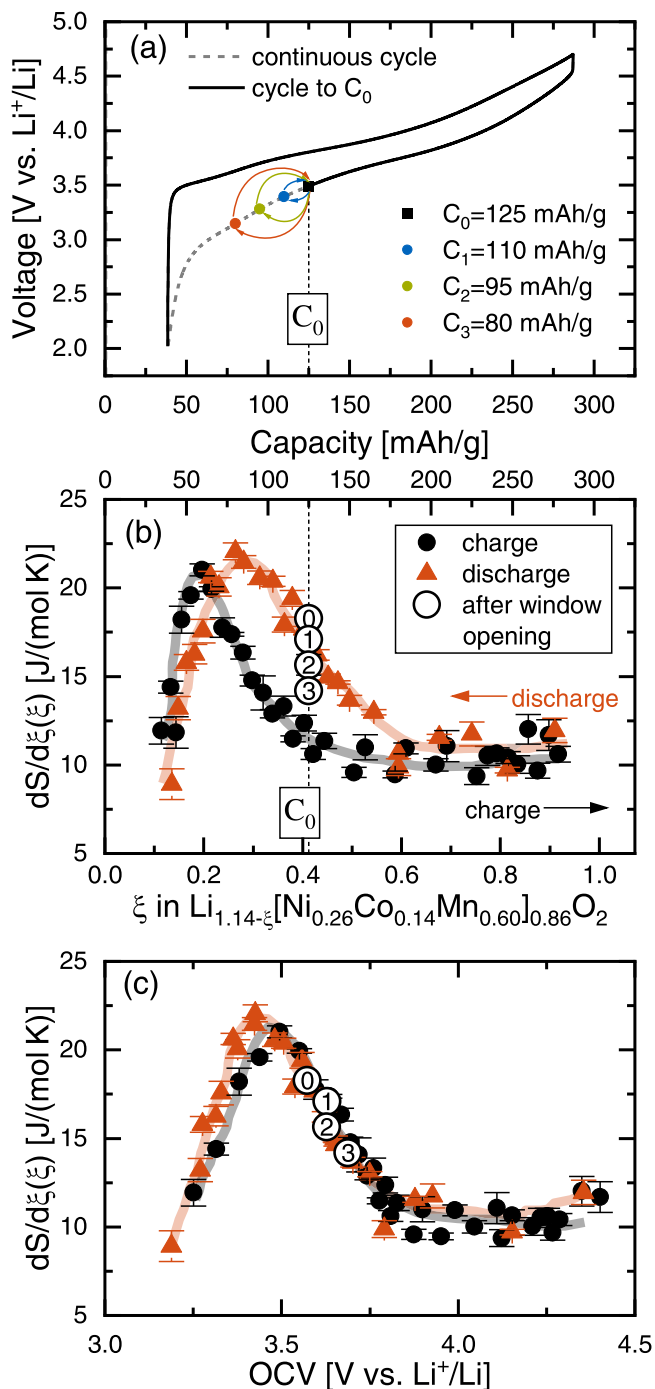


Figure 5. Results from window-opening experiments in discharge direction for 0.33 LMR-NCM/Li cells after activation/stabilization. (a) The voltage curve for the 4th cycle with a continuous cycle indicated by the gray dashed line and the charge/discharge procedure prior to the window-opening marked by the black line. The window-opening loops from the reference point C₀ to the turning points C₁–C₃ are indicated by colored arrows; (b) partial molar entropy during charge (black circles, same data as in Fig. 4) and discharge (orange triangles, same data as in Fig. 4) with trendlines as a function of capacity (upper x-axis) or reaction turnover (lower x-axis); (c) same data as a function of OCV. **Measurement procedure:** (i) after activation/stabilization, cells were charged to 4.7 V and discharged to an absolute capacity of 125 mAh g⁻¹ (C₀) at C/10 and 25 °C; (ii) subsequently, cells were discharged to either C₁ = 110 mAh g⁻¹, C₂ = 95 mAh g⁻¹ or C₃ = 85 mAh g⁻¹ and then charged again to C₀ (all at C/10 and 25 °C); (iii) at C₀, the cells were allowed to rest until the change in OCV was less than ≈ 0.2 mV h⁻¹, after which the cell-TD-OCV was determined. The resulting partial molar entropy data points from the window-opening are labeled according to their maximum discharge capacity window (C₀≡⊙, C₁≡⊖, C₂≡⊗, C₃≡⊕).

modes of the host lattice will be disturbed or suppressed by the presence of Li ions. Possible scenarios are disruptions of vibrations by dislocations of lattice chains, which can be caused by Li (de-) intercalation and its influence on the interlayer distance, transition metal migration, and the formation of clusters. Another reason is a change in the stiffness⁵³ of the host lattice, e.g. by oxidation/reduction of the transition metals or by oxygen redox. In any case, the vibrational entropy is expected to be a function of the energetic state and structure of the host lattice. From XRD studies, it is already known that the LMR-NCM structure changes as a function of OCV and shows a hysteresis as a function of SOC^{5,6}—similar to what is observed for the partial molar entropy. This is why it is reasonable to assume that the entropy profile of LMR-NCM is dominated by changes in the vibrational entropy of the host lattice (expected to be a function of OCV) rather than configurational entropy of the Li atoms in the structure (expected to be a function of SOC).

Typically, a peak in the $\frac{\partial S}{\partial \xi}(\xi)$ profile is correlated to a phase transition.^{54,55} For example, McKinnon et al.⁵⁶ found a broad peak in the entropy profile of Li_xMo₆Se₈ around $x = 2.8$, which they ascribed to the phase transition between the triclinic and the rhombohedral state. They also report a peak in the dQ/dV at the same SOC. Interestingly, they also observe a shift of the peak between charge and discharge direction, translating to a shift in the respective phase boundaries. A broad peak as observed for LMR-NCM is typically ascribed to a second order phase transition. Any phase transition in the electrode should be driven by the chemical potential and should therefore correlate with the OCV, as is the case here. It is therefore conceivable that at an OCV of ≈ 3.5 V (Fig. 4c), the LMR-NCM is transformed in a way that gives rise to the observable peak in the entropy profile. However, it needs to be stressed that what we propose here is no structural phase transition in terms of two crystallographically different symmetries, for which diffraction studies clearly give no evidence.^{5,6} We rather assume an energetic difference between the two phases, similar to what was proposed by Assat et al.⁵⁷ The description of the LMR-NCM structure in terms of energetically different domains was already discussed in the context with impedance measurements, where an asymmetry between the area-specific impedance of LMR-NCM during charge and discharge and an anomalous rise at low SOC during discharge is observed.^{1–3} This path dependence of the impedance shows some similarity with the entropy shown in Fig. 4. Chen et al.² ascribe this phenomenon to bulk rather than interfacial processes within LMR-NCM. They propose that the activated LMR-NCM can be viewed by a percolating network of layered-type, ordered domains with facile Li diffusion, interspersed with disordered domains, which have significantly higher barriers for Li diffusion. Once the layered sites are filled upon discharge, mostly sites in disordered domains remain that represent a considerable barrier for Li diffusion and cause the observable rise in the impedance. Gowda et al.³ follow a similar line of argumentation by describing the LMR-NCM as a nano-composite of Ni- and Co-rich domains with facile Li diffusion and Li- and Mn-rich domains with sluggish Li diffusion. At this point, we want to make clear that we differentiate between the “phase transition” itself and the process causing its path dependence (and the other hysteresis phenomena) as a function of SOC.

Window-opening experiments.—Before we discuss the window-opening experiments, we will briefly summarize the definitions to describe hysteretic phenomena, as for instance summarized by Neumann.⁴³ Hysteresis loops indicate process pathways along thermodynamically metastable states, which are separated by energy barriers from lower equilibrium states. Referring to the CAM in our study, these can in the simplest case originate from interactions between Li ions but may also involve more complicated interactions with the host lattice, for example via charge compensating redox mechanisms. In the latter case, cooperative effects, including domain-like structures, may effectively hinder transitions to the

equilibrium state. Such high energy barriers can be overcome, however, by supplying external energy (e.g. by charging/discharging) whereby the system reaches regions with lower barriers via metastable pathways. There, a relaxation to the more stable state finally occurs, which, if it is sufficiently exothermic, is unidirectional and quasi irreversible. If the process is reversed (e.g. on discharge), the system will return to the initial state along a different metastable pathway, which eventually crosses the initial path. Here again, energy barriers will prevent immediate joining with the initial pathway before the barrier becomes small enough for the backwards relaxation. When the associated interaction domains are not uniform, e.g. because of size or local composition, the energies and barriers contributing to the overall hysteresis pathways will vary accordingly. Then, transitions between both hysteresis branches will not occur uniformly but will be spread throughout the hysteresis loop, which will be a composite of a distribution of individual hysteresis loops. These can be explored with so-called scanning curves, which can give insights into the arrangement of the energy barriers. As long as external perturbations are restricted to regions of metastability, the behavior of a domain is apparently reversible but as soon as the external changes proceed beyond the point, at which the energy barriers can be overcome, a relaxation occurs, which causes the domain to remain in the new stable state even if the original external conditions are re-established. It needs to be stressed here, that when we use the words “equilibration” or “domain” we do not refer to actual crystallographic phase changes and domains (for which there is no evidence), but rather use the general concept of hysteresis and apply it to the situation in LMR-NCM cathode active materials. Thereby, “equilibration” describes all changes in the LMR-NCM phase upon (de-)lithiation (e.g. structural, energetic, ordering, etc.) and ‘domain’ characterizes a structural unit or region in the LMR-NCM (e.g. primary particles, individual crystallites, etc.), which is considered homogeneous, meaning that its elemental units change their state cooperatively.

For 0.33 LMR-NCM/Li cells, the analysis of scanning curves within the hysteresis loop is done by conducting so-called window-opening experiments, in which starting from a certain SOC point, the charge (or discharge) SOC window is sequentially opened. Croy and co-workers have already found a gradual opening of the OCV hysteresis loop for LMR-NCM materials when conducting window-opening experiments.^{44,58} In a similar manner, we investigated the path dependence of the entropy in the discharge branch of the hysteresis. As shown in Fig. 5a, this was accomplished by the following protocol: After the activation and two stabilization cycles (not shown), another C/10 charge up to 4.7 V was conducted, followed by a C/10 discharge (black line) to an absolute capacity of $C_0 = 125 \text{ mAh g}^{-1}$ (black symbol). After relaxation in OCV (until the change in OCV was less than $\approx 0.2 \text{ mV h}^{-1}$), the TD-OCV was measured at this reference point. It is marked with a \odot in Figs. 5b and 5c. Starting from the reference capacity C_0 , discharge-charge loops (window-opening loops, indicated by the colored arrows in Fig. 5a) were conducted with identical cells. After the respective turning points (marked by colored symbols in Fig. 5a) at absolute capacity values of $C_1 = 110 \text{ mAh g}^{-1}$ (blue), $C_2 = 95 \text{ mAh g}^{-1}$ (green), $C_3 = 80 \text{ mAh g}^{-1}$ (orange), the cells were again charged back to C_0 (without any OCV phase in between). There, the cells were allowed to rest in OCV until the change in OCV was less than $\approx 0.2 \text{ mV h}^{-1}$, before the TD-OCV was measured after each window cycle at the same C_0 and compared to that measured during a normal discharge (data point \odot , without previous discharge/charge loops).

Figures 5b and 5c show the entropy data from the window-opening experiment together with the partial molar entropy curves from Fig. 4. When the SOC window is only opened up to point C_1 , the entropy measured at the reference point C_0 has not changed (data point marked by \odot). However, if the SOC window is opened further to point C_2 and C_3 , the entropy measured at C_0 increases and moves towards the entropy curve for charge (\odot and \ominus in Fig. 5b). At the same time, the respective OCV increases as shown in Fig. 5c. Thus,

the relaxations, which gradually close the hysteresis curve during discharge start below $\approx 110 \text{ mAh g}^{-1}$. The further the cell is discharged below this point, the more domains can overcome their individual barriers and remain in the relaxed state with its corresponding entropy and OCV, even if the cell is recharged back to the reference capacity (C_0). This is in agreement with literature reports on the OCV hysteresis^{44,58} and the hysteresis of lattice parameters.^{5,6} For example, Croy et al.,⁴⁴ found that the voltage hysteresis upon discharge in the range between 4.6 V (translates to $\xi \approx 0.96$ in our case) and 3.8 V ($\xi \approx 0.66$) is almost non-existent, but gradually grows when the window is further opened up to 3.3 V ($\xi \approx 0.24$). Also, Teufl et al.,¹ report on an increasing path dependence of the resistance with increasing upper cutoff voltage during charge. Figure S8 in the Supporting Information shows a window-opening experiment during charge, which was conducted in a similar manner as the one shown in Fig. 5 (procedure explained in the SI). Starting at an SOC of $C_0 = 100 \text{ mAh g}^{-1}$, charge-discharge loops to increasing upper cut-offs were conducted. The entropy and OCV measured after reaching C_0 again indicate that the relaxation processes during charge occur when the cell is charged above $\approx 150 \text{ mAh g}^{-1}$.

We can conclude that on the metastable pathways of the hysteresis loop, the LMR-NCM material can behave quasi-reversible in some sections, and endure irreversible relaxations in other sections. The nature of the energy barriers in LMR-NCM cannot be clarified by the applied entropy measurement. Instead, we observe the effect that the hysteresis has on the entropy profile, namely a path-dependence of the entropy curve vs SOC between charge and discharge. We want to stress once more that the peak in the 0.33 LMR-NCM/Li entropy curve, which might indicate a second order phase transition, must be regarded as another phenomenon.

Entropy and reversible heat in LMR-NCM.—The integral of the charge or discharge voltage curve over the SOC corresponds to the electrical energy applied during charge and gained during discharge. The difference of both corresponds to the energy loss in form of heat over a complete cycle. The irreversible heat (Q_{irrev}) due to charge transfer and mass transport overpotential losses leads to a difference between the potential E at an applied current I and the equilibrium potential E_0 at OCV conditions. In Fig. 3, Q_{irrev} corresponds to the area between the black line (voltage while applying a current) and the blue line (OCV curve). The irreversible heat scales with the applied current and is always exothermic. The energy loss corresponding to the OCV hysteresis (blue area in Fig. 3) is independent of the applied current (see Fig. S6 in the SI). The description of this heat term is not trivial and will be the focus of a different study.⁵⁹ Additionally, heat can be released and absorbed reversibly because of entropic changes in the battery. In contrast to the other sources of heat, this cannot be derived from the voltage curve. The reversible heat generation, Q_{rev} , is a function of the partial molar entropy and the temperature. For a reversible process, Q_{rev} is obtained by:

$$Q_{\text{rev}} = \int T \cdot \left(\frac{dS}{d\xi}(\xi) \right) \cdot d\xi \quad [16]$$

In the case of LMR-NCM, however, ξ does not describe the charge/discharge processes unambiguously. Particularly, at the same ξ , the CAM can have two different structures evidenced by the observed differences in lattice parameters^{5,6} and atomic distances.⁷ The OCV hysteresis furthermore underlines that the re-entrant Li environment during discharge is energetically different from that during charge.^{4,46} In fact, it is known that hysteretic processes follow metastable paths away from the thermodynamic equilibrium.^{43,60} The measurement of the cell-TD-OCV, however, can only trace the chemical potential along the accessible metastable pathway. In case of the LMR-NCM, frustrated structural relaxations might induce this metastability. In the course of the hysteresis loop, some of the energetic barriers to equilibrium may eventually sink so that irreversible relaxations can partially or locally restore equilibrium

and release structural or chemical energy. In a closed cycle, all the additionally produced entropy eventually has to be transferred to the surrounding in order to ensure entropy conversion. This entropy transfer does not necessarily occur immediately, as long as it does not arrive at motional degrees of freedom leading to a temperature increase. It can happen later during further progress of charging or discharging. Under isothermal conditions, the entropy will be transferred in a reversible act and so structural or chemical energy is finally carried to the surroundings in form of heat. The total entropy change of the system, dS_{sys} , for materials with a pronounced hysteresis can thus be written as:

$$dS_{\text{sys}} = dS_{\text{equi}} + dS_{\text{int,prod}} \quad [17]$$

dS_{equi} is the entropy change of the system, if it were in equilibrium and could reversibly exchange heat with the surroundings. The corresponding reversible heat is calculated based on integrating dS_{equi} according to Eq. 16. Since entropy is a state function, it is conserved for reversible processes, meaning that $\oint dS_{\text{equi}} = 0$. For LMR-NCM, another term is required, which describes the internal entropy production, $dS_{\text{int,prod}}$.^{43,57,60} This is the additional entropy change of the system, which occurs due to redistribution of energy during structural relaxation. Such relaxations bring any hysteretic deviations of the state functions closer to equilibrium and internally “produce” entropy. Experimentally, only the total entropy change of the system, dS_{sys} , is accessible and we do not know, how large dS_{equi} actually is. It should, however, not suffer from hysteresis and should thus be the same for charging and discharging (with opposite sign) and be zero when a complete cycle is considered. Due to the

additional term of $dS_{\text{int,prod}}$ in case of LMR-NCM, a cyclic integral over the measured partial molar entropy will, however, not be zero but be a measure of the internal entropy production within a complete cycle. Interpretation of this integral requires a bit of care. For clarity, we split the integration of the measured partial molar entropy of LMR-NCM in two parts. The integration of $\frac{dS}{d\xi}(\xi)$ over ξ gives $\approx +10.0 \text{ J (mol K}^{-1})$ for the charge and $\approx -11.2 \text{ J (mol K}^{-1})$ for the discharge process (for $0.11 \leq \xi \leq 0.91$; $d\xi > 0$ for charge and $d\xi < 0$ for discharge). The observed difference is a measure of the internal entropy production. It is surprising that the cyclic integral over the whole charge/discharge process gives has negative sign although entropy production is expected to be positive. The observed difference can hence not solely be explained by irreversible processes with entropy change being strictly positive. The formation of products with lower entropy during charge or higher entropy during discharge could explain this unusual observation. It is well known that LMR-NCM suffers from ongoing voltage decay^{61,62} which is proposed to be caused by progressive irreversible TM migration^{61,63} possibly coupled to oxygen redox⁴⁵ and even oxygen vacancies.⁶⁴ Moreover, the formation of an oxygen depleted surface layer is reported to cause capacity fading over cycling.⁵¹ For such structural transformations, the sign of the entropy change is not known and they might hence explain the observed negative value. A contribution of entropy production (with positive sign) can nevertheless not be excluded. The observed difference between the charge and discharge entropy curve needs to be interpreted with care since we have to consider, how reliable the determination of $\frac{dS}{d\xi}(\xi)$ is. We are confident that the observed shift between the charge and the

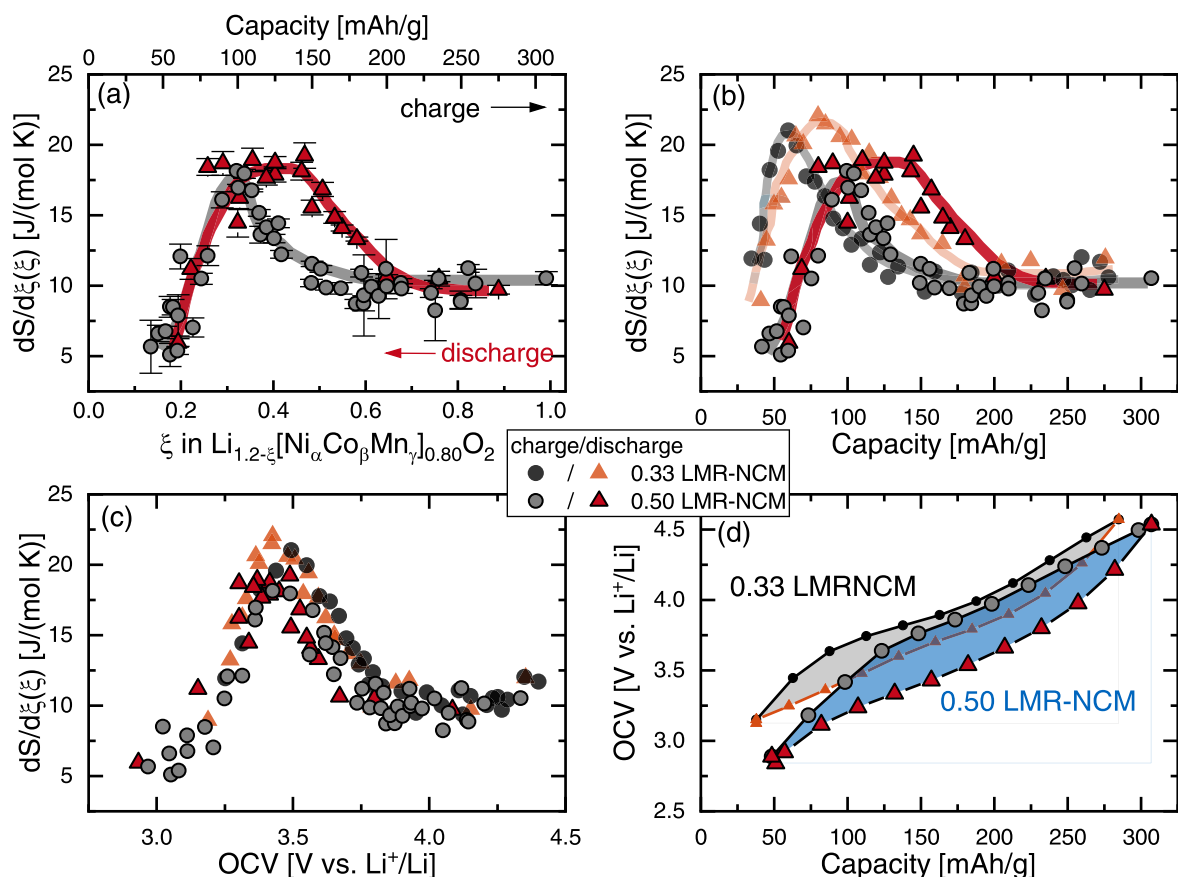


Figure 6. (a) Partial molar entropy data and trendlines (as guide for the eye) vs capacity (upper x-axis) or ξ (lower x-axis) of 0.50 LMR-NCM/Li cells during charge (gray circles) and discharge (red triangles) after one activation and two stabilization cycles. (b) Comparison of $\frac{dS}{d\xi}(\xi)$ vs capacity for 0.50 LMR-NCM/Li (same color code as in panel a) and for 0.33 LMR-NCM/Li cells (black circles for charge, orange triangles for discharge; same data as in Fig. 4b), with error bars removed for clarity. (c) Comparison of the same $\frac{dS}{d\xi}(\xi)$ data but plotted as a function of OCV. (d) OCV curves comparing the OCV hysteresis of 0.50 LMR-NCM/Li (blue) and 0.33 LMR-NCM/Li cells (gray; same data as in Fig. 3) at C/10 (25 °C) after activation and two stabilization cycles.

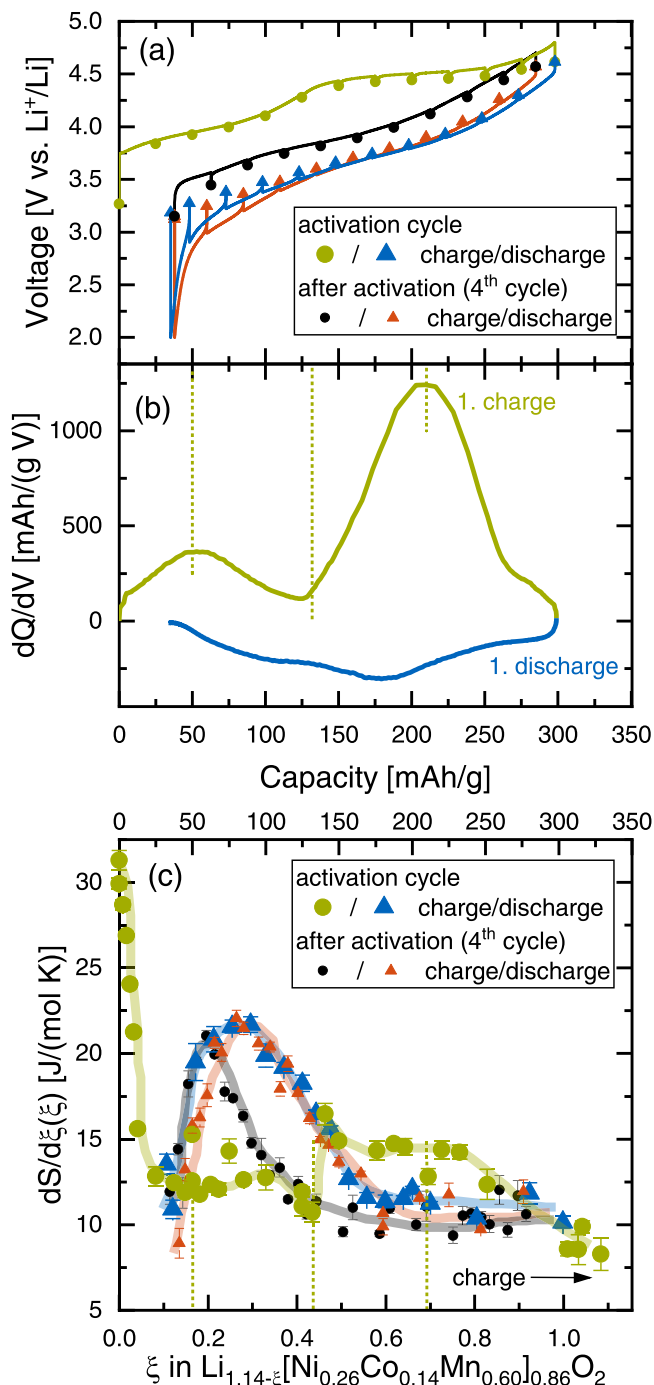


Figure 7. Comparison of voltage and partial molar entropy vs capacity curves during activation and after activation/stabilization (4th cycle) of 0.33 LMR-NCM/Li cells with trendlines as guides for the eye (all at 25 °C): (a) voltage curves with OCV points of the activation cycle at C/15 (charge in green, discharge in blue) and of the 4th cycle (C/10, charge in black, discharge in orange); (b) dQ/dV plot of the activation of a LMR-NCM/Li cell at C/15; (c) partial molar entropy values during charge (circles) and discharge (triangles) in the activation cycle (green/blue) and the 4th cycle (black/orange) as a function of capacity (upper x-axis) and ξ (lower x-axis). The dashed vertical lines highlight common features in the different plots.

discharge entropy curves is true. The shift, however, is not the reason for the observed difference. Instead, the peak of the $\frac{dS}{d\xi}(\xi)$ curve during discharge is slightly broader than during charge. The difference between both only amounts to $\approx 10\%$ of the absolute values. Considering the pronounced scatter of the data points in

Fig. 4, the interpretation of this value requires a bit of care. In summary, we conclude that the calculation of the classical reversible heat according to Eq. 16 as a function of SOC is not applicable for materials with a pronounced hysteresis such as LMR-NCM since the measured entropy includes contributions from internal entropy production.

Effect of overlithiation on the entropy profile of LMR-NCM.—
Entropy profile of 0.50 LMR-NCM.—To further analyze the entropy of this type of CAMs, the measurements were repeated on an LMR-NCM with a higher degree of overlithiation. The standard material of this study was denoted as 0.33 LMR-NCM ($\text{Li}_{1.14}[\text{Ni}_{0.26}\text{Co}_{0.14}\text{Mn}_{0.60}]\text{O}_2$), while 0.50 LMR-NCM refers to the material with the higher Li content, with the overall stoichiometry of $\text{Li}_{1.20}[\text{TM}]_{0.80}\text{O}_2$. The nomenclature and stoichiometry are explained in the Experimental section. It was shown in the literature that the degree of overlithiation in LMR-NCM affects the electrochemical performance of this CAM class in terms of surface degradation and resistance build-up, but also with regards to the lattice parameters.^{6,31,58} As can be seen in Fig. 6d, the size of the OCV hysteresis loop increases with the degree of overlithiation. This is expressed in terms of a ≈ 1.5 -fold increase in the OCV hysteresis related energy loss over the same ΔSOC that is represented by the gray and blue shaded areas in Fig. 6d (45.5 mWh g^{-1} vs 69.2 mWh g^{-1}), caused by a ≈ 1.5 -fold increase in the ΔSOC averaged mean voltage difference between the charge and discharge OCV curves (184 mV vs 268 mV ; obtained by dividing the OCV hysteresis energy by the ΔSOC window of 247 mAh g^{-1} for 0.33 LMR-NCM and 259 mAh g^{-1} for 0.50 LMR-NCM).

Figure 6a shows the $\frac{\partial S}{\partial \xi}(\xi)$ vs SOC (and ξ) profile of 0.50 LMR-NCM/Li cells, obtained from cell-TD-OCV measurements after one activation and two stabilization cycles. Similar to the curves of the 0.33 LMR-NCM/Li (see Fig. 4b), there is a path dependence of the partial molar entropy between charge and discharge, with a peak around $\xi \approx 0.3$ during charge and a broader peak at $\xi \approx 0.4$ during discharge. In Fig. 6b, the $\frac{\partial S}{\partial \xi}(\xi)$ profiles of LMR-NCM/Li cells with either 0.33 LMR-NCM or 0.50 LMR-NCM are contrasted. To enable a comparison of the two materials on the SOC scale, the data are shown as a function of capacity rather than extent of reaction because ξ was defined relative to the total amount of Li, which differs for both materials. The most remarkable difference between the partial molar entropy profiles of the LMR-NCM materials in Fig. 6b is the shift of the partial molar entropy peaks in both charge and discharge to higher SOC values for the 0.50 LMR-NCM (gray and red symbols) compared to the 0.33 LMR-NCM (black and orange symbols); hereby, only the positions of the peak maxima are shifted, while the partial molar entropy values to the right of the peaks (i.e., at higher SOC) become practically identical for both materials in both the charge and the discharge direction. Moreover, the peak maxima of the 0.50 LMR-NCM are lower by an absolute value of $\approx 4 \text{ J/(mol K)}$. Both materials have in common that their discharge peaks are rather broad in comparison to the respective charge peaks and that the partial molar entropy values reach the same plateau values at high degrees of delithiation. The path dependence expressed in terms of peak shifting between charge and discharge is very similar for both materials with $\Delta\text{SOC} \approx 23 \text{ mAh/g}$ ($\approx 6.1\%$ of the total Li amount in $\text{Li}_{1.20}[\text{TM}]_{0.80}\text{O}_2$) for the 0.50 LMR-NCM and $\Delta\text{SOC} \approx 22 \text{ mAh g}^{-1}$ ($\approx 6.4\%$ referenced to $\text{Li}_{1.14}[\text{TM}]_{0.86}\text{O}_2$) for the 0.33 LMR-NCM. From the increased OCV hysteresis loop of the 0.50 LMR-NCM, shown in Fig. 6d, one might have expected that the partial molar entropy profile of this material would show a considerably larger peak shift, which is not the case. Interestingly, when plotted as a function of OCV, as is shown in Fig. 6c, the partial molar entropy profiles in charge and discharge for both materials superimpose aside from the smaller peak heights for the 0.50 LMR-NCM. This means that not only the material specific path dependence has vanished vs OCV but also the difference

between the materials. We conclude that although the OCV hysteresis curves of these materials are different (see Fig. 6d), the entropy profiles coincide when considered as a function of OCV.

Indications for vibrational entropy.—As discussed above, the changes in vibrational entropy are expected to be a function of the OCV and not of the SOC, whereas the configurational entropy should be a function of ξ and hence of the SOC. The fact that the differences in the partial molar entropy profiles between the two LMR-NCM materials plotted vs SOC vanish when they are plotted as a function of OCV suggests that independent of the apparent SOC, the OCV is the actual descriptor of the electrochemical state of the material. In other words, when two LMR-NCM materials are considered to be at the same OCV, they might have a different amount of Li, which can be distributed over the available Li sites, but nevertheless they have the same value for $\frac{dS}{d\xi}(\xi)$. This is another strong indicator that what we observe in the $\frac{dS}{d\xi}(\xi)$ curve cannot be dominated by the configurational entropy but rather by the vibrational entropy of the host lattice. From a theoretical point of view, a thorough simulation of the LMR-NCM structure at different SOCs and the respective derivation of vibrational density of states could shed more light on this issue.

Partial molar entropy during the first-charge activation of LMR-NCM.—*Partial molar entropy of LMR-NCM before and after activation.*—For LMR-NCM cathode active materials, it is well known that during the first charge a so-called activation process occurs, during which oxygen is released from the material^{31,65} and irreversible structural changes^{45,66} occur, including transition metal migration, oxygen redox, and the loss of a honeycomb ordering. These irreversible processes lead to a unique first charge voltage curve and also cause the cell resistance¹ and the lattice parameters⁶ to differ from that of the following cycles. Hence, we also expect a unique partial molar entropy profile during the activation of LMR-NCM. In Fig. 7a, the voltage profile of the first activation cycle is compared to that of the 4th cycle, where all other entropy measurements were typically conducted. In addition to an initial voltage plateau around ≈ 4 V, the first charge curve exhibits a characteristic second plateau at ≈ 4.5 V (green line). Both features become more obvious from the corresponding peaks in the dQ/dV plot in Fig. 7b (green line). In contrast, the first discharge (blue line in Fig. 7a) resembles all following discharge curves after activation, as represented by the 4th cycle (orange line).

In Fig. 7c, the partial molar entropy changes during activation are compared to those after activation (measured in the 4th cycle, as shown in Fig. 4). The entropy curve in the first activation charge (green circles) is completely different from that obtained during the charge of a cell after activation/stabilization (black circles). At the beginning of the first charge ($\xi = 0$), the most positive partial molar entropy is observed, decreasing in a pole-like feature which levels off to a value of ≈ 12 J (mol K⁻¹) at ≈ 50 mAh g⁻¹. This transition point coincides with the first maximum in the dQ/dV plot (marked by the first set of vertical green dashed lines in Fig. 7), i.e., in the mid-point of the first voltage plateau. At a capacity of ≈ 130 mAh g⁻¹, a double pole feature is observed, first going down and then switching to a second pole coming from more positive values of $\frac{dS}{d\xi}(\xi)$. This feature coincides with the transition to the second voltage plateau that is marked by the minimum in the dQ/dV plot in Fig. 7b (second set of green dashed lines in Fig. 7). Subsequently, the $\frac{dS}{d\xi}(\xi)$ profile remains rather flat in the SOC range around ≈ 200 mAh g⁻¹, where another dQ/dV maximum occurs marking the middle of the second voltage plateau (third set of green dashed lines in Fig. 7). Starting at ≈ 250 mAh g⁻¹, $\frac{dS}{d\xi}(\xi)$ gradually decreases to ≈ 8 J (mol K⁻¹) at the end of charge. During the first activation charge, there is no indication of the prominent broad peak at $\xi \approx 0.2$ seen during

charging of LMR-NCM after activation (black circles/lines in Fig. 7c).

In contrast to these striking differences observed during charge, there is no considerable difference between the entropy curve of the first and the 4th discharge (blue and orange symbols in Fig. 7b), in accordance to the associated voltage curves (see Fig. 7a). Window opening experiments in the activation charge show the same trend as was found for the LMR-NCM/Li cells after the initial activation/stabilization cycles. In Fig. S9 in the SI it can be seen that, when the charge window is gradually opened, the entropy values measured at a reference capacity point ($C_0 = 75$ mAh g⁻¹) subsequently change and shift from the first charge profile to that of the first discharge profile.

Although the entropy data of Shi et al.⁴⁸ obtained after the initial activation/stabilization cycles differ from ours, as already noted, they likewise observe significant differences between the entropy profiles during the first charge and the following charge cycles. In their data, the peak at low SOC during charge is also missing during activation, whereas during discharge they see a comparable curve shape as in their following cycles including a peak-like feature at low SOCs.

Configurational entropy during the first charge of LMR-NCM.—In the following we will put our results into context with literature reports that have investigated the activation process in this type of materials with other methods. The positive pole in the $\frac{dS}{d\xi}(\xi)$ curve near $\xi = 0$ (green circles in Fig. 7c) is a typical and strong indication of emerging configurational freedom of Li in the host lattice after the first empty Li-sites become available. In such a case, one expects a typical S-shaped $\frac{dS}{d\xi}(\xi)$ dependence.^{13–15} The corresponding negative pole might appear at $\xi \approx 0.4$ back to back with a second positive pole. A closing negative pole expected from the last exchangeable Li emanating from the host sites appears only in outlines beyond $\xi > 0.9$, if at all. The back to back pole pairs reflect switching between pools of energetically equivalent sites similar to what is reported for the two sub-lattice model^{13–15} mentioned above. Such a discontinuity in the entropy curve at $\xi \approx 0.4$ might be caused by a sufficiently high difference in the interaction energy of the Li with the two sites,¹⁵ which would be consistent with the observations that the mid-points of the low and high voltage plateau, as indicated by the maxima in the dQ/dV plot, differ by ≈ 0.5 V (first and last set of the green dashed lines in Figs. 7b and 7c). The discontinuity could, in principle, also be caused by pronounced repulsive nearest neighbor interactions.¹³ In contrast to the succeeding cycles, where no sign of configurational entropy was found, entropy data of the first charge give strong evidence for free Li exchange between sites being cleared in two consecutive voltage steps. A significant amount of Li sites are therefore energetically equivalent (within thermal energy) between $\xi \approx 0$ and $\xi \approx 0.4$, at which point a second pool of energetically equivalent sites starts to allow for Li exchange. Since there is no clear signature of a final negative pole at high SOC, it cannot be specified up to which values of ξ this exchange persists. Two successive pools of energetically equivalent sites would also be in agreement with the two characteristic plateaus in the first charge voltage profile. Both findings suggest that the delithiation actuates (at least) two different charge compensation mechanisms.^{50,66,67}

During the initial plateau associated with the first peak in the dQ/dV plot, cationic oxidation of Ni and Co occurs. This process is the same as for classical layered transition metal oxide cathodes. When LMR-NCM cathodes are only cycled within this limited SOC range ($\xi < 0.4$), they behave like stoichiometrically lithiated NCMs, meaning that the hysteresis of the voltage,⁴⁴ of the lattice parameters,⁶ and the resistance¹ is minor. Likewise, the entropy profile of LMR-NCM in this first region, also resembles those observed for regular NCMs.^{9,48} Window-opening experiments during the first charge (Figure S9 in the SI) show that the entropy

profile is maintained and is not path dependent as long as the material is not cycled beyond $\xi \approx 0.4$.

In contrast to the initial low-voltage plateau of the activation process, the subsequent high-voltage plateau is reported to include irreversible changes within the LMR-NCM such as O-redox occurring together with TM migration and the removal of Li from the TM layer.^{50,66–68} The oxidation of O^{2-} is reported to be mostly reversible for the bulk oxygen,^{45,66,67} at the surface, however, O_2 is irreversibly lost from the structure.⁶⁵ On charging across the high-voltage plateau, the in-plane honeycomb superstructure ordering of the TMs is irreversibly lost.^{45,66} A coupling between TM migration and bulk anionic redox is discussed in the literature.^{45,66} The fact that the activation charge of LMR-NCM proceeds via two different charge compensation steps, of which the first is reversible while during the second step the LMR-NCM structure is permanently modified, is a strong indication that the interpretation of the corresponding entropy curve with two pools of energetically equivalent sites is valid. As mentioned above, we do not propose two crystallographically different sub-lattices, but rather two energetically different Li deintercalation processes. The contributions of the configurational entropy during the first charge seem to be responsible for the observed entropy curve features (on the order of $\pm 2 \text{ J (mol K}^{-1}\text{)}$), but the entropy offset of $-12 \text{ J (mol K}^{-1}\text{)}$ is not related to configurational contributions.

In contrast to the unique entropy curve upon the first activation charge, there is no considerable difference between the entropy curve of the first and the 4th discharge, which also reflects the behavior of the voltage curves. This means that the (de-)intercalation processes within the LMR-NCM material during the first charge differ significantly from those of the first discharge and of all consecutive cycles. The fact that the features from the configurational entropy are no longer observable in the first discharge indicates that the model of two pools of energetically equivalent Li sites is no longer appropriate to describe the Li (de-)intercalation process. Apparently, the distributional variability of Li among empty lattice sites is effectively hindered. From the literature it is known that the LMR-NCM structure is permanently modified during the activation process. Although the bulk anionic redox is continuously reversed upon discharge, the reordering of the TM layer is not possible and the honeycomb superstructure is lost, which changes the coordination environment around the oxygen.^{45,66} Furthermore, NMR studies show that, in the fully discharged state, the local environment of Li is different from that of the pristine state, revealing a much higher degree of disorder in the TMs surrounding the Li.⁶⁶ These irreversible structural modifications lead to a permanently lowered voltage profile upon subsequent cycling, with an increased slope as compared to the first charge voltage curve^{45,67} and to a smaller peak amplitude in the respective dQ/dV plots (compare Figs. 7b and 4b). As a consequence, the Li sites are energetically wider dispersed, which reduces the configurational freedom of Li within the lattice and hence blurs any features from configurational entropy leaving back the more dominant contribution from the vibrational entropy. Whether the processes which are responsible for the observed disappearance of the configurational entropy are also responsible for the hysteretic behavior of the LMR-NCM remains an open question. Qiu et al.⁶⁹ recently reported that after activation, the pristine state of LMR-NCM cannot be recovered by normal cycling but they demonstrated that the structure of cycled LMR-NCM can be driven close to the original pristine state by heat treatment. For this purpose, they harvested CAM after 50 regular cycles, heat treated the material at up to $300 \text{ }^\circ\text{C}$ and built new cells with the heat treated CAM.⁶⁹ They observe a reappearance of the plateau region at $\approx 4.5 \text{ V}$ in the voltage vs capacity plot, which they ascribe to the lithium ion reinsertion into the TM layer and the reduction of stacking faults and microstrain.⁶⁹ It would be very interesting to investigate if a heat treatment of the LMR-NCM after activation also leads to a recovery of the partial molar entropy curve

from the first charge including the fingerprints from configurational entropy.

Conclusions

The partial molar entropy changes $\frac{dS}{d\xi}(\xi)$ of LMR-NCM/Li cells during lithium (de-)intercalation were investigated. To obtain $\frac{dS}{d\xi}(\xi)$, the OCV variation of the cell needs to be measured as a function of temperature. We evaluated the experimental methods applied so far and found that the widely implemented temperature step method is prone to measurement artefacts. Instead, we implemented a temperature ramp method, where the response of the OCV during a triangular wave variation of the cell temperature is measured. Effects from self-discharge, ongoing voltage relaxation and temperature history can thereby be minimized.

To distinguish between the contribution of the LMR-NCM and the Li electrode, the latter was first analyzed by means of spatially non-isothermal experiments. We have found that the contribution of Li ($\approx 1.1 \text{ mV K}^{-1}$) is in the same order of magnitude as the contribution of the cathode and only the difference between the two leads to the small values ($\approx -0.1 \text{ mV K}^{-1}$) observed for the LMR-NCM/Li cell under spatially isothermal conditions. Since we measure the OCV of LMR-NCM vs the Li reference electrode in all following experiments, we can assume that the contribution of Li is constant as a function of SOC and that all features observed in the $\frac{dS}{d\xi}(\xi)$ curve of LMR-NCM/Li cells originate from processes in the cathode.

The cathode active material in the focus of this study is LMR-NCM, which exhibits a unique hysteresis in the OCV. The resulting partial molar entropy curves of LMR-NCM/Li cells show no typical fingerprint features of the configurational entropy indicating that there is hardly any configurational freedom of Li within the LMR-NCM. In fact, from the steepness of the OCV curve, we do not expect to find enough exchangeable Li within the Li layers to contribute to configurational entropy. Instead, the entropy profile is dominated by the changes in the lattice entropy (vibrational entropy). We found a broad peak in the $\frac{dS}{d\xi}(\xi)$ curve, similar to a feature of a second order phase transition. Since diffraction studies have not reported any evidence for a second phase, we propose that there is no crystallographic phase transition but rather a change in the local ordering or the energetics of the lattice (e.g. lattice strain). We observed a hysteresis of the characteristic peak in the $\frac{dS}{d\xi}(\xi)$ curve as a function of SOC, which vanishes if mapped as a function of OCV revealing that the entropy changes in LMR-NCM are governed by the OCV and thus by the Gibbs free energy and not by the amount of Li in the structure (ξ). This trend was also observed for an LMR-NCM material with a higher degree of overlithiation. Clearly, ξ is no unique descriptor of the (de-)lithiation processes within LMR-NCM because at the same ξ , LMR-NCM has a different structure evidenced by OCV and $\frac{dS}{d\xi}(\xi)$ values. This means that the charge and discharge processes do not follow reversible pathways when a full cycle is considered, which was further shown by window-opening experiments. We conclude that the (de-)lithiation of LMR-NCM follows metastable paths away from thermodynamic equilibrium, as is common for hysteretic processes. In order to determine the reversible heat of a battery, the partial molar entropy curve is typically integrated. For LMR-NCM, this, however, also includes an additional term caused by internal entropy production.

In addition to the analysis of a reversible cycle (after activation and stabilization), the entropy profile of LMR-NCM/Li was also investigated during the first activation cycle. The resulting $\frac{dS}{d\xi}(\xi)$ curve obtained during the first charge differs significantly from that

of the first discharge and of subsequent cycles. We explain the observed curve features with changes in the configurational entropy according to a two sub-lattice model. Apparently, the material undergoes a permanent transformation during this activation, which diminishes the distributional variability of Li ions in the structure and hence blurs the contribution from the configurational entropy for all subsequent charge/discharge processes.

Our findings on hysteresis, the resonance feature detected in entropy and the observed dependence on OCV should stimulate and focus detailed investigations with other experimental methods on these features, which could lay the basis for extensive quantum chemical calculations.

Acknowledgments

This work was supported by BASF SE within its Battery Research Network. The authors want to thank Alexander Ogrodnik for his contributions to this manuscript.

ORCID

Franziska Friedrich  <https://orcid.org/0000-0001-9400-1212>
Hubert A. Gasteiger  <https://orcid.org/0000-0001-8199-8703>

References

1. T. Teufl, D. Pritzl, S. Solchenbach, H. A. Gasteiger, and M. A. Mendez, *J. Electrochem. Soc.*, **166**, A1275 (2019).
2. J. Chen, A. Gutierrez, M. T. Saray, R. S. Yassar, M. Balasubramanian, Y. Wang, and J. R. Croy, *J. Electrochem. Soc.*, **168**, 080506 (2021).
3. S. R. Gowda, D. W. Dees, A. N. Jansen, and K. G. Gallagher, *J. Electrochem. Soc.*, **162**, A1374 (2015).
4. F. Dogan, B. R. Long, J. R. Croy, K. G. Gallagher, H. Iddir, J. T. Russell, M. Balasubramanian, and B. Key, *J. Am. Chem. Soc.*, **137**, 2328 (2015).
5. H. Konishi, T. Hirano, D. Takamatsu, A. Gunji, X. Feng, S. Furutsuki, T. Okumura, S. Terada, and K. Tamura, *J. Solid State Chem.*, **262**, 294 (2018).
6. B. Strehle, T. Zünd, S. Siculo, A. Kießling, V. Baran, and H. A. Gasteiger, *J. Electrochem. Soc.* (2021), In Press.
7. H. Koga, L. Croguennec, M. Ménétrier, P. Mannesiez, F. Weill, C. Delmas, and S. Belin, *J. Phys. Chem. C.*, **118**, 5700 (2014).
8. K. Maher and R. Yazami, *J. Power Sources*, **247**, 527 (2014).
9. E. Schuster, C. Ziebert, A. Melcher, M. Rohde, and H. J. Seifert, *J. Power Sources*, **286**, 580 (2015).
10. V. V. Viswanathan, D. Choi, D. Wang, W. Xu, S. Towne, R. E. Williford, J. G. Zhang, J. Liu, and Z. Yang, *J. Power Sources*, **195**, 3720 (2010).
11. A. Eddahech, O. Briat, and J. Vinassa, *Energy*, **61**, 432 (2013).
12. K. Takano, Y. Saito, K. Kanari, K. Nozaki, K. Kato, A. Negishi, and T. Kato, *J. Appl. Electrochem.*, **32**, 251 (2002).
13. S. Schlüter, R. Genieser, D. Richards, H. E. Hoster, and M. P. Mercer, *Phys. Chem. Chem. Phys.*, **20**, 21417 (2018).
14. M. P. Mercer, S. Finnigan, D. Kramer, D. Richards, and H. E. Hoster, *Electrochim. Acta*, **241**, 141 (2017).
15. E. P. M. Leiva, E. Perassi, and D. Barraco, *J. Electrochem. Soc.*, **164**, A6154 (2017).
16. T. Liebmann, C. Heubner, M. Schneider, and A. Michaelis, *J. Solid State Electrochem.*, **23**, 245 (2019).
17. M. Song, Y. Hu, S.-Y. Choe, and T. R. Garrick, *J. Electrochem. Soc.*, **167**, 120503 (2020).
18. K. Kai, Y. Kobayashi, H. Miyashiro, G. Oyama, S.-I. Nishimura, M. Okubo, and A. Yamada, *ChemPhysChem*, **15**, 2156 (2014).
19. S. L. Glazier, S. A. Odom, A. P. Kaur, and J. R. Dahn, *J. Electrochem. Soc.*, **165**, A3449 (2018).
20. Y. Reynier, J. Graetz, T. Swan-Wood, P. Rez, R. Yazami, and B. Fultz, *Phys. Rev. B*, **70**, 174304 (2004).
21. Y. Reynier, R. Yazami, and B. Fultz, *J. Power Sources*, **119–121**, 850 (2003).
22. X.-F. Zhang, Y. Zhao, Y. Patel, T. Zhang, W.-M. Liu, M. Chen, G. J. Offer, and Y. Yan, *Phys. Chem. Chem. Phys.*, **19**, 9833 (2017).
23. P. Gröndler, A. Kirbs, and L. Dunsch, *ChemPhysChem*, **10**, 1722 (2009).
24. J. R. Dahn and R. R. Haering, *Can. J. Phys.*, **61**, 1093 (1983).
25. A. Swiderska-Mocek, E. Rudnicka, and A. Lewandowski, *Phys. Chem. Chem. Phys.*, **21**, 2115 (2019).
26. A. J. DeBethune, T. S. Licht, and N. Swendeman, *J. Electrochem. Soc.*, **106**, 616 (1959).
27. J. L. Valdes and B. Miller, *J. Phys. Chem.*, **92**, 4483 (1988).
28. E. Maciá-Barber, *Thermoelectric Materials: Advances and Applications* (CRC Press, Boca Raton) (2015).
29. J. K. Platten, *J. Appl. Mech.*, **73**, 5 (2006).
30. M. A. Rahman and M. Z. Saghir, *Exp. Therm. Fluid Sci.*, **49**, 31 (2013).
31. T. Teufl, B. Strehle, P. Müller, H. A. Gasteiger, and M. A. Mendez, *J. Electrochem. Soc.*, **165**, A2718 (2018).
32. D. Schreiner, T. Zünd, F. J. Günter, L. Kraft, B. Stumper, F. Linsenmann, M. Schüller, R. Wilhelm, A. Jossen, G. Reinhart, and H. A. Gasteiger, *J. Electrochem. Soc.*, **168**, 030507 (2021).
33. S. Solchenbach, D. Pritzl, E. J. Y. Kong, J. Landesfeind, and H. A. Gasteiger, *J. Electrochem. Soc.*, **163**, A2265 (2016).
34. K. Jalkanen, T. Aho, and K. Vuorihehto, *J. Power Sources*, **243**, 354 (2013).
35. Y. Abdul-Quadir, T. Laurila, J. Karppinen, K. Jalkanen, K. Vuorihehto, L. Skogström, and M. Paulasto-Kröckel, *Int. J. Energy Res.*, **38**, 1424 (2014).
36. Y. F. Reynier, R. Yazami, and B. Fultz, *J. Electrochem. Soc.*, **151**, A422 (2004).
37. I. Zilberman, A. Rheinfeld, and A. Jossen, *J. Power Sources*, **395**, 179 (2018).
38. L. M. Housel, W. Li, C. D. Quilty, M. N. Vila, L. Wang, C. R. Tang, D. C. Bock, Q. Wu, X. Tong, A. R. Head, K. J. Takeuchi, A. C. Marschilok, and E. S. Takeuchi, *ACS Appl. Mater. Interfaces*, **11**, 37567 (2019).
39. P. J. Osswald, M. del Rosario, J. Garce, A. Jossen, and H. E. Hoster, *Electrochim. Acta*, **177**, 270 (2015).
40. K. E. Thomas, C. Bogatu, and J. Newman, *J. Electrochem. Soc.*, **148**, A570 (2001).
41. Q. Huang, M. Yan, and Z. Jiang, *J. Power Sources*, **156**, 541 (2006).
42. P. J. Linstrom and W. G. Mallard, *NIST Chemistry WebBook* (National Institute of Standards and Technology, Gaithersburg MD) (2020).
43. E. Neumann (ed.), *Angew. Chem. Int. Ed. Engl.*, **12**, 356 (1973).
44. J. R. Croy, K. G. Gallagher, M. Balasubramanian, Z. Chen, Y. Ren, D. Kim, S.-H. Kang, D. W. Dees, and M. M. Thackeray, *J. Phys. Chem. C*, **117**, 6525 (2013).
45. W. E. Gent, K. Lim, Y. Liang, Q. Li, T. Barnes, S. Ahn, K. H. Stone, M. McIntire, J. Hong, J. H. Song, Y. Li, A. Mehta, S. Ermon, T. Tyliczczyk, D. Kilcoyne, D. Vine, J. Park, S. Doo, M. F. Toney, W. Yang, D. Prendergast, and W. C. Chueh, *Nat. Commun.*, **8**, 2091 (2017).
46. K. Ariyoshi, T. Inoue, and Y. Yamada, *J. Electrochem. Soc.*, **165**, A2675 (2018).
47. T. Ohzuku, M. Nagayama, K. Tsuji, and K. Ariyoshi, *J. Mater. Chem.*, **21**, 10179 (2011).
48. W. Shi, J. Zheng, J. Xiao, X. Chen, B. J. Polzin, and J.-G. Zhang, *J. Electrochem. Soc.*, **163**, A571 (2016).
49. B. Manikandan, C. Yap, and P. Balaya, *J. Electrochem. Soc.*, **164**, A2794 (2017).
50. G. Assat and J. Tarascon, *Nat. Energy*, **3**, 373 (2018).
51. Y. Saito, K. Takano, K. Kanari, A. Negishi, K. Nozaki, and K. Kato, *J. Power Sources*, **97–98**, 688 (2001).
52. C. Heubner, S. Heiden, M. Schneider, and A. Michaelis, *Electrochim. Acta*, **233**, 78 (2017).
53. X. Gong, J. Huang, Y. Chen, M. Wu, G. Liu, X. Lei, J. Liang, H. Cao, F. Tang, B. Xu, and C. Ouyang, *Int. J. Electrochem. Sci.*, **8**, 10549 (2013).
54. N. P. Butch, M. E. Manley, J. R. Jeffries, M. Janoschek, K. Huang, M. B. Maple, A. H. Said, B. M. Leu, and J. W. Lynn, *Phys. Rev. B*, **91**, 035128 (2015).
55. J. R. Morris and R. J. Gooding, *Phys. Rev. Lett.*, **65**, 1769 (1990).
56. W. R. McKinnon, J. R. Dahn, J. J. Murray, R. R. Haering, R. S. McMillan, and A. H. Rivers-Bowerman, *J. Phys. C Solid State Phys.*, **19**, 5135 (1986).
57. G. Assat, S. L. Glazier, C. Delacourt, and J.-M. Tarascon, *Nat. Energy*, **4**, 647 (2019).
58. J. R. Croy, K. G. Gallagher, M. Balasubramanian, B. R. Long, and M. M. Thackeray, *J. Electrochem. Soc.*, **161**, A318 (2014).
59. F. Friedrich, T. Zünd, A. Hoefling, J. Tübke, and H. A. Gasteiger, Manuscript in preparation.
60. T. B. Flanagan, C. N. Park, and D. H. Everett, *J. Chem. Educ.*, **64**, 944 (1987).
61. K. G. Gallagher, J. R. Croy, M. Balasubramanian, M. Bettge, D. P. Abraham, A. K. Burrell, and M. M. Thackeray, *Electrochem. Commun.*, **33**, 96 (2013).
62. J. R. Croy, D. Kim, M. Balasubramanian, K. Gallagher, S.-H. Kang, and M. M. Thackeray, *J. Electrochem. Soc.*, **159**, A781 (2012).
63. K. Kleiner, B. Strehle, A. R. Baker, S. J. Day, C. C. Tang, I. Buchberger, F. F. Chesneau, H. A. Gasteiger, and M. Piana, *Chem. Mater.*, **30**, 3656 (2018).
64. P. M. Csernica, S. S. Kalirai, W. E. Gent, K. Lim, Y.-S. Yu, Y. Liu, S.-J. Ahn, E. Kaeli, X. Xu, K. H. Stone, A. F. Marshall, R. Sinclair, D. A. Shapiro, M. F. Toney, and W. C. Chueh, *Nat. Energy*, **6**, 642 (2021).
65. B. Strehle, K. Kleiner, R. Jung, F. Chesneau, M. Mendez, H. A. Gasteiger, and M. Piana, *J. Electrochem. Soc.*, **164**, A400 (2017).
66. R. A. House, G. J. Rees, M. A. Pérez-Osorio, J.-J. Marie, E. Boivin, A. W. Robertson, A. Nag, M. Garcia-Fernandez, K.-J. Zhou, and P. G. Bruce, *Nat. Energy*, **5**, 777 (2020).
67. G. Assat, D. Foix, C. Delacourt, A. Iadecola, R. Dedryvère, and J.-M. Tarascon, *Nat. Commun.*, **8**, 2219 (2017).
68. H. Liu, Y. Chen, S. Hy, K. An, S. Venkatchalam, D. Qian, M. Zhang, and Y. S. Meng, *Adv. Energy Mater.*, **6**, 1502143 (2016).
69. B. Qiu, M. Zhang, S.-Y. Lee, H. Liu, T. A. Wynn, L. Wu, Y. Zhu, W. Wen, C. M. Brown, D. Zhou, Z. Liu, and Y. S. Meng, *Cell Reports Phys. Sci.*, **1**, 100028 (2020).

Supporting Information

Entropy Measurements of Li-Ion Battery Cells with Li- and Mn-Rich Layered Transition Metal Oxides via Linear Temperature Variation

Franziska Friedrich^a, Susanne Pieper^a, and Hubert A. Gasteiger^a

^a *Chair of Technical Electrochemistry, Department of Chemistry and Catalysis Research Center,*

Technical University of Munich, Munich, Germany

franziska.friedrich@tum.de

Contents

Spatially non-isothermal measurement setup	2
Comparison of different methods to determine the TD-OCV	3
Contribution of the Li counter electrode to the entropy of LMR-NCM/Li cells.....	6
OCV hysteresis phenomena in LMR-NCM.....	7
Window-opening experiment in charge direction with activated/stabilized cells	9
Window-opening experiment in charge direction for the first activation charge	10

Spatially non-isothermal measurement setup

As was mentioned in the experimental section, U-shaped pouch-cells were built to conduct spatially non-isothermal measurements. Figure S 1 shows a schematic drawing of such a U-cell. In case of the symmetric Li/Li U-cells, Li (and a Ni-tab) was used at both sides of the cell.

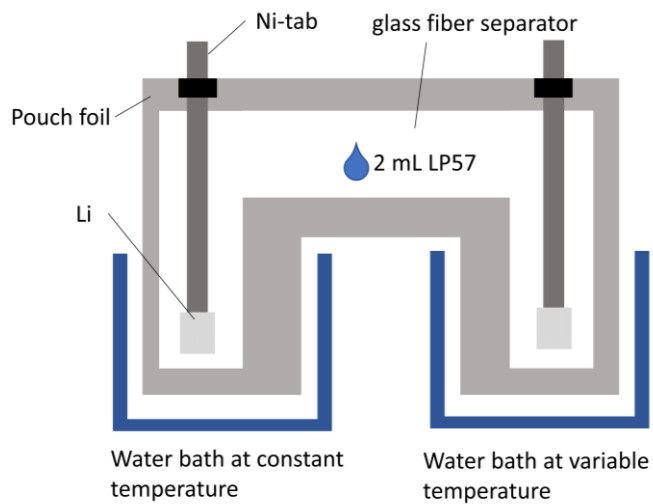


Figure S 1: Schematic drawing of the U-shaped pouch-cell used for spatially non-isothermal measurements of TD-OCVs.

Comparison of different methods to determine the TD-OCV

To illustrate the effect of voltage relaxation, which is especially pronounced at high SOCs, Figure S2 and Figure S3 show OCV data as a function of relaxation time. Both data sets were obtained during pre-experiments with a different cycling procedure as described in the main text. Here, we used a CCCV cycling method with a CV hold at 4.7 V for 2h. Thereby, Figure S2 shows the OCV response recorded when applying the step method. Please note, that the step method for this case differs from the one presented in Figure 1 in the main text since the temperature steps were applied in a different order. Figure S3a shows that the voltage relaxation is still ongoing, even after more than 90 h of relaxation. Figure S3b illustrates that the ongoing voltage decay leads to three different OCV values for the three measurements at 25°C. Since with the step method, one OCV value is determined for each temperature, an ongoing voltage relaxation leads to a falsification of the calculation of the TD-OCV.

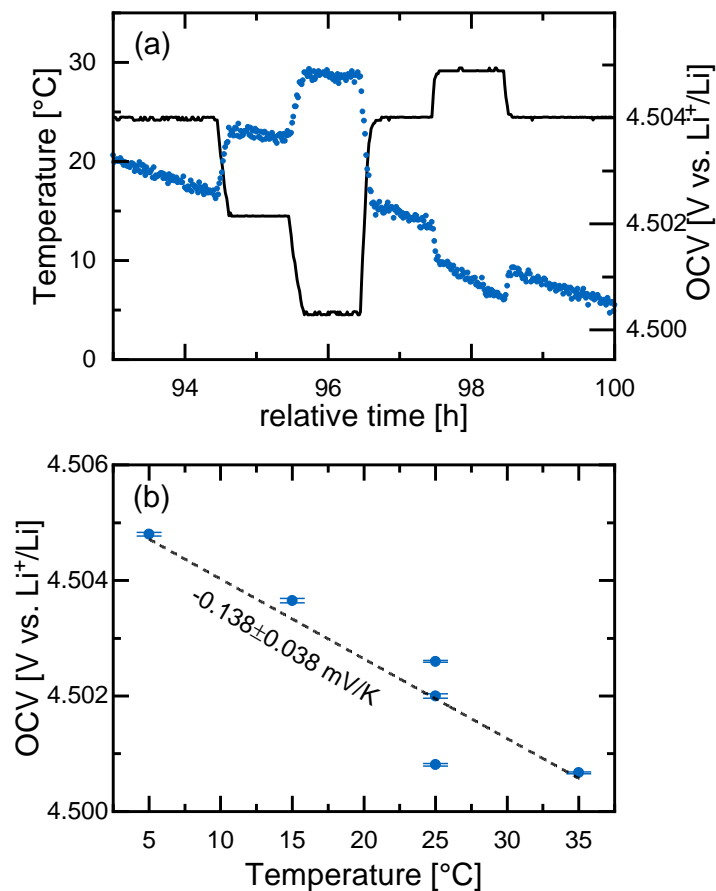


Figure S 2: (a) Example of a temperature profile (black line) and the corresponding OCV response (blue symbols) when applying the temperature step method. After equilibrating at OCV conditions for ≈ 94 h at 25°C, the temperature of the battery is varied in steps with a thermal equilibration time of 1 h per step. Here, data from a 0.33 LMR-NCM/Li T-cell at a nominal SOC of ≈ 310 mAh/g during the 4th charge is shown. (b) The cell-TD-OCV is the slope of a linear fit (black dashed line) of the determined OCV values (blue symbols) as a function of the respective temperatures. The error bars of the OCV data are the standard deviation calculated from averaging over the last 5 minutes of every 1 h temperature step. The error of the resulting cell-TD-OCV includes the error from the linear fitting and the errors of the data points.

Figure S3 shows a comparable data set collected at ≈ 300 mAh/g during the 4th charge using the ramp method. Voltage relaxation is also pronounced in this case leading to slightly higher value for the heating ramps (red lines in Figure S3) than for the cooling ramps (blue in Figure S3). By averaging over the three heating and three cooling ramps, this effect can be minimized. The resulting TD-OCV is -0.097 ± 0.003 mV/K. Hence, the error of the ramp method is considerably smaller compared to the step method, in agreement with what is shown in Table 1 in the manuscript.

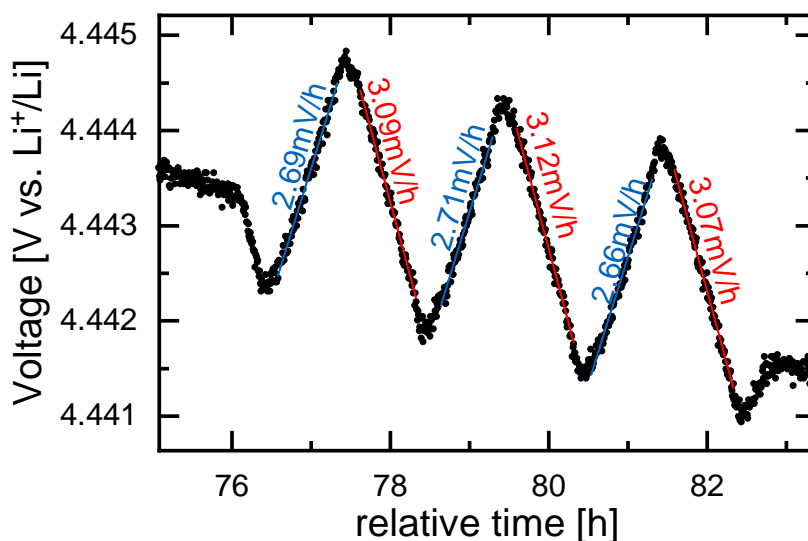


Figure S 3: Typical OCV profile during the application of the temperature ramp method where the temperature is varied linearly between 5°C and 35°C with a rate of 0.5 K/min (as described in the main text) while the OCV is recorded (black symbols). The red lines illustrate linear fits through the data collected during heating and the blue lines during cooling of the cell. The calculated slope of the OCV variation as a function of time is given in the respective colors. Here, data from a 0.33 LMR-NCM/Li T-cell at a nominal SOC of ≈ 300 mAh/g during the 4th charge is shown after equilibrating the cell at OCV conditions for ≈ 76 h at 25°C

The discrepancy between the two TD-OCV values determined by the step and the ramp method in Figure S2 and Figure S3 arises from cell-to-cell variations, which were clearly observable during these pre-experiments due to the (at this point of the study) not optimized experimental approach. Both cells underwent several entropy measurements every $\approx 10\%$ SOC before the data shown here was collected. Due to accumulated self-discharge, the nominal SOC of the respective cells is not reliable anymore. This is also evident by the different OCV values of both cells prior to the entropy measurements. For this reason, we decided to use a set of identical cells to collect the data for the manuscript, with every cell being measured only two to three times in order to avoid accumulated self-discharging and an ambiguous SOC determination as was observed during these pre-experiments. Nevertheless, the data is still helpful to illustrate the effects of high SOCs on the measurement of the TD-OCV with the step and the ramp method.

To validate the herein implemented temperature ramp method, the TD-OCV was determined *via* the temperature step procedure, a consecutive temperature ramping with a rate of 0.5 K/min and 1 K/min. The results are shown in Figure S 4 and prove that the TD-OCV of the temperature ramp method agrees with that obtained by the temperature step procedure. Moreover, the TD-OCV is independent of the applied rate. Minor deviations arise from the ongoing OCV relaxation during the experiment, which introduces a higher error in case of the temperature step method.

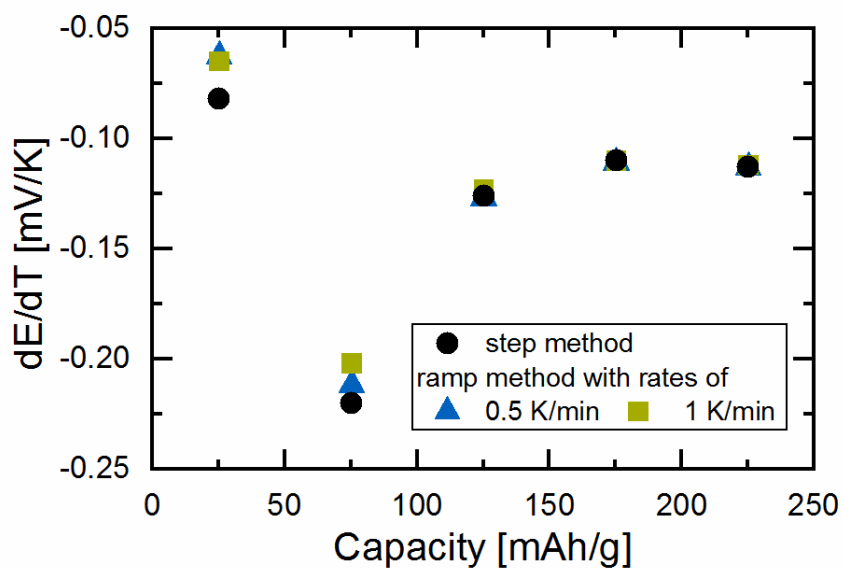


Figure S 4: Comparison of the cell-TD-OCV values determined by the temperature step method (black symbols) and the temperature ramp method with two different rates (0.5 K/min: blue symbols, 1 K/min: green symbols).

Contribution of the Li counter electrode to the entropy of LMR-NCM/Li cells

Symmetrical Li/Li U-cells were analyzed in the spatially non-isothermal setup. By doing so, the electrode-TD-OCV of Li, could be determined to be 1.12 mV/K on average. An exemplary data set of such a measurement is shown in Figure S 5. The electrode-TD-OCV results from the slope of the potential difference versus the temperature difference between the two Li electrodes.

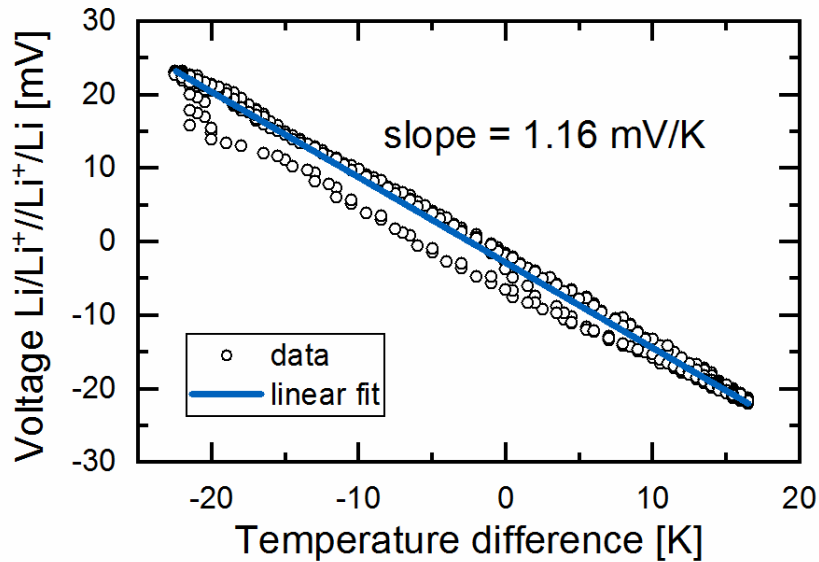


Figure S 5: Spatially non-isothermal measurement of a symmetric Li/Li U-cell with one Li-electrode exposed to linear temperature changes between 0-40°C and one kept at a constant temperature of 25°C. The slope of the potential versus temperature difference gives the electrode-TD-OCV of the Li electrode 1.16 mV/K.

OCV hysteresis phenomena in LMR-NCM

As mentioned in the main part of the manuscript, there are several parameters, which were analyzed with respect to their effect on the OCV hysteresis in LMR-NCM. It needs to be stressed that, for these experiments, the SOC window had to be controlled by a capacity cutoff procedure to ensure that the cycling was conducted in a fixed SOC window - independent of current and temperature. For the results shown in Figure S 4 and Figure S 5, a different initial capacity was chosen.

For the investigation of the effect of the C-rate (Figure S 4), LMR-NCM/Li cells (after one activation and two stabilization cycles) were charged to an absolute capacity of 90 mAh/g where the first 1 h rest phase was conducted to collect an OCV data point. Subsequently, seven equidistant charging steps ($\Delta\text{SOC}=25$ mAh/g) each followed by a 1 h rest phase were done and the same procedure was repeated for the discharge direction until the cells reached the initial capacity again. The thus recorded OCV curves plotted in Figure S 6 show that the C-rate has no effect on the OCV hysteresis.

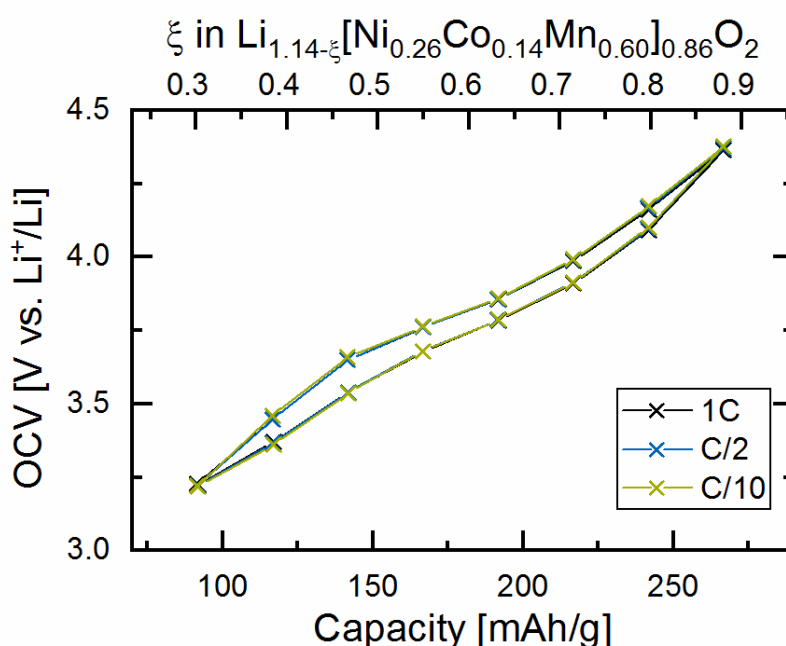


Figure S 6: Comparison of the OCV curves of 0.33 LMR-NCM/Li cells at different C-rates (1C black, C/2 blue, C/10 green) in a capacity limited SOC range after regular activation (i.e. after one formation and two stabilization cycles; see experimental section in the main text). The resulting OCV data at all C-rates superimpose.

In Figure S 7, the OCV curves collected with LMR-NCM/Li cells at 0°C and 45°C are contrasted. After activation/stabilization at 25°C, the cells were charged to an absolute capacity of 65 mAh/g at either 45°C or 0°C. Subsequently, seven equidistant charging steps ($\Delta\text{SOC}=25$ mAh/g) each followed by a 1 h rest phase were done and the same procedure was repeated for the discharge direction. The data in Figure S 7 therefore show a different SOC range than those in Figure S 6. Figure S 7 shows that the OCV values at 45°C are generally lower than at 0°C. Partly, this is caused by the temperature dependence of the OCV (on the order of -0.15 mV/K, see Figure 4a) that could account for on the order of ≈ 7 mV lower OCV values at the higher temperature, but this cannot explain the whole shift in the OCV curves that is on the order of ≈ 200 mV. There might be further factors, such as faster kinetics and relaxation, which still need to be clarified. Apart from this, the specific energy loss associated with the OCV hysteresis shows an interesting behavior, namely that it is clearly larger at higher temperatures.

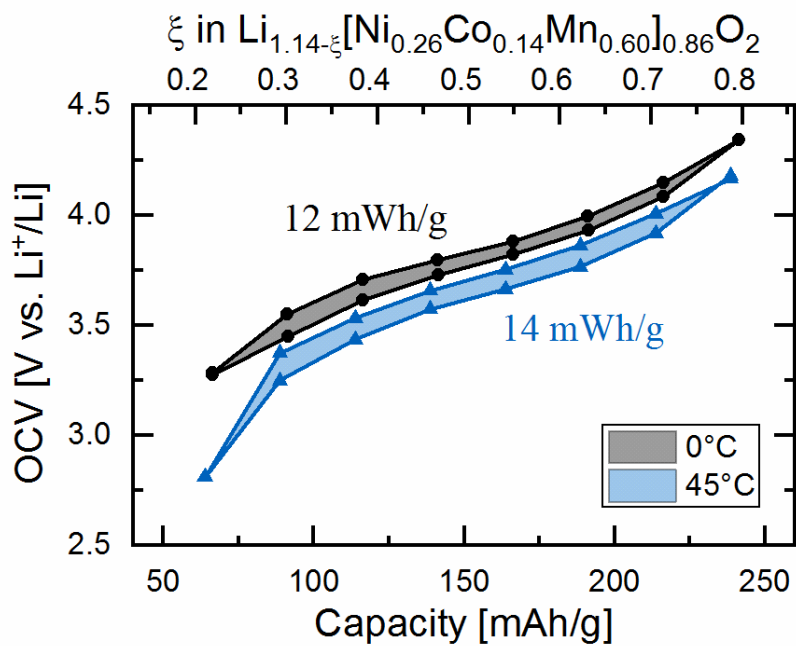


Figure S 7: OCV hysteresis curves of 0.33 LMR-NCM/Li at C/10 obtained at 0°C (black line and symbols) and 45°C (blue line and symbols) in the 4th cycle after regular activation and stabilization at 25°C. The ≈200 mV lower OCV values at 45°C are not only caused by the temperature dependence of the OCV. It could be a convolution of entropy coefficient, faster relaxation, and other kinetic processes. However, this effect needs more investigation.

Window-opening experiment in charge direction with activated/stabilized cells

Similar to the window-opening experiment in discharge direction that were conducted with LMR-NCM/Li cells after the initial activation/stabilization cycles (see Figure 7 in the main text), another window-opening experiment was conducted in charge direction, also using cells after the initial activation/stabilization cycles. As shown in Figure S 8a, the cells were initially charged to $C_0 = 100$ mAh/g, where the partial molar entropy was determined (marked by ① in Figure S 6b and Figure S 6c). When cells were charged to other upper cut-offs ($C_1 = 150$ mAh/g, $C_2 = 225$ mAh/g, $C_3 = 275$ mAh/g), and again discharged to C_0 , the TD-OCV measured at C_0 (after 100-200 h relaxation) differs from the initial one (①) the further the charge window is opened (① → ③).

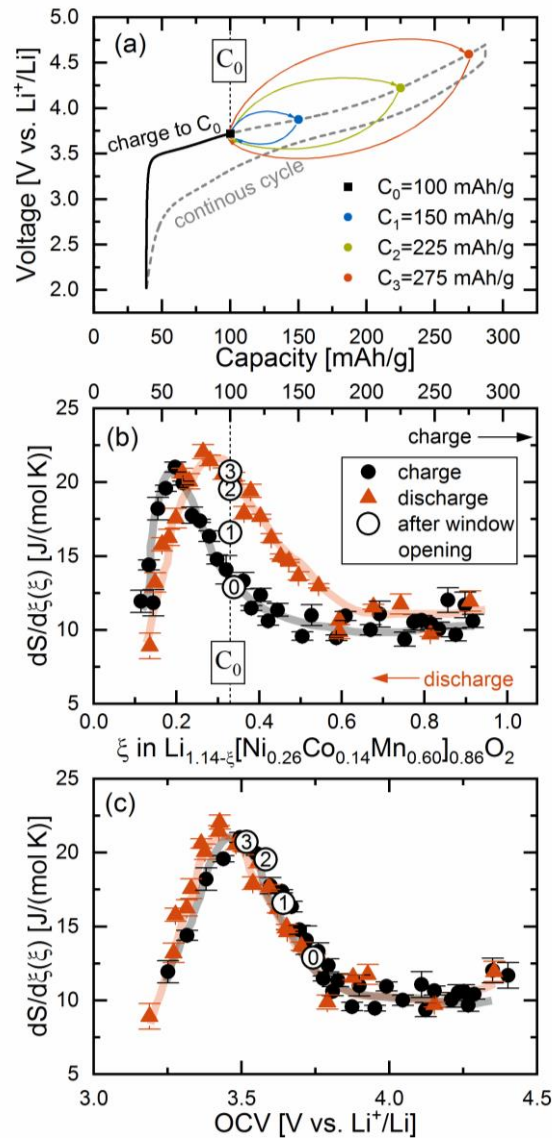


Figure S 8: Results from the window-opening experiments in charge direction with 0.33 LMR-NCM/Li cells after activation/stabilization: (a) The voltage curve for the 4th cycle with a continuous cycle indicated by the gray dashed line and the charge procedure prior to the window-opening marked by the black line. The window-opening loops from the reference point C_0 to the turning points C_1 - C_3 are indicated by colored arrows; (b) partial molar entropy during charge (black circles; same data as in Figure 6) and discharge (orange triangles; same data as in Figure 6) with trendlines as a function of capacity (upper x-axis) or reaction turnover (lower x-axis); (c) same data as a function of OCV. Measurement procedure: (i) after activation/stabilization, cells were charged to $C_0 = 100$ mAh/g at $C/10$ and 25°C ; (ii) subsequently, cells were charged to either $C_1 = 150$ mAh/g, $C_2 = 225$ mAh/g, or to $C_3 = 275$ mAh/g and then discharged again to $C_0 = 100$ mAh/g (all at $C/10$ and 25°C); (iii) at this final charge of 100 mAh/g, the cells were rested at OCV for ≈ 100 -200 h, after which the cell-TD-OCV was measured. The partial molar entropy data points from the window-opening and the resulting OCV values are labeled according to the maximum capacity window ($C_0 \equiv$ ①; $C_1 \equiv$ ②; $C_2 \equiv$ ③; $C_3 \equiv$ ④).

Window-opening experiment in charge direction for the first activation charge

Similar to the window-opening experiment in charge direction that was conducted after the initial activation/stabilization cycles (see Figure S 8), another window-opening experiment in charge direction was done during the first activation charge. For this purpose, the cells were charged to a capacity of either 100 mAh/g (marked by ① in Figure S 9), 200 mAh/g (marked by ②), 250 mAh/g (marked by ③), or 280 mAh/g (marked by ④), after which the cell was discharged again to $C_0=75$ mAh/g, where it was rested at OCV for ≈ 100 -200 h, after which the cell-TD-OCV was determined. For reference, the partial molar entropy data obtained without a window-opening loop are shown for the first activation charge (green circles; same data as in Figure 9c) and for the first discharge (blue triangles; same data as in Figure 9c). In agreement with the other experiments, it was found that the resulting partial molar entropy values at $C_0=75$ mAh/g gradually decrease from the charge curve value (≈ 12 J/(mol K)) to the discharge curve value (≈ 22 J/(mol K)), as the capacity window increases from 100 to 250 mAh/g (i.e. from ① to ④). This means that also during activation the path dependence between charge and discharge grows with increasing SOC window, together with a gradual transformation of the LMR-NCM material.

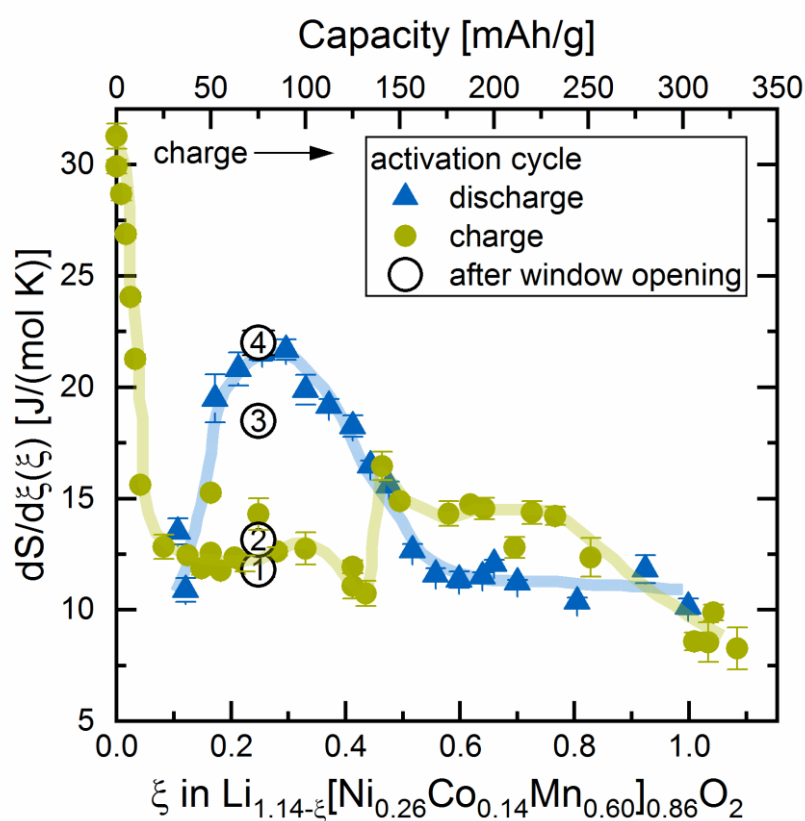


Figure S 9: Window-opening experiment in charge direction with 0.33 LMR-NCM/Li cells during the first activation charge, showing the partial molar entropy versus capacity (upper x-axis) and versus reaction turnover (lower x-axis). For reference, the partial molar entropy data acquired during the first activation charge (green circles; same as in Figure 9c) and the first discharge (blue triangles; same as in Figure 9c). Window-opening measurement procedure: i) first activation charge of the cells to $C_0=75$ mAh/g at C/15 and 25°C; ii) subsequently, the cells were further charged to either $C_1=100$ mAh/g, $C_2=200$ mAh/g, $C_3=250$ mAh/g, or to $C_4=280$ mAh/g, and then discharged again to $C_0=75$ mAh/g (all at C/15 and 25°C); iii) at this final SOC of 75 mAh/g, the cells were rested at OCV for ≈ 100 -200 h, after which the cell-TD-OCV was measured. The partial molar entropy data points from the window-opening are labeled according to the maximum capacity window ($C_1=$ ①; $C_2=$ ②; $C_3=$ ③; $C_4=$ ④).

3.2.2 Implications of hysteresis on heat generation during cycling

The article “Classification of Heat Evolution Terms in Li-ion Batteries regarding the OCV Hysteresis in a Li- and Mn-Rich NCM Cathode Material in Comparison to NCA” was submitted to the peer-reviewed Journal of the Electrochemical Society in February 2022 and was published in April 2022 as an “open access” article under the terms of the Creative Commons Attribution Non-Commercial No Derivates 4.0 License. The permanent web link of this work is available under: <https://iopscience.iop.org/article/10.1149/1945-7111/ac6541>.

As outlined in the previous section and in section 1.3, the commercial application of LMR-NCM as cathode active material in LIBs is impeded by its pronounced OCV hysteresis. It is the reason for a significantly reduced electrical energy round-trip efficiency compared to NCMs and NCA. Since the OCV hysteresis is a material specific property, its extent does not depend on the applied current. The corresponding energy loss is expected to be converted into waste heat, posing an additional challenge for the thermal management of the battery. In order to investigate the energy loss caused by the OCV hysteresis, we conducted an isothermal micro-calorimetry (IMC) study with LMR-NCM/Li cells, whereby NCA/Li cells served as reference system, because NCA shows a relatively high energy density (see Figure 1.2) but no significant OCV hysteresis.

In the article presented here, we aimed at answering the following questions with regards to the LMR-NCM material: (i) Is the energy lost due to the OCV hysteresis fully converted into waste heat? (ii) When is this heat dissipated (during charge or discharge and at which SOC)? (iii) What conclusions can be drawn from the IMC results regarding the underlying thermodynamic mechanisms behind the hysteresis? For this purpose, we cycled both half-cell types in an IMC at the Helmholtz Institute Ulm after we had conducted a few formation cycles in-house. We investigated different C-rates (C/10, C/5, C/2, 1C; all at 25°C) and implemented a 6 h rest phase after each half-cycle of interest in order to separate the heat flow signal of the charge from that of the discharge. Revisiting equation (2.3) in section 2.3, the heat generation due to OCV hysteresis (\dot{Q}_{hys}) is accessible by measuring the total heat flow (\dot{Q}) using IMC and subtracting the other sources of

heat (irreversible, reversible and parasitic heat). The calculation of the different sources of heat is discussed in the article.

Considering the questions raised above, we found that (i) the energy loss due to OCV hysteresis is fully converted into waste heat and that (ii) the majority of it is dissipated during discharge. During charge, \dot{Q}_{hys} is mainly evolved at a high SOC (>200 mAh/g), while during discharge, it is dissipated over the whole SOC range and especially at SOC<170 mAh/g. Our results therefore indicate that (iii) the underlying processes causing the OCV hysteresis evolve waste heat and occur mainly at high SOC during charge and at low SOC during discharge.

The comparison between LMR-NCM/Li and NCA/Li cells clearly shows that the generation of waste heat is much higher in case of the LMR-NCM cathode. This also means that the energy round-trip efficiency is considerably lower. One reason is that LMR-NCM exhibits a larger irreversible heat generation caused by a higher cathode resistance. The other important factor is the OCV hysteresis, which amounts up to 55% of the lost electrical work (at C/10) and hence causes a significant contribution to the overall energy loss, which is not the case for NCA. Our results hence underline the importance of an IMC analysis for electrode materials with a pronounced hysteresis.

Author contributions

F.F. and T.Z. conducted electrochemical measurements and built the cells analyzed in the calorimeter. A.H. was in charge of the calorimetric measurements. F.F. and T.Z. analyzed all results and wrote the manuscript. All authors discussed the data and revised the manuscript. F.F. and T.Z. contributed equally to this work as co-shared first authors.



Classification of Heat Evolution Terms in Li-Ion Batteries Regarding the OCV Hysteresis in a Li- and Mn-Rich NCM Cathode Material in Comparison to NCA

Franziska Friedrich,^{1,=z}  Tanja Zünd,^{1,=}  Alexander Hoefling,² Jens Tübke,³ and Hubert A. Gasteiger¹ 

¹Chair of Technical Electrochemistry, Department of Chemistry and Catalysis Research Center, Technical University of Munich, Munich, Germany

²Helmholtz Institute Ulm, Electrochemical Energy Storage, Ulm, Germany

³Karlsruhe Institute of Technology, Karlsruhe, Germany

We investigate the heat release of Li- and Mn-rich NCM (LMR-NCM) and NCA half-cells during cycling at different C-rates and quantify the individual contributions to the overall heat flow using a combination of isothermal micro-calorimetry and electrochemical methods. The paper focuses in particular on the open-circuit voltage (OCV) hysteresis of the LMR-NCM material, which results in a significant reduction in energy round-trip efficiency ($\approx 90\%$ for LMR-NCM/Li cells vs $\approx 99\%$ for NCA/Li cells at C/10) and therefore in an additional source of heat that has to be considered for the thermal management of the cell. The total heat release of the LMR-NCM/Li cells is found to be nine times higher than that of the corresponding NCA/Li cells (at C/10). In the case of the LMR-NCM cathode, the heat due to OCV hysteresis is responsible for up to 55% of the total energy loss. Using the applied approach, the OCV hysteresis heat is separated into its share during charge and discharge and is furthermore presented as a function of SOC. Additional sources of heat, such as reversible entropic heat, parasitic effects, and measurement limitations, are discussed in terms of their contribution to the overall energy balance of the two cell chemistries.

© 2022 The Author(s). Published on behalf of The Electrochemical Society by IOP Publishing Limited. This is an open access article distributed under the terms of the Creative Commons Attribution Non-Commercial No Derivatives 4.0 License (CC BY-NC-ND, <http://creativecommons.org/licenses/by-nc-nd/4.0/>), which permits non-commercial reuse, distribution, and reproduction in any medium, provided the original work is not changed in any way and is properly cited. For permission for commercial reuse, please email: permissions@iopublishing.org. [DOI: [10.1149/1945-7111/ac6541](https://doi.org/10.1149/1945-7111/ac6541)]



Manuscript submitted February 4, 2022; revised manuscript received March 27, 2022. Published April 25, 2022.

Lithium-ion batteries (LIB) for use in portable electronic devices and in battery electric vehicles (BEVs) dominate the battery market. For the latter application, high-energy density batteries are required ($> 350 \text{ Wh kg}_{\text{cell}}^{-1}$),¹ so that a significant challenge is to create a suitable thermal management system, since the reduced surface area to volume ratio in large batteries can result in insufficient heat transfer from the cells to the surroundings.² Thus, the design of large batteries requires an accurate prediction of the heat flow rate from the LIB for the current loads applied.

Heat is produced and absorbed through various processes during electrochemical cycling of a battery. These processes generally include reversible entropic heat, irreversible heat due to the effects of polarization, heat from side reactions, and heat of mixing caused by the effects of the relaxation of lithium ion concentration gradients after interruption of the current. This study does not take into account the heat generation from side reactions because after several formation cycles and compared to the other sources of heat, it is typically negligible for cells that can be reversibly cycled.^{3,4} Heat evolution due to mixing was also neglected, since it is a diffusional effect after current interruption, which is only significant for electrodes with large active material particles and at high current densities.⁵ In the isothermal calorimetric measurements applied here, the heat absorbed by the cell remains close to zero, since the cell is maintained at a constant temperature. This means that only entropic and polarization effects contribute to the total heat generation. Usually, the heat flow rate of a LIB is dominated by irreversible heat at high current densities, while at lower currents, reversible heat can make a significant contribution. A recently published study, comparing the cycling behavior of 7 Ah pouch full-cells with Li- and Mn-rich layered oxide (LMR-NCM) cathodes to that of NCA cathodes, points out an additional significant heat evolution term for LMR-NCM cathode active materials (CAMs) that is caused by its large open-circuit voltage hysteresis (OCV hysteresis) and that largely affects thermal management.^{6,7} Hence, apart from the applied current, the heat generation is also closely related to the

cell chemistry and for active materials with a significant voltage hysteresis like Li- and Mn-rich NCMs and silicon, an additional heat term due to the OCV hysteresis needs to be considered. The thermal properties of electrode active materials are therefore critical for the design of large-scale high-energy density batteries. These thermodynamic data are essential input parameters in the modeling and development of thermal management systems.

The aim of the present study is therefore to enable a thorough understanding of the heat generation processes taking place in cells with an LMR-NCM ($\text{Li}_{1.14}\text{Ni}_{0.26}\text{Co}_{0.14}\text{Mn}_{0.6}\text{O}_{2}$) CAM that exhibits a significant OCV hysteresis in comparison to cells with NCA ($\text{LiNi}_{0.81}\text{Co}_{0.15}\text{Al}_{0.04}\text{O}_{2}$). We will compare these two CAMs cycled in half-cells with a lithium anode, whereby NCA serves as a reference CAM with a negligible OCV hysteresis that has been commercialized by Tesla in its electric vehicles and is incorporated in projections for grid-connected applications.⁸ The scientific focus of this study is on LMR-NCM, which has a high gravimetric capacity ($\approx 250 \text{ mAh g}_{\text{CAM}}^{-1}$) and a low material cost compared to other state-of-the-art CAMs, as it has a high manganese content instead of cobalt and nickel. However, issues such as oxygen evolution, gradual voltage fade during cycling, and a large OCV hysteresis still hamper the commercialization of LMR-NCM.^{9–11} As mentioned by Kraft et al.,⁶ its OCV hysteresis, which is largely independent of the applied current and thus a material-specific property, negatively affects the round-trip efficiency of LMR-NCM based cells when compared to NCA based cells. At low C-rates, the energy round-trip efficiency for LMR-NCM/Li cells is $\approx 90\%$, while it is $\approx 99\%$ for NCA/Li cells. If this energy inefficiency is dissipated as heat, it not only constitutes an additional source of heat in the overall energy balance, but it is also a challenge for the development of a thermal management system of such batteries. Hence, the following questions need to be addressed for materials like LMR-NCM that have a pronounced OCV hysteresis: (i) Is the energy loss due to the OCV hysteresis dissipated as heat? (ii) In what proportions is this heat dissipated in charge and discharge? (iii) At what point during charge and discharge is the heat evolved? (iv) What conclusions can be drawn from the heat evolution profiles with regard to the underlying thermodynamic mechanisms behind voltage hysteresis?

⁼These authors contributed equally to this work.

^zE-mail: franziska.friedrich@tum.de

The current independent OCV hysteresis of LMR-NCM has previously been studied from several perspectives. Literature reports show correlations between OCV hysteresis, impedance response,¹² lattice parameters,¹³ entropy,¹⁴ and oxygen redox behavior.^{15,16} Shi et al. showed that the entropy and overpotential behavior of LMR-NCM is unique compared to that of regular layered oxide materials.¹⁷ Using only electrochemical methods, their study mainly correlates the gradual voltage decay (shown to be ≈ 100 mV over 100 cycles by Kraft et al.⁶) with the entropy change within the material, whereas we focus on the OCV hysteresis between the charge and discharge voltage curve of a single cycle (\approx up to 300 mV), which has a significant impact on the thermal behavior of the cell. The application of isothermal micro-calorimetry (IMC) in the precise thermal analysis of batteries was demonstrated long ago with the measurement of parasitic reactions in LIBs.¹⁸ In a similar approach to ours, Housel et al.¹⁹ analyzed the heat evolution of silicon anodes by combining IMC with the measurement of polarization induced and entropic heat flows. A recent study by Assat et al.²⁰ addressed some of our questions for an LMR-NCM model system (viz., $\text{Li}_2\text{Ru}_{0.75}\text{Sn}_{0.25}\text{O}_3$) and showed how the thermal characterization of a cathode active material with a pronounced OCV hysteresis could be accomplished with the help of isothermal micro-calorimetry (IMC). Chevrier et al.²¹ used IMC in a similar manner to study silicon as an anode material, which also shows a path dependent behavior and heat generation for zero-current hysteresis.

The present study uses isothermal micro-calorimetry to analyze the thermal behavior during cycling of NCA/Li and LMR-NCM/Li half-cells at different C-rates. The data obtained relating to the generated heat are complemented by measurements of reversible and irreversible heat in order to quantify the different heat sources measured by IMC. Reversible heat is determined by entropy measurements,¹⁴ while irreversible heat is calculated using impedance spectroscopy and overpotential data from an intermittent cycling protocol (constant-current charge intervals followed by OCV periods). In the case of LMR-NCM, the combination of all data sets enables the quantification of the evolved heat due to OCV hysteresis during charge and discharge, along with the calculation of a respective heat evolution profile.

Theoretical Considerations

Derivation of total heat generation in a battery.—The heat flow (\dot{Q}) generated by an electrochemical cell is described by Eq. 1. The interpretation of IMC data is based on the thermodynamics of a battery. A detailed derivation of Eq. 1 is provided by Housel et al.¹⁹ in their Supporting Information.

$$\dot{Q} = I \cdot (E_{load} - E_{eq}) + T \cdot I \cdot \frac{\partial E_{eq}}{\partial T} \quad [1]$$

The first term on the right-hand side of Eq. 1 denotes irreversible heat generation (\dot{Q}_{irrev}), which originates from the polarization processes that cause the measured cell potential under load (E_{load}) to deviate from the thermodynamic equilibrium potential (E_{eq}). The difference between E_{load} and E_{eq} is generally called overpotential (η). It is further illustrated in Fig. 3 (whereby E_{OC} is used instead of E_{eq} as explained below). Note here, that E_{load} is a function of the applied current (I). \dot{Q}_{irrev} is always exothermic. The second term is the reversible heat generation (\dot{Q}_{rev}) caused by an entropic heat flow arising from changes in entropy as a result of the electrochemical reaction. \dot{Q}_{rev} can be calculated based on the change in E_{eq} with temperature. Entropic heat flow is reversible, hence it has different signs in the charge and discharge directions and should, by definition, have a zero contribution if a complete charge/discharge cycle is considered. In addition to these conventional heat flows, another term might be added to Eq. 1 to describe the parasitic heat flow (\dot{Q}_{par}) caused by any side or parasitic reactions, such as

electrolyte decomposition²² or SEI formation.¹⁹ Although the contribution from parasitic heat flow is not equal to zero, it is not further analyzed in the present study, because it can be assumed to be small in comparison to the other sources of heat for a reversibly cycling cell, as will be shown later. As outlined in the Experimental section, a correction for minor parasitic heat flow is applied similar to what is reported by Assat et al.²⁰ Other non-Faradaic heat sources include the heat of mixing and the heat absorbed by the cell from the surroundings. As the measurements are conducted in an isothermal environment, the latter heat term is considered to be close to zero. The heat of mixing is reported to be only important at high current densities ($>2\text{C}$) and for electrodes with large particles ($d \approx 40 \mu\text{m}$),⁵ which is not the case in the present paper (max. 1C and particles with $d \approx 10\text{--}15 \mu\text{m}$).

However, particularly in the case of LMR-NCM, heat generation is not adequately described by Eq. 1. This is due to the hysteresis of the open-circuit voltage between charge and discharge. For a given state-of-charge (SOC), a cell with an LMR-NCM cathode has different OCVs upon charge and discharge, meaning that the OCV is path-dependent. The OCV hysteresis thus translates into a yet undescribed energy loss term. The whole situation thus becomes more complicated, and Eq. 1 has to be extended. To adapt the commonly used energy balance established above to a system with an OCV hysteresis, the voltage measured under open-circuit conditions will not be considered as a reversible equilibrium potential (E_{eq}) but as E_{OC} . Consequently, a similar situation to that of the polarization effect is created by establishing a difference (ΔE) between a (hypothetical) equilibrium potential (E_{eq}) without hysteresis and the measurable potential under open-circuit conditions (E_{OC}). To account for this conceptually, the first term in Eq. 1 can be expanded into two separate terms, one describing nominally the heat evolution term due to a current induced polarization ($\equiv \dot{Q}_{irrev}$, first term in Eq. 2) and one describing nominally the heat evolution induced by the OCV hysteresis ($\equiv \dot{Q}_{hys}$, first term in Eq. 2), whereby the true reversible voltage (E_{eq}) is unknown:

$$\begin{aligned} \dot{Q} &= I \cdot (E_{load} - E_{OC}) + I \cdot (E_{OC} - E_{eq}) + T \cdot I \cdot \frac{\partial E_{eq}}{\partial T} \\ &= \dot{Q}_{irrev} + \dot{Q}_{hys} + \dot{Q}_{rev} \end{aligned} \quad [2]$$

We want to underline that, unlike in classical intercalation materials, the position of E_{eq} cannot simply be assumed to be halfway between the charge and discharge E_{OC} because E_{OC} is highly path-dependent. The position of E_{eq} is thus not directly accessible by experimental methods. Instead of the equilibrium potential, Assat et al.²⁰ and Chevrier et al.²¹ constructed the so-called enthalpy potential based on calorimetric data. In the usual case with active materials that show no OCV hysteresis, i.e., where $E_{OC} = E_{eq}$ (as for NCA/Li cells), Eq. 2 again simplifies to the form of Eq. 1. Note that there is an important difference between the calculation of \dot{Q}_{irrev} and \dot{Q}_{hys} although in both cases, the heat flow is based on the product of current and a potential difference. However, \dot{Q}_{irrev} becomes very small when the current is reduced because E_{load} is a function of the applied current and approaches E_{OC} for small currents, thus $\Delta E(I) = E_{load}(I) - E_{OC} \approx 0$ for small I . In contrast, since both E_{OC} and E_{eq} are a material specific property, their potential difference $\Delta E = E_{OC} - E_{eq}$ is independent of the applied current and hence leads to a significant contribution even at low currents. Strictly speaking, the entropic heat for LMR-NCM is also determined from the change in E_{OC} with temperature, since the (hypothetical) E_{eq} is not accessible. However, this is more of a theoretical problem, and since the contributions from entropic heat flow are minor in the case of LMR-NCM, it will not be discussed further here. The interested reader is referred to a detailed discussion of the entropy of LMR-NCM by Friedrich et al.¹⁴ The essential conclusion from Eq. 2 is that the heat flow due to OCV hysteresis

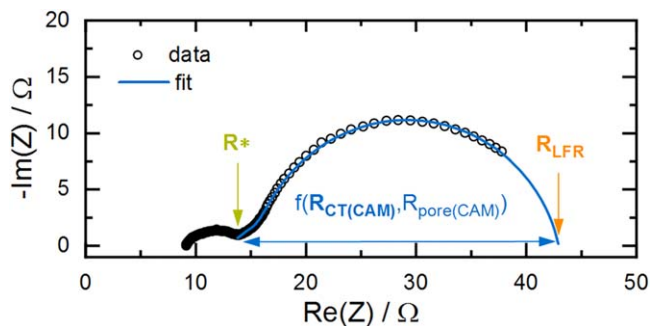


Figure 1. Exemplary impedance spectrum of an LMR-NCM/Li cell at a nominal SOC of ≈ 260 mAh/g_{CAM} during a C/10 charge, with data depicted as black circles and the applied fit as a blue line. Only the low-frequency semi-circle was fitted by the equivalent circuit $R^* + TLM(R_{pore} + R_{CT(CAM)})/Q$. From this spectrum, the pore resistance of this cell was determined as $12.2 \Omega \text{ cm}^2$. The arrows mark the parameters extracted from the fit: (i) R^* , which includes the high frequency resistance of the cell, contact resistances, and contributions of the Li anode impedance; (ii) the charge transfer resistance of the cathode, $R_{CT(CAM)}$, which was extracted from the transmission line model; and, (iii) the low frequency resistance R_{LFR} , as described above. The high frequency semi-circle was not taken into account for fitting.

\dot{Q}_{hys}) can be calculated from the difference between the total heat flow \dot{Q} measured by IMC and the sum of the reversible (\dot{Q}_{rev}) and irreversible heat flow terms (\dot{Q}_{irrev}).

We want to make clear that the current (I) in Eq. 1 is defined to be positive in the discharge direction (voluntary process, lithiation of the cathode) and negative in the charge direction. By this definition, a positive \dot{Q} represents heat absorbed by the cell (endothermic), while a negative \dot{Q} means that heat is generated by the cell (exothermic). It should be noted, however, that in contrast to this thermodynamic definition, the sign convention used in this study is based on the perspective of the calorimeter, as is common in the literature. Thus, if the IMC measures heat generated by the cell (exothermic reaction) the heat flow has a positive sign, while it takes a negative value for heat absorbed by the cell (endothermic process).

Contributions to irreversible heat.—Irreversible heat arises from the internal battery resistance and is calculated either as the current multiplied by the polarization induced overpotential (η) or as the product of the current squared and the total cell resistance (R_{tot}).

$$\dot{Q}_{irrev} = I \cdot (E_{load} - E_{OC}) = I \cdot \eta = I^2 \cdot R_{tot} \quad [3]$$

The full voltage relaxation during the applied intermittent cycling protocol (constant-current charge intervals followed by OCV periods; Experimental section) gives the polarization induced overpotential η for each relaxation phase at this specific current (see Fig. 3), from which the total irreversible heat flow (\dot{Q}_{irrev}) can be calculated.

The contributions to the total cell resistance can be further analyzed by impedance spectroscopy. As shown in Fig. 1, the impedance spectra in this study were fitted with a simplified transmission line model. The fitted equivalent circuit is described by $R^* + TLM(R_{pore} + R_{CT(CAM)})/Q$. Hereby, R^* represents the sum of several contributions: (i) the high frequency resistance, which includes the ionic resistance of the separator and the electrical resistance of the external cell contacts; (ii) the resistance of the Li anode; and, (iii) the contact resistance between the cathode and the Al current collector. As can be seen from the example in Fig. 1, R^* is defined as being at the end of the high-frequency semi-circle. The low-frequency semi-circle corresponds to a complex convolution of the pore resistance due to the lithium ion conduction across the

porous cathode (R_{pore}) and the cathode charge transfer resistance ($R_{CT(CAM)}$). In case of the LMR-NCM/Li cells, the low-frequency semi-circle was fitted by a transmission line model.²³ The assignment of the fitting parameters to the semi-circles is verified by experiments with a micro-reference electrode (not shown here) and by comparison to literature reports.¹² In the case of NCA/Li cells, the pore resistance could not be clearly distinguished. In this case, the second semi-circle was fitted by a simplified R_{CAM}/Q_{CAM} element where R_{CAM} includes $R_{CT(CAM)}$ and R_{pore} . More details on the analysis and fitting of the impedance data can be found in the Experimental section. Since R_{pore} is assumed to be constant and independent of the SOC, we will focus on the analysis of R^* and R_{CT} . However, to compare the results of the impedance analysis to those of intermittent cycling, the low frequency resistance R_{LFR} needs to be calculated from the fitting parameters:²³

$$R_{LFR} = R^* + 1/3 R_{pore} + R_{CT(CAM)} \quad [4]$$

Equation 4 was applied for the impedance spectra of the LMR-NCM/Li cells within its validity criteria.²⁴ For NCA, R_{LFR} is calculated from the sum of R^* and R_{CAM} . Both, R^* and R_{CAM} , are only shown for NCA where they were clearly distinguishable (at high and low SOC). The difference between R_{LFR} and the total resistance determined by the intermittent cycling (R_{tot}) is a result of diffusion limitations. For a more advanced impedance analysis of cells with LMR-NCM cathodes, the reader is referred to the work by Teuff et al.¹² However, the aim of this study is not to conduct a detailed impedance analysis, but to deconvolute the different sources of irreversible heat, in particular the contributions of the cathode, which justifies the applied simplification.

Thermal energy per cycle.—So far, only heat flows, i.e., the evolution of heat over time, have been discussed. However, the total heat generated during a complete charge/discharge cycle, the thermal energy per cycle, can be obtained from them. This parameter can be accessed by various means: (i) as the sum of the integration of all calculated heat flow terms over time; (ii) as the integration of the voltage curve over a whole cycle; and, (iii) as the sum of the integrated heat evolution during a charge/discharge cycle measured by IMC. Therefore, the contributions of different heat sources can be quantified by calculating (i) and (ii) and then comparing it to the thermal energy measured by IMC (iii). An essential requirement for the validity of this analysis is that the total thermal energy per cycle calculated by all three methods is equal. This means that the electrical energy lost according to the voltage curve is fully converted into heat and that there are no other (non-Faradaic) heat sources.

For calculation method (i), the heat generated during charge Q_{cha} (during discharge Q_{dis}) is integrated from time t_0 , where the charge (discharge) commenced, to t_c (t_d), where the charge (discharge) half-cycle ends. The sum of the heat generated during charge and discharge gives the total heat generated per cycle, Q_{cycle} . Since reversible heat has opposite signs on charge and discharge, it cancels out and thus does not contribute to the thermal energy per cycle.

$$Q_{cycle} = \int_{t_0}^{t_c} \dot{Q}_{cha} dt + \int_{t_0}^{t_d} \dot{Q}_{dis} dt = Q_{irrev,cha} + Q_{irrev,dis} + Q_{hys,cha} + Q_{hys,dis} \quad [5]$$

Thus, only the irreversible heat and the energy loss due to hysteresis (in the case of LMR-NCM), both separated into their charge and discharge components, contribute to the thermal energy per cycle.

Using calculation method (ii), the integration over the voltage curve on load, only one value, which is the sum of all heat sources, can be obtained:

$$Q_{\text{cycle}} = \int_{t_0}^{t_c} I_{\text{cha}} \cdot E_{\text{load,cha}} dt - \int_{t_0}^{t_d} I_{\text{dis}} \cdot E_{\text{load,dis}} dt \quad [6]$$

However, when applying intermittent charging, the voltage under load can be distinguished from that under open-circuit conditions. This enables the quantification of individual contributions to the thermal energy per cycle. The generated irreversible heat can be calculated for the charge ($Q_{\text{irrev,cha}}$) and discharge ($Q_{\text{irrev,dis}}$). For example, the energy loss caused by the effects of polarization during charge is the integrated area between the upper voltage curve under load and the upper OCV curve (analogously for the discharge):

$$Q_{\text{irrev,cha}} = \int_{t_0}^{t_c} I_{\text{cha}} (E_{\text{load,cha}} - E_{\text{OC,cha}}) dt \quad [7]$$

The energy loss caused by OCV hysteresis is calculated by integrating the area enclosed by the OCV points upon charge and discharge. Only the sum of the charge and discharge contributions to Q_{hys} is accessible from integration of the OCV data.

$$Q_{\text{hys}} = \oint_{t_0}^{t_d} I \cdot (E_{\text{OC,cha}} - E_{\text{OC,dis}}) dt \quad [8]$$

It is important to keep in mind that the integration over the whole charge/discharge voltage curve is not a closed loop due to the coulombic inefficiency of the cell. When Eq. 6 is thus strictly applied, Q_{cycle} is overestimated as compared to reconstructing Q_{cycle} according to Eq. 5 from $Q_{\text{irrev,cha}}$, $Q_{\text{irrev,dis}}$ and Q_{hys} calculated according to Eqs. 7 and 8. The resulting inaccuracy of the analysis and how to best minimize it will be discussed later in the Results section.

For method (iii), the heat flow signal measured by IMC is integrated over time to give the total generated heat. When a sufficiently long OCV phase is applied at the end of each charge/discharge half-cycle, the total heat generated during charge can be separated from that during discharge. The heat evolution is measured by IMC both during current flow and the consecutive OCV phase, in which the heat signal levels off while the cell cools down. When comparing with calculated heat flows, only the signal during current flow is considered, while for the calculation of the total heat generation, the heat evolution at zero current also needs to be taken into account. However, for this part of the IMC signal, the time delay of the instrument needs to be taken into consideration, in order to determine a reasonable time frame during which the IMC signal at open-circuit conditions is included in the integration. The applied method is explained in more detail in the Experimental section.

The combination of all three methods enables the differentiation and identification of the different sources of heat contributing to the experimental IMC data. In particular, when the irreversible heat calculated by Eq. 7 is subtracted from the calorimetric data of the respective half-cycle, Q_{hys} can be determined for the charge and discharge half-cycles. However, when calculating Q_{hys} with this method, the reversible heat, Q_{rev} , cannot be neglected, although the fact that Q_{rev} cancels out in Eq. 5 might give this impression. This is because, unlike a whole cycle, the reversible heat during a half-cycle, e.g., $Q_{\text{rev,cha}}$ during charge, contributes to the heat evolution measured by IMC. However, when calculating the heat evolution of a half-cycle by method (ii), the reversible heat is not included because it cannot be calculated from the voltage data collected during intermittent cycling. Thus, when comparing both values, the inconsistency with regard to Q_{rev} constitutes an error source for determining the share of Q_{hys} for individual half-cycles. Therefore, we use the term Q_{residual} instead of Q_{hys} (see Fig. 10) to make it more clear that what is determined by method (ii) is the residual heat for each charge/discharge half-cycle. In other words, Q_{residual} only

equals Q_{hys} if Q_{rev} were zero. This will be discussed in more detail in the Results section.

Experimental

Battery assembly and cycling.—LMR-NCM of the composition $\text{Li}_{1.14}(\text{Ni}_{0.26}\text{Co}_{0.14}\text{Mn}_{0.6})_{0.86}\text{O}_2$, which corresponds to the nomenclature $0.33 \text{Li}_2\text{MnO}_3 \cdot 0.67 \text{LiNi}_{0.38}\text{Co}_{0.21}\text{Mn}_{0.41}\text{O}_2$ as used by Teuff et al.⁹ and NCA of the composition $\text{LiNi}_{0.81}\text{Co}_{0.15}\text{Al}_{0.04}\text{O}_2$ were obtained from BASF SE (Germany). For electrode preparation, inks of the cathode active material (CAM) were prepared by mixing 92.5 wt% CAM (NCA or LMR-NCM), 3.5 wt% polyvinylidene-fluoride binder (PVdF, Solef 5130, Solvay, Belgium), and 4 wt% conductive carbon (Super-C65, Timal, Switzerland) with N-methyl pyrrolidine (NMP, anhydrous, Sigma-Aldrich, Germany). The dispersion was mixed in a planetary orbital mixer (solid content ≈ 58 wt%; Thinky, USA). The resulting ink was coated onto aluminum foil ($\approx 15 \mu\text{m}$, MTI, USA) and the dried coatings were calendered (GK 300 L, Saueressig, Germany) to a porosity of $\approx 42\%$ – 45% . For electrochemical testing, the electrodes were dried for a minimum of 12 h at 120°C under dynamic vacuum (Büchi, Switzerland). The loading of the LMR-NCM electrodes was $\approx 12 \text{ mg cm}^{-2}$, which corresponds to $\approx 3 \text{ mAh cm}^{-2}$, (based on a nominal reversible capacity of $250 \text{ mAh g}_{\text{LMR-NCM}}^{-1}$). The NCA electrode loading was $\approx 13 \text{ mg cm}^{-2}$, which corresponds to $\approx 2.6 \text{ mAh cm}^{-2}$, (based on a nominal reversible capacity of $200 \text{ mAh g}_{\text{NCA}}^{-1}$).

Coin cells (type CR2032) were assembled in an argon-filled glovebox (O_2 , $\text{H}_2\text{O} < 0.1$ ppm, MBraun, Germany) with the manufactured cathodes (14 mm diameter), two glass fiber separators (17 mm diameter, glass microfiber #691, VWR, Germany), and a Li counter electrode (15 mm diameter, $450 \mu\text{m}$ thickness, 99.9%, Rockwood Lithium, USA). A volume of $100 \mu\text{l}$ of electrolyte was added, composed of 1 M LiPF_6 in a FEC:DEC-based (12:64 v:v) solvent with 24 vol% of an additional fluorinated co-solvent (BASF SE, Germany). Electrochemical testing was performed at 25°C in a temperature-controlled oven (Binder, Germany) using a potentiostat (VMP300, Biologic, France). First, a formation cycle at a C-rate of C/15 (voltage cutoffs for LMR-NCM were 2.0–4.8 V and for NCA 3.0–4.4 V; all voltages reported vs Li^+/Li) and two stabilization cycles at C/10 (2.0–4.7 V for LMR-NCM and 3.0–4.4 V for NCA) were conducted. All C-rates reported here refer to the above stated nominal capacities of the CAMs. The cells analyzed in this study can be divided into two groups: (i) those used for the IMC measurements (red box in Fig. 2); and (ii) those used to determine the irreversible heat (blue box in Fig. 2).

Isothermal micro-calorimetry measurements.—Following the initial formation cycles, which were conducted in-house, the calorimeter cells were transferred to an isothermal micro-calorimeter at the Helmholtz Institute Ulm to record the heat generation during cycling. A TAM IV calorimeter equipped with a 20 ml micro-calorimeter (stability $\pm 50 \mu\text{K}$, accuracy $\pm 300 \text{ nW}$, precision $\pm 100 \text{ nW}$, TA Instruments, USA) was used for this purpose. All measurements were performed at 25°C under isothermal conditions, following internal gain calibration. During the course of the experiments, the baseline drift did not exceed 700 nW . The step response of the heat flow is of second order, and the two characteristic time constants are $T_1 = T_2 = 158 \pm 1 \text{ s}$. This results in a time delay of $\approx 1050 \text{ s}$ until 99% of the heat flow signal is detected. Here, a positive sign in the observed heat flow indicates that heat is generated by the cell.

The cells were cycled in a custom-made coin cell holder, which was connected by Cu-P bronze wires (36 AWG, Lakeshore, USA) to a potentiostat (VSP, BioLogic, France). Galvanostatic cycling was conducted, as shown in the red box in Fig. 2, at a number of current levels (C/10, C/5, C/2, 1C). For each C-rate, one first continuous charge/discharge cycle was performed and ended by a 6 h equilibration phase in the discharged state under open-circuit conditions. This

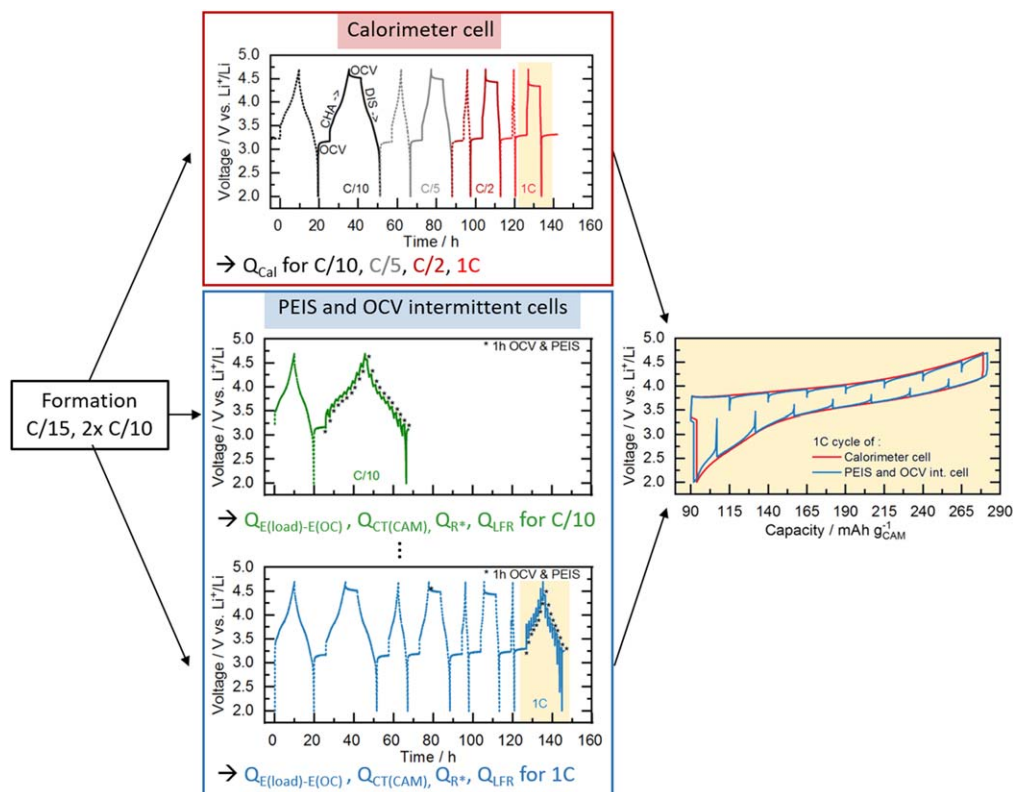


Figure 2. Graphic representation of the cycling procedures used in this study, with the initial formation cycle at C/15 (2.0–4.8 V for LMR-NCM/Li and 3.0–4.4 V for NCA/Li) and two stabilization cycles at C/10 (2.0–4.7 V for LMR-NCM/Li and 3.0–4.4 V for NCA/Li) conducted in-house (black box, left). The subsequent actual test protocols differ for the two types of experiments: (i) for the IMC measurements (red box), cells were cycled inside the calorimeter with a loop of one stabilization cycle and one cycle with 6 h rest phases at the beginning and end of each half-cycle, repeated for each applied C-rate (C/10, C/5, C/2, 1C); (ii) for the determination of the different sources of heat (blue box), an intermittent cycling protocol with 10% SOC steps and 1 h OCV phases was applied. For each C-rate, two identical cells were cycled with the same protocol as the IMC cells but for the C-rate of interest, where the intermittent cycling was applied (see example for C/10 and 1C in the blue box). The panel on the right presents a comparison of the data at 1C for a calorimeter cell and the cell with intermittent cycling.

first cycle was intended for the purpose of adapting to a new C-rate, and the heat generated during this process was not considered. The heat flows were determined from the second cycle, commencing with a constant-current charge to the respective upper cutoff voltage (4.7 V for LMR-NCM and 4.4 V for NCA) at the particular C-rate, followed by a further 6 h equilibration phase to enable separation of the heat flow during charge and discharge, and finally discharging to the respective lower cutoff voltage (2.0 V for LMR-NCM and 3.0 V

for NCA). The discharge was followed by a 6 h open-circuit phase before the whole loop of two cycles was repeated for the next C-rate. Two identical cells were measured for each CAM. A constant baseline was used for integration of the data, which was determined as the minimum heat flow at each C-rate section. By subtraction of this constant background signal, a correction for minor parasitic heat flows is achieved.²⁰ However, it must be kept in mind this is not the true value of the parasitic heat of this cell, which depends on complex relationships among all cell components, the SOC and voltage of the cell and its cycling history. This simplification is acceptable for the scope of this study but it does not describe the nature of the parasitic heat flow. Due to the time delay, the integration of the heat flow of an individual charge or discharge half-cycle includes not only the heat signal during current flow, but also that during the subsequent relaxation phase. Of the applied 6 h relaxation phase, we only included the first 1.5 h into the calculation, which is sufficient to obtain most of the actual heat signal, considering the time delay of ≈ 18 min (until 99% of the signal is detected), while being short enough to minimize contributions from parasitic heat flows.

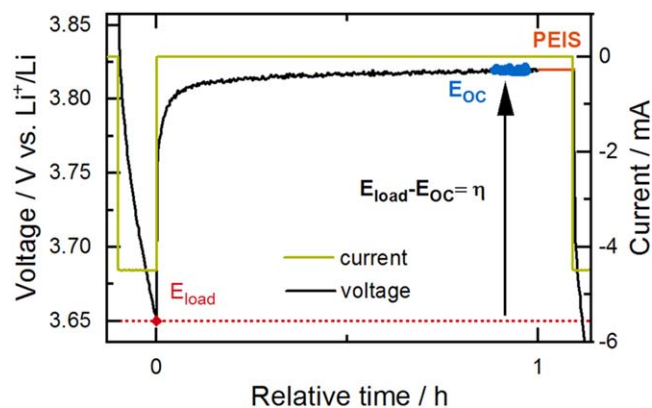


Figure 3. Application of intermittent cycling to determine the polarization induced overpotential $\eta = E_{load} - E_{OC}$. The current (green) and voltage (black) during a 1C discharge ($\Delta SOC = 10\%$) and a consecutive 1 h OCV phase are shown. E_{OC} is determined by averaging over the final 300 s of the OCV phase (data marked in blue). After relaxation, a PEIS measurement is conducted, whose duration is only shown schematically here (orange).

Determination of irreversible heat by intermittent cycling and impedance analysis.—As shown in Eq. 3, the irreversible heat generation rate (\dot{Q}_{irrev}) is a function of the voltage difference η between the voltage on load (E_{load}) and after relaxation at open-circuit conditions (E_{OC}). During intermittent cycling, η is determined after a certain time t of the intermittent relaxation phase, as shown in Fig. 3. The applied cycling protocol was similar to a galvanostatic intermittent titration and included (dis)charging steps of $\Delta SOC = 10\%$ followed by a relaxation phase of $t = 1$ h. This was repeated

until the upper (lower) voltage cutoff was reached. To determine η for the first SOC point during charging, the method shown in Fig. 3 is not applicable, because there is no preceding voltage relaxation in the charge direction. Therefore, for this data point, it was only possible to determine the instantaneous voltage jump upon applying the charging current. The same holds for the first point on discharge. The underlying resistance to this instantaneous voltage change was calculated using Ohm's law, and it was observed that it agrees well with the low-frequency resistance calculated from the impedance analysis. Hence, for the first SOC point of each half-cycle, the intermittent technique complies with the impedance and does not include any effects of diffusion, as is the case if η can be determined from full voltage relaxation.

The intermittent cycling, shown in the blue box in Fig. 2, was conducted with identical cells, as used in the IMC measurement with two cells for each C-rate. To ensure applicability of the herein determined irreversible heat to the data obtained from IMC experiments, the intermittent cycling protocol mimics the cycling protocol for the IMC. This means that to determine η at a specific C-rate, the cell first underwent the same loop of continuous cycling and charging/discharging with a 6 h rest phase in between at each C-rate preceding the C-rate of interest, such that the irreversible heat data are from the exact same cycle with the same cycling history as the heat data from the IMC (illustrated in the bottom panel of Fig. 2 for acquiring intermittent cycling data at 1C). Furthermore, the OCV data shown in this paper were determined by a Matlab script averaging over the final 300 s of the intermittent relaxation phase (see data given in blue in Fig. 3).

In addition to determining the overpotential by intermittent cycling, the cell resistance was further analyzed by means of impedance spectroscopy. As marked in Fig. 3, an impedance measurement (PEIS) was conducted at the end of each 1 h intermittent relaxation phase of the protocol described above. A potentiostat (VMP300, Biologic, France) was used in a frequency range of 200 kHz to 100 mHz with an AC voltage perturbation of 10 mV (taking 20 data points per decade and 3 period repetitions). As explained in the Theoretical Considerations above, data were fitted by the equivalent circuit $R^* + TLM(R_{pore} + R_{CT(CAM)}/Q)$. Here, R^* includes the high frequency resistance of the cell, the impedance of the Li anode, and the contact resistance of the cathode. The data of the high-frequency semi-circle was not taken into account for the fit, and R^* was set to the end of the first semi-circle, as shown in Fig. 1. The low-frequency semi-circle was fitted by the transmission line model, including contributions from the pore resistance, R_{pore} , and the charge transfer resistance of the cathode, $R_{CT(CAM)}$. The pore resistance of the LMR-NCM/Li cells was extracted from a fit of an impedance spectrum at high SOC during

charge, in which the characteristic 45° line²³ was clearly observable and kept constant for all other impedance fits of this cell. In the case of NCA/Li cells, the pore resistance could not be clearly distinguished and is therefore a part of $R_{CT(CAM)}$. Furthermore, we only show R^* and the sum of $R_{CT(CAM)}$ and R_{pore} for NCA where they were clearly distinguishable (at high and low SOC) and otherwise report R_{LFR} . Due to the generally much smaller $R_{CT(CAM)}$ of NCA/Li cells compared to LMR-NCM/Li cells, the impedance contribution of the lithium counter electrode in the mid-SOC region is of a similar order as $R_{CT(CAM)}$, which results in the two semi-circles merging. Hence, for the respective spectra, $R_{CT(CAM)}$ cannot be assigned unambiguously.

Figure 1 shows an example of an impedance spectrum for an LMR-NCM/Li cell. Unfortunately, we did not collect any data under blocking conditions, as would usually be performed to determine R_{pore} .²³ The results for R_{pore} are 12.2 $\Omega \text{ cm}^2$ and 10.1 $\Omega \text{ cm}^2$ for the two nominally identical LMR-NCM/Li cells at C/10. The charge transfer resistance of the cathode was extracted from the transmission line model. It was verified by impedance experiments using a gold wire micro-reference electrode (not shown here), which, furthermore, correspond with the data in the literature.¹² The difference between the irreversible heat calculated from the polarization induced overpotential $\eta = E_{load} - E_{OC}$ and that calculated from the low-frequency resistance (R_{LFR}) determined from the PEIS data is due to the mass-transport limitations within the electrolyte and the porous electrode, which are not captured by the PEIS measurements in the applied frequency range.

Determination of reversible heat.—As shown in Eq. 2, reversible heat is calculated as a product of the current, temperature and temperature-dependent OCV value, $\frac{\partial E_{eq}}{\partial T}$. The latter was measured as a function of SOC after (dis)charging the cell to a certain SOC point and allowing it to relax until the change in OCV over time was less than 0.2 mV/h. After this relaxation, $\frac{\partial E_{eq}}{\partial T}$ was determined by linearly varying the temperature of the cell between 5 °C and 35 °C in an Espec temperature chamber (LU114, Espec, Japan), while recording the respective OCV variation (VMP300, Biologic, France). A detailed description of the method applied is reported elsewhere.¹⁴ The obtained values for $\frac{\partial E_{eq}}{\partial T}$ are shown in the appendix (Figure A-1).

Results and Discussion

Lost electrical energy.—Lost electrical energy is the difference between the charge and the discharge energy of one cycle, and is expected to dissipate as waste heat. The two cathode active materials

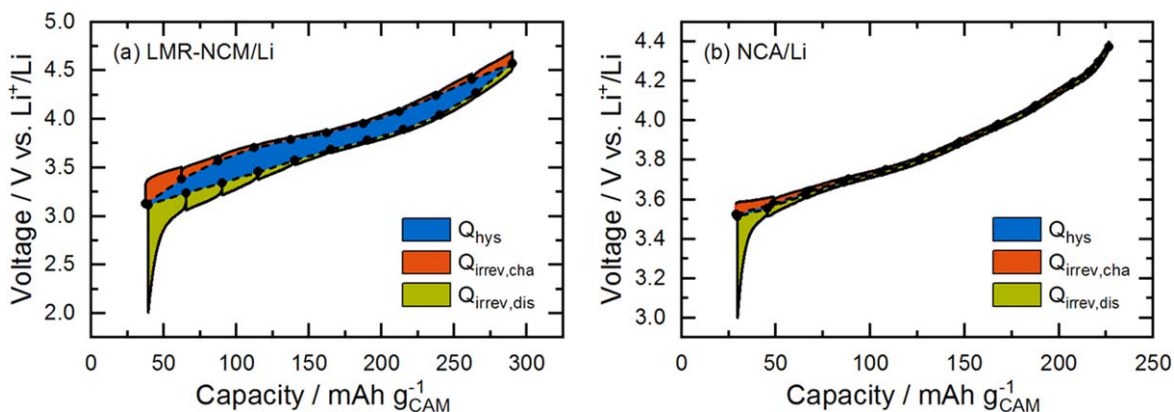


Figure 4. Voltage vs SOC charge/discharge curves of (a) LMR-NCM/Li and (b) NCA/Li in the 5th cycle at C/10 obtained during intermittent cycling with 1 h OCV holds at every 10% SOC interval. The charge curve is shown as a black solid line and the OCV points are shown as black circles connected by a dashed line. The integral of the whole curve is the total lost electrical energy, which can be separated into three parts: irreversible losses during charge (orange) and discharge (green) due to polarization induced overpotential, and the lost energy due to OCV hysteresis (blue).

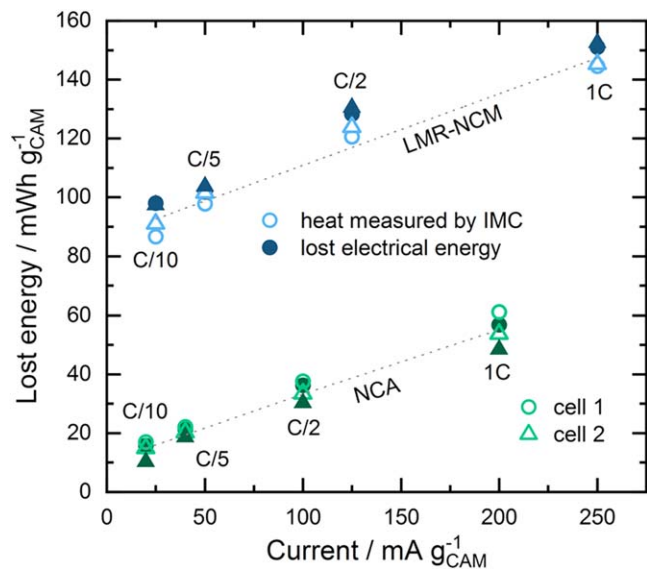


Figure 5. Comparison of the lost electrical energy calculated from the voltage vs SOC curve (dark, filled symbols) and the heat measured by IMC (pale, empty symbols) for two identical LMR-NCM/Li cells (blue) and NCA/Li cells (green) for different mass-specific current densities (corresponding to the C-rates indicated in the figure). The dashed lines represent a linear fit through the average of all data points of one cell chemistry at each C rate.

of interest, LMR-NCM and NCA, exhibit considerably different energy efficiencies. While an LMR-NCM/Li cell has an energy efficiency of $\approx 90\%$ in the 5th cycle at C/10, that of an NCA/Li cell reaches $\approx 99\%$. Figure 4 shows a voltage vs SOC charge/discharge curve for both cell types in a C/10 cycle. According to Eq. 6, the total energy loss corresponds to the integration of the geometrical area enclosed by the charge and discharge voltage curve (sum of orange, blue, and green shaded areas in Fig. 4). This total energy loss can be further separated into three parts: (i) the irreversible energy loss during charge ($Q_{irrev,cha}$), i.e., the difference between the voltage curve on load and the OCV curve during charge (orange shaded area), as described by Eq. 7; (ii) the irreversible losses during discharge ($Q_{irrev,dis}$; green shaded area); and, (iii) the energy loss due to OCV hysteresis (Q_{hys} ; blue shaded area), as described by Eq. 8.

Note here, that the coulombic inefficiency of the cell means that the end of the discharge curve does not meet the start of the charge curve. For clarity, the resulting “gap” is not colored in Fig. 4. The deconvolution of these different energy loss terms as a function of the C-rate is shown in Table I for LMR-NCM and NCA half-cells. Thereby, the values for Q_{irrev} for charge and discharge were calculated by applying Eq. 7. The calculation of Q_{hys} was based on Eq. 8. However, the last E_{OC} value upon discharge did not agree with the first E_{OC} on charge due to the coulombic inefficiency of the cell. If Eq. 8 were exactly applied, this would lead to an obvious overestimation of Q_{hys} , which is physically not meaningful. In other words, the blue area in Fig. 4 would extend down to zero volts because there is no matching discharge voltage curve. Instead, we applied a small correction, so that the last $E_{OC,dis}$ value agrees with the first $E_{OC,cha}$ value. Q_{hys} is thus calculated by integrating over a closed OCV hysteresis curve. This assumption minimizes the error of the coulombic inefficiency but does not exclude it all together. The resulting implications will be discussed throughout this work. For an absolutely accurate calculation the error introduced by the coulombic inefficiency should be ruled out by the design of the experiment using capacity limited cycling procedures (instead of voltage limited), so that the discharge capacity is equal to the charge capacity. This might be a starting point for future research activities striving for the exact quantification of individual heat terms.

As outlined in the Theory section, irreversible energy losses due to overpotential (Q_{irrev}) are dependent on the applied current, while the hysteresis of the OCV is expected to be independent of the C-rate. As expected, the polarization induced overpotential losses in Table I increase with increasing current for both cell chemistries. In the case of LMR-NCM, the irreversible heat during discharge is larger than during charge and becomes more and more dominant for increasing current values, until it reaches 50% of total heat generation at 1C. In Fig. 4a, it can be seen that the potential difference between the voltage curve on load and the OCV curve increases drastically at the end of the discharge (to a lesser degree also at the end of the charge). Hence, the end of the lithiation process of the cathode active material seems to be accompanied by significant kinetic limitations, leading to high overpotentials and, in turn, to high irreversible heat evolution. The asymmetry of the LMR-NCM cathode resistance between the charge and discharge direction was previously demonstrated by Teufl et al.¹²

Energy loss due to overpotential is significantly smaller for NCA, as can be clearly seen in Fig. 4b and Table I. Still, the resistance behavior of NCA at low SOC during discharge is similar to that of LMR-NCM, with a steep increase at the end of the discharge. This was attributed to an increase in the charge transfer resistance, as reported by Weber et al.²⁵ More important is the OCV hysteresis comparison, since there is no significant contribution from this term for NCA/Li cells and the determined contribution of the OCV hysteresis to the overall energy loss of 0.1%–0.3% (see last row in Table I) are most probably due to the fact that the E_{OC} is not yet exactly equal to E_{eq} after the 1 h rest phase. In contrast, the cells with an LMR-NCM cathode suffer a considerable energy loss due to OCV hysteresis of up to 55% of the total energy loss at C/10. At first sight surprising is the observation that the energy loss due to the OCV hysteresis of the LMR-NCM/Li cells decreases with increasing C-rate. The reason for this is that the applied cycling protocol is voltage-limited, meaning that a smaller overall SOC range is accessed when cycling at higher C-rates, and therefore only a smaller part of the OCV hysteresis is observable. We have shown elsewhere (see Fig S6 (available online at stacks.iop.org/JES/169/040547/mmedia) in Ref. 14) that when applying a capacity-limited cycling procedure, the OCV hysteresis is independent of the C-rate. The energy loss due to OCV hysteresis results in an undesirable energy inefficiency, which is presumably dissipated as heat. To clarify this, IMC measurements were conducted to analyze the different sources of heat, particularly the heat due to OCV hysteresis in such materials and to compare it to the thermal behavior of a classical CAM such as NCA.

Accuracy of the isothermal micro-calorimeter.—In order to establish a quantitative correlation between the lost electrical energy calculated from the voltage vs SOC curve by method (ii), as described in the Theory section, and the heat measured by IMC (method (iii)), the accuracy of the calorimetric measurement first has to be validated. For this purpose, the heat evolution from the IMC data (pale, empty symbols) and that calculated from the respective voltage curves (dark, filled symbols) are contrasted in Fig. 5. Ideally, both data sets should show perfect agreement, which is indicated by the dashed lines that represent linear regression lines through all the data. For the LMR-NCM/Li cell, the deviation is between -2% and -6% , with one outlier of -12% for the LMR-NCM/Li cell for one of the two cells (cell number 1) at C/10. This means that the measured heat by calorimetry is generally slightly below the expected value, which may be due to instrument errors such as the loss of heat through the cables connecting the coin cell holder with the potentiostat. Also, it should be noted that if the integration of the calorimeter heat signal in the 6 h OCV rest phase at the end of discharge had been chosen to be longer than 1.5 h, the deviations would become smaller. However, since the estimated time delay for detection of 99% of the heat signal is ≈ 18 min, any extension of the

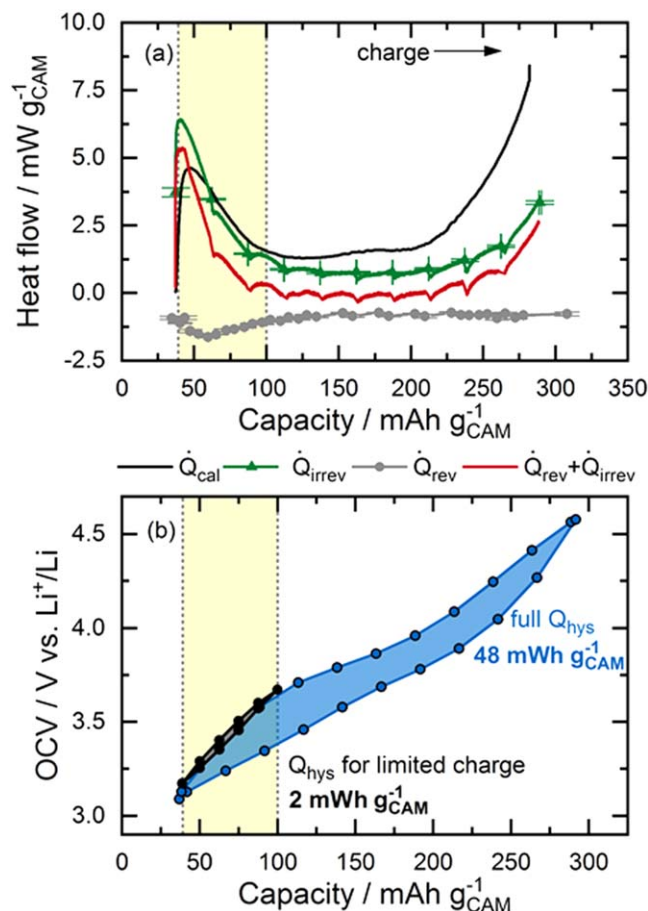


Figure 6. (a) Heat flow of an LMR-NCM/Li cell in charge at C/10 as a function of SOC. The heat flow measured by IMC (black) for cell 2 is compared to the calculated profiles of \dot{Q}_{irrev} , based on the polarization induced overpotential (green, error bars from two measurements; the green line representing a linear interpolation of the OCV data points), and \dot{Q}_{rev} , as determined from entropy measurements (gray, error bars from the calculation). The sum of \dot{Q}_{irrev} and \dot{Q}_{rev} is shown in red. (b) OCV curve at C/10 of a complete cycle (blue) and a cycle limited to a nominal capacity of 100 mAh g_{CAM}^{-1} during charge (black). The yellow shaded area highlights the SOC range in which no significant OCV hysteresis is expected (thus, $\dot{Q}_{hys} \approx 0$).

integration window would increase the risk of including contributions from non-faradaic heat (e.g., through parasitic side reactions). In the case of NCA, the deviations are between +4% and +10%, i.e., the heat measured by calorimetry is more than that obtained by the integration of the voltage vs SOC curves. One of the two NCA/Li cells (cell number 2) showed an outlier of +45% at C/10, but since a fluctuation in the applied electrical current was detected, we did not include this data point in our calculations. Due to the much smaller absolute amount of produced heat in case of the NCA/Li cell, any contributions from undesired side reactions and parasitic heat terms result in a much higher relative error, which might be the reason why the integrated IMC signal is higher than expected. Nevertheless, since the deviations between the expected and measured heat are below $\pm 10\%$ (with the exception of the two above mentioned cases) for both cell chemistries, our original assumption that the lost electrical energy is converted into heat and that parasitic side reactions play no major role is confirmed within the error of the measurements. Another conclusion that can be drawn from Fig. 5 is that the experiments are reproducible, since the energy losses for both cells correspond fairly well (the deviation between two repeat cells at the same C-rate is less than 6% in all cases, except for the two instances mentioned above). For all further calculations, we considered LMR-NCM/Li cell 2 and NCA/Li cell 1.

When comparing the total electrical energy loss/heat production measured by the continuous constant-current (CC) cycling protocol used in the calorimeter experiments (data in Fig. 5) with the total electrical energy loss measured in the intermittent cycling protocol (first row in Table I), it becomes apparent that there is a reasonably good agreement at the low C-rate of C/10, with the intermittent cycling yielding slightly lower energy losses, but that at higher C-rates, this deviation increases substantially, so that at 1C the intermittent cycling procedure results in a $\approx 25\%$ – 35% lower total energy loss. This is mainly due to three factors. First, the CC-cycling procedure, particularly at higher C-rates, leads to a higher overall voltage polarization compared to the intermittent cycling procedure, for which the intermittent OCV holds allow for a repeated relaxation of the concentration gradients in the liquid and solid phase. This can be seen by the comparison of the resulting voltage vs SOC curves shown in the right-hand panel of Fig. 2. Thus, integrating a voltage vs SOC curve from an intermittent cycling protocol always resulted in a smaller value compared to that from a CC-cycling protocol, meaning that the energy losses from intermittent cycling are slightly lower (by $\approx 4\%$ – 7% for the LMR-NCM/Li cells and by up to $\approx 25\%$ for NCA/Li cells). The second reason is that the Coulombic efficiency of each cycle is slightly less than 100%. This irreversible capacity leads to a small ‘gap’ between the charge and the discharge voltage curves, so that the integration of the voltage vs SOC curve cannot be performed 100% accurately. The calculation of total electrical energy loss from the voltage vs SOC curves of the cells tested in the calorimeter energy loss caused by the integration of the gap. For the cells from the intermittent cycling, the electrical energy loss is calculated based on Eq. 6. This mathematical approach, however, does not include the integration of the ‘gap’ since it can neither be ascribed to \dot{Q}_{irrev} during charge or discharge, nor to \dot{Q}_{hys} . Thus, the calculated electrical energy loss is lower in case of the cells from intermittent cycling due to the integration of the voltage vs SOC curve. The third reason is the slightly higher contact resistance of the custom-made coin cell holder for the experiments conducted in the calorimeter ($\approx 9 \Omega$). As these three factors yield reasonably small differences in the total lost electrical energy determined from the voltage vs SOC curves obtained by the two different cycling protocols at C/10, but yield increasingly large differences at higher C-rates, the analysis in the following sections for which both cycling protocols are required will be limited to C/10.

Although the limits of the applied IMC method become clear from Fig. 5, it also provides an answer to the first question in the introduction to this paper: the energy loss due to the OCV hysteresis in LMR-NCM is indeed dissipated as heat (note that another, albeit unlikely possibility would have been that the OCV hysteresis presents a continuous chemical conversion of the bulk of the LMR-NCM material). Moreover, there is an important difference between the two cell chemistries, which is visualized in Fig. 5: the y-axis intercepts of the linear relationship between lost electrical work and measured heat vs mass-specific current density (dashed lines in Fig. 5) is rather small for the NCA/Li cells ($\approx 12.1 \text{ mWh } g_{CAM}^{-1}$ and $\approx 12.4 \text{ mWh } g_{CAM}^{-1}$ for cell 1), while it is quite large ($\approx 93.1 \text{ mWh } g_{CAM}^{-1}$ and $\approx 88.9 \text{ mWh } g_{CAM}^{-1}$ for cell 2) for the LMR-NCM/Li cells, caused by the quasi-static OCV hysteresis, as discussed by Assat et al.²⁰ for the $\text{Li}_2\text{Ru}_{0.75}\text{Sn}_{0.25}\text{O}_3$ model compound. Chevrier et al.²¹ also report a significant heat production at zero current for silicon anodes, and thereby correlate their observation to the current independent nature of the voltage hysteresis. We conclude that even at very low rates, there is significant hysteresis between the OCV curve on charge and discharge, indicating that the underlying processes are far from the thermodynamic equilibrium. The fact that the intercept for the NCA/Li measurement results is not zero, however, underlines the limits of the applied IMC method especially at such small observable heat signals. One would have expected the intercept to be zero because both contributions of reversible and irreversible heat should ideally vanish to zero at infinitesimally small currents. Apart from the accuracy of the method at such small heat

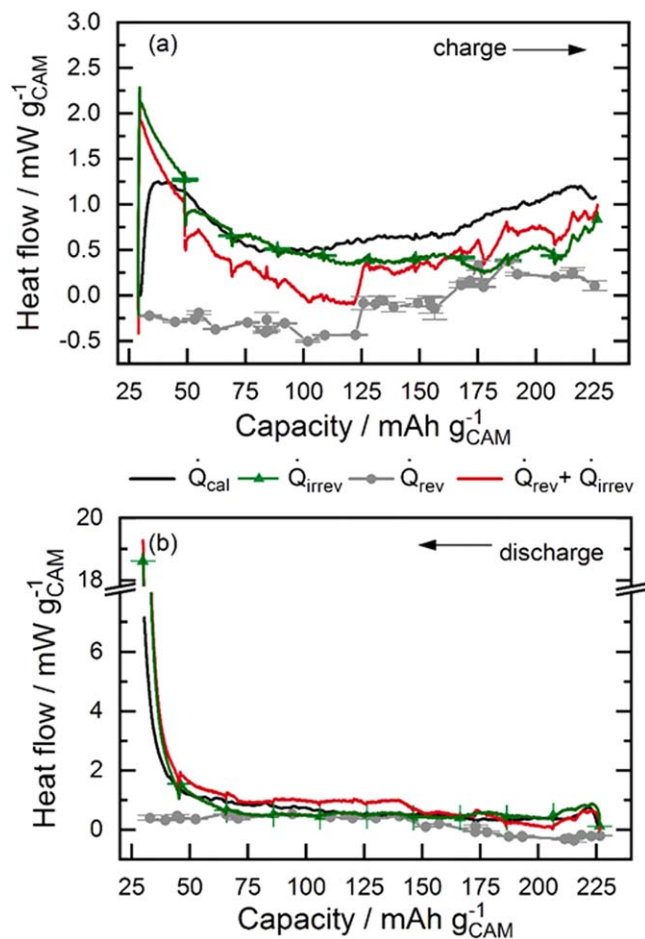


Figure 7. (a) Heat flow of an NCA/Li cell in charge at C/10 as a function of SOC. The heat flow measured by IMC (black) for cell 1 is compared to the calculated profiles of \dot{Q}_{irrev} , based on the polarization induced overpotential (green, error bars from two measurements), and \dot{Q}_{rev} as determined from entropy measurements (gray, error bars from the calculation). The sum of \dot{Q}_{irrev} and \dot{Q}_{rev} is shown in red. In panel (b) the same analysis is shown for the discharge process.

signal amplitudes, any assumptions and simplifications made during the calculation (e.g. correction for Q_{par} , integrating the voltage curve although the coulombic efficiency is less than 100%, etc.) are possible error sources, which might lead to the observed deviation from zero.

Conventional contributions to the heat flow profile.—In addition to the integration of the IMC heat signal to a total heat value, it is also possible to analyze the heat flow profile as a function of the SOC. This analysis involves calculating different heat sources, as outlined in the Theory section of the paper. Figs. 6 and 7 show the heat flow signal measured by IMC (black) together with various heat flow profiles calculated as a function of SOC for LMR-NCM/Li and NCA/Li, respectively. According to Eq. 2, three contributions to the total heat flow can be identified: irreversible heat (\dot{Q}_{irrev}), reversible heat (\dot{Q}_{rev}) and heat due to OCV hysteresis (\dot{Q}_{hys}); while the first two terms can be observed for any electrode material, the latter is only observable in materials with a pronounced OCV hysteresis, such as LMR-NCM. The discussion in this section will focus on the conventional sources of heat, \dot{Q}_{irrev} and \dot{Q}_{rev} .

To compare the measured heat flow with the calculated values, two assumptions have to be made: (i) only the heat signal during current flow is analyzed, which means that heat dissipated after the current is removed is disregarded; (ii) the time delay of the IMC is

assumed to be virtually negligible, so the heat flow profile measured as a function of time can be directly translated to the SOC. Since both the time resolution and the heat dissipation after switching off the current increase with increasing C-rates, this heat flow analysis is only reliable for low currents. For example, with a C-rate of 1C, a time delay of ≈ 18 min already corresponds to a deviation of $\approx 30\%$ SOC, which substantially falsifies the translation of the time axis into an SOC axis, whereas for a C-rate of C/10, this time delay only represents a deviation of 3%. Furthermore, with a C-rate of C/10, the heat evolved after switching off the current at the end of charge is $\approx 12\%$ of the total heat measured for the charge half-cycle of an LMR-NCM/Li cell ($\approx 4\%$ for NCA). In the discharge direction, $\approx 7\%$ of the total heat is evolved at zero current for both cells. In contrast, for the cycle at 1C, these terms increase to $\approx 19\%$ for the charge and $\approx 27\%$ for the discharge in case of LMR-NCM/Li ($\approx 11\%$ and $\approx 22\%$ for NCA), which would clearly not lead to a meaningful analysis. However, even with the slowest C-rate, it is important to bear in mind that measured heat flow profiles are never completely accurate.

Reversible heat contributions to the overall heat flow.—As mentioned above, the reversible heat is included in the calorimetric signal but cannot be calculated from the voltage curve. As shown in Eq. 2, \dot{Q}_{rev} is determined on the basis of the variation of OCV with temperature. These measurements were conducted with the same cathode active material but the OCV was measured against a Li reference electrode, which did not undergo any electrochemical cycling as the Li counter electrode used in this study. Details of the experiment and a discussion of the entropy profile of LMR-NCM are reported elsewhere,¹⁴ but the results from the entropy measurements of the two cathode active materials are plotted in the appendix. For the present study, the most important aspect of our previous publication is that the reversible heat of LMR-NCM/Li cells cannot be calculated from the measured partial molar entropy data because of the path dependence of the entropy curve as a function of SOC. Its integration would include non-reversible pathways, as is generally the case for material that shows a hysteresis in the partial molar entropy vs SOC. This means that a theoretical \dot{Q}_{rev} curve calculated from the entropy data would include an unknown contribution of entropy production in the material. Hence, although mathematically possible, this would not produce a physically meaningful result for the reversible heat flow as a function of SOC. However, this means that we cannot determine what share of the theoretical \dot{Q}_{rev} curve corresponds to the heat term that is reversibly evolved as a function of SOC.

Yet, with the IMC data we can estimate what effect neglecting \dot{Q}_{rev} has on the total heat evolution within a limited SOC range. For this purpose, Fig. 6 shows the IMC heat signal (\dot{Q}_{cal} , black) together with the irreversible heat calculated from the difference between the voltage vs SOC curve on load and under OCV conditions (\dot{Q}_{irrev} , green) and the theoretical reversible heat, which was calculated from the entropy data as explained in Eq. 2, although we already know that this is physically not meaningful (gray). Nevertheless, we will use these calculated data sets in our approach and focus on the heat flow in the low SOC region ($< 100 \text{ mAh g}_{CAM}^{-1}$) during charge. There are two reasons why this SOC region is of special interest: (i) the theoretically calculated reversible heat flow profile exhibits a peak at around $\approx 60 \text{ mAh g}_{CAM}^{-1}$ meaning that in the low SOC region, the contribution of \dot{Q}_{rev} is expected to be most significant; (ii) from cycling experiments it is known that when LMR-NCM is only charged to $\approx 100 \text{ mAh g}_{CAM}^{-1}$ and then discharged again, there is no significant OCV hysteresis (see black data points in Fig. 6b), which means that the heat measured by IMC is exclusively attributable to \dot{Q}_{irrev} and \dot{Q}_{rev} , from which the first one can be easily determined. Figure 6b shows the OCV curve of a cell charged to $100 \text{ mAh g}_{CAM}^{-1}$ together with an OCV curve that is obtained for a full charge/discharge. As is also known from window-opening

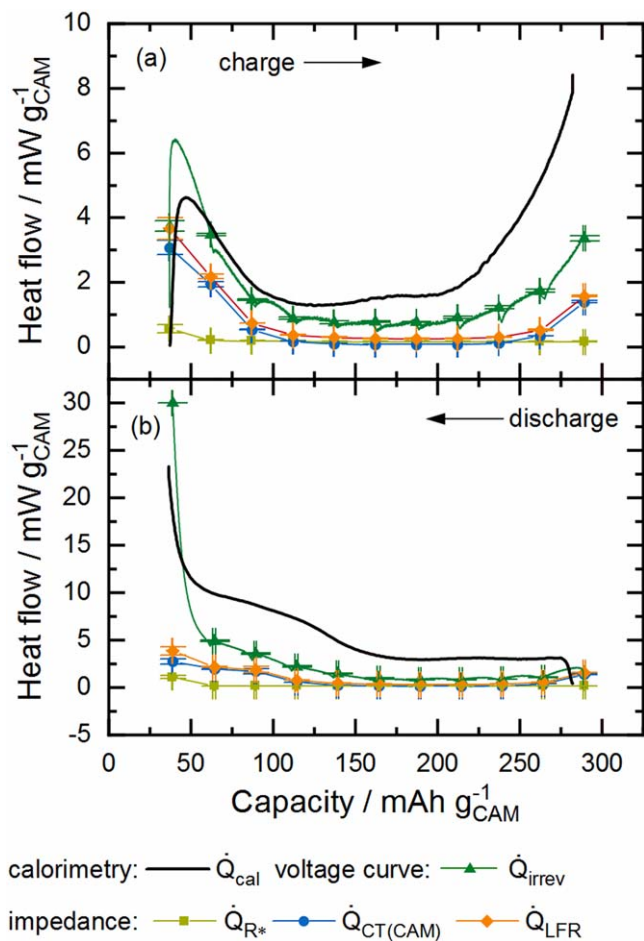


Figure 8. Heat flow during (a) charge and (b) discharge of the LMR-NCM/Li cell (number 2) at C/10 as a function of SOC. The heat flow measured by IMC (black) is compared to calculated heat flow profiles based on data from identical cells. Calculated heat flows are based on the voltage drop measured during intermittent cycling (\dot{Q}_{irrev} , green triangles), and impedance measurements including the LFR (orange), the $R_{CT(CAM)}$ (blue) and the “ohmic” resistance R^* (light green). Error bars are shown for two measurements. The line connecting the voltage drop points (green triangles) results from the subtraction of the OCV curve from the voltage curve on load for the respective half-cycle.

experiments in the literature,²⁶ the OCV hysteresis of LMR-NCM is not pronounced if the charge window is not opened up to higher SOCs. Thus, Eq. 2 simplifies, since $\dot{Q}_{hys} = 0$. This means that any difference between the heat flow measured by IMC and the irreversible heat generation determined from the polarization induced overpotential has to be caused by \dot{Q}_{rev} . However, as shown in Fig. 6a, the measured heat flow (black line) in the yellow shaded region, for which $\dot{Q}_{hys} = 0$, corresponds very closely with the irreversible heat generation (green line and symbols), indicating that the contribution from \dot{Q}_{rev} is not significant. The only deviation between the two heat signals is at the very beginning of charge, when the calculated irreversible heat exceeds the measured signal. This might be an artifact which comes from the fact that \dot{Q}_{irrev} is determined by interpolating between the first and the second OCV points whereby the first OCV point is obtained differently from the subsequent OCV points, as outlined in the Experimental part. The interpretation of this apparent overshoot should be considered carefully. Another reason for the observed mismatch between \dot{Q}_{irrev} and \dot{Q}_{cal} at the beginning of charge might be the above-mentioned time lag of the IMC signal detection. Another possibility is that at the beginning of charge, the endothermic reversible heat

indeed makes a contribution and hence partly compensates for the irreversible heat. However, when the heat flow calculated from the sum of the exothermic irreversible heat and the endothermic reversible heat (red curve in Fig. 6a) is compared to the measured data, no agreement is observed. This further underlines the conclusion drawn by Friedrich et al.¹⁴ that the entropy measurements for LMR-NCM cannot be directly translated into a heat flow curve. The observation that the entropy does not significantly contribute to the measured heat flow profile in the low SOC range, where its values are maximum indicates that also for the rest of the cycle, its contribution can be neglected. Further IMC studies are required to quantify the reversible heat in this type of material. For the investigation conducted here, the reversible heat flow was neglected. Still, we want to emphasize that this simplification is a possible error source regarding the quantification of \dot{Q}_{hys} . What we report here as \dot{Q}_{hys} hence includes an unknown but comparably small contribution of the reversible heat.

The rather complicated discussion regarding the LMR-NCM material becomes simpler with a regular cathode active material, such as NCA, where no hysteresis is present and \dot{Q}_{rev} can be directly calculated from the measurement of $\frac{\partial E_{eq}}{\partial T}$, as explained in the Theory and Experimental sections. Since there is virtually no heat due to OCV hysteresis, Eq. 2 simplifies to $\dot{Q} = \dot{Q}_{irrev} + \dot{Q}_{rev}$. As discussed above, neglecting the SOC dependence of \dot{Q}_{par} results in a rough simplification of the energy balance for NCA. However, as can be seen in Fig. 7, this simplification is acceptable for a semi-quantitative analysis of heat flow as a function of SOC. In Fig. 7, the IMC signal (black) is shown together with the irreversible heat flow calculated from the intermittent cycling (green), the reversible heat calculated from entropy measurements (grey), and the sum $\dot{Q}_{irrev} + \dot{Q}_{rev}$ (red). For the charge half-cycle in Fig. 7a, the irreversible heat is slightly higher than the measured heat at low SOC, while it is clearly smaller at a high SOC. By adding the reversible and irreversible heat, the calculated curve (red) moves closer to the measured one. However, there is still a gap, especially at a high SOC, between the measured signal and the calculated heat flow, which might be attributable to parasitic heat, or simply the inaccuracy of calculating and scaling such small heat flows. For the discharge direction, shown in Fig. 7b, the agreement of the calculated and measured heat flow is similar to that of the charge direction. However, it should be stressed that the absolute signal amplitude is nearly seven times higher, especially at the end of discharge, which makes a direct comparison of the two figure panels difficult.

Based on the data discussed, we conclude that the effect of reversible heat on total heat flow is a source of error, in particular for NCA/Li cells. While it is acceptable to assume a minor contribution of \dot{Q}_{rev} for the LMR-NCM/Li cell due to the comparably very high contribution from the OCV hysteresis heat, \dot{Q}_{rev} has a more significant effect on the overall heat flow for the NCA/Li cell, in which the measurement uncertainties are of the same order of magnitude as \dot{Q}_{rev} . Nevertheless, we want to stress that the exact contribution of \dot{Q}_{rev} was not quantified for either one of the two cells in this study, meaning that it is still contained in the additional heat term, \dot{Q}_{hys} , which will be discussed in the following. Since the significance of \dot{Q}_{rev} was shown to be rather minor for LMR-NCM/Li cells, its contribution to \dot{Q}_{hys} is not considered to be falsifying the analysis.

Irreversible heat.—So far, only the irreversible heat calculated from the potential drop during intermittent cycling has been shown. However, the resistances due to overpotential induced polarization can be further analyzed, using the impedances obtained by EIS analysis. Figures 8a and 8b show the heat flow profiles measured by

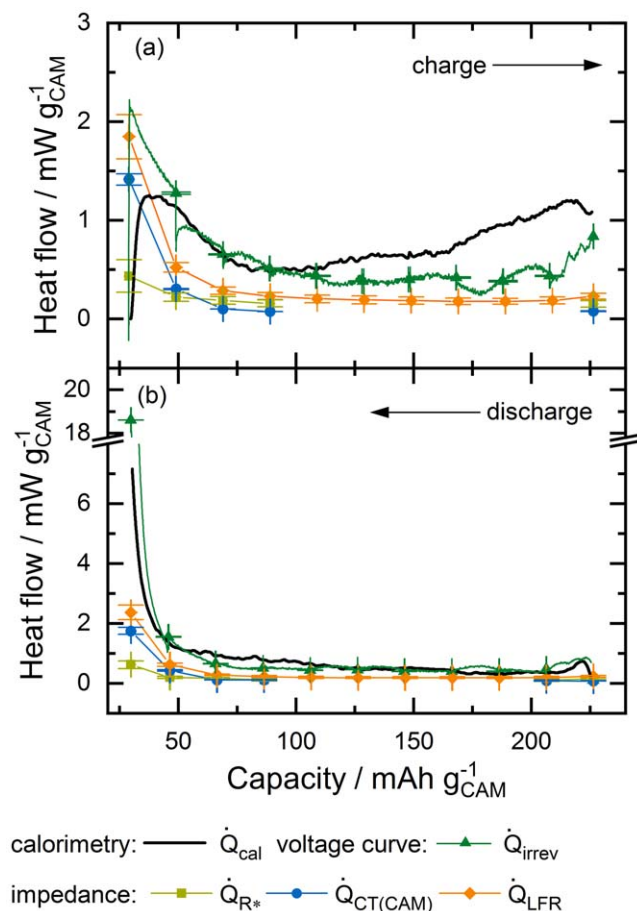


Figure 9. Heat flow during (a) charge and (b) discharge of NCA/Li cells at C/10 as a function of SOC. The heat flow measured by IMC (black) for cell 1 is compared to calculated profiles based on data from identical cells. Calculated heat flows are based on the voltage drop (\dot{Q}_{irrev} , green), and data calculated from impedance measurements including the LFR (orange), the $R_{CT(CAM)}$ (blue) and the “ohmic” resistance R^* (light green). Error bars are shown for two measurements. The line connecting the voltage drop points (green triangles) results from the subtraction of the OCV curve from the voltage curve on load for the respective half-cycle.

IMC for the LMR-NCM/Li cell (black), together with those calculated from the impedance data based on Eq. 3 but using R_{LFR} instead of R_{tot} (orange). Figure 8 also includes the heat flow curves calculated from the individual components of R_{LFR} , namely $R_{CT(CAM)}$ (blue) and R^* (light green) as explained by Eq. 4 and the polarization induced overpotentials (i.e., $E(load) - E(OC)$) determined by the intermittent cycling protocol, using the first part of Eq. 3 (\dot{Q}_{irrev} , green triangles).

In a first comparison of the calorimetric data (black), a clear asymmetry between the charge and discharge heat flow profiles can be observed (see Figs. 8a and 8b). At the beginning of charge cycle, there is a peak in the heat evolution, with a maximum at $\approx 55 \text{ mAh g}_{CAM}^{-1}$, which levels off at around $100 \text{ mAh g}_{CAM}^{-1}$, after which a plateau is observed. At around $225 \text{ mAh g}_{CAM}^{-1}$, the heat flow increases again and reaches a maximum at the end of charge. For the charge half-cycle, the heat flow values over most of the charge are in a range of $1.3 \text{ mW g}_{CAM}^{-1}$ to $8 \text{ mW g}_{CAM}^{-1}$, while for the discharge, these values are much larger, varying between $3 \text{ mW g}_{CAM}^{-1}$ and $36 \text{ mW g}_{CAM}^{-1}$. Besides the absolute values, the profile shape between charge and discharge also differs. During discharge, the heat flow is constant in the high SOC region but starts to increase when discharging below $\approx 170 \text{ mAh g}_{CAM}^{-1}$. Following a steady increase in heat flow in this lower SOC region, a sharp increase is observed when discharging below $\approx 65 \text{ mAh g}_{CAM}^{-1}$.

Irreversible heat flow can be calculated with Eq. 3 based on the voltage drop occurring when the current is switched off during an intermittent cycling, as indicated by the green triangles in Fig. 8. In addition, the OCV curve of a charge/discharge half-cycle (linear interpolation between OCV points) can be subtracted from the respective voltage curve on load (green curve, which is identical with that shown in Fig. 6a), which in principle should give the same results as the data based on the potential drop after one hour of OCV. As a matter of fact, both data sets agree except for the first point during charge, at which the calculation of the voltage drop is based on the instantaneous voltage jump upon connecting the current, as described in the Experimental section. Thus, for the first 10% SOC range, the subtraction line is a better measure for the irreversible heat.

Since the generation of irreversible heat is based on the resistances within a battery cell, impedance spectroscopy is a complementary tool that can be used to further distinguish the underlying resistive phenomena that cause irreversible heat flow. The applied equivalent circuit model includes the charge transfer resistance of the cathode ($R_{CT(CAM)}$, shown in blue in Fig. 8), the low-frequency resistance (LFR, orange) and a so-called R^* (light green), which includes contributions from the high frequency resistance, cathode contact resistance, and anode impedance, as discussed in the Theory and Experimental sections. An example impedance spectrum is shown in Fig. 1. These resistances were translated into a heat flow with Eq. 3. As can be seen in Fig. 8, the profile of the total irreversible heat flow \dot{Q}_{irrev} as determined from the voltage drop agrees with the shape of that calculated from impedance data, \dot{Q}_{LFR} . Both exhibit a U-shape as a function of SOC during charge, which is typical for this type of material.¹² Furthermore, the impedance measurements prove that the dominating contribution to the irreversible heat flow is the charge-transfer resistance, $\dot{Q}_{CT(CAM)}$, while all other resistances, summarized as \dot{Q}_{R^*} , make only minor contributions. The offset between the irreversible heat calculated from the voltage drop (\dot{Q}_{irrev}) and the heat obtained from the impedance data (\dot{Q}_{LFR}) is due to diffusion limitations, which are not captured in the impedance experiment with a lower frequency limit of 0.1 Hz but are included in the voltage drop. These limitations include liquid and solid diffusion, which seem to be rather constant in the middle of the SOC window, with increasing values at low and high SOC. The overall diffusion resistance can be estimated from the difference of the two heat profiles by translating the respective heat flow into an apparent resistance based on Eq. 3. In the constant region, it is around $\approx 60 \Omega \text{ cm}^2$ while at high SOC during charge, it increases to $\approx 140 \Omega \text{ cm}^2$ and at low SOC during discharge up to $\approx 215 \Omega \text{ cm}^2$, with an extremely high value at the end of discharge in the k Ω -range.

We performed a similar analysis for the NCA/Li cells, shown in Figs. 9a and 9b. The heat flow measured by IMC (\dot{Q}_{cal} , black) displays some interesting differences to that of the LMR-NCM/Li cells. Most strikingly, the overall measured heat flow (black curve) is significantly lower. The curve of the IMC signal during charge has its maximum of $\approx 1.2 \text{ mW g}_{CAM}^{-1}$ at the beginning of charge, after which the heat flow levels off until $\approx 75 \text{ mAh g}_{CAM}^{-1}$ and gradually increases again until the end of the half-cycle. Overall, the heat flow curve during charge of the NCA/Li cell is rather flat compared to that of the LMR-NCM/Li cell. The IMC signal of the NCA/Li cell during discharge, shown in Fig. 9b, has a similarly flat shape as during charge, and its absolute values are of the same order of magnitude until the cell is discharged below $\approx 50 \text{ mAh g}_{CAM}^{-1}$, at which point the heat signal displays a steep increase up to $\approx 7 \text{ mW g}_{CAM}^{-1}$. The deviation between the irreversible heat flow (\dot{Q}_{irrev} , green curve) and the measured signal (black curve), which is especially prominent at the end of the charge process, was discussed above and arises from a combination of reversible heat and measurement inaccuracy. The diffusion limitations causing the difference between \dot{Q}_{irrev} (green) and \dot{Q}_{LFR} (orange) cover $\approx 50\%$

Table I. Lost electrical energy for LMR-NCM and NCA half-cells calculated from the voltage vs SOC charge/discharge curve as a function of C-rate, using an intermittent cycling protocol. The total energy loss is shown in absolute numbers and relative to the charge energy of the respective cycle. The different energy terms as defined by Eqs. 7 and 8 are shown as absolute numbers and relative shares of Q_{total} .

Electrical energy loss	C/10		C/5		C/2		1C	
	LMR-NCM	NCA	LMR-NCM	NCA	LMR-NCM	NCA	LMR-NCM	NCA
Q_{total} [mWh/g _{CAM}]	84.1	9.3	88.1	14	99.7	23.8	114.6	34.8
% of charge energy	8%	1.2%	9%	1.9%	12%	3.4%	15%	5.2%
$Q_{irrev,cha}$ [mWh/g _{CAM}]	15.0	3.1	19.8	4.9	28.7	10.6	37.7	15.6
% of Q_{total}	18%	33%	23%	35%	29%	45%	33%	45%
$Q_{irrev,dis}$ [mWh/g _{CAM}]	23.0	4.8	31.2	7.2	42.6	12.5	57.6	18.4
% of Q_{total}	27%	52%	35%	51%	43%	53%	50%	53%
Q_{hys} [mWh/g _{CAM}]	46.1	1.4	37.1	1.9	28.4	0.7	19.4	0.8
% of Q_{total}	55%	15%	42%	14%	28%	3%	17%	2%

of the irreversible heat flow. They translate into diffusion resistances similar to those found for the LMR-NCM/Li cells of around $50 \Omega \text{ cm}^2$ in the mid-SOC region with increasing values at the end of charge ($120 \Omega \text{ cm}^2$) and discharge ($>200 \Omega \text{ cm}^2$). The cathode related resistance (R_{CAM}) dominates the impedance response in the lower SOC region, with values of up to $250 \Omega \text{ cm}^2$. In contrast to the impedance spectra of the LMR-NCM/Li cells (see Fig. 1), the two semi-circles of the NCA spectra, from which R^* and R_{CAM} were determined, are merged together in the middle SOC range ($40 \text{ mAh g}_{CAM}^{-1} < \text{SOC} < 200 \text{ mAh g}_{CAM}^{-1}$). This means that the two resistances could not be deconvoluted using the transmission line model. This is why, in this SOC region, only the LFR was

determined from the impedance spectra of NCA. Another difference to the impedance response of LMR-NCM is that, at the end of charge, R_{CAM} of NCA does not increase significantly, due to the simple fact that the cut-off potential for the NCA cells is lower and a larger amount of cyclable lithium is still available in the material at the end of the charge process.

As outlined in Eq. 2, another heat generation term exists for materials with an OCV hysteresis, such as LMR-NCM, which is Q_{hys} , i.e., the heat due to OCV hysteresis. This will be discussed in more detail in the following.

Deconvolution of energy losses.—Valuable information on the allocation of heat due to OCV hysteresis (Q_{hys}) to a charge and discharge half-cycle can be gained by comparing the heat measured by IMC with the electrical energy loss terms. In Fig. 10, this analysis is conducted for the lowest C-rate of C/10 with the integrated calorimetric heat signal shown in the left-hand column (charge and discharge heat stacked) and the electrical energy losses in the right-hand column for both the LMR-NCM/Li and the NCA/Li cell. The analysis is based on the combination of electrochemical and calorimetric data visualized in Fig. 2. Thereby, the IMC signal is integrated over the charge or discharge half-cycle including the first 1.5 h of the consecutive relaxation phase at zero current as described above. In contrast to the heat flow data (\dot{Q}_{cal} in mW/g_{CAM}) shown in Figs. 6 to 9, the integration over time leads to the amount of evolved heat Q_{cal} (in mWh/g_{CAM}). For example, from IMC, the evolved heat during charge ($Q_{cal,cha}$) is accessible, which is a sum of the following terms:

$$Q_{cal,cha} = Q_{irrev,cha} + Q_{hys,cha} + |Q_{rev,cha}| \quad [9]$$

Solving for $Q_{hys,cha}$, this yields:

$$Q_{hys,cha} = Q_{cal,cha} - Q_{irrev,cha} - |Q_{rev,cha}| \quad [10]$$

$Q_{irrev,cha}$ is calculated from the electrochemical measurements by integrating over the voltage curve as shown in Fig. 4 and Table I. To obtain values for $Q_{hys,cha}$, one has to assume that the contribution of $Q_{rev,cha}$ is negligible since the moment $Q_{rev,cha}$ becomes comparable

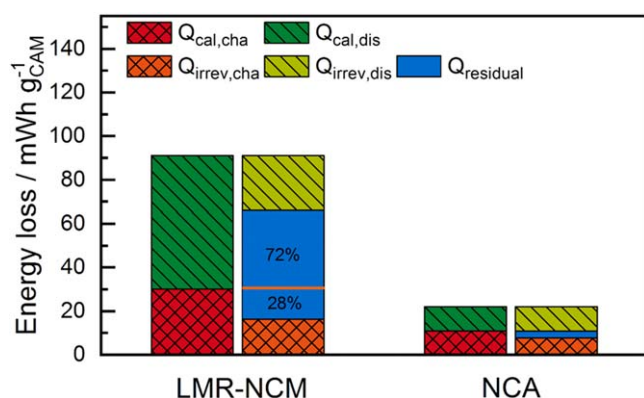


Figure 10. Allocation of different sources of heat according to the results from intermittent cycling to the heat measured by IMC for the lowest C-rate of C/10 for the LMR-NCM/Li cell (number 2) and for the NCA/Li cell (number 1). For each cell, the left-hand column contains the stacked IMC heat data from the charge (red) and discharge (green) half-cycle. The expected electrical energy loss determined from intermittent cycling is shown for each cell by the right-hand column. Thereby, the relative shares for the polarization induced overpotential in charge (orange) and discharge (light green) are shown (see Table I) together with the residual energy loss ($Q_{residual}$, blue). In case of LMR-NCM/Li, this corresponds to the OCV hysteresis. The orange line and relative numbers indicate its share in charge and discharge.

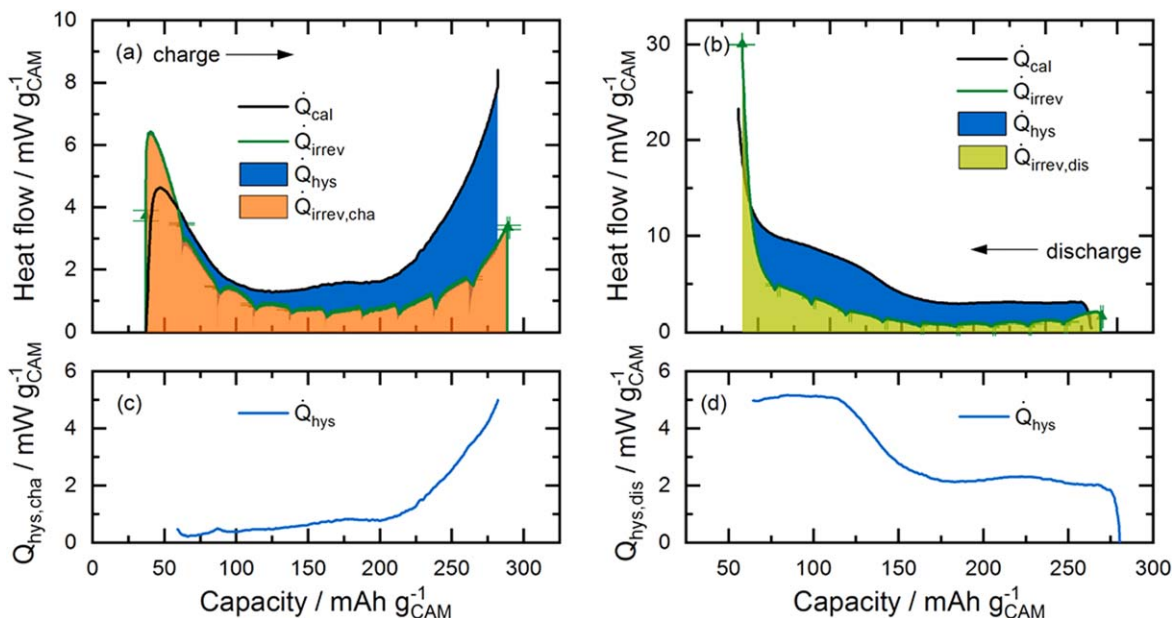


Figure 11. Heat flow during (a) charge and (b) discharge of the LMR-NCM/Li cell (cell number 2) at C/10 as a function of SOC. The heat flow measured by IMC (black) is compared to the irreversible heat generation calculated from the difference between the voltage at load and the OCV curve obtained by the intermittent cycling protocol (green line, error bars from two measurements). The shaded areas correspond to the irreversible heat in charge (orange) and discharge (green) and the heat due to OCV hysteresis (blue). The heat flow of \dot{Q}_{hys} in (c) charge and (d) discharge is calculated by $\dot{Q}_{cal} - \dot{Q}_{irrev}$ (only exothermic signal is shown).

to any of the other heat terms, independent values for $Q_{hys,cha}$ cannot be obtained by this approach anymore. For the analysis shown in Fig. 10, we therefore deliberately use the term $Q_{residual}$ instead of Q_{hys} to make the difference between both values more clear. The effect on the accuracy of the results will be discussed below. For the discharge, an equivalent derivation can be made.

The results from the IMC measurements ($Q_{cal,cha}$ and $Q_{cal,dis}$) are shown by the left-hand column for both the LMR-NCM/Li and the NCA/Li cell. The right-hand column for each cell marks the expected total electrical energy loss. To allocate the different sources of heat, determined by intermittent cycling, to the heat measured by IMC, the relative shares, as shown in Table I, were applied to the calorimeter signal. Note that by this definition, the height of the right-hand column agrees with that of the left-hand column since it simply illustrates the relative distribution of heat sources. For example, it is known from the intermittent cycling at C/10 that 18% of the total energy loss is attributable to $Q_{irrev,cha}$ and 27% to $Q_{irrev,dis}$. Hence, the remaining heat, which is measured by IMC ($Q_{residual}$ in Fig. 10), can be allocated to the OCV hysteresis and can furthermore be separated into its shares during the charge and discharge half-cycles, respectively. This is illustrated by the orange line in Fig. 10 and the percentage values in the blue section.

The left part of Fig. 10 shows the allocation of the different sources of heat to the IMC signal for the LMR-NCM/Li cell, indicating that the heat measured by IMC during charge (red column) is only about half of that measured during discharge (green column). As can be seen in the right-hand column for the LMR-NCM/Li cell in Fig. 10, the polarization induced overpotential losses during discharge ($Q_{irrev,dis}$, light green) are larger than during charge ($Q_{irrev,cha}$, orange), which means that more irreversible heat is evolved during discharge. The heat caused by these overpotential losses is directly attributable to the respective charge and discharge IMC heat signal. The additional heat, which is observed by IMC for each half-cycle ($Q_{residual}$), is assigned to the OCV hysteresis. It can be seen that the ratio between discharge and charge is around 70:30, meaning that most of the heat due to OCV hysteresis is evolved in the discharge process. Together with the higher irreversible heat

evolved during discharge, this leads to a considerable asymmetric heat evolution between the two half-cycles.

As mentioned above, this analysis is somewhat compromised by the reversible heat due to entropic changes, which is assumed to be negligible for the construction of $Q_{residual}$ in Fig. 10. It needs to be noted, however, that any contribution of the reversible heat is recorded by the calorimeter but cannot be observed in the voltage vs SOC curve. Hence, this heat term contributes to the overall heat observed by IMC (left-hand columns in 10) but is not considered for the construction of the right-hand ones. As explained in the Theory section, reversible heat has opposite signs on charge and discharge and is therefore, by definition, equal to zero for a whole cycle. This means that both the total heat measured by IMC and the electrical energy loss have no net contribution from Q_{rev} . However, Q_{rev} influences the respective half-cycles by adding another exothermic heat source to one direction (discharge in the case of the LMR-NCM)¹⁴ and an endothermic source to the other one (charge for the LMR-NCM).¹⁴ The reversible heat can be determined from entropy measurement. However, in the case of LMR-NCM, these experiments revealed that the entropy is path-dependent between charge and discharge, which suggests that the integration of Q_{rev} would include non-reversible pathways, and hence would not give a meaningful value for Q_{rev} .¹⁴ Rather, we assume that the entropy curve indicates that entropy production is being observed.¹⁴ For a detailed discussion on the entropy and reversible heat in LMR-NCM and the implications of non-reversible pathways, the interested reader is referred to our previous work (in particular the discussion of Eq. 17 in Friedrich et al.¹⁴). However, the effect of the reversible heat can be analyzed when the heat flow is considered instead of the total integrated heat. As is shown in Fig. 6, the reversible heat can be assumed to be negligible in the case of the LMR-NCM/Li cell investigated here, so that the analysis shown in Fig. 10 should be reasonably accurate.

Figure 10 also shows the IMC results of the NCA/Li cell, comparing them with the energy loss data expected from the intermittent cycling (Table I and Fig. 5) in the same way as for the LMR-NCM/Li cell. The generated heat of the NCA/Li cell is clearly less than for the LMR-NCM/Li cell. For the results from

calorimetry, a symmetrical heat release between charge and discharge is observed. The electrochemical data, however, suggest that the irreversible heat in charge direction should be slightly smaller than the heat determined by calorimetry, while for the discharge direction it should be slightly larger. The mismatch between the heat measured by IMC and the calculated heat in charge and discharge is most likely attributable to the simplifications made with the calculation of the different heat terms. As mentioned above, the irreversible capacity loss results in a relatively large error when calculating the total electrical energy loss in the case of NCA, because of the rather small absolute heat flow signal. When the relative shares of the energy terms calculated from the intermittent cycling are then applied to deconvolute the different contributions to the IMC signal, this additional heat term is evenly distributed between $Q_{irrev,cha}$, $Q_{irrev,dis}$ and $Q_{residual}$. However, it seems that by doing so, $Q_{irrev,dis}$ is overestimated while $Q_{irrev,cha}$ is underestimated. For materials with small absolute heat signals, such as NCA, neglect of this energy loss term is not justified when aiming at a quantitative analysis. We therefore recommend determining this heat term separately so as to be able to allocate it to the charge or discharge direction or analyze the heat flow signal as a function of SOC.

Heat evolution due to OCV hysteresis of LMR-NCM.—Figure 8 shows the various sources of irreversible heat, while Fig. 6 elucidates the rather minor contribution of reversible heat for LMR-NCM. The lost electrical energy, which can be calculated by integrating the OCV curve, as shown in Fig. 4a and Table I, is an additional source of heat for cells with LMR-NCM compared to normal cathodes like NCA. In Fig. 10, we discussed what share of this heat is evolved in each charge and discharge half-cycle at C/10 of LMR-NCM/Li cells. Besides absolute numbers, another interesting question, which we posed at the beginning of the paper, is how \dot{Q}_{hys} is evolved as a function of the SOC. To answer it, we will compare the heat evolution measured by IMC with the total irreversible heat flow determined from the intermittent cycling protocol, as shown in Figs. 11a and 11b. The data are the same as in Fig. 8, but focus only on the two sources of heat that are essential for determining \dot{Q}_{hys} , i.e., ignoring the minor contribution from reversible heat. The difference between the measured heat flow (\dot{Q}_{cal} , black curve) and the expected irreversible heat flow (\dot{Q}_{irrev} , green curve) is a measure of the evolution of \dot{Q}_{hys} (blue shaded area). The difference curve, $\dot{Q}_{cal} - \dot{Q}_{irrev}$, is shown in Figs. 11c and 11d for the charge and discharge half-cycle, respectively.

As can be seen from the difference plot in Fig. 11c for the charge half-cycle, the heat flow due to the OCV hysteresis is small up to an SOC of ≈ 200 mAh g_{CAM}^{-1} , after which it increases steadily. At the beginning of charge, however, the irreversible heat flow is greater than the measured signal. This apparent overshoot in the green curve is most likely due to the way how \dot{Q}_{irrev} is constructed by linear interpolation between the OCV points as mentioned above. This is supported by the observation that the two first data points (green triangles; direct result of taking the difference between E_{load} and at this SOC) agree rather well with the IMC heat flow curve (black line). Other sources of errors include the time delay of the measurement setup and the inaccuracy in the determination of $\dot{Q}_{irrev,cha}$. Since this deviation is considered to be an artifact from the calculation, no endothermic \dot{Q}_{hys} signal is shown in Fig. 11c. A more detailed analysis of this lower SOC range, for instance with a smaller Δ SOC spacing in the intermittent cycling, could shed further light on the thermal effects at the beginning of charge. During discharge, \dot{Q}_{hys} is evolved over the whole SOC window with a constant value of ≈ 2 mW g_{CAM}^{-1} during the initial discharge and an increasing heat flow when the cell is discharged below ≈ 170 mAh g_{CAM}^{-1} ; this forms a plateau at ≈ 5 mW g_{CAM}^{-1} towards the end of discharge, where the irreversible heat strongly dominates the total heat flow. A comparison with the total heat flow of NCA serves to

classify the magnitude of the evolution of \dot{Q}_{hys} . While for the NCA/Li cells the total measured IMC signal is between 0.5 mW g_{CAM}^{-1} and 2 mW g_{CAM}^{-1} for most of the SOC range, the heat evolution only due to the OCV hysteresis for the LMR-NCM/Li cells is between 0.5–5 mW g_{CAM}^{-1} in charge and between 2–5 mW g_{CAM}^{-1} in discharge. Hence, for LMR-NCM/Li cells, the material-specific \dot{Q}_{hys} , is of the same order of magnitude (or even greater) as the total heat flow of the reference material NCA.

The profile of the total heat evolution of LMR-NCM in charge is dominated by the shape of the irreversible heat flow (up to ≈ 100 mAh g_{CAM}^{-1}), while in the discharge direction, \dot{Q}_{hys} makes a significant contribution to the heat flow profile, especially in the SOC range between ≈ 250 mAh g_{CAM}^{-1} and ≈ 65 mAh g_{CAM}^{-1} . The SOC ranges at which \dot{Q}_{hys} is mainly evolved in charge and discharge (see Figs. 11c and 11d) suggest that the underlying phenomena for OCV hysteresis in LMR-NCM occur particularly at high SOC during charge (>200 mAh g_{CAM}^{-1}) and at low SOC during discharge (<170 mAh g_{CAM}^{-1}). From window-opening experiments, it is known that the hysteresis of the OCV curve,^{26,27} the lattice parameters,¹³ and the entropy profile¹⁴ grow gradually, becoming more and more pronounced as the charge or discharge window are continuously opened. The evolution of \dot{Q}_{hys} reflects the behavior of these other properties and hence indicates that the underlying processes leading to the reported hysteresis phenomena cause waste heat, which is observed at high SOC in charge and at low SOC during discharge. However, as discussed above, the accuracy of this analysis method is limited due to the time-delay of the calorimeter, and we can therefore only report a trend in \dot{Q}_{hys} evolution as a function of SOC. In an extreme case, a pronounced time lag would lead to a relative shift on the SOC axis, meaning that the SOC for the \dot{Q}_{hys} evolution in charge is generally overestimated, while in discharge it is underestimated. For the data shown in Fig. 11, this potential error is rather small, as outlined above (i.e., the time lag ≈ 18 min until 99% of the heat signal is detected corresponds to a Δ SOC of $\approx 3\%$). However, as mentioned above, there is still some heat flow present after removing the current, and there is also an excess of irreversible heat at the beginning of charge. This means that not all heat is detected at the moment of its production. The heat evolution towards the end of each half-cycle might therefore include some share of the heat produced at lower SOC, leading to an overestimation of the heat flow at high SOC. As mentioned above for Figs. 6 and 8, the heat signal after disconnecting the current was also neglected in the analysis shown in Fig. 11. Moreover, the heat flow observed by IMC might contain contributions from parasitic heat sources, such as electrolyte decomposition, leading to an overestimation of \dot{Q}_{hys} . Probably the most significant source of error is the unknown but evidentially minor contribution of \dot{Q}_{rev} to the herein determined \dot{Q}_{hys} , which might lead to an overestimation of \dot{Q}_{hys} in case of an exothermic \dot{Q}_{rev} (and an underestimated for an endothermic \dot{Q}_{rev}). In conclusion, we wish to emphasize that what is reported here is a semi-quantitative trend in the evolution of \dot{Q}_{hys} in charge and discharge and that further measurements are required for a more accurate quantitative analysis.

Conclusions

We conducted a comparative study comprising an investigation of the heat release of LMR-NCM/Li and NCA/Li coin cells at different C-rates using isothermal micro-calorimetry. Impedance spectroscopy and an intermittent cycling protocol were applied as complementary methods to analyze the various heat sources. The focus of this study is on the LMR-NCM cathode active material (CAM), which has a unique OCV hysteresis. The electrochemical and calorimetric data sets were analyzed employing two different approaches: (i) integrating the heat flow for an individual half-cycle

to get the total generated heat for the respective charge or discharge direction (in $\text{mWh g}_{\text{CAM}}^{-1}$), and (ii) converting the heat flow over time to a heat flow as a function of SOC (in $\text{mW g}_{\text{CAM}}^{-1}$). Using the first approach, we observed that the total heat generation for LMR-NCM is much higher than for NCA (decreasing from a factor of 9 to 3 for increasing the C-rate from C/10 to 1C), leading to a lower energy round-trip efficiency. For both CAMs, the overall released heat shows a linear correlation with the applied C-rate. However, while the heat release extrapolated to a zero C-rate is rather small for the NCA/Li cells, it is significantly higher for the LMR-NCM/Li cells due to the quasi-static OCV hysteresis being a material-specific property present even under zero current conditions.

The OCV hysteresis was further analyzed by intermittent cycling, in which a 1 h rest phase was applied after each 10% SOC step to collect OCV points during charging and discharging at different C-rates. These electrochemical measurements indicate that the OCV hysteresis of the LMR-NCM material is responsible for up to 55% of the total electrical energy loss of LMR-NCM/Li cells at C/10. The irreversible heat generated during charge and discharge was also calculated by this method. The share of the heat generation due to OCV hysteresis was attributed to either the charge or discharge direction on the basis of the calculated heat terms and the heat measured by IMC for the individual half-cycles assuming that the reversible heat due to entropy is negligible. We found that most of the heat due to OCV hysteresis in the LMR-NCM/Li cells is dissipated during discharge (72% for C/10).

Using approach (ii) above, we compared the measured heat flow signal with the profile calculated from electrochemical data. For the NCA/Li cells, the sum of the irreversible heat determined by intermittent cycling and the reversible heat calculated from entropy measurements corresponded well with the heat flow measured by IMC. The heat flow is clearly dominated by irreversible heat while the reversible heat serves more as a small correction for the calculated curve. However, the very small absolute level of the heat flow signal for the NCA material means that the limit of the applied approach's accuracy is reached, especially with regard to the combination of the measurement results from different cells and methods with an irreversible capacity leading to a source of error, which is in the order of the measured data. In contrast, due to the higher absolute signal for LMR-NCM/Li cells (≈ 4 times), the analysis is more accurate in this case. Using impedance spectroscopy, the irreversible heat determined from intermittent cycling was further differentiated into the underlying resistive phenomena, which lead to the observed potential drop. We found that for both cathode active materials, the charge transfer resistance of the cathode dominates the irreversible heat flow curve. For LMR-NCM, the $R_{\text{CT}(\text{CAM})}$ shows a characteristic U-shape as a function of SOC and

further contributions from diffusional limitations are rather small. For the NCA/Li cells, the diffusion resistances are very similar, while the charge transfer resistance is generally much smaller and covers only $\approx 50\%$ of the overpotential losses. The contribution of the Li anode is included in the fitting parameters but makes only a minor contribution to the low frequency resistance at very low and high SOC.

With LMR-NCM/Li cells, the analysis of the heat flow profiles provides detailed information about the OCV hysteresis. The heat evolution due to OCV hysteresis is determined as a function of SOC by subtracting the calculated irreversible heat flow from the measured heat signal. During charge, \dot{Q}_{hys} is mainly evolved at a high SOC ($>200 \text{ mAh g}_{\text{CAM}}^{-1}$), while during discharge, it is released over the whole SOC range at a constant evolution rate until $170 \text{ mAh g}_{\text{CAM}}^{-1}$ and an increasing rate below that. The heat evolved due to OCV hysteresis in LMR-NCM is of the same order of magnitude as the total heat release of the reference material NCA, which underlines the importance of the analysis of this heat source.

To revisit the questions raised at the beginning of this paper, we found that (i) the energy loss due to OCV hysteresis is fully dissipated as heat and (ii) the majority is evolved during discharge. The fact that (iii) the heat due to OCV hysteresis is mainly generated at high SOC during charge and at low SOC during discharge indicates that (iv) the underlying processes leading to the hysteresis phenomena in LMR-NCM occur in these SOC ranges, which agrees with observations from literature reports on parameters, such as the LMR-NCM lattice parameters.

Acknowledgments

We want to acknowledge BASF SE for the support within its Scientific Network on Electrochemistry and Batteries and the German Federal Ministry of Education and Research (BMBF) for its financial support within the ExZellTUM II project (grant no. 03XP0081). We gratefully thank See Tow Wei Hao for his contribution to the entropy measurements of NCA and Viola Knödler for her support with the NCA/Li cell building.

Appendix

As shown in Eq. 2, reversible heat is calculated as a product of the current, temperature and temperature-dependent OCV value, $\frac{\partial E_{\text{eq}}}{\partial T}$. The latter was determined for both LMR-NCM/Li and NCA/Li cells as described in the Experimental section. A detailed discussion of the method and the results for LMR-NCM/Li cells is reported elsewhere.¹⁴ The obtained $\frac{\partial E_{\text{eq}}}{\partial T}$ values are shown in Figure A.1.

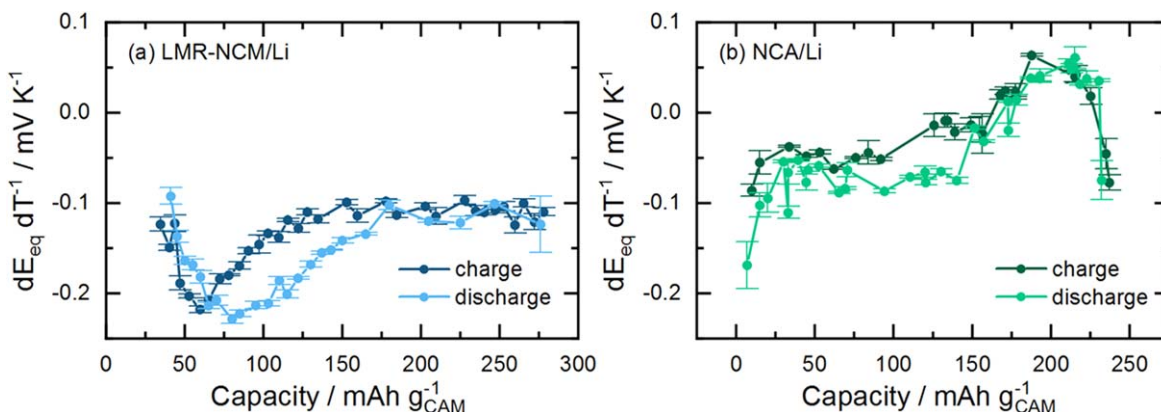


Figure A.1. Temperature-dependent OCV value, $\frac{\partial E_{\text{eq}}}{\partial T}$, for (a) LMR-NCM/Li and (b) NCA/Li cells during charge and discharge as a function of specific capacity. The variation of the OCV with temperature was measured as described above and discussed by Friedrich et al.¹⁴

ORCID

Franziska Friedrich  <https://orcid.org/0000-0001-9400-1212>
 Tanja Zünd  <https://orcid.org/0000-0002-1650-3636>
 Hubert A. Gasteiger  <https://orcid.org/0000-0001-8199-8703>

References

1. R. Schmuck, R. Wagner, G. Hörpel, T. Placke, and M. Winter, *Nat. Energy*, **3**, 267 (2018).
2. K. Onda, T. Ohshima, M. Nakayama, K. Fukuda, and T. Araki, *J. Power Sources*, **158**, 535 (2006).
3. H. Bang, H. Yang, Y. K. Sun, and J. Prakash, *J. Electrochem. Soc.*, **152**, A421 (2005).
4. H. Yang and J. Prakash, *J. Electrochem. Soc.*, **151**, A1222 (2004).
5. K. E. Thomas and J. Newman, *J. Electrochem. Soc.*, **150**, A176 (2003).
6. L. Kraft, T. Zünd, D. Schreiner, R. Wilhelm, F. Günter, G. Reinhart, H. A. Gasteiger, and A. Jossen, *J. Electrochem. Soc.*, **168**, 020537 (2021).
7. L. Kraft, A. Hoeffling, T. Zünd, A. Kunz, M. Steinhardt, J. Tübke, and A. Jossen, *J. Electrochem. Soc.*, **168**, 053505 (2021).
8. G. Zubi, R. Dufo-López, M. Carvalho, and G. Pasaoglu, *Renew. Sustain. Energy Rev.*, **89**, 292 (2018).
9. T. Teuff, B. Strehle, P. Müller, H. A. Gasteiger, and M. A. Mendez, *J. Electrochem. Soc.*, **165**, A2718 (2018).
10. K. G. Gallagher, J. R. Croy, M. Balasubramanian, M. Bettge, D. P. Abraham, A. K. Burrell, and M. M. Thackeray, *Electrochem. Commun.*, **33**, 96 (2013).
11. J. R. Croy, D. Kim, M. Balasubramanian, K. Gallagher, S.-H. Kang, and M. M. Thackeray, *J. Electrochem. Soc.*, **159**, A781 (2012).
12. T. Teuff, D. Pritzl, S. Solchenbach, H. A. Gasteiger, and M. A. Mendez, *J. Electrochem. Soc.*, **166**, A1275 (2019).
13. B. Strehle, T. Zünd, S. Siculo, A. Kiebling, V. Baran, and H. A. Gasteiger, *J. Electrochem. Soc.*, **169**, 020554 (2022).
14. F. Friedrich, S. Pieper, and H. A. Gasteiger, *J. Electrochem. Soc.*, **168**, 120502 (2021).
15. G. Assat, D. Foix, C. Delacourt, A. Iadecola, R. Dedryvère, and J.-M. Tarascon, *Nat. Commun.*, **8**, 2219 (2017).
16. W. E. Gent et al., *Nat. Commun.*, **8**, 2091 (2017).
17. W. Shi, J. Zheng, J. Xiao, X. Chen, B. J. Polzin, and J.-G. Zhang, *J. Electrochem. Soc.*, **163**, A571 (2016).
18. L. J. Krause, L. D. Jensen, and J. R. Dahn, *J. Electrochem. Soc.*, **159**, A937 (2012).
19. L. M. Housel et al., *ACS Appl. Mater. Interfaces*, **11**, 37567 (2019).
20. G. Assat, S. L. Glazier, C. Delacourt, and J.-M. Tarascon, *Nat. Energy*, **4**, 647 (2019).
21. V. L. Chevrier, Z. Yan, S. L. Glazier, M. N. Obrovac, and L. J. Krause, *J. Electrochem. Soc.*, **168**, 030504 (2021).
22. L. E. Downie, S. R. Hyatt, A. T. B. Wright, and J. R. Dahn, *J. Phys. Chem. C*, **118**, 29533 (2014).
23. J. Landesfeind, D. Pritzl, and H. A. Gasteiger, *J. Electrochem. Soc.*, **164**, A1773 (2017).
24. R. Morasch, J. Keilhofer, H. A. Gasteiger, and B. Suthar, *J. Electrochem. Soc.*, **168**, 080519 (2021).
25. R. Weber, A. J. Louli, K. P. Plucknett, and J. R. Dahn, *J. Electrochem. Soc.*, **166**, A1779 (2019).
26. J. R. Croy, K. G. Gallagher, M. Balasubramanian, Z. Chen, Y. Ren, D. Kim, S.-H. Kang, D. W. Dees, and M. M. Thackeray, *J. Phys. Chem. C*, **117**, 6525 (2013).
27. J. R. Croy, K. G. Gallagher, M. Balasubramanian, B. R. Long, and M. M. Thackeray, *J. Electrochem. Soc.*, **161**, A318 (2014).

3.2.3 Heat generation during the first activation cycle

The manuscript with the title “Heat Generation During the First Activation Cycle in Li-Ion Batteries with Li- and Mn-rich Layered Oxides Measured by Isothermal Micro-calorimetry” will soon be submitted to a peer-reviewed journal. Since the results are not published yet, the manuscript is shown in the Appendix in its current version.

In the previous sections, the OCV hysteresis of LMR-NCM and its implications on the heat generation were discussed in detail. Interestingly, this hysteresis only occurs for an activated CAM. The activation happens when the LMR-NCM is charged to 4.8 V vs. Li⁺/Li. The corresponding charge voltage curve has a unique shape and exhibits a characteristic plateau at ≈ 4.5 V, during which irreversible structural rearrangements occur, including the loss of the “honey-comb” ordering^{106,136}, irreversible oxidation of lattice oxygen,^{93,94} partly reversible TM migration^{97,106,107}, the formation of Li/TM dumbbells^{97,102} and of dislocations¹³⁷. In the activation cycle, an anomalously high charge capacity of more than 300 mAh/g is reached. The afore mentioned processes however lead to a loss of chemically available Li sites, thereby causing a substantial irreversible capacity loss during the first cycle. The subsequent discharge occurs at a significantly lower voltage. The loss of average voltage together with the large irreversible capacity loss lead to a very low electrical energy efficiency of only $\approx 73\%$ for the first cycle (at C/10 and 25°C).

In the article presented here, we investigate how much of the electrical energy lost during the first cycle is converted into waste heat and what conclusions can be drawn from the heat evolution profiles on the underlying activation processes. For this purpose, we used IMC in combination with electrochemical cycling experiments. In contrast to the study presented in section 3.2.2, we conducted the IMC measurements in-house at an identical calorimeter as used previously but with a modified cell holder. The details of the cell holder are subject to an upcoming publication by Kunz and Berg et al.¹²² Based on an intermittent cycling protocol, we determined the irreversible heat generation similar to what was done in the previous study. The contributions from reversible heat and parasitic heat are also discussed in the article.

We found that only $\approx 43\%$ of the electrical work lost during the first cycle is converted into heat. During the first charge, a unique heat flow curve is obtained. The irreversible heat thereby only accounts for $\approx 19\%$ of this heat generation suggesting that the major part is caused by the afore mentioned activation processes. The heat generation during the first discharge is similar to that of the following cycles and the results agree with what is shown in section 3.2.2. The quantification of the heat generation during the activation of LMR-NCM is presented here for the first time and indicates the underlying processes cause a unique heat evolution profile.

Author contributions

F.F. conducted the electrochemical and calorimetric measurements and interpreted the data. A.K. was in charge of setting up the improved calorimetric setup, which will be subject to an upcoming publication. F.F. wrote the manuscript. All authors discussed the data and revised the manuscript.

4 Conclusions

This PhD thesis investigated two types of cathode active material for use in LIBs. In the first part, a Ni-rich layered oxide (NCM-811) was analyzed regarding its capacity fading over long-term cycling. To gain an understanding of the mechanisms leading to capacity fading, the electrochemical data were complemented with X-ray diffraction and other diagnostics such as impedance spectroscopy. The second part of this thesis deals with Li- and Mn-rich layered oxides (LMR-NCM) and their intrinsic OCV hysteresis. This hysteresis phenomenon was investigated by conducting entropy measurements and the corresponding energy loss was analyzed by means of calorimetry.

In the first research project (section 3.1), we investigated the capacity fading mechanisms of NCM-811 during long-term cycling and compared the results obtained at room temperature (section 3.1.1) to those obtained at 45°C (section 3.1.2). The capacity loss during C/2 cycling (3.0-4.5 V) was more than doubled for the operation at 45°C. As illustrated in Figure 1.3, there are several possible degradation processes leading to a deterioration of the cell performance. By design of experiment, we minimized all other contributions (such as Li loss, electrolyte consumption, etc.) in order to focus solely on the degradation phenomena originating from the CAM. By collecting XPDs in regular intervals in both charged and discharged state, we were able to analyze the CAM structural degradation over the course of cycling. We found that the bulk structure remained reasonably stable, since the Li-Ni mixing only increased by $\approx 1-2\%$ at 45°C (700 cycles) and was constant at room temperature (1000 cycles). In the diffractograms we could moreover find no indication for electronically isolated particles. Particle cracking could therefore not be observed. By combining the XPD results from the long-term studies with XPDs collected over a complete cycle, we were able to establish a quantitative correlation between the NCM-811 lattice parameters and the capacity losses. We conclude that the formation of an oxygen-deficient, reconstructed surface layer causes the observed capacity losses.

Figure 4.1a shows the implications of such a surface layer on the cell performance. There is an irreversible capacity loss due to the material lost for the formation of the surface layer. The second effect describes a shrinkage of the effective SOC window as a result of an increasing overpotential caused by the resistive nature of the surface layer. Impedance spectroscopy further evidenced that an increasing charge-transfer resistance is responsible for the growing overpotential over the course of cycling. Further XPD experiments have shown that the surface layer is formed around the primary CAM particles, as illustrated in Figure 4.1b (sketched in blue). The thickness of this layer was estimated based on BET measurements to be ≈ 6 nm after 1000 cycles at 22°C and ≈ 12 -14 nm after 700 cycles at 45°C. We conclude that the instability of the surface is the “Achilles heel” of Ni-rich layered oxides. Potential countermeasures are less resistive, protective coatings or a lowering of the exposed surface area, e.g., by using single crystalline CAMs¹³⁸.

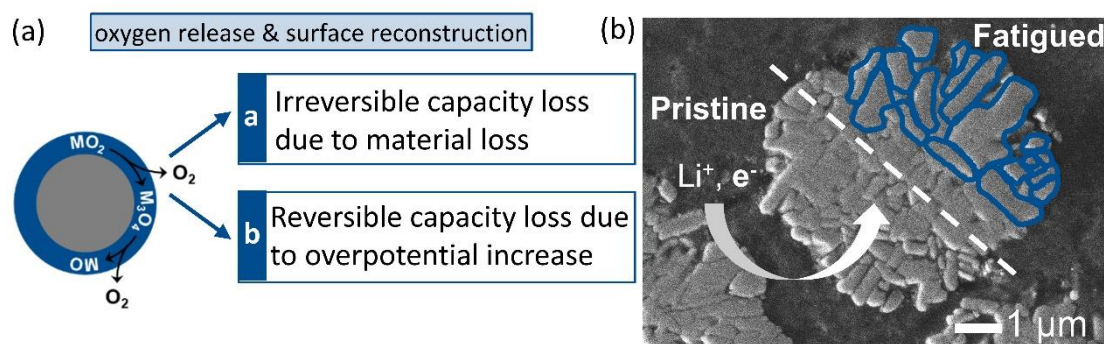


Figure 4.1: (a) Illustration of the CAM degradation mechanism of oxygen release and surface reconstruction according to Figure 1.3, including the two effects on the cycling performance observed in our studies.^{139,140} (b) SEM-Image with an illustration of the reconstructed, O-deficient surface layer (sketched in blue), which is suggested to form on the surface of the NCM-811 primary particles upon prolonged cycling. Figure adapted from Friedrich et al.¹³⁹

The second part of this thesis deals with LMR-NCM (section 3.2). Due to its high specific capacity and low material cost (see Figure 1.2), it is a promising candidate to be used as CAM in future LIBs. LMR-NCM, however, suffers from a significant OCV hysteresis, which complicates the SOC determination in commercial applications and severely reduces the energy round-trip efficiency. In order to investigate the OCV hysteresis, entropy measurements were conducted (section 3.2.1). The partial molar entropy of a battery is determined by measuring the variation of the OCV as a function of temperature. For this purpose, a temperature ramping method was implemented and validated in comparison to the typically used temperature step

procedure. In order to determine the contribution of the lithium counter electrode to the entropy of the LMR-NCM/Li cell, a spatially non-isothermal cell setup was developed. Our results prove that the contribution of the lithium electrode is in the same order of magnitude as the contribution of the cathode (≈ 1 mV/K) and only the difference between these two values gives the relatively small overall experimental response (≈ 0.1 mV/K). Since the contribution of Li is independent of the SOC of the cell and only gives a constant offset, any changes in the entropy profile are caused by the cathode. For the LMR-NCM/Li system, we found a peak in the partial molar entropy curve, which we ascribe to a second order phase transition. The entropy curves during charge and discharge show a hysteresis when plotted as a function of SOC, which vanishes when mapped versus OCV. The lack of typical fingerprints of the configurational entropy together with the observed path dependence and the relatively steep voltage curve prove that the vibrational and not the configurational entropy dominates the partial molar entropy curve. In contrast, during the first activation cycle, indications for changes in the configurational entropy were found, which however vanish after the first cycle. Generally, the reversible heat can be calculated from entropy data as shown in equation (2.14). Since the (de-)lithiation of LMR-NCM, however, does not follow fully reversible pathways when a whole cycle is considered, the calculation of the reversible heat is not possible for a charge/discharge cycle. Our entropy study has generated insights into the hysteresis phenomena in LMR-NCM, but has also raised new questions to be addressed by researchers with other experimental methods or theoretical calculations.

In order to quantify the energy lost due to the OCV hysteresis (\dot{Q}_{hys}), calorimetric measurements were conducted (section 3.2.2). We thereby compared the heat evolution in LMR-NCM/Li to that of NCA/Li cells. NCA serves as a reference material, since it does not exhibit a significant OCV hysteresis. We found that the heat generation during charging/discharging of cells with LMR-NCM cathodes is up to 9 times higher (at C/10) compared to cells with NCA cathodes. The heat release of both materials shows a linear correlation with the electrical current applied to the cells. While for NCA/Li cells the zero current intercept is close to zero, there is a considerable offset for LMR-NCM/Li due to the OCV hysteresis, which is present

even at zero current conditions, since it is a material specific property. At low currents (i.e. C/10), the energy loss due to the OCV hysteresis amounts to $\approx 55\%$ of the total energy loss for LMR-NCM. Our analysis shows that the main part of the heat due to OCV hysteresis is generated during discharge. The evolution of \dot{Q}_{hys} as a function of SOC was determined by subtracting the expected irreversible heat flow from the heat signal measured by IMC. The irreversible heat was calculated based on the overpotential measured every 10% SOC by an intermittent cycling protocol. We found that \dot{Q}_{hys} is generated over the whole SOC range during discharge but especially at low SOC (< 170 mAh/g). During charge, we observed the evolution of \dot{Q}_{hys} at high SOC (> 200 mAh/g). These observations are in agreement with literature reports on the hysteresis of the OCV^{19,97}, the lattice parameters^{100,104}, and our results for the path dependence of the entropy curves (section 3.2.1)¹³², indicating that the hysteresis phenomena in LMR-NCM arise when it is charged to high SOC and discharged to low SOC. Our results evidence that the underlying processes leading to the hysteresis generate waste heat. For LMR-NCM, \dot{Q}_{hys} is thereby of the same order of magnitude as the total heat released from NCA/Li cells. This underlines the importance of calorimetric measurements for active materials with a pronounced OCV hysteresis such as LMR-NCM. For the thermal management of the cell in an application like a BEV, it is essential to know the heat flow as a function of SOC.

In addition to the OCV hysteresis in regular cycles, LMR-NCM also exhibits a considerable hysteresis in the voltage curve during the initial activation cycle. The first charge voltage curve has a unique shape, with a plateau at ≈ 4.5 V vs. Li⁺/Li. When LMR-NCM is charged to this upper plateau, irreversible structural changes occur.^{93,94,97,106,136} The consecutive discharge voltage curve has a considerably lower average voltage and not all Li that was extracted during charge can be re-intercalated during discharge. This means, that the energy round-trip efficiency is significantly reduced ($\approx 73\%$ at C/10). To investigate how much of this energy loss is converted into waste heat, calorimetric measurements were conducted with LMR-NCM/Li cells during the first activation cycle (section 3.2.3). We found that only $\approx 43\%$ of the electrical work lost during the first cycle is evolved as waste heat. Similar to our previous study, we compared the expected irreversible heat flow to

the measured IMC signal and ascribed the difference to the heat due to activation processes. During the first charge, more than 80% of the observed heat flow is caused by these activation processes. The onset of this heat evolution coincides with the beginning of the upper voltage plateau, which further evidences that it is directly related to the irreversible structural processes happening during activation of LMR-NCM. The heat observed is a measure of the enthalpy of the structural rearrangements during activation. The heat evolution during the first discharge is comparable to that during subsequent regular cycles. Window-opening experiments, in which the upper SOC limit is gradually increased, furthermore prove that the heat evolution due to activation in charge and due to hysteresis in discharge is only observable when LMR-NCM is charged (i.e., activated) beyond the beginning of the upper voltage plateau (>100 mAh/g). The results presented in this PhD thesis therefore give new insights on the OCV hysteresis in LMR-NCM. Our entropy and IMC results could be the basis for in-depth computational studies allowing a fundamental understanding of the mechanisms underlying the OCV hysteresis.

Following up on this work, research questions for future studies arise. For the X-ray diffraction studies on Ni-rich CAMs presented in the first part of this thesis (section 3.1), an interesting follow-up question is the aging behavior of single-crystalline CAMs in contrast to the poly-crystalline CAMs investigated in our work. Since single-crystalline NCM has primary particles with a size in the μm range, they have a significantly lower surface-to-bulk ratio, which would substantially decrease the loss of electrochemically active material. This holds true as long as intragranular cracking of the single crystallites does not generate new surfaces, and if the active material loss mostly occurs on CAM surfaces exposed to the electrolyte. To test these hypothesis and compare the degradation mechanisms between the two types of CAMs, an identical long-term aging study with single-crystalline NCM811 would be interesting to look at in the future.

The methods of entropy measurements and IMC, presented in the second part of this thesis (section 3.2), can be applied in various further ways to gain more information on LMR-NCM, but also on other active materials of interest. Possible options are the measurement of the partial molar entropy and the heat flow by IMC

at different cycling temperatures. Since the extent of the OCV hysteresis loop depends on the temperature,^{132,141} it is an interesting question how the temperature affects the partial molar entropy as well as the observable heat flow, in particular the heat flow due to the OCV hysteresis. Another factor influencing the OCV hysteresis loop is the degree of activation during the initial formation cycle.^{97,100} When the activation is not fully completed during the first cycle, literature reports suggest that the activation processes proceed during the subsequent cycles when high charge voltages are reached.^{96,142} Thus, an interesting question for future research is the effect of the degree of activation on the heat flow curves during subsequent cycling. The proposed working hypothesis is that the accumulated heat over the first five to ten cycles is the same when normalized to the exchanged charge/discharge capacity, independent of the activation protocol during the first cycle, but this still needs to be proven, and could be subject to further research.

Regarding the experimental approach in the IMC study conducted in Ulm (section 3.2.2),¹¹⁰ our recently established in-house calorimeter offers the advantage of more possible complementary methods to be combined with the IMC measurement. For example, there is no need to use two sets of identical cells in future IMC studies with one set analyzed in the calorimeter and the other set used for electrochemical tests. With our IMC set-up in house, it is possible to conduct e.g. impedance measurements in-situ on the cells in the calorimeter. Furthermore, it is possible to conduct long-term cycling experiments where the cells are cycled in the temperature chambers in the lab and analyzed by IMC in regular intervals. Thereby, a similar design of experiment, as for the in-house diffraction study presented earlier (see section 3.1.2),¹⁴⁰ is possible, where cells are cycled for several hundreds of cycles at a constant temperature and every 50 cycles, a charge/discharge cycle is conducted inside the calorimeter in order to measure the heat evolution over the course of cycling. By doing so, the heat flow due to the OCV hysteresis could be investigated as a function of cycle number and possible effects from aging on the OCV hysteresis could be revealed. In that context, a combination of XPD and IMC would also be an interesting approach. The structural information gained from XPD correlated with the heat flow data from IMC could give a new perspective especially for active materials where structural processes are strongly correlated with heat

evolution. For silicon negative electrodes for example, operando XPD was successfully combined with IMC showing a correlation of a decrease in silicon crystallinity to a decrease in the measured entropic heat flow.¹²⁰ The groundwork for such research activities is laid within this thesis, and many interesting research questions for the future follow from this work.

5 Appendix

The manuscript with the title “Heat Generation During the First Activation Cycle in Li-Ion Batteries with Li- and Mn-rich Layered Oxides Measured by Isothermal Micro-calorimetry” is shown here since the results are not published yet. The manuscript will soon be submitted to a peer-reviewed journal.

Heat Generation during the First Activation Cycle in Li-ion Batteries with Li- and Mn-rich Layered Oxides Measured by Isothermal Micro-calorimetry

Franziska Friedrich^{a,~}, Alexander Kunz^b, Andreas Jossen^b and Hubert A. Gasteiger^a

^a Chair of Technical Electrochemistry, Department of Chemistry and Catalysis Research Center, Technical University of Munich (TUM), Munich, Germany

^b Institute for Electrical Energy Storage Technology, Technical University of Munich (TUM), Munich, Germany.

[~] E-mail: franziska.friedrich@tum.de

Abstract

Using isothermal micro-calorimetry, we investigate the heat generation of lithium- and manganese-rich layered oxides (LMR-NCMs) during the first cycle in which LMR-NCM exhibits a pronounced voltage hysteresis leading to a low energy efficiency ($\approx 73\%$). In the first charge, LMR-NCM shows a unique voltage plateau at ≈ 4.5 V where irreversible structural rearrangements lead to an activation of the material as well as the large voltage hysteresis. We found that only a fraction of the lost electrical work ($\approx 43\%$) is converted into waste heat. Thereby, the heat flow profile of the first charge is unique and shows considerable heat generation during the voltage plateau. With complementary electrochemical methods, contributions of conventional sources of heat, i.e., because of polarization and entropy, are determined. However, they do not cause the considerable generation of heat during the voltage plateau. Our results therefore suggest that the structural rearrangements during activation lead to a significant generation of heat. In window-opening experiments, we demonstrate that the activation is a gradual process and that the heat generated during the first discharge is directly linked to the extent of activation during the preceding charge. We also investigate the effect of the degree of overlithiation on the heat generated during activation.

1 **1 Introduction**

2 Lithium- and manganese-rich layered oxides (LMR-NCMs) such as $\text{Li}_{1.14}(\text{Ni}_{0.26}\text{Co}_{0.13}\text{Mn}_{0.6})_{0.86}\text{O}_2$ are
3 promising candidates for next-generation Li-ion batteries. Compared with conventional layered NCMs,
4 they provide higher reversible capacities of up to 250 mAh/g. This is because a part of the transition
5 metals (TMs) in the TM layer is replaced by lithium, thereby leading to an overlithiation of the
6 structure. By using inexpensive manganese, a low material cost compared with other state-of-the-art
7 cathode materials, which contain high amounts of nickel and cobalt, is achieved.¹

8 However, the practical applications of LMR-NCM are still limited by several challenges such as voltage
9 fading², oxygen evolution^{3,4}, high resistances⁵, and a pronounced voltage hysteresis^{1,6,7}. The hysteresis
10 of the voltage is still present under open-circuit conditions and is thus an intrinsic bulk property of
11 LMR-NCM. In addition to the open-circuit voltage (OCV), other parameters show a path-dependence
12 as a function of state of charge (SOC), i.e., the cathode resistance⁵, the lattice parameters⁸, and the
13 entropy curve⁹. Interestingly, all of these hysteresis phenomena occur only for an activated material
14 i.e., after charging the LMR-NCM to 4.8 V vs. Li/Li⁺. Thereby, the activation of the LMR-NCM is a gradual
15 process and the first charge occurs via a two-step voltage profile. During the initial sloping region,
16 lithium (Li) is removed from the Li-sites, and the charge is compensated by the oxidation of the
17 transition metals (TMs). In this first region (below ≈ 125 mAh/g or ≈ 4.4 V vs. Li/Li⁺), the material cycles
18 are reversible (i.e., the coulombic efficiency is close to 100%, the peaks in the dQ/dV profile are
19 symmetrical^{1,10}, and the lattice parameters⁸, resistance⁵, and entropy⁹ of the charge and discharge
20 direction coincide). Upon further charging, the voltage curve shows a plateau at ≈ 4.5 V, and the charge
21 compensation includes oxygen redox, which enables the anomalously high first charge capacity of
22 more than 300 mAh/g and leads to irreversible structural rearrangements. During the upper voltage
23 plateau, the long-range “honey-comb” ordering disappears^{10,11}, and chemically available Li sites are
24 lost, thereby leading to a large irreversible capacity loss during the first cycle. Several structural and
25 electronic changes are associated with the activation process and discussed in literature. These include
26 irreversible^{3,12} and reversible^{13,14} oxidation of oxygen species, partly reversible TM migration^{1,7,10}, the
27 formation of Li/TM dumbbells^{1,15}, and the formation of dislocations¹⁶. All of these processes happen
28 during the upper voltage plateau and cause a substantial hysteresis between the first charge and
29 discharge voltage curve. This loss of voltage combined with the large irreversible capacity loss leads to
30 a very low electrical energy efficiency of $\approx 73\%$ for the first cycle (at C/10 and 25°C).

31 The aim of the present study is to investigate the heat generated during the first cycle and answer the
32 following questions: (i) How much of the electrical work, which is lost during the first cycle, is converted
33 into waste heat? (ii) What can we learn from the heat generation profile as a function of SOC on
34 activation processes? (iii) What effect does the activation have on the generation of heat during the
35 subsequent discharge? (iv) How does the degree of overlithiation influence the generation of heat

1 during activation? The lost electrical work, measured by galvanostatic cycling, can usually be directly
2 converted into the expected waste heat of a battery when a full, reversible charge/discharge cycle is
3 considered. However, because LMR-NCM undergoes irreversible processes during the first activation
4 cycle, the material at the end of the cycle clearly differs from the pristine one. The irreversible capacity
5 loss observed and the substantially lower voltage on discharge are direct consequences. Thus, the
6 difference between the charge and discharge energy is only a measure of lost electrical work and does
7 not provide information about the amount of waste heat or its generation during charge and discharge.
8 The heat generation during the activation of LMR-NCM can be analyzed only by means of calorimetry.
9 By applying in operando isothermal micro-calorimetry (IMC), we aim to analyze the generation of heat
10 as a function of state-of-charge (SOC), thereby gaining insight into the activation processes. With the
11 investigation of parasitic reactions, the Dahn group demonstrated that IMC is a reliable technique for
12 precisely analyzing the thermal behavior of batteries¹⁷⁻¹⁹. In our previous IMC study²⁰, we discuss the
13 heat generation of LMR-NCMs during regular cycling and introduce a new heat source into the general
14 energy balance model: the heat resulting from OCV hysteresis, \dot{Q}_{hys} . This term is required to describe
15 the thermal behavior of active materials with a pronounced OCV hysteresis such as LMR-NCM. Using
16 IMC, Assat et al.²¹ investigated the heat generation of $\text{Li}_2\text{Ru}_{0.75}\text{Sn}_{0.25}\text{O}_3$, which serves as a model system
17 for LMR-NCM materials. They report a large heat release during the upper voltage plateau in the first
18 charge. This is ascribed to a chemical stabilization process correlated to the irreversible structural
19 rearrangements during activation.

20 We use IMC to measure the heat generated during activation of LMR-NCM/Li half-cells at C/10 and
21 25°C. We also determine the irreversible heat using a galvanostatic intermittent cycling protocol. The
22 reversible heat is calculated based on potentiometric entropy measurements⁹. However, this is shown
23 to be negligible for the present study. Thus, from the difference between the observed heat and the
24 calculated expectation value, the heat resulting from activation and hysteresis is determined as a
25 function of SOC.

1 **2 Experimental**

2 **2.1 Calculation approach**

3 When a battery is charged or discharged, heat is generated. Under isothermal conditions, the total
4 heat flow can be expressed according to equation (1). In general, three main contributions to the heat
5 generation can be identified: (i) the irreversible heat, \dot{Q}_{irrev} , (ii) the reversible heat, \dot{Q}_{rev} , and (iii) the
6 parasitic heat flow, \dot{Q}_p .

$$\begin{aligned}\dot{Q}_{tot} &= I \cdot (E_{load} - E_{eq}) + T \cdot I \cdot \frac{\partial E_{eq}}{\partial T} + \dot{Q}_p \\ &= \dot{Q}_{irrev} + \dot{Q}_{rev} + \dot{Q}_p\end{aligned}\quad (1)$$

7 Irreversible heat originates from cell polarization, which causes the cell voltage under load, E_{load} , to
8 differ from that under open-circuit conditions, E_{eq} . This term, which is the first one on the right hand
9 side of equation (1), is always exothermic. It can be calculated from electrochemical cycling data with
10 an intermittent protocol explained in Section 2.4. The second term, the reversible heat, is caused by
11 the changes in the entropy of the cathode and anode as a function of SOC. Depending on the sign of
12 the applied current, I , this contribution can be either exothermic or endothermic. For reversible
13 processes, \dot{Q}_{rev} is equal to zero if a complete charge-discharge cycle is considered (under isothermal
14 conditions). The reversible heat was determined from entropy measurements described in Section 2.5
15 and is discussed in more detail elsewhere.⁹ The third term on the right hand side of equation (1)
16 summarizes all heat flow from sources other than charge/discharge. This can include any side reactions
17 such as electrolyte decomposition¹⁷⁻¹⁹ or SEI formation²². A detailed discussion of the different sources
18 of heat can be found in our previous IMC study²⁰ in which we also elucidated the necessity to add
19 another term to the general heat equation for materials such as LMR-NCM, which show a significant
20 hysteresis in their open-circuit voltage (OCV). We introduced the heat resulting from OCV hysteresis,
21 \dot{Q}_{hys} . For this purpose, we assume that the voltage measured under OCV conditions, E_{OC} , is not equal
22 to the (theoretical) thermodynamic equilibrium potential, E_{eq} , which cannot be measured. A potential
23 difference and thus a similar expression as for the irreversible heat generated by polarization is
24 created. The heat flow of LMR-NCM/Li cells is thus as follows:

$$\begin{aligned}\dot{Q}_{tot} &= I \cdot (E_{load} - E_{OC}) + T \cdot I \cdot \frac{\partial E_{eq}}{\partial T} + \dot{Q}_p + I \cdot (E_{OC} - E_{eq}) \\ &= \dot{Q}_{irrev} + \dot{Q}_{rev} + \dot{Q}_p + \dot{Q}_{hys}\end{aligned}\quad (2)$$

25 However, this theoretical heat balance must be adjusted for the present study. For the first cycle of
26 LMR-NCM/Li cells, the contribution from \dot{Q}_{rev} was found to be negligible. A detailed discussion of this
27 simplification can be found in Section 3.5. There, we also explain why the parasitic heat, which was
28 estimated from measurements of a symmetrical Li/Li cell, is assumed to be insignificant. The heat
29 balance used for the calorimetry study presented here thus simplifies to:

$$\begin{aligned}\dot{Q}_{tot} &= I \cdot (E_{load} - E_{OC}) + I \cdot (E_{OC} - E_{eq}) \\ &= \dot{Q}_{irrev} + \dot{Q}_{hys}\end{aligned}\quad (3)$$

1 The total heat generation is measured by isothermal micro-calorimetry (IMC) described in Section 2.3.
 2 Thus, the additional heat term resulting from OCV hysteresis and activation, \dot{Q}_{hys} , is determined from
 3 the difference between the total measured heat flow, $\dot{Q}_{IMC} \equiv \dot{Q}_{tot}$, and the calculated irreversible
 4 heat. This simplification means that what we identify as \dot{Q}_{hys} includes contributions from \dot{Q}_p and \dot{Q}_{rev} .
 5 In Section 3.5, we will demonstrate that these contributions are insignificant. Nevertheless, we still
 6 want to make clear that they are not zero, even though this is assumed for the calculation in
 7 equation (3).

8 **2.2 Electrode fabrication and battery assembly**

9 We used three different Li- and Mn-rich layered oxides (LMR-NCM) with varying degrees of
 10 overlithiation. According to the notation $\text{Li}[\text{Li}_\delta\text{TM}_{\delta-1}]\text{O}_2$, BASF SE (Germany) provided us with a low-
 11 ($\delta = 0.14$), mid- (0.17), and high-lithium material (0.20), which correspond to 0.33 Li_2MnO_3 , 0.42
 12 Li_2MnO_3 , and 0.50 Li_2MnO_3 in the notation applied by Teufl et al.³ This study focuses on the low-lithium
 13 material, which has been analyzed by means of calorimetry^{6,20} and entropy⁹. Its exact composition is
 14 $\text{Li}_{1.14}(\text{Ni}_{0.26}\text{Co}_{0.13}\text{Mn}_{0.6})_{0.86}\text{O}_2$. For electrode preparation, inks of the cathode active material (CAM) were
 15 prepared by mixing 92.5 wt% LMR-NCM, 3.5 wt% polyvinylidene-fluoride binder (PVdF, Solef 5130,
 16 Solvay, Belgium), and 4 wt% conductive carbon (Super-C65, Timcal, Switzerland) with N-methyl
 17 pyrrolidine (anhydrous, Sigma-Aldrich, Germany). The dispersion was mixed in a planetary orbital
 18 mixer (solid content ≈ 58 wt%; Thinky, USA), and the resulting ink was coated onto aluminum foil
 19 (≈ 15 μm , MTI, USA). After drying, the coatings were calandered (GK 300L, Saueressig, Germany) to a
 20 porosity of ≈ 42 – 45% . For electrochemical testing, the electrodes were dried for a minimum of 12 h at
 21 120°C in a dynamic vacuum (Büchi, Switzerland). The loading of the LMR-NCM electrodes was
 22 ≈ 11.6 mg/cm^2 , which corresponds to ≈ 2.9 mAh/cm^2 based on a nominal reversible capacity of
 23 250 $\text{mAh}/\text{g}_{\text{LMR-NCM}}$.

24 Coin cells (type CR2032) were assembled in an argon-filled glovebox (O_2 , $\text{H}_2\text{O} < 0.1$ ppm, MBraun,
 25 Germany) with the manufactured cathodes (14 mm diameter), two glass fiber separators (17 mm
 26 diameter, glass microfiber #691, VWR, Germany), and a Li counter electrode (15 mm diameter,
 27 450 μm thickness, 99.9%, Rockwood Lithium, USA). The electrolyte was composed of 100 μL of a 1M
 28 LiPF_6 in a FEC:DEC-based (12:64 v:v) solvent with 24 vol% of an additional fluorinated co-solvent (BASF
 29 SE, Germany). All data reported here originate from constant current (CC) cycling at a C-rate of C/10,
 30 whereby the C-rate refers to the reversible capacity of LMR-NCM (250 mAh/g). We use the term “state
 31 of charge” (SOC) to describe the nominal specific capacity (in $\text{mAh}/\text{g}_{\text{CAM}}$), which was extracted from
 32 the cathode. It can hence be directly converted into the amount of Li in the cathode. An SOC of 0 mAh/g

1 means that the material is fully lithiated ($\text{Li}_{1.14}(\text{Ni}_{0.26}\text{Co}_{0.13}\text{Mn}_{0.6})_{0.86}\text{O}_2$) while at an SOC of 345.6 mAh/g,
2 the LMR-NCM would be fully delithiated. Two sets of identical cells were analyzed in this study: (i) one
3 set was cycled inside the calorimeter as described in Section 2.3; (ii) the second set of cells was used
4 to determine the irreversible heat by intermittent cycling described in Section 2.4.

5 **2.3 Isothermal micro-calorimetry**

6 The LMR-NCM/Li coin cells were transferred to the isothermal micro-calorimeter directly after
7 assembly. A TAM IV calorimeter equipped with a 20 mL micro-calorimeter (stability $\pm 50 \mu\text{K}$, accuracy
8 $\pm 300 \text{ nW}$, precision $\pm 100 \text{ nW}$, TA Instruments, USA) was used. All measurements were performed at
9 25°C under isothermal conditions after internal gain calibration. On the reference site of the
10 calorimeter, a dummy cell with the same content as the actual sample cell but without the cathode
11 active material was used in order to ensure high measurement accuracy by a comparable heat capacity
12 of both cells. Before the experiment was started, we waited for the signal to reach certain stability
13 criteria (drift $< 10 \text{ nW/h}$, standard deviation $< 150 \text{ nW}$ for 60 minutes). As the system identification
14 process suggests, the calorimetric setup can be described as dynamical system 2nd order (PT2 system).
15 Typically, such systems can be empirically characterized by the according unit step-response when a
16 rectangular heat flow is applied as an input signal. The two time-constants T_1 , T_2 of the systems
17 transfer-function we derived during the calibration process and are found to be $T_1 = 57 \text{ s}$ and $T_2 =$
18 131 s . This results in a time delay of 682 s until 99% of the steady-state heat flow value is detected. A
19 positive sign in the observed heat flow indicates that heat is generated by the cell.

20 The cells were cycled inside the IMC in a custom-made coin cell holder, which was connected by Cu-P
21 bronze wires (Duo-Twist wire WDT-36-25, 36 AWG, Lakeshore, USA) to a potentiostat (SP200, BioLogic,
22 France). A publication with a detailed description of the coin cell holder is in preparation.²³
23 Galvanostatic cycling was done at C/10. First, a formation cycle was conducted between 2.0–4.8 V (all
24 voltages reported vs. Li^+/Li), followed by a stabilization cycle (2.0–4.7 V), which was not further
25 analyzed, and another cycle (2.0–4.7 V) representative of the following reversible cycling behavior of
26 this material. After each half-cycle (i.e., whenever the upper or lower cutoff was reached), the CC phase
27 was followed by a 6 h open-circuit phase in order to enable separation of the heat flow during charge
28 and discharge. Two identical cells were measured for each experiment in order to ensure the
29 reproducibility of the results. The raw heat flow data obtained by IMC were normalized by the cathode
30 active material mass and corrected for their relative y-offset by subtracting a baseline. For the charge
31 half-cycles, a constant y-offset was determined prior to the start of the CC phase. For the discharge
32 half-cycles, an exponential decay function fitted to the subsiding heat flow signal observed during the
33 preceding OCV phase was used as baseline. Because the heat flow signal in the rest phase after
34 charging did not converge to a stable value within the 6 h of relaxation, we were unable to use a simple

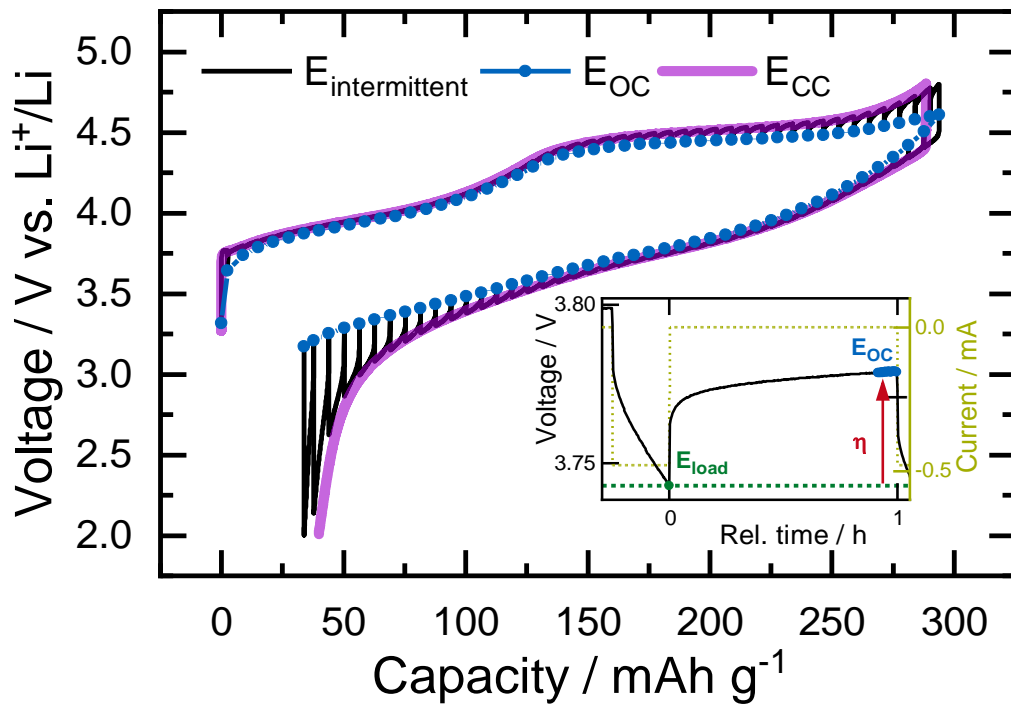
1 y-offset for the discharge half-cycles. Because of the time delay, the integration of the heat flow of an
2 individual charge or discharge half-cycle includes not only the heat signal obtained during current flow
3 but also that obtained during the subsequent relaxation phase. Of the 6 h relaxation phase applied,
4 we included only the first 1.5 h into the calculation. This is sufficient to obtain most of the actual heat
5 signal, yet not so long that parasitic heat flows might be erroneously included in the calculation. A
6 waiting time of 1.5 h might seem ineptly long considering the time delay of ≈ 11 minutes until 99% of
7 the signal is observed in the calibration measurement. However, the determined time delay needs to
8 be classified as a signal response of an ideal system, i.e. an electrical resistor, whose heat generation
9 strictly follows the applied current profile. The reported value hence solely describes the time delay of
10 the IMC instrument. When the applied current of a coin cell with a real cell chemistry is switched off
11 at the beginning of a rest phase, equilibration processes within the electrodes occur and lead to heat
12 generation with much longer time constants. For a reliable analysis of IMC data, it is hence crucial to
13 critically assess how much of the rest phase will be included into the integration of the heat signal. This
14 value should be reported to allow comparison to other reports and instruments.

15 **2.4 Determination of irreversible heat by intermittent cycling**

16 Complementary to the IMC measurements, electrochemical testing was performed with identical cells
17 at 25°C in a temperature-controlled oven (Binder, Germany) using a Biologic potentiostat (VMP300,
18 Biologic, France). In order to calculate the irreversible heat according to equation (3), the
19 overpotential, $\eta = E_{load} - E_{OC}$, was determined by intermittent cycling. The cycling protocol applied
20 is similar to a galvanostatic intermittent titration and was used as in our previous study²⁰ in which the
21 approach is described in more detail. The first cycle was conducted between 2.0–4.8 V, followed by a
22 stabilization cycle (2.0–4.7 V), which was not further analyzed, and another cycle (2.0–4.7 V)
23 representative of the following reversible cycling behavior of this material. All cycles were conducted
24 at C/10. Figure 1 shows the voltage curve of a 0.33 LMR-NCM/Li cell obtained by intermittent cycling
25 during the first charge and discharge (black solid line). The cycling procedure includes (dis)charging
26 steps of $\Delta SOC = 2.5\%$ followed by a relaxation phase of $t = 1$ h. This was repeated until the upper
27 (lower) voltage cutoff was reached. Using this approach, η is determined as the difference between
28 the last voltage value at current flow, E_{load} , and the open-circuit voltage, E_{OC} , at the end of the
29 intermittent relaxation phase, as shown in the inset of Figure 1. The average of the final 300 s of the
30 OCV phase are used as E_{OC} . The intermittent cycling method is not applicable for determining η for
31 the first SOC point during charging or discharging because there is no preceding voltage relaxation in
32 the charge (discharge) direction. By applying small ΔSOC steps, we aim to minimize the effect of this
33 missing data point.

1 The measurement of E_{OC} after 1 h of relaxation means that slow relaxation processes that happen on
2 the order of hours or even weeks (i.e. solid diffusion) are not included into the calculation of the
3 overpotential and hence the irreversible heat. However, prolonged relaxation phases at every $\Delta SOC =$
4 2.5% would lead to severe self-discharge effects and an uncertainty in the determination of the
5 nominal SOC. From previous experiments, we know that a 1 h OCV phase leads to reliable SOC data
6 and a tolerable inaccuracy in the determination of E_{OC} . For example, when the last discharging step in
7 Figure 1 is considered, the overpotential η determined after $t = 1$ h amounts to $\approx 96\%$ of that after $t =$
8 6 h. Nevertheless, we want to emphasize that a longer rest phase would generally lead to higher values
9 for Q_{irrev} . Since Q_{hys} is calculated by subtracting Q_{irrev} from the total heat signal, this means that the
10 heat because of hysteresis and activation would be slightly smaller when a longer rest phase was
11 chosen. However, the error is small in comparison to other measurement inaccuracies.

12 As can be seen in Figure 1, the charge and discharge capacities of a Li/LMR-NCM cell from constant
13 current cycling (as applied for the IMC cells, purple line) are slightly lower than from the intermittent
14 cycling (solid black line). These deviations amount to $\approx -2\%$ for the charge capacity and $\approx -4\%$ for the
15 discharge capacity and can be explained by the different cycling procedures. Because in the
16 intermittent protocol, a 1 h rest phase is applied every $\Delta SOC = 2.5\%$, any concentration gradients,
17 which are formed in the cell during cycling (e.g., because of liquid or solid diffusion limitations) are
18 continuously minimized. This means that the intercalation processes are closer to equilibrium and that
19 more Li-ions can be (de-)intercalated during intermittent cycling compared with a constant current
20 cycling. In addition, self-discharge phenomena might occur for the cells of the intermittent cycling,
21 especially at high SOCs during charge because they spend more time at high voltages. When the upper
22 voltage plateau is considered ($SOC > 125$ mAh/g), both cell types spend ≈ 6 h in this region during the
23 constant current phase. However, while for the IMC cells, only another 6 h during the subsequent OCV
24 phase must be added, the cells from intermittent cycling go through ≈ 27 OCV phases of 1 h each in this
25 region. This may enhance self-discharge phenomena and lead to a higher observable charge capacity.
26 Because the deviations are rather small, the results from intermittent cycling can still be used to
27 complement those from the IMC cells.



1

2 *Figure 1: Voltage curves of the first cycle of a 0.33 LMR-NCM/Li cell at C/10. During intermittent cycling, the (dis)charging was*
 3 *interrupted every $\Delta\text{SOC} = 2.5\%$ for 1 h and when the upper or lower cutoff potential was reached. The OCV values (E_{OC}) at the*
 4 *end of each rest phase are depicted as blue circles and the measured voltage ($E_{intermittent}$) as a solid black line. A voltage*
 5 *curve from a continuous cycle of an identical cell is shown for comparison (purple line). The inset shows voltage and current*
 6 *of the cell from intermittent cycling as a function of time at an $\text{SOC} \approx 180 \text{ mAh/g}$ during discharge. This illustrates how the*
 7 *overpotential, η , is calculated from the difference between the last voltage point on load, E_{load} , and E_{OC} .*

8 **2.5 Determination of reversible heat**

9 As shown in equation (2), the reversible heat is calculated as a product of the applied current,
 10 temperature, and temperature-dependent OCV value, $\frac{\partial E_{eq}}{\partial T}$. The latter was measured as a function of
 11 SOC after (dis)charging the cell to a certain SOC point and allowing it to relax until the change in OCV
 12 over time was less than $\approx 0.2 \text{ mV/h}$. After this relaxation, $\frac{\partial E_{eq}}{\partial T}$ was determined by linearly varying the
 13 temperature of the cell between 5°C and 35°C in an Espec temperature chamber (LU114, Espec, Japan)
 14 while recording the respective OCV variation (VMP300, Biologic, France). A detailed description of the
 15 method applied and the results for the low- and high-lithium material are reported elsewhere.⁹

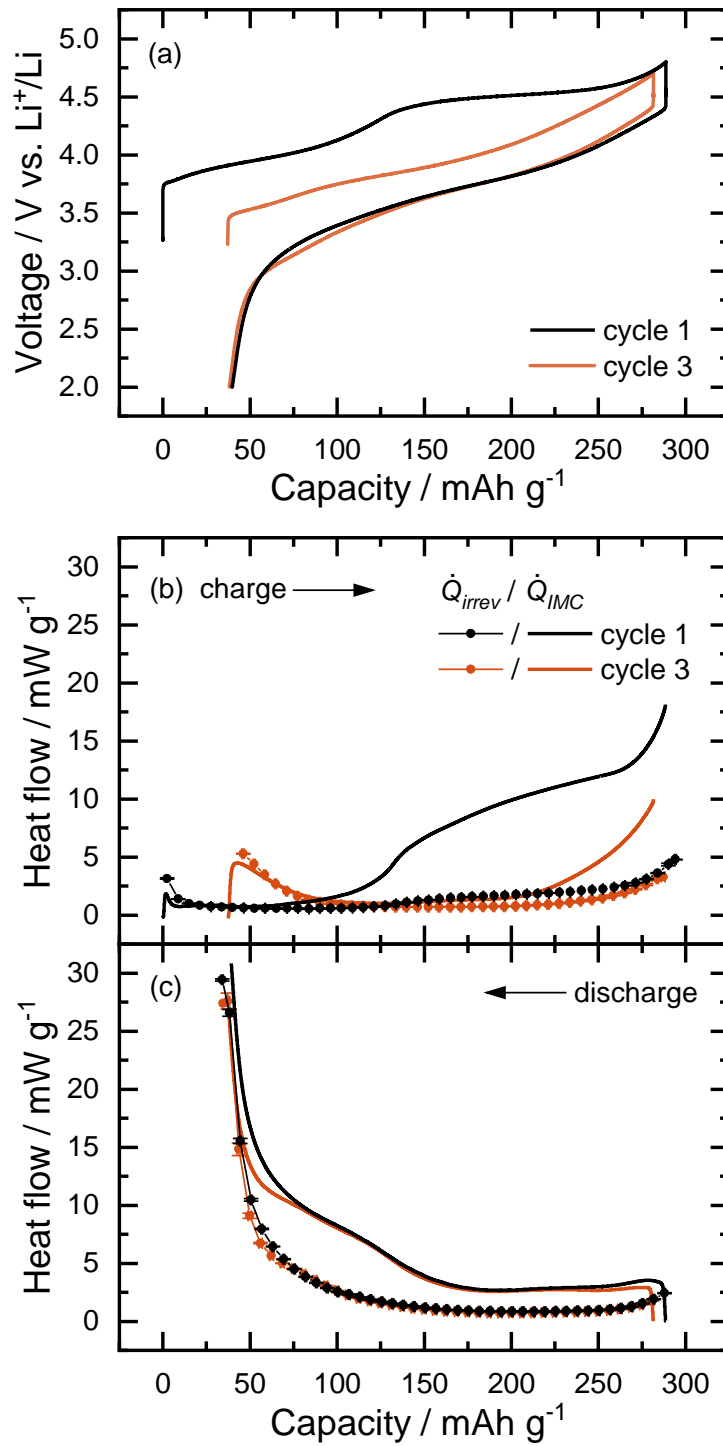
1 **3 Results and discussion**

2 **3.1 Heat generation during activation of LMR-NCM**

3 The cyclic voltage curves of the first and the third cycle of an 0.33 LMR-NCM/Li cell at C/10 are shown
4 in Figure 2a. The second cycle is not shown because it is not representative of the continuous cycling.
5 The first charge-discharge profile (black curve in Figure 2a) starts with an initial sloping region, which
6 is associated with the oxidation of transition metals (Ni and Co), followed by a voltage plateau at ≈ 4.5 V
7 during which irreversible structural changes such as transition metal migration^{1,7,10}, oxygen redox^{13,14},
8 and the loss of a honeycomb ordering^{10,11} occur. The first charge of LMR-NCM thus includes unique
9 activation processes, which cause the cell resistance⁵, the lattice parameters⁸, and the entropy curve⁹
10 to differ from those of the following cycles. Furthermore, at high SOCs (voltage > 4.6 V), oxygen is
11 released from the material.^{3,12} The voltage profile of the first charge differs significantly from that of
12 the following cycles (e.g. the third cycle shown in orange in Figure 2a). In contrast, the first discharge
13 voltage curve agrees with those of following cycles. Compared with the charge, the discharge occurs
14 at a much lower average potential, and the discharge capacity that can be achieved is ≈ 40 mAh/g lower
15 because of an irreversible loss of capacity. Both of these factors combined lead to a significantly lower
16 discharge energy and a considerable loss of electrical energy during the first cycle, which is shown in
17 Table 1 ($E_{cha} - E_{dis}$). In other words, the energy efficiency ($\frac{E_{dis}}{E_{cha}} \cdot 100\%$) of the first cycle ($\approx 73\%$) is
18 significantly lower than that of the third cycle ($\approx 90\%$).

19 Table 1 furthermore illustrates that for the third cycle, the electrical energy lost is almost completely
20 observed as waste heat by IMC ($Q_{IMC,total}$). With 93%, the accuracy of this measurement is
21 comparable to our previous study²⁰ in which we discuss possible error sources that might had led to
22 the deviation observed. These include the cables connecting the coin cell holder, which might remove
23 heat from the cell and hence the detector. Another issue is the choice of the integration limit for the
24 calculation of the IMC heat. From the 6 h OCV phase at the end of each half-cycle, only the first 1.5 h
25 were considered for the calculation as explained in Section 2.3. This should be enough time to include
26 the diminishing heat generation resulting from the time delay of the calorimeter and the equilibration
27 processes within the cell yet not too long to erroneously include too much heat from parasitic
28 processes, such as electrolyte decomposition. However, if the heat signal of the complete rest phase
29 was taken instead, the resulting total IMC heat would correspond to 97% of the electrical work lost.
30 Overall, we conclude that the accuracy of the IMC is sufficient to detect the electrical energy lost as
31 waste heat. In the third cycle, $\approx 33\%$ of the waste heat is dissipated during charge and $\approx 67\%$ during
32 discharge. The irreversible heat determined from intermittent cycling thereby covers $\approx 43\%$ of the heat
33 generated during charge and $\approx 47\%$ of the heat observed during discharge. The residual part of the heat
34 is caused by the OCV hysteresis, which is discussed in detail in our previous IMC study.²⁰

1 For the first cycle, the electrical energy lost far exceeds the waste heat observed by IMC. In fact, only
2 $\approx 43\%$ of the energy lost is converted into heat. From the analysis of the third cycle, we know that this
3 is not caused by instrumental errors. The questions thus arises as to why the electrical work lost cannot
4 be observed as waste heat. In order to clarify this, we need to revisit the cyclic voltage curve in Figure
5 2a, which shows that the charge–discharge process is not a closed loop for the first cycle. The large
6 irreversible loss of capacity (≈ 40 mAh/g) together with the fact that the first charge profile is unique
7 and includes irreversible processes mean that the first cycle is not a thermodynamically reversible
8 process. Simply speaking, the LMR-NCM material at the end of the first cycle differs from the pristine
9 material at the beginning. The difference in the charge and discharge energy therefore includes not
10 only waste heat but also a considerable amount of electrical energy, which is consumed by irreversible
11 processes in the active material or which cannot be extracted anymore during discharge because of
12 the restructuring of the LMR-NCM leading to the loss of chemically available Li sites.²⁴ From the voltage
13 curve alone, it is therefore not possible to assess how much waste heat will be released during the first
14 cycle. IMC measurements enable us to quantify the heat generated during the activation cycle of LMR-
15 NCM as a function of SOC and separate it into its share in charge and discharge direction, which, to our
16 knowledge, is reported here for the first time. Table 1 shows that only $\approx 43\%$ of the electrical energy
17 loss is observed as waste heat; of this $\approx 55\%$ is generated during charge and $\approx 45\%$ during discharge.
18 The irreversible heat determined by intermittent cycling accounts for $\approx 19\%$ of the heat during charge
19 and $\approx 41\%$ of the heat during discharge. A comparison of the absolute numbers of $Q_{IMC,dis}$ in Table 1
20 indicates that the heat generated during discharge is similar for the first and the third cycle and that a
21 comparable proportion of the heat observed is due to polarization effects. In contrast, with $Q_{IMC,cha} =$
22 78.8 mWh/g, the total heat released during the first charge is almost three-fold of that released during
23 the third charge. The relative contribution of the irreversible heat to the heat generation in charge is
24 much smaller during the activation (19%) as was the case during the third cycle (57%). However,
25 because of the different absolute $Q_{IMC,cha}$ values, these relative numbers are misleading. The absolute
26 values of the irreversible heat during the first (≈ 15 mWh/g) and the third charge (≈ 16 mWh/g) are quite
27 similar. The fact that only a small share of the heat generated during the first charge is due to
28 polarization effects means that a considerable amount is caused by another heat source. This will be
29 discussed in more detail in Section 3.2.



1

2 Figure 2: (a) Voltage curve of the first cycle (blue) and the third cycle (black) of a 0.33 LMR-NCM/Li cell at C/10. Panels (b) and
 3 (c) show the heat flow profiles during charge and discharge, respectively with the heat flow of the first cycle in blue and the
 4 third cycle in black. The heat measured by IMC is shown as solid line and originates from the same cell from which the voltage
 5 curves are shown in (a). The irreversible heat calculated from intermittent cycling is depicted as filled symbols with error bars
 6 from two different cells. Intermittent cycling was conducted with identical cells as used for the IMC experiments.

1 *Table 1: Measured and calculated energy losses for a 0.33 LMR-NCM/Li cell at C/10 and 25°C for the first and third cycle.*
2 *Electrical energy loss, total heat generation measured by IMC, and the ratio total heat/electrical loss for the whole cycle are*
3 *shown together with the heat measured by IMC during charge and discharge as well as the respective proportion of the*
4 *irreversible heat. Energy terms in mWh/g and ratios in %.*

Cycle	$E_{cha} - E_{dis}$ [mWh/g]	$Q_{IMC,total}$ [mWh/g]	$\frac{Q_{IMC,total}}{E_{cha} - E_{dis}}$ [%]	$Q_{IMC,cha}$ [mWh/g]	$\frac{Q_{irrev,cha}}{Q_{IMC,cha}}$ [%]	$Q_{IMC,dis}$ [mWh/g]	$\frac{Q_{irrev,dis}}{Q_{IMC,dis}}$ [%]
1	333.6	143.0	43	78.8	19	64.2	41
3	94.1	87.7	93	28.7	57	59.0	47

5

6 In addition to the overall heat generation, the heat flow profiles provide valuable information resolved
7 as a function of SOC. The heat flow curves of the first and the third cycle of an LMR-NCM/Li cell
8 measured by IMC at C/10 are shown in Figure 2b for the charge direction and in Figure 2c for the
9 discharge direction. In both plots, the heat flow measured by IMC, \dot{Q}_{IMC} (solid lines), is contrasted with
10 the irreversible heat generation, \dot{Q}_{irrev} (filled symbols), determined from identical cells by intermittent
11 cycling. As explained in Section 2.3, a 6 h rest phase was applied between charge and discharge of the
12 IMC cells in order to enable separation of the heat flow of the two respective half-cycles. The heat flow
13 was measured as a function of time and with the applied constant current this time axis was converted
14 into an SOC scale. However, we wish to emphasize that with this approach, the time delay of the
15 calorimeter is neglected. As was already discussed in our previous IMC study²⁰, the resulting error is
16 small for slow C-rates. With the C/10 current applied here, it is in the order of $\approx 2\%$ when the time delay
17 of ≈ 11 minutes, until 99% of the signal is observed, is compared to the duration of the first charge
18 (≈ 12 h).

19 Figure 2c shows that the heat generated during the first discharge agrees well with that during the
20 third cycle – similar to what is expected from the voltage curve. In the first part of the discharge process
21 ($300 \text{ mAh/g} > \text{SOC} > 175 \text{ mAh/g}$), heat generation is relatively constant ($\approx 3 \text{ mW/g}$). When the cell is
22 discharged below $\approx 175 \text{ mAh/g}$, the heat signal increases to $\approx 10 \text{ mW/g}$ and at the end of discharge,
23 another sharp increase in the heat generation is observed. The irreversible heat is rather constant
24 ($\approx 1 \text{ mW/g}$) over a wide SOC range and increases exponentially when the cell is discharged below
25 $\approx 125 \text{ mAh/g}$. Irreversible heat is caused by polarization effects in the cell. These include the ionic
26 resistance of the separator, the electric resistance of the external cell contacts, the resistance of the Li
27 anode, the charge transfer resistance of the cathode, the contact resistance between the cathode
28 coating and the current collector, and the ionic resistance of the electron and ion conduction across
29 the cathode. For reversible cycles such as the third cycle shown in Figure 2, a detailed discussion on
30 the underlying resistances causing \dot{Q}_{irrev} can be found in our previous publication²⁰ in which we
31 conducted impedance measurements and concluded that the charge transfer resistance of the

1 cathode dominates the polarization effects. Its increasing values at low and high SOC give rise to the
2 observed curve shape as a function of SOC, which is in agreement with the results of Teufl et al.⁵ The
3 data in Figure 2c suggest that the polarization effects in the first discharge agree with those of the third
4 cycle. The difference observed between \dot{Q}_{IMC} and \dot{Q}_{irrev} will be discussed in more detail in the
5 Section 3.2.

6 In contrast to the discharge direction, the heat generation observed by IMC during the first charge
7 differs significantly from the profile during the third charge as can be seen in Figure 2b. During
8 activation, \dot{Q}_{IMC} has a constant region with values between 1 and 2 mW/g at the beginning of charge
9 until the cell reaches an SOC of ≈ 100 mAh/g, where the heat signal starts to increase. At
10 SOC > 125 mAh/g, the heat flow profile then shows a saturation behavior, where \dot{Q}_{IMC} is between
11 ≈ 7 mW/g and ≈ 12 mW/g. At the end of charge, another steep increase is observed. In contrast, during
12 the third charge, the heat flow profile exhibits a U-shape starting at ≈ 4.5 mW/g at low SOC. This is
13 followed by a plateau around ≈ 1.5 mW/g in the mid-SOC region and an increase up to ≈ 10 mW/g at the
14 end of the charge. The heat flow curves during activation and the following cycles thus differ
15 significantly in case of the charge direction. With the results from intermittent cycling, we can analyze
16 whether the observed mismatch is caused by differences in the irreversible heat profile. For the low
17 SOC region, both heat flow profiles are dominated by the irreversible heat. In the third charge, which
18 starts at ≈ 40 mAh/g because of the irreversible capacity loss in the first cycle (see voltage profile in
19 Figure 2a), the irreversible heat and IMC signal agree well below ≈ 200 mAh/g, which means that the
20 measured heat is caused mainly by polarization effects. In the first charge, \dot{Q}_{IMC} is close to \dot{Q}_{irrev} in
21 the SOC region < 100 mAh/g. The observed mismatch in the low SOC region is thus caused by the
22 irreversible heat flow. For the third charge, the results for \dot{Q}_{irrev} agree with those previously
23 reported²⁰, thereby indicating that the charge transfer resistance of the cathode dominates the
24 underlying polarization effects. Based on the impedance measurements by Teufl et al.⁵, it is known
25 that for a cell with an LMR-NCM cathode that has not yet been charged beyond 100 mAh/g, the
26 polarization effects are significantly lower and have a different profile as a function of SOC compared
27 to a cell that underwent a full activation cycle. The observed mismatch in the \dot{Q}_{IMC} curves of the first
28 and the third charge in the SOC region below ≈ 100 mAh/g are thus caused by differences in the
29 underlying cathode resistance, which dominate the irreversible heat. However, for the SOC range in
30 which the mismatch between the \dot{Q}_{IMC} curves of the first and the third charge is most striking
31 (> 100 mAh/g), the results from intermittent cycling prove that this is not caused by the irreversible
32 heat. When comparing the curves for \dot{Q}_{irrev} in the first (black symbols) and the third charge (orange
33 symbols) in Figure 2b, we observe that in this SOC range, the curves for \dot{Q}_{irrev} agree well for both
34 cycles. For the first charge, there must therefore be an additional source of heat, which is no longer

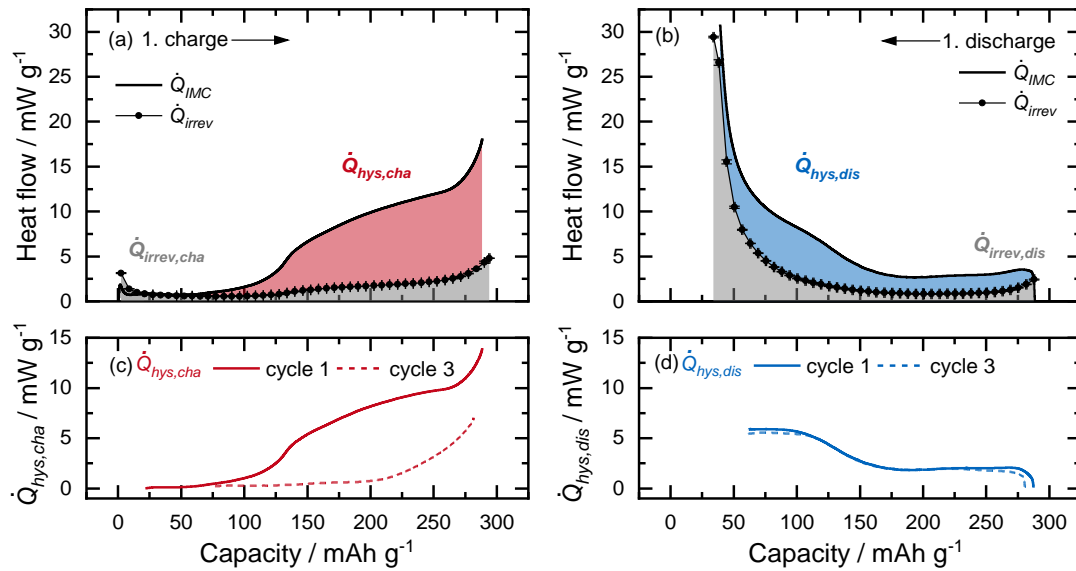
1 observable in the following cycles. This additional heat generation will be discussed in detail in the
2 following.

3 **3.2 Heat resulting from activation and hysteresis**

4 Figure 3a and Figure 3b show a detailed analysis of the heat flow, which is observed during the first
5 activation charge and discharge. There, heat generation measured by IMC (solid lines) is compared
6 with the irreversible heat flow determined by intermittent cycling (black circles and shaded gray area).
7 As mentioned in the Experimental Section, the intermittent cycling was conducted with identical cells
8 as used for the IMC experiments. The apparent charge and discharge capacity of the cells from
9 intermittent cycling is slightly higher than that of the IMC cells because of the different cycling
10 procedures (see Section 2.4).

11 For the charge half-cycle, the IMC signal agrees with the calculated expectation value of \dot{Q}_{irrev} until
12 SOC \approx 100 mAh/g. When the cell is charged further than this, \dot{Q}_{IMC} increases significantly, while \dot{Q}_{irrev}
13 remains constant, indicating that, at SOC values above \approx 125 mAh/g, an additional source of heat is
14 present for LMR-NCM. When comparing the heat generation profiles in Figure 3a to the voltage curve
15 in Figure 2a, it becomes clear that the onset of this large heat generation coincides with the beginning
16 of the upper voltage plateau during which irreversible structural rearrangements lead to the activation
17 of the LMR-NCM. We thus ascribe this large generation of heat to these activation processes as
18 suggested by Assat et al²¹ for the first cycle of $\text{Li}_2\text{Ru}_{0.75}\text{Sn}_{0.25}\text{O}_3$. The additional heat source is termed
19 \dot{Q}_{hys} and is illustrated by the red shaded area in Figure 3a for the first charge. Above \approx 125 mAh/g, \dot{Q}_{hys}
20 is the main source of heat. For the discharge direction, the IMC signal deviates from the irreversible
21 heat over the whole SOC range. This means that there is a continuous \dot{Q}_{hys} generation corresponding
22 to the area shaded in blue in Figure 3b. To better analyze the profile of the \dot{Q}_{hys} generation, Figure 3c
23 and Figure 3d show the difference curve, which is obtained by subtracting \dot{Q}_{irrev} from \dot{Q}_{IMC} in the
24 respective upper panels (solid lines for the first cycle). For the charge direction, the generation of
25 $\dot{Q}_{hys,cha}$ starts at \approx 100 mAh/g with a steep increase until \approx 140 mAh/g, where the curvature changes
26 into an approximately linear slope. In the SOC range between \approx 140 mAh/g and \approx 260 mAh/g, the \dot{Q}_{hys}
27 generation continuously rises from \approx 4.5 mW/g to \approx 10 mW/g. At the end of charge, another steep
28 increase to \approx 14 mW/g is observed. Figure 3d shows that, during the discharge half-cycle, $\dot{Q}_{hys,dis}$ is
29 generated over the entire SOC range. The heat flow profile of $\dot{Q}_{hys,dis}$ can be described with two
30 plateaus at high and low SOC that are connected by a step-like feature. At the beginning of discharge,
31 a constant value around \approx 2 mW/g is observed, which increases when the cell is discharged below
32 \approx 170 mAh/g. The second plateau is reached at SOC $<$ 100 mAh/g, where $\dot{Q}_{hys,dis}$ is around \approx 5 mW/g.
33 The \dot{Q}_{hys} generation thus shows a clear asymmetry between the first charge and discharge.

1 When we compare the generation of \dot{Q}_{hys} during the first cycle with that during the third cycle (solid
 2 versus dashed lines in Figure 3c and Figure 3d), we see a clear difference for the charge direction. For
 3 the discharge, on the other hand, both $\dot{Q}_{hys,dis}$ curves agree. This outcome was to be expected from
 4 the heat flow profiles in Figure 2b and Figure 2c. Because for the discharge direction, the total heat
 5 flow and the irreversible heat generation agree for both cycles, $\dot{Q}_{hys,dis}$ is equal. The fact that the heat
 6 evolution during discharge in the first and the consecutive cycles agrees is in accordance with literature
 7 reports on the lattice parameters⁸ and the entropy curve⁹ of LMR-NCM. In contrast, while the
 8 irreversible heat during charge at SOCs above ≈ 100 mAh/g is fairly comparable for the first and the
 9 third cycle, the overall heat signal differs significantly. This, in turn, leads to a considerably different
 10 $\dot{Q}_{hys,cha}$ generation profile. In the third cycle, $\dot{Q}_{hys,cha}$ is observed only at high SOCs (>200 mAh/g),
 11 where it increases steadily and reaches a maximum of ≈ 7 mW/g at the end of charge as reported in
 12 our previous study²⁰. On the other hand, in the first charge, the onset of $\dot{Q}_{hys,cha}$ is earlier
 13 (≈ 100 mAh/g), and the overall heat generation observed is substantially higher
 14 ($Q_{hys,3,cha} \approx 12.3$ mWh/g, $Q_{hys,1,cha} \approx 63.8$ mWh/g). Thus, what we label here as $\dot{Q}_{hys,cha}$ is not the
 15 same for the first and any consecutive cycle because during the first charge, $\dot{Q}_{hys,cha}$ includes heat
 16 generation from irreversible activation processes, which occur only during the upper voltage plateau
 17 of the first charge half-cycle.



18

19 Figure 3: Heat flow of a 0.33 LMR-NCM/Li cell during activation at C/10: (a) and (b) show the heat flow measured by IMC,
 20 \dot{Q}_{IMC} , (solid black lines) together with the irreversible heat flow determined by intermittent cycling, \dot{Q}_{irrev} , (black circles)
 21 during charge and discharge (same data as shown in black in Figure 2b and Figure 2c). The colored areas in (a) and (b)
 22 correspond to the irreversible heat (gray) and the heat resulting from OCV hysteresis (red for charge, blue for discharge). The
 23 generation of \dot{Q}_{hys} for charge and discharge is plotted in (c) and (d) (calculated from the difference between \dot{Q}_{IMC} and \dot{Q}_{irrev} ;
 24 the solid lines correspond to the \dot{Q}_{hys} generation during the first cycle, and the dashed lines represent the third cycle. The
 25 error bars for \dot{Q}_{irrev} are calculated from the measurement of two identical cells. Intermittent cycling was conducted with
 26 identical cells as used for the IMC experiments.

1 Interestingly, for the charge direction, the onset of $\dot{Q}_{hys,cha}$ occurs in the same SOC region
2 (≈ 100 mAh/g) in which the step of the voltage curve is observed. Thus, in the SOC window between
3 ≈ 100 mAh/g and ≈ 125 mAh/g, both the voltage curve and the $\dot{Q}_{hys,cha}$ curve show a steep increase.
4 At SOCs above ≈ 150 mAh/g, the upper voltage plateau is reached, and the voltage curve flattens out.
5 In this SOC range, the $\dot{Q}_{hys,cha}$ profile increases in an approximately linear manner. The major
6 proportion of $\dot{Q}_{hys,cha}$ is generated in this high SOC region, which coincides with the upper voltage
7 plateau of the cell. As explained above, irreversible processes^{10,13} occur during the upper voltage
8 plateau. Our results clearly indicate that this activation process generates a significant amount of waste
9 heat.

10 There are also some similarities between the $\dot{Q}_{hys,cha}$ generation during activation and the gas release
11 measured by on-line electrochemical mass spectrometry (OEMS). For the same LMR-NCM active
12 material as used in the present study, Strehle et al.¹² and Teufl et al.³ report that the CO₂ generation
13 during the first charge starts between ≈ 100 mAh/g and ≈ 125 mAh/g. This coincides with the sloping
14 region at the beginning of the upper voltage plateau and the onset of the $\dot{Q}_{hys,cha}$ generation observed
15 here. The increase of the CO₂ concentration as a function of SOC is comparable to the shape of the
16 $\dot{Q}_{hys,cha}$ signal up to ≈ 270 mAh/g. When the cell is charged even higher, both the $\dot{Q}_{hys,cha}$ and the CO₂
17 generation show a steep increase. In this high SOC range, O₂ generation is observed by OEMS. The CO₂
18 evolution below 4.6 V (≈ 270 mAh/g) is attributed to the chemical decomposition of Li₂CO₃, which
19 reacts with protons formed by either the anionic oxidation of the electrolyte or trace impurities.^{3,12,25}
20 The CO₂ and O₂ evolution at high SOC are ascribed to the formation of singlet O₂ at the surface of the
21 LMR-NCM particles, which either reacts with the electrolyte to form CO₂ or is evolved as triplet O₂.⁴ An
22 O-depleted spinel/rock salt surface layer is thereby formed around the LMR-NCM particles.^{3,12,13} Let us
23 first discuss the decomposition of Li₂CO₃. According to the enthalpies of formation listed in the NIST
24 database²⁶, the enthalpy of reaction for $\text{Li}_2\text{CO}_3 + 2 \text{HF} \rightarrow 2 \text{LiF} + \text{H}_2\text{O} + \text{CO}_2$ is ≈ -155.6 kJ/mol_{Li₂CO₃} and
25 thus exothermic. The decomposition of Li₂CO₃ as a surface impurity is reported to be in the order of
26 ≈ 0.6 wt%¹², which means that per gram of LMR-NCM active material, only about 80 μmol of Li₂CO₃ are
27 decomposed. The enthalpy of the decomposition thus translates to a heat generation of
28 ≈ 3.5 mWh/g_{CAM}. When we calculate absolute numbers for $Q_{hys,cha}$ based on the difference between
29 the total heat measured by IMC and the irreversible heat determined by intermittent cycling shown in
30 Table 1 and Table 2, we observe that $Q_{hys,cha}$ amounts to ≈ 63.8 mWh/g (≈ 20 kJ/mol) for the first
31 charge of LMR-NCM. Compared to this value, the decomposition reaction can explain only a small
32 fraction of the observed heat generation. We can therefore exclude that it is the source of the $\dot{Q}_{hys,cha}$
33 generation. However, as mentioned in Section 2.1, other sources of heat, such as reversible and
34 parasitic heat, contribute to the overall heat signal. The significance of these heat terms for the present

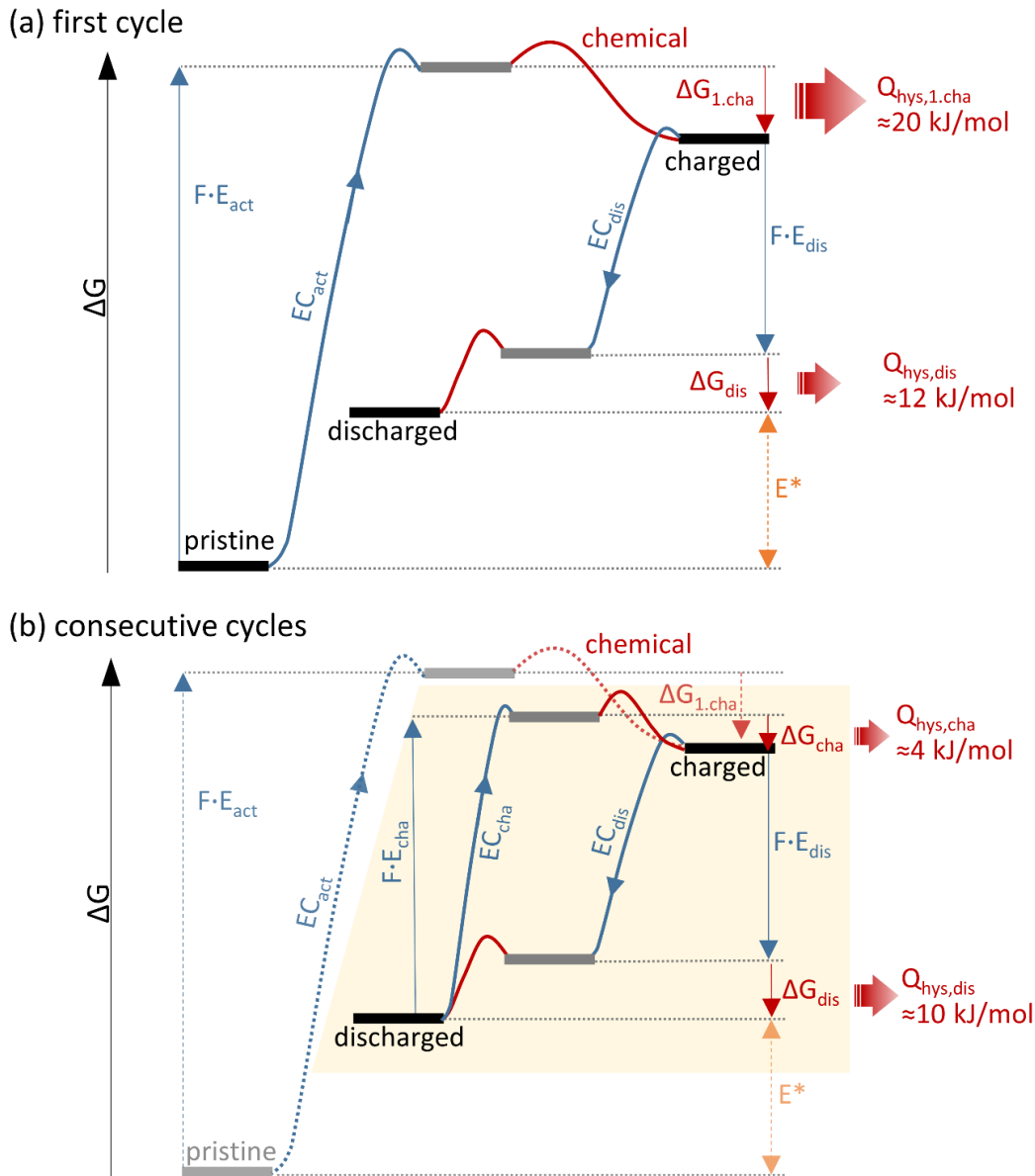
1 study will be further discussed in Section 3.5. However, we can already say that they are negligible
2 compared with the magnitude of the heat generation observed. Nevertheless, the assumptions mean
3 that the results for Q_{hys} constitute a maximum value. The second process, which causes gas evolution
4 at high SOCs, is the transformation of the LMR-NCM surface from a layered to a spinel/rock salt
5 structure.^{3,12,13} At high degrees of delithiation, this process is reported to be exothermic.^{27,28} According
6 to DFT calculations by Wang et al.²⁷, layered $\text{Li}_{0.25}\text{NiO}_2$ can be transformed to rock salt NiO and/or spinel
7 LiNi_2O_4 with reaction enthalpies of ≈ -10 kJ/mol to ≈ -15 kJ/mol. However, in the presence of
8 electrolyte, which reacts with the evolved O_2 , the heat is reported to be approximately 10 times higher
9 with numbers between ≈ -75 kJ/mol for $\text{Li}_{0.45}\text{Ni}_{0.33}\text{Co}_{0.33}\text{Mn}_{0.33}\text{O}_2$ and ≈ -130 kJ/mol for
10 $\text{Li}_{0.45}\text{Ni}_{0.8}\text{Co}_{0.15}\text{Al}_{0.05}\text{O}_2$ in 1.2M $\text{LiPF}_6/\text{EC}:\text{EMC}$ (3:7 wt%).²⁸ It needs to be stressed that these literature
11 values refer to a complete material decomposition while in the present study, we expect that only a
12 few mol% of the CAM at the particle surface are restructured.^{3,12} For the first charge, we observe that
13 $Q_{hys,cha}$ amounts to ≈ 63.8 mWh/g (≈ 20 kJ/mol). However, these calculated numbers refer to the
14 whole SOC range, whereas O_2 evolution from the CAM restructuring is observed only at high SOC.
15 By fitting a baseline through the $\dot{Q}_{hys,cha}$ profile between 100 mAh/g and 250 mAh/g, the heat
16 generation, which is observed on top of this baseline at higher SOCs, can be integrated. We thus
17 estimate the additional heat generated above 250 mAh/g to be ≈ 1.1 mWh/g (≈ 0.36 kJ/mol). Assuming
18 that ≈ 3 mol% of CAM at the surface are transformed to a spinel/rock salt structure^{3,12}, the expected
19 energy values are between 0.3 kJ/mol and 0.45 kJ/mol assuming no reaction of the evolving O_2 with
20 the electrolyte²⁷ and between 2.25 kJ/mol and 3.9 kJ/mol with electrolyte decomposition²⁸. Because
21 the OEMS studies indicate that the CO_2 signal increases once O_2 is detected^{3,12}, a combination of both
22 reactions is observed. We therefore conclude that the increase in the $\dot{Q}_{hys,cha}$ profile above
23 ≈ 250 mAh/g might be correlated to the restructuring of the CAM particle surface from a layered to an
24 O-depleted spinel/rock salt structure. The heat of this reaction together with the heat generated when
25 the evolved O_2 reacts with the electrolyte might be the cause of the sharp increase in the IMC signal
26 towards the end of charge. However, a more thorough analysis is required to prove this hypothesis.
27 Moreover, it is important to stress that the O_2 evolution of the CAM can explain only this rather small
28 part of the overall $Q_{hys,cha}$ heat. Most of the heat generation observed is thus caused by bulk
29 phenomena and not by the gassing of the surface.

30 The findings discussed above feed into a scheme for the reaction energy landscape of LMR-NCM shown
31 in Figure 4. It is similar to previously reported hysteresis loops for molecular hysteresis^{29,30} and a model
32 Li-rich layered cathode²¹, $\text{Li}[\text{Li}_{0.33}\text{Ru}_{0.5}\text{Sn}_{0.17}]\text{O}_2$. The first cycle (Figure 4a) starts from the pristine
33 material, which is electrochemically oxidized on charge requiring the electrical charge energy $F \cdot E_{act}$.
34 This electrochemical reaction (termed as "EC" and marked in blue in Figure 4) is followed by a chemical

1 process (red), in which the LMR-NCM structure is rearranged. In the scheme in Figure 4a, this is
2 visualized by the transition from the intermediate (gray) to the stable charged state (black). The
3 structural modification happens during the upper voltage plateau and is most likely caused by a
4 combination of irreversible processes (e.g., anionic redox, TM migration, or the loss of the honeycomb
5 ordering), whereby the definite mechanism is still under debate.^{8,13,31} With our approach, we cannot
6 make any statement on the mechanistic processes during activation. However, we are able to measure
7 the waste heat associated with these activation processes. The stabilizing chemical step thus explains
8 the considerable heat generation observed during the upper voltage plateau, $Q_{hys,1.cha}$ as indicated
9 by the red arrow in Figure 4a. In other words, the $Q_{hys,1.cha}$ generation observed is a measure of the
10 enthalpy of reaction for the activation process. Because of the irreversible structural rearrangements,
11 the discharge occurs via a different pathway, which generates the electrical discharge energy, $F \cdot E_{dis}$.
12 The electrochemical process is again followed by a chemical step, which generates the heat $Q_{hys,dis}$.
13 An important finding is that, after the first cycle, the material has not returned to its initial state
14 because of the irreversible processes that occurred during the first charge. As a result, the voltage
15 curve is not a closed loop. Thus, from the electrochemical data alone, it cannot be determined how
16 much energy is lost as waste heat during the first cycle. In contrast, for conventional active materials,
17 the waste heat is equal to the electrical energy lost during a reversible cycle with a closed voltage
18 curve, and the CAM returns to its initial state after a complete cycle. There, it can be calculated from
19 the integration of the voltage curve. In the case of the first cycle of LMR-NCM, we observe that the
20 electrical discharge energy is significantly lower than the charge energy due to three main factors: (i)
21 polarization effects cause the mean charge voltage to increase and the mean discharge voltage to
22 decrease, thereby creating an irreversible heat source, Q_{irrev} , (not shown in Figure 4); (ii) the
23 stabilizing chemical steps convert electrochemical energy into waste heat, Q_{hys} ; (iii) the irreversible
24 modifications during activation change the CAM in such a way that not all Li extracted during charge
25 can be re-inserted during discharge (irreversible capacity loss); and (iv) these irreversible
26 rearrangements lead to a lower discharge potential, even under OCV conditions, thereby lowering the
27 discharge energy. By quantifying the energy lost as waste heat, using IMC, we determine (i) Q_{irrev} and
28 (ii) Q_{hys} and are thus able to assess how much of the electrical energy is lost as a result of the
29 irreversible rearrangements (iii + iv). Based on Table 1, this energy loss term, E^* , amounts to
30 190.6 mWh/g, which corresponds to 15% of the charge energy and accounts for 57% of the total
31 energy loss. This energy was put into the system in the form of electrical energy upon charge ($F \cdot E_{act}$
32 in Figure 4a) but was neither lost as waste heat nor extracted as electrical energy during discharge. It
33 is visualized as orange double arrow in Figure 4. However, it cannot be determined what proportion of
34 this energy loss E^* is simply due to the loss of chemically available Li sites in the CAM (irreversible
35 capacity loss) and to what extent E^* corresponds to electrochemical energy, which was consumed by

1 the LMR-NCM in order to enable the structural rearrangements during the activation process. What is
2 reported here as E^* is thus a measure of the lost electrical work not converted into waste heat and a
3 maximum possible value for the electrochemical energy consumed for structural rearrangements. This
4 energy term can be determined only by quantifying the other sources of energy loss by IMC. To the
5 best of our knowledge, this is reported here for the first time. Qiu et al.³² recently reported that
6 although the pristine state of LMR-NCM cannot be recovered through natural processes, the structure
7 of cycled LMR-NCM can be driven close to the original state by heat treatment at up to 300°C. For the
8 heat treated CAM, they observed a reappearance of the voltage plateau at ≈ 4.5 V suggesting that the
9 structural rearrangements during activation can to some extent be reversed by a heat treatment. It
10 would be interesting to investigate if also the IMC signal of such a treated LMR-NCM resembles that of
11 a pristine electrode.

12 Figure 4b illustrates the reaction energy landscape for the following reversible cycles as suggested by
13 Assat et al.²¹ The charge process occurs via a different pathway than during the first cycle, and the
14 electrical charge energy $F \cdot E_{cha}$ is less than during activation. Again, the redox step is followed by a
15 stabilizing structural rearrangement. For the charge after activation, this chemical step generates
16 significantly less heat, $Q_{hys,cha}$, than during the first cycle. The consecutive discharge is analogous to
17 that observed during the first cycle. The $Q_{hys,dis}$ value calculated is only slightly lower than during the
18 first cycle because the SOC window has slightly decreased from the first to the third cycle. Because all
19 consecutive cycles are reversible, the proposed reaction mechanism is now a closed loop (highlighted
20 by the yellow area in Figure 4b). Nevertheless, it is a hysteresis loop because of the path-dependence
21 between the charge and discharge direction, thereby implying that (de-)lithiation occurs via
22 metastable pathways. A more detailed discussion on the hysteresis phenomena in LMR-NCM during
23 regular cycles can be found in our previous entropy study⁹ as well as in the IMC study by Assat et al.²¹
24 A quantitative analysis of the corresponding Q_{hys} heat terms for LMR-NCM/Li cells is reported in our
25 previous publication.²⁰ The comparison of the reversible cycle and the first charge in Figure 4b (dashed
26 lines) further underlines that the first charge is a unique process, which irreversibly changes the LMR-
27 NCM and leads to a different energy landscape for the following cycles.



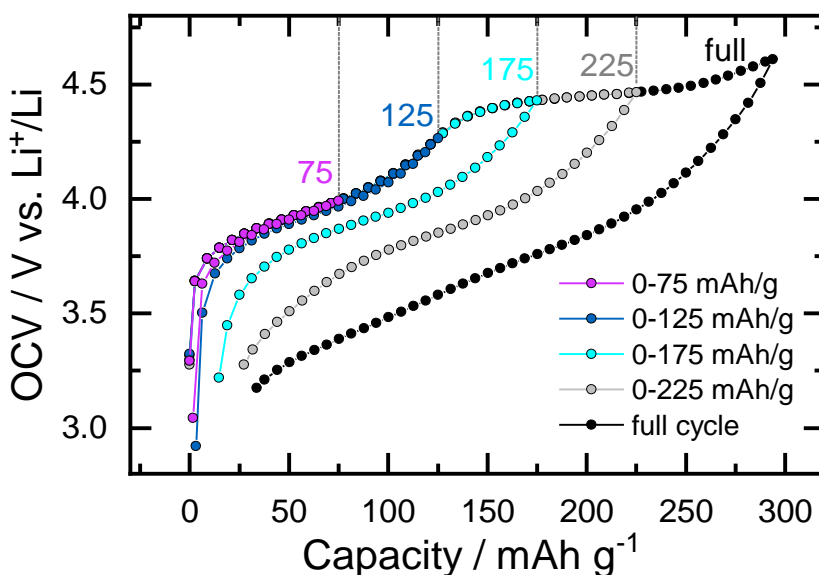
1

2 *Figure 4: Scheme of a reaction energy landscape (not true to scale) for (a) the first cycle and (b) all consecutive cycles (region*
 3 *marked in yellow) of LMR-NCM/Li cells at C/10 and 25°C. Blue lines indicate electrochemical processes (EC) with the conversion*
 4 *of the respective electrical energy ($F \cdot E$), and red lines indicate chemical processes with the respective chemical energy (ΔG),*
 5 *which is evolved as heat (Q). The heat terms calculated are based on the Q_{hys} results discussed in the text. Black bars indicated*
 6 *stable energy levels (pristine/charged/discharged), and gray bars indicate intermediate states. Essential findings of the*
 7 *scheme are: (i) The first charge is an irreversible process, meaning that its energetic pathway in panel (a) is unique and can no*
 8 *longer be accessed once the material is activated, (ii) the difference between the first charge and discharge energy is explained*
 9 *by the conversion of electrochemical energy into heat (Q_{hys}) and by the energy loss (E^*) caused by the structural*
 10 *rearrangements during activation.*

11 **3.3 Window-opening experiments**

12 As described above in context with Figure 4, the first charge includes irreversible processes that occur
 13 during the upper voltage plateau and which lead to waste heat, $\dot{Q}_{hys,cha}$, which can be observed at
 14 SOC > 100 mAh/g. In order to further analyze this heat generation during activation, charge window
 15 opening experiments were conducted. In these experiments, identical cells were charged to different
 16 upper SOC limits and discharged to 2.0 V. Figure 5 shows the OCV curves resulting from intermittent

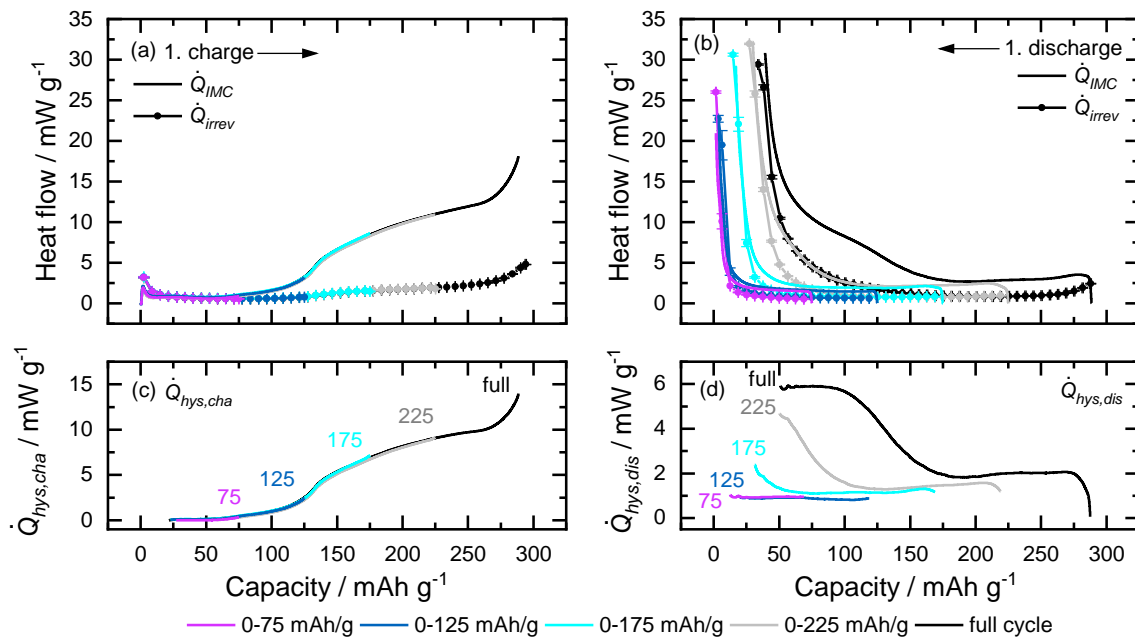
1 cycling to the upper limits of 75 mAh/g, 125 mAh/g, 175 mAh/g, and 225 mAh/g and compares them
 2 to a full cycle, which was conducted until the upper voltage cutoff of 4.8 V (≈ 290 mAh/g). For each of
 3 these curves, a new set of cells was used so that all started from the pristine state. For the first two
 4 sets of cells, which were charged only in the initial sloping region of the voltage curve, the charge and
 5 discharge OCV curves agree and no hysteresis is observable, which is in agreement with the
 6 literature^{1,8}. However, as soon as a cell is charged beyond ≈ 125 mAh/g, where the upper voltage
 7 plateau starts, there is a path dependence between the charge and discharge OCV curves. The resulting
 8 hysteresis loop grows continuously with increasing upper charge window. Those intermediate
 9 scanning curves can provide valuable insight into the nature of the structural rearrangement and the
 10 corresponding energy barrier that lead to the hysteresis phenomena.³⁰ As long as the SOC window is
 11 restricted to the region below ≈ 125 mAh/g, the LMR-NCM behaves apparently reversible. However, as
 12 soon as the delithiation proceeds beyond this critical point, which is the beginning of the upper voltage
 13 plateau, the energy barriers can be overcome and the irreversible material transformation occurs. This
 14 causes the system to remain in the new stable state even if the LMR-NCM is relithiated. The gradual
 15 growth of the hysteresis loop observed for the OCV is also reported for other material properties, such
 16 as the cell resistance⁵ and the partial molar entropy⁹. The lattice parameters of LMR-NCM show a
 17 reversible behavior when the material is charged to an upper limit of ≈ 100 mAh/g, which is in contrast
 18 to the path dependence that can be observed for a full activation cycle.⁸



19
 20 *Figure 5: OCV curves of identical 0.33 LMR-NCM/Li cells during activation at C/10 collected during intermittent cycling to*
 21 *various upper SOC limits. During this window-opening experiment, the cells were charged to different upper SOC limits and*
 22 *discharged to 2.0 V with a 1 h rest phase every Δ SOC = 2.5%. The OCV values determined at the end of each rest phase are*
 23 *shown as function of the upper SOC limit with a color as indicated (i) 75 mAh/g (pink), (ii) 125 mAh/g (dark blue), (iii)*
 24 *175 mAh/g (light blue) and (iv) 225 mAh/g (grey). Data from a full cycle, which was conducted until the cutoff voltage of 4.8 V,*
 25 *is shown in black (≈ 290 mAh/g).*

1 To analyze whether the heat signal of LMR-NCM/Li cells also shows such intermediate scanning curves,
2 we conducted IMC measurements with identical cells as used above. They were charged at constant
3 current to the upper SOC values of 75 mAh/g, 125 mAh/g, 175 mAh/g, or 225 mAh/g followed by a 6 h
4 rest phase and a discharge to 2.0 V. Figure 6a shows the resulting IMC curves together with the
5 irreversible heat determined from intermittent cycling for the first charge to various upper charge
6 limits (color gradient as indicated in the figure caption). Reference data for a full first cycle with charge
7 to the cutoff voltage of 4.8 V (≈ 290 mAh/g) is shown in black. As expected, the heat flow profiles of
8 $\dot{Q}_{IMC,cha}$ and $\dot{Q}_{irrev,cha}$ in Figure 6a agree with the reference data set of the full charge until they reach
9 their respective charge limit. The corresponding $\dot{Q}_{hys,cha}$ curves in Figure 6c indicate that with
10 increasing charge window, the generation of $\dot{Q}_{hys,cha}$ increases but that the onset and profile shape
11 are independent of the SOC limit. The cells, which were charged only until 75 mAh/g, did not show any
12 $\dot{Q}_{hys,cha}$ generation. Figure 6b shows the heat generation curves for the discharge after charging the
13 cells to the various SOC limits. The observed $\dot{Q}_{IMC,dis}$ signals for the cells charged to 75 mAh/g and
14 125 mAh/g are close to their respective irreversible heat curves. There is thus no significant $\dot{Q}_{hys,dis}$
15 generation in Figure 6d. In contrast, the cells that were charged to higher SOC values exhibit a growing
16 difference between $\dot{Q}_{IMC,dis}$ and $\dot{Q}_{irrev,dis}$. This translates into an increasingly more pronounced
17 $\dot{Q}_{hys,dis}$ generation in Figure 6d. Apart from the growing $\dot{Q}_{hys,dis}$ signal amplitude with increasing
18 charge window, the onset of the steep increase in the $\dot{Q}_{hys,dis}$ curves also changes. The onset of this
19 step-like feature is around ≈ 175 mAh/g for a cell after full activation and is observed at later points
20 during discharge (lower SOC) for cells that were charged only to 225 mAh/g (onset at ≈ 120 mAh/g)
21 and 175 mAh/g (onset at ≈ 65 mAh/g). Thus, the more the LMR-NCM becomes “activated” during the
22 first charge, the more and the earlier $\dot{Q}_{hys,dis}$ is generated in the consecutive discharge. This
23 observation proves that the heat resulting from hysteresis, which is observed in the first and every
24 other discharge, is a consequence of the activation processes during the first charge. In agreement
25 with literature reports on the behavior of the cell resistance⁵, the partial molar entropy⁹ and the lattice
26 parameters⁸ of LMR-NCM, our IMC measurements suggest that the activation that occurs during the
27 upper voltage plateau is a gradual process. The irreversible rearrangements become increasingly more
28 complete the more the cell is delithiated, which results in an increasing \dot{Q}_{hys} generation in both the
29 charge and discharge direction. The critical point for this activation process is the onset of the upper
30 voltage plateau at an SOC of ≈ 125 mAh/g. The presence of intermediate scanning curves for all these
31 bulk phenomena indicates that the structural rearrangement is not a sequential process that occurs
32 via individual domains (e.g. first small particles and then large ones) or from the surface to the center
33 of the CAM particles but rather is a continuous process within the entire bulk LMR-NCM structure.

34



1

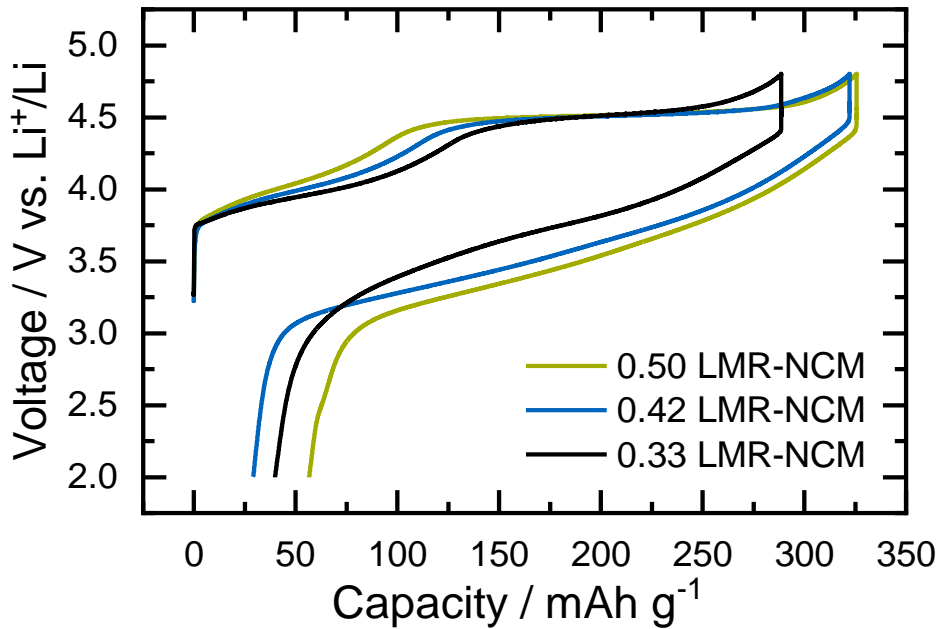
2 Figure 6: Heat flow of 0.33 LMR-NCM/Li cells during activation at C/10. In this window-opening experiment, identical cells
 3 were charged to different upper SOC limits and discharged to 2.0 V. The resulting heat profiles are colored as indicated for the
 4 upper SOC limits of (i) 75 mAh/g (pink), (ii) 125 mAh/g (dark blue), (iii) 175 mAh/g (light blue), and (iv) 225 mAh/g (grey). Data
 5 from a full cycle, which was conducted until the cutoff voltage of 4.8 V, is shown in black (≈ 290 mAh/g). Panels (a) and (b)
 6 show the heat flow measured by IMC, \dot{Q}_{IMC} , (solid lines) together with the irreversible heat flow determined by intermittent
 7 cycling, \dot{Q}_{irrev} , (circles) during charge and discharge. The generation of \dot{Q}_{hys} for charge and discharge is plotted in (c) and (d).
 8 The error bars for \dot{Q}_{irrev} are calculated from the measurement of two identical cells. Intermittent cycling was conducted with
 9 identical cells as the IMC experiments.

10

11 3.4 Effect of the degree of overlithiation on the heat generation

12 The degree of overlithiation (the amount of Li in the TM layer) influences the electrochemical
 13 performance of LMR-NCM but also plays an important role for the hysteresis phenomena. A higher
 14 degree of overlithiation leads to a higher theoretical capacity of the LMR-NCM material.³ Figure 7
 15 shows the voltage curves during the first cycle for LMR-NCM/Li half-cells with various degree of
 16 overlithiation, namely 0.33 LMR-NCM (black), 0.42 LMR-NCM (blue), and 0.50 LMR-NCM (green) cells.
 17 The previous discussion focused on the 0.33 LMR-NCM material with the lowest degree of
 18 overlithiation. In agreement with literature^{1,3}, the charge capacity increases with increasing degree of
 19 overlithiation and reaches 289 mAh/g for 0.33 LMR-NCM, 322 mAh/g for 0.42 LMR-NCM, and
 20 325 mAh/g for 0.50 LMR-NCM. Moreover, a longer activation plateau is observed for a higher degree
 21 of overlithiation as was reported by Croy et al. and Teufl et al.^{1,3}. The charge energy thus increases
 22 with the degree of overlithiation. The first charge energy is 1240 mWh/g for 0.33, 1401 mWh/g for
 23 0.42, and 1427 mWh/g for 0.50 LMR-NCM. The irreversible loss of capacity shows no clear trend as a
 24 function of overlithiation. It is 40 mAh/g for the 0.33, 29 mAh/g for the 0.42, and 57 mAh/g for the
 25 0.50 LMR-NCM material. The discharge energy is highest for the 0.42 LMR-NCM material

1 (1048 mWh/g), which shows the lowest irreversible loss of capacity. For the 0.33 LMR-NCM, the first
 2 discharge energy is 907 mWh/g, for 0.50 LMR-NCM, it is 949 mWh/g. The electrical energy loss
 3 resulting from the difference between the charge and the discharge energy is summarized in Table 2.
 4 It increases with increasing degree of overlithiation. In agreement with literature^{1,3}, the hysteresis loop
 5 of the charge and discharge voltage increases with the degree of overlithiation. Moreover, for the
 6 same types of CAM as used in this study, the variation of the lattice parameters as a function of SOC
 7 depends on the degree of overlithiation.⁸ In a previous entropy study on 0.33 LMR-NCM and 0.50 LMR-
 8 NCM, we found that the partial molar entropy curves of LMR-NCM/Li cells differ when plotted as a
 9 function of SOC but agree when plotted as a function of OCV. We thus aim to analyze the different
 10 LMR-NCM materials by means of IMC in order to determine whether the heat generation is also
 11 influenced by the degree of overlithiation.



12

13 *Figure 7: Voltage curves during the first cycle at C/10 for 0.33 LMR-NCM/Li (black), 0.42 LMR-NCM/Li (blue), and 0.50 LMR-NCM/Li cells.*
 14

15 *Table 2: Measured and calculated energy losses for the first cycle of LMR-NCM/Li cells at C/10 and 25°C with various degrees of overlithiation (0.33, 0.42, and 0.50 LMR-NCM as explained in Experimental Section 2.2). Electrical energy loss, total heat generation measured by IMC, and the ratio total heat/electrical loss for the whole cycle are shown together with the integrated IMC signal and the determined heat resulting from hysteresis in charge and discharge.*
 16
 17
 18

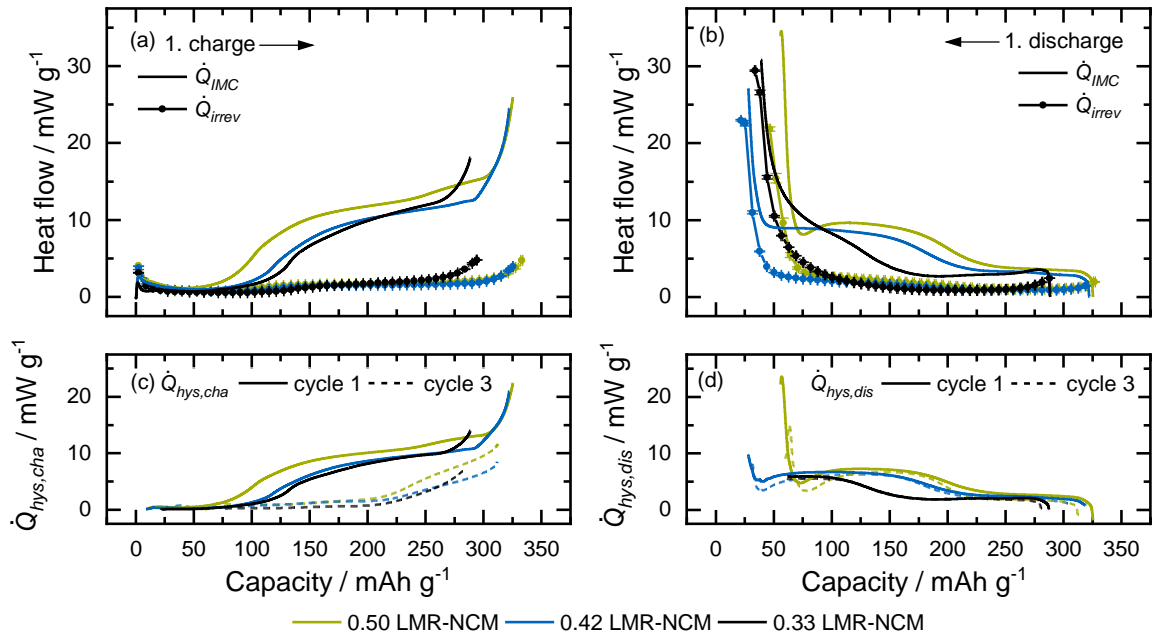
LMR-NCM	$E_{cha} - E_{dis}$ [mWh/g]	$Q_{IMC,total}$ [mWh/g]	$\frac{Q_{IMC,total}}{E_{cha} - E_{dis}}$ [%]	$Q_{IMC,cha}$ [mWh/g]	$Q_{hys,cha}$ [mWh/g]	$Q_{IMC,dis}$ [mWh/g]	$Q_{hys,dis}$ [mWh/g]
0.33	333.6	143.0	43	78.8	63.8	64.2	38.0
0.42	353.3	183.9	52	106.7	91.5	77.3	56.5
0.50	478.4	211.4	44	129.5	111.9	211.4	60.9

1 Figure 8a and Figure 8b show the heat flow curves measured by IMC \dot{Q}_{IMC} (solid lines) and \dot{Q}_{irrev}
 2 determined from intermittent cycling (symbols) for LMR-NCM/Li half-cells during activation at C/10
 3 with 0.33 LMR-NCM (black), 0.42 LMR-NCM (blue), and 0.50 LMR-NCM (green) for the charge and
 4 discharge direction. Table 2 summarizes the integrated heat terms, including the consecutive rest
 5 phase, which is not shown in Figure 8. For the first cycle, the heat measured by IMC, Q_{IMC} , increases
 6 with increasing degree of overlithiation for both the charge and discharge direction. This is in
 7 agreement with the increasing electrical energy loss, $E_{cha} - E_{dis}$. For all LMR-NCM materials, the
 8 waste heat observed is not more than half of the electrical energy loss. This means that a comparable
 9 proportion of the charge energy is lost as a result of irreversible rearrangement processes during
 10 activation for all LMR-NCM materials. Figure 8a and Figure 8b show that while the irreversible heat
 11 flow is similar for the different materials, the \dot{Q}_{IMC} profiles differ. During the first charge, the $\dot{Q}_{irrev,cha}$
 12 curves of the different CAMs agree until the cells reach their respective end of charge, where an
 13 increase in the cell polarization is observed. For example, for the 0.33 LMR-NCM/Li cells, the
 14 polarization within the cell increases starting at ≈ 275 mAh/g, which is also visible in the voltage curve
 15 in Figure 7. For the cells with 0.42 and 0.50 LMR-NCM, this feature occurs at higher SOC because of
 16 the higher amount of available Li^+ . However, for the rest of the charge, the irreversible heat generation
 17 is fairly comparable for all CAMs. A similar trend is found for the discharge direction, where the
 18 $\dot{Q}_{irrev,dis}$ curves of the different LMR-NCM/Li cells agree until the respective end of discharge is
 19 reached, where the polarization then begins to increase again. The $\dot{Q}_{IMC,cha}$ signals shown in Figure 8a
 20 indicate that with increasing degree of overlithiation, the overall heat generation increases, while the
 21 general profile shape is still comparable. In Figure 8c, the generation of $\dot{Q}_{hys,cha}$ is shown for the three
 22 different LMR-NCM materials. The solid lines thus correspond to the heat generation during the first
 23 charge, while the dashed lines were determined for the third charge. If we focus on the first cycle, the
 24 $\dot{Q}_{hys,cha}$ signals of the 0.33 and the 0.42 LMR-NCM are comparable for most of the first charge. The
 25 only difference is the onset and amplitude of the steep increase at the end of charge, which occurs at
 26 ≈ 265 mAh/g for the 0.33 LMR-NCM and at ≈ 292 mAh/g for the 0.42 LMR-NCM material. For the
 27 0.50 LMR-NCM, the $\dot{Q}_{hys,cha}$ signal is generally higher over the whole SOC range, and its onset around
 28 ≈ 60 mAh/g is earlier than for the other two materials investigated, which leads to the significantly
 29 increased $Q_{hys,cha}$ value in Table 2. Furthermore, an additional feature emerges at ≈ 250 mAh/g where
 30 the curvature of the $\dot{Q}_{hys,cha}$ signal increases slightly. The onset of the steep increase at the end of
 31 charge is around ≈ 300 mAh/g and therefore later than for the other two materials. Because we closely
 32 correlate the $\dot{Q}_{hys,cha}$ generation during the first charge with the irreversible structural
 33 rearrangements within the LMR-NCM, this calorimetric analysis suggests that for a higher degree of

1 overlithiation, a more pronounced activation process is observed. This is in agreement with the higher
2 amount of Li^+ in the TM layer of LMR-NCMs with a high degree of overlithiation.

3 The heat generated during the first discharge is shown in Figure 8b. While the $\dot{Q}_{irrev,dis}$ curves
4 generally agree for the various materials, the $\dot{Q}_{IMC,dis}$ profiles show clear differences. Because of the
5 higher charge capacity (Figure 7), the heat flow curves of 0.42 and 0.50 LMR-NCM start at a higher
6 SOC. For the materials with a higher degree of overlithiation, the onset of the increase in $\dot{Q}_{IMC,dis}$ is
7 observed earlier during discharge (at higher SOC). Moreover, while for the 0.33 LMR-NCM, the
8 $\dot{Q}_{IMC,dis}$ signal continuously increases after the onset around ≈ 175 mAh/g, the $\dot{Q}_{IMC,dis}$ values of
9 0.42 LMR-NCM display a saturation behavior. In case of the 0.50 LMR-NCM, the $\dot{Q}_{IMC,dis}$ signal even
10 decreases at ≈ 75 mAh/g prior to the steep increase at the end of discharge. The resulting $\dot{Q}_{hys,dis}$
11 profiles are compared in Figure 8d. For all materials, $\dot{Q}_{hys,dis}$ is generated over the whole SOC range,
12 and all curve shapes can be roughly described by two plateaus connected by a step-like feature. The
13 signal amplitude during the first plateau at high SOC is fairly similar for all materials. However, the
14 onset of the consecutive step-like feature is shifted to higher SOC for a higher degree of overlithiation.
15 For 0.33 LMR-NCM, it is at ≈ 170 mAh/g, for 0.42 LMR-NCM, at ≈ 225 mAh/g, and for 0.50 LMR-NCM, at
16 ≈ 240 mAh/g. For a higher degree of overlithiation, the signal amplitude during the second plateau is
17 slightly higher. A remarkable difference between the $\dot{Q}_{hys,dis}$ profiles is that the curves of 0.42 and
18 0.50 LMR-NCM show a decreasing signal towards the end of the respective discharge before the heat
19 generation increases steeply at the end of the discharge. This dip is observed at ≈ 75 mAh/g for
20 0.50 LMR-NCM and at ≈ 40 mAh/g for 0.42 LMR-NCM, whereby it is more pronounced for the
21 0.50 LMR-NCM. A possible reason for this decreasing heat signal can be the occurrence of an
22 endothermic processes, which, together with the exothermic processes (which were also present
23 before), leads to a decrease in the net heat signal. Another possibility is the disappearance of an
24 exothermic process at the respective SOC values. It cannot be clarified whether the absence of the dip
25 in the heat flow profile of 0.33 LMR-NCM is a material specific property or due to the smaller effective
26 SOC window. Further studies are necessary to address these questions. In summary, it can be
27 concluded that the heat flow resulting from hysteresis and activation, \dot{Q}_{hys} , differs when the degree
28 of overlithiation is varied. In agreement with the earlier beginning of the upper voltage plateau in
29 Figure 7, the onset and amplitude of $\dot{Q}_{hys,cha}$ are shifted so that the total heat generation during the
30 first charge increases with increasing degree of overlithiation. For the first discharge, the $\dot{Q}_{hys,dis}$
31 profile is also altered in such a way that the heat generated is higher for a higher degree of
32 overlithiation.

33



1
2 *Figure 8: Heat during activation of LMR-NCM/Li cells at C/10 as a function of the degree of overlithiation of the LMR-NCM*
3 *material: 0.33 LMR-NCM (black, same data as in Figure 3), 0.42 LMR-NCM (blue) and 0.50 LMR-NCM (green). Panels (a) and*
4 *(b) show the heat flow measured by IMC, \dot{Q}_{IMC} , (solid lines) together with the irreversible heat flow determined by intermittent*
5 *cycling, \dot{Q}_{irrev} , (circles) during charge and discharge. The generation of \dot{Q}_{hys} for charge and discharge is plotted in (c) and (d);*
6 *the solid lines correspond to the \dot{Q}_{hys} generation during the first cycle, and the dashed lines represent the third cycle.*
7 *Intermittent cycling was conducted with identical cells as used for the IMC experiments.*

8 In Figure 8c and Figure 8d, the \dot{Q}_{hys} generation during the first (solid lines) and the third cycle (dashed
9 lines) are compared. For the third cycle, only \dot{Q}_{hys} is depicted in Figure 8. It was obtained by subtracting
10 the irreversible heat determined by intermittent cycling from \dot{Q}_{IMC} for the third cycle (raw data not
11 shown here). Table 3 furthermore summarizes the integrated heat generation and the electrical energy
12 loss terms for the different LMR-NCM materials in the third cycle at C/10. With increasing degree of
13 overlithiation, the loss of electrical energy and with it the waste heat increases. Thus, 91–97% of the
14 expected heat are measured by the applied method. A comparison with Table 2 underlines that the
15 heat generation during the third cycle is considerably less than during the first cycle for all materials.
16 For the heat flow profiles during charge (Figure 8c), a mismatch between $\dot{Q}_{hys,1,cha}$ and $\dot{Q}_{hys,3,cha}$ is
17 clearly observable for all materials, which is in agreement with the analysis of the 0.33 LMR-NCM
18 material in Figure 3. Compared with the first cycle (see Table 2), the heat resulting from hysteresis is
19 considerably less during the third cycle but still shows an increasing trend with increasing degree of
20 overlithiation. The $\dot{Q}_{hys,3,cha}$ profile is thus quite similar for the various CAMs. All curves show no
21 significant \dot{Q}_{hys} generation until an SOC of ≈ 200 mAh/g is reached but the maximum amplitude of the
22 heat generation is higher for a higher degree of overlithiation. The $\dot{Q}_{hys,dis}$ curves of the third and the
23 first cycle shown in Figure 8d, agree for each type of LMR-NCM. However, for the 0.42 and 0.50 LMR-
24 NCM, the signal amplitude of $\dot{Q}_{hys,3,dis}$ is slightly lower than that observed during the first discharge.

1 In general, the same trend as for the 0.33 LMR-NCM is also observed for the CAMs with a higher degree
 2 of overlithiation: While the heat generation during the first and the third charge are significantly
 3 different in shape and total integral, the first discharge is similar to the consecutive ones.

4 *Table 3: Measured and calculated energy losses for the third cycle of LMR-NCM/Li cells at C/10 and 25°C with various degrees*
 5 *of overlithiation (0.33, 0.42, and 0.50 LMR-NCM as explained in Experimental Section 2.2). Electrical energy loss, total heat*
 6 *generation measured by IMC, and the ratio total heat/electrical loss for the whole cycle are shown together with the*
 7 *integrated IMC signal and the determined heat resulting from hysteresis in charge and discharge.*

LMR- NCM	$E_{cha} - E_{dis}$ [mWh/g]	$Q_{IMC,total}$ [mWh/g]	$\frac{Q_{IMC,total}}{E_{cha} - E_{dis}}$ [%]	$Q_{IMC,3,cha}$ [mWh/g]	$Q_{hys,3,cha}$ [mWh/g]	$Q_{IMC,3,dis}$ [mWh/g]	$Q_{hys,3,dis}$ [mWh/g]
0.33	94.1	87.7	93	28.7	12.3	59.0	31.3
0.42	119.8	109.3	91	43.4	29.1	65.9	45.0
0.50	123.2	119.8	97	55.4	41.7	64.4	44.5

8

9 **3.5. Short digression on other sources of heat during activation**

10 As was briefly outlined in the Experimental Section 2.1, the general heat balance shown in equation (2)
 11 was simplified in the present study. Neglecting the reversible and parasitic heat leads to equation (3).
 12 We now discuss why this simplification was possible and first focus on the parasitic heat. Parasitic heat
 13 refers to all heat sources from processes other than regular intercalation, which can include any side
 14 reactions, such as electrolyte decomposition¹⁷⁻¹⁹ or SEI formation²². These processes can happen
 15 during cycling but also open-circuit conditions, where they might lead to self-discharge. The Dahn
 16 group has published several studies investigating parasitic reactions and the corresponding heat
 17 generation.¹⁷⁻¹⁹ By combining high precision coulometry and IMC, they are able to analyze the parasitic
 18 heat flow in pouch full-cells with nominal capacities over 200 mAh. In our present study, we used coin
 19 cells with a nominal capacity of ≈ 4 mAh and a custom-made coin cell holder for the IMC experiments.
 20 We therefore do not meet the required accuracy and signal-to-noise ratio necessary to reliably
 21 measure small heat flows such as parasitic heat. Nevertheless, we tried to estimate the contribution
 22 of the Li counter-electrode to the observed heat flow profiles of LMR-NCM/Li cells. For this purpose,
 23 we used symmetrical Li/Li coin cells with the same separator and electrolyte as in the half-cells. The
 24 Li/Li cells were cycled inside the IMC with the same current density as used in the regular cells and
 25 time-limited so that the cycling protocol of the LMR-NCM/Li cells was mimicked with regard to current
 26 density and capacity. The heat flow observed from the Li/Li cells thus enables us to estimate the
 27 thermal effect of Li plating and stripping during cycling. However, because the voltage is much lower
 28 than in the actual cells, these experiments cannot elucidate the effect of electrolyte oxidation at high
 29 potentials (e.g. at the end of the charge). The heat balance of the Li/Li cells is as follows:

$$\dot{Q}(\text{Li}/\text{Li}) = \dot{Q}_{\text{irrev,ox}} + \dot{Q}_{\text{rev,ox}} + \dot{Q}_{\text{irrev,red}} + \dot{Q}_{\text{rev,red}} + \dot{Q}_{p,\text{Li}} \quad (4)$$

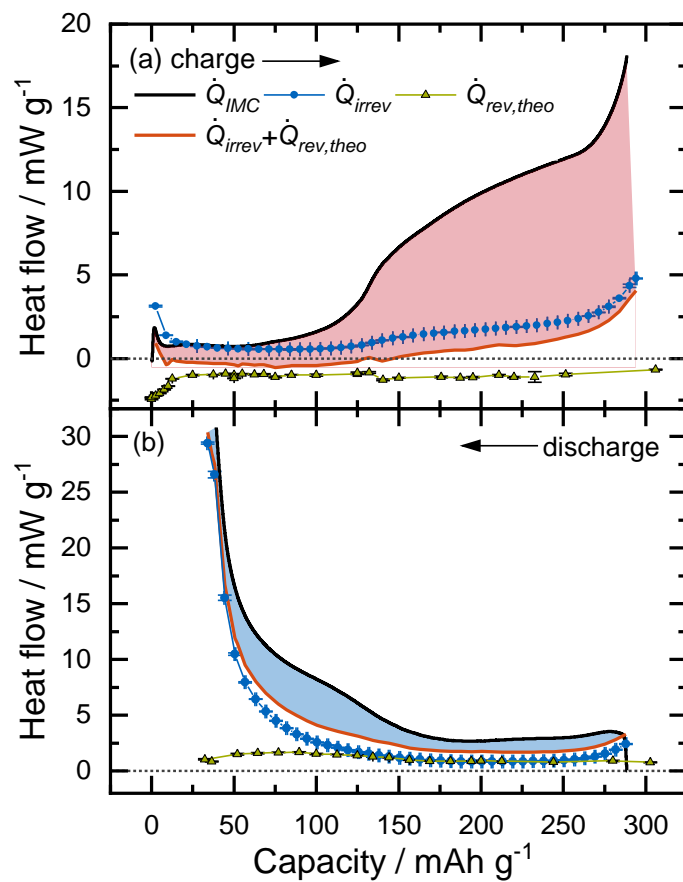
1 The indices “ox” and “red” indicate the oxidation and reduction reaction of Li, which occur
 2 simultaneously in the symmetrical cells. If we assume that the entropy of Li plating and stripping is the
 3 same and that only the sign is opposite, the contribution of \dot{Q}_{rev} is cancelled out in equation (4).
 4 Moreover, the irreversible heat can directly be determined from the potential of the Li/Li cell, which,
 5 under ideal equilibrium conditions, must be equal to zero. Because no reference electrode is used in
 6 this setup, we can monitor only the sum of both \dot{Q}_{irrev} terms. $\dot{Q}_{p,\text{Li}}$ can thus be calculated by
 7 subtracting \dot{Q}_{irrev} from the total heat flow. In order to transfer the calculated parasitic heat to the
 8 LMR-NCM/Li half-cell, the value obtained needs to be halved because only one Li electrode is present
 9 in the actual cell. The resulting values for $\dot{Q}_{p,\text{Li}}$ are between $\approx 5 \mu\text{W}$ and $\approx 10 \mu\text{W}$. They are relatively
 10 constant over most of the SOC range and only increase slightly towards the lower and upper limit,
 11 presumably because of enhanced Li plating and stripping at high and low SOCs. In comparison, the
 12 signal amplitude of the LMR-NCM/Li cells is between $\approx 100 \mu\text{W}$ and $\approx 300 \mu\text{W}$ at SOCs $> 125 \text{ mAh/g}$ and
 13 around $20\text{--}50 \mu\text{W}$ at the beginning of charge. The effect of the parasitic heat from Li on the analysis of
 14 \dot{Q}_{hys} , which is generated starting at $\approx 100 \text{ mAh/g}$, is thus negligible. If \dot{Q}_p is included in the integration
 15 of \dot{Q}_{hys} , a relative error of $\approx 5\%$ is observed for the charge direction and $\approx 7\%$ for the discharge direction.
 16 Because the heat flow profile of $\dot{Q}_{p,\text{Li}}$ is rather constant, it does not affect the analysis of the \dot{Q}_{hys}
 17 generation with regard to onset and curve features. We can conclude that the reported values for \dot{Q}_{hys}
 18 to some extent include the parasitic heat resulting from Li plating and stripping and thus tend to
 19 overestimate the heat resulting from OCV hysteresis and activation. We were also unable to quantify
 20 the contribution of other parasitic reactions such as electrolyte oxidation at high potentials. After the
 21 cells were charged to 4.8 V , the heat signal showed a rather slow decay and did not approach zero
 22 even after 6 h of relaxation at open-circuit conditions. This clearly indicates that parasitic processes
 23 are taking place at high potentials. Further studies are required to analyze these processes and quantify
 24 the corresponding heat terms in order to exactly determine the value of \dot{Q}_{hys} .

25 The second term, which was omitted in equation (2) is the reversible heat. This heat is caused by
 26 changes in entropy of the cathode and anode as a result of the (de-)lithiation during cycling. According
 27 to equation (2), the reversible heat is calculated based on the variation of the OCV with temperature,
 28 $\frac{\partial E_{\text{eq}}}{\partial T}$, the temperature, and the applied current. From potentiometric entropy measurements (see
 29 Experimental Section 2.5), $\frac{\partial E_{\text{eq}}}{\partial T}$ was determined for LMR-NCM/Li cells during the first cycle. The values
 30 of $\frac{\partial E_{\text{eq}}}{\partial T}$ are categorically negative for both charge and discharge direction in the first cycle. With the
 31 applied current in equation (2) being positive for the charge and negative for the discharge direction,
 32 the reversible heat has a negative sign upon charge (endothermic) and a positive sign upon discharge

1 (exothermic). The following discussion is based on this sign convention but the conclusions drawn in
 2 the following might as well be reached by using the opposite signs. The resulting entropy curves are
 3 discussed in our previous publication⁹, and the calculated theoretical reversible heat flow, $\dot{Q}_{rev,theo}$,
 4 is shown as green triangles in Figure 9 together with the heat observed by IMC, \dot{Q}_{IMC} (black) and the
 5 irreversible heat flow determined by intermittent cycling, \dot{Q}_{irrev} (blue circles). Figure 9a shows that
 6 $\dot{Q}_{rev,theo}$ is endothermic for the charge direction and is especially pronounced at the beginning of
 7 charge at SOC < 25 mAh/g. For the first discharge (Figure 9b), the sign of $\dot{Q}_{rev,theo}$ is opposite because
 8 of the changed current direction. Our previous publication on the partial molar entropy in LMR-NCM
 9 investigated the entropy during activation and showed that the entropy curve during the first charge
 10 is unique and deviates significantly from those of following charge half-cycles but also from that of the
 11 consecutive discharge.⁹ The mismatch between the charge and discharge entropy curves observed
 12 provides clear evidence for irreversible processes that happen during the first cycle and lead to a
 13 restructuring of the material. This is in agreement with the aforementioned irreversible structural
 14 rearrangements, which ultimately lead to the generation of \dot{Q}_{hys} . Although based on the entropy data,
 15 the theoretical reversible heat can be calculated, it does actually not reflect the true reversible heat
 16 since the activation is an irreversible process. The calculated $\dot{Q}_{rev,theo}$ value thus includes an unknown
 17 proportion from the irreversible structural rearrangements in LMR-NCM. This is why we clearly
 18 differentiate between the calculated value, $\dot{Q}_{rev,theo}$, and the true reversible heat, \dot{Q}_{rev} , which is not
 19 accessible to us by electrochemical measurements. To assess the importance of the reversible heat for
 20 the investigation of \dot{Q}_{hys} , the following analysis is helpful. The observed total heat flow, \dot{Q}_{IMC} , is first
 21 compared to the sum of the theoretical reversible heat and the irreversible heat, $\dot{Q}_{rev,theo} + \dot{Q}_{irrev}$
 22 (orange line in Figure 9) as suggested by the general energy balance model in equation (2) (but
 23 neglecting the parasitic heat). In a second approach, \dot{Q}_{IMC} is only compared to \dot{Q}_{irrev} as was done in
 24 the present study and equation (3). In the first case, $\dot{Q}_{hys} = \dot{Q}_{IMC} - (\dot{Q}_{rev,theo} + \dot{Q}_{irrev})$. This is
 25 shown as the colored area in Figure 9 (red during charge, blue during discharge). In the second case,
 26 \dot{Q}_{hys} is calculated based on equation (3): $\dot{Q}_{hys} = \dot{Q}_{IMC} - \dot{Q}_{irrev}$. The heat resulting from OCV
 27 hysteresis and activation is shown as colored area in Figure 3. A comparison of both equations and
 28 Figure 3 and Figure 9 makes it clear that with approach (i) the contribution of the reversible heat is
 29 overestimated because it includes unknown contributions from the material restructuring, which is
 30 not necessarily generated as heat, and thus leads to an overestimation of \dot{Q}_{hys} in charge and an
 31 underestimation during discharge. In contrast, the second approach neglects \dot{Q}_{rev} and thus
 32 underestimates \dot{Q}_{hys} during charge and overestimates it during discharge. Here, \dot{Q}_{hys} conclusively
 33 includes an unknown proportion of the true reversible heat. In summary, neither of the two analysis
 34 approaches reflects the exact result of \dot{Q}_{hys} since the true value of \dot{Q}_{rev} is not known.

1 However, by comparing the observed heat \dot{Q}_{IMC} to both calculated expectation values, we can assess
 2 how important the effect of the reversible heat is for the analysis of \dot{Q}_{hys} . For this, it is helpful to focus
 3 on an SOC region in which the generation of \dot{Q}_{hys} is expected to be minimal. Any difference between
 4 \dot{Q}_{IMC} and \dot{Q}_{irrev} is thus predominantly caused by the reversible heat. From the window-opening
 5 experiments presented in Figure 5, we know that in the low SOC region (<100 mAh/g) during charge
 6 no OCV hysteresis is observed and that the contribution of \dot{Q}_{hys} is thus minimal. When applying
 7 calculation approach (i), the expected heat flow is the sum of \dot{Q}_{irrev} and $\dot{Q}_{rev,theo}$, which is depicted
 8 as orange line in Figure 9a. Because of the relatively large endothermic contribution of $\dot{Q}_{rev,theo}$, the
 9 overall expected heat flow is also endothermic below an SOC of ≈ 125 mAh/g. A comparison with the
 10 observed heat (black line) shows a clear mismatch. Thus, based on this analysis, \dot{Q}_{hys} would give a
 11 considerable contribution in this low SOC region (red shaded area in Figure 9a) to compensate for the
 12 endothermic heat flow calculated. However, from the OCV curves in Figure 5, no evidence for an OCV
 13 hysteresis can be found because the LMR-NCM/Li cells cycle reversibly in the SOC window below
 14 125 mAh/g. This, however, also suggests that during the low SOC region, no irreversible processes
 15 occur, which would falsify the determination of the reversible heat based on the entropy data. The
 16 calculation of $\dot{Q}_{rev,theo}$ should thus be reliable in this SOC region. This would, however, result in the
 17 considerable offset between the measured and the expected heat flow shown in Figure 9a, which
 18 cannot be explained by \dot{Q}_{hys} . In contrast, when comparing the observed heat flow in Figure 9a only to
 19 the irreversible heat (blue circles), a reasonably good agreement is found for the low SOC region. This
 20 means that no significant \dot{Q}_{hys} generation is expected below 100 mAh/g with this analysis approach
 21 (see Figure 3c), which agrees with the OCV curves from Figure 5. In conclusion, for the low SOC range
 22 (<100 mAh/g), the contribution of the reversible heat seems to be negligible although no irreversible
 23 processes occur. The reason for this, however, needs to be investigated. According to the entropy
 24 measurements, the low SOC region coincides with the largest $\dot{Q}_{rev,theo}$ values (≈ 2.4 mW/g at the
 25 beginning of charge). For the rest of the charge, $\dot{Q}_{rev,theo}$ is only around ≈ 1 mW/g. Thus, although we
 26 cannot exclude the contribution of the reversible heat completely, we can assume that the relative
 27 error resulting from neglecting the reversible heat is low for two reasons. First, the effect of $\dot{Q}_{rev,theo}$
 28 was found to be negligible in the low SOC region eventhough the highest values of $\dot{Q}_{rev,theo}$ are
 29 observed there. Its effect at higher SOC is thus assumed to be insignificant. Second, at SOC >
 30 125 mAh/g, the relative effect of $\dot{Q}_{rev,theo}$ is small compared with the large \dot{Q}_{hys} generation. If only
 31 the $\dot{Q}_{hys,1,cha}$ generation above 125 mAh/g is considered, the relative error between the two
 32 calculation methods is $\approx 13\%$. For the first discharge, the relative error for the calculation of the
 33 integrated $Q_{hys,1,dis}$ amounts to $\approx 24\%$. Figure 9b shows that the general trend of the $\dot{Q}_{hys,1,dis}$ is not
 34 changed when $\dot{Q}_{rev,theo}$ is considered.

1 In summary, we want to emphasize that the simplifications used in the present study mean that the
 2 reported \dot{Q}_{hys} includes an unknown but small contribution of reversible heat as well as heat from
 3 parasitic side reactions such as Li plating/stripping and electrolyte oxidation. Using the entropy data
 4 and results from a Li/Li IMC measurement, the possible errors for the reversible heat and the parasitic
 5 heat resulting from Li plating and stripping were estimated. We want to underline that the focus of
 6 our study is to semi-quantitatively describe the onset, generation, and integral of \dot{Q}_{hys} during the
 7 activation of LMR-NCM. For a more accurate quantitative analysis, further experiments are required.



8

9 *Figure 9: Heat generation of a 0.33 LMR-NCM/Li cell during activation at C/10 in the (a) charge and (b) discharge direction.*
 10 *The heat flow measured by IMC, \dot{Q}_{IMC} , (solid black lines) is shown together with the irreversible heat flow determined by*
 11 *intermittent cycling, \dot{Q}_{irrev} , (blue circles), the theoretical reversible heat, $\dot{Q}_{rev,theo}$, calculated from entropy measurements*
 12 *(green triangles) and the sum of \dot{Q}_{irrev} and $\dot{Q}_{rev,theo}$ (orange line). The colored areas correspond to the difference between*
 13 *\dot{Q}_{IMC} and the sum of \dot{Q}_{irrev} and $\dot{Q}_{rev,theo}$. The error bars for \dot{Q}_{irrev} are calculated from the measurement of two identical*
 14 *cells. The error of $\dot{Q}_{rev,theo}$ is based on the calculation of the OCV variation with temperature.⁹*

1 **4 Conclusion**

2 The first cycle of LMR-NCM is governed by unique, irreversible processes, which occur during the upper
3 voltage plateau during charging. These irreversible structural rearrangements lead to a pronounced
4 voltage hysteresis in the first cycle. This involves a substantial loss of voltage and capacity in the first
5 discharge and leads to a very low energy efficiency of $\approx 73\%$. In this study, the heat generation of LMR-
6 NCM during the first activation cycle was studied by isothermal micro-calorimetry focusing on the
7 0.33 LMR-NCM material. We found that only $\approx 43\%$ of the electrical work lost during the first cycle is
8 converted into heat. To further analyze this heat evolution, complementary methods were used to
9 calculate the reversible and irreversible heat of LMR-NCM/Li cells. The contributions from reversible
10 heat and parasitic heat from Li plating/stripping are negligible with respect to the relatively large heat
11 generation during the first cycle. They were therefore neglected in the energy balance model. Using
12 an intermittent cycling procedure, the irreversible heat generation resulting from polarization effects
13 was determined. During the first charge, the irreversible heat can explain only 19% of the measured
14 heat signal. The observed mismatch is caused by heat resulting from activation processes and
15 hysteresis, which we termed \dot{Q}_{hys} . The onset of this heat evolution coincides with the beginning of the
16 upper voltage plateau (≈ 100 mAh/g) and is therefore directly related to the irreversible structural
17 rearrangements during activation. Window-opening experiments, in which the upper SOC limit is
18 gradually increased, indicate that when LMR-NCM is not cycled beyond this SOC, there is no evolution
19 of \dot{Q}_{hys} during charge and discharge. This agrees with the absence of an OCV hysteresis in this limited
20 SOC region and also with the absence of a path dependence reported for other parameters such as the
21 cathode resistance⁵, lattice parameters⁸, and entropy⁹. In contrast, when LMR-NCM is charged beyond
22 ≈ 100 mAh/g, a path dependence of all these parameters gradually arises. We show that this is also
23 true for the heat generation. This again underlines the correlation between the reported structural
24 rearrangements during the upper voltage plateau and the heat generation observed. Moreover, the
25 window-opening experiments indicate that the generation of $\dot{Q}_{hys,1.dis}$ in the first discharge is linked
26 to the preceding $\dot{Q}_{hys,1.cha}$ evolution during charge and is thus a direct consequence of the activation
27 processes. We then analyzed the effect of the degree of overlithiation on the heat generation of LMR-
28 NCM. The electrical energy loss during the first cycle and the generation of heat resulting from
29 activation and hysteresis increase with an increasing amount of Li in the TM layer. This is in agreement
30 with the prolonged upper voltage plateau observed and indicates that the activation processes are
31 more pronounced for a higher degree of overlithiation.

32 In summary, we demonstrate by IMC that the heat generation during the first charge of LMR-NCM
33 shows a unique profile. This is dominated by heat resulting from activation processes during the upper
34 voltage plateau. Because of the irreversibility of the first cycle, the electrical energy loss, which is easily
35 accessible from electrochemical data, does not translate into an expected value for the generation of

1 waste heat. IMC is thus an irreplaceable tool for quantifying the heat generation of LMR-NCM. The
2 heat observed is a measure of the enthalpy of the structural rearrangements during activation. Further
3 research effort is required to accurately determine parasitic heat flow (e.g. because of electrolyte
4 decomposition) in order to obtain an exact value for the enthalpy of LMR-NCM activation. A
5 combination of IMC and theoretical calculations may open new doors in the understanding of the
6 structural and/or energetic processes that cause the activation of LMR-NCM during the first charge.

7

8

9 **Acknowledgements**

10 We would like to acknowledge BASF SE for the support within its Scientific Network on
11 Electrochemistry and Batteries. This work was financially supported by the German Federal Ministry
12 of Education and Research (BMBF) within the AQua HysKaDi project (grant no. 03XP0312B). We
13 gratefully thank Alexander Hoefling for sharing his experiences in setting up an IMC.

1 Literature

- 2 1. J. R. Croy, K. G. Gallagher, M. Balasubramanian, Z. Chen, Y. Ren, D. Kim, S.-H. Kang, D. W. Dees, and
3 M. M. Thackeray, *J. Phys. Chem. C*, **117**, 6525–6536 (2013).
- 4 2. J. R. Croy, M. Balasubramanian, K. G. Gallagher, and A. K. Burrell, *Acc. Chem. Res.*, **48**, 2813–2821
5 (2015).
- 6 3. T. Teufl, B. Strehle, P. Müller, H. A. Gasteiger, and M. A. Mendez, *J. Electrochem. Soc.*, **165**, A2718–
7 A2731 (2018).
- 8 4. J. Wandt, A. T. S. Freiberg, A. Ogrodnik, and H. A. Gasteiger, *Mater. Today*, **21**, 825–833 (2018).
- 9 5. T. Teufl, D. Pritzl, S. Solchenbach, H. A. Gasteiger, and M. A. Mendez, *J. Electrochem. Soc.*, **166**,
10 A1275–A1284 (2019).
- 11 6. L. Kraft, T. Zünd, D. Schreiner, R. Wilhelm, F. Günter, G. Reinhart, H. A. Gasteiger, and A. Jossen, *J.*
12 *Electrochem. Soc.*, **168**, 020537–020547 (2021).
- 13 7. K. G. Gallagher, J. R. Croy, M. Balasubramanian, M. Bettge, D. P. Abraham, A. K. Burrell, and M. M.
14 Thackeray, *Electrochem. commun.*, **33**, 96–98 (2013).
- 15 8. B. Strehle, T. Zünd, S. Siculo, A. Kiessling, V. Baran, and H. A. Gasteiger, *J. Electrochem. Soc.*, **169**,
16 020554 (2022).
- 17 9. F. Friedrich, S. Pieper, and H. A. Gasteiger, *J. Electrochem. Soc.*, **168**, 120502 (2021).
- 18 10. W. E. Gent, K. Lim, Y. Liang, Q. Li, T. Barnes, S. Ahn, K. H. Stone, M. McIntire, J. Hong, J. H. Song, Y.
19 Li, A. Mehta, S. Ermon, T. Tyliczszak, D. Kilcoyne, D. Vine, J. Park, S. Doo, M. F. Toney, et al., *Nat.*
20 *Commun.*, **8**, 2091–2102 (2017).
- 21 11. R. A. House, U. Maitra, M. A. Pérez-Osorio, J. G. Lozano, L. Jin, J. W. Somerville, L. C. Duda, A. Nag,
22 A. Walters, K.-J. Zhou, M. R. Roberts, and P. G. Bruce, *Nature*, **577**, 502–508 (2020).
- 23 12. B. Strehle, K. Kleiner, R. Jung, F. Chesneau, M. Mendez, H. A. Gasteiger, and M. Piana, *J.*
24 *Electrochem. Soc.*, **164**, A400–A406 (2017).
- 25 13. R. A. House, G. J. Rees, M. A. Pérez-Osorio, J.-J. Marie, E. Boivin, A. W. Robertson, A. Nag, M.
26 Garcia-Fernandez, K.-J. Zhou, and P. G. Bruce, *Nat. Energy*, **5**, 777 (2020).
- 27 14. G. Assat, D. Foix, C. Delacourt, A. Iadecola, R. Dedryvère, and J.-M. Tarascon, *Nat. Commun.*, **8**,
28 2219–2230 (2017).
- 29 15. F. Dogan, B. R. Long, J. R. Croy, K. G. Gallagher, H. Iddir, J. T. Russell, M. Balasubramanian, and B.
30 Key, *J. Am. Chem. Soc.*, **137**, 2328–2335 (2015).
- 31 16. A. Singer, M. Zhang, S. Hy, D. Cela, C. Fang, T. A. Wynn, B. Qiu, Y. Xia, Z. Liu, A. Ulvestad, N. Hua, J.
32 Wingert, H. Liu, M. Sprung, A. V. Zozulya, E. Maxey, R. Harder, Y. S. Meng, and O. G. Shpyrko, *Nat.*
33 *Energy*, **3**, 641–647 (2018).
- 34 17. L. J. Krause, L. D. Jensen, and J. R. Dahn, *J. Electrochem. Soc.*, **159**, A937–A943 (2012).
- 35 18. L. E. Downie, S. R. Hyatt, A. T. B. Wright, and J. R. Dahn, *J. Phys. Chem. C*, **118**, 29533–29541
36 (2014).
- 37 19. S. L. Glazier, S. A. Odom, A. P. Kaur, and J. R. Dahn, *J. Electrochem. Soc.*, **165**, A3449 (2018).
- 38 20. F. Friedrich, T. Zünd, A. Hoefling, J. Tübke, and H. A. Gasteiger, *Submitted to J. Electrochem. Soc.*
- 39 21. G. Assat, S. L. Glazier, C. Delacourt, and J.-M. Tarascon, *Nat. Energy*, **4**, 647–656 (2019).
- 40 22. L. M. Housel, W. Li, C. D. Quilty, M. N. Vila, L. Wang, C. R. Tang, D. C. Bock, Q. Wu, X. Tong, A. R.
41 Head, K. J. Takeuchi, A. C. Marschilok, and E. S. Takeuchi, *ACS Appl. Mater. Interfaces*, **11**, 37567–
42 37577 (2019).
- 43 23. A. Kunz, C. Berg, F. Friedrich, H. A. Gasteiger, and A. Jossen, *Manuscript in Preparation*.

- 1 24. L. de Biasi, B. Schwarz, T. Brezesinski, P. Hartmann, J. Janek, and H. Ehrenberg, *Adv. Mater.*, **31**
2 (2019).
- 3 25. A. T. S. Freiberg, J. Sicklinger, S. Solchenbach, and H. A. Gasteiger, *Electrochim. Acta*, **346**, 136271
4 (2020).
- 5 26. P. J. Linstrom and W. G. Mallard, *NIST Chemistry WebBook, NIST Standard Reference Database*
6 *Number 69*, National Institute of Standards and Technology, Gaithersburg MD, (2020).
- 7 27. L. Wang, T. Maxisch, and G. Ceder, *Chem. Mater.*, **19**, 543–552 (2007).
- 8 28. I. Belharouak, W. Lu, D. Vissers, and K. Amine, *Electrochem. commun.*, **8**, 329–335 (2006).
- 9 29. M. Sano and H. Taube, *Inorg.Chem.*, **33**, 705–709 (1994).
- 10 30. E. Neumann, *Angew. Chem. Int. Ed. Engl.*, **12**, 356–369 (1973).
- 11 31. G. Assat and J. Tarascon, *Nat. Energy*, **3**, 373 (2018).
- 12 32. B. Qiu, M. Zhang, S.-Y. Lee, H. Liu, T. A. Wynn, L. Wu, Y. Zhu, W. Wen, C. M. Brown, D. Zhou, Z. Liu,
13 and Y. S. Meng, *Cell Reports Phys. Sci.*, **1**, 100028 (2020).
- 14

References

1. Umweltbundesamt. Nationale Trendtabellen für die deutsche Berichterstattung atmosphärischer Emissionen 1990-2018. <https://www.umweltbundesamt.de/daten/energie/energiebedingte-emissionen#energiebedingte-treibhausgas-emissionen>; accessed March 18, 2022.
2. Hornberg, C., Niekisch, M., Calliess, C., Kemfert, C., Lucht, W., Messari-Becker, L. & Rotter, V. S. Umsteuern erforderlich: Klimaschutz im Verkehrssektor - Sondergutachten. https://www.umweltrat.de/SharedDocs/Downloads/DE/02_Sondergutachten/2016_2020/2017_11_SG_Klimaschutz_im_Verkehrssektor.pdf?__blob=publicationFile&v=25; accessed March 18, 2022.
3. Kobiela, D. G., Samadi, D. S., Kurwan, J., Tönjes, A., Fishedick, M., Koska, T., Lechtenböhmer, S., März, S. & Schüwer, D. CO₂-neutral bis 2035: Eckpunkte eines deutschen Beitrags zur Einhaltung der 1.5°C-Grenze. https://epub.wupperinst.org/frontdoor/deliver/index/docId/7606/file/7606_CO2-neutral_2035.pdf; accessed March 18, 2022.
4. Bundesministerium für Verkehr und digitale Infrastruktur. Verkehr in Zahlen 2020/2021. https://www.bmvi.de/SharedDocs/DE/Publikationen/G/verkehr-in-zahlen-2020-pdf.pdf?__blob=publicationFile; accessed March 18, 2022.
5. Ding, Y., Cano, Z. P., Yu, A., Lu, J. & Chen, Z. Automotive Li-Ion Batteries: Current Status and Future Perspectives. *Electrochem. Energy Rev.* **2**, 1–28 (2019).
6. Andre, D., Kim, S. J., Lamp, P., Lux, S. F., Maglia, F., Paschos, O. & Stiaszny, B. Future generations of cathode materials: An automotive industry perspective. *J. Mater. Chem. A* **3**, 6709–6732 (2015).
7. Whittingham, M. S. Electrical Energy Storage and Intercalation Chemistry. *Science*. **192**, 1126-1127 (1976).
8. Mizushima, K., Jones, P. C., Wiseman, P. J. & Goodenough, J. B. Li_xCoO₂ (0<x<1): A new cathode material for batteries of high energy density. *Mater. Res. Bull.* **15**, 783–789 (1980).
9. Blomgren, G. E. The Development and Future of Lithium Ion Batteries. *J. Electrochem. Soc.* **164**, A5019–A5025 (2017).
10. Nishi, Y. Lithium ion secondary batteries; past 10 years and the future. *J. Power Sources* **100**, 101–106 (2001).
11. The Royal Swedish Academy of Science. The Nobel Prize in Chemistry 2019 - Press Release. <https://www.nobelprize.org/prizes/chemistry/2019/press-release/>; accessed March 18, 2022.

12. Schmuch, R., Wagner, R., Hörpel, G., Placke, T. & Winter, M. Performance and cost of materials for lithium-based rechargeable automotive batteries. *Nat. Energy* **3**, 267–278 (2018).
13. Li, W., Erickson, E. M. & Manthiram, A. High-nickel layered oxide cathodes for lithium-based automotive batteries. *Nat. Energy* **5**, 26–34 (2020).
14. US Council for Automotive Research. US DRIVE Electrochemical Energy Storage Technical Team Roadmap. https://www.energy.gov/sites/prod/files/2017/11/f39/EESTT_roadmap_2017-10-16_Final.pdf; accessed March 18, 2022.
15. Kwade, A., Haselrieder, W., Leithoff, R., Modlinger, A., Dietrich, F. & Droeder, K. Current status and challenges for automotive battery production technologies. *Nat. Energy* **3**, 290–300 (2018).
16. Pillot, C. The Rechargeable Battery Market and Main Trends 2012-2025. https://rechargebatteries.org/wp-content/uploads/2019/02/Keynote_2_AVICENNE_Christophe-Pillot.pdf; accessed March 18, 2022.
17. SMM Information & Technology Co Ltd. Nickel Sulfate (Battery Grade). <https://www.metal.com/Nickel/201908270001> accessed March 18, 2022.
18. SMM Information & Technology Co Ltd. Manganese Sulfate (Battery Level). <https://www.metal.com/Manganese/201805300001>; accessed March 18, 2022.
19. Croy, J. R., Gallagher, K. G., Balasubramanian, M., Long, B. R. & Thackeray, M. M. Quantifying Hysteresis and Voltage Fade in $x\text{Li}_2\text{MnO}_3 \cdot (1-x)\text{LiMn}_{0.5}\text{Ni}_{0.5}\text{O}_2$ Electrodes as a Function of Li_2MnO_3 Content. *J. Electrochem. Soc.* **161**, A318–A325 (2014).
20. Chen, W. C., Song, Y. F., Wang, C. C., Liu, Y., Morris, D. T., Pianetta, P. A., Andrews, J. C., Wu, H. C. & Wu, N. L. Study on the synthesis-microstructure-performance relationship of layered Li-excess nickel-manganese oxide as a Li-ion battery cathode prepared by high-temperature calcination. *J. Mater. Chem. A* **1**, 10847–10856 (2013).
21. Zheng, J., Myeong, S., Cho, W., Yan, P., Xiao, J., Wang, C., Cho, J. & Zhang, J. G. Li- and Mn-Rich Cathode Materials: Challenges to Commercialization. *Adv. Energy Mater.* **7**, 1601284–1601308 (2017).
22. Hausbrand, R., Cherkashinin, G., Ehrenberg, H., Gröting, M., Albe, K., Hess, C. & Jaegermann, W. Fundamental degradation mechanisms of layered oxide Li-ion battery cathode materials: Methodology, insights and novel approaches. *Mater. Sci. Eng. B* **192**, 3–25 (2015).
23. Dahn, J. R. Phase diagram of Li_xC_6 . *Phys. Rev. B* **44**, 9170–9177 (1991).
24. Lin, D., Liu, Y. & Cui, Y. Reviving the lithium metal anode for high-energy batteries. *Nat. Nanotechnol.* **12**, 194–206 (2017).
25. Peled, E. The Electrochemical Behavior of Alkali and Alkaline Earth Metals in Nonaqueous Battery Systems—The Solid Electrolyte Interphase Model. *J. Electrochem. Soc.* **126**, 2047–2051 (1979).

26. Peled, E., Golodnitsky, D. & Ardel, G. Advanced Model for Solid Electrolyte Interphase Electrodes in Liquid and Polymer Electrolytes. *J. Electrochem. Soc.* **144**, L208–L210 (1997).
27. Aurbach, D., Daroux, M. L., Faguy, P. W. & Yeager, E. Identification of Surface Films Formed on Lithium in Propylene Carbonate Solutions. *J. Electrochem. Soc.* **134**, 1611–1620 (1987).
28. Daniel, C. & Besenhard, J. O. *Handbook of Battery Materials*. pp.433 ff. (2011).
29. Joshi, T., Eom, K., Yushin, G. & Fuller, T. F. Effects of Dissolved Transition Metals on the Electrochemical Performance and SEI Growth in Lithium-Ion Batteries. *J. Electrochem. Soc.* **161**, A1915–A1921 (2014).
30. Vetter, J., Novák, P., Wagner, M. R., Veit, C., Möller, K. C., Besenhard, J. O., Winter, M., Wohlfahrt-Mehrens, M., Vogler, C. & Hammouche, A. Ageing mechanisms in lithium-ion batteries. *J. Power Sources* **147**, 269–281 (2005).
31. Ferg, E., Gummow, R. J., de Kock, A. & Thackeray, M. M. Spinel Anodes for Lithium-Ion Batteries. *J. Electrochem. Soc.* **141**, L147–L150 (1994).
32. Zhao, B., Ran, R., Liu, M. & Shao, Z. A comprehensive review of $\text{Li}_4\text{Ti}_5\text{O}_{12}$ -based electrodes for lithium-ion batteries: The latest advancements and future perspectives. *Mater. Sci. Eng. R Reports* **98**, 1–71 (2015).
33. He, Y. B., Li, B., Liu, M., Zhang, C., Lv, W., Yang, C., Li, J., Du, H., Zhang, B., Yang, Q. H., Kim, J. K. & Kang, F. Gassing in $\text{Li}_4\text{Ti}_5\text{O}_{12}$ -based batteries and its remedy. *Sci. Rep.* **2**, 33–35 (2012).
34. Chevrier, V. L., Liu, L., Le, D. B., Lund, J., Molla, B., Reimer, K., Krause, L. J., Jensen, L. D., Figgemeier, E. & Eberman, K. W. Evaluating Si-Based Materials for Li-Ion Batteries in Commercially Relevant Negative Electrodes. *J. Electrochem. Soc.* **161**, A783–A791 (2014).
35. Nitta, N., Wu, F., Lee, J. T. & Yushin, G. Li-ion battery materials: Present and future. *Mater. Today* **18**, 252–264 (2015).
36. McDowell, M. T., Lee, S. W., Nix, W. D. & Cui, Y. 25th anniversary article: Understanding the lithiation of silicon and other alloying anodes for lithium-ion batteries. *Adv. Mater.* **25**, 4966–4985 (2013).
37. Besenhard, J. O., Yang, J. & Winter, M. Will advanced lithium-alloy anodes have a chance in lithium-ion batteries? *J. Power Sources* **68**, 87–90 (1997).
38. Zhang, W. J. A review of the electrochemical performance of alloy anodes for lithium-ion batteries. *J. Power Sources* **196**, 13–24 (2011).
39. Brandt, K. Historical development of secondary lithium batteries. *Solid State Ionics* **69**, 173–183 (1994).
40. Zhang, X. & Devine, T. M. Factors That Influence Formation of AlF_3 Passive Film on Aluminum in Li-Ion Battery Electrolytes with LiPF_6 . *J. Electrochem. Soc.* **153**, B375–B383 (2006).
41. Yang, H., Zhuang, G. V. & Ross, P. N. Thermal stability of LiPF_6 salt and Li-ion battery electrolytes containing LiPF_6 . *J. Power Sources* **161**, 573–579 (2006).
42. Xu, K. Nonaqueous liquid electrolytes for lithium-based rechargeable

- batteries. *Chem. Rev.* **104**, 4303–4417 (2004).
43. Strmcnik, D., Castelli, I. E., Connell, J. G., Haering, D., Zorko, M., Martins, P., Lopes, P. P., Genorio, B., Østergaard, T., Gasteiger, H. A., Maglia, F., Antonopoulos, B. K., Stamenkovic, V. R., Rossmeisl, J. & Markovic, N. M. Electrocatalytic transformation of HF impurity to H₂ and LiF in lithium-ion batteries. *Nat. Catal.* **1**, 255–262 (2018).
 44. Zhang, S. S. A review on electrolyte additives for lithium-ion batteries. *J. Power Sources* **162**, 1379–1394 (2006).
 45. Imhof, R. & Novák, P. In Situ Investigation of the Electrochemical Reduction of Carbonate Electrolyte Solutions at Graphite Electrodes. *J. Electrochem. Soc.* **145**, 1081–1087 (1998).
 46. Erickson, E. M., Schipper, F., Penki, T. R., Shin, J.-Y., Erk, C., Chesneau, F.-F., Markovsky, B. & Aurbach, D. Review—Recent Advances and Remaining Challenges for Lithium Ion Battery Cathodes. *J. Electrochem. Soc.* **164**, A6341–A6348 (2017).
 47. SMM Information & Technology Co Ltd. Cobalt Sulfate. <https://www.metal.com/Chemical-Compound/201102250381>; accessed March 18, 2022.
 48. SMM Information & Technology Co Ltd. Iron Phosphate. <https://www.metal.com/Ternary-precursor-material/202111010002>; accessed March 18, 2022.
 49. US Geological Survey. Mineral Commodity Summaries 2022. <https://pubs.usgs.gov/periodicals/mcs2022/mcs2022.pdf>; accessed March 18, 2022.
 50. Roland Berger. The Lithium Ion (EV) battery market and supply chain - Part 1: Market drivers and emerging supply chain risks. <https://mobex.io/webinars/the-lithium-ion-ev-battery-market-part-one-market-drivers-and-emerging-supply-chain-risks/>; accessed March 18, 2022.
 51. SMM Information & Technology Co Ltd. Lithium Carbonate (99.5% Battery Grade). <https://www.metal.com/Chemical-Compound/2011022500592>; accessed March 18, 2022 .
 52. Manthiram, A. A reflection on lithium-ion battery cathode chemistry. *Nat. Commun.* **11**, 1550–1558 (2020).
 53. Jung, R., Metzger, M., Maglia, F., Stinner, C. & Gasteiger, A. H. Oxygen Release and its Effect on the Cycling Stability of LiNi_xMn_yCo_zO₂ (NMC) Cathode Materials for Li-Ion Batteries. *J. Electrochem. Soc.* **164**, A1361–A1377 (2017).
 54. Li, H., Cormier, M., Zhang, N., Inglis, J., Li, J. & Dahn, J. R. Is Cobalt Needed in Ni-Rich Positive Electrode Materials for Lithium Ion Batteries? *J. Electrochem. Soc.* **166**, A429–A439 (2019).
 55. Belharouak, I., Sun, Y. K., Liu, J. & Amine, K. Li(Ni_{1/3}Co_{1/3}Mn_{1/3})O₂ as a suitable cathode for high power applications. *J. Power Sources* **123**, 247–252 (2003).
 56. Nelson, A. P., Gallagher, K. G., Bloom, I. & Dees, D. W. Modeling the

- Performance and Cost of Lithium-Ion Batteries for Electric-Drive Vehicles. *Argonne National Laboratory* <https://publications.anl.gov/anlpubs/2015/05/75574.pdf>; accessed March 18, 2022. **(2012)**
57. Thackeray, M. M., David, W. I. F., Bruce, P. G. & Goodenough, J. B. Lithium insertion into Manganese spinels. *Mater. Res. Bull.* **18**, 461–472 **(1983)**.
 58. Thackeray, M. M. Manganese oxides for lithium batteries. *Prog. Solid State Chem.* **25**, 1–71 **(1997)**.
 59. Pritzl, D., Solchenbach, S., Wetjen, M. & Gasteiger, H. A. Analysis of Vinylene Carbonate (VC) as Additive in Graphite/LiNi_{0.5}Mn_{1.5}O₄ Cells. *J. Electrochem. Soc.* **164**, A2625–A2635 **(2017)**.
 60. Solchenbach, S., Hong, G., Freiberg, A. T. S., Jung, R. & Gasteiger, H. A. Electrolyte and SEI Decomposition Reactions of Transition Metal Ions Investigated by On-Line Electrochemical Mass Spectrometry. **165**, 3304–3312 **(2018)**.
 61. Ellingsen, L. A. W., Hung, C. R., Majeau-Bettez, G., Singh, B., Chen, Z., Whittingham, M. S. & Strømman, A. H. Nanotechnology for environmentally sustainable electromobility. *Nat. Nanotechnol.* **11**, 1039–1051 **(2016)**.
 62. Noh, H. J., Youn, S., Yoon, C. S. & Sun, Y. K. Comparison of the structural and electrochemical properties of layered Li[Ni_xCo_yMn_z]O₂ (x = 1/3, 0.5, 0.6, 0.7, 0.8 and 0.85) cathode material for lithium-ion batteries. *J. Power Sources* **233**, 121–130 **(2013)**.
 63. Whittingham, M. S. Lithium batteries and cathode materials. *Chem. Rev.* **104**, 4271–4301 **(2004)**.
 64. Lima, P. Comparison of different EV batteries in 2020 (update). <https://pushevs.com/2020/04/04/comparison-of-different-ev-batteries-in-2020/>; accessed March 18, 2022.
 65. Bruch, W. The efficient drivetrain for the purely electric BMW iX3. <https://www.press.bmwgroup.com/global/article/detail/T0303834EN/the-efficient-drivetrain-for-the-purely-electric-bmw-ix3>; accessed March 18, 2022.
 66. Manthiram, A., Knight, J. C., Myung, S. T., Oh, S. M. & Sun, Y. K. Nickel-Rich and Lithium-Rich Layered Oxide Cathodes: Progress and Perspectives. *Adv. Energy Mater.* **6**, 1501010–1501032 **(2016)**.
 67. Sicklinger, J., Metzger, M., Beyer, H., Pritzl, D. & Gasteiger, H. A. Ambient Storage Derived Surface Contamination of NCM811 and NCM111: Performance Implications and Mitigation Strategies. *J. Electrochem. Soc.* **166**, A2322–A2335 **(2019)**.
 68. Jung, R., Morasch, R., Karayaylali, P., Phillips, K., Maglia, F., Stinner, C., Shao-Horn, Y. & Gasteiger, H. A. Effect of Ambient Storage on the Degradation of Ni-rich Positive Electrode Materials for Li-Ion Batteries. *J. Electrochem. Soc.* **165**, A132–A141 **(2018)**.
 69. Jung, R., Strobl, P., Maglia, F., Stinner, C. & Gasteiger, H. A. Temperature Dependence of Oxygen Release from LiNi_{0.6}Mn_{0.2}Co_{0.2}O₂ (NMC622) Cathode

- Materials for Li-Ion Batteries. *J. Electrochem. Soc.* **165**, A2869–A2879 (2018).
70. Abraham, D. P., Twesten, R. D., Balasubramanian, M., Kropf, J., Fischer, D., McBreen, J., Petrov, I. & Amine, K. Microscopy and Spectroscopy of Lithium Nickel Oxide-Based Particles Used in High Power Lithium-Ion Cells. *J. Electrochem. Soc.* **150**, A1450–A1456 (2003).
 71. Watanabe, S., Kinoshita, M., Hosokawa, T., Morigaki, K. & Nakura, K. Capacity fade of $\text{LiAl}_y\text{Ni}_{1-x-y}\text{Co}_x\text{O}_2$ cathode for lithium-ion batteries during accelerated calendar and cycle life tests (surface analysis of $\text{LiAl}_y\text{Ni}_{1-x-y}\text{Co}_x\text{O}_2$ cathode after cycle tests in restricted depth of discharge ranges). *J. Power Sources* **258**, 210–217 (2014).
 72. Wandt, J., Freiberg, A. T. S., Ogrodnik, A. & Gasteiger, H. A. Singlet oxygen evolution from layered transition metal oxide cathode materials and its implications for lithium-ion batteries. *Mater. Today* **21**, 825–833 (2018).
 73. Freiberg, A. T. S., Roos, M. K., Wandt, J., De Vivie-Riedle, R. & Gasteiger, H. A. Singlet Oxygen Reactivity with Carbonate Solvents Used for Li-Ion Battery Electrolytes. *J. Phys. Chem. A* **122**, 8828–8839 (2018).
 74. Buchberger, I., Seidlmayer, S., Pokharel, A., Piana, M., Hattendorff, J., Kudejova, P., Gilles, R. & Gasteiger, H. A. Aging Analysis of Graphite/ $\text{LiNi}_{1/3}\text{Mn}_{1/3}\text{Co}_{1/3}\text{O}_2$ Cells Using XRD, PGAA, and AC Impedance. *J. Electrochem. Soc.* **162**, A2737–A2746 (2015).
 75. Wandt, J., Freiberg, A., Thomas, R., Gorlin, Y., Siebel, A., Jung, R., Gasteiger, H. A. & Tromp, M. Transition metal dissolution and deposition in Li-ion batteries investigated by operando X-ray absorption spectroscopy. *J. Mater. Chem. A* **4**, 18300–18305 (2016).
 76. Zheng, H., Sun, Q., Liu, G., Song, X. & Battaglia, V. S. Correlation between dissolution behavior and electrochemical cycling performance for $\text{LiNi}_{1/3}\text{Co}_{1/3}\text{Mn}_{1/3}\text{O}_2$ -based cells. *J. Power Sources* **207**, 134–140 (2012).
 77. Jung, R., Metzger, M., Maglia, F., Stinner, C. & Gasteiger, H. A. Chemical versus Electrochemical Electrolyte Oxidation on NMC111, NMC622, NMC811, LNMO, and Conductive Carbon. *J. Phys. Chem. Lett.* **8**, 4820–4825 (2017).
 78. Burns, J. C., Kassam, A., Sinha, N. N., Downie, L. E., Solnickova, L., Way, B. M. & Dahn, J. R. Predicting and Extending the Lifetime of Li-Ion Batteries. *J. Electrochem. Soc.* **160**, A1451–A1456 (2013).
 79. de Biasi, L., Kondrakov, A. O., Geßwein, H., Brezesinski, T., Hartmann, P. & Janek, J. Between Scylla and Charybdis – Balancing Among Structural Stability and Energy Density of Layered NCM Cathode Materials for Advanced Lithium-Ion Batteries. *J. Phys. Chem. C* **121**, 26163–26171 (2017).
 80. Li, H., Liu, A., Zhang, N., Wang, Y., Yin, S., Wu, H. & Dahn, J. R. An Unavoidable Challenge for Ni-Rich Positive Electrode Materials for Lithium-Ion Batteries. *Chem. Mater.* **31**, 7574–7583 (2019).
 81. Kondrakov, A. O., Schmidt, A., Xu, J., Geßwein, H., Mönig, R., Hartmann, P., Sommer, H., Brezesinski, T. & Janek, J. On the Anisotropic Lattice Strain and Mechanical Degradation of High- and Low-Nickel NCM Cathode Materials for Li-Ion Batteries. *J. Phys. Chem. C* **121**, 3286–3294 (2017).

-
82. Park, K. J., Hwang, J. Y., Ryu, H. H., Maglia, F., Kim, S. J., Lamp, P., Yoon, C. S. & Sun, Y. K. Degradation Mechanism of Ni-Enriched NCA Cathode for Lithium Batteries: Are Microcracks Really Critical? *ACS Energy Lett.* **4**, 1394–1400 (2019).
 83. Liu, H., Wolf, M., Karki, K., Yu, Y., Stach, E. A., Cabana, J., Chapman, K. W. & Chupas, P. J. Intergranular Cracking as a Major Cause of Long-Term Capacity Fading of Layered Cathodes. *Nano Lett.* **17**, 3452–3457 (2017).
 84. Schweidler, S., De Biasi, L., Garcia, G., Mazilkin, A., Hartmann, P., Brezesinski, T. & Janek, J. Investigation into Mechanical Degradation and Fatigue of High-Ni NCM Cathode Material: A Long-Term Cycling Study of Full Cells. *ACS Appl. Energy Mater.* **2**, 7375–7384 (2019).
 85. Oswald, S., Pritzl, D., Wetjen, M. & Gasteiger, H. A. Novel Method for Monitoring the Electrochemical Capacitance by In Situ Impedance Spectroscopy as Indicator for Particle Cracking of Nickel-Rich NCMs: Part I. Theory and Validation. *J. Electrochem. Soc.* **167**, 100511–100526 (2020).
 86. Makimura, Y., Sasaki, T., Nonaka, T., Nishimura, Y. F., Uyama, T., Okuda, C., Itou, Y. & Takeuchi, Y. Factors affecting cycling life of NCA for LIBs. *J. Mater. Chem. A* **4**, 8350–8358 (2016).
 87. Liu, W., Oh, P., Liu, X., Lee, M. J., Cho, W., Chae, S., Kim, Y. & Cho, J. Nickel-Rich Layered Lithium Transition-Metal Oxide for High-Energy Lithium-Ion Batteries. *Angew. Chemie - Int. Ed.* **54**, 4440–4457 (2015).
 88. Sharabi, R., Markevich, E., Borgel, V., Salitra, G., Aurbach, D., Semrau, G., Schmidt, M. A., Schall, N. & Stinner, C. Significantly improved cycling performance of LiCoPO₄ cathodes. *Electrochem. commun.* **13**, 800–802 (2011).
 89. Yim, T., Ha, H. J., Park, M. S., Kim, K. J., Yu, J. S. & Kim, Y. J. A facile method for construction of a functionalized multi-layered separator to enhance cycle performance of lithium manganese oxide. *RSC Adv.* **3**, 25657–25661 (2013).
 90. Thackeray, M. M., Kang, S. H., Johnson, C. S., Vaughey, J. T., Benedek, R. & Hackney, S. A. Li₂MnO₃-stabilized LiMO₂ (M = Mn, Ni, Co) electrodes for lithium-ion batteries. *J. Mater. Chem.* **17**, 3112–3125 (2007).
 91. Croy, J. R., Balasubramanian, M., Gallagher, K. G. & Burrell, A. K. Review of the U.S. Department of Energy's 'deep Dive' Effort to Understand Voltage Fade in Li- and Mn-Rich Cathodes. *Acc. Chem. Res.* **48**, 2813–2821 (2015).
 92. Hong, J., Gwon, H., Jung, S.-K., Ku, K. & Kang, K. Review—Lithium-Excess Layered Cathodes for Lithium Rechargeable Batteries. *J. Electrochem. Soc.* **162**, A2447–A2467 (2015).
 93. Teufl, T., Strehle, B., Müller, P., Gasteiger, H. A. & Mendez, M. A. Oxygen release and surface degradation of Li- and Mn-Rich Layered Oxides in variation of the Li₂MnO₃ content. *J. Electrochem. Soc.* **165**, A2718–A2731 (2018).
 94. Strehle, B., Kleiner, K., Jung, R., Chesneau, F., Mendez, M., Gasteiger, H. A. & Piana, M. The Role of Oxygen Release from Li- and Mn-Rich Layered Oxides during the First Cycles Investigated by On-Line Electrochemical Mass Spectrometry. *J. Electrochem. Soc.* **164**, A400–A406 (2017).

95. Luo, K., Roberts, M. R., Hao, R., Guerrini, N., Pickup, D. M., Liu, Y. S., Edström, K., Guo, J., Chadwick, A. V., Duda, L. C. & Bruce, P. G. Charge-compensation in 3d-transition-metal-oxide intercalation cathodes through the generation of localized electron holes on oxygen. *Nat. Chem.* **8**, 684–691 (2016).
96. Schreiner, D., Zünd, T., Günter, F. J., Kraft, L., Stumper, B., Linsenmann, F., Schüßler, M., Wilhelm, R., Jossen, A., Reinhart, G. & Gasteiger, H. A. Comparative Evaluation of LMR-NCM and NCA Cathode Active Materials in Multilayer Lithium-Ion Pouch Cells: Part I. Production, Electrode Characterization, and Formation. *J. Electrochem. Soc.* **168**, 030507–03528 (2021).
97. Croy, J. R., Gallagher, K. G., Balasubramanian, M., Chen, Z., Ren, Y., Kim, D., Kang, S.-H., Dees, D. W. & Thackeray, M. M. Examining Hysteresis in Composite $x\text{Li}_2\text{MnO}_3 \cdot (1-x)\text{LiMO}_2$ Cathode Structures. *J. Phys. Chem. C* **117**, 6525–6536 (2013).
98. Rozier, P. & Tarascon, J. M. Review—Li-Rich Layered Oxide Cathodes for Next-Generation Li-Ion Batteries: Chances and Challenges. *J. Electrochem. Soc.* **162**, A2490–A2499 (2015).
99. Kraft, L., Zünd, T., Schreiner, D., Wilhelm, R., Günter, F., Reinhart, G., Gasteiger, H. A. & Jossen, A. Comparative Evaluation of LMR-NCM and NCA Cathode Materials in Multilayer Lithium-Ion Pouch Cells - Part II: Rate Capability, Long-Term Stability and Thermal Behavior. *J. Electrochem. Soc.* **168**, 020537–020547 (2021).
100. Strehle, B., Zünd, T., Sicolo, S., Kiessling, A., Baran, V. & Gasteiger, H. A. Correlating the Voltage Hysteresis in Li- and Mn-Rich Layered Oxides to Reversible Structural Changes by Using X-ray and Neutron Powder Diffraction. *J. Electrochem. Soc.* **169**, 020554 (2022).
101. Teufl, T., Pritzl, D., Solchenbach, S., Gasteiger, H. A. & Mendez, M. A. SOC dependent Resistance Builds-up in Li- and Mn-rich layered oxides during Li extraction and insertion. *J. Electrochem. Soc.* **166**, A1275–A1284 (2019).
102. Dogan, F., Long, B. R., Croy, J. R., Gallagher, K. G., Iddir, H., Russell, J. T., Balasubramanian, M. & Key, B. Re-entrant lithium local environments and defect driven electrochemistry of Li- and Mn-Rich Li-Ion battery cathodes. *J. Am. Chem. Soc.* **137**, 2328–2335 (2015).
103. Koga, H., Croguennec, L., Ménétrier, M., Mannessiez, P., Weill, F., Delmas, C. & Belin, S. Operando X-ray Absorption Study of the Redox Processes Involved Li Ion Batteries. *J. Phys. Chem. C.* **118**, 5700–5709 (2014).
104. Konishi, H., Hirano, T., Takamatsu, D., Gunji, A., Feng, X., Furutsuki, S., Okumura, T., Terada, S. & Tamura, K. Electrochemical reaction mechanisms under various charge-discharge operating conditions for $\text{Li}_{1.2}\text{Ni}_{0.13}\text{Mn}_{0.54}\text{Co}_{0.13}\text{O}_2$ in a lithium-ion battery. *J. Solid State Chem.* **262**, 294–300 (2018).
105. Assat, G., Foix, D., Delacourt, C., Iadecola, A., Dedryvère, R. & Tarascon, J.-M. Fundamental interplay between anionic/cationic redox governing the kinetics and thermodynamics of lithium-rich cathodes. *Nat. Commun.* **8**, 2219–2230 (2017).

-
106. Gent, W. E., Lim, K., Liang, Y., Li, Q., Barnes, T., Ahn, S., Stone, K. H., McIntire, M., Hong, J., Song, J. H., Li, Y., Mehta, A., Ermon, S., Tyliczszak, T., Kilcoyne, D., Vine, D., Park, J.-H., Doo, S.-K., Toney, M.F., Yang, W., Prendergast, D., Chueh, W. Coupling between oxygen redox and cation migration explains unusual electrochemistry in lithium-rich layered oxides. *Nat. Commun.* **8**, 2091–2102 (2017).
 107. Gallagher, K. G., Croy, J. R., Balasubramanian, M., Bettge, M., Abraham, D. P., Burrell, A. K. & Thackeray, M. M. Correlating hysteresis and voltage fade in lithium- and manganese-rich layered transition-metal oxide electrodes. *Electrochem. commun.* **33**, 96–98 (2013).
 108. Mohanty, D., Li, J., Abraham, D. P., Huq, A., Payzant, E. A., Wood, D. L. & Daniel, C. Unraveling the voltage-fade mechanism in high-energy-density lithium-ion batteries: Origin of the tetrahedral cations for spinel conversion. *Chem. Mater.* **26**, 6272–6280 (2014).
 109. Ariyoshi, K., Inoue, T. & Yamada, Y. Quantitative Analysis of Large Voltage Hysteresis of Lithium Excess Materials by Backstitch Charge and Discharge Method. *J. Electrochem. Soc.* **165**, A2675–A2681 (2018).
 110. Friedrich, F., Zünd, T., Hoefling, A., Tübke, J. & Gasteiger, H. A. Classification of Heat Evolution Terms in Li-ion Batteries regarding the OCV Hysteresis in a Li- and Mn-Rich NCM Cathode Material in Comparison to NCA. *Submitted*
 111. Kondrakov, A. O., Geßwein, H., Galdina, K., de Biasi, L., Meded, V., Filatova, E. O., Schumacher, G., Wenzel, W., Hartmann, P., Brezesinski, T. & Janek, J. Charge Transfer-Induced Lattice Collapse in Ni-Rich NCM Cathode Materials during Delithiation. *J. Phys. Chem. C* **121**, 24381–24388 (2017).
 112. Ryu, H. H., Park, K. J., Yoon, C. S. & Sun, Y. K. Capacity fading of Ni-rich $\text{Li}[\text{Ni}_x\text{Co}_y\text{Mn}_{1-x-y}]\text{O}_2$ ($0.6 \leq x \leq 0.95$) Cathodes for High-Energy-Density Lithium-Ion Batteries: Bulk or Surface Degradation? *Chem. Mater.* **30**, 1155–1163 (2018).
 113. Coelho, A. Coelho Software. (2016).
 114. Murray, C. A., Potter, J., Day, S. J., Baker, A. R., Thompson, S. P., Kelly, J., Morris, C. G., Yang, S. & Tang, C. C. New synchrotron powder diffraction facility for long-duration experiments. *J. Appl. Crystallogr.* **50**, 172–183 (2017).
 115. Solchenbach, S., Pritzl, D., Kong, E. J. Y., Landesfeind, J. & Gasteiger, H. A. A Gold Micro-Reference Electrode for Impedance and Potential Measurements in Lithium Ion Batteries. *J. Electrochem. Soc.* **163**, A2265–A2272 (2016).
 116. Morasch, R., Suthar, B. & Gasteiger, H. A. Simple Way of Making Free-Standing Battery Electrodes and their Use in Enabling Half-Cell Impedance Measurements via μ -Reference Electrode. *J. Electrochem. Soc.* **167**, 100540–100547 (2020).
 117. Landesfeind, J., Pritzl, D. & Gasteiger, H. A. An Analysis Protocol for Three-Electrode Li-Ion Battery Impedance Spectra: Part I. Analysis of a High-Voltage Positive Electrode. *J. Electrochem. Soc.* **164**, A1773–A1783 (2017).
 118. Schuster, E., Ziebert, C., Melcher, A., Rohde, M. & Seifert, H. J. Thermal behavior and electrochemical heat generation in a commercial 40 Ah lithium

- ion pouch cell. *J. Power Sources* **286**, 580–589 (2015).
119. Krause, L. J., Jensen, L. D. & Dahn, J. R. Measurement of Parasitic Reactions in Li Ion Cells by Electrochemical Calorimetry. *J. Electrochem. Soc.* **159**, A937–A943 (2012).
120. Housel, L. M., Li, W., Quilty, C. D., Vila, M. N., Wang, L., Tang, C. R., Bock, D. C., Wu, Q., Tong, X., Head, A. R., Takeuchi, K. J., Marschilok, A. C. & Takeuchi, E. S. Insights into Reactivity of Silicon Negative Electrodes: Analysis Using Isothermal Microcalorimetry. *ACS Appl. Mater. Interfaces* **11**, 37567–37577 (2019).
121. Assat, G., Glazier, S. L., Delacourt, C. & Tarascon, J.-M. Probing the thermal effects of voltage hysteresis in anionic redox-based lithium-rich cathodes using isothermal calorimetry. *Nat. Energy* **4**, 647–656 (2019).
122. Kunz, A., Berg, C., Friedrich, F., Gasteiger, H. A. & Jossen, A. Time-resolved Electrochemical Heat Flow Calorimetry for the Analysis of Highly Dynamic Processes in Li-Ion Batteries. *Manuscript in Preparation*.
123. Downie, L. E. PhD thesis - The application of isothermal microcalorimetry to the study of parasitic reactions in lithium ion batteries. pp. 56 ff. (2015).
124. TA Instruments. *TAM Basic Theory and Applications Training*. (2015).
125. Sarge, S. M., Höhne, G. W. H. & Hemminger, W. *Calorimetry - Fundamentals, Instrumentation and Applications*. pp. 59 ff. (2014).
126. Liebmann, T., Heubner, C., Schneider, M. & Michaelis, A. Investigations on the reversible heat generation rates of blended Li-insertion electrodes. *J. Solid State Electrochem.* **23**, 245–250 (2019).
127. Kai, K., Kobayashi, Y., Miyashiro, H., Oyama, G., Nishimura, S.-I., Okubo, M. & Yamada, A. Particle-size effects on the entropy behavior of a Li_xFePO_4 electrode. *ChemPhysChem* **15**, 2156–2161 (2014).
128. Song, M., Hu, Y., Choe, S.-Y. & Garrick, T. R. Analysis of the Heat Generation Rate of Lithium-Ion Battery Using an Electrochemical Thermal Model. *J. Electrochem. Soc.* **167**, 120503–120514 (2020).
129. DeBethune, A. J., Licht, T. S. & Swendeman, N. The Temperature Coefficients of Electrode Potentials. *J. Electrochem. Soc.* **106**, 616–625 (1959).
130. Valdes, J. L. & Miller, B. Contribution of Thermodiffusion to the Electrochemical Response of Thermally Modulated Rotating Disk Electrodes. *J. Phys. Chem.* **92**, 4483–4490 (1988).
131. Swiderska-Mocek, A., Rudnicka, E. & Lewandowski, A. Temperature coefficients of Li-ion battery single electrode potentials and related entropy changes - revisited. *Phys. Chem. Chem. Phys.* **21**, 2115–2120 (2019).
132. Friedrich, F., Pieper, S. & Gasteiger, H. A. Entropy Measurements of Li-Ion Battery Cells with Li- and Mn-Rich Layered Transition Metal Oxides via Linear Temperature Variation. *J. Electrochem. Soc.* **168**, 120502 (2021).
133. Kim, M. H., Shin, H. S., Shin, D. & Sun, Y. K. Synthesis and electrochemical properties of $\text{Li}[\text{Ni}_{0.8}\text{Co}_{0.1}\text{Mn}_{0.1}]\text{O}_2$ and $\text{Li}[\text{Ni}_{0.8}\text{Co}_{0.2}]\text{O}_2$ via co-precipitation. *J. Power Sources* **159**, 1328–1333 (2006).

-
134. Ohzuku, T., Ueda, A. & Nagayama, M. Electrochemistry and Structural Chemistry of LiNiO_2 (R-3m) for 4 Volt Secondary Lithium Cells. *J. Electrochem. Soc.* **140**, 1862–1870 (1993).
 135. Li, H., Zhang, N., Li, J. & Dahn, J. R. Updating the Structure and Electrochemistry of Li_xNiO_2 for $0 \leq x \leq 1$. *J. Electrochem. Soc.* **165**, A2985–A2993 (2018).
 136. House, R. A., Maitra, U., Pérez-Osorio, M. A., Lozano, J. G., Jin, L., Somerville, J. W., Duda, L. C., Nag, A., Walters, A., Zhou, K.-J., Roberts, M. R. & Bruce, P. G. Superstructure control of first-cycle voltage hysteresis in oxygen-redox cathodes. *Nature* **577**, 502–508 (2020).
 137. Singer, A., Zhang, M., Hy, S., Cela, D., Fang, C., Wynn, T. A., Qiu, B., Xia, Y., Liu, Z., Ulvestad, A., Hua, N., Wingert, J., Liu, H., Sprung, M., Zozulya, A.V., Maxey, E., Harder, R., Meng, Y.S., Shpyrko, O.G. Nucleation of dislocations and their dynamics in layered oxide cathode materials during battery charging. *Nat. Energy* **3**, 641–647 (2018).
 138. Sun, H. H., Ryu, H. H., Kim, U. H., Weeks, J. A., Heller, A., Sun, Y. K. & Mullins, C. B. Beyond Doping and Coating: Prospective Strategies for Stable High-Capacity Layered Ni-Rich Cathodes. *ACS Energy Lett.* **5**, 1136–1146 (2020).
 139. Friedrich, F., Strehle, B., Freiberg, A. T. S., Kleiner, K., Day, S. J., Erk, C., Piana, M. & Gasteiger, H. A. Capacity fading mechanisms of NCM-811 cathodes in lithium-ion batteries studied by X-ray diffraction and other diagnostics. *J. Electrochem. Soc.* **166**, A3760–A3774 (2019).
 140. Strehle, B., Friedrich, F. & Gasteiger, H. A. A Comparative Study of Structural Changes during Long-Term Cycling of NCM-811 at Ambient and Elevated Temperatures. *J. Electrochem. Soc.* **168**, 050512–050526 (2021).
 141. Ohzuku, T., Nagayama, M., Tsuji, K. & Ariyoshi, K. High-capacity lithium insertion materials of lithium nickel manganese oxides for advanced lithium-ion batteries: toward rechargeable capacity more than 300 mAh/g. *J. Mater. Chem.* **21**, 10179 (2011).
 142. Twu, N., Metzger, M., Balasubramanian, M., Marino, C., Li, X., Chen, H., Gasteiger, H. & Ceder, G. Understanding the Origins of Higher Capacities at Faster Rates in Lithium-Excess $\text{Li}_x\text{Ni}_{2-4x/3}\text{Sb}_{x/3}\text{O}_2$. *Chem. Mater.* **29**, 2584–2593 (2017).

List of figures

- Figure 1.1:** Schematic illustration of the main components and the operating principle of a Li-ion battery taken from Hausbrand et al.²². Reprinted under a Creative Commons BY-NC-ND 3.0 license..... 4
- Figure 1.2:** Classification of the most relevant cathode active materials (CAMs) according to their practical energy density^{9,21,52-55} (in Wh/kg referenced to the CAM mass) and the cathode cost^{17,18,47-49} (in €/kWh referenced to the CAM energy density). The calculation is based on the values shown in Table 1.1. For the cathode cost, only the raw material prices were considered as described in the text.10
- Figure 1.3:** Schematic illustration of the most important aging mechanisms in a Li-ion battery with a graphite anode and an NCM cathode. Text in colored boxes describes the respective process. The yellow arrows indicate the effect on the cell performance. The right hand side shows the three major degradation phenomena of the cathode active material in more detail. For further explanations, see text...14
- Figure 1.4:** Examples of 0.33 LMR-NCM (0.33 Li₂MnO₃ · 0.67 LiMO₂; M = Ni, Co, Mn) material properties that show a path dependent behavior between charge and discharge direction as a function of state-of-charge (=capacity, given in mAh/g_{CAM}). Charge direction indicated by black triangles, discharge direction by white circles. The resulting hysteresis is highlighted in blue. All data shown here originate from LMR-NCM/Li cells after complete activation, cycled at a C-rate of C/10 at 25°C between 2.0 – 4.7 V vs. Li⁺/Li: (a) open-circuit voltage (OCV, 4th cycle); (b) unit cell volume obtained from in-situ X-ray diffraction in accordance with data reported by Strehle et al.¹⁰⁰ (2nd cycle); (c) charge-transfer resistance as published¹¹⁰ and presented in the Results section 3.2.2 (4th cycle). For experimental details, see section 2.19
- Figure 2.1:** Schematic drawing of the NCM-811/graphite pouch cell used for XPD experiments with NCM-811 working electrode (WE, 30x30 mm², contacted by an aluminum tab), a pre-lithiated graphite as counter electrode (CE, 33x33 mm², contacted by a nickel tab), and two glass-fiber separators in between (GF, 36x36 mm²). The potential of the cathode was controlled versus a lithium reference electrode (RE).22
- Figure 2.2:** Comparison of measurement results from the calorimeters B, C, and E. The mass-normalized heat flow is shown as a function of time for coin cells with LMR-NCM cathodes discharged at C/10 and 25°C. The constant-current phases (CC) with heat generation from the cell are highlighted in yellow, the subsequent open-circuit phases (OCV) in gray. The baseline determined prior to the CC-phase is indicated by the dashed orange line.32
- Figure 2.3:** Pictures of the micro-calorimeter assembly used for measurements in section 3.2.3, with the whole assembly in (a), the custom-made cell holder in (b),

and the opened cell holder in (c). A detailed discussion of the setup will be published by Kunz and Berg et al.¹²² 35

Figure 4.1: (a) Illustration of the CAM degradation mechanism of oxygen release and surface reconstruction according to Figure 1.3, including the two effects on the cycling performance observed in our studies.^{139,140} (b) SEM-Image with an illustration of the reconstructed, O-deficient surface layer (sketched in blue), which is suggested to form on the surface of the NCM-811 primary particles upon prolonged cycling. Figure adapted from Friedrich et al.¹³⁹160

Acknowledgements

First of all, I would like to express my deep gratitude to **Prof. Hubert A. Gasteiger** for giving me the opportunity to conduct my PhD thesis at his Chair for Technical Electrochemistry at TUM. You are an exceptional supervisor who inspires, motivates and empowers us to become diligent and passionate researchers. I appreciate all the time you spend with us (even at late night) to discuss our results and support us in our professional development. You are a source of knowledge and wisdom when it comes to electrochemistry. Your door is always open and you have created a working atmosphere of respect and trust. I deeply admire your never-ending inquisitiveness and thank you for giving me the chance to develop and pursue my own ideas. You have made my PhD time an enriching journey on both personal and professional level, for which I will always be grateful!

I would like to thank **Veronika Pichler** for being the organizational talent you are. Without you, none of our scientific work would be possible because you keep the chair running and support us with all the administrative work in the background.

I would also like to express my gratitude to **Benjamin Strehle**, who supervised my Master's thesis together with **Karin Kleiner**. They gave me the opportunity to get into the field of lithium-ion battery research and helped me open the door for my PhD thesis. I want to thank Benjamin for his support during my thesis and far beyond that. Thank you for all I could learn from you and for always having an open ear for me.

Many thanks also go to my former students **Tobias Käter**, **Susanne Pieper**, **See Tow Wei Hao** and **Simon Qian** for their curiosity, motivation and the good teamwork.

I would like to thank all current and former TEC members for their support, the fruitful discussions and the pleasant working atmosphere. Special thanks go to **Benjamin Strehle**, **Tanja Zünd**, **Anna Freiberg**, **Paulette Loichet**, **Mohammad Fathi Tovini**, **Simon Qian**, and **Clara Berg** for their active support and great teamwork in our cooperation projects. I am thankful to **Alexander Hoefling** from

HIU and **Alexander Kunz** from EES for their support with the calorimetry. Moreover, I would like to thank the beamline scientists at Diamond Light Source for the long-duration experiments and their hospitality during our visits.

I am especially grateful to my “**Lunch Buddies**” for being much more than colleagues – you are real friends! You were always there when I needed professional or personal support. I had the time of my life with you! I would also like to thank **Robert Morasch** for the countless discussions on the most varied topics under the sun and his support with any impedance question.

I would like to acknowledge the financial support and scientific exchange provided by BASF SE through its “Network on Electrochemistry and Batteries”. Many thanks go to my former and current colleagues in the BASF project group at TUM: **Sophie Solchenbach, Daniel Pritzl, Johannes Sicklinger, Benjamin Strehle, Stefan Oswald, Louis Hartmann** and **Jiyoung Yoon**. Thank you for the fruitful discussions in the BASF meetings.

Lastly, I want to deeply thank my parents **Gitti** and **Hubert**, my sister **Vroni**, my best friend **Andi** and my husband **Tim** for their invaluable support. You make me whole.

Scientific Contributions

Peer-reviewed publications

- **F. Friedrich**[≠], T. Zünd[≠], A. Hoefling, J. Tübke, H.A. Gasteiger: „Classification of Heat Evolution Terms in Li-ion Batteries regarding the OCV Hysteresis in a Li- and Mn-Rich NCM Cathode Material in Comparison to a Regular NCA”, J. Electrochem. Soc., 169, 040547 (2022).
<https://iopscience.iop.org/article/10.1149/1945-7111/ac6541/pdf>
- **F. Friedrich**, S. Pieper, H.A. Gasteiger: „Entropy Measurements of Cells with Li- and Mn-rich Layered Oxides via Linear Temperature Variation”, J. Electrochem. Soc., 168, 120502 (2021).
<https://iopscience.iop.org/article/10.1149/1945-7111/ac3938/pdf>
- B. Strehle[≠], **F. Friedrich**[≠], H.A. Gasteiger: “A Comparative Study of Structural Changes during Long-Term Cycling of NCM-811 at Ambient and Elevated Temperatures”, J. Electrochem. Soc., 168, 050512 (2021).
<https://iopscience.iop.org/article/10.1149/1945-7111/abf780/pdf>
- P.A. Loichet Torres, H.A. El-Sayed, J.N. Schwämmlein, **F. Friedrich**, H.A. Gasteiger: “Hydrogen Gas Promoted Self-Limiting Copper Monolayer Deposition on Platinum”, J. Electrochem. Soc., 168, 052508 (2021).
<https://iopscience.iop.org/article/10.1149/1945-7111/abfe79/pdf>
- **F. Friedrich**[≠], B. Strehle[≠], A.T.S. Freiberg, K. Kleiner, S.J. Day, C. Erk, M. Piana, H.A. Gasteiger: “Editor’s Choice-Capacity Fading Mechanisms of NCM-811 Cathodes in Lithium-Ion Batteries Studied by X-Ray Diffraction and Other Diagnostics”, J. Electrochem. Soc., 166, A3760 (2019).
<https://iopscience.iop.org/article/10.1149/2.0821915jes/pdf>
- B. Strehle, J. Yoon, **F. Friedrich**, H.A. Gasteiger: “Specific Surface Area and Bulk Strain – Important Material Metrics Determining the Electrochemical Performance of Li- and Mn-Rich Layered Oxides”, J. Electrochem. Soc., 169, 060521 (2022).
<https://iopscience.iop.org/article/10.1149/1945-7111/ac766c/pdf>

Submitted manuscripts

- A. Kunz[≠], C. Berg[≠], **F. Friedrich**, H.A. Gasteiger, A. Jossen: “Time-Resolved Electrochemical Heat Flow Calorimetry for the Analysis of Highly Dynamic Processes in Li-Ion Batteries”, submitted to J. Electrochem. Soc. in June 2022.

Manuscripts to be submitted

- **F. Friedrich**, A. Kunz, A. Jossen, H.A. Gasteiger: „Heat evolution during the First Activation Cycle in Li-Ion Batteries with Li- and Mn-rich Layered Oxides Measured by Isothermal Micro-calorimetry”.
- S. Qian[‡], A.T.S. Freiberg[‡], **F. Friedrich**, H.A. Gasteiger: “Structural and Electrochemical Properties of ‘Disordered, Spinel-like’ Structures Derived from NCM Materials by Chemical Delithiation”.

Oral presentations

- **F. Friedrich**, B. Strehle, H.A. Gasteiger: “A Comparative Study of Structural Changes during Long-Term Cycling of NCM-811 at Ambient and Elevated Temperatures”, Pacific Rim Meeting Electrochemical Society, online, 2020.
- **F. Friedrich**, A. Ogrodnik, S. Pieper, H.A. Gasteiger: “Entropy in Li- and Mn-rich Layered Oxides Measured via Linear Temperature Variation”, Pacific Rim Meeting Electrochemical Society, online, 2020.

Poster presentations

- **F. Friedrich**, B. Strehle, K. Kleiner, H.A. Gasteiger: “Investigation of Structural Changes over Long-Term Cycling of Ni-rich Layered Oxides Used as Cathode Materials in LIBs”, Electrochemistry Conference Gesellschaft Deutscher Chemiker, Ulm, 2018.
- **F. Friedrich**, B. Strehle, K. Kleiner, A. Baker, S. Day, C. Tang, M. Piana, H. Gasteiger: “Correlation of structural changes and capacity fading of Ni-rich layered oxides”, 649. WE-Heraeus-Seminar, Bad Honnef, 2017.

[‡] = These authors contribute equally.

Curriculum Vitae



PERSONAL DETAILS

📍 14.08.1993
in Bad Aibling
🏠 Hauptstraße 11
85386 Eching
☎ +49 157 36985905
franziska.friedrich@outlook.de

EXTRACURRICULAR ACTIVITIES

Scientists for Future Munich

- Public talks and podcast about electromobility

TUM Entdeckerinnen

- MINT project day for female students
- Workshop leader

Electrochemical Society – Student Chapter Munich

- Organisation of talks and panel discussions

HOBBIES

- Mountain biking
- Bike travelling
- Taking my horse and dog for a walk
- Yoga

WORK EXPERIENCE

since
10/2021

Specialist Battery Cell Technology

BMW Group

- Research and Development of All-Solid-State-Batteries
- Project leader for cooperation with universities (TUM, WWU Münster) and start-ups

03/2018
- 09/2021

PhD Thesis

Chair of Technical Electrochemistry (Prof. H. A. Gasteiger),
Technical University of Munich

- Topic: Cathode material research for Lithium-ion Batteries
- Focus: Aging mechanisms and heat generation during cycling
- Cooperation projects with BASF, Helmholtz Institut Ulm, Institute for Electrical Energy Storage Technology TUM

01/2016-
03/2017

Research Assistant

Bavarian Center for Applied Energy Research e.V., Garching

- Topic: Vanadium-Redox-Flow Battery
- Focus: Modification of the electrode surfaces
- Methods: Electrochemical experiments at the test station

EDUCATION

04/2016-
01/2018

Master Chemistry (M. Sc., grade 1.0)

Ludwig-Maximilians-University of Munich

- Master thesis at TUM (Prof. H. A. Gasteiger)
Topic: Long-term aging study on Ni-rich cathodes used in Lithium-ion Batteries
- Major subjects: Physical chemistry, inorganic chemistry, minor subject: Material sciences

09/2012-
03/2016

Bachelor Chemistry and Biochemistry (B. Sc., grade 1.45)

Ludwig-Maximilians-University of Munich

Major subjects: Inorganic and organic chemistry

06/2012

Abitur (grade 1.0)

Gymnasium Bad Aibling

SKILLS

LANGUAGES

German ●●●●●
English ●●●●○
Russian ●○○○○

SOFTWARE

MS Office ●●●●●
Origin ●●●●○
Matlab ●●○○○
EC-Lab ●●●●●